1.0 | 4.5 | 2.8 | 2.5
1.1 | 5.0 5.6 6.3 | 3.2 3.6 4.0 | 2.2 2.0
1.8
1.25 | 1.4 | 1.6

MICROCOPY RESOLUTION TEST CHART
NATIONAL BUREAU OF STANDARDS-1963-A

AGARD-CP-351

AD A139749

AGARD CONFERENCE PROCEEDINGS No. 351

Viscous Effects in Turbomachines

DTIC
ELECTE
FEB 16 1984
S D
B

FILE COPY

84 03 16 070

COMPONENT PART NOTICE

THIS PAPER IS A COMPONENT PART OF THE FOLLOWING COMPILATION REPORT:

(TITLE): Proceedings of the Conference on Viscous Effects in Turbomachines

Held at Copenhagen, Denmark on 1-3 June 1983,

(SOURCE): Advisory Group for Aerospace Research and Development Neuilly-sur-Seine

(France)

To ORDER THE COMPLETE COMPILATION REPORT USE __AD-A139 749__ .

THE COMPONENT PART IS PROVIDED HERE TO ALLOW USERS ACCESS TO INDIVIDUALLY AUTHORED SECTIONS OF PROCEEDINGS, ANNALS, SYMPOSIA, ETC. HOWEVER, THE COMPONENT SHOULD BE CONSIDERED WITHIN THE CONTEXT OF THE OVERALL COMPILATION REPORT AND NOT AS A STAND-ALONE TECHNICAL REPORT.

THE FOLLOWING COMPONENT PART NUMBERS COMPRISE THE COMPILATION REPORT:

AD#: P003 088 **TITLE:** Flow Measurements in the Stator Row of a Single-Stage Transonic Axial-Flow Compressor with Controlled Diffusion Stator Blades.

P003 089   Compressor Rotor Aerodynamics.

P003 090   Experimental Verification of an End Wall Boundary Layer Prediction Method.

DTIC
ELECTE
APR 1 2 1984
S   D
A

Accession For	
NTIS GRA&I	☑
DTIC TAB	☐
Unannounced	☐
Justification	
By	
Distribution/	
Availability Codes	
Dist	Avail and/or Special
A-1	

AGARD-CP-351

NORTH ATLANTIC TREATY ORGANIZATION

ADVISORY GROUP FOR AEROSPACE RESEARCH AND DEVELOPMENT

(ORGANISATION DU TRAITE DE L'ATLANTIQUE NORD)

AGARD Conference Proceedings No.351

VISCOUS EFFECTS IN TURBOMACHINES

DTIC
ELECTE
FEB 16 1984
S D
B

THE MISSION OF AGARD

The mission of AGARD is to bring together the leading personalities of the NATO nations in the fields of science and technology relating to aerospace for the following purposes:

— Exchanging of scientific and technical information;

— Continuously stimulating advances in the aerospace sciences relevant to strengthening the common defence posture;

— Improving the co-operation among member nations in aerospace research and development;

— Providing scientific and technical advice and assistance to the North Atlantic Military Committee in the field of aerospace research and development;

— Rendering scientific and technical assistance, as requested, to other NATO bodies and to member nations in connection with research and development problems in the aerospace field;

— Providing assistance to member nations for the purpose of increasing their scientific and technical potential;

— Recommending effective ways for the member nations to use their research and development capabilities for the common benefit of the NATO community.

The highest authority within AGARD is the National Delegates Board consisting of officially appointed senior representatives from each member nation. The mission of AGARD is carried out through the Panels which are composed of experts appointed by the National Delegates, the Consultant and Exchange Programme and the Aerospace Applications Studies Programme. The results of AGARD work are reported to the member nations and the NATO Authorities through the AGARD series of publications of which this is one.

Participation in AGARD activities is by invitation only and is normally limited to citizens of the NATO nations.

PROPULSION AND ENERGETICS PANEL

CHAIRMAN: Professor Ch. Hirsch
Vrije Universiteit Brussel
Dienst Stromingsmechanica
Pleinlaan 2
1050 Brussel, Belgium

DEPUTY CHAIRMAN: Professor Ir. H.Wittenberg
Delft University of Technology
Dept. of Aerospace Engineering
Kluyverweg 1
2629 HS Delft, Netherlands

PROGRAMME COMMITTEE

Dr A.J.Wennerstrom (Chairman)
Air Force Wright Aeronautical Labs/POTX
Wright-Patterson AFB, Ohio 45433, US

Dr J.Dunham
Royal Aircraft Establishment
Pyestock
Farnborough, Hants GU14 OLS, UK

Dr D.K.Hennecke
Motoren und Turbinen Union GmbH
Abt EW
Dachauerstrasse 665
8000 München 50, Germany

Professor Dr B.Qvale
Laboratoriet for Energiteknik
Polytechniske Laereanstalt
Bygning 403B, Lundtoftvej 100
2800 Lyngby, Denmark

Professor D.Dini
Università degli studi
Istituto di Macchine
Via Diotisalvi 3
56100 Pisa, Italy

Mr J.Fabri
ONERA
29 Avenue de la Division Leclerc
92320 Châtillon sous Bagneux, France

Professor Ch. Hirsch
Vrije Universiteit Brussel
Dienst Stromingsmechanica
Pleinlaan 2
1050 Brussel, Belgium

HOST NATION COORDINATOR

Captain N.Frøsig
Danish Defence Research Establishment
Ved Idraetsparken 4
2100 Copenhagen K, Denmark

HOST REPRESENTATIVE

Professor Dr B.Qvale

PANEL EXECUTIVE

Dr-Ing. E.Riester
AGARD-NATO
7 rue Ancelle
92200 Neuilly sur Seine
France

ACKNOWLEDGEMENT

CONTENTS

TECHNICAL EVALUATION REPORT

by

Leroy H.Smith, Jr

1. TECHNICAL EVALUATION SUMMARY

Twenty-three papers related to viscous flow in turbomachines were presented and discussed at the meeting. Nearly half of these dealt with analysis of the flow over relatively simple isolated geometries, such as cascade blades with uniform inlet conditions, but Mach numbers from zero into the transonic range were employed, and two-dimensional flow separations were sometimes treated. All workers employed a boundary layer approach, and all were able to show good, or reasonably good, agreement with experiment.

Four of the papers involved detailed studies of cascade flows with non-uniform inlet conditions, spacially non-uniform (due to end walls) in three cases and temporally non-uniform (due to a moving upstream blade row) in the fourth case. In all cases the effects of these non-uniformities were dramatic. Adequate analytical treatments for these cases were not presented at this meeting, although it is believed that progress is being made elsewhere on so-called Navier-Stokes solvers that can be expected to be applicable.

The remainder of the papers dealt with multi-blade-row flows. Some of these included attempts at analysis using endwall boundary layer integral approaches, which appear to work reasonably well for the cases treated, but, in the opinion of this evaluator, much more work is needed before they can be used with confidence on untested designs.

Since capabilities for the treatment of isolated goemetries with uniform inflow are now reasonably satisfactory, it is recommended that researchers now focus more on multi-blade-row effects such as unsteady inflow, skewed annulus boundary layers and flow mixing. The employment of large low-speed multistage turbomachines for this research is recommended.

2. INTRODUCTION

For at least two reasons it was appropriate to hold a Specialists' Meeting on Viscous Effects in Turbomachines at this time.

First, gas turbine manufacturers have by now largely learned how to avoid or cope with most of the major development problems of earlier days — such as compressor stall — and currently there is great interest in efficiency improvement, which can result from a more accurate treatment of viscous flows.

Second, computational fluid dynamics has received much attention in recent years in many different areas, so a comparison of progress among workers is appropriate. This was foreseen at the 1977 Specialists' Meeting on Secondary Flows in Turbomachines, where it was recommended that the same subject be considered at a future meeting when new theoretical and experimental results are again available.

This general subject is an important one, and future meetings at roughly five year intervals can be anticipated.

3. CONTENT OF THE MEETING

In this section the twenty-three papers presented have been organised into six groups according to subject matter, although the grouping is somewhat arbitrary. The number in parentheses after each author's name is his paper number.

Group 1: Treatment of External Flow.

Le Balleur (1) presented calculations o   e flow around aircraft wings; these showed good agreement with experiment even when the flow was transonic and the wing geometry was rather complex. The basic approach used for the calculations involved an inviscid free-stream analysis coupled with a boundary-layer integral analysis, the boundary layer displacement thickness being represented by fictitious blowing and suction. The Prandtl boundary layer approach to the treatment of viscous flow problems was thus verified for external flows, which is a necessary condition for its

application to internal flows. This is fortunate because, as we shall see, all of the analysts who presented viscous flow analyses at this meeting employed a boundary layer approach. Lambropoulos, Ktenidis and Papailiou (18) showed that the flow around a spinner is best treated in the relative frame of reference because, in that frame, boundary layer skew is found to be minimal.

Group 2: Treatment of Cascade and Passage Flows

Calvert (2) showed that the boundary layer approach also works well for some internal flows of interest, namely transonic compressor cascades. Other workers generally supported this approach. Meauze and Delery (7) gave solutions for channel flows with shocks, and Fourmaux (8) showed it was possible to find a displacement streamline that matched input (from test) static pressures using an inviscid time-marching free stream solution. Werle (9) discussed more specifically how the boundary layer can be treated when a two-dimensional separation is involved. Psarudakis (12) showed us that good results for low Mach number two-dimensional cascades could be obtained by coupling a boundary layer method with a Martensen-type calculation, and Janssens and Hirsch (3) got good results for highly loaded subsonic two-dimensional cascades with separation present using a finite element free stream analysis iteratively with a boundary layer analysis. Janssens and Hirsch (3) also pointed out the need to include curvature and rotation effects in turbulent stresses when appropriate as did Aupoix and Cousteix (14), who also dealt with certain three-dimensional features of boundary layer behaviour. Lewis and Porthouse (13) presents a novel method for treating airfoils in stall in which shed vortices are convected away by the total flow field and are dispersed statistically. Although this method (13) provides useful insight into stall phenomena, the long computational time involved limits its usefulness as a design tool.

Group 3: Unsteady Boundary Layers

Hodson (10) found that the wakes from an upstream blade row can cause a 50% loss increase at the mean diameter of a high aspect ratio, lightly loaded turbine rotor, and his beautifully executed measurements showed that periodic movements of the suction surface transition point are responsible for this. This important finding deserves further attention.

Group 4: Three-Dimensional Flow in Cascades

Measurements by Moore (5) demonstrated how dominant are secondary flows in a low aspect ratio turbine cascade, and Gregory-Smith and Graves (17), with a somewhat higher aspect ratio turbine cascade, also found secondary flows to be quite significant in loss generation. Tests by Boletis and Sieverding (16) on a turbine nozzle annular cascade showed that, with colateral inlet annulus boundary layers, endwall losses were confined to the endwall regions, i.e. a free stream region with low losses existed near mid span. However, when the inlet hub boundary layer was skewed, as in a multistage turbine, the hub secondary flow was enhanced to the extent that it penetrated the midspan region with high loss fluid. Other researchers should take note of this.

Group 5: Multi-Blade-Row Analyses and Tests

All of the work in this category dealt with axial-flow compressors. de Ruyck and Hirsch (19) have further developed their defect force models and are showing generally good agreement with experience, as are Leboeuf and Naviere (20) with their secondary flow approach. The effects of casing roughness, porosity, and clearance were studied by Elrod and Bettner (25), who found that roughness adversely affects stall margin but porosity (simulated by perforated plates) enhances it. Fottner and Lichtfuss (4) gave laser measurements inside the first rotor of a three-stage transonic fan, the design of which had been based on cascade analysis and experiments. Sandel (15) described a multistage through flow analysis that is under development and which includes viscous effects.

Group 6: Multi-Blade-Row Experimental Data Sets

Again, only axial-flow compressor results were presented at this meeting. Lakshminarayana, Govindan and Murthy (21), Ball, Reid and Schmidt (22), Dunker (23), and Dring, Joslyn and Wagner (24) presented data sets (two at high speed and two at low speed) that provide insights and potential verification cases for future analyses.

4. CONCLUSIONS

(1) The approach employed by all authors for the calculation of viscous flows embodied the Prandtl concept of an inviscid free stream plus viscous boundary layers. The authors succeeded in showing that their analyses and their data could be brought into good agreement with this approach for the relatively simple geometries (airfoils and cascades) for which analysis and experiment were compared in detail.

(2) Wakes from an upstream stator were found by Hodson (10) to significantly affect the development of a turbine rotor blade suction surface boundary layer. Over the majority of the rotor suction surface, the boundary layer was found to oscillate between characteristic laminar and turbulent states in sympathy with the passage of the stator wakes. As a result of this oscillating change of state, and because the free stream velocity is in anti-phase with the fluctuations of free stream turbulence, the levels of velocity fluctuations within the boundary layer are much greater

than those found in conventional laminar or turbulent unsteady boundary layers. This caused the profile loss to be 50% greater than was measured in a two-dimensional cascade of identical blade profiles with uniform inflow. This is an important finding and other researchers should consider whether it affects their work.

(3) The secondary flows in high deflection turbine bladings were shown once again to be highly complex, and no good way to analyze them was presented. As had been concluded at the 49th Specialists' Meeting on Secondary Flows in Turbomachines in 1977, the classical Hawthorne approach was found (17) to be inadequate for these cases, although one discusser felt that that approach might give reasonable results for the pitch-average transverse velocity distribution as it often does on lower deflection compressor cascades. Skewing of the inlet hub boundary layer was found (16) to significantly affect the secondary flow in an annular turbine nozzle cascade.

(4) Multi-blade-row endwall boundary layer integral analyses (19), (20), (25) have progressed to the point where reasonable agreement with experiment can be expected in most cases, although flow details are often not correctly deduced. This is, presumably, all that can be expected for some time to come because such complex features as steps and gaps, clearances, leakages, unsteady effects, and local flow separation are prevalent.

5. **EVALUATION AND RECOMMENDATIONS**

The meeting well served its purpose of providing a forum for disseminating information on progress by research workers in this very important field, and there was a significant amount of discussion among the authors and other specialists present. As is usually the case, designers and manufacturers had relatively little to say, but we were listening and will incorporate many of the results into our thinking and our work.

This evaluator recommends that the work by Hodson (10) be given special attention, and that it be expanded at Cambridge and elsewhere. Hodson showed that the proximity of an adjacent bladerow can be very important to the development of blade boundary layers and therefore blade losses. This work brings into question whether boundary layer methods that ignore free stream unsteadiness, (or at best respond only to isotropic turbulence) are adequate for use in optimizing blade designs in multi-blade-row turbomachines. The type of research facility employed by Hodson, i.e. a large scale low-speed machine running at Reynolds numbers typical of those encountered in aircraft engine low pressure turbines, is ideally suited for this kind of research. Additional work should include experiments with more two- or three-stage configurations.

An important subject that was not discussed at the meeting is the development of so-called Navier-Stokes computer codes, or three-dimensional solvers that contain laminar and turbulent shear stress models that are active at the flow boundaries and in wakes. Work on such codes is quietly going on at several places, and, as computer capacity and availability increase, we can expect to see these codes in general use for turbomachinery design in a few years.

PROGRES DANS LE CALCUL DE L'INTERACTION

FLUIDE PARFAIT - FLUIDE VISQUEUX

J.C. LE BALLEUR

Office National d'Etudes et de Recherches Aérospatiales (ONERA)
29, Avenue de la Division Leclerc - 92320 Châtillon - FRANCE

RESUME

Les techniques numériques d'interaction fluide parfait - fluide visqueux sont analysées d'une manière très globale, précisant les grands objectifs de développement, leurs possibilités et leurs contraintes.

Se limitant ensuite aux méthodes intégrales couplées en Formulation Déficitaire, on présente quelques exemples-types de calcul d'écoulements décollés obtenus en aérodynamique externe, dans l'approximation potentielle du fluide-parfait.

On présente enfin des résultats nouveaux obtenus en aérodynamique interne par une méthode intégrale déficitaire couplée aux équations d'Euler, sur une configuration de canal transsonique bloqué, avec interaction onde de choc-couche limite turbulente, conduisant à un petit décollement. Le couplage est réalisé par la technique de relaxation mixte précédemment proposée, directe ou semi-inverse par zones, avec contrôle automatique local de la stabilité numérique.

PROGRESS IN COMPUTATION OF VISCOUS INVISCID INTERACTION

SUMMARY

The numerical techniques based on viscous-inviscid interaction are surveyed with a very global view, to get the main developments areas, the capacities and constraints.

Then restricting to the integral methods interacted with a Defect Formulation, typical examples are presented for the calculation of separated flows in external aérodynamics, using the approximation of a potential inviscid flow.

At last are presented new results achieved in internal aerodynamics, using a defect integral method interacted with the full Euler equations. The calculated flow is a choked transonic channel flow, with a turbulent shock wave-boundary layer interaction which generates a very small separation. The coupling is converged with the previously suggested zonal relaxation technique, Direct or Semi-inverse, including a local and automatic control of the numerical stability.

1. INTRODUCTION

La valorisation pratique des progrès obtenus ces dernières années dans les techniques numériques du fluide parfait, tant en aérodynamique externe qu'interne, requiert une attention croissante à la prise en compte de la viscosité, notamment pour les écoulements des régimes hors-adaptation.

Aux nombres de Reynolds élevés des applications, l'un des objectifs principaux consiste à déterminer des écoulements qui peuvent encore être assimilés à ceux d'un fluide parfait dans leur plus grande partie, mais dans lesquels les conditions aux limites de glissement (ou de Joukowski), devenues insuffisantes, doivent être remplacées par des conditions d'interaction avec le calcul des couches visqueuses. Ce phénomène de conditionnement total du fluide parfait par des couches visqueuses en interaction, éventuellement très minces, est la source de difficultés de calcul bien connues, le plus souvent multiples dans un même écoulement, telles que les bulbes de décollement de bord d'attaque, de bord de fuite, de charge-arrière d'intrados, de culot et de proche sillage, ainsi que les interactions couche limite-onde de choc.

Les techniques numériques les plus directes consistent à résoudre globalement des équations de Navier-Stokes moyennées (NS) complétées d'un modèle de turbulence sur l'ensemble du domaine fluide, en utilisant des méthodes instationnaires. Bien que très fructueuses [1, 2,4], ces techniques numériques globales ne s'appuient pas sur la physique des nombres de Reynolds élevés et des couches visqueuses minces. Elles sont de ce fait confrontées, dans le domaine de l'Aérodynamique, à des difficultés de coût numérique et de discrétisations fines des couches ou sous-couches visqueuses, en l'absence desquelles la qualité de l'approche devient illusoire.

Les techniques numériques d'interaction se différencient à priori seulement par la nature indirecte de la résolution du problème global NS précédent, et par l'incorporation d'une méthode numérique du type fluide parfait. Cette dernière assure le calcul de l'écoulement réel dans les régions à viscosité négligeable et comporte en dehors de celles-ci des modifications de conditions aux limites ou d'équations, de telle sorte que le calcul Pseudo-

Fluide-Parfait obtenu (Prédicteur) puisse être *effectivement conditionné* par un calcul
visqueux complémentaire (correcteur). Cette simple dichoto mie du problème global équivaut
à une simulation numérique composite sans hiérarchisation des influences du prédicteur
et du correcteur, souvent résolus sur des domaines de calcul superposés [3-4]. Prédicteur
et correcteur sont notamment assujettis à un couplage réciproque (couplage fort). Voisine
de la *physique des phénomènes, cette approche composite* est par nature plus apte qu'une
approche directe NS à la simulation précise ou économique des nombres de Reynolds élevés.
Elle est en contre-partie plus complexe et nécessite la maitrise simultanée de trois algo-
rithmes numériques différents, résolvant respectivement le prédicteur, le correcteur, et
le couplage.

Historiquement, cette complexité a d'abord conduit à associer largement l'approximation aux
techniques numériques d'interaction, notamment au niveau des équations visqueuses résolues
et du degré de couplage, les premiers objectifs ayant été ceux de calculs économiques, rela-
tivement empiriques, utilisable dans la pratique pour des applications déterminées. Le bilan
suscité par Monnerie, Quinn[5] lors d'un récent Symposium AGARD pour l'Aérodynamique externe
a cependant montré [6] que cet objectif primaire a déjà été largement dépassé. Les nombreux
résultats recueillis par exemple par Kline et Al. lors de la Conférence AFOSR-Stanford 1981
[7], ainsi que par Cebeci lors d'un Symposium très récent [8], confirment que les *progrès*
réalisés, tant au niveau de l'extrapolation des méthodes de couche limite couplées que
des algorithmes de couplage [3, 9], permettent d'incorporer le traitement automatique d'in-
teraction multiples au sein d'un même écoulement, décollements minces ou interaction couche
limite - onde de choc, en bidimensionnel.

Au stade actuel, l'objectif des techniques numériques d'interaction n'est plus équivalent
à la recherche d'une solution "approximative" au problème global NS, et la facilité offerte
pour introduire des approximations reste seulement l'une des options intéressantes. Il est
ainsi possible de rechercher des résolutions numériques visqueuses ayant des discrétisations
spatiales et des coûts minimaux, *tout en conservant un minimum d'universalité vis à vis des*
problèmes de décollement et d'interaction choc-couche limite. Cet objectif peut être atteint
par exemple en généralisant aux régimes turbulents décollés ou hors-équilibre les méthodes
intégrales issues des techniques de couches limites, une fois ces méthodes convenablement
couplées à un écoulement de fluide parfait [10].

Rien à priori n'exclut cependant plus, en s'appuyant sur les mêmes algorithmes numériques
d'interaction, d'envisager la construction de solveurs indirects pour des équations vis-
queuses moins restrictives, telles que les équations de Navier-Stokes parabolisées ou
complètes. Des démarches préliminaires de cette nature ont par exemple été données par
Dodge [11], Rubin, Khosla [12].

Une analyse complète des techniques numériques d'interaction étant ici hors de portée,
on se bornera d'abord à examiner brièvement les contraintes et les objectifs de dévelop-
pement. Des analyses moins restreintes sont accessibles par exemple dans les références
[3, 4, 9, 13, 14, 5, 8].Se limitant ensuite aux techniques numériques à discrétisation
minimale, obtenues au moyen de méthodes intégrales "Déficitaires" rigoureusement cou-
plées, ou examine la qualité très remarquable de la modélisation économique qu'elles
fournissent. Celle-ci est à priori meilleure que celle donnée par *des équations de Prandtl*
raccordée au fluide parfait,en raison d'une prise en compte approximative des gradients
de pression normaux. Il a en outre été établi [16, 17, 4, 15] que cette modélisation est
capable de traiter le décollement et l'interaction choc-couche limite des régimes trans- et
super-soniques, et notamment d'éliminer l'écueil dit de "couche limite supercritique",
observé dans le passé par Crocco, *Lees* [21] *en raison de l'inaptitude des équations de*
Prandtl raccordées à décrire la pénétration des ondes de choc de décollement au sein des
couches visqueuses.

Outre des exemples de résultats caractéristiques de l'Aérodynamique externe, où l'approxi-
mation potentielle du fluide *parfait a été* retenue, on présente les premiers résultats
obtenus en écoulement interne par couplage avec les équations d'Euler complètes, sur une
configuration d'interaction couche limite-onde de choc dans un canal transsonique.

2. OBJECTIFS ET CONTRAINTES DES TECHNIQUES NUMERIQUES D'INTERACTION

2.1. Différents objectifs et voies de développements :

Globalement, et indépendamment du rôle de valorisation directe des techniques existantes
en fluide parfait, les techniques numériques d'interaction se regroupent sur trois objec-
tifs principaux :

2.1.1. Solveurs numériques par zones ou sous-domaines :

En extension des solveurs numériques NS directs, un premier objectif consiste à restreindre
le domaine de calcul NS au strict voisinage des zones visqueuses, et à coupler les conditions
aux limites avec une solution de fluide parfait externe raccordée. Cette approche, dite de
couplage par zones ou sous-domaines, possède quelques analogies avec celle du calcul raccordé
"Equations de Prandtl - Fluide Parfait", en ce qui concerne les problèmes analytiques de
raccordement des conditions aux limites, ainsi que des multiples algorithmes numériques de
couplage possibles.

Toutefois, la zone visqueuse NS ne bénéficiant pas, à la différence des solveurs d'équations
de Prandtl, d'une technique numérique rapide marchant d'amont en aval, la principale diffi-

culté consiste à ne pas compromettre l'économie modérée résultant d'un domaine de calcul NS
réduit, en utilisant une relaxation à convergence lente au niveau de l'algorithme de couplage
[18, 19]. Bien que le traitement réel de ce problème reste à acquérir, des résultats ont pu
être obtenus à l'ONERA [20] en faisant appel à une résolution instationnaire, explicite et
simultanée, des sytèmes visqueux et non-visqueux, sensiblement hyperboliques au raccord. Les
propriétés de cette technique relèvent cependant encore davantage des méthodes d'évolution
et des solveurs NS directs que des méthodes numériques d'interaction.

2.1.2. Solveurs économiques avec approximations de couches minces couplées :

En extension des méthodes de couche limite, le second objectif consiste à développer des
méthodes numériques économiques, incluant le traitement du décollement et de l'interaction
couche limite-onde de choc, capables de calculer globalement des écoulements complexes à
interaction forte et multiples sans autre donnée que la géométrie, mais fondées sur une
certaine approximation du problème NS. L'approximation la plus simple est celle des équations
de Prandtl raccordées au fluide parfait, et constitue l'extension de l'idée développée par
Crocco [21] en supersonique.

L'idée plus récente de "Formulation Déficitaire" [3, 15, 10] du calcul visqueux , par rapport
à un écoulement de fluide parfait superposé (prédicteur), a permis d'établir la supériorité
théorique du concept de couplage par "vitesse de transpiration à la paroi", èt de prodiguer
notamment un traitement général de l'interaction choc-couche limite qui faisait défaut au
modèle de Crocco. La Formulation Déficitaire permet en outre [10, 15] d'introduire naturel-
lement les méthodes intégrales du type couche limite, et de constater qu'elles sont en fait
moins restrictives que le modèle de Prandtl au niveau des équations, cet avantage étant
toutefois pondéré par l'empirisme plus important introduit dans la modélisation de fermeture
des sytèmes d'équations intégrales. Enfin, le progrès sur les équations de Prandtl apporté
aux méthodes intégrales par la "Formulation Déficitaire", qui consiste à modéliser le gradient
de pression normal interne aux couches visqueuses au moyen du champ de pression fluide-
parfait superposé [10, 15], a pu également être utilisé sans difficulté dans des techniques
numériques construites pour les équations de Prandtl, notamment par Carter [22], Werle [23],
Wilmoth [24].

Ainsi qu'il a été mentionné, la technique des équations intégrales déficitaires, qui réduit
le problème visqueux à des équations aux dérivées partielles "interactives" intervenant ex-
clusivement sur les frontières ou surfaces de discontinuités du fluide parfait, offre l'avan-
tage de minimiser la discrétisation des problèmes de fortes interactions visqueuses. Elle
est de ce fait capable de minimiser la mémoire de stockage et le coût d'ordinateur néces-
saires, ou encore de maximiser la complexité des écoulements accessibles au calcul. Elle
constitue la première étape naturelle de généralisation des méthodes du fluide parfait.

Les techniques interactives de couche limite généralisée , ou de méthodes intégrales défi-
citaires actuelles, possèdent conceptuellement une généralité suffisante pour offrir de
nombreux développements non encore atteints, tant en bidimensionnel, qu'en tridimensionnel
et en ṡ ıstationnaire, en incluant la présence de décollements non généralisés. Cette étape
est sans doute essentiellement conditionnée par la maitrise d'algorithmes numériques de
couplage rigoureux plus nombreux. Elle demande encore également, dans le cas des corps
fuselés tridimensionnels, un effort de compréhension pour la modélisation visqueuse du
problème des lignes de séparation des nappes tourbillonnaires.

Conceptuellement, les limitations de ces modélisations de couche mince interactive appa-
raissent essentiellement au niveau des couches limites épaisses se développant dans les
coins, en tridimensionnel, ainsi qu'au niveau des nappes de sillages à géométries
complexes, enroulées, intermittentes , ou confluentes avec les couches limites. Il faut
noter cependant que le recours à des solveurs NS, appropriés à de telles configurations,
suppose une échelle de discrétisation bien inférieure aux structures tourbillonnaires,
sous peine de voir dégénérer le solveur NS en un simple solveur "Fluide-Parfait", c'est-
à-dire à un niveau d'approximation inclus dans les techniques de couches minces inte-
ractives.

2.1.3. Solveurs numériques composites :

Conservant parmi les progrès obtenus en 2.1.2. ceux qui consistent à résoudre les problèmes
prédicteurs pseudo-fluide-parfait et correcteur visqueux sur des domaines de calcul super-
posés, à résoudre le correcteur visqueux par des techniques numériques marchant itérati-
vement d'amont en aval, à résoudre enfin le couplage prédicteur-correcteur au moyen d'algo-
rithmes itératifs, il est désormais concevable [9, 10, 15, 11, 12, 25] d'introduire au
niveau du correcteur les termes visqueux négligés en 2.1.2. et de donner ainsi accès à
des solveurs numériques NS indirects, au moins au niveau des équations dites "NS Couche Mince".

Cette génération de solveurs NS composites correspond à opérer la dissociation prédicteur-
correcteur comme un éclatement des équations, les sous-systèmes d'équations équivalents
obtenus étant résolus par des techniques numériques mieux conditionnées aux nombres de
Reynolds élevés.

Contrairement à l'approche du couplage par sous-domaines 2.1.1., une économie et un meilleur
conditionnement numérique sont ici accessibles au niveau du prédicteur et du correcteur,
par le recours aux solveurs numériques rapides de fluide parfait et de couches visqueuses
minces. La difficulté principale reste cependant de ne pas compromettre cet avantage au ni-

veau d'une convergence lente ou mal contrôlée de l'algorithme de couplage. En ce domaine, les progrès réalisés dans les solveurs approchés 2.1.2. devraient pouvoir être mis à profit directement. Enfin, un avantage supplémentaire pouvant résulter des solveurs NS composites est celui d'une dégénérescence mieux contrôlée des performances en cas d'application sur des maillages grossiers, cette dégénérescence conduisant sensiblement au niveau 2.1.2. Une commutation par zones du calcul, entre les niveaux 2.1.3. et 2.1.2., peut d'ailleurs être envisagée simplement.

2.2. Contraintes des calculs : -

2.2.1. Echelles de discrétisation :

Comparativement aux contraintes habituelles en fluide parfait, une échelle de discrétisation plus réduite est généralement indispensable, au moins dans les zones de forte interaction. Cette contrainte porte d'abord évidemment sur le calcul visqueux correcteur qui, à l'exception des méthodes intégrales, doit résoudre numériquement les gradients intenses dans la direction normale aux couches et sous-couches, turbulentes ou visqueuses, tant pour les grandeurs moyennes que pour la turbulence.

La contrainte de discrétisation fine porte également d'autre part sur la direction tangentielle aux couches visqueuses, dans les zones de forte interaction. Celle-ci conditionne aussi bien le prédicteur pseudo-fluide-parfait que le correcteur, l'aspect interactif de la solution composite globale rendant illusoire un sous-maillage unilatéral de l'un ou l'autre calcul selon cette direction. L'échelle de "discrétisation minimale" est celle qui est capable de résoudre la perturbation apportée au fluide parfait externe par les couches visqueuses. En régime turbulent, l'échelle de cette perturbation, déduite de l'analyse asymptotique [14] ou expérimentale, est de l'ordre de l'épaisseur de la couche visqueuse turbulente locale en amont du phénomène. Cette échelle de discrétisation "minimale" pour résoudre les problèmes visqueux d'interaction forte est effectivement une échelle suffisante en cas d'utilisation d'une méthode intégrale interactive.

Cette discrétisation minimale, bien que moins contraignante que l'échelle nécessaire au correcteur visqueux dans la direction normale, peut constituer une contrainte importante qui pénalise le calcul du fluide parfait externe toutes les fois que les couches visqueuses en interaction sont très minces par rapport à léchelle de l'écoulement global. Il en est ainsi par exemple en cas de décollement on d'interaction couche limite-onde de choc dans les régions de bord d'attaque. Une discrétisation locale plus fine de l'écoulement non-visqueux est cependant le prix minimal nécessaire pour donner accès au calcul des régimes de forte interaction visqueuse.

2.2.2. Modélisation de la turbulence

Il est clair que les difficultés et limitations rencontrées pour modéliser la turbulence dans les solveurs NS directs sont retrouvées en totalité dans les solveurs indirects que constituent les techniques d'interaction. Les problèmes supplémentaires spécifiques à ces techniques apparaissent au niveau des modélisations simplifiées mises en jeu pour la fermeture des méthodes intégrales. Plus empiriques à priori, ces fermetures exigent non seulement une modélisation des termes turbulents, mais encore une modélisation complémentaire portant sur les profils de vitesse moyenne des couches visqueuses. En contre-partie de ce double empirisme, une modélisation très précise des sous-couches visqueuses, tant au niveau des vitesses moyennes que de la turbulence locale, n'est plus un facteur déterminant pour la précision globale de ces méthodes, qui résulte avant tout des grandeurs macroscopiques à l'échelle de la couche visqueuse.

A cette échelle, une représentation très satisfaisante des profils de vitesse moyenne a pû être obtenue, tant en bidimensionnel et en instationnaire [15] qu'en tridimensionnel [10], grâce à une extension de la représentation composite de Coles [26], qui combine une loi logarithmique de paroi et une loi de sillage "universelle". L'extension comporte un changement de la loi de sillage et permet une représentation unique, couvrant le domaine complet des paramètres de formes de couches limites ou sillages, avec ou sans courants de retour[10]. En tridimensionnel notamment, la représentation n'est pas limitée aux petits décollements exempts de courants de retour par rapport aux lignes de courants du fluide parfait externe. Dans ce repère, l'écoulement transversal est supposé à déversement unilatéral, fig. 1, le profil de vitesse visqueux $\vec{q}\,(\delta, C_2, C_3)$ étant décrit vectoriellement, δ étant l'épaisseur de la couche visqueuse, C_2 et C_3 deux paramètres de forme indépendants. Les vecteurs unitaires $\vec{x}$ et $\vec{y}$ sont respectivement tangent et normal au vecteur vitesse fluide-parfait $\vec{q}$. Si $z = \delta.\eta$:

$$(1) \quad \begin{cases} \vec{q} = \vec{q} - \vec{W}.\tilde{F}(\eta) + \vec{c}.\,Log\,\eta \\[2mm] \vec{W} = q\,(C_2\,\vec{x} + C_3\,\vec{y}) \\[2mm] \vec{c} = q\,\dfrac{C_1}{C_4}\left[(1-C_2)\vec{x} - C_3\,\vec{y}\right] \end{cases}$$

$$(2) \quad \begin{cases} C_4 = \sqrt{(1-C_2)^2 + C_3^2} \qquad\qquad C_1 = \dfrac{1}{0,41} \sqrt{\dfrac{Cf}{2}} \\[3mm] C_4 = \sqrt{\dfrac{Cf}{2}} \left[\dfrac{1}{0,41} \log\left(R_\delta \sqrt{\dfrac{Cf}{2}} \right) + 5,25 \right] \end{cases}$$

La description combine une composante logarithmique de cisaillement $\vec{z}$ et une composante déficitaire plane de sillage $\vec{W}$, $\vec{z}$ et $\vec{W}$ n'étant pas coplanaires. La "loi universelle de paroi" fournit Cf et C_1 selon (2). La fonction de sillage $\tilde{F}(\eta)$ est celle proposée en bidimensionnel [15]. Elle incorpore une relation relativement empirique $\eta^*(C_1, C_2)$ pour dissocier la couche de cisaillement principale de la paroi en cas de décollements intenses et contrôler la vitesse de retour maximale (η^* est nul pour les écoulements attachés ou les décollements naissants) :

$$(3) \quad \tilde{F}(\eta) = F\left[\frac{\eta - \eta^*}{1 - \eta^*} \right] \qquad\qquad F(\eta) = \left[1 - \eta^{\frac{3}{2}} \right]^2$$

A titre de première approximation, le frottement pariétal peut être considéré comme colinéaire à $\vec{z}$. Aux grands nombres de Reynolds, C_1 décroit, et le profil polaire donné par (1) devient approximativement triangulaire. La représentation (1) avec $C_1 = 0$ fournit enfin une modélisation des profils de sillage, par moitiés supérieure ou inférieure. Les mêmes profils conviennent en écoulement compressible ou instationnaire, les profils de densité s'en déduisant à partir de l'enthalpie totale, assimilable à celle de l'écoulement externe dans le cas adiabatique.

En supplément de la modélisation du frottement pariétal (2), les méthodes intégrales demandent la modélisation de grandeurs caractérisant globalement la turbulence de la couche visqueuse, telles que la dissipation globale d'énergie par unité de longueur $\emptyset$, ou le taux d'entrainement turbulent E. Il est aisé de constater [15] que la fermeture par l'entrainement, qui est systématiquement utilisée dans les exemples donnés ci-dessous, se déduit directement des propriétés locales des profils de vitesses et de la turbulence au voisinage immédiat de la frontière externe des couches visqueuses.

Dans le cas des turbulences d'équilibres, pour lesquelles un modèle algébrique simple peut suffire à déterminer les contraintes de Reynolds, la fermeture turbulente des méthodes intégrale peut en être déduite directement en faisant appel à la modélisation des profils de vitesses, tant pour la dissipation globale que pour l'entrainement. Dans l'hypothèse d'un modèle de longueur de mélange construit sur l'échelle $\delta = (1-\eta^*)\delta$ de la couche de cisaillement principale, l'entrainement d'équilibre est proportionnel à la courbure du profil de vitesse en $\jmath = \delta$ et peut être déduit de (1), même en présence de courants de retour. En incompressible bidimensionnel, l'entrainement et la dissipation d'équilibre E_{eq} , ϕ_{eq} s'expriment ainsi approximativement [15] :

$$(4) \quad \begin{cases} \tilde{u}_w = 1 - \dfrac{2,22}{1 + 1,22\,\eta^*} \dfrac{\delta_1}{\delta} \\[3mm] E_{eq} = \left[0,053\,(1 - \tilde{u}_w) - 0,182 \dfrac{Cf}{\sqrt{|Cf|}} \right] \lambda_1\, \lambda_2\, \lambda_3 \\[3mm] \phi_{eq} = \left[|Cf| . |\tilde{u}_w| + 0,018\,(1 - \tilde{u}_w)^3 \right] \lambda_1\, \lambda_2\, \lambda_3 \end{cases}$$

δ_1 est l'épaisseur de déplacement (incompressible). Les termes correctifs $\lambda_1, \lambda_2, \lambda_3$ sont liés au coefficient de longueur de mélange, de telle sorte que $\lambda_1 = \lambda_2 = \lambda_3 = 1$ pour une couche limite simple. Les valeurs $\lambda_1 = 2$, $Cf = 0$ conviennent pour un sillage simple. Les termes λ_2, λ_3 correspondent à des corrections en cas de turbulence extérieure ou de courbure des lignes de courant importantes, précisées en [15].

La fermeture turbulente des méthodes intégrales, à priori plus empirique, conduit paradoxalement à une robustesse accrue des performances pratiques vis à vis des écoulements turbulents complexes, qui s'explique par une restitution moins détaillée des phénomènes. Il serait cependant illusoire de penser qu'une modélisation d'équilibre puisse suffire à décrire universellement l'entrainement, la connection entre l'écoulement moyen et la turbulence ayant été concentrée sur cet unique scalaire par l'approche intégrale. Une modélisation hors-équilibre de la fermeture intégrale par l'entrainement turbulent conduit à des effets similaires à ceux d'équations de transport pour la turbulence ou pour les tensions de Reynolds. Elle s'avère nécessaire et déterminante pour les régimes de forte interaction à décollement rapide ou interaction couche limite-onde de choc. Dans les exemples bidimensionnels ci-dessous, on utilise un modèle d'écart à l'équilibre à deux équations différentielles auxiliaires, détaillé en [15, 10]. Le modèle suppose que l'écart à l'équilibre $\lambda(x)$ du cisaillement turbulent $\vec{z}(x,\jmath)$ est indépendant de $\jmath$. Il suppose en outre que $\lambda(x)$ est déterminé par des équations de transport simplifiées, régissant les valeurs $\tilde{k}(x)$, $\tilde{\varepsilon}(x)$, $\tilde{z}(x)$ des grandeurs turbulentes moyennées sur l'épaisseur de la couche visqueuse. Les équations sont déduites de celles de Launder, Hanjalic, Rodi. Elles font appel à des niveaux d'équilibre de l'énergie $k_{eq}(x)$, de la dissipation locale $\tilde{\varepsilon}_{eq}(x)$ et du cisaillement $\vec{z}_{eq}(x)$, qui peuvent être exprimées [15,10] en fonction de $\delta, q, \tilde{u}_w$ et ϕ_{eq} . Le modèle s'écrit:

$$(5) \quad \begin{bmatrix} \mathcal{C}\,(x,\mathfrak{z}) \\ E\,(x) \\ \phi\,(x) \end{bmatrix} = \lambda\,(x) \begin{bmatrix} \mathcal{C}_{eq}\,(x,\mathfrak{z}) \\ E_{eq}\,(x) \\ \phi_{eq}\,(x) \end{bmatrix} \quad , \quad \lambda\,(x) = \frac{\tilde{\mathcal{C}}(x)}{\tilde{\mathcal{C}}_{eq}\,(x)}$$

$$(6) \quad \begin{cases} \dfrac{D\tilde{k}}{Dt} = \dfrac{\tilde{\mathcal{C}}}{\tilde{\mathcal{C}}_{eq}} \; \phi_{eq} \; \dfrac{q^3}{2} - \tilde{\mathcal{C}}\,\tilde{\delta} \\[3mm] \dfrac{D\tilde{\mathcal{C}}}{Dt} = 1{,}5 \; \dfrac{\hat{\mathcal{C}}\tilde{\delta}}{\tilde{k}} \left[\left(\dfrac{\tilde{k}}{\tilde{k}_{eq}} \right)^2 \dfrac{\hat{\mathcal{C}}_{eq}}{\hat{\mathcal{C}}} \; \tilde{\mathcal{C}}_{eq} - \tilde{\mathcal{C}} \right] \\[3mm] \dfrac{\tilde{\mathcal{C}}}{\tilde{\mathcal{C}}_{eq}} = \left(\dfrac{\tilde{k}}{\tilde{k}_{eq}} \right)^{\frac{3}{2}} \end{cases}$$

2.2.3 - Singularités - Influence amont - Méthodes inverses ou couplées

L'utilisation d'équations de quantité de mouvement simplifiées pour le calcul des couches visqueuses minces, telles que des équations de Prandtl ou des équations intégrales défi-citaires, peut conduire à des singularités dans les solutions. Sans réalité physique, ces singularités dépendent du type de conditions aux limites imposées au problème visqueux. Elles apparaissent notamment en théorie de couche limite ordinaire, c'est-à-dire en l'absen-ce de couplage au fluide parfait, avec pression externe imposée. Des exemples typiques sont ici ceux de la singularité de décollement en bidimensionnel stationnaire, ainsi que l'exis-tence de solutions faibles aux systèmes hyperboliques des équations intégrales instation-naires ou tridimensionnelles.

Il a maintenant été bien établi sur les exemples précédents, par voie analytique ou essais numériques, que ces singularités ne diagnostiquent pas la limite de validité des équations simplifiées utilisées, mais essentiellement la limite de validité d'une résolution visqueuse découplée du calcul de la pression. Le couplage au calcul du fluide parfait permet de ce fait d'éliminer les singularités. Il permet de restaurer simultanément dans le calcul visqueux la possibilité d'une convection d'influence vers l'amont (même en l'absence de courants de retour) par le biais du champ de pression interactif externe, et de retrouver ainsi une modélisation des domaines d'influence similaire à celle offerte par les solveurs NS.

Cette restitution de l'influence amont dans les calculs visqueux simplifiés au moyen du champ de pression ne peut toutefois être assurée exclusivement par le fluide parfait dans les zones où celui-ci est localement supersonique. Dans ce cas, l'influence amont (ou pseudo-ellipiticité du problème) doit résulter exclusivement de l'effet de "couplage fort", et peut être effectivement restituée dans les modèles dits "subcritiques". Elle peut aussi parfois être éliminée, comme dans le cas des couches "supercritiques" de Crocco-Lees [21], le traitement du décollement supersonique et de l'interaction choc-couche limite devenant alors impossible.

De la même manière que pour les singularités des calculs visqueux découplés, il a été éta-bli [16, 4] que le comportement supercritique, physiquement irréaliste, ne constituent pas une propriété intrinsèque des équations visqueuses résolues, mais fait aussi intervenir le modèle de couplage mis en oeuvre. La conclusion déterminante est que le couplage par vi-tesse de transpiration à la paroi, ou la "Formulation Déficitaire", procurent des modèles toujours "subcritiques", capables de restituer pleinement l'influence amont en transsonique ou supersonique. Il en résulte en particulier que les ondes de choc présentes au sein de l'écoulement non-visqueux couplé (prédicteur) sont toujours atténuées avant d'atteindre les parois, le cas échéant à l'intérieur même des couches visqueuses, et que les distributions de pression pariétales calculées sont toujours continues.

Il est clair que la suppression des singularités visqueuses par couplage suppose en pratique que les calculs visqueux et non-visqueux puissent être résolus simultanément. Dans le cas le plus fréquent d'une technique numérique de couplage itérative, fondée sur des calculs visqueux et non-visqueux alternés, les singularités doivent également être éliminées à chaque itération. Le procédé habituel consiste à définir des problèmes visqueux inverses, dans lesquels la pression devient une grandeur calculée. La sélection des conditions aux limites du problème inverse est un facteur déterminant. Le choix de l'épaisseur de dépla-cement peut en particulier conduire, en supersonique, à des difficultés ayant un lien direct avec le problème des modèles "supercritiques" [16, 9]. En bidimensionnel, le choix optimal est toujours, semble-t'il [9], celui de la vitesse de transpiration à la paroi définie par le couplage.

2.2.4. Algorithmes numériques de couplage fort :

La dissociation du problème global en sous-problèmes prédicteur et correcteur visqueux conduit en général à des sous-problèmes numériques discrétisés dont la résolution couplée directe est hors de portée. Des algorithmes de résolution itérative doivent de ce fait être mis au point. L'aspect numérique de ce problème spécifique et complexe a parfois été occulté

par l'idée de le restreindre au simple choix d'un enchainement des calculs prédicteurs et correcteurs, ainsi que le suggère par exemple l' itération de point fixe appliquée à l'épaisseur de déplacement en théorie de couche limite. Cette approche n'est cependant fondée que si le couplage est faible, c'est-à-dire si la convergence de l'itération n'est pas exigée. Il a été établi en particulier [17] que cette itération, discrétisée par des schémas numériques consistants, peut toujours être rendue instable par l'utilisation de maillages suffisamment fins, même dans le cas simple d'une couche limite de plaque plane.

Outre la consistance de la discrétisation des équations de couplage (qui exclut les techniques de lissage) et la stabilité des algorithmes, la convergence des itérations donnant accès au couplage fort doit respecter la propagation de l'influence visqueuse vers l'amont, notamment dans les zones supersoniques. Dans ces zones, une discrétisation totalement décentrée vers l'amont serait de ce fait inconsistante. Elle serait aussi incapable d'incorporer les conditions aux limites à l'aval qui sont nécessaires à un calcul visqueux. Les premiers algorithmes de couplage présentant une généralité suffisante, en écoulement supersonique, ont été recherchés par Werle, Vatsa [27] dans des techniques pseudo-instationnaires, fondées sur l'addition de termes instationnaires fictifs aux équations de base, et destinées aux problèmes de décollements supersoniques multiples sur des rampes de compression supersoniques successives.

La plupart des autres techiques numériques de couplage disponibles sont des méthodes de relaxation, détaillées en [3, 9] . Les premières méthodes ici ont été simplement des techniques de sous-relaxation uniforme et arbitraire, introduites dans l'itération sur l'épaisseur de déplacement, et ajustées par tâtonnements numériques. Elles sont utilisables en l'absence de décollement, sur des maillages standard, assez lâches par rapport à l'échelle de couches visqueuses, notamment vis à vis des problèmes d'interaction choc-couche limite ou de bord de fuite. Elles constituent encore l'un des rares accès au couplage fort en instationnaire ou en tridimensionnel.

En écoulement bidimensionnel stationnaire, une technique de relaxation véritable, apportant un contrôle automatique de la stabilité, a pû être obtenue [17] à partir de la même itération de point fixe sur l'effet de déplacement. L'analyse s'appuie sur une approximation linéarisée de la stabilité de la solution du fluide-parfait vis à vis de petites perturbations des conditions aux limites. Cette approximation donne accès aux coefficients d'amplification de l'itération de couplage dans l'espace de Fourier, et permet de déterminer une relaxation optimale. En pratique, la stabilité numérique peut être contrôlée par le calcul en chaque noeud d'un coefficient de relaxation, fonction de la taille des mailles, du nombre de Mach et d'un paramètre de forme de la couche visqueuse. Le contrôle de relaxation devient cependant impossible au décollement.

En présence des zones décollées, le nécessaire recours à des méthodes inverses pour éliminer les singularites des calculs visqueux a d'abord conduit à réaliser le couplage par des itérations de point fixe "inverses". Dans celles-ci la pression résultant du calcul visqueux est imposée comme condition aux limites d'un calcul inverse de fluide parfait, lequel délivre à son tour une condition aux limites du calcul visqueux, épaisseur de déplacement ou vitesse de transpiration. Dans les cas simples, la stabilité numérique de l'itération peut encore être obtenue par une simple sous-relaxation uniforme et arbitraire. De même que pour l'itération de point fixe directe, une technique de relaxation inverse véritable a pu être définie [17], en introduisant en chaque noeud un contrôle local du coefficient de relaxation stabilisateur. Cette analyse démontre cependant que la stabilité de la relaxation inverse n'est plus conditionnée par la taille locale des mailles, mais par l'étendue maximale du domaine de calcul inverse qui, s'il est suffisamment important, peut rendre difficile ou incertaine la stabilisation par relaxation. Le recours possible à une commutation par zones entre la "relaxation directe" et la "relaxation inverse" n'élimine pas totalement la difficulté, et conduit à une très grande complexité du calcul non-visqueux, parfois prohibitive, notamment en transsonique.

La difficulté peut être surmontée par des méthodes de relaxation plus complexes que celles de point fixe "directes" ou "inverses". L'une des voies est celle de techniques un peu plus implicites dans la direction parallèle à la frontière de couplage, voir [3, 9]. Des résultats ont été essentiellement obtenus en subsonique, avec des méthodes du type Gauss-Seidel proposées par Veldman [28], Moses, Kline [29]. Des méthodes de type Newton ont pû aussi être mises en oeuvre en incompressible [30].

L'autre voie est celle des méthodes de "relaxation semi-inverse" [17]. Leur convergence à priori plus lente, liée à un caractère explicite analogue à celui des méthodes directes ou inverses, est compensée par la possibilité d'utiliser la même technique avec divers solveurs de fluide parfait. Dans le cas des solveurs par relaxation, les convergences du fluide parfait et du couplage visqueux sont en outre simultanées. La technique consiste à corriger itérativement l'épaisseur de déplacement ou bien la vitesse de transpiration, à partir de l'erreur mesurée entre les distributions de pression d'un calcul fluide-parfait direct et d'un calcul visqueux inverse.

La méthode numérique originelle de Le Balleur [17] est fonctionnelle en subsonique comme en supersonique, et comporte en chaque noeud un contrôle de la stabilité du type sur-relaxation. De nombreux résultats ont aussi été obtenus avec la méthode plus récemment définie par Carter [31], qui est directement une forme intégrale de la précédente [3, 9]. En supersonique, un aménagement de la méthode originelle a été proposé par Wigton, Holt [32]. La méthode a par ailleurs été étendue au problème des sillages totalement dissymétriques, ainsi que des écoulements quasi-tridimensionnels [15, 10]. Enfin, une première tentative heuristique a été faite par Wigton, Yoshihara [33] pour réaliser une méthode semi-inverse en tridimensionnel.

La méthode de relaxation semi-inverse originelle peut être facilement commutée par zones avec la méthode de relaxation directe. L'ensemble des résultats ci-dessous correspondent à une commutation automatique liée au paramètre de forme de la couche visqueuse à l'itération considérée ($H_i \simeq 1.8$ en turbulent).

3. EXEMPLES DE SOLVEURS PAR METHODE INTEGRALE DEFICITAIRE EN AERODYNAMIQUE EXTERNE

Moyennant une adaptation des épaisseurs intégrales mises en jeu dans les équations, ainsi qu'un couplage fort avec un écoulement de fluide parfait superposé aux couches visqueuses, les équations intégrales traditionnelles délivrent une approximation au premier ordre de la "Formulation Déficitaire" proposée pour les équations de Navier-Stokes [3, 15, 10]. Elles délivrent l'effet de déplacement. Une modélisation complémentaire de second ordre est généralement appliquée à l'effet de courbure des sillages.

3.1. Formulation Déficitaire - Méthodes intégrales approchées :

Considérant en bidimensionnel par exemple un contour $\xi = 0$ de courbure K (x), définissant un repère curviligne orthogonal tangent, on note $\bar{u}, \bar{w}$ les composantes de la vitesse, $\bar{\rho}$ la densité, $\bar{p}$ la pression, u, w, ρ, p les inconnues homologues dans un calcul prédicteur superposé au champ visqueux, $\hbar = 1 + K_{\xi}$ la métrique, $\bar{V}$ les termes de contraintes visqueuses. Le problème dynamique NS s'écrit :

$$(7) \qquad \frac{\partial \bar{U}}{\partial t} + \frac{\partial \bar{F}}{\partial x} + \frac{\partial \bar{G}\hbar}{\partial \xi} + K\bar{H} = \bar{V}$$

$$(8) \qquad \bar{U} = \begin{bmatrix} \bar{\rho} \\ \bar{\rho}\bar{u} \\ \bar{\rho}\bar{w} \end{bmatrix} \quad \bar{F} = \begin{bmatrix} \bar{\rho}\bar{u} \\ \bar{\rho}\bar{u}^2 + \bar{p} \\ \bar{\rho}\bar{u}\bar{w} \end{bmatrix} \quad \bar{G} = \begin{bmatrix} \bar{\rho}\bar{w} \\ \bar{\rho}\bar{u}\bar{w} \\ \bar{\rho}\bar{w}^2 + \bar{p} \end{bmatrix} \quad \bar{H} = \begin{bmatrix} 0 \\ -\bar{\rho}\bar{u}\bar{w} \\ \bar{\rho}\bar{u}^2 + \bar{p} \end{bmatrix}$$

$$(9) \qquad 0 = \lim_{\xi \to \infty} (f - \bar{f}) \qquad f = \{u, w, p, \rho\}$$

En addition des conditions d'adhérence aux parois, les équations (9) correspondent à un couplage analytique continu (matching) avec le champ lointain non-visqueux. La Formulation Déficitaire suppose que le prédicteur vérifie les équations du fluide parfait, le système (7) (8) (9) étant décomposé en un système équivalent :

$$(10) \qquad \frac{\partial U}{\partial t} + \frac{\partial F}{\partial x} + \frac{\partial G\hbar}{\partial \xi} - KH = 0$$

$$(11) \qquad \frac{\partial}{\partial t}(U - \bar{U}) + \frac{\partial}{\partial x}(F - \bar{F}) + \frac{\partial}{\partial \xi}(G - \bar{G})\hbar - K(H - \bar{H}) = -\bar{V}$$

$$(12) \qquad \begin{cases} \text{Parois} : \rho w(x,0,t) = \frac{\partial}{\partial t}\int_0^\infty (\rho - \bar{\rho})\,d\xi + \frac{\partial}{\partial x}\int_0^\infty (\rho u - \bar{\rho}\bar{u})\,d\xi \\ \text{Sillages} : \rho w(x,0+,t) - \rho w(x,0-,t) = \frac{\partial}{\partial t}\int_{-\infty}^{+\infty}(\rho - \bar{\rho})\,d\xi + \frac{\partial}{\partial x}\int_{-\infty}^{+\infty}(\rho u - \bar{\rho}\bar{u})\,d\xi \end{cases}$$

$$(13) \qquad \text{Sillages} : p(x,0+,t) - p(x,0-,t) = \int_{-\infty}^{+\infty} - \frac{\partial(p - \bar{p})}{\partial \xi}\,d\xi$$

Les équations déficitaires (11) pilotent les écarts induits par la viscosité, directement sur les flux U, F, G, H. Leur intégration selon ξ au travers des couches visqueuses, avec le couplage (9), fournit des conditions aux limites "exactes" pour le fluide parfait, en effet de déplacement (12), et en effet de courbure (13). La différence avec la théorie de la couche limite réside ici dans la prise en compte des variations selon ξ de $\rho, \rho u, p, \bar{p}$.

Si dans la suite le terme visqueux $\bar{V}$ est simplifié dans l'hypothèse d'équations NS-couche-mince, et si de surcroit un développement en δ (échelle de la couche visqueuse) est appliqué, les flux simplifiés s'écrivent au premier ordre :

$$(14) \qquad \bar{U} = \begin{bmatrix} \bar{\rho} \\ \bar{\rho}\bar{u} \\ 0 \end{bmatrix} \quad \bar{F} = \begin{bmatrix} \bar{\rho}\bar{u} \\ \bar{\rho}\bar{u}^2 + \bar{p} \\ 0 \end{bmatrix} \quad \bar{G}\hbar = \begin{bmatrix} \bar{\rho}\bar{w} \\ \bar{\rho}\bar{u}\bar{w} \\ \bar{p} \end{bmatrix} \quad \bar{H} = 0 \quad \bar{V} = \begin{bmatrix} 0 \\ \partial \tau / \partial \xi \\ 0 \end{bmatrix}$$

avec des simplifications similaires pour les flux non-visqueux. L'équation déficitaire de quantité de mouvement normale, compte tenu de (9) dégénère au premier ordre en $\bar{p}(x, z, t) = p(x, z, t)$, ce qui annule l'effet de courbure (13), sans toutefois annuler le gradient de pression normal. Les équations déficitaires intégrales de continuité et de quantité de mouvement longitudinale, ainsi que l'équation déficitaire de quantité de mouvement en $\xi = \delta(x,t)$ (équation d'entrainement), s'écrivent au premier ordre ($\bar{p} = p$) :

$$(15) \qquad \left[\frac{1}{\rho q}\frac{\partial \rho \delta_0}{\partial t} + \frac{1}{\rho q}\frac{\partial \rho q \delta_1}{\partial x} - \frac{w}{q} \right](x,0,t) = 0$$

$$(16) \quad \left[\frac{1}{\rho q^2} \frac{\partial \rho q \delta_1}{\partial t} + \frac{1}{\rho q^2} \frac{\partial \rho q^2 (\delta_1 + \theta_{11})}{\partial x} - \frac{u w}{q^2} \right]_{(x,0,t)} = \frac{Cf}{2}$$

$$(17) \quad \left[\frac{1}{u} \frac{\partial \delta}{\partial t} + \frac{\partial \delta}{\partial x} - \frac{w}{u} \right]_{(x,\delta,t)} = E = \left[\frac{\partial \tau / \partial z}{\rho u \cdot \partial (u - \bar{u}) / \partial z} \right]_{(x,\delta,t)}$$

Ce système d'équations intégrales traditionnelles, qui peut être fermé par la modélisation turbulente (1) (2) (3) (4) (5) (6), détermine en fait des épaisseurs intégrales "déficitaires", c'est-à-dire mesurant l'écart au fluide parfait compte tenu de la variation en z de ρ, ρu, ρu^2 :

$$(18) \quad \begin{cases} \delta_1 \, \rho q \, (x,0,t) = \int_0^\infty \left[\rho u \, (x,z,t) - \bar{\rho} \bar{u} \, (x,z,t) \right] dz \\[2mm] (\delta_1 + \theta_{11}) \, \rho q^2 (x,0,t) = \int_0^\infty \left[\rho u^2 \, (x,z,t) - \bar{\rho} \bar{u}^2 (x,z,t) \right] dz \\[2mm] \delta_0 \, \rho \, (x,0,t) = \int_0^\infty \left[\rho \, (x,z,t) - \bar{\rho} \, (x,z,t) \right] dz \end{cases}$$

Cette définition de δ_0, δ_1 élimine d'ailleurs toute approximation sur (15), qui est identique à (12). Au second ordre, une modélisation de l'équation déficitaire de quantité de mouvement normale peut s'appuyer sur la courbure "induite" des lignes de courants non-visqueuses, moyennée selon z, $K^*(x,0\pm,t)$:

$$(19) \quad \frac{\partial}{\partial z} (p - \bar{p}) = K^*(x,t) \left[\rho u^2 \, (x,z,t) - \bar{\rho} \bar{u}^2 (x,z,t) \right]$$

$$(20) \quad p \, (x,0+,t) - p (x,0-,t) = -\left[K^*(\delta_1 + \theta_{11}) \rho q^2 \right]_{(x,0+,t)} + \left[K^*(\delta_1 + \theta_{11}) \rho q^2 \right]_{(x,0-,t)}$$

La valeur du modèle repose sur un couplage fort aux effets visqueux de la courbure induite, K^* pouvant être assimilée à la courbure de la surface de déplacement. Près d'un bord de fuite, la valeur du modèle repose en outre sur le respect de la dissymétrie du sillage, tant pour les épaisseurs δ_1, θ_{11} que pour les courbures induites $K^*(x+,t)$ et $K^*(x-,t)$, dont les signes sont généralement opposés.

3.2. Couplage - Relaxation directe - Relaxation semi-inverse

Dans les exemples ci-dessous, seuls les calculs instationnaires ou tridimensionnels, encore restreints aux écoulements sans décollement, font appel à un couplage par simple itération sur la vitesse de transpiration w^n (x, y, o, t), avec sous-relaxation uniforme et empirique entre les itérations n et n+1. La convergence (sans lissage), en chaque noeud et à chaque pas de temps, assure cependant l'accès au couplage fort, avec influence .ont.

Dans les calculs bidimensionnels ou quasi-tridimensionnels (flèche infinie), la méthode numérique de couplage est toujours la méthode de relaxation mixte, directe ou semi-inverse par zones, évoquée en 2.2.4. Pourvu que le maillage soit adapté à l'échelle de la couche visqueuse locale, elle offre la capacité de résoudre les décollements ou interactions choc-couche limites multiples, et assure le contrôle automatique de la stabilité numérique.

Dans le cas des profils, elle détermine aussi le positionnement de la ligne moyenne des sillages (lieu du minimum de vitesse $\bar{u}$), sur laquelle est adaptée itérativement la coupure du maillage en C utilisé pour le calcul du fluide parfait. La méthode numérique, détaillée en [15], inclut le calcul et le couplage des sillages dissymétriques. Les équations intégrales (15) (16) (17) (5) (6) sont alors résolues pour les moitiés supérieures et inférieures du sillage, fermées par modélisation des demi-profils de vitesse (1) (2) (3) (4), et couplées sur la ligne moyenne. En cas de sillages décollés, le calcul visqueux local est résolu en problème inverse, les effets de déplacement et de courbure étant alors donnés, puis couplés itérativement au fluide parfait par relaxation semi-inverse [15].

Dans les zones de calcul visqueux en problème direct, la relaxation directe de couplage s'écrit en chaque noeud :

$$(21) \quad \begin{cases} \left[w^{n+1} - w^n = \omega \cdot \omega_1 \left(\tilde{w} - w^n \pm R \right) \right]_{(x,0\pm)} \\[2mm] 0 < \omega < 2 \qquad \omega_1 = \omega_{opt} \left[\mu_0^2 \left(\kappa_{max} \right) \right] \qquad \alpha_{max} = \frac{\pi}{\Delta x} \end{cases}$$

La vitesse normale $\widetilde{\mathcal{V}}$ est celle issue du calcul visqueux. Le symbole $^+$ correspond au cas du sillage. R est nul pour une couche limite, et représente l'erreur angulaire de positionnement du sillage à l'itération n, nulle à convergence. ω_{opt} est le coefficient de relaxation optimal associé au coefficient d'amplification μ_D de l'itération directe aux nombres d'ondes α , précisé en [15]. Dans les zones de problème visqueux inverse, la relaxation semi-inverse s'écrit :

$$\begin{cases} \left[\mathcal{V}^{n+1} - \mathcal{V}^n = \omega \cdot \omega_2 \left(\dfrac{d\widetilde{q}}{dx} - \dfrac{dq^n}{dx} \right) + \omega \cdot \omega_3 \left(\dfrac{d^2\widetilde{q}}{dx^2} - \dfrac{d^2q^n}{dx^2} \right) \right] (x, 0t) \\[4mm] 0 < \omega < 2 \qquad \omega_4 = \omega_{opt} \left[\mu_I \left(\alpha_{max} \right) \right] \qquad \mu_D \cdot \mu_I = 1 \end{cases}$$

(22)

La vitesse $\widetilde{q}$ est celle délivrée par le calcul visqueux inverse, q^n étant la vitesse déduite du fluide parfait. On utilise $\omega_2 = \omega_4$ et $\omega_3 = 0$ aux noeuds subsoniques, $\omega_3 = 0$ et $\omega_3 = \omega_4$ aux noeuds supersoniques. La dissymétrie du sillage agit ici sur le calcul des coefficients d'amplification $\mu_I^{\pm}$, voir [15].

3.3. Solveur transsonique bidimensionnel :

La résolution interactive des équations intégrales complètes (15) (16) (17) (5) (6) (20), fermées en turbulent par (1) (2) (3) (4), conduit à un solveur pour les écoulements compressibles portants avec décollements [15]. En stationnaire, le couplage fort inclut les couches limites laminaires-turbulentes avec transition douce, ainsi que les sillages dissymétriques, compte étant tenu des effets de déplacement, de courbure et de position du sillage. Les bulbes de décollement, ainsi que d'importants décollements de bord de fuite ont pu être résolus sur des profils d'ailes, sensiblement jusqu'à la portance maximale. L'approximation de l'équation du potentiel complète a été utilisée par le fluide parfait, résolu par différences finies selon les techniques de relaxation conservatives ou non-conservatives de Chattot [34], la relaxation (21) (22) du couplage visqueux étant opérée simultanément, de même que les adaptations visqueuses du maillage.

La figure 2 montre l'aspect du maillage à convergence pour un profil NACA0012 à basse vitesse et 16° d'incidence (portance maximale). La figure 3 montre l'aspect des lignes de courant du fluide parfait prédicteur et l'importance des effets de vitesse de transpiration sur le champ lointain, la valeur nulle de la fonction du courant, en pointillé, reconstituant indirectement la surface de déplacement exacte. La description analytique (1) des profils de vitesse visqueux correcteurs, respectant la dissymétrie du sillage, permet de reconstituer la solution composite prédicteur-correcteur globalement calculée. La figure 4 en donne l'exemple pour un décollement de bord de fuite sur la section NACA4412 à basse vitesse, au maximum de portance, sur le cas-test de la Conférence AFOSR-Stanford-1980-81 du "profil décroché". La distribution de pression correspondante apparaît figure 5.

Les figures 6 et 7 illustrent les résultats transsoniques typiques obtenus pour des profils supercritiques, sur les cas-test de Stanford-1980-81. La charge arrière, avec décollement éventuel, est généralement bien restituée. Les maillages standard sont cependant encore trop grossiers pour résoudre correctement la zone d'interaction choc-couche limite, le pas de discrétisation étant souvent du même ordre que la zone d'interaction complète. Sur ces maillages, le décollement induit par un choc n'est pas accessible au calcul. En l'absence de décollement, un simple excès de recompression après choc est généralement observé lorsque sont utilisées les techniques numériques conservatives, à priori cependant les plus rigoureuses (figure 7).

3.4. Solveur incompressible - Profils multi-corps :

La même méthode numérique de calcul et de cou. ...ge des couches limites ou sillages a été mis en oeuvre pour les profils multiples, en incompressible. Elle utilise pour le fluide parfait potentiel une méthode de singularités très précise développée par Néron [35]. Les itérations de couplage sont effectuées après détermination de la matrice d'influence du fluide parfait. La méthode est valide tant que les couches limites et sillages multiples ne sont pas confluents dans la zone utile de l'écoulement. La figure 9 illustre les distributions de pression obtenues par Néron en utilisant le couplage visqueux, dans un cas difficile comportant bec et volet, figure 8. Des décollements importants sont calculés à l'intrados du bec, à l'intrados du corps principal à forte charge arrière, à l'extrados du volet à demi-décroché. La géométrie réelle du bec, présentant une arête vive et une cavité à l'intrados, a cependant dû être adoucie (exclusivement dans la région d'eau morte, bien en amont du recollement) pour réaliser le calcul, figure 8.

3.5. Culots - Volets spoilers :

Le solveur transsonique a été aménagé [36] pour modéliser les problèmes de culot ou de spoilers, ceux-ci étant assimilés à des marches descendantes, figure 10. Par simplicité, le calcul potentiel est réalisé sur une géométrie approchée exempte de discontinuités, l'erreur angulaire de géométrie étant transformée en une vitesse de transpiration à la paroi équivalente, qui est cumulée avec celle induite par le couplage fort aux couches visqueuses. Des volumes de contrôle globaux évaluent les surépaississements brusques des couches visqueuses aux stations de discontuités, induisant ou non le décollement. Le re-

collement est calculé, qu'il intervienne à la paroi ou dans le sillage. Les figures 11,
12, 13 illustrent les résultats obtenus dans le cas d'un profil épais légèrement super-
critique, présentant une portance négative induite par braquage de 10° d'un spoiler d'ex-
trados. L'écoulement est proche du décollement à l'articulation du spoiler. Un décolle-
ment important est induit à l'aval du spoiler, un plateau de pression étant assez bien
prévu, de même que le rejet du recollement dans le sillage épais.

3.6. Ailes transsoniques en flèches infinies

Une extension du solveur transsonique aux écoulements décollés quasi-tridimensionnels tur-
bulents a également été obtenue, présentement dans l'approximation symétrique du sillage.
La méthode intégrale visqueuse introduit la modélisation pleinement tridimensionnelle des
profils de vitesse incluant les courants de retour (1). Elle résout en problème inverse
les zones décollées avec ou sans courants de retour. La technique numérique reste cependant
quasi-bidimensionnelle. Le couplage fort est réalisé par une extension des méthodes de re-
laxation directe et semi-inverse, dans lesquelles l'effet de flèche des calculs visqueux
et non-visqueux vient modifier le contrôle local et automatique de la stabilité numérique.
Les figures 14, 15 montrent des résultats obtenus par Blaise [37] pour une aile supercri-
tique sans décollement. Si la comparaison à l'expérience est peu significative en raison
de la tridimensionnalité expérimentale, la figure 15 indique qu'une différence sensible
existe entre les solutions bidimensionnelles et quasi-tridimensionnelles recalées.

3.7. Profils transsoniques en instationnaire :

Une première technique numérique consistante, en instationnaire, pour résoudre les équations
intégrales bidimensionnelles (15) (16) (17), fermées par (1) (2) (3) (4), avec couplage
fort à l'écoulement pseudo-fluide-parfait, a été définie par Le Balleur, Girodroux-Lavigne
[38], dans le cas des profils transsoniques exempts de décollement. La méthode résout à
chaque pas de temps les équations intégrales instationnaires en problème direct par une
technique implicite marchant d'amont en aval. Elle utilise pour le fluide parfait une
méthode implicite de petites perturbations transsoniques pour l'équation du potentiel
instationnaire, développée par Couston, Angelini. Le couplage est obtenu par simple ité-
ration sous-relaxée de la vitesse de transpiration déterminée par le calcul visqueux des
couches limites et du sillage, la convergence de l'itération étant exigée à chaque pas de
temps (couplage fort consistant). La figure 16 illustre les distributions de pression ins-
tationnaires obtenues pour le profil NACA64A010 en régime supercritique, en oscillation
de tangage à 25% de corde, à la fréquence réduite k = 0.40 basée sur la corde, le premier
harmonique étant analysé en module et phase.

3.8. Voilures transsoniques

Bien que la Formulation Déficitaire ainsi que les équations intégrales puissent être aisé-
ment écrites en tridimensionnel, et fermées par la modélisation générale (1) (2) (3) (4),
l'extension en 3D du solveur transsonique bidimensionnel, capable de calculer les décolle-
ments, soulève encore des difficultés non résolues au niveau des techniques numériques
intimement liées que nécessitent le calcul visqueux et le couplage fort.

Dans les cas non-décollés, des résultats tridimensionnels sont cependant déjà accessibles
par des techniques numériques plus simples. Les figures 17, 18 illustrent les résultats
de la méthode définie par Lazareff, Le Balleur [39] pour les voilures transsoniques. Le
couplage fort sur la voilure est obtenu par simple itération sous-relaxée de la vitesse
de transpiration déterminée après calcul des couches limites (sillage exclu). La méthode
utilise la technique non-conservative de Chattot [34] pour l'équation du potentiel, et la
méthode de couche limite de Cousteix [40]. La figure 17 visualise par sections la direction
du frottement à l'intrados, où l'effet de charge arrière est visible, pour la voilure
DFVLR-F4 en supercritique. La figure 18 visualise la pression.

4. EXEMPLE D'EXTENSION A L'AERODYNAMIQUE INTERNE EN TRANSSONIQUE

Numériquement, l'ensemble des exemples de calcul précédents peut être directement mis en
oeuvre pour des écoulements internes, du type canal ou profils d'aubes notamment, aussi
longtemps que l'approximation potentielle de l'écoulement externe est utilisable, et que
les couches visqueuses multiples, décollées ou non, ne sont pas confluentes. Si nécessaire,
une modélisation plus fine de l'entrainement turbulent pour les effets de turbulence ex-
terne, de rotation ou de transition, peut être envisagée.

L'aspect numérique le plus nouveau est sans doute le nécessaire recours à la résolution
des équations d'Euler complètes à l'apparition du blocage, ainsi que l'importance accrue
de la viscosité et des décollements pour déterminer le positionnement et la structure des
réseaux d'ondes de choc, à contre-pression donnée. Le recours aux équations d'Euler sou-
lève d'abord des problèmes nouveaux de conditions aux limites, liés à la présence d'une
"vitesse de transpiration" des parois dans la Formulation Déficitaire. D'autre part, la
convergence relativement lente sur des maillages fins des techniques pseudo-instationnaires
[20] résolvant les équations d'Euler rend assez peu performantes les techniques numériques
de couplage existantes, par relaxation, fondées sur une succession de résolutions station-
naires du fluide parfait.

4.1. <u>Conditions aux limites supplémentaires des équations d'Euler</u> :

La Formulation Déficitaire des équations NS (10) (11) (12) (13) conduit pour le prédicteur
pseudo-fluide-parfait à une condition aux limites de vitesse normale non-nulle sur les
parois, la donnée de cette vitesse normale étant suffisante pour déterminer l'écoulement
dans l'approximation potentielle. Dans le cas des équations d'Euler stationnaires, la
vitesse normale reste encore une condition aux limites suffisante pour les zones où la
viscosité induit un effet de suction à la paroi. Dans les zones d'injection au contraire,
des conditions aux limites supplémentaires doivent être imposées pour déterminer les niveaux
d'entropie et d'enthalpie. Cette difficulté est en particulier évoquée par Johnston, Sockol
[40], Murman, Bussing [41], Whitfield et al. [42].

Ce problème ne constitue cependant qu'une difficulté apparente, donnant au contraire une
marge d'adaptation accrue lorsqu'un modèle simple est sélectionné pour calculer le correc-
teur visqueux déficitaire. Le problème est lié à la non-unicité des solutions "Euler" ca-
pables de représenter le fluide visqueux dans une solution composite faisant appel à un
problème "correcteur visqueux" complémentaire. Si la Formulation Déficitaire NS complète
est résolue, les conditions aux limites supplémentaires du pseudo-fluide-parfait sont in-
déterminées, un choix quelconque de l'entropie du calcul prédicteur pouvant toujours être
compensé, par résolution des équations déficitaires complètes (11) au correcteur.

Si au contraire une modélisation simple est appliquée au correcteur visqueux, le choix de
l'entropie à la paroi dans le calcul prédicteur doit être optimisé de façon à minimiser
les approximations mises en jeu. Au premier ordre par exemple, équations (14), l'entropie
non-visqueuse à la paroi devra être choisie de façon à minimiser l'écart des pressions vis-
queuses et non-visqueuses, de telle sorte que $\bar{p}$ (x, z, t,) $\cong$ p (x, z, t).

Dans le cas des équations intégrales déficitaires, un critère d'optimisation supplémentaire
sera celui de la validité de la modélisation adoptée pour les profils de vitesse défici-
taires (1) (2) (3). Dans les premiers résultats de calcul présentés ci-dessous, on a pro-
visoirement adopté, faute d'une optimisation précise, et par analogie avec les calculs dé-
veloppés dans l'approximation potentielle, une condition de dérivée normale nulle de l'en-
tropie à la paroi, ce qui est sensiblement équivalent à une extrapolation suivant la normale.

4.2. <u>Exemple d'un canal transsonique avec interaction choc-couche limite</u> :

La méthode, développée conjointement avec D. Blaise, utilise exactement les mêmes modules
numériques de calcul visqueux et de couplage que le solveur transsonique bidimentionnel
décrit en 3.3., voir [15]. Il résout les équations intégrales déficitaires stationnaires (15)
(16) (17) avec deux équations de transport turbulent (5) (6), fermées par la modélisation
des profils (1) (2) (3) (4). Le couplage fort est obtenu par les méthodes de relaxation di-
rectes et semi-inverses avec contrôle automatique de la stabilité numérique. L'itération de
couplage est effectuée en utilisant pour les équations d'Euler des cycles d'environ 100 pas
de temps de la méthode pseudo-instationnaire explicite à enthalpie totale constante de
Veuillot, Viviand [44].

La configuration calculée est celle d'un diffuseur plan symétrique à faible divergence
conduisant à un choc de recompression au voisinage de M = 1.3, expérimenté par Délery (43),
et ayant servi de support à des calculs par solveur NS (20). La figure 19 montre le do-
maine utile du calcul appliqué à la moitié inférieure du diffuseur, et le maillage fin
nécessaire à la résolution de la zone amont de l'interaction choc-couche limite en régime
turbulent. Compte tenu de la faible divergence de veine, la valeur numérique de la contre-
pression, supposée uniforme dans la section de sortie, a du faire l'objet d'un ajustement
délicat par essais successifs, afin de positionner au mieux l'onde de choc par rapport à
l'expérience. Un positionnement plus optimisé reste cependant possible.

Les figures 20 et 21 montrent les distributions de pression obtenues à la paroi pour deux
calculs effectués, l'un avec un entrainement turbulent d'équilibre, fig. 20, l'autre avec
le modèle à deux équations, fig. 21, qui semble améliorer la comparaison à l'expérience.
Les figures 22, 23 comparent aux mesures les grandeurs intégrales d'épaisseur de dépla-
cement et de paramètre de forme. La figure 25 montre les lignes isobares du pseudo-
fluide-parfait, qui constituent une approximation des lignes isobares visqueuses. On note
en particulier la partie incurvée vers l'amont du pied de choc, associée à l'influence
amont visqueuse, l'étalement de la compression au niveau de la paroi, le gradient de
pression normal non-nul dans la couche visqueuse au pied du choc. La figure 25 montre
les lignes iso-Mach de la solution composite reconstituée avec les profils de vitesse
turbulents (1). Enfin, la figure 26 montre que les lignes isochores de la solution nu-
mérique composite présentent une analogie étroite avec celles déduites de l'expérience
par un interférogramme en teinte plate.

5. <u>CONCLUSIONS</u>

Les progrès des méthodes numériques d'interaction permettent de réaliser, tout en valo-
risant les techniques de fluide parfait existantes, des solveurs indirects pour calculer
globalement (ou simuler) une large part des écoulements complexes à grand nombre de Reynolds,
en aérodynamique externe ou interne. Ces méthodes offrent trois voies principales et complé-
mentaires de développements :

(i) le couplage par zones ou sous-domaines, avec raccordement des conditions aux limites
sur les contours, capable d'intégrer localement des solveurs directs NS.

(ii) les techniques de couches minces interactives, avec recouvrement des domaines de
calcul visqueux et non-visqueux, fondées sur le concept d'une approximation à la
"Formulation Déficitaire", capables d'intégrer les techniques de couche-limite et
d'offrir des solveurs économiques incluant le décollement et l'interaction choc-
couche limite.

(iii) la génération de solveurs indirects NS composites, fondés sur la décomposition en
sous-problèmes numériques de type visqueux et non-visqueux couplés, avec recouvre-
ment des domaines de calcul, capable d'intégrer les méthodes numériques de (ii) et
de résoudre le problème NS par des techniques de relaxation.

Parmi les solveurs économiques du niveau (ii), des résultats très performants peuvent être
obtenus par couplage fort d'équations intégrales déficitaires aux techniques numériques de
fluide parfait, avec modélisation des profils de vitesse visqueux et de l'entrainement tur-
bulent hors-équilibre. Ce modèle autorise le calcul des interactions fortes multiples, in-
cluant les problèmes de décollement, d'interaction choc-couche limite, de sillage ou de
culot. Il conduit pour ces problèmes au solveur numérique à discrétisation minimale, per-
mettant donc de maximiser la complexité des écoulements accessibles au calcul.

Dans cette optique, des résultats nouveaux très encourageants ont été obtenus par une
méthode intégrale déficitaire couplée à des équations d'Euler, pour le traitement des
écoulements internes transsoniques bloqués, dans le cas d'une interaction choc-couche
limite avec léger décollement.

REFERENCES

[1]   METHA U., LOMAX H. - Reynolds-averadged Navier-Stokes computations of tran-
sonic flows. The state of the art - Proceed. Symp. Transonic Perspective,
ed. D. Nixon, Progress in Astronautics vol. 81 (1982) -

[2]   VIVIAND H. - Traitement des problèmes d'interaction Fluide-parfait - Fluide
visqueux en écoulement bidimensionnel compressible à partir des équations
de Navier-Stokes - AGARD-LS-94 (1978) -

[3]   LE BALLEUR J.C. - Calcul des écoulements à forte interaction visqueuse au
moyen de méthodes de couplage - AGARD-CP-291 (1981), Introduction Générale,
ou ONERA-TP 1980-121 -

[4]   LE BALLEUR J.C., PEYRET R., VIVIAND H. - Numerical studies in high Reynolds
number aerodynamics - Computers and fluids, vol. 8, n° 1, p. 1-30 (March 1980) -

[5]   MONNERIE B., QUINN B. - Editors, AGARD-CP-291 (1981), on Computation of Viscous
Inviscid Interactions, Colorado-Springs -

[6]   LE BALLEUR J.C. - Technical evaluation report on the FDP Symposium on Computa-
tion of Viscous-Inviscid Interactions - AGARD-AR-171 (Oct. 1981) -

[7]   KLINE S.J. - Editor, Proceedings of the 1980-81-AFOSR-HTTM-STANFORD Conference
on Complex turbulent flows, Stanford University, California, USA (Oct. 1981) -

[8]   CEBECI T. - Editor, Proceedings of the 2nd Symposium on Numerical and Physical
Aspects of Aerodynamic Flows, California St. University, Long Beach, USA
(Jan. 1983) - (and Springer Verlag, to appear) -

[9]   LE BALLEUR J.C. - Viscid-Inviscid Coupling Calculations for Two and Three-
dimensional flows - Lectures series 1982-04, Von Karman Institute, Computa-
tional fluids dynamics, Belgium, (March 1982) -

[10]   LE BALLEUR J.C. - Numerical Viscid-Inviscid interaction in steady and unsteady
flows - Proceed. 2nd Symp. Numerical-Physical Aspects of Aerodynamic Flows,
California State University, Long Beach, USA (Jan. 1983), or ONERA-TP-1983-8,
(Springer Verlag, to appear) -

[11]   DODGE P.R. - Numerical method for 2D and 3D flows - AIAA Journal, Vol. 15,
n° 7, p. 961-965 (July 1977) -

[12]   KHOSLA P.K., RUBIN S.G. - A composite velocity procedure for the compressible
          Navier-Stokes equations - AIAA Paper n° 82.0099 (Jan. 1982) -

[13]   LOCK R.C., FIRMIN M.C.P. - Survey of techniques for estimating viscous effects
          in external aerodynamics - RAE Tech. Memo. Aero. 1900, (April 1981) -

[14]   MELNIK R.E. - Turbulent interactions on airfoils at transonic speeds - Recent
          developments - AGARD-CP-291, Lecture 10, (1981), Colorado-Springs -

[15]   LE BALLEUR J.C. - Strong matching method for computing transonic viscous flows
          including wakes and separations. Lifting airfoils - La Recherche Aérospatiale
          1981-3, p. 21-45, English and French editions, (May 1981) -

[16]   LE BALLEUR J.C. - Couplage visqueux - non visqueux : Analyse du problème
          incluant décollements et ondes de choc - La Recherche Aérospatiale 1977-6,
          p. 349-358, (Nov. 1977), English translation ESA-TT-476 -

[17]   LE BALLEUR J.C. - Couplage visqueux-non visqueux : Méthode numérique et
          applications aux écoulements bidimensionnels transsoniques et supersoniques -
          La Recherche Aérospatiale 1978-2, p. 67-76, (March 1978), English translation
          ESA-TT-496 -

[18]   BRUNE G.W., RUBBERT P.E., FORESTER C.K. - The analytic of flow fields with
          separation by numerical matching - AGARD-CP-168 (1975) -

[19]   SEGINER A., ROSE W.C. - An approximate calculation of strong interaction over
          a transonic airfoil including strong schock-inducted flow separation - AIAA
          Paper n° 76-333, San Diego (July 1976) -

[20]   CAMBIER L., GHAZZI W., VEUILLOT J.P., VIVIAND H. - Une approche par domaines
          pour le calcul d'écoulements compressibles - Proceed. 5th Symp. Computing
          Methods in Applied Sciences and Engineering, Glowinsky and Lions ed., North-
          Holland - INRIA (1982) -

[21]   CROCCO L., LEES L. - A mixing theory for the interaction between dissipative
          flows and nearly iseutropic streams - J. Aero. Sci., vol. 19, n° 10,
          (Oct. 1952) -

[22]   CARTER J.E., VATSA V.N. - Analysis of separated boundary layer flows -
          Proceed 8th Conf. Num. Methods in Fl. Dyn., Aachen, Lecture notes in
          Physics, Springer-Verlag (June 1982) -

[23]   WERLE M.J. - Compressor an Turbine Blade Boundary layer separation -
          61st AGARD- PEP Meeting on Viscous Effects in turbomachines, Copenhagen,
          Denmark (June 1983) -

[24]   WILMOTH R.G., DASH S.M. - A viscous-inviscid interaction model of jet
          entrainment - AGARD-CP-291, Paper 13, (1981) -

[25]   COSNER R.R. - Relaxation solution for Viscous transonic flow about fighter-
          type Forebodies and Afterbodies - AIAA Paper 82-0252, Orlando (Janv. 1982) -

[26]   COLES P.E. - The law of the wake in turbulent boundary layer - J.F.M., Vol. 1,
          Part. 2, (1956) -

[27]   WERLE M.J., VATSA V.N. - New method for supersonic boundary layers separations-
          AIAA Journal Vol. 12, n° 11, (Nov. 1974) -

[28]   VELDMAN A.E.P. - New, quasi-simultaneous method to calculate interacting boun-
          dary layers - AIAA J., Vol. 19, n° 1, p. 79-85 (Janv. 1981) -

[29]   MOSES H.L., JONES R.R., O'BRIEN W.F. - Simultaneous solution of the boundary
          and freestream with separated flow - AIAA J., Vol. 16, n° 1, p. 61-66,
          (Jan. 1978) -

[30]   GILMER B.R., BRISTOW D.R. - Analysis of stalled airfoils by simultaneous
          perturbations to viscous and inviscid equations - AIAA Paper n° 81-1239,
          Palo-Alto, (June 1981) -

[31]   CARTER J.E. - A new boundary layer iteration technique for separated flow -
          4th Comput. Fl. Dyn. Conf., AIAA Paper n° 79-1450 (July 1979) -

[32]   WIGTON L.B., HOLT M. - Viscous Inviscid interaction in transonic flow -
          5th Comput. Fl. Dyn. Conf., AIAA Paper n° 81-1003, Palo Alto (June 1981) -

[33]   WIGTON L.B., YOSHIHARA H. - Viscous-Inviscid interaction with a three-
          dimensional inverse boundary layer code - Proceed. 2nd Symp. Physical
          Numerical Aspects Aerodyn. Flows, California State University, Long Beach,
          USA, (Jan. 1983) -

[34]   CHATTOT J.J., COULOMBEIX C., TOME C. - Calcul d'écoulements transsoniques
          autour d'ailes - La Recherche Aérospatiale n° 1978-4, p. 143-159, English
          Transl. ESA-TT-561 (July 1979) -

[35]   LE BALLEUR J.C., NERON M. - Calcul d'écoulements visqueux décollés sur
         profils d'ailes par une approche de couplage - AGARD-CP-291, Paper 11,
         (1981) -

[36]   LE BALLEUR J.C. - Calculation method for transonic separated flows over
         airfoils including spoiles effects - Proceed. 8th Conf. Num. Meth. un
         Fl. Dyn., Aachen, Lecture Notes in Physics, Springer-Verlag (June 1982),
         or ONERA-TP 1982-66 -

[37]   BLAISE D. - Mise en oeuvre et développement d'une méthode de couplage fort
         pour le calcul d'écoulements autour d'ailes en flèches infinies -
         Doct. Thesis 3e Cycle, Université Lille 1 (1982) -

[38]   COUSTON M., ANGELINI J.J., LE BALLEUR J.C., GIRODROUX-LAVIGNE P. - Prise
         en compte d'effets de couche limite instationnaire dans un calcul bidi-
         mensionnel transsonique - AGARD-CP-296, Aix-en-Provence, (1981) -

[39]   LAZAREFF M., LE BALLEUR J.C. - Computation of three-dimensional viscous flows
         on transonic wings via boundary layer - inviscid flow interaction - La
         Recherche Aérospatiale n° 1983-3, English and French edition (May 1983),
         to be published -

[40]   JOHNSTON W., SOCKOL P. - A viscouc-inviscid interactive procedure for
         rotational flow in cascades of Two-dimensional airfoils of arbitrary shape -
         AIAA Paper n° 83-0256, Reno, (Jan. 1983) -

[41]   MURMAN E.M., BUSSING R.A. - On the coupling of boundary layer and Euler
         equation solutions. Proceed. 2nd Symp. Numerical Physical Aspects Aerodyn.
         Flows, California State University, Long Beach, USA, (Jan. 1983) -

[42]   WHITFIELD D.L., THOMAS J.J., JAMESON A., SCHMIDT W. - Computation of tran-
         sonic viscous-inviscid interacting flow - Proceed. 2nd Symp. Numerical
         Physical Aspects Aerodyn. Flows, California State University, Long Beach,
         USA, (Jan. 1983), (Springer Verlag to appear) -

[43]   DELERY J.M. - Experimental investigation of turbulence properties in Transonic
         Shock/Boundary-layer interactions - AIAA Journal, Vol. 21, n° 2, p. 180-185,
         (Febr. 1983) -

[44]   VIVIAND H., VEUILLOT J.P. - Méthodes Pseudo-Instationnaires pour le calcul
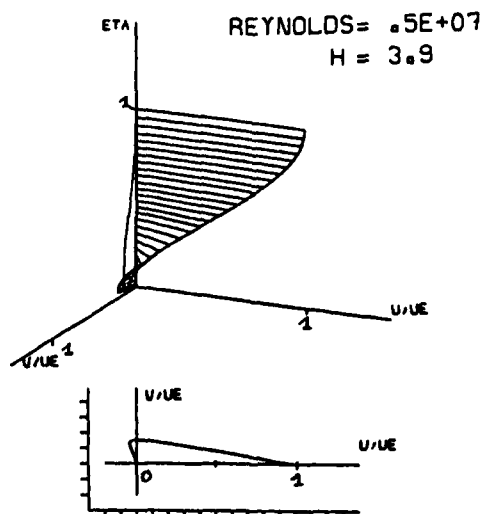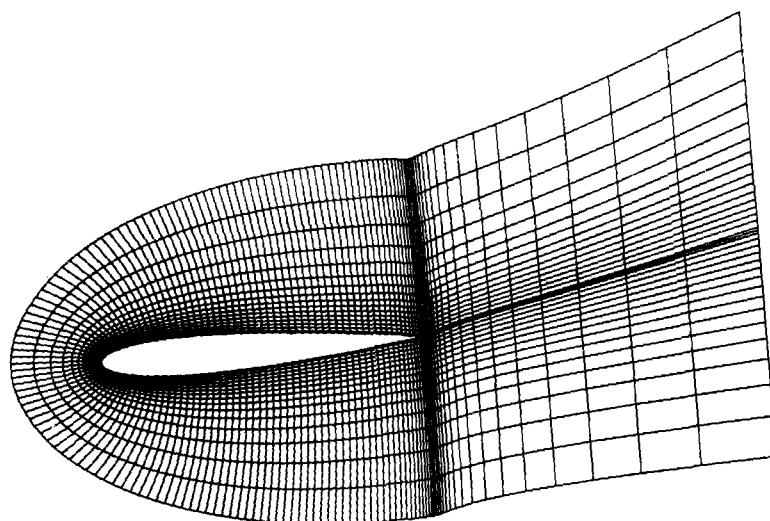   d'écoulements transsoniques - ONERA Publication n° 1978-4 (1978) -

Fig. 1 — Modélisation des profils de vitesse turbulents.

NACA0012 I=16 - JCFOIL9 - 181X27

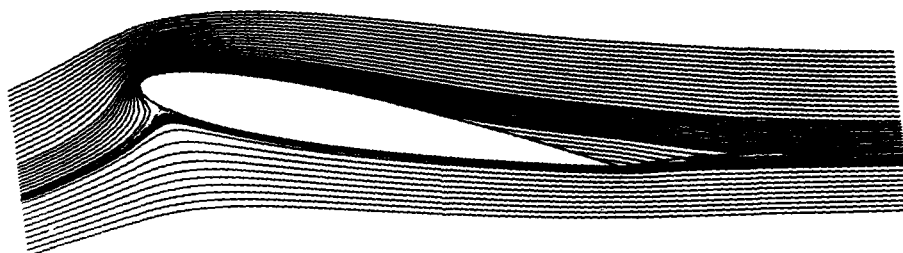Fig. 2 — Maillage adapté aux effets visqueux. Profil NACA 0012 ($M = 0,116$, $\alpha = 16°$, $R = 2 \times 10^6$).

Fig. 3 — Lignes de courant du prédicteur fluide parfait couplé. (NACA 0012, $M = 0,116$, $\alpha = 16°$, $R = 2 \times 10^6$).
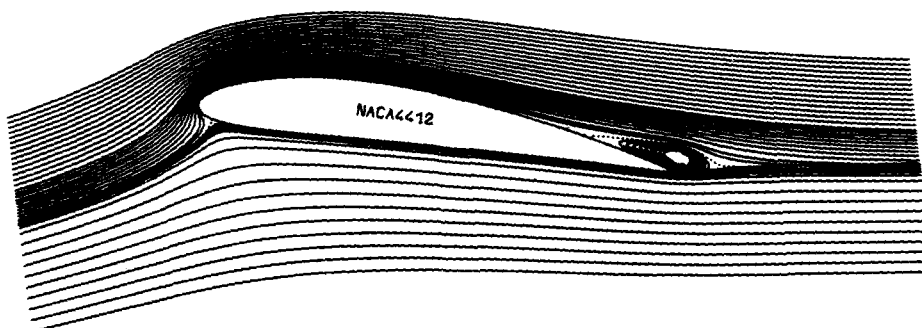

NACA4412

Fig. 4 — Solveur transsonique à basse vitesse. Solution composite (NACA 4412, $V = 20$ m/s, $\alpha = 13,5°$, $R = 1,5 \times 10^6$).
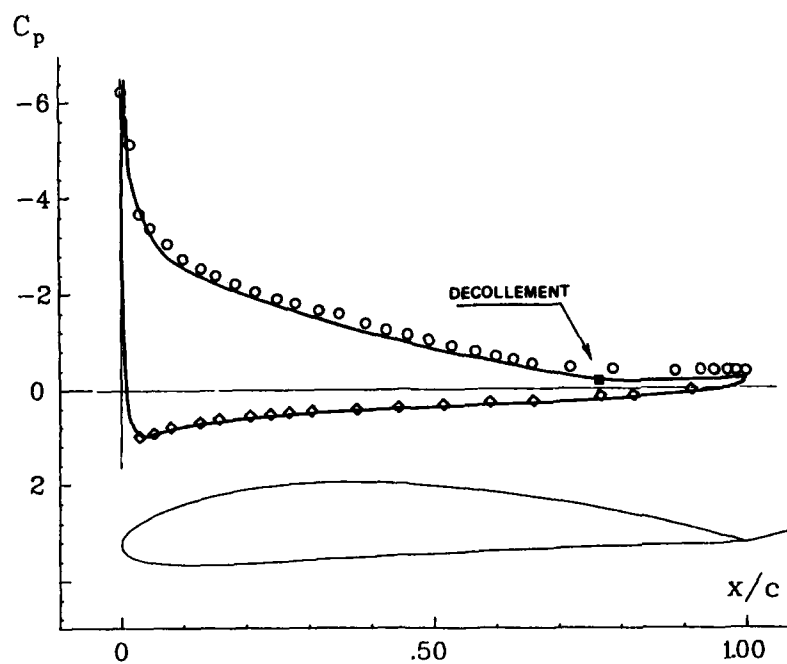
Fig. 5 – Distribution de pression (NACA 4412, V = 20 m/s, α = 13,6°, R = 1,5 x 10⁴).
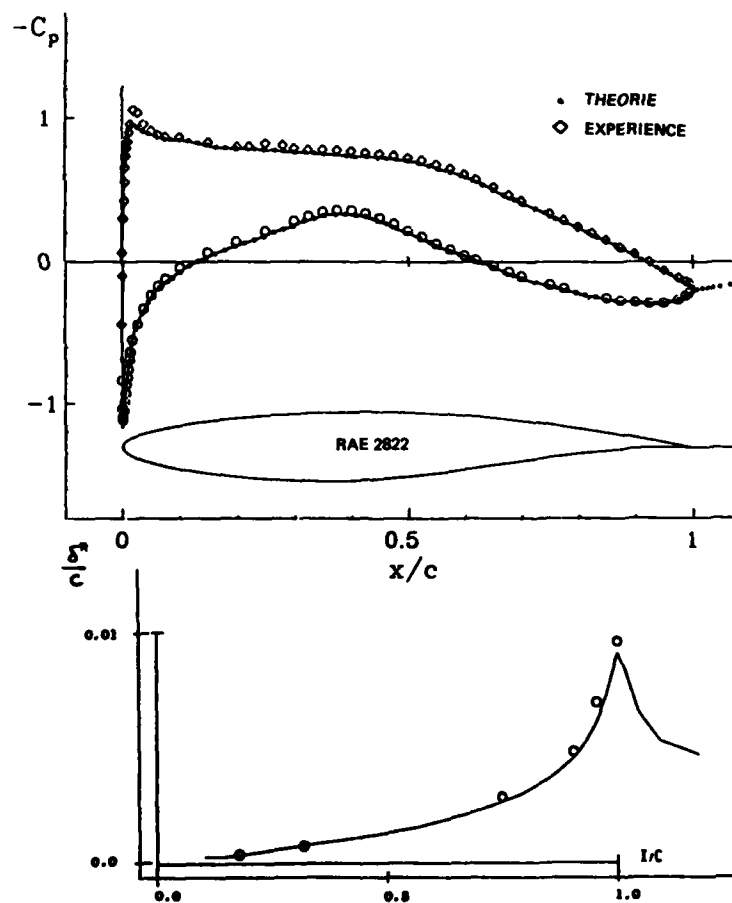
Fig. 6 – Solveur transsonique en subcritique (RAE 2822, M = 0,676, α = 2,40°, R = 6,7 x 10⁴).
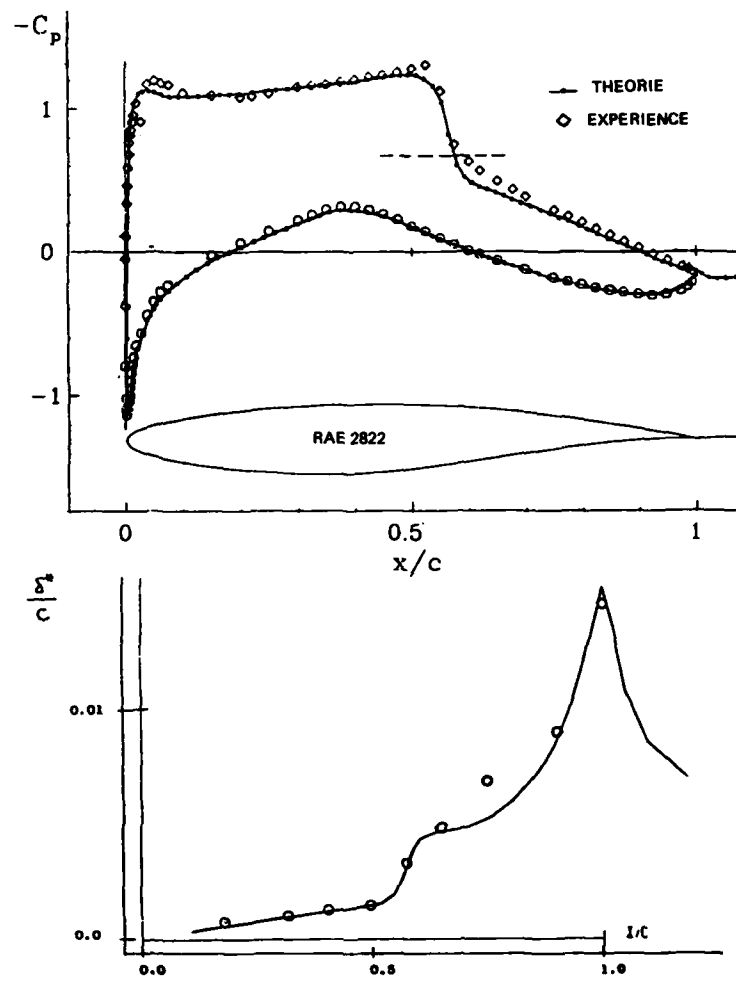
Fig. 7 — Solveur transsonique en supercritique (RAE 2822, M = 0,730, α = 3,19°, R = 6,5 x 10⁶).
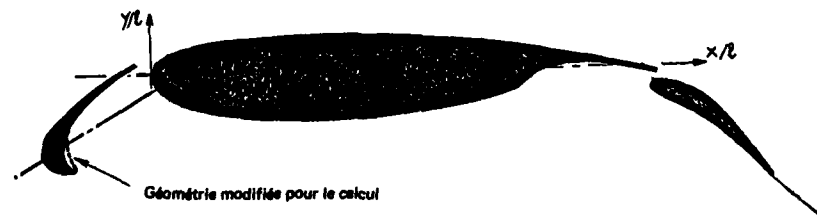
Fig. 8 — Profil RA 16SC1 avec bec et volet (40°).
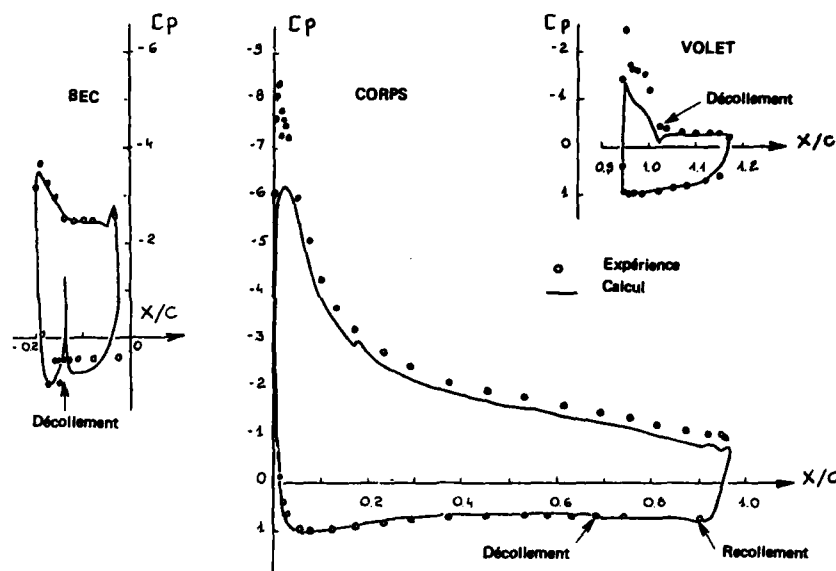
Fig. 9 — Distribution de pression sur le profil triple-corps de la figure 8 en incompressible $(\alpha = 12°, \delta_{volet} = 40°, R \cong 2 \times 10^6)$.
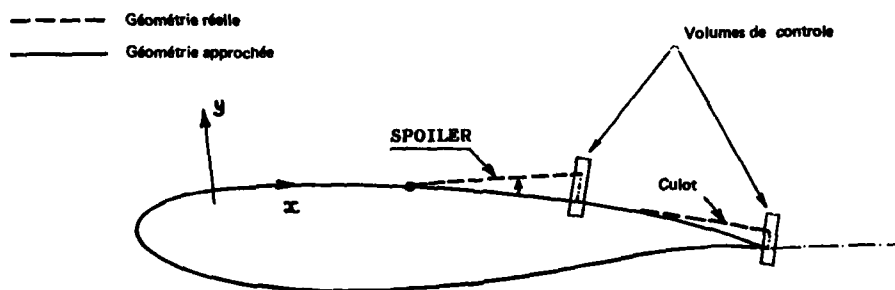
Fig. 10 — Modélisation des culots et volets spoiler.
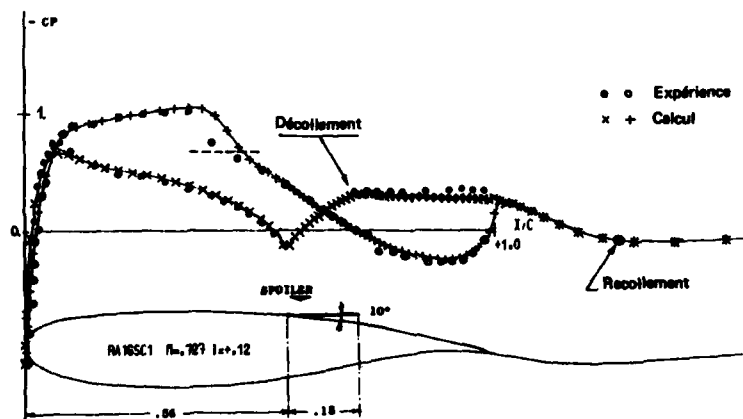
Fig. 11 — Solveur transsonique avec volet spoiler sur le profil supercritique RA 16SC1
$(M = 0,727, \alpha = 0°, R = 4,2 \times 10^6, \delta_{SPOILER} = 10°)$.
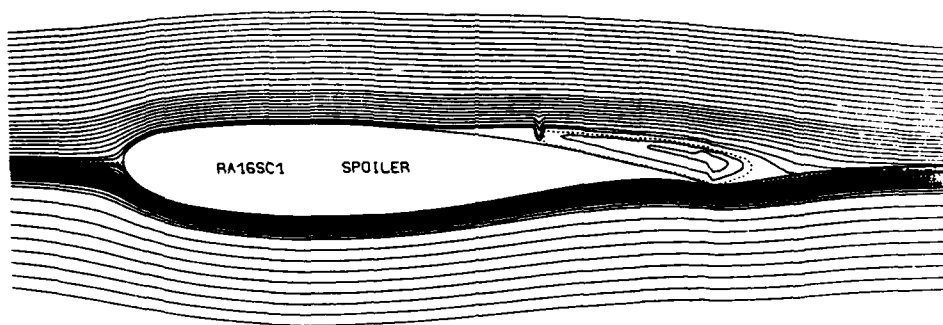
Fig. 12 – Solveur transsonique avec volet spoiler. Lignes de courant de la solution composite
(RA 16SC1, M = 0,727, α = 0°, R = 4,2 x 10⁶, δSPOILER = 10°).
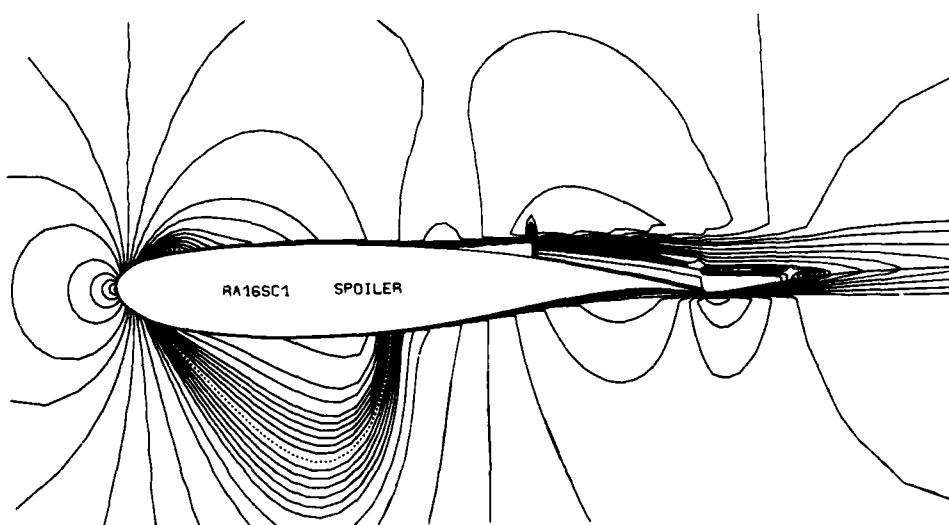
Fig. 13 – Solveur transsonique avec volet spoiler. Lignes Iso-Mach (RA 16SC1, M = 0,727, α = 0°, R = 4,2 x 10⁶, δSPOILER = 10°).
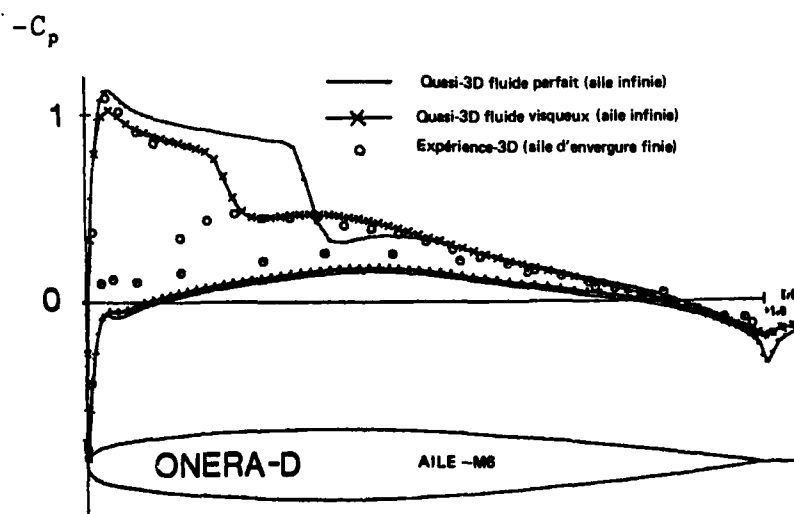
Fig. 14 – Solveur transsonique quasi-tridimensionnel. Aile en flèche infinie
(ONERA-D, M = 0,84, α = 2°, R = 2,5 x 10⁶, φ = 30°).

Fig. 15 – Comparaison des calculs bidimensionnel et quasi-tridimensionnel sur l'aile en flèche infinie (ONERA-D, $M = 0,84$, $\alpha = 2°$, $R = 2,5 \times 10^6$, $\varphi = 30°$).
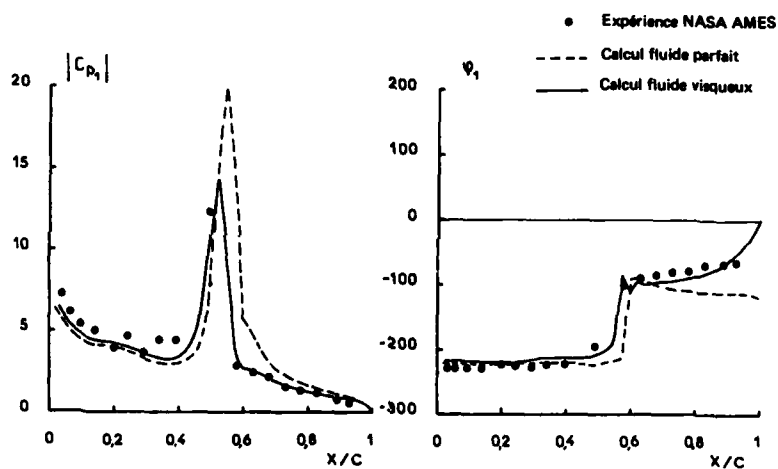
Fig. 16 – Calcul instationnaire consistant sur profil supercritique oscillant en tangage: Pression. Premier harmonique. (NACA64A010, $M = 0,80$, $\alpha = 0°$, $R = 12 \times 10^6$, $k = 0,40$).
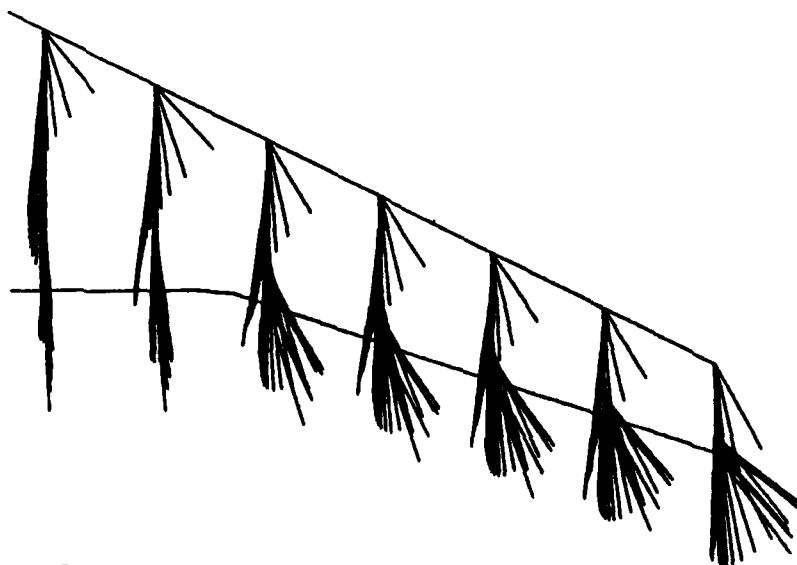
Fig. 17 – Calcul tridimensionnel transsonique sur l'aile DFVLR-F4. Direction du frottement pariétal à l'intrados. ($M = 0,75$, $\alpha = 0,1°$, $R = 3 \times 10^6$).
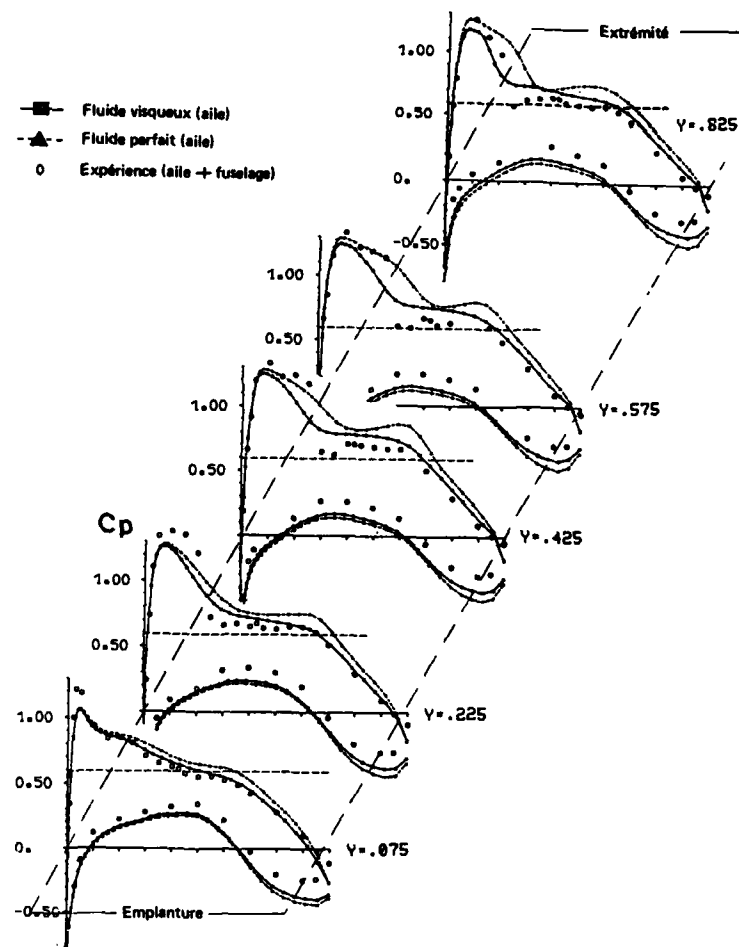
Fig. 18 — Distributions de pression calculées sur l'aile DFVLR-F4 (M = 0,75, α = 0,1°, R = 3 x 10⁶).
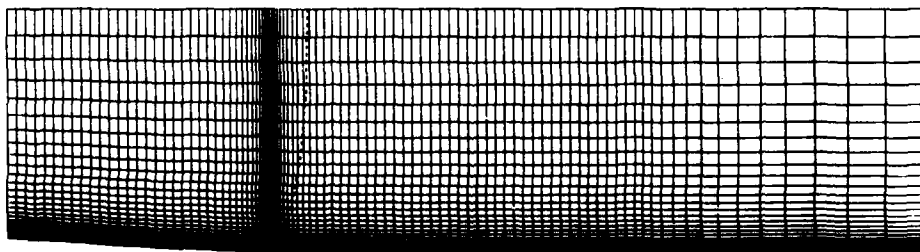
Fig. 19 — Demi-maillage pour le calcul de l'interaction couche limite-onde de choc dans un diffuseur transsonique.
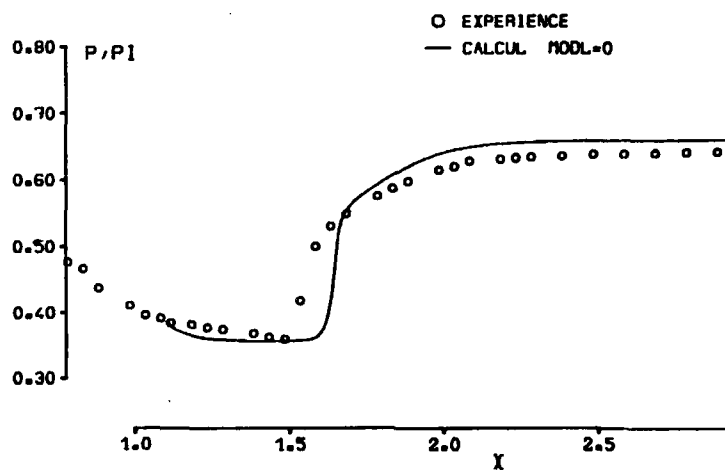
Fig. 20 — *Distribution de pression à la paroi du diffuseur dans la zone d'interaction choc-couche limite. Calcul couplé avec entraînement turbulent d'équilibre.*
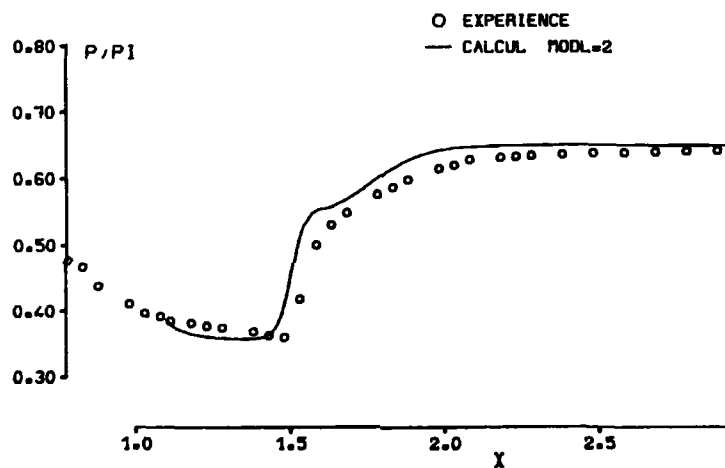
Fig. 21 — *Distribution de pression à la paroi dans la zone d'interaction choc-couche limite. Calcul couplé avec modèle à deux équations de transport pour l'entraînement.*
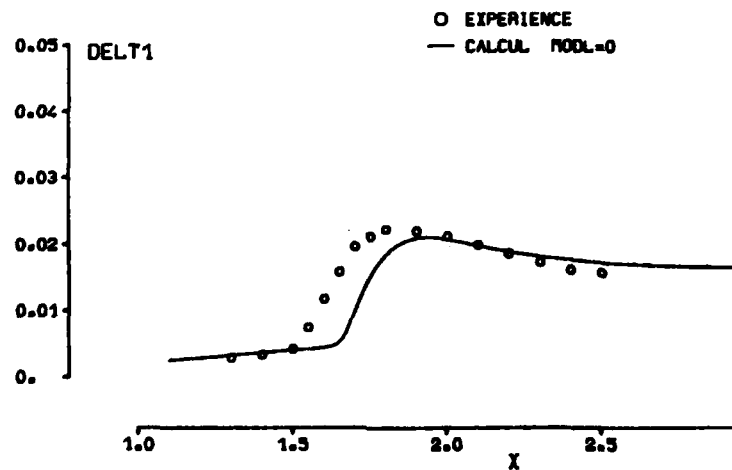
Fig. 22 — *Epaisseur de déplacement.*
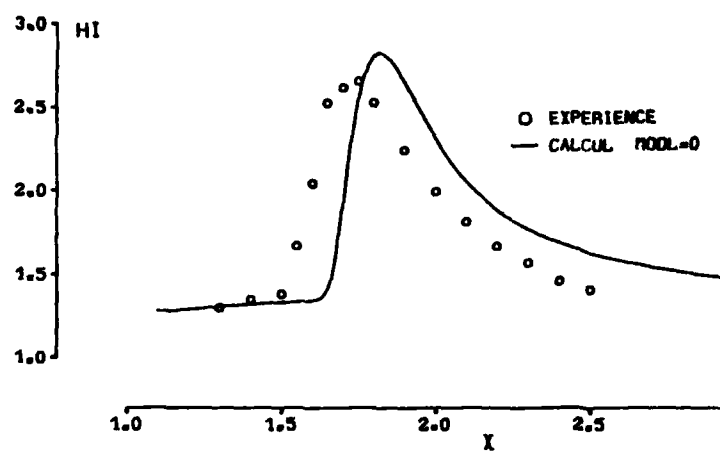
Fig. 23 — Paramètre de forme incompressible.
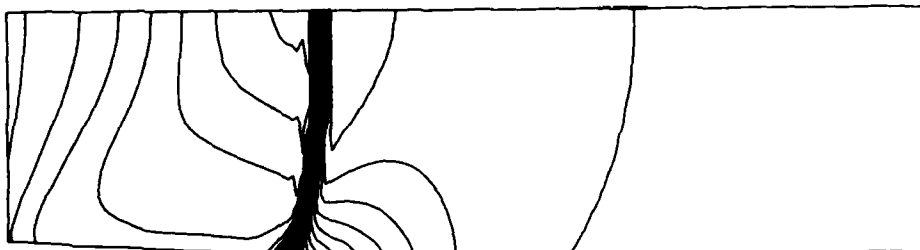
Fig. 24 — Lignes isobares. Champ du pseudo-fluide-parfait couplé.

Fig. 25 — Lignes Iso-Mach. Solution composite.

Fig. 26 — Lignes isochores de la solution composite et comparaison à l'expérience par interférogramme.

DISCUSSION

Ph.Ramette.Fr

(1) Dans le cas de la résolution des équations d'Euler, vous avez fait une distinction entre les zones d'émission à la paroi pour lesquelles il faut se donner 3 valeurs à la paroi (vitesse normale, pression totale et température totale) et les zones de succion pour lesquelles la vitesse normale seule est suffisante. Comment expliquez-vous cette dissymétrie de traitement des zones d'émission et de succion?

(2) Avec la méthode de couplage semi-directe (non visqueux direct et visqueux inverse), il est possible de traiter les cas de décollement. Est-ce que cette méthode permet également le traitement des chocs en resserrant le maillage au niveau de l'onde de choc?

Si oui, est-ce également le cas pour un écoulement entre deux parois?

Réponse d'Auteur

(1) La "Formulation Déficitaire" impose au moins une condition au limites "visqueuse" au fluide-parfait, celle d'une vitesse normale non-nulle déterminée par les équations visqueuses. La dissymétrie de traitement des conditions aux limites entre les zones d'injection et de succion, dans le cas des équations d'Euler complètes, résulte seulement de l'analyse du fluide parfait, le nombre de directions caractéristiques dirigées vers l'intérieur du domaine de calcul étant identifié au nombre de conditions aux limites nécessaires. Pour une vitesse de transpiration subsonique, une condition suffit en cas de succion, trois conditions étant nécessaires en cas d'injection. Les deux conditions supplémentaires, qui correspondent à la possibilité d'injecter un écoulement stratifié en dessous de la surface de déplacement, peuvent être mises à profit le cas échéant pour améliorer la modélisation appliquée aux équations visqueuses de quantité de mouvement.

(2) La technique numérique de relaxation "semi-inverse" permet le couplage visqueux non-visqueux en présence de décollements en nombre quelconque, sur un nombre quelconque de parois ou d'obstacles présents dans l'écoulement. Elle peut de plus propager vers l'amont l'influence induite par les effets visqueux au sein des zones supersoniques. Par son principe, la méthode est donc effectivement capable, sans autre donnée que la géométrie et la pression "aval", de calculer des écoulements à interaction choc-couche limite multiples, induisant ou non des décollements, pourvu que le maillage local soit assez fin. L'échelle du phénomène est de l'ordre de l'épaisseur de la couche visqueuse en début d'interaction. Cette échelle peut être obtenue si nécessaire au moyen de resserrements locaux du maillage, adaptés à la position des chocs par itérations. Pour le couplage des équations d'Euler complètes, les premiers résultats obtenus ici sur un écoulement interne symétrique résolvent une interaction choc-couche limite sur une seule paroi, avec un maillage suffisant, dans le cas d'un très petit décollement. L'application à priori possible, au calcul d'un canal dissymétrique n'a pas encore été tentée, mais ne demande aucune modification majeure du calcul.

K.Papailiou, Gr

(1) Could you comment on the Kutta condition you are using, when a separation is present near the trailing edge?

(2) Do you take into account the turbulent normal fluctuation terms in your turbulent model?

Réponse d'Auteur

(1) La "Formulation Déficitaire" et la modélisation du gradient de pression normal déterminent les conditions aux limites appliquées au fluide-parfait dans le proche sillage, le long d'une coupure. Celle-ci prend toujours origine au point anguleux du bord de fuite, dont la courbure infinie est supposée éliminer le contournement. La direction d'émission de la coupure au bord de fuite est cependant déterminée par le couplage, et diffère notablement de la bissectrice du bord de fuite. En chaque noeud de couplage sur la coupure, l'effet de déplacement introduit un saut de vitesse normale, et l'effet de courbure un saut de pression. Le sauts (qui seraient nuls en fluide parfait) sont assujettis à un couplage fort aux équations de mouvement visqueuses tangentielles et normales, respectant la dissymétrie du sillage. Pour l'effet de courbure, le couplage "fort" utilise la courbure "induite" des surfaces de déplacement supérieures et inférieures, dont les signes sont souvent opposés, contrairement aux zones de sillage lointain. Il en résulte que la valeur de la pression visqueuse réelle sur la coupure n'est pas toujours à l'intérieur de l'intervalle défini par les niveaux de pression du fluide parfait de part et d'autre de la coupure, cet effet de couplage fort au bord de fuite étant conforme à l'expérience.

Par ailleurs, des problèmes purement numérique peuvent être soulevés en fonction des techniques de résolution de fluide parfait. Une condition "de type Kutta" peut parfois être appliquée en un noeud de bord de fuite distinct des noeuds de couplage, les conditions de sauts correspondantes étant alors interpolées dans les valeurs calculées aux noeuds de couplage. De même un traitement spécial du couplage numérique "Direct" ou "Semi-Inverse" est généralement nécessaire au noeud de bord de fuite.

(2) Le seul terme turbulent pris en compte est la contrainte de cisaillement $\overline{u'v'}$ qui agit sur le frottement, l'entrainement et la dissipation. Le calcul de l'écart à l'équilibre de $\overline{u'v'}$ fait aussi intervenir une modélisation de l'énergie cinétique turbulente. Il est vrai que les termes liés aux contraintes normales du tenseur de Reynolds pourraient éventuellement avoir une influence sur le bilan visqueux de quantité de mouvement normal, au second ordre, et par conséquent influer sur le gradient de pression normal qui définit l'effet de

courbure du proche sillage. Aucun évaluation de cet effet n'a encore été tentée dans les présents calculs. Une modélisation serait sans doute réalisable.

F.Leboeuf, Fr

Votre modèle est-il plus performant dans le cas de décollements d'étendue limitée ou de décollements complets sur une paroi?

Réponse d'Auteur

Les équations intégrales déficitaires avec du décollement modélisent les équations de Navier-Stokes (NS) de Couches Minces. De ce fait, et sauf introduction de conditions aux limites supplémentaires, le calcul des décollements n'a de sens qu si le recollement est lui aussi calculé, éventuellement dans le sillage. L'étendue géométrique du décollement est donc celle d'une bulbe. L'épaisseur du bulbe doit en principe rester modérée pour justifier l'approximation NS — Couche Mince, mais des épaisseurs de 20% de l'échelle de référence du fluid parfait ne semblent pas excessives en pratique. De même la longueur du bulbe n'est pas significative d'une limite d'application.

La limitation intrinsèque et la modélisation appliquée aux profils de vitesse pour résoudre l'équation de quantité de mouvement longitudinale. "L'universabilité" de ces profils est sans doute d'autant plus incertaines que la paramètre de forme est plus grand. Les bulbes secondaires ne sont par exemple pas représentés. En outre, les grands *paramètres de forme rendent aussi plus incertaine la modélisation "hors-équilibre" appliquée à l'entrainement* turbulent, de la même manière que les modèles de turbulence des solveurs NS. La tendance vers une pression "plateau" aux grands paramètres de forme est cependant incluse dans les équations, la pression d'eau morte étant alors peu sensible au détail des vitesses de retour dans le voisinage de la paroi. Enfin, en écoulement interne, le confinement doit conduire à des décollements étendus dans lesquels le paramètre de forme maximal reste modéré.

B.Lakshminarayana

(1) Most of the examples you showed are for external flows, where the method seems to work well. Many of the assumptions you made in deriving the viscid/inviscid interaction equations are not valid for internal flows, such as a cascade with thick boundary layer or when the shock-boundary layer interaction is present. Do you think this method is good for internal flows as well? If so, do you have any examples to show it.

(2) In your formulations you neglected the turbulence quantities. Inclusion of these quantities (especially for the near wake) may change the equations. What is the error introduced in neglecting these quantities?

Réponse d'Auteur

(1) Au niveau des équations intégrales déficitaires, rien ne distingue les écoulements externes et internes. La "Formulation Déficitaire" calculant l'écoulement visqueux réel en terms d'écarts à un écoulement de fluide parfait fictif, superposé et couplé, ce dernier délivre toujours une approximation minimale des gradients normaux existant dans les couches limites épaisses, quelques soient les hypothèses simplificatrices des équations visqueuses "Déficitaires" complémentaires. En cas d'interaction choc-couche limite, la pénétration des ondes de choc dans l'épaisseur de la couche limite, ainsi que leur atténuation progressive qui conduit à une compression continue à la paroi, sont ainsi pris en compte par la composante "Fluide-Parfait-superposé" du modèle.

La limitation véritable est celle des relations algébriques de fermeture appliquées pour l'entraînement turbulent, ainsi que pour l'une des épaisseurs intégrales turbulentes. Cette fermeture, fondée sur une modélisation des *profils de vitesse turbulents, peut a priori sembler restrictive. La diversité des exemples d'applications, ainsi* que le dernier exemple du calcul de l'interaction choc-couche limite dans un écoulement interne symétrique, montrent cependant que cette fermeture intégrale déficitaire, sans être "universelle", se compare favorablement aux modèles complexes pour une large gamme d'applications dont le point commun est l'existence d'une direction privilégiée pour le cisaillement (couches minces). Le calcul des décollements de spoiler constitue un exemple d'application avec couches limites épaisses.

(2) La seconde partie de la question rejoint celle du Dr Papailiou sur l'importance des différents termes turbulents dans les équations. Le modèle de calcul étant une simplification des équations "Navier-Stokes-Couches Minces" seul le terme de cisaillement principal $\overline{u'v'}$ est retenu. L'erreur introduite par cette simplification est difficile à estimer compte tenu de l'incertitude attachée à la modélisation du terme de cisaillement pris en compte.

APPLICATION OF AN INVISCID-VISCOUS INTERACTION METHOD
TO TRANSONIC COMPRESSOR CASCADES

W J Calvert
Turbomachinery and Installations Department
National Gas Turbine Establishment
Pyestock, Farnborough, Hampshire, UK

SUMMARY

A recent ASME paper by the author described an inviscid-viscous interaction method to predict the blade-to-blade flow in axial compressors. This paper presents comparisons between the predictions from the method and experimental data from a number of transonic linear cascades. The cascades cover a wide range of duties, with inlet Mach numbers varying from 0.8 to 1.46 and flow deflections from 7° to 50°. Generally the predictions are in good agreement with the test data.

NOTATION

AR	aspect ratio of cascade, ie span at mid chord/chord
c	blade chord
$\bar{H}$	transformed boundary layer shape parameter $= \dfrac{1}{\theta} \int \dfrac{\rho}{\rho_{fs}} \left(1 - \dfrac{V}{V_{fs}}\right) dy$
M	Mach number
p	static pressure
P_T	total pressure
Re_θ	Reynolds number based on momentum thickness
s	blade pitch, or surface distance
t	blade maximum thickness
V	flow velocity
x	distance in chordwise direction
α	flow angle, degrees
δ^*	boundary layer displacement thickness
ζ	blade stagger angle, degrees
θ	boundary layer momentum thickness
ϕ	blade camber angle, degrees
ρ	static density
ω	loss coefficient based on upstream conditions $= \left(\dfrac{P_{T_1} - P_{T_2}}{P_{T_1} - P_1}\right)$
Ω	stream tube contraction (upstream/downstream)

Subscripts

1	conditions at upstream boundary
2	conditions at downstream boundary
Des	design value
fs	free stream
ss	suction surface

1   INTRODUCTION

The blade-to-blade flow in axial compressors for aircraft gas turbine engines is very complex. The flow is generally transonic, sometimes with strong shock waves present, and the blade surface boundary layers are likely to come close to separation or to separate. These phenomena make it difficult to produce accurate predictions of the detailed flow and overall performance of compressor blade sections, and in the past the designer has often been forced to rely on correlations of the performance of existing profiles in order to estimate the performance of a new profile. Such empirical correlations provide little or no help in developing better blade profiles.

With recent advances in numerical algorithms for inviscid and viscous flows and the techniques for matching them together, it is now possible to produce inviscid-viscous solutions for the blade-to-blade

flow around many types of compressor blade section. Reference 1 describes one such calculation method for sections with leading edge normal shock waves, and this method has since been developed so that it can cater for other types of compressor blade section as well. In the present work the method is applied to a range of linear compressor cascades and the predictions are compared with experimental data in order to determine the accuracy and limitations of the technique.

2   CALCULATION METHOD

The general form of the calculation method is described in Reference 1. It is basically a mixed mode inviscid-viscous interaction technique for quasi-3 dimensional (Q3D) blade-to-blade flows, ie the blade-to-blade flow surface is assumed to be axisymmetric, but the effects of rotation and of varying radius and stream tube thickness in the axial direction are included. The inviscid calculation is based on the improved Denton time marching technique[2], and it is therefore capable of calculating transonic flows, including the positions and strengths of shock waves. The viscous calculation is an integral technique consisting of three parts to estimate laminar boundary layer development, transition point and turbulent boundary layer development respectively.

The procedure used to match the inviscid and viscous parts of the calculation features a mixed mode technique in order to handle both attached and separated boundary layer flows. On the pressure surface of the blade and the first part of the suction surface where the boundary layers should be attached, a forward mode of operation is used, in which the inviscid calculation determines the pressure distribution for a given blade geometry and the viscous calculation estimates the boundary layer growth (and hence the effective blade shape) corresponding to the inviscid pressure distribution. On the second part of the suction surface where the boundary layer may be close to separation or completely separated, the forward mode may become unstable. The method therefore switches to an inverse mode, in which the inviscid calculation determines the effective blade geometry (and hence boundary layer displacement thickness) for a given surface pressure distribution, and the viscous calculation estimates the surface pressure distribution corresponding to the specified boundary layer displacement thickness. The displacement surface model, as opposed to the surface transpiration model, is employed, and second order boundary layer effects such as the variation in static pressure across the layer are ignored at present.

The above matching procedure was initially chosen for use with compressor sections operating with leading edge normal shock waves. However, it is also applicable to other situations and the calculation method has now been developed to allow other types of compressor blades to be studied. For example the method can also handle high deflection transonic (but substantially shock free) blades such as the V1 and V2 cascades considered in Reference 3. The predicted results for V1 and V2 using the present method are similar to those obtained by the technique used in Reference 3, as would be expected since they both use an inviscid-viscous approach with the same viscous calculation.

After the inviscid-viscous interaction has converged, usually taken to be when the maximum error in effective geometry between one cycle and the next is less than 0.05% of blade pitch, a compressible flow mixing calculation[4] is carried out to determine the mean flow conditions at the downstream plane. The inviscid-viscous calculation generally takes about twice the number of time steps required for an inviscid solution. The viscous part of the calculation is relatively quick and so total computation times are roughly twice those for inviscid solutions. Typically an inviscid-viscous solution with a 21 × 100 calculating grid would require 2 minutes CPU on the VAX 11/780 computer + 10 minutes CPU on the FPS 164 attached processor. These times are sufficiently short for the method to be used as a design tool.

3   STREAM TUBE THICKNESS DISTRIBUTION

A major and recurring problem in comparing the theoretical predictions with experimental results from cascade tests is the distribution of stream tube thickness. In the experiment, flow conditions are measured at planes upstream and downstream of the cascade and from these measurements a value of overall stream tube contraction (Ω) can be calculated. However, there is generally no information available regarding the variation of stream tube thickness between these two measuring planes, so some assumption must be made. Transonic flows are likely to be very sensitive to small differences in flow area and so the accuracy of this assumption will set a limit to the accuracy of the predictions, independent of the imperfections in the calculation method. The same point applies to any variations of stream tube thickness in the pitchwise direction – in this case the use of a Q3D calculation method means that a constant value has to be assumed, though this can sometimes be far from the truth (see Reference 5 for example).

4   COMPARISONS WITH MEASURED CASCADE DATA

4.1   DFVLR L030-4 cascade[6,7]

This cascade is derived from the blade section at 45% height of the rotor of a DFVLR transonic compressor stage. It has a multiple circular arc profile and is designed for an inlet Mach number of 1.09 and a flow deflection of 12.5°. Other geometric and aerodynamic design parameters are given in Table I. The cascade was tested over a range of inlet Mach numbers, inlet flow angles, back pressures and stream tube contractions. In addition to measurements of up and downstream flow conditions and blade surface static pressures, the shock patterns were observed by a Schlieren system and at one condition near the design point the flow field was also investigated using laser anemometry. For the theoretical predictions of the flow, it was suggested[7] that a linear variation of stream tube thickness should be taken between the cascade leading edge and trailing edge planes with constant values up and downstream. This assumption was made for all the predictions for this cascade.

The predictions and test data for the condition near design point are compared in Figures 1 and 2. Apart from a slight overestimation of the peak suction surface value there is a very close match between the surface pressure coefficient distributions. Also, despite the shock smearing inherent in the time marching calculation, the predicted blade-to-blade Mach number contours are in remarkably good agreement with those derived from the laser anemometry and surface pressure measurements (Figure 16 of Reference 6). The predicted suction surface boundary layer growth is shown in the bottom half of Figure 1. Transition

to a turbulent boundary layer occurs at 16% chord at a value of Re_θ of 300. The shock compression starts at 40% chord and it causes a rapid rise in boundary layer shape factor and displacement thickness, though no actual separation is predicted. The boundary layer then recovers before once again approaching separation near the blade trailing edge. The blade therefore appears to be well matched to its duty. The predicted overall performance in terms of static pressure rise and exit flow angle is in good agreement with the test data (see Table II), but the predicted total loss is below the measured value.

In view of the fact that the blade surface boundary layers are predicted to remain attached in this case, it might be expected that an inviscid solution would give a reasonable approximation to the measured data. However, as can be seen from Figure 1 the inviscid solution has significantly higher loading and the flow deflection is increased from 12.8° to 15.0°; the predicted static pressure ratio across the cascade is increased from 1.48 to 1.57. Thus even though the blade surface boundary layers remain attached they have a significant effect on the overall performance of the cascade.

Reference 6 also presents test results for the LO30-4 cascade at four different values of inlet flow angle and back pressure, the inlet Mach number being kept approximately constant at 1.02. Predictions for these four conditions are compared with the measured surface pressure coefficients in Figure 3, and the predicted Mach number contours at the two extreme points are shown in Figure 4 - the contours are in good qualitative agreement with the Schlieren photographs given in Figure 12 of Reference 6. At high positive incidence there is a normal shock wave well detached from the blade leading edge (Figure 4a). Considerable spillage of flow occurs from one blade passage to the next and there are very high local incidence angles onto the blade leading edge - values of about 15° to the blade camber line are predicted. This type of situation was discussed in Reference 3, and it was suggested that the likely result was immediate separation of the suction surface boundary layer followed by reattachment as a turbulent layer at some point downstream. The present inviscid-viscous method cannot resolve this detail using a finite difference grid within practical limits, and so it fails to predict the correct suction surface boundary layer development. Thus the boundary layer blockage over the rear part of the suction surface is underestimated, and the predicted surface pressure coefficients (Figure 3a) are much too low. Better agreement with the test data can be achieved, as noted in Reference 3, by specifying suitable starting conditions for the suction surface boundary layer calculation, but in this case a very high initial value of Re_θ of about 1000 would be required. A more detailed model of the leading edge flow is obviously needed to investigate the matter further.

As the upstream incidence angle is reduced, the normal shock moves downstream and the flow spillage is considerably reduced. The predictions from the inviscid-viscous technique for the rest of the operating range are in much better agreement with the test data, both in terms of surface pressure distribution (Figures 3b, c, d) and overall performance (Table II). At the design inlet flow angle of 58.5° (Figure 3b) the cascade still operates with a detached shock. The unique incidence condition occurs at a flow angle of 57° (Figure 3c) and this value is accurately predicted. Further reductions in back pressure then have no effect on the upstream conditions, but cause a supersonic acceleration within the blade passage (Figures 3d and 4b). This is terminated by a normal shock which causes complete separation of the suction surface boundary layer - at the trailing edge the boundary layer displacement thickness is predicted to be 3.9% of chord with a shape factor of 6.5.

4.2   DFVLR LO30-6 cascade[6,7]

This cascade corresponds to the blade section at 68% height of the same transonic rotor from which LO30-4 was derived. It again has a multiple circular arc profile and it is designed for an inlet Mach number of 1.22 and a flow deflection of 7.9° (see Table I for other details). As for the LO30-4 cascade, stream tube thickness was assumed to vary linearly between the cascade leading edge and trailing edge planes. The predicted performance for a point near design conditions is generally in good agreement with the test data (Figure 5 and Table II), though loss coefficient is again underestimated. The prediction indicates that the suction surface boundary layer separates immediately downstream of the shock wave, but soon reattaches and then remains attached over the rest of the surface. The displacement thickness at the trailing edge is 1.1% of blade chord.

4.3   DDA cascade[8]

This cascade which was tested by Detroit Diesel Allison is once again derived from the rotor of a compressor stage. The stage was designed for a pressure ratio of 3.0/1 which results in a very arduous duty for the blade sections. The cascade represents the section at 63% height and it is intended to turn the flow from 66.85° to 34.46° at an inlet Mach number of 1.46. The duty is made slightly easier by a spanwise height contraction of 50% and the blades are more closely spaced (s/c = 0.526) than would be possible in a fan stage with lower hub/tip ratio. Other details are given in Table I. For prediction purposes the stream tube height at mid span of the cascade was assumed to be proportional to the local spanwise height up to the blade trailing edge and then to reduce by a further 7½% of the upstream value to match up with the value deduced from the flow measurements 1 axial chord downstream of the cascade.

The cascade was tested over a range of back pressures, producing conditions which varied between slight spilling of flow from one passage to the next and completely choked with a shock wave well back in the blade passage. Predictions were done for the design value of inlet Mach number at three levels of back pressure within this range, and the predicted surface pressure distributions are compared with the test data in Figure 6. At the highest back pressure (2.06), the shock wave is situated at inlet to the blade passage, as can be seen from the predicted Mach number contours in Figure 7: its interaction with the suction surface boundary layer causes immediate separation, and the boundary layer displacement thickness increases by 12 times across the interaction. The boundary layer reattaches between 70 and 90% chord, but it separates again at the trailing edge and reaches a value of displacement thickness of 6% of blade chord (12% of the blade pitch and 33 times the pre-shock value). In view of these large viscous effects, the agreement between the measured and predicted surface pressure distributions (Figure 6a) is very encouraging. The general form of the distributions and in particular the high loading near the trailing edge is well modelled. Part of the difference in pressure levels on the pressure surface and the rear of the suction surface is probably because the calculation underestimates the drop in free stream

total pressure by 4% of total pressure - the measured values are in fact greater than would be expected due to a normal shock wave at the peak predicted Mach numbers. The predicted profile loss is in better agreement with that deduced from the test data. The mean exit flow angle is also well predicted (see Table II).

As the back pressure is reduced, the shock moves downstream into the passage and the two regions of separated flow on the suction surface merge together. The predicted surface pressure distributions are in good agreement with the test data (Figure 6b), despite the fact that the suction surface flow is now completely supersonic. The calculation correctly predicts that the loss in free stream total pressure is reduced, but it is still optimistic by about 2%. This reduction in shock loss is in line with the effect noted in Reference 1 whereby a strong shock/boundary layer interaction reduces the size of the shock loss, but at the expense of increased profile losses. In this case the suction surface boundary layer displacement thickness is predicted to reach 8% of chord (15% of blade pitch) at the blade trailing edge.

The same trends continue with further reductions in back pressure (Figure 6c) - the shock moves rearwards and the interaction with the suction surface boundary layer becomes even stronger. The interaction between the passage shock and the pressure surface boundary layer is also becoming stronger and the pressure surface boundary layer now produces 18% of the predicted profile loss, compared with 15% at the highest back pressure. It is interesting that although the total predicted losses are roughly the same for all three levels of back pressure, the profile loss coefficient has increased from 0.056 at the highest back pressure, to 0.098 at this condition.

4.4 DFVLR SKG 2.7 supercritical cascade[7,9]

Turning now to cascades with subsonic inlet flow, DFVLR SKG 2.7 is a supercritical cascade with a pitch/chord ratio of 0.821. It was designed to remove 36.7° of swirl from a flow with an inlet Mach number of 0.80. Other data are given in Table I. The cascade was tested at DFVLR over a range of inlet Mach numbers, inlet flow angles and stream tube contractions. The tests indicated that the cascade worked efficiently at the design inlet flow angle for Mach numbers up to about 0.77, but that the losses increased rapidly if the Mach number was increased further. Since some of the measured stream tube contraction was thought to occur upstream of the blades, it was considered that the design target of inlet Mach number had been achieved.

For the predictions, it was assumed that the stream tube thickness varied linearly between a point 0.2 axial chords upstream of the cascade to a point 0.2 axial chords downstream. Solutions were then produced at the design inlet flow angle for a number of values of Mach number. The solutions indicated that the cascade would operate efficiently without significant shock waves or boundary layer separation up to and including an inlet Mach number of 0.76, but that at higher values a shock formed on the suction surface and produced a large boundary layer separation. The inviscid-viscous method thus estimated the maximum useful operating Mach number to within about 0.01. The predicted blade surface Mach numbers at an inlet Mach number of 0.76 are compared with the measured values at an inlet Mach number of 0.77 in Figure 8. There is generally good agreement except that the predicted values on the first 25% of the suction surface are rather low. The overall performance of the cascade is also well predicted (Table II), the overestimation of loss coefficient being due to total pressure errors in the time marching solution at the blade leading edge. At this condition the blade surface boundary layers are estimated to remain attached throughout, although the suction surface layer comes very close to separation between 45 and 80% chord. However, if the inlet Mach number is increased, the region of high diffusion starting at about 40% chord on the suction surface (Figure 9) steepens up into a shock wave which then causes complete separation of the boundary layer and hence high losses and reduced pressure recovery.

4.5 ONERA 115 stator cascade[10,11]

The final test case is the ONERA 115 stator cascade. As for the previous example, it has a subsonic inlet Mach number, but the pitch/chord ratio is much lower (0.29) since the cascade is required to remove over 50° of flow swirl. Other geometric and aerodynamic data are given in Table I. The cascade was tested over a range of inlet Mach numbers and flow angles, but thankfully the flow was two-dimensional overall and so it was obvious what assumption should be made about stream tube thickness variation. Boundary layer traverses were taken on the blade suction surface at inlet Mach numbers of 0.70 and 0.85 and at a range of inlet flow angles.

For an inlet flow angle of 51° there is excellent agreement between the measured and predicted suction surface boundary layer development at both levels of inlet Mach number (Figures 10a and b). In both cases the boundary layer remains attached along the whole surface, but with such closely spaced blades it still produces a blockage of 5 to 7% in the trailing edge region. When the inlet flow angle is increased to 53° the agreement between measurement and prediction becomes significantly worse (Figures 10c and d) - the measurements indicate that the boundary layer actually separates over the rear part of the surface, while the standard predictions show little change from those at the lower inlet flow angle. This result is consistent with the predictions at higher than optimum incidence for the L030-4 cascade (above) and for the V2 cascade (Reference 3). The current inviscid-viscous method is unable to predict the leading edge flow in sufficient detail to set up the correct starting conditions for the turbulent boundary layer, and hence it underestimates the suction surface boundary layer growth. For the case at an inlet Mach number of 0.7, an improved prediction is possible, as noted in Reference 3, if the suction surface boundary layer calculation is assumed to start as a turbulent layer with a momentum thickness Reynolds number of 300. The modified predictions of both boundary layer growth and blade surface pressure distribution are then in good agreement with the test data (Figures 10c and 11). At an inlet Mach number of 0.85 the above modification produces a prediction which overestimates the actual boundary layer growth (Figure 10d); it would thus appear that this may be a borderline case.

5. CONCLUDING REMARKS

The inviscid-viscous blade-to-blade method described in Reference 1 has been applied to seven transonic compressor cascades and the predictions compared with test data. Results for five of the

cascades are discussed in this Paper - the results for the other two (V1 and V2 cascades) are similar to those produced by an earlier inviscid-viscous method (see Reference 3) and so only the comparison of overall parameters is included here (see Tables I and II). The cascades cover a wide range of geometries and design flow conditions, as can be seen from Table I. Pitch/chord ratio varies from 0.29 to 0.82 and stagger angle from 14° to 56°, while the design values of inlet Mach number vary from 0.80 to 1.46 with flow deflections from 7° to over 50°. The test points considered correspond to a wide range of conditions for both the inviscid and viscous parts of the flow. Both shock-free flows and flows with shock waves are encountered, the shock positions ranging from highly detached to well swallowed, while the predictions of blade surface boundary layers vary from completely attached to highly separated. It is encouraging that the same inviscid-viscous matching procedure can produce converged solutions for all the cases.

In most cases the solutions are in good agreement with the test data, in terms of both internal flow details such as blade surface pressure distributions (see figures), and overall performance parameters such as static pressure ratio and exit flow angle (see Table II). Predicted overall loss levels are less satisfactory, but they might be improved by using finer calculating grids to improve the estimation of shock loss by the inviscid part of the calculation. It is therefore considered that an inviscid-viscous method is capable of modelling the main features of the flows in transonic compressor cascades and thus should be a useful tool for the designer of compressor blades.

The major area where the present method requires improvement is in treating blades operating at high incidence. It appears that it cannot resolve the leading edge flow in sufficient detail to set up the correct starting conditions for the boundary layer calculation, and hence it fails to predict the measured increases in boundary layer thickness and profile loss. To some extent this situation can be detected by examination of the inviscid flow, and revised starting conditions for the surface boundary layer may then be specified. This provides a guide to the optimum incidence range of the cascade until a better model of the leading edge flow can be developed.

REFERENCES

No.	Author(s)	Title, etc
1	W J Calvert	An inviscid-viscous interaction treatment to predict the blade-to-blade performance of axial compressors with leading edge normal shock waves ASME Paper 82-GT-135 (1982)
2	J D Denton	An improved time marching method for turbomachinery flow calculation ASME Paper 82-GT-239 (1982)
3	W J Calvert M V Herbert	An inviscid-viscous interaction method to predict the blade-to-blade performance of axial compressors Aeronautical Quarterly, Vol XXXI, Part 3 (August 1980)
4	W L Stewart	Analysis of two-dimensional compressible flow loss characteristics downstream of turbomachine blade rows in terms of basic boundary layer characteristics NACA TN 3515 (1955)
5	J Dunham	The effect of stream surface convergence on turbomachine blade boundary layers Aeronautical Journal, Vol 78, No. 758/759, p 90 (1974)
6	H-A Schreiber H Starken	Evaluation of blade element performance of compressor rotor blade cascades in transonic and low supersonic flow range Fifth International Symposium on Airbreathing Engines Bangalore, India (1981)
7		Private communication, DFVLR (1982)
8	R L Holtman G D Huffman R B McClure	Test of a supersonic compressor cascade. Volume I General Motors Corp (Detroit Diesel Allison) AD-756 870 ARL-72-0170-Vol-1 (1972)
9	H Rechter P Schimming H Starken	Design and testing of two supercritical compressor cascades ASME Paper 79-GT-11 (1979)
10	G Meauzé	Transonic boundary layer on compressor stator blades as calculated and measured in wind tunnel 4th International Symposium on Airbreathing Engines, Orlando (1979)
11	G Meauzé	Calculation-experiment comparisons of the transonic two-dimensional flow in a high deflection cascade La Recherche Aérospatiale, p 175-180 (1978-4)

TABLE I

CASCADE GEOMETRIC AND AERODYNAMIC DESIGN PARAMETERS

Cascade	Chord mm	a/c	ζ	ϕ	t/c	AR	M_{1Des}	α_{1Des}	α_{2Des}
LO30-4	90.0	0.621	48.5	14.9	0.050	1.86	1.091	58.7	46.2
LO30-6	90.0	0.678	55.7	7.9	0.040	1.86	1.224	62.0	54.0
DDA	76.3	0.526	52.3	40.9	0.036	0.69	1.460	66.9	34.5
SKG 2.7	70.0	0.821	13.6	~38	~0.08	2.40	0.799	36.7	0.0
ONERA 115	94.9	0.295	16.5	~53	~0.04	1.27	~0.85	~52°	0.0
V1	80.0	0.450	26.0	54.0	0.070	3.75	0.850	50.0	0.0
V2	80.0	0.450	19.2	56.8	0.070	3.75	0.850	50.0	0.0

TABLE II

CASCADE OVERALL PERFORMANCE PARAMETERS

Cascade	Ω	Measured					Predicted				
		M_1	α_1	α_2	p_2/p_1	ω	M_1	α_1	α_2	p_2/p_1	ω
LO30-4	1.18	1.08	58.5	45.4	1.45	0.083	1.08	58.6	45.8	1.48	0.052
	⌁1.23	1.0	63	45.5	1.36	0.14	1.01	62.2	45.2	1.42	0.087
	1.10	1.03	58.5	45.3	1.49	0.057	1.02	58.5	46.6	1.47	0.046
	1.10	1.03	57.0	45.7	1.40	0.069	1.02	57.0	46.8	1.40	0.042
	1.08	1.02	56.8	47.3	1.34	0.091	1.02	57.0	48.6	1.33	0.069
LO30-6	1.20	1.20	62.2	53.6	1.52	0.082	1.20	62.3	54.5	1.53	0.058
DDA	2.27	1.46	66.9	30.9	2.06	0.179	1.456	67.1	30.8	2.03	0.114
	2.27	1.46	66.9	31.2	1.95	0.142	1.456	67.1	32.3	1.92	0.113
	2.27	1.46	66.9	33.0	1.75	0.121	1.456	67.1	32.7	1.82	0.118
SKG 2.7	1.09	0.77	36.7	1.0	1.16	0.025	0.76	36.7	-0.1	1.15	0.037
ONERA 115*	1.0	0.72	51.2	0.2	1.275	0.031	0.70	51.0	0.9	1.254	0.035
	1.0	0.85	51.2	0.5	1.404	0.048	0.85	51.0	1.2	1.407	0.057
	⌁1.0	0.70	53.0	0	1.256	0.050	0.70	53.0	0.9	1.266	0.034
	⌁1.0	0.85	53.0	0.5	1.413	0.050	0.85	53.0	1.3	1.424	0.050
V1⌁	1.23	0.80	54.5	{ 8.8 / 9.1	1.273 / 1.273	0.100 / 0.085	0.80	54.5	7.8	1.274	0.087
V2⌁	1.15	0.80	49.5	{ 2.2 / 1.9	1.278 / 1.273	0.048 / 0.053	0.80	49.5	0.6	1.270	0.055
	1.12	0.85	49.5	{ 2.4 / 1.5	1.329 / 1.314	0.058 / 0.088	0.85	49.5	1.0	1.328	0.067
	⌁1.12	0.80	52.5	0.5	1.275	0.116	0.80	52.5	1.3	1.317	0.056

*Test results for ONERA 115 cascade correspond to tests with similar inlet conditions to those reported in Reference 10.

⌁Cascades V1 and V2 were tested both with solid side walls and with porous side walls and so there are two sets of test data.

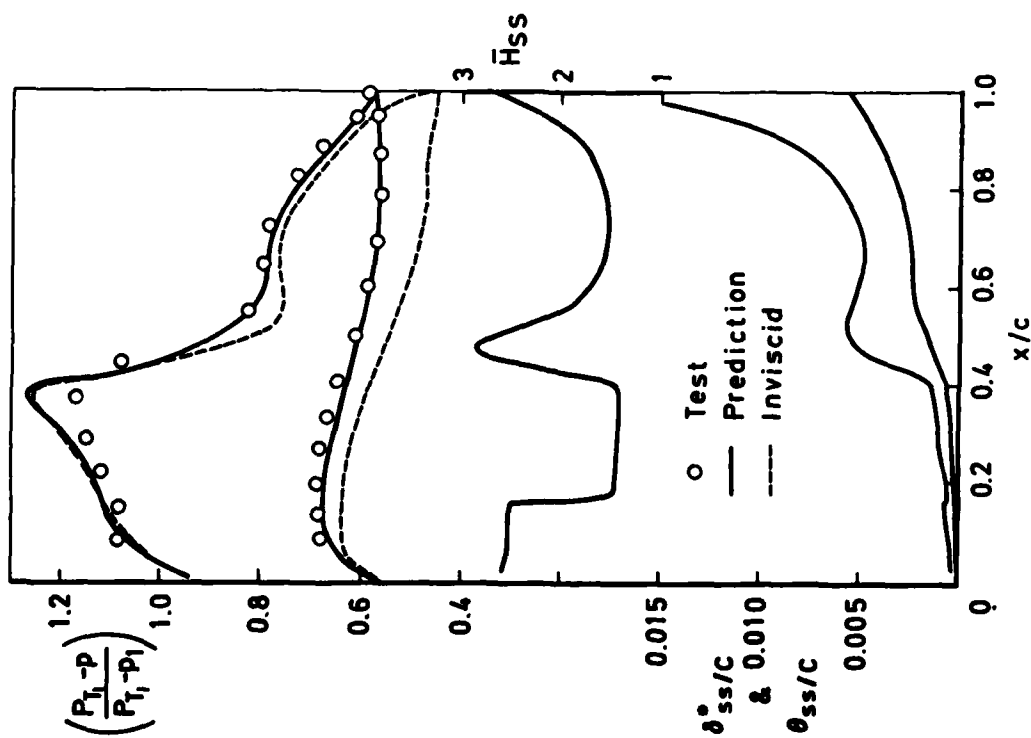⌁Conditions at higher than optimum incidence (NB. Predicted results are for the standard method).

a. Measured (Fig 16 of reference 6)

b. Predicted

Fig 2 LO30-4 cascade Mach number contours at design point

Fig 1 LO30-4 cascade design point

○ Test
— Prediction
--- Inviscid

o Test   —— Prediction

a. $M_1=1.0, \alpha_1=63°, \Omega=1.23$

b. $M_1=1.03, \alpha_1=58.5°, \Omega=1.10$

c. $M_1=1.03, \alpha_1=57.0°, \Omega=1.10$

d. $M_1=1.02, \alpha_1=56.8°, \Omega=1.08$

$\dfrac{P_{T_1}-p}{P_{T_1}-p_1}$

x/c
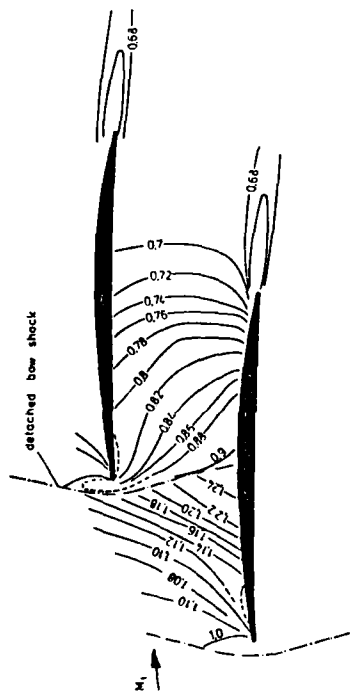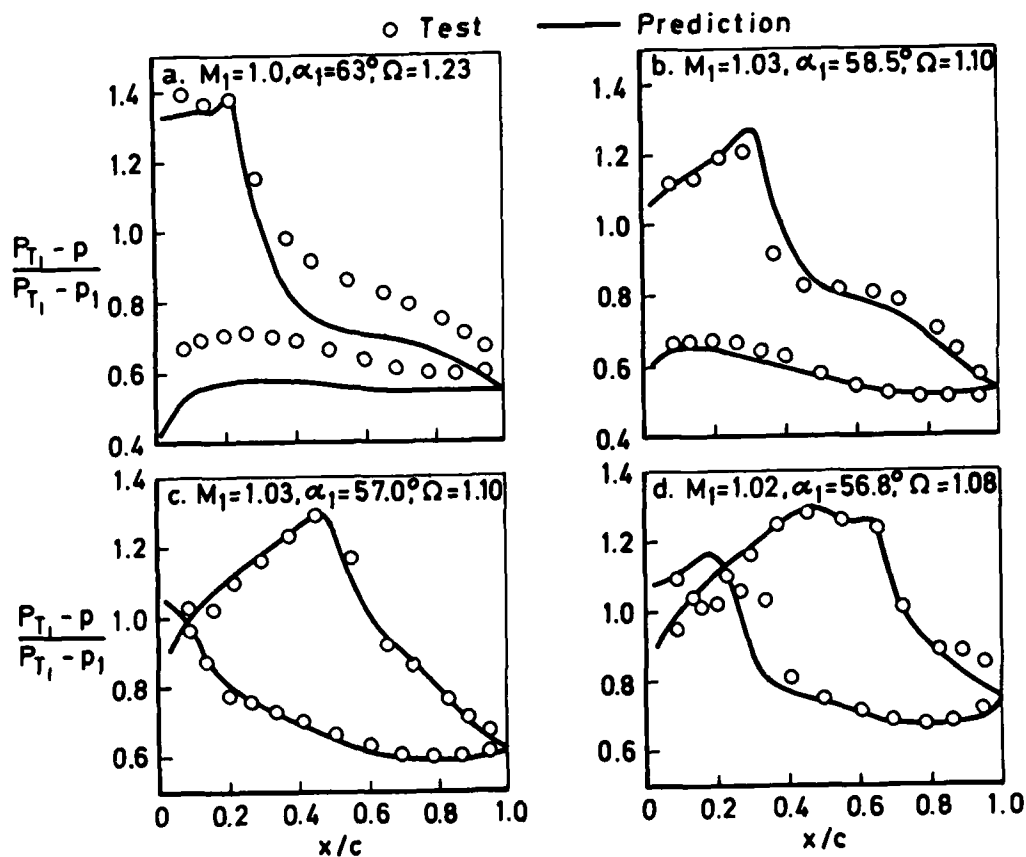
Fig 3   L030-4 cascade blade pressure distributions at different inlet flow angles $M_1=1.0$

a. $\alpha_1=63°$

b. $\alpha_1=56.8°$
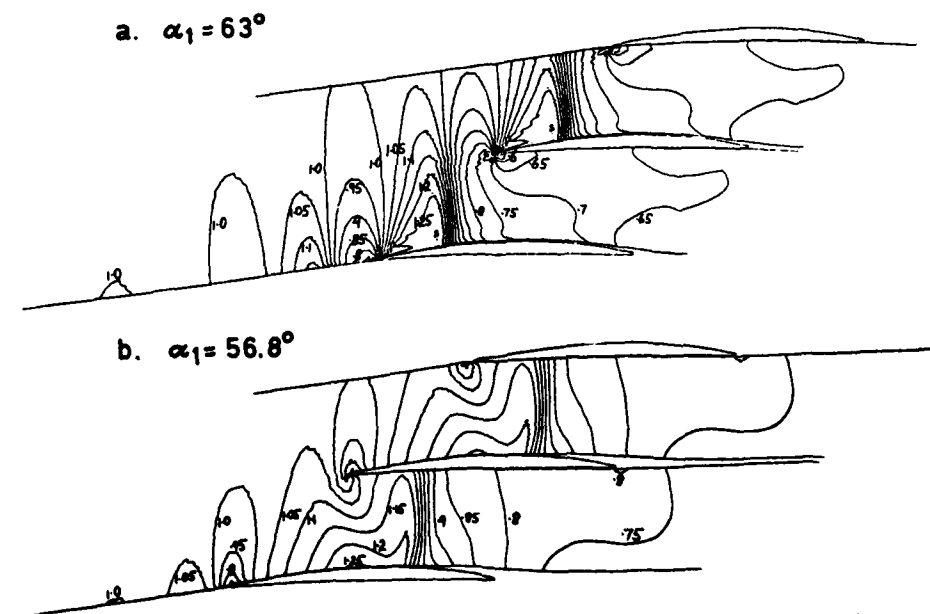
Fig 4   L030-4 cascade predicted Mach number contours at $M_1-1.0$

Fig 5 L030-6 cascade near design point

Fig 7 DDA cascade predicted Mach
number contours $M_1 = 1.46$, $P_2/P_1 = 2.03$

Fig 6 DDA cascade blade pressure
distributions $M_1 = 1.46$

Fig 9 SKG 2.7 cascade predicted Mach
number contours $M_1=0.76, \alpha_1=36.7$

Fig 8 SKG 2.7 cascade blade
Mach number distribution
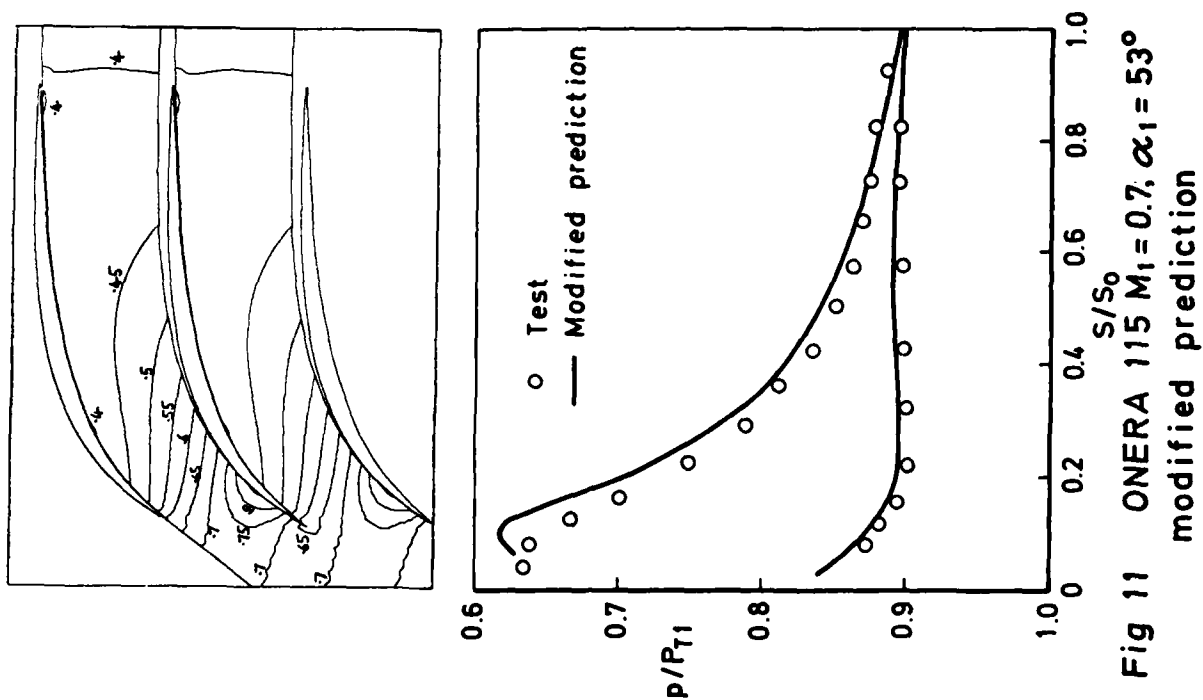$M_1=0.77, \alpha_1=36.7°$

Fig 11 ONERA 115 $M_1 = 0.7$, $\alpha_1 = 53°$
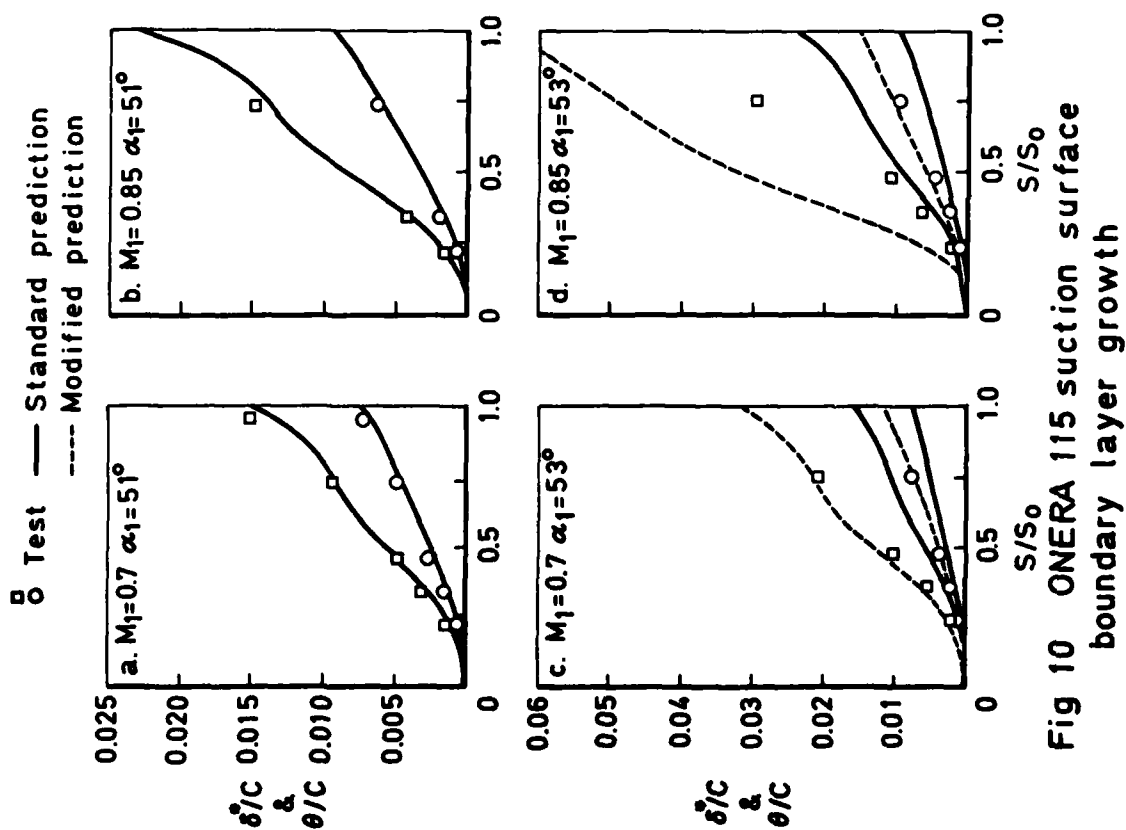modified prediction

Fig 10 ONERA 115 suction surface
boundary layer growth

DISCUSSION

Ph.Ramette, Fr

Pour la grille d'aubes SKG 2.7 du DFVLR représenté sur la figure 9 avec un écoulement d'entrée subsonique, pourriez vous préciser le maillage utilisé pour le bord d'attaque des aubes?

Author's Reply

No special treatment was used for the leading edge region of the SKG 2.7 cascade. In this region the calculating grid for the inviscid solution had calculating planes at intervals of 1% axial chord in the axial direction and there were 21 points uniformly spaced across the blade pitch.

H-J.Lichtfuss, Ge

The difference between the viscous and inviscid blade pressure distributions, shown in Figure 1, results in different loading and outlet flow angle, as mentioned. To see the influence of viscous effects it is necessary to compare pressure distributions with the same loading. Within the inviscid calculation, this means to set a Kutta-Joukowsky condition which fulfills this constraint. Maybe the discrepancy comes from the fact that all known time-marching (inviscid) Euler calculations will give automatically the outlet flow angle without any explicit additional setting. This phenomenon is not really understood in my eyes.

Author's Reply

The inviscid solution shown in Figure 1 was produced by assuming that the static pressures on the blade suction and pressure surfaces were equal at the trailing edge. I agree that closer agreement with the inviscid-viscous blade pressure distribution would be achieved by an inviscid solution with the outlet flow angle set equal to the inviscid-viscous value: However, this inviscid solution would not satisfy the requirement for zero loading (equal static pressure) at the blade trailing edge. Also, such a calculation is only possible if the outlet flow angle is known, either from test data or from a calculation which includes viscous effects.

M.J.Werle, US

What transition criterion is used in the calculations?

Author's Reply

The transition treatment is based on that suggested by Dunham*. Bubble transition occurs if the pressure gradient parameter falls below -0.09 and in that case the bubble length and the conditions at reattachment are determined by empirical correlations. Otherwise, transition is deemed to take place instantaneously (i.e. neglecting considerations of intermittency) when the momentum thickness Reynolds number reaches a critical value dependent on pressure gradient parameter and turbulence level.

K.Papailiou, Gr

Concerning Figure 10, conditions $M_1 = 0.85$ and $\alpha = 53°$, I think that the reasons you evoke concerning the discrepancy may not be true. We know that boundary layer behaviour is cumulative and we may observe that, in this case, it is calculated correctly up to 50% of the chord. It seems, then, that the trouble doesn't come from the leading edge region.

Author's Reply

I do not ageee that the standard prediction calculates boundary layer growth accurately up to 50% chord for the ONERA 115 cascade at $\alpha_1 = 53°$, $M_1 = 0.85$; although the differences between test and prediction are fairly small, they may be sufficient to account for the error at 75% surface distance since (as you say) the effects are cumulative. I consider that the leading edge region is the most likely cause of the discrepancy between prediction and test because it is the only part where there is a significant change in the blade surface pressure distribution.

J.Moore, US

I would like to ask about the calculations in Figure 1 showing results for the DFVLR cascade – L030-4. The calculation gives a higher Mach number, just upstream of the shock on the suction surface, than the measurements. But, in Table II, the calculated loss coefficient for the cascade is lower than the measured value. Can you comment on this apparent discrepancy?

Author's Reply

I agree that the over-estimation of the peak suction surface Mach number by the inviscid-viscous method would be expected to give a predicted loss which is slightly too high. At present I cannot explain why the predicted loss is lower than the measured value. It seems unlikely that the predicted shock loss (2.6%) is too low considering the measured values of Mach number, and so the difference is presumably due either to errors in the viscous calculation or in the measured data.

* Reference: Dunham, J. – "Predictions of boundary layer transition on turbomachinery blades". AGARD-AG-164, 1972.

A VISCID INVISCID INTERACTION PROCEDURE FOR TWO DIMENSIONAL CASCADES.

by

P. JANSSENS   and   Ch. HIRSCH
Research ass.   Professor

Department of Fluid Mechanics, Vrije Universiteit Brussel
Pleinlaan 2, 1050 BRUSSELS
BELGIUM

SUMMARY.

A viscous inviscid interaction scheme (woos) has been developed in order to predict fluid turning and loss coefficients for arbitrary cascade bladings of axial and centrifugal turbomachines. The effects of the blade surface boundary layers, separation of these boundary layers and the wake downstream of the trailing edge are taken into account by the wake displacement body method. The effective separation line between the inviscid outer flow, separated boundary layers and the wake is iteratively searched using a free streamline method. A Kutta Joukowsky condition at the trailing edge corrects the outlet flow angle and ensures zero loading on the wake. The outer potential flow is solved in a finite element Galerkin approximation and the boundary layer development is predicted with an integral method. Corrections based on Richardson numbers are included for streamline curvature and Coriolis effects on turbulence.

NOMENCLATURE.

B   blockage factor
c   blade chord
C_D dissipation function
ΔC_D correction on C_D
C_p, C_v specific heat coefficients
h   enthalpy
$H_{12} = \delta_1/\delta_2$ momentum shape factor
$H_{23} = \delta_3/\delta_2$ energy shape factor
I   rothalpy
l   mixing length
m   meridional coordinate
n   normal
p   static pressure
r   radius, gas constant ($=C_p - C_v$)
R   radius of curvature
R_i local Richardson number
$\bar{R}_i$ mean Richardson number
s   curvilinear coordinate
T   temperature
$u = \omega r$ rotational speed
v   absolute velocity vector
w   relative velocity vector

β flow angle, Monin Oboukhov factor
$\gamma = C_p / C_v$ specific heat ratio
Γ circulation
δ boundary layer thickness

$$\delta_1 = \int_0^\delta (1 - \frac{\rho w}{\rho_\delta w_\delta})\, dn \qquad \text{displacement th.}$$

$$\delta_2 = \int_0^\delta (1 - \frac{w}{w_\delta}) \frac{\rho w}{\rho_\delta w_\delta}\, dn \qquad \text{momentum th.}$$

$$\delta_3 = \int_0^\delta (1 - (\frac{w}{w_\delta})^2) \frac{\rho w}{\rho_\delta w_\delta}\, dn \qquad \text{energy th.}$$

ϕ potential function
ρ density
θ tangential angular coordinate
ω rotor angular velocity
Ω effective angular velocity

Subscripts:
0   without correction
1   inlet
2   outlet
e   at boundary layer edge
TE   at trailing edge

1. INTRODUCTION.

Loss and turning information of the flow in turbomachines is largely based on empirical data correlations from experimental research. The continuous trend to increase the aerodynamic loading of the stages leads to designs where separated regions can occur. Hence computational methods which are able to accurately predict the boundary layer growth along the section of a blade and which can treat flows with separated regions, become more and more important. With such procedures more efficient optimisations of the blade and higher machine performances can be achieved.

Several methods have been developed to calculate the flow field around airfoils as well as in cascades. To introduce viscosity, a first approach consists in solving the full Navier Stokes equations. An alternative approach is based on a viscous inviscid interaction model, which involves separate calculations of the viscous shear layers over the blade and in the wake and of the inviscid flow, together with a matching process to build up the mutual interaction of these flows. This allows the use of already existing boundary layer and inviscid flow calculation methods. General overviews of existing viscous inviscid procedures can be found in Hansen [1978] and in Le Bailleur [1980].

Downstream of the separation point the classical boundary layer methods fail and techniques are to be developed in order to extend the range of the calculated regions. This can be achieved by adapting the boundary layer calculation itself as in Assassa [1976], Bario [1978], Hansen [1978],[1979] and to continue in the direct mode of calculation, under more or less restrictive assumptions imposed on the used mathematical

model. The validity of these methods is however mostly limited to small separations. Since the singular behaviour of the boundary layer equations in two dimensional stationary flow is tied to the direct mode of calculation, it has most commonly been removed by employing inverse calculations as described in Assassa [1976], Kwon and Pletcher [1979]. Over separated boundary layer regions, Calvert and Herbert [1980] perform an inverse integral boundary layer calculation, corresponding to a prescribed parabolic displacement surface. All these methods work under the assumption that the boundary layer equations are still representative in separated flows regions. More global inviscid treatments exist for separated flows. Applications, were some flow boundaries are left free, are almost exclusively found in external aerodynamics and are well-adapted to singularity methods, Jacob [1969], Geller [1972], and especially to panel methods, Gross [1978], Henderson [1978]. Some applications to general free flow problems were developed in finite element calculations, O'Carroll and Harrison [1975], O'Carroll [1978], Morice [1977], [1979], Obee and De Witt [1980]. Up to now free streamline techniques have not been used in finite element methods for turbomachinery performance predictions.

In the present paper a viscous inviscid interaction procedure is described which predicts the blade to blade flow through axial and centrifugal turbomachines, for fixed or rotating blade rows. The aim of the method is to handle flow conditions where large separated boundary layers occur, in order to predict outlet angles and loss coefficients. The inviscid flow is calculated by the Galerkin finite element method in terms of a potential function with biquadratic isoparametric elements. Streamtube thickness variations and radius variations are included. The boundary layer development and the separation points are calculated with a compressible integral method with the inclusion of Coriolis and curvature effects on the turbulence through the introduction of Richardson numbers.
The influence of the viscous regions is introduced by the wake displacement body method, where the displacement thickness is added to the blade surface. The effective flow boundaries for the outer potential flow are treated as streamlines. Therefore an efficient combination is made of both the surface transpiration and the solid displacement surface models.
Separated boundary layer regions and the wake region downstream of the trailing edge are treated as an inviscid problem by introducing the free streamline concept. The flow within the viscous regions is however not calculated.
The outlet flow angle is corrected by introducing a Kutta Joukowsky condition at the trailing edge on the calculated effective flow boundaries of the outer flow. Zero loading is ensured at the trailing edge and anywhere downstream along the wake. Total pressure loss coefficients are obtained with a mixing calculation, assuming fixed values for the shape factor to obtain the momentum thickness in the separated regions.
Results are presented and discussed for axial bladings and compared with experimental data. Different pressure distributions for the blade separated regions are examined in order to calibrate the pressure evolution to be prescribed over the separated blade region. Wide ranges of incidences are considered and the predicted total pressure loss coefficients are compared with experimental values.

2. DESCRIPTION OF THE METHOD.

2.1 Inviscid blade to blade flow equations.

The blade to blade flow in a turbomachine can be considered along an axisymmetric streamsheet of a given thickness B and as irrotational in the absolute frame of reference. The inviscid blade to blade flow is then governed by the potential equation, written in cylindrical coordinates (m,θ) :

$$\frac{\partial}{\partial m} (\rho \ Br \ \frac{\partial \phi}{\partial m}) + \frac{\partial}{\partial \theta} (\frac{\rho B}{r} \frac{\partial \phi}{\partial \theta}) = \omega \frac{\partial (\rho \ Br)}{\partial \theta} \qquad (2.1)$$

where

m   is the distance along a streamline in the meridional plane (r,z). The blade to blade surface is assumed to be the surface of revolution obtained by rotation of this meridional streamline

r(m)   is the radius of the blade to blade surface

B(m)   the blockage factor or the streamtube thickness as shown in Fig.2.1.

A solution of the meridional throughflow, Hirsch and Warzee [1978], provides the functions r(m) and B(m) as well as the boundary conditions for the blade to blade flow.

Since no entropy can be created in an irrotational flow, the density is obtained by the isentropic relation

$$\rho = \rho_{tR} \left[1 - \frac{\gamma - 1}{2 \gamma r T_{tR}} (w_m^2 + w_\theta^2) \right]^{1/(\gamma-1)} \qquad (2.2)$$

where ρ_{tR} and T_{tR} are the relative stagnation density and temperature. The relative velocities w_m and w_θ are obtained from the potential function :

$$w_m = v_m = \frac{\partial \phi}{\partial m} \quad ; \quad w_\theta = v_\theta - \omega r = \frac{1}{r} \frac{\partial \phi}{\partial \theta} - \omega r \qquad (2.3)$$

Since all the streamlines in the flow passage originate in a region of uniform flow, the rothalpy is constant everywhere

$$I = h + \frac{w^2}{2} - \frac{u^2}{2} = h + \frac{v^2}{2} - u \ v_\theta \qquad (2.4)$$

It is clear that only three independent quantities can be specified for both upstream (A-Al) and downstream (F-Fl) boundaries including periodicity, see Fig. 2.1. Hence inlet Mach number and inlet angle together with the outlet Mach number or alternately the outlet angle, completely determine the flow for a given geometrical configuration and blockage. Applying in addition a Kutta Joukowsky condition, which determines the circulation,

$$\Gamma = s_2 \, v_{\theta 2} - s_1 \, v_{\theta 1} \qquad (2.5)$$

by estimating the outlet angle, only two independent quantities are left.

2.2 Boundary layer calculation with corrections for streamline curvature and Coriolis force.

As we are mainly interested in the displacement thickness and other overall boundary layer parameters a compressible integral method was selected to predict the development of attached boundary layers. The Walz [1969] procedure is used, which is based upon the integral boundary layer equations of momentum and energy. Separation is detected when the energy shape factor falls below a given value.

Within this integral method, corrections for streamline curvature and Coriolis force were introduced following the procedure of Van Den Braembussche and Zunino [1979], [1981], by adding a correction term to the dissipation factor in the energy integral equation.

Observations on boundary layers over curved surfaces and in rotating systems strongly confirm the sensitivity of turbulent boundary layers to normal pressure gradients. Bradshaw [1973] mentioned the "surprisingly" large influences and observed that the effects of curvature start to be appreciable, for ratios of boundary layer thickness to surface curvature (δ/R) larger than 1/300. Some important experiments investigated the stabilizing and destabilizing effects on the turbulent properties, either for streamline curvature, Schubauer and Klebanoff [1951], Patel [1968], So and Mellor [1972], Meroney and Bradshaw [1975] or for Coriolis force effects, Johnston [1971], Johnston et al. [1972], Moore [1973], Watanabe et al. [1979]. Stabilisation, occuring on the convex curved side and on the suction side of rotating blades, reduces the mixing between the fluid layers and the entrainment and thus leads to reduced Reynolds stress, wall shear stress, eddy viscosity and mixing length. On concave walls and pressure sides, destabilisation has precisely the opposite effects. The observed trend is that essentially the momentum shape factor and the skin friction coefficient are modified, while the momentum thickness is altered very little.

These stabilizing and destabilizing effects play an important role in turbomachinery flows, particularly on the boundary layer development as well as on the whole flow passage. The separation on the suction side and the formation of the jet-wake structure within centrifugal impellers is entirely due to wall curvature and Coriolis force fields, Dean [1971], Eckhardt [1976], Johnston and Eide [1976], Balje [1977]. High stabilisation may even suppress turbulence totally and the transition from laminar to turbulent flow, Johnston [1971], Johnston et al. [1972]. Strong stabilisation may lead to the formation of large scale streamwise vortices of the Taylor Görtler type, as investigated in the concave wall measurements of So and Mellor [1972] and Meroney and Bradshaw [1975] and the pressure side measurements of Johnston et al. [1972].

The presence of Coriolis force and streamline curvature does not generally require a drastic change of the boundary layer calculation method itself. One normally accounts for them by modifying some parameter, as Head's entrainment function or eddy viscosity. Most common used is the well-known Monin Oboukhov relation, resulting from Bradshaw's analysis [1967], [1973], which gives the modified mixing length l in terms of the mixing length l_o, calculated in the absence of a normal pressure gradient

$$\ell = \ell_o \, (1 - 2 \, \beta \, R_i) \qquad (2.6)$$

The magnitude of the correction is defined by β which is an experimental constant for which Bradshaw proposed values of 7 for stabilisation and 4 for destabilisation. The local influence of centrifugal and Coriolis forces is most commonly expressed in terms of non-dimensional Richardson numbers, R_i :

$$R_{iC} = \frac{v_s/R}{\partial w_s/\partial n} \qquad R_{iR} = \frac{\Omega}{\partial w_s/\partial n} \qquad \begin{array}{c} (2.7) \\ \\ (2.8) \end{array}$$

The radius of curvature is denoted by R while Ω stands for the effective velocity of rotation, i.e. that part of the angular velocity ω , which corresponds to the Coriolis acceleration component normal to the considered streamline, see also Johnston and Eide [1976]. The signs of R and Ω are defined so that positive Richardson numbers correspond to stabilisation, while destabilisation gives negative values. These Richardson numbers are a measure of the relative importance of the local centrifugal and Coriolis forces, to the inertia forces. In finite difference methods which use the mixing length model for turbulence closure, the correction (2.6) can directly be introduced and many applications can be mentioned in the literature, Bradshaw [1967], [1973], Johnston [1971], So and Mellor [1972], Parsons and Hill [1973], Johnston and Eide [1976], Watanabe et al. [1979], Cebeci et al. [1979].

Since the correction (2.6) is a function of the distance to the wall, this fact seems to limit its application to differential methods only. Based on the same theoretical considerations, a correction was derived at VKI which is applicable to integral methods using the energy equation. First a curvature correction was derived by Papailliou et al. [1970], [1972], [1973], afterwards Van Den Braembussche and Zunino [1979], [1981] derived a similar correction for Coriolis force and combined the two. Good agreement is obtained with experimental results, for a wide range of curvature and rotation numbers as encountered in turbomachinery applications.

The method is based on the idea that, even though detailed information of the Reynolds stress distribution perpendicular to the wall is lost by integration of the momentum equation, a different Reynolds stress distribution still results in a different dissipation factor in the energy equation. Introducing relation (2.6) and the definition for the Richardson number, relation (2.7) or (2.8), into the dissipation function definition, leads to corrections of the following form .

$$\Delta c_D^C = - \beta \bar{R}_{iC} [A - \beta \bar{R}_{iC} B] \tag{2.9}$$

$$\Delta c_D^R = - \beta \bar{R}_{iR} [A' - \beta \bar{R}_{iR} B'] \tag{2.10}$$

so that the corrected dissipation function C_D becomes:

$$C_D = C_{Do} + \Delta c_D^C + \Delta c_D^R \tag{2.11}$$

The functions A,B,A'and B' are, within a neglected dependence on δ_2 of 1%, functions of H_{12} only. The mean Richardson numbers appearing from this procedure are obtained by integration over the boundary layer thickness:

$$\bar{R}_{iC} = \frac{\delta}{R} \qquad \bar{R}_{iR} = \frac{\Omega \delta}{w_e} \tag{2.12), (2.13}$$

To be able to treat flows where high $\bar{R}_i$ values occur, up to .25, Van Den Braembussche and Zunino left the concept of constant β values. They demonstrated why β must decrease with increasing $\bar{R}_i$ numbers and calibrated then $\beta(\bar{R}_i)$ curves, one for $R_i > 0$ and one for $R_i < 0$ values, however with the use of a global mean Richardson number in relation (2.9) :

$$\bar{R}_{iC}^* = \delta \left(\frac{1}{R} + 1.4 \frac{\Omega}{w_e} \right) \tag{2.14}$$

since A' $\simeq$ 1.4A and B' $\simeq$ 1.9B for a wide range of H12.

The corrections on the dissipation function are calculated here separately for curvature and Coriolis effects and are then added. Based on a relevant number of experimental comparisons, the two $\beta(\bar{R}_i)$ functions were therefore calibrated again as shown in Fig. 2.2.

To illustrate the performance of the present method, the predictions for the convex side of the curved channel flows of So and Mellor [1972] are compared with the experimental data, followed by the suction and pressure side boundary layer developments on Moore's rotating diffusor [1973]. Results obtained with previously developed procedures for turbulence correction, indicate that the most difficult flow cases to treat are those associated with destabilisation and with strong Richardson numbers in general.
To investigate a turbulent flow only affected by curvature , So and Mellor arranged the cross section and radius of curvature in a first, high aspect ratio geometry, to result in a zero convex side longitudinal pressure gradient. In the corresponding velocity distribution of Fig. 2.3a the only apparent pressure drop at x=48" is due to the rapid change in curvature at the entrance from the straight channel to the curved test section. As can be seen in Fig. 2.3b the curvature Richardson number, eq. (2.12), is rather high from there, with values of .075 at the entrance of the bend. Figs. 2.3c-2.3g show the most important boundary layer parameters obtained with Ri number correction (continuous lines) and without correction (dotted lines). Stabilisation causes the boundary layer thickness to decrease, Fig. 2.3g, while the displacement thickness is increased, Fig. 2.3e and the momentum thickness is slightly decreased, Fig. 2.3f. This relaminarisation of the turbulent boundary layer increases the momentum shape factor, Fig. 2.3c and decreases the skin friction coefficient, Fig. 2.3d. As already mentioned, H , Cf and also δ_1 and δ are the most sensitive parameters, while δ_2 is changed only slightly. The corresponding β values can be derived in Fig. 2.2 from the mean $\bar{R}_i$ numbers of Fig. 2.3b and vary around 1. Boundary layer separation is not reached at the end of this test section. For the separating test, Fig. 2.4a, the results are analogous, besides the fact that the mean $\bar{R}_i$ number now does not decrease as much after the bend entrance as in the constant pressure case, see Fig 2.4b. This enhances the corrections and causes the boundary layer to separate. From Fig. 2.4d it is obvious that no evidence is found for this separation without correction, while the shape factor does not increase enough, Fig 2.4 c. With the corrections introduced, the reduction in mixing is well predicted as δ decreases, Fig 2.4g, while H_{12} increases strongly, Fig. 2.4c. Again δ_2 varies only slightly, Fig. 2.4f.
Moore's rotating diffusor tests [1973] clearly show how Coriolis forces may bring a boundary layer to separation as shown in Fig. 2.5, while they might prevent separation altogether as shown in Fig. 2.6. The experimental data for the suction side at large mass flow do not agree very well, Figs. 2.5c-f. The same discrepancy was also found by Johnston and Eide [1976] and Baljé [1977] with differential methods and by Papailliou [1979] and Van Den Braembussche and Zunino [1981] with integral calculations, and is probably due to secondary flows from the end walls which cause the flow to be three dimensional in the diffusor. Nevertheless, separation is predicted at approximately the

correct position, Fig. 2.5d. The stabilizing effects of The Coriolis forces are very strong, although the mean Richardson number, eq. (2.13), is below 1%, see Fig. 2.5b. Without corrections the boundary layer calculation proceeds to the end of the diffusor without separation, Figs. 2.5c-f. The rapid growth of the momentum shape factor in the vicinity of the separation, Fig. 2.5c, was not predicted by Johnston and Eide who used a constant value of 6 for β.
Along the pressure side the agreement is much better, Figs. 2.6c-e. The qualitative behavior of the skin friction coefficient which first decreases and then increases, is well predicted in Fig. 2.6d. Johnston and Eide used a constant β factor of 6 and were not able to predict this increase. As shows Fig. 2.6b the mean Richardson number varies strongly. A non corrected boundary layer calculation predicts almost immediately separation, Figs. 2.6d,e., which emphasises once more how important normal pressure gradients are for the location and the occurence of flow separation.

2.3. The viscous inviscid interaction.

The interaction is modelled by the wake displacement body method, whereby the displacement thickness of the viscous regions is added to the blade surface, so that the new "effective" wall shape induces streamline deflections in the inviscid solution, compatible with the boundary layer thickness variation. This effective boundary concept is identical for the viscous flow regions over the blade contour and in the downstream wake. Separated flow regions and the decaying wakes call for additional iterations in the viscous inviscid scheme. Fig. 2.7 shows the resulting effective blade to blade calculation domain.

Within the wake displacement body method, basically two different techniques can be applied to express the boundary conditions on the equivalent inviscid flow. In the "solid displacement surface" method one calculates the inviscid flow around the thickened blade BC'E-B1C1'E1. The "surface transpiration" model injects along the blade walls BC-B1C1, a fictitious mass flow, which is a function of the evolution of the displacement thickness. Downstream of the trailing edge, the injected mass has to be removed along sink lines CE-C1E1, with an arbitrary distribution. As long as the boundary layers remain relatively thin, either of these matching models is an equally valid representation of the displacement effect of the viscous layers.
One of the advantages of the finite element method is that mixed type boundary conditions can be easily and axactly introduced along curved boundaries without losing accuracy. Fictitious mass injection would thus be the most appropriate way to simulate the wall boundary condition in this viscous inviscid interaction scheme, because the finite element mesh could be kept unchanged, Deconinck and Hirsch [1979]. This method is however only valid for small displacements of the effective flow boundaries of the outer potential flow. Mesh redefinitions are thus necessarily introduced in the overall iterations, since the present method is intended to treat flows where large separations occur. But to avoid relative time-expensive finite element mesh redefinitions, when small geometry changes have to be introduced, fictitious mass injection is also used and coupled with the mesh redefinitions. A choice is made during the iterations, either to displace the whole mesh to fit the effective flow boundaries, or to introduce a fictitious mass flow distribution. In the latter case, mass injection is performed along the mesh boundaries, which are not necessarily the blade walls BCD-B1C1D1, but the lines BC'D'-B1C1'D1' of the most recent mesh. Another particularity in the present approach is that mass injection is performed up to downstream of the trailing edge (to points D' and D1' in Fig. 2.7), over the largest part of the wake region. For the modelling of the wake body C'D'E,C1'D1'E1, (i) the effective flow boundaries C'D' and C1'D1' are calculated with the free streamline method and (ii) the lines D'E and D1'E1 are determined by the used suction law.

The modelling problem of separated flows and wakes consits in finding the effective limiting streamline of the viscous region. Therefore a free streamline method has been developed, where the viscous flow within these regions is however not calculated. In order to find the unknown position of this line, the two following conditions are imposed :

    a. The separation line is a streamline. This condition is fulfilled in the inviscid flow calculation.

    b. The static pressure distribution is specified :

$$p(s) = p^e(s) \qquad (2.15)$$

In an iterative search for the correct free streamline position, the pressure condition is satisfied by gradually changing the position of the mesh points on this line. The displacement thickness is corrected as a function of the local difference between the value of the computed pressure p, obtained from the inviscid flow solution, and the specified pressure p^e. Generally a constant pressure is imposed over the blade separated flow regions of isolated airfoils. Experiments in cascade configurations however indicate that the static pressure over the blades in separated boundary layer regions is generally not constant. Within centrifugal and radial turbomachines the static pressure evolution is moreover strongly affected by rotation. In a previous paper, Janssens and Hirsch [1982], only two different pressure laws were investigated, namely a constant pressure level and a distribution varying with the inverse of the arc length of the free streamline. Further calibrations against experiments were found necessarily. The following general expression is therefore introduced for the imposed pressure distribution over the separated blade regions, from the separation point (S) to the trailing edge

$$p^e(s) = p_2 + (p_S - p_2) \ e^{-\frac{s - s_S}{s_{TE} - s_S} \frac{1}{PB}} \tag{2.16}$$

The arc length s of the free streamlines is measured from the leading edge. Index 2 corresponds to the uniform outlet station far behind the cascade, line PP1 in figure 2.7. Large values of PB correspond to the already mentioned constant pressure level over the blade region. In the wake downstream of the trailing edge the pressure varies linearly from its trailing edge value to p2.

A Kutta Joukowsky condition is imposed which corrects the outlet flow angle and ensures zero load on the wake. Various forms for the Kutta Joukowsky condition in inviscid flow calculations are reviewed by Scholz [1977] and Hirsch and Denton [1981]. Most usually the Wilkinson [1967] trailing edge condition is followed whereby equal pressures or velocities are imposed on opposite points on the contour near the trailing edge. Here, the trailing edge closure condition is expressed by the requirement of equal velocities in the trailing edge plane, at the calculated effective flow boundaries, points C' and C1' in Fig. 2.7. This is achieved iteratively by correcting the mean outlet tangential velocity component. Associated with the trailing edge closure , an additional condition is required, which ensures that no loading is created over the wake. This is realised by imposing on the potential function a constant value of the periodicity constant, from the trailing edge on over the whole downstream flow extension.

2.4 Numerical solution.

The numerical procedure for the outer potential flow, based on finite elements, and the computational details are extensively described by Hirsch and Warzee [1974], [1976]. Within the present method however the finite element mesh can be redefined and different boundary conditions are applied

If the viscous regions become too important, the finite element mesh is redefined. Then the usual wall boundary condition is imposed

$$\rho w_n = 0 \tag{2.17}$$

When fictitious mass is injected, the finite element geometry of a previous iteration is maintained and the wall displacement is replaced by a source-sink distribution according to the expression :

$$\rho \, B \, w_n = - \frac{\partial}{\partial s} \left(\rho \, B \, (d \, \delta_1) \, w_s \right) \tag{2.18}$$

$d \, \delta_1 = \delta_1 - \delta_1^{mesh}$ is the local displacement of the effective flow boundary to be introduced at the considered iteration with respect to the already displaced mesh distance δ_1^{mesh} . To preserve the mass flow of the outer potential flow one has to remove the fictitious injected mass flow. This is done over a short extend of the last part of the wake region D'E and D1'E1 by a sink distribution with a mass rate of :

$$\dot{m}_f(s) = - \rho \, B \, (d \, \delta_1) \, w_s \, \Big|_{D' \ or \ D1'} \cdot f(s) \tag{2.19}$$

where f(s) is the used suction law.

The details of the interactive procedure are described in Janssens and Hirsch [1982] and will not be repeated here.

The loss coefficients are computed from a compressible mixing law based on Scholz [1977]. The continuity and momentum integral laws are expressed between the real non homogenous viscous flow at the trailing edge plane and the homogenous flow far downstream, which contains the losses due to the boundary layer formation and separation over the blade and due to the mixing in the wake. Since the real viscous flow pattern at the trailing edge plane is not known, the corresponding integrals in the conservation laws cannot be calculated directly. This is done through an equivalent discharge flow, which is defined at the trailing edge plane and based on the inviscid flow solutions in the outlet region and on the integral boundary layer properties at the trailing edge plane. The equivalent discharge flow has the same mass flow, mean outlet angle and density as the inviscid flow obtained with the viscous inviscid interaction solution, but the velocity is corrected for the displacement effect of the viscous regions and its energy loss is the same as in the real flow. The loss coefficient is then obtained as the difference, referred to the inlet dynamic pressure (for compressors), of the total relative pressures of the inviscid flow and the homogenous discharge flow far downstream with the same rothalpy.

3. RESULTS.

Based on the theory described in the previous sections, a viscous inviscid interaction method was developed and applied to a number of cascade tests. This resulted also in a numerical scheme wherein the different interactions are efficiently balanced. Based on experimentally measured profile Mach number distributions and displacement thicknesses, outlet angles and loss coefficients, the calibrations were performed for the pressure distributions to be imposed over blade separated flow regions.

For the selection of experimental data it is extremely important to have accurate knowledge of the measuring details especially concerning inlet and outlet flow conditions and blockage factors. Although a considerable number of cascade tests are available in the literature, only few include measurements of separated regions.

A first set of considered tests concerns a high cambered DCA blade experimented at the VKI, Meauze, Starken and Van Den Braembussche [1976]. Blade Mach number distributions, outlet angles and loss coefficients are available. At ONERA, Meauze [1978]a and [1978]b, experiments were investigated for highly separated cascade flows. For the first blade, Mach number distributions are reported, while for the other blade, boundary layer thicknesses were measured for four incidences.

3.1 The DCA cascade.

The DCA cascade has 48 degrees of camber and the range of inlet flow angles varied from 31.9 to 44.5 degrees. The inlet Mach number is .60. Sidewall suction has been necessary to preserve the two dimensionality of the flow especially for the positive incidences.

For the same case results were reported in a previous paper, Janssens and Hirsch [1982], without interaction on the separation point position and without turbulence correction for curvature. No blockage was introduced (B=1) for all the incidences. Loss coefficients were estimated from the empirical relation from Lieblein [1965] :

$$\bar{\omega} = 2 \sigma \frac{\Theta}{\cos \beta_2} (\frac{\cos \beta_1}{\cos \beta_2})^2 \quad \text{with} \quad \Theta \cdot c = \delta_{2TE}^{suct.} + \delta_{2TE}^{press.} \tag{3.1}$$

This estimation provides an underlimit of the profile losses. Over the separated blade regions the free streamlines were fitted to a constant pressure law, equal to the pressure at separation.

To accurately predict Mach number distributions the blockage factor is important. Because the experimental values were variable a linearly varying blockage from .95 to .85 was taken corresponding respectively to the range of considered inlet angles from 31.9 to 48.5 degrees.

Figure 3.1 shows the results for one typical incidence. First the Mach number evolution is drawn without viscous inviscid interaction, with and without trailing edge condition. In a next figure the obtained distribution agrees fairly well with the experiment and it can be clearly seen that a constant pressure level is far from realistic here over the separated zone.

During calibration of the pressure law it was tried to either satisfy the Mach number evolutions for each incidence and to predict the measured outlet angles and loss coefficients for all incidences as good as possible. A large number of calculations thereby demonstrated that the optimum value of the pressure law factor, PB in eq. (2.16), changes with incidence. The tendency is that as separation moves upstream a flatter pressure law is required. Based on the read in parameter PB a continuously decreasing function with the separation point position was selected. So all the incidences can be treated and also changes in the separation point position during convergence for each individual incidence. The loss and turning evolutions are given in figure 3.2. In the low incidence range the outlet angles are below the experimentally values. These angles could be increased by increasing the displacement thickness at trailing edge by choosing a more flatter pressure level in the separated region, but this unavoidedly should result in unrealistic increased loss coefficients and Mach distributions in the vicinity of the trailing edge. Therefore it was preferred to pay more attention on the loss coefficients and the Mach number distributions. To show the increasing trend of loss and turning in the range of the higher incidences additional cases were calculated up to 48.5 degrees of inlet angle.

3.2 ONERA blades.

The first case in this considered group of tests is a cascade geometry with a blade chord length of 123.5 mm and a pitch of 33.58 mm. The Mach number distribution along the blade.walls is given for an inlet Mach number of .847 and inlet flow angle of 53. degrees. Separation of the suction side boundary layer is predicted by the present method at 23% of the chord. Along the other 77% blade length the separation line between the viscous and inviscid regions was calculated with the free streamline method, resulting in a Mach number distribution shown in Fig. 3.3. A nearly forizontal line drawn from the indicated separation point position to the trailing edge should result from a constant pressure law. This test case is particularly suited to demonstrate that good results can be obtained with an exponentially evoluting pressure from the separation point to the trailing edge. Compared with the results obtained in [1982] with a 1/s pressure law the Mach number evolution is now predicted much better. Note here that separation is predicted 5% of chord more upstream due to the curvature effects. The isoMach lines and the final finite element mesh together with the effective blade contour are shown in Fig. 3.4.

The developed viscous inviscid interaction procedure has also been tested on the so called "115" blade with a chord length of 95.mm and mounted in cascade with a pitch of 28.mm. For an inlet Mach number of .70 four inlet angles are considered namely 49., 51.,

53. and 55. degrees. The obtained displacement thickness distributions along the blade suction side are compared with the experiments in Fig. 3.5. As for the DCA cascade these results were obtained with the same value of pressure law coefficient for the four incidences. Although the results still differ considerably from the measured ones, the displacement thicknesses are much more dispersed than those obtained with a 1/s pressure law, see [1982]. For the highest incidence the results indicate clearly that in cascade flow the presence of a next blade avoids the highly separated boundary layer to grow as much as would be expected from external flow experiences. The final mesh, isoMach lines and Mach number distributions are shown in Fig. 3.6 for the highest incidence.

4. CONCLUSIONS.

An efficient viscous inviscid procedure has been developed for blade to blade flows taking into account even large separated boundary layer regions however without computing the viscous separated components. The boundary layer calculation is corrected for Coriolis and centrifugal effects on turbulence. A coupled prediction is obtained for the losses and outlet flow angles. A calibration was derived for the pressure distribution in the separated regions resulting in satisfactory comparisons with experimental data.

REFERENCES.

[1]   Assassa G.M. 1976. Calcul par des methodes integrales de couches limites laminaires ou turbulentes incompressibles ou compressibles et incluant des zones faiblement decollees. These de Doctorat d'Etat, Universite de Lyon, No d'ordre 76-22, Mai 1976

[2]   Balje O.E. 1978. A flow model for centrifugal compressor rotors. Transactions of the ASME, Vol. 100 : 148-158. Jan. 1978

[3]   Bario F. 1978. Contribution a l'etude du developpement des couches limites sur des aubages de turbomachines. Ecole Centrale de Lyon, Laboratoire de Mecanique des Fluides, No d'ordre 734.

[4]   Bradshaw P. 1967. The analogy between streamline curvature and buoyancy in turbulent shear flow. Journal of Fluid Mechanics, Vol.36 part 1 : 171-191.

[5]   Bradshaw P. 1973. Effects of streamline curvature on turbulent flow. AGARDo-graph 169, 1973

[6]   Breugelmans F.A.E. 1973. The cascade and rotor section performance of a 48 degrees cambered airfoil. In : Transonic Flows in Turbomachinery, May 1973. VKI Lecture Series 59.

[7]   Calvert W.J., Herbert M.V. 1980. An inviscid vicous interaction method to predict the blade to blade performance of axial compressors. NGTE M80012. Feb. 1980.

[8]   Cebeci T., Hirsh R.S., Whitelaw J.H. 1979. On the calculation of laminar and turbulent boundary layers on longitudinally curved surfaces. AIAA Journal Vol.17, No.4 Apr. 1979.

[9]   Dean jr. R.C. 1971. On the unresolved fluid dynamics of the centrifugal compressor. In : Advanced centrifugal compressors. ASME publication, New York.

[10]   Deconinck H., Hirsch Ch. 1979. A finite element method solving the full potential equation with boundary layer interaction in transonic cascade flow. AIAA paper 78-1148, 1979.

[11]   Eckhardt D. 1976. Detailed flow investigations within a high-speed centrifugal compressor impeller. Journal of Fluids Engineering, TRANS. ASME, Sep. 1976.

[12]   Geller W. 1972. Incompressible flow through cascades with separation. In : Boundary Layer Effects in Turbomachines : 171-186. AGARD-AG-164.

[13]   Gross L.W. 1978. The prediction of two dimensional stall progression. AIAA 16th Aerospace Sciences Meeting. Paper 78-155. Jan. 1978

[14]   Hansen E. 1978. Blade-surface boundary layer and wake computational models for estimation of axial-flow compressor and fan blade-row fluid turning angles and losses. Iowa State University, Ph. Doctor Thesis 1978, University Microfilm 7813230.

[15]   Hansen E., Serovy C.P.M., Sockol P.M. 1979. Axial-flow compressor turning angle and loss by inciscid-viscous interaction blade to blade computation. ASME paper 79-GT-5.

[16]   Henderson M.L. 1978. A solution to the 2D separated wake modeling problem and its use to predict CL max of arbitrary airfoil sections. AIAA 16th Aerospace Sciences Meeting. Paper 78-156. Jan. 1978.

[17]   Hirsch Ch., Warzee G. 1974. A finite element method for flow calculations in turbomachines. Vrije Universiteit Brussel, Department of Fluid Mechanics, Report VUB-STR-5, 1974.

[18] Hirsch Ch., Warzee G. 1976. A finite element method for through flow calculations in turbomachines. ASME Journal of Fluids Engineering, Vol.98, 1976 : 403-421.

[19] Hirsch Ch., Warzee G. 1978. An integrated quasi 3D finite element calculation program for turbomachinery flows. ASME paper 78-GT-56.

[20] Hirsch Ch., Denton J.D. (editors) 1981. Through flow calculations in axial turbomachines. AGARD-AR-175.

[21] Jacob K. 1969. Berechnung der abgelosten inkompressiblen Stromung um Tragflugelprofile und Bestimmung des maximalen Auftriebs. Zeitschrift fur Flugwissenschaften, Vol.17, No.7, Jul. 1969.

[22] Janssens P., Hirsch Ch. 1982. Viscous inviscid interactions in cascades. 16Tth Israel Conference on Mechanical Engineering, Haifa, Jul. 1982. Published in : Israel Journal of Technology, Vol.20.

[23] Johnston J.P. 1971. The suppression of shear layer turbulence in rotating systems. In : Turbulent shear flows, AGARD, CP 93, 1971.

[24] Johnston J.P., Halleen R., Lezuis D. 1972. Effects of spanwise rotation of two dimensional fully developed turbulent channel flow. Journal of Fluid Mechanics, Vol.56 part 3 : 533-557, 1972.

[25] Johnston J.P., Eide S.A. 1976. Turbulent boundary layers in centrifugal compressor blades and prediction of the effects of surface curvature and rotation. ASME paper 76-FE-10, 1976.

[26] Kwon O.K., Pletcher R.H. 1979. Prediction of incompressible separated boundary layers including viscous inviscid interaction. Transactions of the ASME, Vol. 101, Dec. 1979 : 466-472

[27] Le Bailleur J.C. 1980. Calcul des ecoulements a forte interaction visqueuse au moyen de methodes de couplage. In : Computation of viscous inviscid interactions, AGARD CP 291, 1980.

[28] Lieblein S. 1965. Experimental flow in two dimensional cascades. In : Aerodynamic Design of Axial Flow Compressors. Chapter VI, NASA SP-36. 1965

[29] Meauze G., Starken H., Van Den Braembussche R. 1976. Turbine and compressor cascade test cases. In : Transonic Flows in Axial Turbomachinery, February 1976. VKI Lecture Series 84.

[30] Meauze G. 1978a. Comparaison calcul-experience de l'ecoulement transsonique bidimensionnel dans une grille d'aubes a forte deviation. La Recherche Aerospatiale 1978-4 : 175-180.

[31] Meauze G. 1978b. Transonic boundary layer on compressor stator blades as calculated and measured in wind tunnel. 4th ISABE Meeting.

[32] Meroney R.N., Bradshaw P. 1975. Turbulent boundary layer growth over a longitudinal curved surface. AIAA Journal Vol.13, Nr.11 : 1148-1153.

[33] Moore J. 1973. A wake and an eddy in a rotating radial flow passage. Parts 1 and 2. ASME papaers 73 GT 57 and 73 GT 58.

[34] Morice Ph. 1977. A variational principle and a finite element method for compressible flow with free boundaries. ONERA T.P. No 1977-151.

[35] Morice Ph. 1979. Finite element approximation of a variational principle for perfect fluid flows with free boundaries. In : Notes on Numerical Fluid Mechanics, Vol.2 : 202-210. Vieweg & Sons, Wiesbaden 1979.

[36] Obee T.N., De Witt K.J. 1980. Finite element analysis of free jet inpingement. International journal for numerical methods in engineering, Vol. 15 : 63-85, John Wiley & Sons 1980.

[37] O'Carroll M.J., Harrison H.T. 1975. A variational method for free boundary problems. In : The Mathemathics of Finite Elements and Applications II, Mafelap 1975. Academic Press, London 1975.

[38] O'Carroll M.J. 1978. Variational methods for free surfaces of cavitation, jets, open channel flows, separation and wakes. In : Finite Elements in Fluids, Vol.3, John Wiley & Sons, Chichester, New York 1978.

[39] Papailliou K.D., Nurzia F., Satta A. 1970. The inclusion of surface curvature effects in the calculation of the turbulent boundary layer with integral methods. Internal Note 37, VKI 1970.

[40] Papailliou K.D., Nurzia F., Satta A. 1972. On the two dimensional boundary layers as they appear on turbomachine blades. In : Boundary layer effects in turbomachines. AGARD AG 164 : 5-27, 1972.

[41] Papailliou K.D., Nurzia F., Satta A. 1973. *The inclusion of surface curvature effects in the calculation of the turbulent boundary layer with integral methods.* Internal Note 44, VKI 1973.

[42] Papailliou K.D. 1979. *The Coriolis force influence when we calculate turbulent boundary layers in centrilugal compressors.* Haifa Israel Jul. 1979.

[43] Parsons D.J., Hill P.G. 1973. *Effects of curvature on two dimensional diffusor flow.* Journal of Fluids Engineering : 349-360, Sep. 1973

[44] Patel V.C. 1968. *The effects of curvature on the turbulent boundary layer.* R.M. No. 3599, Cambridge University, Aug. 1968

[45] Scholz N. 1977. *Aerodynamics of cascades.* Translated and revised by Klein A. AGARD AG 220

[46] Schubauer G.B., Klebanoff P.S. 1951. *Investigation of separation of the turbulent boundary layer.* NACA TR 1030, 1951.

[47] So R.M., Mellor G.L. 1972. *An experimental investigation of turbulent boundary layers along curved surfaces.* NASA CR 1940, 1972.

[48] Van Den Braembussche R., Zunino P. 1979. *Corrections for streamline curvature and Coriolis force in boundary layer integral methods.* Project Report 1979-6, VKI.

[49] Van Den Braembussche R., Zunino P. 1981. *Correction for streamline curvature and Coriolis force in a boundary layer integral method.* ASME paper 81 GT 97.

[50] Walz A. 1969. *Boundary layers of flow and temperature.* The MIT Press, London.

[51] Watanabe I, Koyama H., Ariga I. 1979. *Stabilizing and destabilizing effects of Coriolis force on two dimensional laminar and turbulent boundary layers.* Journal of Engineering for Power, Vol.101 : 23-31, Jan. 1979.

[52] Wilkinson D.H. 1967. *A numerical solution of the analysis and design problems for the flow past one or more aerofoils or cascades.* ARC Rep. and Memo 3545.
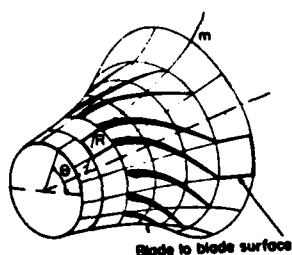
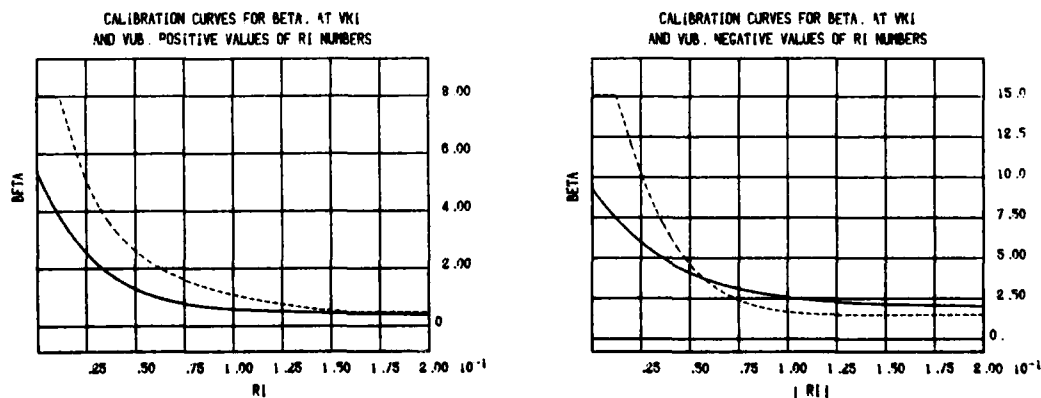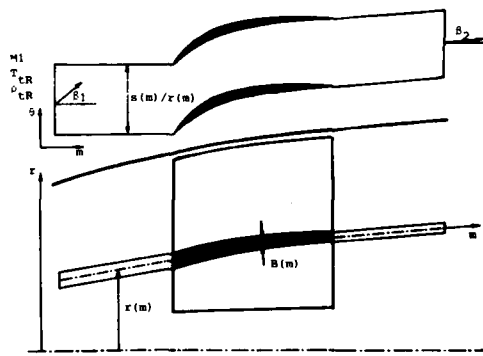**Fig. 2.1.** View of a turbomachine and typical blade to blade domain for inviscid flow calculation.

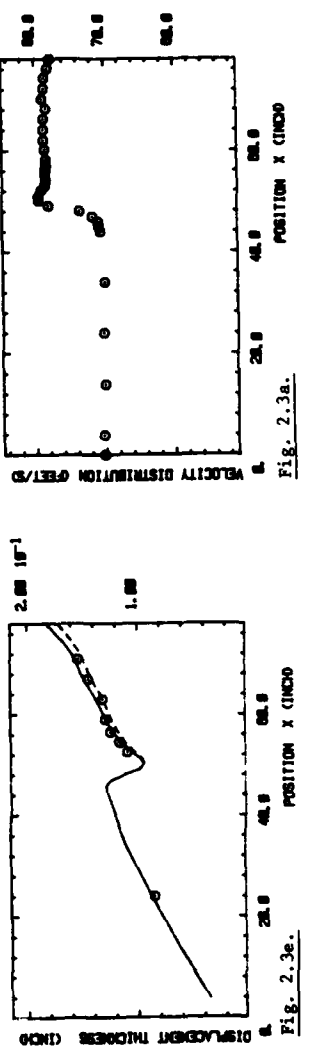**Fig. 2.2.** Calibration curves for $\beta(R_i)$: ——— at VUB
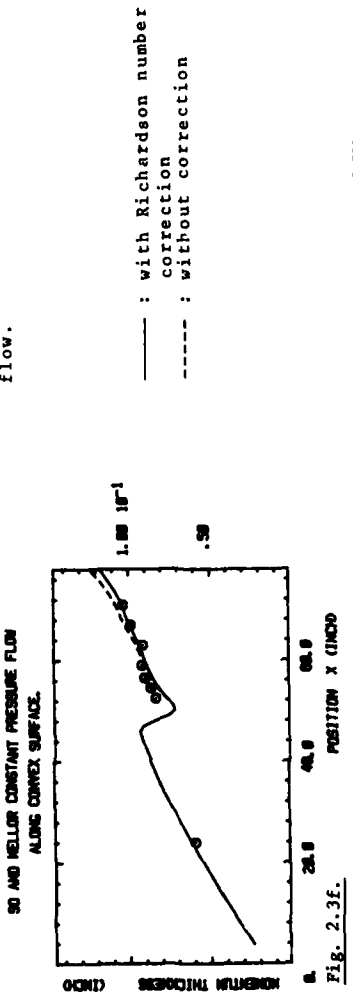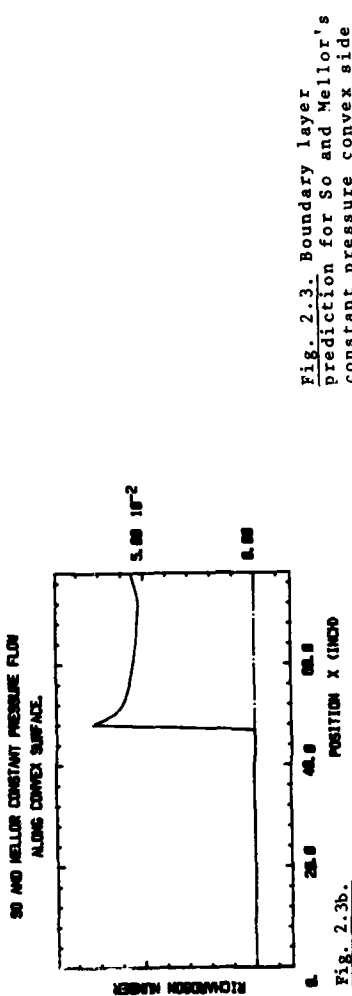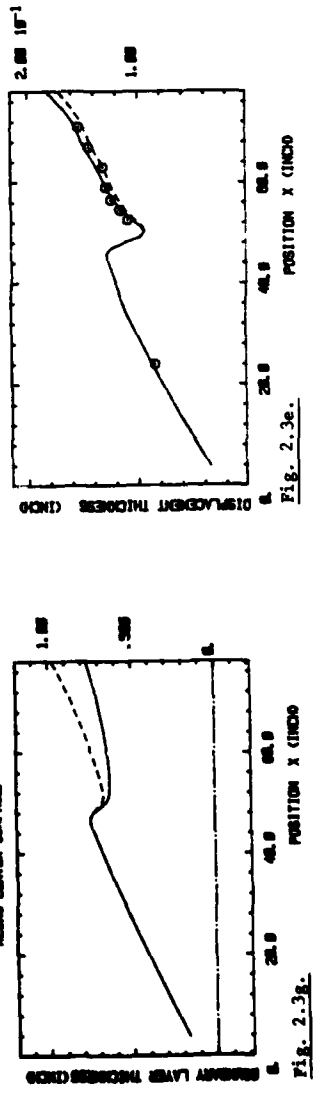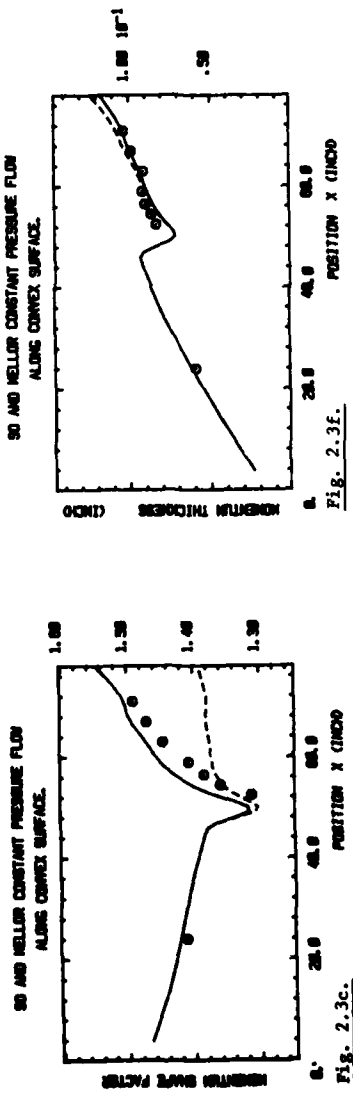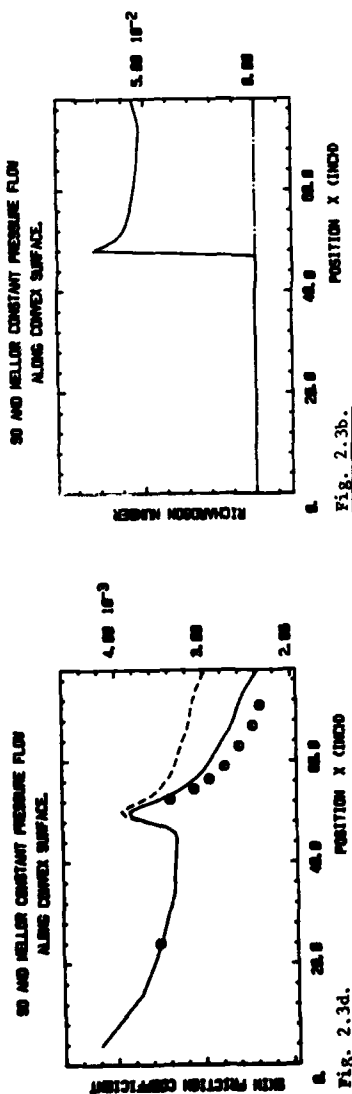---- at VKI

Fig. 2.3. Boundary layer
prediction for So and Mellor's
constant pressure convex side
flow.

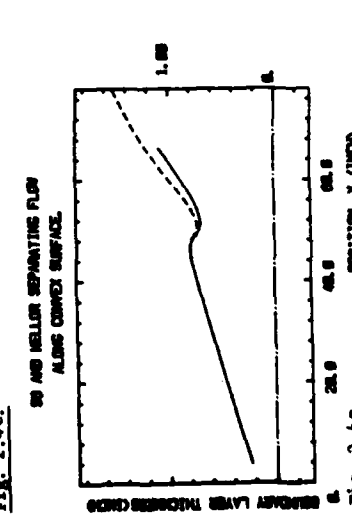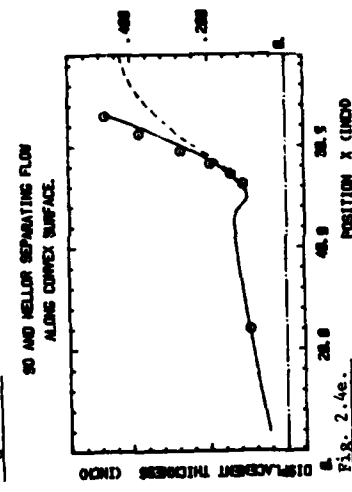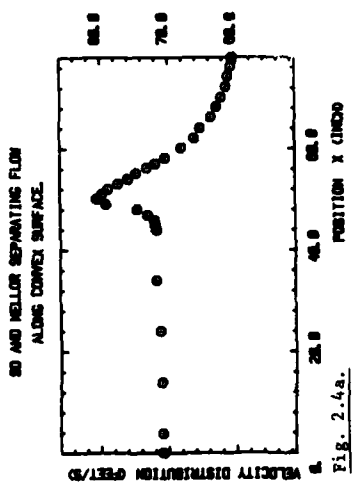——— : with Richardson number
correction
----- : without correction

Fig. 2.3a.

Fig. 2.3b.

Fig. 2.3f.

Fig. 2.3e.

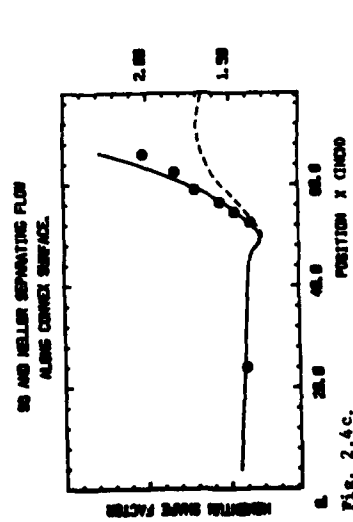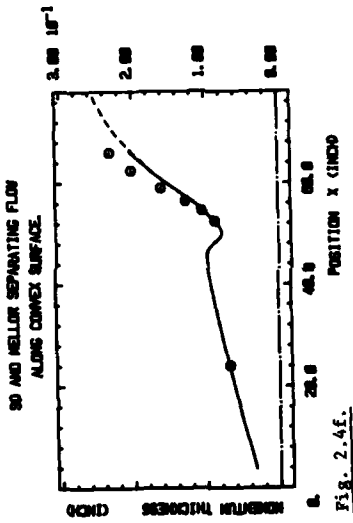
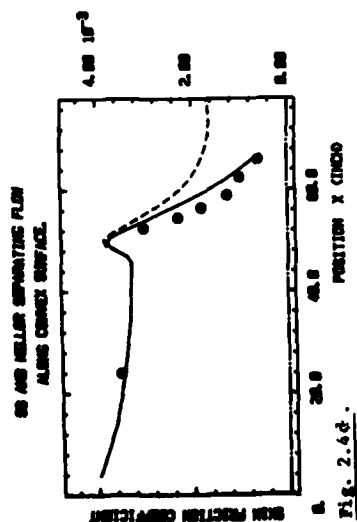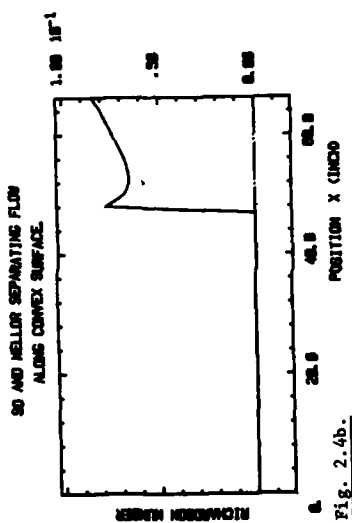Fig. 2.3d.

Fig. 2.3c.

Fig. 2.3g.

Fig. 2.4. Boundary layer
prediction for So and Mellor's
separating convex side flow

—— : with Richardson number
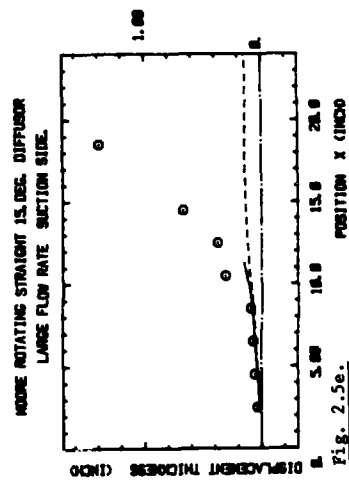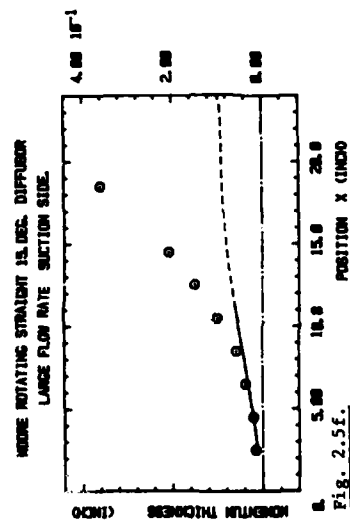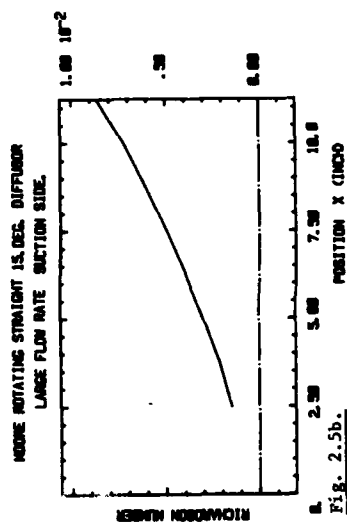correction
----- : without correction

SO AND MELLOR SEPARATING FLOW
ALONG CONVEX SURFACE.

VELOCITY DISTRIBUTION (ZET/B)

POSITION X (INCH)

Fig. 2.4a.

SO AND MELLOR SEPARATING FLOW
ALONG CONVEX SURFACE.

RICHARDSON NUMBER

POSITION X (INCH)

Fig. 2.4b.

SO AND MELLOR SEPARATING FLOW
ALONG CONVEX SURFACE.

MOMENTUM THICKNESS (INCH)

POSITION X (INCH)

Fig. 2.4f.

SO AND MELLOR SEPARATING FLOW
ALONG CONVEX SURFACE.

DISPLACEMENT THICKNESS (INCH)

POSITION X (INCH)

Fig. 2.4e.

SO AND MELLOR SEPARATING FLOW
ALONG CONVEX SURFACE.

SKIN FRICTION COEFFICIENT

POSITION X (INCH)

Fig. 2.4d.

SO AND MELLOR SEPARATING FLOW
ALONG CONVEX SURFACE.

MOMENTUM SHAPE FACTOR

POSITION X (INCH)

Fig. 2.4c.

SO AND MELLOR SEPARATING FLOW
ALONG CONVEX SURFACE.

BOUNDARY LAYER THICKNESS (INCH)
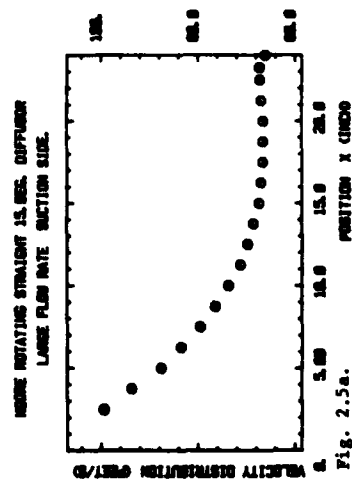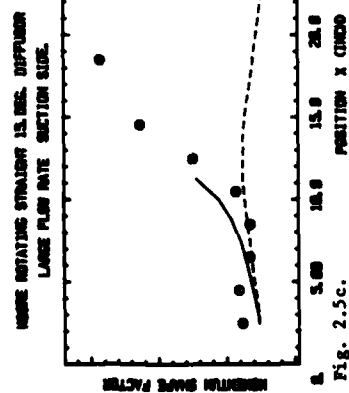
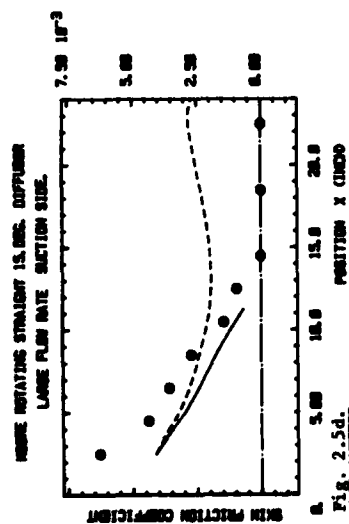POSITION X (INCH)

Fig. 2.4g.

Fig. 2.5. Boundary layer prediction for Moore's suction side diffusor flow.

——— : with Richardson number correction
------ : without correction

Fig. 2.5b.

Fig. 2.5f.

Fig. 2.5e.

Fig. 2.5d.

Fig. 2.5c.

Fig. 2.5a.
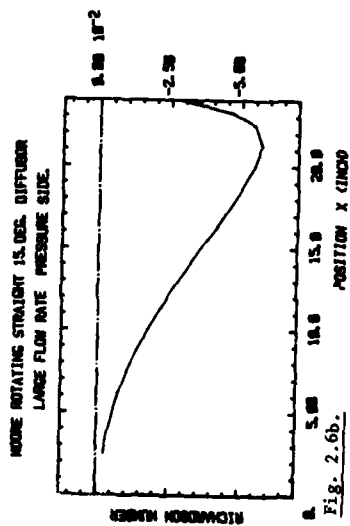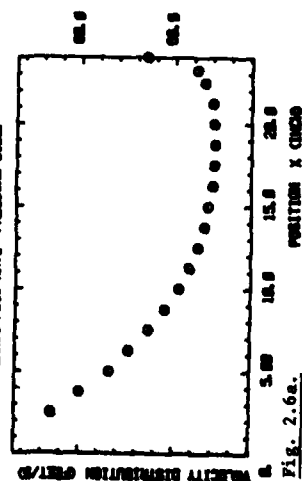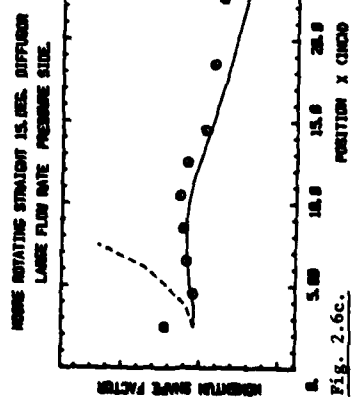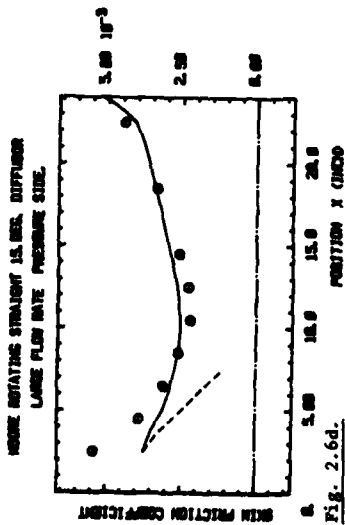
Fig. 2.6. Boundary layer prediction for Moore's pressure side diffusor flow.

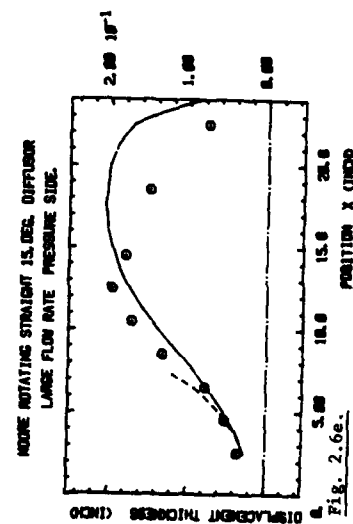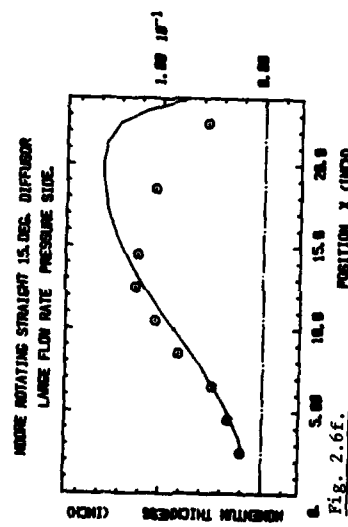———— : with Richardson number correction

------ : without correction

Fig. 2.6b.

Fig. 2.6f.

Fig. 2.6e.

Fig. 2.6d.

Fig. 2.6c.

Fig. 2.6a.
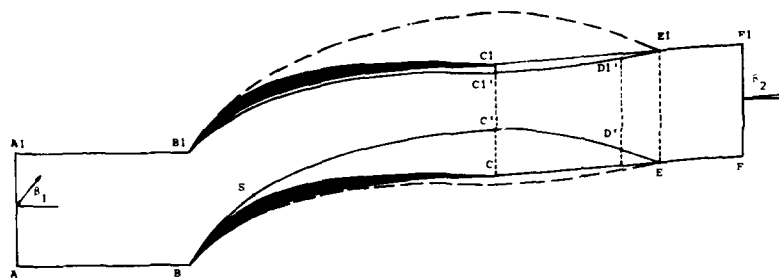
Fig. 2.7. Effective calculation domain
with presence of separated region and
wake.

Without *Kutta Joukowsky*
condition

With *Kutta Joukowsky*
condition

Pure inviscid calculation

Complete viscous inviscid
interaction
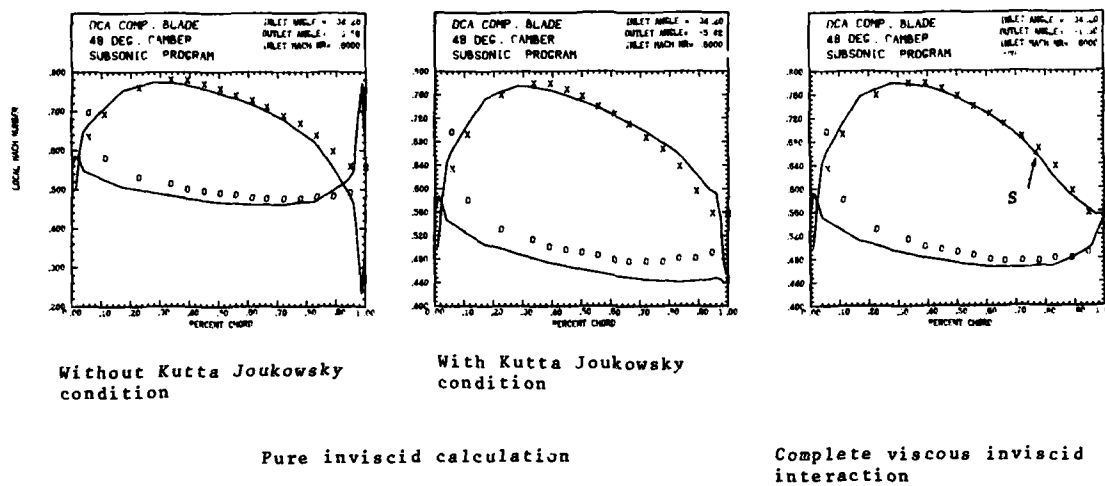
Fig. 3.1. Results for the DCA cascade
Inlet flow angle = 34.2°
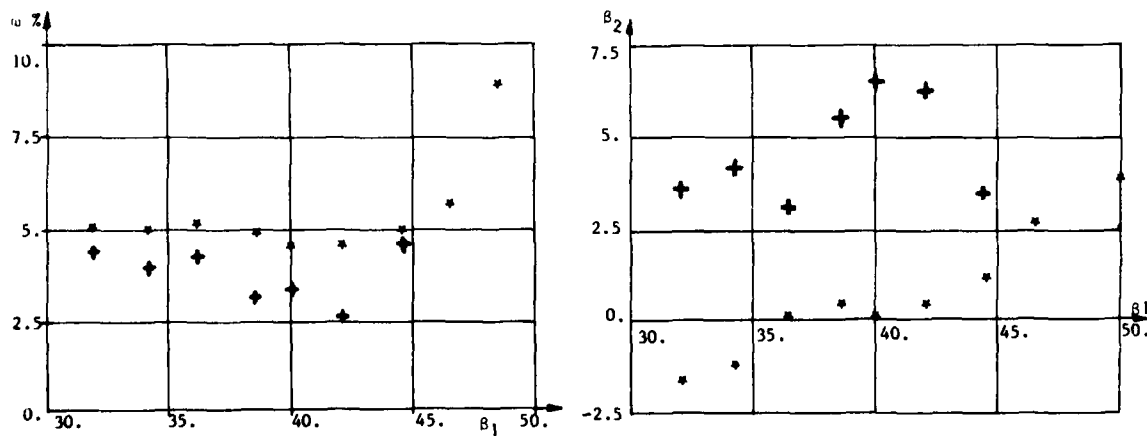
Fig. 3.2. Comparison of the predicted outlet angles and
loss coefficients with experimental data for the DCA cas-
cade at an inlet Mach number of .60.

* : calculated
+ : experiment
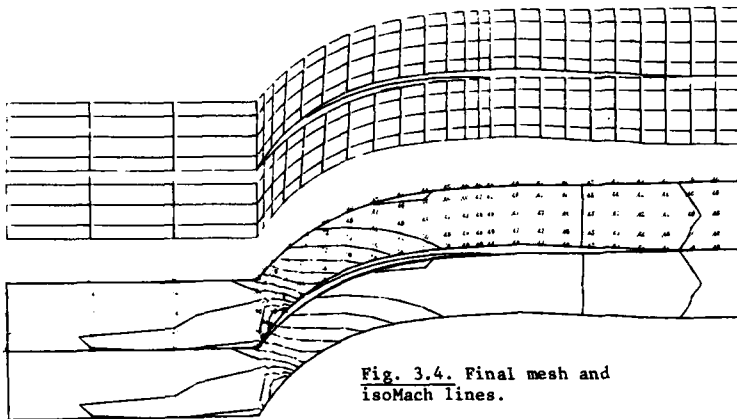
Fig. 3.4. Final mesh and isoMach lines.
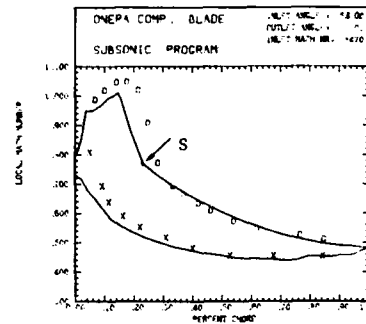
Fig. 3.3. Mach number distribution for the first ONERA blade.

ONERA 115 blade.

----- : measured

———— : calculated

S : separation point
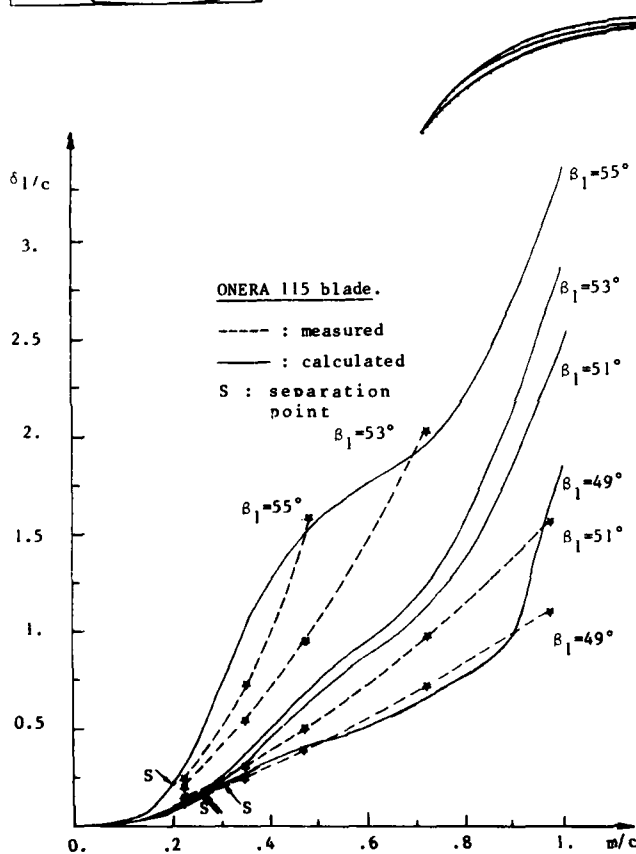
Fig. 3.5. Comparison between the measured and calculated boundary layer thicknesses for the ONERA 115 blade.
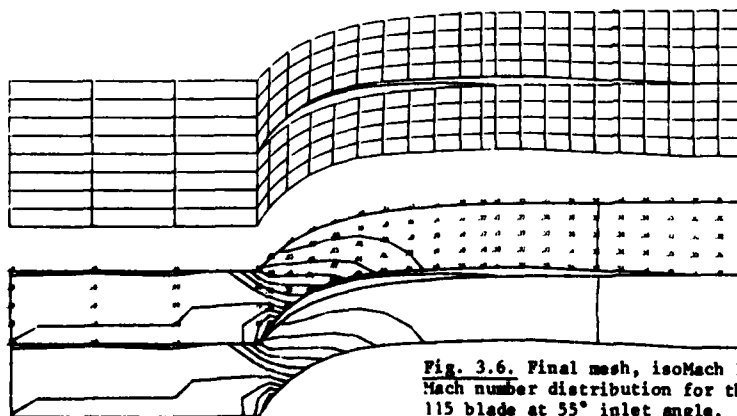
Fig. 3.6. Final mesh, isoMach lines and Mach number distribution for the ONERA 115 blade at 55° inlet angle.
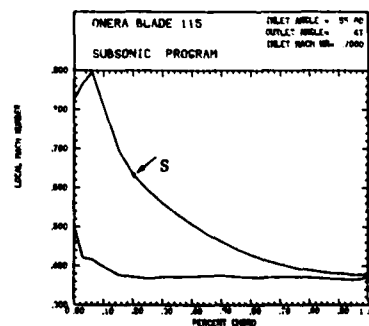
DISCUSSION

R.I.Lewis, UK

Could I ask for clarification of the free streamline model? For a true free streamline the static pressure at the edge of the shear layer is constant since velocity is zero in the separation zone. To sustain a pressure rise, as implied by Equation 2.16 would thus require fluid motion in the separation zone. How important do the authors consider the neglect of this recirculating motion in the present model? Perhaps more advanced Navier-Stokes solutions could be used to check these simplifying assumptions.

Author's Reply

It is customary to assume a constant static pressure along a separation line on isolated airfoils. In cascades, however, the interaction between the velocity variation along the free streamline and the requirements of mass flow conservation through the remaining inviscid region allows for non-constant static pressures along that streamline.

Actually, this assumption is also implied by the "inverse" methods for viscid-inviscid interactions whereby the integral Von Kármán equation is solved with vanishing wall shear stress, solving for $\delta_2 = \delta_2(U_e)$ through

$$\frac{d\delta_2}{dU_e} = -\frac{\delta_2}{U_e}(H + 2)$$

written for an incompressible flow.

No assumptions are made with regard to the flow behaviour in the separated region, since this region is excluded from the calculation domain. But, we fully agree that full Navier-Stokes solutions would be an important help for assessing the limits of validity of the simplified models used in the present work.

M.J.Werle, US

(1) Is the wake closure to zero thickness imposed or calculated.

(2) Are viscous mixing terms active in the wake closure region of your model.

Author's Reply

The wake closure is introduced in the computation as a simple way of stimulating the mixing of the physical wakes, which are not computed explicitly.

This allows to consider the flow quantities at the downstream end of the computational domain as mixed out, uniform, quantities and recover the full pitch spacing at the exit station.

Since the viscous regions are not computed, there is no physical viscous mechanism introduced in the wake simulation.

K.Papailiou, Gr

(1) Comment: The formulation that you are using for the calculation of the Coriolis and curvature effects on turbulence is the same as the one presented in References (1) and (2), appearing below, including the dependance of β on the overall curvature and Coriolis Richardson numbers.

It would be interesting, as one of the references appears already in your reference list, to compare the values of functions A and B that you are using (Equations (2.9) and (2.10) of your paper) with those appearing in Reference (2) below. It should be noted also, that the curve (Ri) appearing in Reference (2), covers a wider range of Richardson numbers, (covering the radial compressor applications also).

References

1. K.D.Papailiou   *Viscous Flows in Centrifugal Compressors.* VKI Lecture Series 95 on Industrial Centrifugal Compressors, 1977.

2. K.D.Papailiou   *The Coriolis Force Influence, when we Calculate Turbulent Boundary Layers in Centrifugal Compressors.* Haifa, Israel, 1979.

Question: A separated shear layer sustains, usually, a very limited deceleration. This is, in fact, one of the reasons for the difficulties encountered in calculating separated shear layers and for using an interaction procedure. In Figure 3.1 of your paper, there appears an impressive deceleration after separation. Have you any experimental evidence that this separation is there?

Author's Reply

The boundary layer code used in the interaction program is very sensitive to adverse pressure gradients and hence to separation detection. The experimental data of Meauze (1978b) concerning the ONERA "15" cascade confirm, for the higher incidences, the early separation which is detected around 30–40% chord.

Actually, from the point of view of the overall interaction procedure, since the imposed pressure law, Equation (2.16), assures a continuity of the pressure variation, the exact position of the separation point S is not at all critical and may not correspond always with a physical boundary layer separation. In this case, it is to be interpreted as the starting point of the free streamline without implying necessarily that the physical separation occurs at that point.

DESIGN OF TRANSONIC COMPRESSOR CASCADES FOR MINIMAL SHOCK LOSSES AND COMPARISON WITH TEST RESULTS

by

L. Fottner*, H.-J. Lichtfuß**

* Prof. Dr.-Ing., Hochschule der Bundeswehr München
  Werner-Heisenberg-Weg 39
  D-8014 Neubiberg, Germany

** Dr.-Ing., MTU Motoren- und Turbinen-Union München GmbH
   Postfach 50 06 40
   D-8000 München 50, Germany

SUMMARY

New blading concepts with respect to optimal profile shape take into account the close interdependence between the pressure distribution on profile suction and pressure side and the boundary-layer development (i.e. the losses) on these surfaces. For transonic compressor bladings with minimal losses the shock and shock/boundary-layer interaction losses have to be carefully considered. For supersonic inlet conditions these losses have been reduced by using wedge-type profile shapes in the supersonic part of the profile (wedge-type). On the other hand, the diffusion losses in the subsonic region (rear part of the blade) can be reduced by reducing subsonic deflection of a given vector triangle, resulting in a limited supersonic expansion (MCA-type). Thus, a very careful optimisation process has to be done for the partition of supersonic and subsonic deflection.
Detailed cascade tests have been carried out for the mid section of a rotor blade of a three-stage transonic compressor. The analysis of these tests and additional laser anemometry measurements within the compressor showed good agreement between design and test and proved the low loss design of the special profile types.

LIST OF SYMBOLS

B	stream tube height
c	chord length
h	local coordinate along blade height
La	Laval Number
Ma	Mach Number
p	static pressure
p_t	total pressure
r	radius
s	pitch
T_t	total temperature
t	max. profile thickness
w	relative velocity
x	local coordinate along chord
ß	flow angle
$ß_s$	stagger angle
$δ_u$	camber angle
$δ_{uss}$	supersonic expansion
η	local coordinate along pitch
ϰ	ratio of specific heat
ω	loss coefficient
Ω	axial velocitiy density ratio

INDICES

1	cascade inlet
2	cascade exit
comp	compressible
crit	critical
inc	incompressible
'	relativ to blade
∧	downstream of a compression shock

CONTENTS

1. INTRODUCTION

The efficiency of advanced turbojet aero engines is considerably affected by the aerodynamic characteristics of the turbo components. Using the latest knowledge regarding the flow deflection behaviour of the cascades and as a result of better understanding of the actual flow, the efficiency of these components has been considerably increased in the last years. Future development will have the following objectives:

-   high or even higher efficiency
-   large working range, also taking into account inlet distortions
-   lower manufacturing effort and cost, which means a reduction in size, weight, and number of blades. This requirement can only be met by reducing the number of stages, which means increasing the aerodynamic stage loading.

At these conditions the aerodynamic qualitiy of the blading is of great importance. The objective of the blading design is to realize a given design velocity triangle (result of through-flow calculation) with minimal losses and to have a sufficient working range at off-design conditions. Up to now the blading is designed with the aid of empirical methods. Compressor bladings are mainly designed using profile families which have been developed years ago. Cascade test results are the basis for the empirical design of such cascades, consisting of NACA 65, NGTE or DCA profile shapes (ref.1/2). The profile shape is strongly influenced by the Mach Number level. As an example, _Fig. 1_ shows the radial Laval Number distribution for the cascades of a 3-stage transonic compressor. The relativ Laval Number of the first rotor reaches $La_1' = 1.45$ at the tip and remains supersonic over a large region of the blade height. The inlet velocities of the following cascades decrease to lower Laval Number values. The stator cascades are subsonic, but the Laval Number sometimes exceeds the critical value, thus producing local supersonic fields terminated by a compression shock. The profile type to be chosen for optimal flow deflection is directly dependent on the Laval Number level. The areas of application of some profile types are also indicated in Fig. 1. At Laval Numbers higher than $La_1' = 1.2$ special profile types (transonic profiles) should be used to reduce the shock losses at these supersonic inlet conditions. Double circular arc profiles have shown good results for the Laval Number region between $La_1' = 0.8$ and 1.1. For lower Laval Number values NACA 65 profile blades are widely used. But, as has been already mentioned, for Laval Numbers higher than the critical value local supersonic fields with a terminating compression shock are experienced with conventional blades. Thus the compression shock should be minimised and it had been verified that it is possible to design cascades for supercritical inlet conditions without any compression shock (supercritical profiles).

Within the last years it has been shown that the use of new concepts for the bladings will increase their flow deflection behaviour, i.e. efficiency and working range. These methodes are of the inverse type, i.e. they calculate the profile shape for a given pressure distribution on suction and pressure surface. Thus, the pressure distribution as an input for these design methods has to be optimised with respect to high efficiency and sufficient safe working range.

2. FLOW BEHAVIOUR OF TRANSONIC COMPRESSOR CASCADES, SHOCK CONFIGURATION

2.1 Flowfield in Transonic Compressor Cascades

Before going in more detail for some of the mechanism associated with deceleration of supersonic flows in the next two paragraphs, a survey shall be given on the typical manifestations of cascade flow fields incorporating more or less extended supersonic areas. The presentation of different flow behaviours is best done by illustrating the flow field through its shock waves, the sonic line and expansion fans. This is shown in **Fig. 2** for cascades having all types of inlet and outlet flow conditions, i.e., Mach Number and flow angle. For the aspired classification the most important parameter will be the axial component of the in- and outlet flow Mach Number. This axial component is in either case subsonic for the configurations I to VI and supersonic for the configuration XI, whereas for the examples IX and X only the inlet flow has an axial supersonic component combined with an axial subsonic downstream region. In contrast to the last mentioned one the flow configurations VII and VIII represent an axial subsonic inlet but an axial supersonic outlet.

Physically the axial component uniquely determines the number of independable flow parameters of a geometrically given cascade. If we assume for this consideration a constant total temperature as well as a constant total pressure the individual flow conditions are only determined by Mach Number and flow angle. Now assuming an axial supersonic outlet flow means, that no information from downstream can reach the cascade so that the cascade exit condition is totally fixed by the cascade itself and its inlet flow conditions. If on the other hand the axial inlet flow is supersonic, there exists no influence of the cascade and of course much less of the exit into the upstream direction. Due to this, both upstream variables (Ma_1, β_1) are for free choice in this case. Assuming that the axial component of the inlet is subsonic there will be only one inlet variable which can be chosen independently, because the other one is then uniquely defined by the cascade itself (choking = cases II, III, V, VI, VII and VIII) or by the setting of the downstream throttling device (case I and IV). Regarding the last possibilty where the axial outlet velocity is subsonic means that now one of the two outlet parameters can be chosen as desired because now the information of the downstream throttle setting can be transmitted upstream and can so reach the cascade itself. In summary we have two independent variables in cases where the flow conditions at both ends are either axial subsonic (one inlet, one outlet) or supersonic (two inlet), but there is only one choice *in one of the mixed cases*, i.e., if the exit flow is axial supersonic and the inlet is axial subsonic, whereas in the contrary combination of an axial supersonic inlet and an axial subsonic outlet there are three (two at the inlet and one at the outlet) parameters to be chosen.

After this overall view we will now concentrate only on such behaviour which will be typical for transonic compressors. From all the various kinds shown in Fig. 2 especially the configurations I and V are typical for design point conditions of transonic compressor cascades. For some part load conditions at low back pressures also cases II, III and VI may occur and for very high back pressures the configuration IV will come in scene. First of all there is the subsonic configuration where in transonic stages, due to the high subsonic inlet Mach Numbers, normally a supersonic pocket on the profile suction surface will occur. These flow conditions are typical for rotor hub sections and for all radial sections of the stators with the higher Mach Numbers normally at the hub. The second flow configuration typical for transsonic compressors is those shown as case V. Here the inlet flow is supersonic but the axial component is far away from sonic. The outlet flow is throttled to subsonic or near sonic conditions. These flow configurations are realized especially in the outer parts of the first rotors of transonic compressors.

For part speed conditions when the throttling area is decreased the supersonic conditions change to the configurations shown as case IV. Now the inlet flow is still supersonic but not fixed by the cascade geometry but by the throttle area. Thus, the oblique shock system at the inlet has moved upstream and the cascade supersonic inlet conditions are strongly dependent on the downstream throttle settings. If in contrast the relative back pressure is lowered in comparison to case V the subsonic exit flow is accelerated up to supersonic conditions and the flow condition will be more similar to those shown as case VI. Regarding part speed conditions for the subsonic design (case I) results at increasing back pressure to lower inlet Mach Numbers and higher incidences. Is the back pressure lowered in contrary, the inlet flow is accelerated up to the limit at which the cascade chokes. This choking may be of the normal subsonic type (case II) or for higher inlet angles of the supersonic type (unique incidence). In both cases the inlet no longer can be influenced from behind. But if the decreasing of back pressure prolonge the outlet flow is still further accelerated up to supersonic velocities comparable to cases III and VI.

At last it shall be mentioned that for all choked supersonic inlet flows with an axial subsonic component there may be one additional limiting situation if the cascade passage is formed in such a manner, that there exists a remarkable throat area (minimum area). Under all these circumstances one is always confronted with the so-called starting problem. Due to the additional shock losses produced upstream of the throat its area is relatively small, so that in spite of the supersonic inlet Mach Number a large subsonic region across the whole passage is established and in the cascade throat the flow is accelerated up to sonic condition. Therefore there is a subsonic choking of the flow in spite of the supersonic inlet flow. This means, that the inlet is influenced by the cascade geometry and the losses produced upstream of the throat. If it is possible to swallow the intermediate subsonic flow due to short term increasing of inlet Mach Number or of throat opening, and so to avoid most of the shock losses, another flow configuration can be established, where now a supersonic choking (unique incidence) is reached as it is shown in Fig. 2 (cases V - VII).

In **Fig. 3** the normal flow condition of a transonic compressor section is shown in some more detail. As can be seen in this figure there is an oblique shock wave (S-C) moving upstream (axial) of the cascade. Near the leading edge of the blade (S-B) this oblique shock changes to the center part of a bow wave, where the strong solution of the shock polar comes into action. Finally at the cascade channel entrance the bow wave forms a nearly normal shock (B-A) at this high back pressure condition. As long as the outlet pressure cannot influence the inlet flow the unique incidence condition still is fulfilled. In all real applications the shock losses due to the oblique part of the entrance shock wave are negligible whereas the normal shock at the channel entrance produces entropy losses comparable to the usual profile losses at Mach Numbers of Ma_1 1.3. At lower inlet flow Mach Numbers these shock losses become weaker but they are strongly increasing at higher inlet flow velocities.

2.2 Basic considerations on shock losses

The total pressure loss of a normal shock is given by the recovery factor:

$$\frac{\hat{P}_t}{P_t} = La^2 \left\{ \frac{1 - \frac{\varkappa-1}{\varkappa+1} La^2}{1 - \frac{\varkappa-1}{\varkappa+1} \frac{1}{La^2}} \right\}^{\frac{1}{\varkappa-1}}$$

In this equation La is the Laval Number immediately upstream of the shock. This local Laval Number can be calculated for supersonic inlet flow as a function of the inlet Laval Number and a supersonic expansion from the leading edge to the position of the compression shock. This supersonic expansion results from the expansion around the leading edge shape and the change of the contour angle between the inlet flow direction (begin of supersonic expansion due to unique incidence condition, see ref. 3) and the position of the shock. **Fig. 4** shows the recovery factor of a normal compression shock as a function of supersonic expansion for several values of the inlet Laval Number. Thus, for given inlet Laval Number, the supersonic expansion should be minimized. This will result in a sharp leading edge and a straight contour shape up to the compression shock position. In this case the supersonic expansion can be neglected and the Laval Number in front of the compression shock is nearly equal to the inlet value which is the lowest possible value. Thus, the losses due to the compression shock will be minimal.

2.3 Shock/boundary-layer interaction loss model

For supersonic cascade inlet conditions there is a shock system consisting of an oblique shock which influences the region upstream of the cascade (for subsonic axial velocity) and a normal shock within the blade passage. It has been experienced that the oblique shock in front of the cascade produces very low losses, whereas the normal shock within the blade passage produces considerably high losses for high shock Laval Numbers. The strong increase of losses in transonic compressor cascades at high inlet Mach Numbers cannot only be attributed to shock losses according to normal shock correlations, but primarily to the shock/boundary-layer interaction which results in boundary-layer separation due to the strong pressure gradient of the compression shock. The very complicated flow conditions made it impossible up to now to calculate the shock losses with analytical methods sufficiently accurate. Therefore, most of the published methods are derived using very simple shock models and empirical shock loss correlations (ref. 4). The first published correlation for shock loss prediction is given in ref. 5 and is also used today with some modifications. One of these modified correlations has been applied to the profile types of this paper with very good success and contains two steps (see **Fig. 5**):

- a normal shock correlation for a shock Mach Number equal to the inlet Mach Number. This could be done because the investigated profiles had been designed for zero or nearly zero supersonic expansion in the supersonic part of the profile.

- the well known correlation of ref. 6 to take into account for compressibility effects and shock/boundary-layer interaction.

The profile losses at supersonic inlet conditions are calculated by superposition of the two correlations:

$$\bar{\omega} = \frac{P_{t1} - P_{t2}}{P_{t1} - P_1} = La_1 \left\{ \frac{1 - \frac{\varkappa-1}{\varkappa+1} \, La_1^{\,2}}{1 - \frac{\varkappa-1}{\varkappa+1} \, \frac{1}{La_1^{\,2}}} \right\}^{-\frac{1}{\varkappa-1}} + \bar{\omega}_{inc} \left[1,8 \; (Ma_1 - Ma_{1crit}) + 1 \right]$$

This correlation had been applied to relevant cascade measurements done at DFVLR on supersonic profiles for transonic compressors. Fig. 6 shows the results of the correlation in good agreement with the measurements.

3. TRANSONIC PROFILE DESIGN CONCEPTS

According to the above mentioned criteria for design of transonic compressor cascades for minimal shock losses the objective of a blading design is to reduce the shock Mach Number by minimizing the supersonic expansion. These ideal conditions cannot be realized in every case (for instance sharp leading edge). A further consideration has to be directed to the subsonic part of the cascade behind the compression shock. For the case of a straight contour shape from the inlet to the shock position the whole flow deflection has to be done by the rear part of the cascade. For a given flow deflection this can lead to an overloading with subsequent boundary-layer separation. Therefore, the optimisation of transonic profiles should take into account this boundary-layer behaviour, resulting in a small supersonic expansion in the supersonic part and a tolerable diffusion in the subsonic part. Although compression shock losses will be increased due to higher supersonic expansion, the total losses can be decreased due to the elimination of boundary-layer separation. The design of such transonic profiles for a given velocity triangle has to take into account the following conditions:

- profile thickness according to structural considerations
- space/chord ratio for sufficient choke margin
- unique incidence condition to fix the suction surface direction with respet to the inlet flow direction (also taking into account supersonic expansion around the leading edge)
- the splitting point between supersonic and subsonic part is given by a shock model of a normal shock emanating from the leading edge of the adjacent blade and normal to the suction surface of the considered blade. The profile contours at this point have an identical tangent.
- deviation at the trailing edge according to empirical correlations for subsonic cascades consisting of NACA 65 blades (see ref. 1).

3.1 Wedge-type profile shape

The consequent realisation of the above mentioned optimisation criteria for the supersonic part of transonic profiles (lowest Laval Number in front of the compression shock) leads to a straight suction surface from the leading edge to the shock position. This wedge-type profile (MTU-1, Fig. 7) is composed of a straight camber line in the supersonic region and a circular arc camber line in the subsonic region behind the compression shock. The profile shape is given by a superposition of this camber line and a thickness distribution consisting of the leading edge circle and a wedge shape within the supersonic region and of a NACA 65 thickness distribution within the subsonic part behind the compression shock.

3.2 Multiple circular arc type profile shape (MCA)

In order to reduce the aerodynamic loading of the subsonic part of the cascade, this type of blades has a small amount of supersonic expansion from the leading edge to the shock position. As has been mentioned, the supersonic expansion has to be chosen with respect to avoiding separation of the boundary-layer at the shock position. The camber line of these MCA-type blades (MTU-2, MTU-3) is composed of two circular arcs. The profile shape is given by a superposition of this camber line and a thickness distribution in the supersonic part as explained above. For the subsonic part two different profile shapes have been investigated:

- according to good experience for high subsonic flow conditions a NACA T1 thickness distribution has been chosen (MTU-2)
- similar to the wedge-type profile shape, also a NACA 65 thickness distribution has been used for the subsonic part (MTU-3).

3.3 Design of test cascades

Due to insufficient accuracy of available calculation methods for viscous transonic cascade flows, the quality of the design methods and the deflection behaviour of the designed profile shape has to be verified by cascade testing. The cascade geometry chosen for the cascade tests was taken from the aerodynamic design at mid section of rotor 1 of a 3-stage transonic compressor (ref. 7) with the aerodynamic data:

Section: mid $r = 0.2565$ m
$Ma_1 = 1.3$ $\quad \beta_1 = 27.1°$ $\beta_2 = 34.0°$ $\quad \Omega = 1.21$
$t/c = 0.042$ $\quad s/c = 0.7086$

According to the above explained design concepts a wedge-type profile cascade as well as MCA-type profile cascades were designed (Fig. 8):

- The blading data for the wedge-type profile (MTU-1) are:
  $\delta_u = 7.9°$ $\delta_{uss} = 0°$ $\beta_s = 31.0°$

- The blading data for the MCA-type profile are strongly effected by the supersonic expansion δ_{uss}. This value has to be carefully chosen with respect to low choke Mach Number for the section investigated, but also with respect to radial distribution of this value. Thus, for the mid-section of rotor 1 blading $\delta_{uss} = 2.0°$ has been chosen.
  The blading data of MTU-2 type profile section are:
  $\delta_u = 9.3°$ $\delta_{uss} = 2.0°$ $\beta_s = 31.4°$

  The blading data of MTU-3 type profile section are:
  $\delta_u = 8.8°$ $\delta_{uss} = 2.0$ $\beta_s = 31.7°$

4. ANALYSIS OF TEST RESULTS

4.1 Cascade Test Results

The cascade investigations were performed in the transonic cascade wind tunnel of DFVLR in Cologne. The details of this facility and all the measuring equipments are summarized in ref. 8. In spite of the two-dimensional cascade model there exists in a real tunnel a flow area contraction due to the growing boundary layers on the tunnel side walls, see Fig. 9. This contraction which is identical to the axial velocity density ratio (AVDR)

$$\Omega = B_1/B_2 = (\rho_2 \, w_2 \, \sin \beta_2)/(\rho_1 \, w_1 \, \sin \beta_1)$$

has to be incorporated in all investigations or must be controlled by boundary layer suction during the tests. Within the present tests it was impossible to install such a suction device because it was necessary to make Schlieren-pictures in order to see the shock-system and to control and adjust the periodicity during the different throttling set-ups. Therefore all the measured data are not at a constant AVDR and some scatter may be the result. To overcome this difficulty at least partly only measurements where the AVDR is of the same magnitude are compared. A detailed documentation of all test results is given in ref. 9.

Within the test program measurements were taken in front of the cascade (wall statics) and behind (wake traverses) as well as profile statics on the suction and pressure side of the blade and in addition also Schlieren measurements are done as already mentioned. For the analysis especially the downstream wake results are of interest to compare the net turning and the associated losses with design and also to judge the three different profile types against each other. The first is of interest to see how far design and reality diverge whereas the second question may result in some alternative compressor profiling if the MTU-2 or MTU-3 blades shows some remarkable advantage against the standard MTU-1 compressor blade. Whereas in the test series a lot of different back pressures are realized for the analysis only the highest static outlet pressure is mainly recognized because this condition is nearest to the compressor design configuration as the original Schlieren pictures clearly show.

In Fig. 10 the inlet flow angle is shown as function of inlet Mach Number. In this case only the low back pressure results are shown to be sure to show the started supersonic inlet conditions (unique incidence). In Fig. 11 the outlet flow angle now at highest outlet static pressure is shown again as function of the inlet Mach Number. In addition in both figures the compressor design values are shown yielding quite good agreement with measurements especially if the difference in AVDR (design Ω = 1.21 test: Ω = 1.05 - 1.10) is taken into account which is of some influence on the outlet flow angle. Fig. 12 shows the integrated total pressure loss for all three types of profile. As can be seen the differences for all three configurations are very small. The MTU-2 profile seams to have some small advantages at higher Mach Numbers but care has to be taken due to some scatter in AVDR and also the usual accuracy scatter of measured values and of blade shape geometry may narrow the gap between the MTU-2 losses and those of the two other profiles. Fig. 13 shows the wake traverses at highest back pressure for the three profiles at near design conditions. As is in accordance with the integrated losses also the wakes of the different MTU profiles show quite the same total pressure loss distribution in the circumferential direction indicating no differences in separation zones for these three profile types, especially at the shown design Mach Number. In Fig. 14 the profile Mach Number distributions of the three profiles is shown again for the same flow conditions as before.

4.2 Experience in a transonic compressor

To see whether the theoretical considerations and the cascade results could be realized in a concrete machine, the first rotor of a three stage fan was analyzed in more detail. This fan is sketched in Fig. 15. As can be seen the first two rotors are designed with profiles of the MTU-1 type, as discussed in the foregoing sections. The last rotor on the other hand uses double-circular-arc blades whereas all stators are from the conventional NACA 65 series. The reduced performance characteristics of this compressor is shown in Fig. 16 from which a satisfying distance from surge can be deduced over the whole working range of an associated military fighter engine. Additionally this map shows a clear tendency to improved efficiency in the part speed regime at a reduced speed of ninety percent.

To analyse the interior flow behaviour of this compressor different measuring devices are used. In addition to standard up- and downstream set-ups several profiles of all three stator rows are instrumented with total pressure and total temperature probes at the leading edges (see Fig. 17) in order to get the radial information at the stator entries. But to get also some information of the flow velocities within a blade row it was necessary to use a Laser-2-Focus velocity anemometer (ref. 10). This instrument yields detailed velocity vectors within a complete three-dimensional blade passage of rotor 1 (ref. 11). All the axial and radial Laser measuring locations are shown in Fig. 18, where also is indicated at how many circumferential positions the flow is detected within one spacing. In Fig. 19 to 22 the interblade flow Laval Numbers are shown at four different radial stations. For all shown flow conditions the compressor working point is fixed at design speed and a pressure ratio at the associated engine working line. In addition to the sketched relative Laval Number at all measuring stations the measured relative Laval Number and relative flow angle are indicated numerically. In Fig. 19 the radial height is 19 %, i.e. near the hub. The flow configuration clearly shows the near sonic subsonic inlet velocities but due to the supercritical condition a limited supersonic pocket is formed at the front part of the suction surface. This pocket is bounded downstream by a nearly normal shock reducing the supersonic flow again to subsonic velocity. At the more inward stations of 34,5 % radial height the inlet flow has reached a supersonic condition and the supersonic pocket increases up to infinity. Crossing the compressor radial mid section the inlet flow velocity further increases and reaches a Laval Number of 1.22 at the shown radial station of 60 %. As can be seen on Fig. 21 the front bow wave can be divided into two parts. The upward running weak shock induced by the front suction surface geometry which fixes the final cascade inlet condition (unique incidence) is continued into the blade passage as a nearly normal shock. In the shown flow case there exists a second acceleration to supersonic velocities within the cascade channel which finally is terminated by a second normal shock yielding the final subsonic outlet conditions. Finally Fig. 22 shows the flow conditions near the rotor tip (at a radial height of 90 %). In this case the inlet Laval Number has further increased to La_1 = 1.4 and the bow wave has moved downstream nearer to the blade leading edge. Addidtionally in the shown configuration the back pressure is so low, that the deceleration to the downstream conditions is possible by means of several reflected oblique shock waves resulting from the blade passage part of the front bow wave. In this case the relative outlet Laval Number is near sonic so that no velocity reduction to subsonic velocities will occur downstream.

In addition to the detailed flow analysis within the blade passages it is possible too, to use the measured velocities and flow directions in front and aft of the blades to get the radial distribution of magnitude and angle of the flow velocity. In this case the different values along the pitch are area averaged. In those radial positions where only one single position is focused this value which is located near the middle of the pitch is used. The relative Laval Numbers are shown in Fig. 23 whereas the rela-

tive flow angles are given in Fig. 24. In both figures also the theoretical values used during the compressor design are sketched. To give an imagination of the rotor loss in Fig. 25 the relative total pressure at the rotor exit is shown. This figure clearly shows the radial and circumferential loss distribution of this rotor. Due to the high Mach Number and the associated shock losses at the rotor tip the total-pressure loss in this region is markedly increased in comparison to the low Mach Number hub-region.

5. CONCLUSIONS

On the basis of a detailed investigation of the flow conditions in a transonic compressor cascade design criteria for the supersonic part of these profiles are derived. The main design feature is to reduce the shock Mach Number by applying wedge-type profiles. With respect to the loss behaviour of the subsonic part a moderate supersonic deflection has been investigated (MCA-type blades). The subsonic part of these profiles consists of conventional NACA thickness distribution. According to these design criteria three different cascades have been tested. Cascade tunnel results as well as Laser-2-Focus measurements, in the first rotor of a three-stage transonic compressor proved the low-loss design of these blades. A further improvement in loss reduction at high inlet Mach Numbers will be possible by applying modern numerical methods. But a real progress can only be made if the viscous effects are treated in a realistic way.

6. REFERENCES

Ref. 1 Johnsen I.A., Bullock R.O.
Aerodynamic design of axial flow compressors (revised)
NASA SP-36 (1965)

Ref. 2 Scholz N.
Aerodynamik der Schaufelgitter, Band 1
Verlag G. Braun (1965)

Ref. 3 Starken H.
Untersuchung der Strömung in ebenen Überschallverzögerungsgittern
DLR FB 71-99 (1971)

Ref. 4 Hirsch Ch., Denton J.D. (Edts.)
Through Flow Calculations in Axial Turbomachines
AGARD-AR-175 (1981)

Ref. 5 Schwenk F.C., Lewis G.W., Hartmann M.J.
A preliminary analysis of the magnitude of the shock losses in transonic compressors
NACA RM E 57 A 30 (1967)

Ref. 6 Jansen W., Moffat W.C.
The Off-Design Analysis of Axial Flow Compressors
Trans. ASME, J. of Eng. for Power, Oct. 1967, 453-462

Ref. 7 Volkmann H., Fottner L., Scholz N.
Aerodynamische Entwicklung eines dreistufigen Transonik-Frontgebläses
ZfW 22 (1974) Heft 4, 135 - 144

Ref. 8 Starken H., Breugelmans F.A.E., Schimming P.,
Investigation of the axial velocity density ratio in a high turning cascade
ASME-paper 75-GT-25 (1975)

Ref. 9 Schreiber H.A., Schimming P.,
Zweidimensionale Gitteruntersuchungen an den Profilen MTU-1, MTU-2 und MTU-3 im Machzahlbereich $1.0 \leq Ma_1 \leq 1.4$
DFVLR IB 352-77/15 (1977)

Ref. 10 Schodl R.,
On the Development of a New Optical Method for Flow Measurements in Turbomachines
ASME-paper No. 74-GT-157 (1974)

Ref. 11 MTU München GmbH
Strömungsuntersuchungen im ersten Rotor des fortschrittlichen ND-Verdichters mit dem Laser-2-Focus-Geschwindigkeitsmeßverfahren der DFVLR.
MTU TB 78/008 (1978)

ACKNOWLEDGEMENT

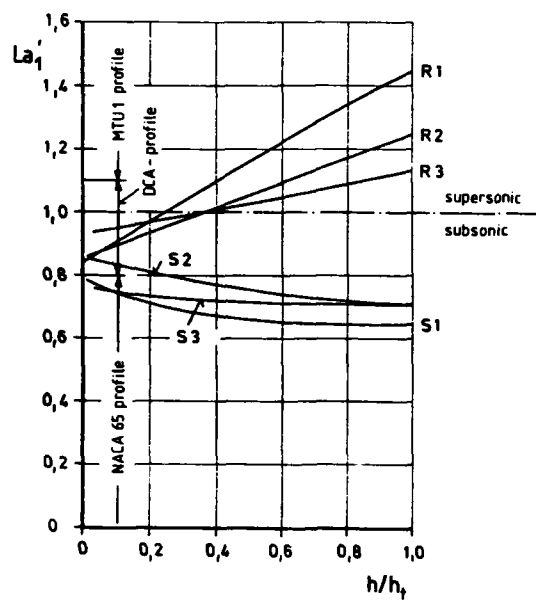Fig. 1   Radial distribution of Laval Number for a 3-stage transonic compressor
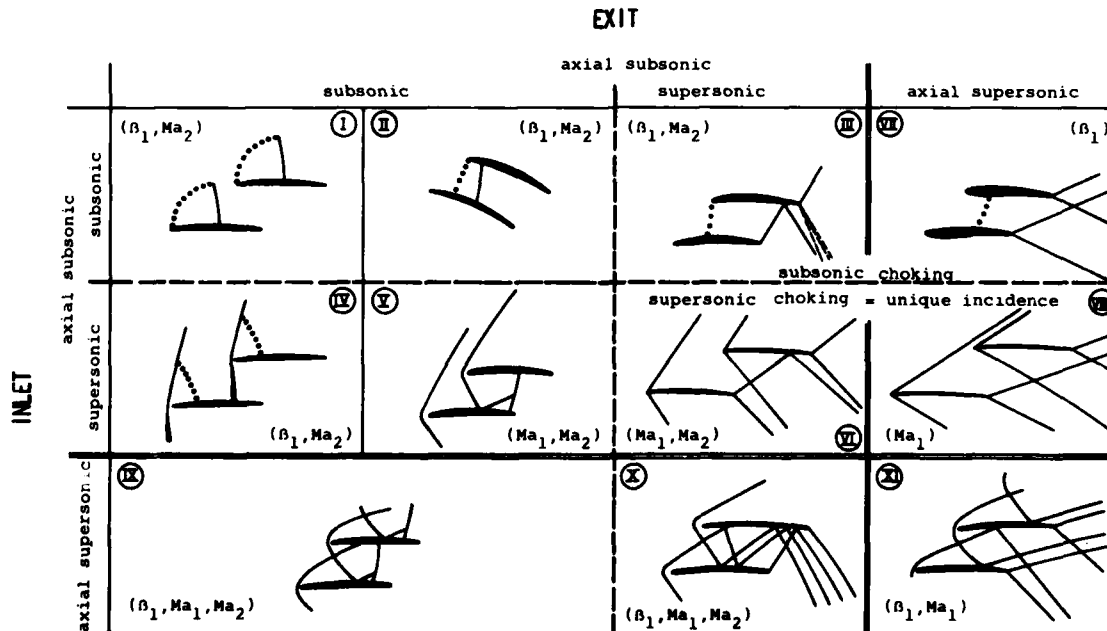
Fig. 2   Principal flow conditions of plane cascades
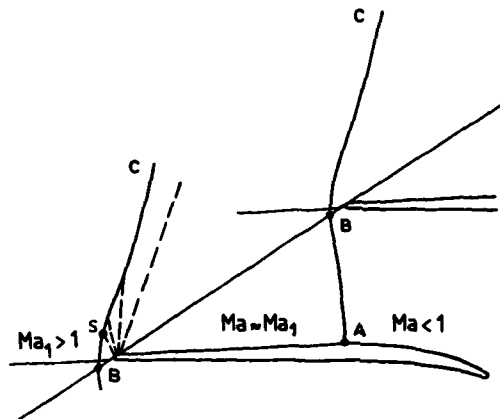
Fig. 3   Shock configuration of a transonic cascade with supersonic inlet condition
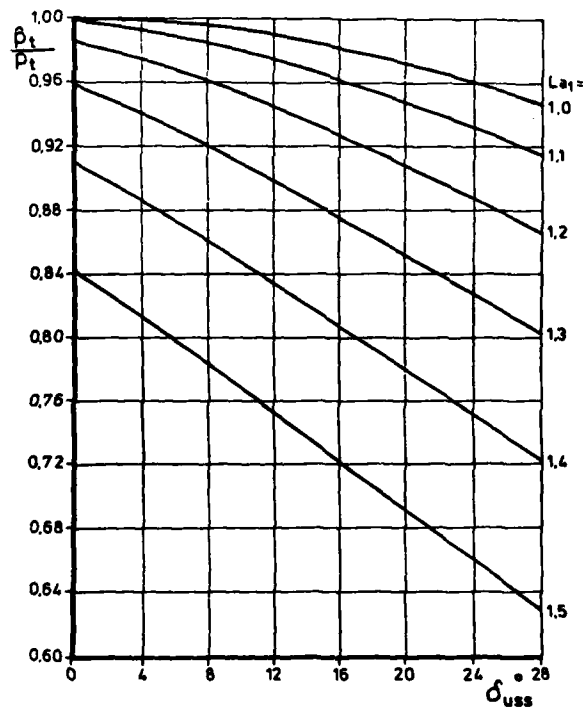
Fig. 4   Recovery factor of a normal compression shock
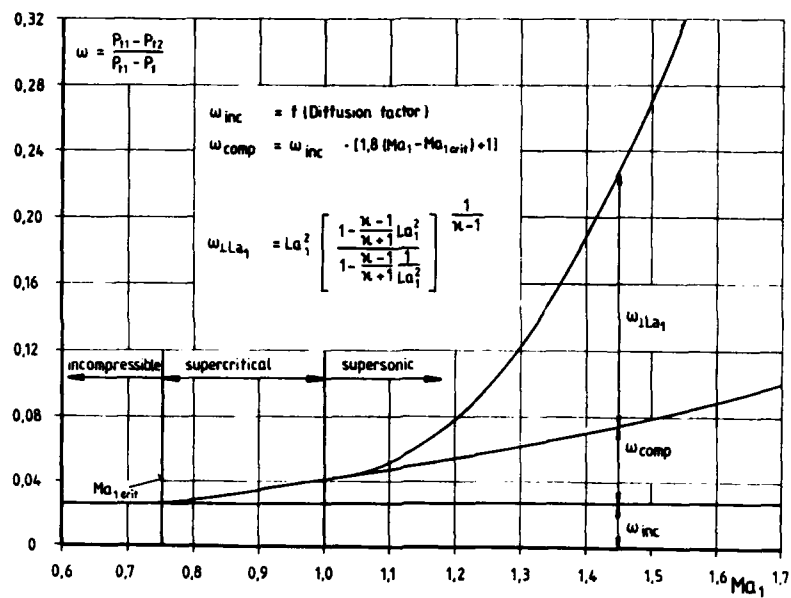
Fig. 5   Loss correlation as a function of inlet Mach Number
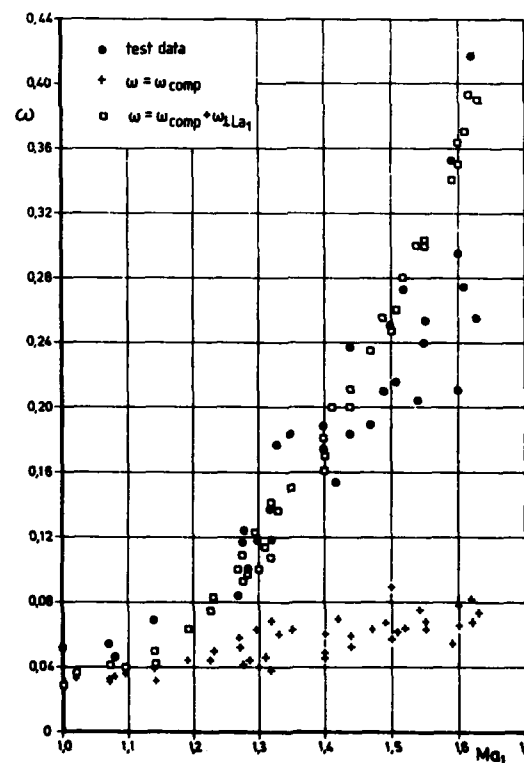
Fig. 6   Comparison of profile loss coefficients
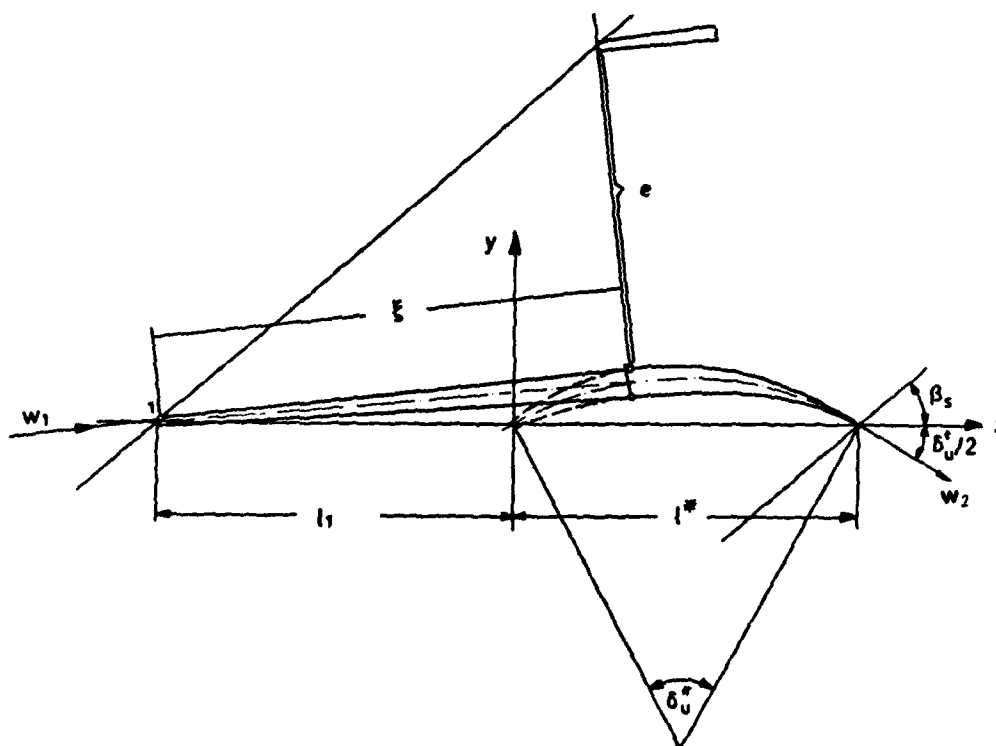
Fig. 7   Geometrical definition for a wedge type profile

MTU 1

MTU 2

MTU 3
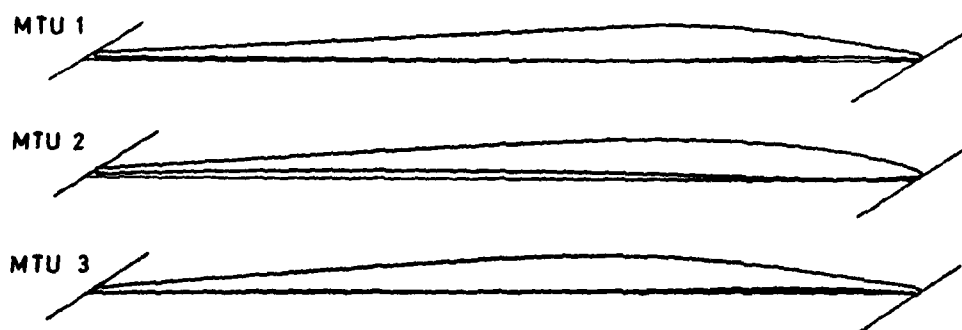
Design Data for mid section of rotor 1:

$Ma_1 = 1.3$ $\beta_1 = 27.1^\circ$ $\beta_2 \approx 34.0^\circ$

$t/c = 0.042$ $s/c = 0.7086$

Fig. 8   Different profile shapes of transonic profiles
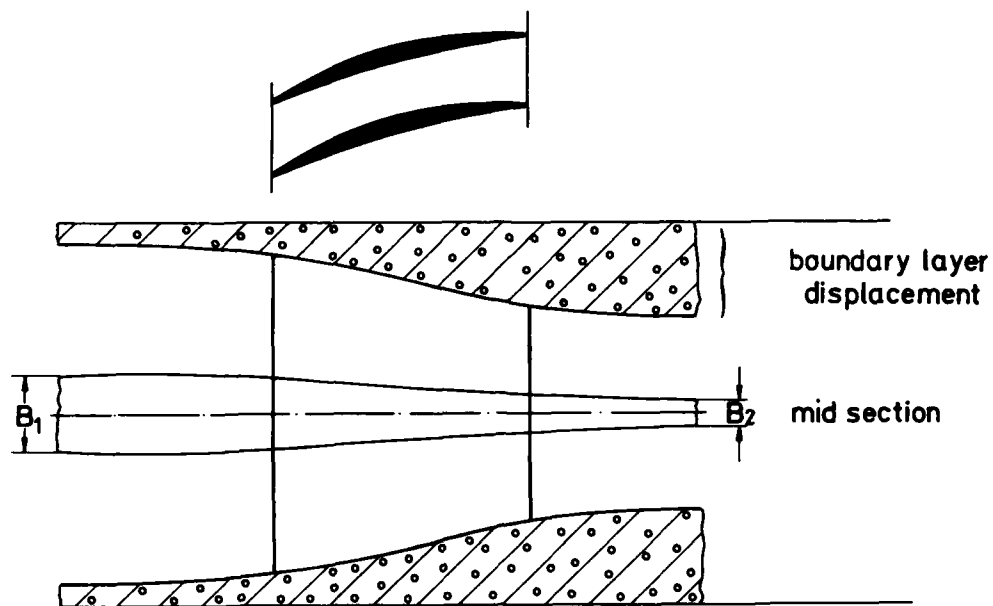
Fig. 9   Plane cascade arrangement and the associated contraction due to side-
wall boundary-layer growth
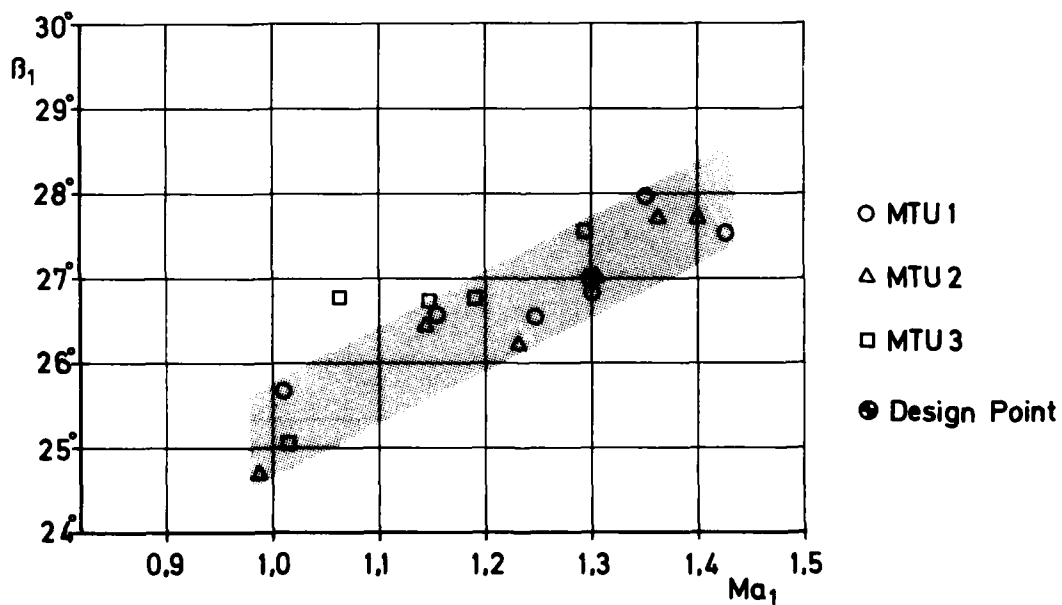
Fig. 10   Inlet flow angle at lowest back pressure (unique incidence condition)
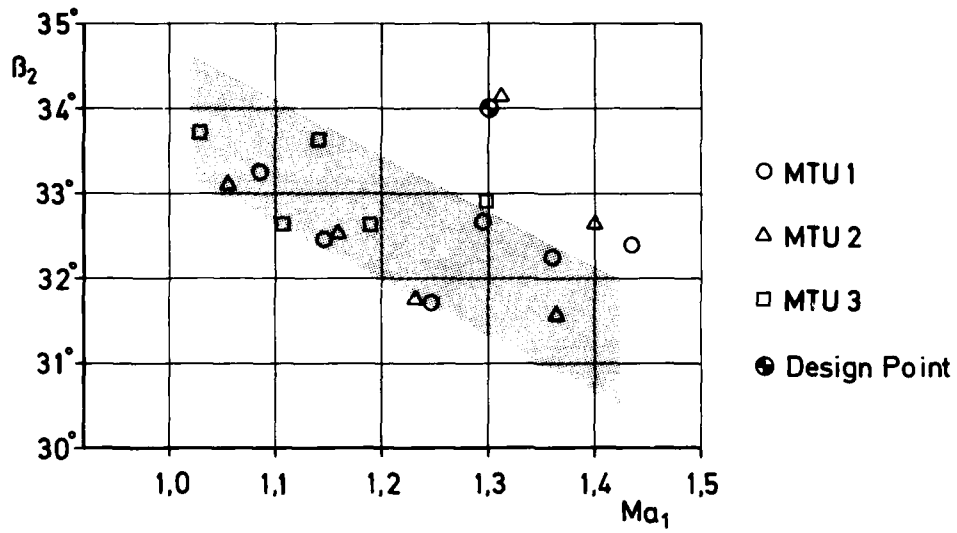
Fig. 11   Outlet flow angle as function of inlet Mach Number at highest throttling
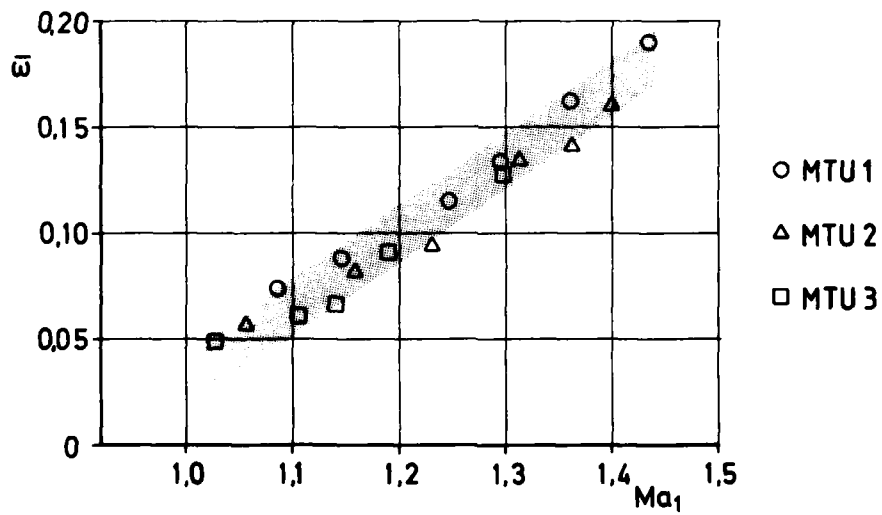
Fig. 12   Profile loss coefficient at highest back pressure
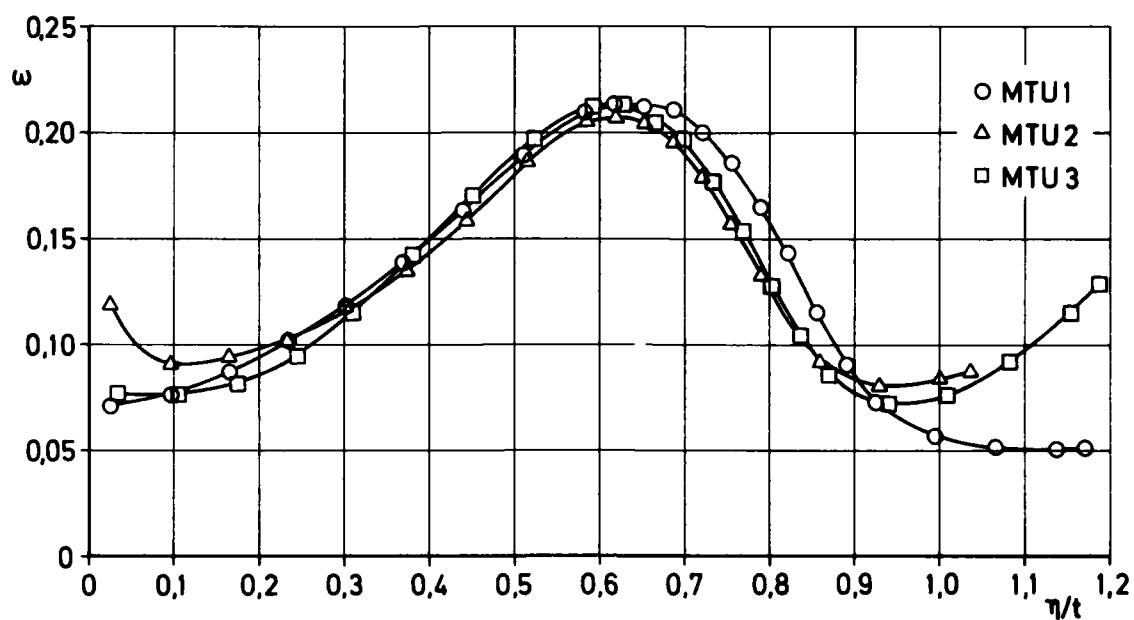
Fig. 13 Wake measurement at near design conditions
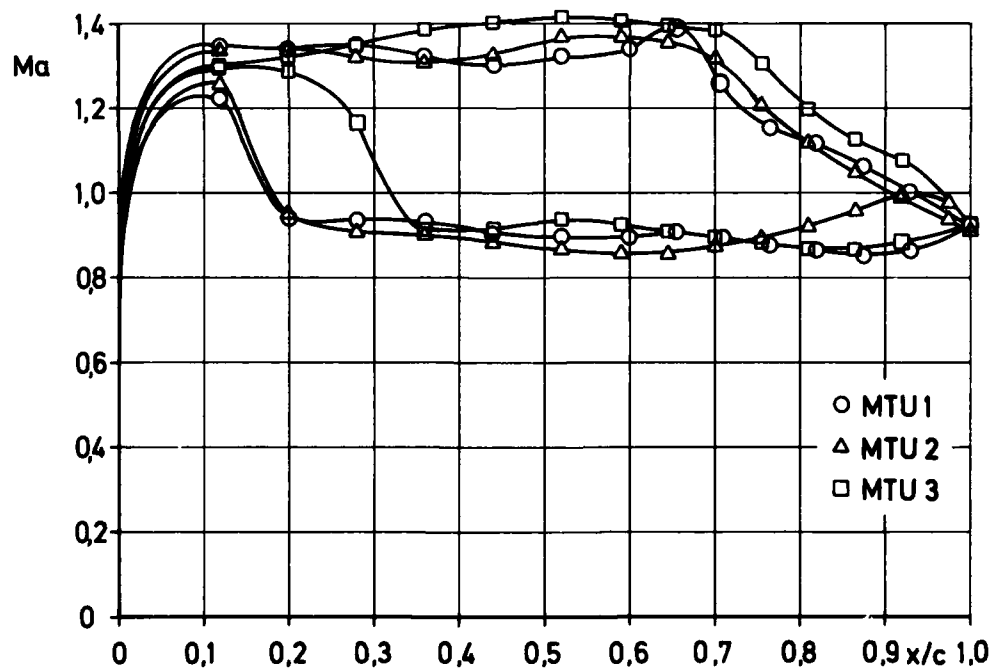
Fig. 14 Profile Mach Number distribution at near design conditions
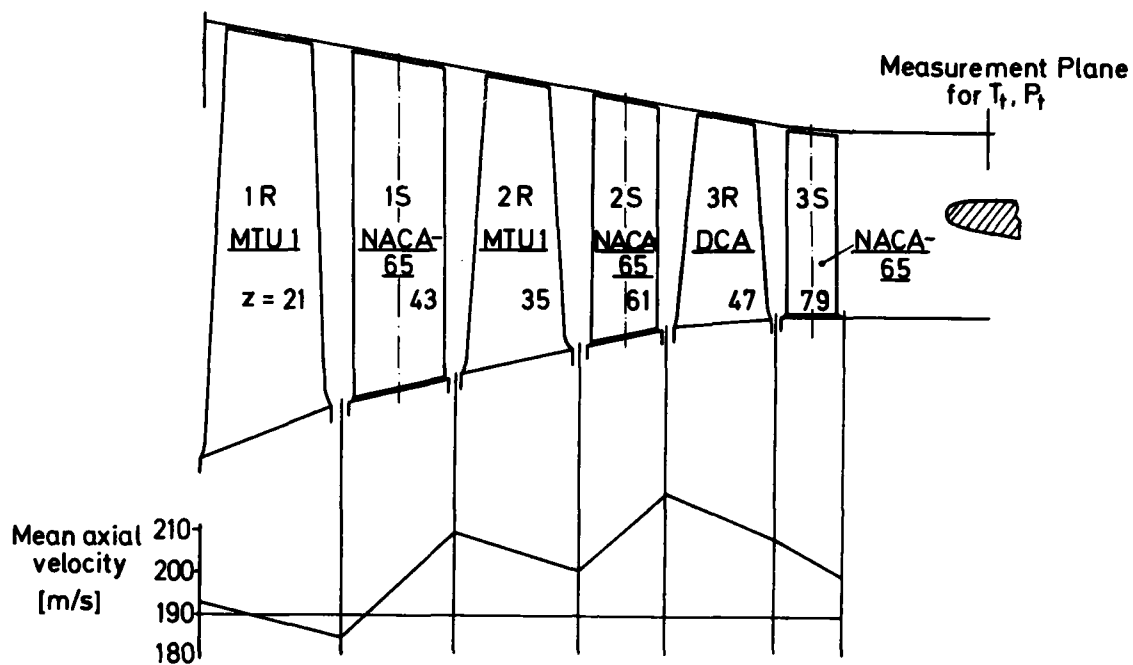
Fig. 15   Flow path of three-stage low-pressure compressor
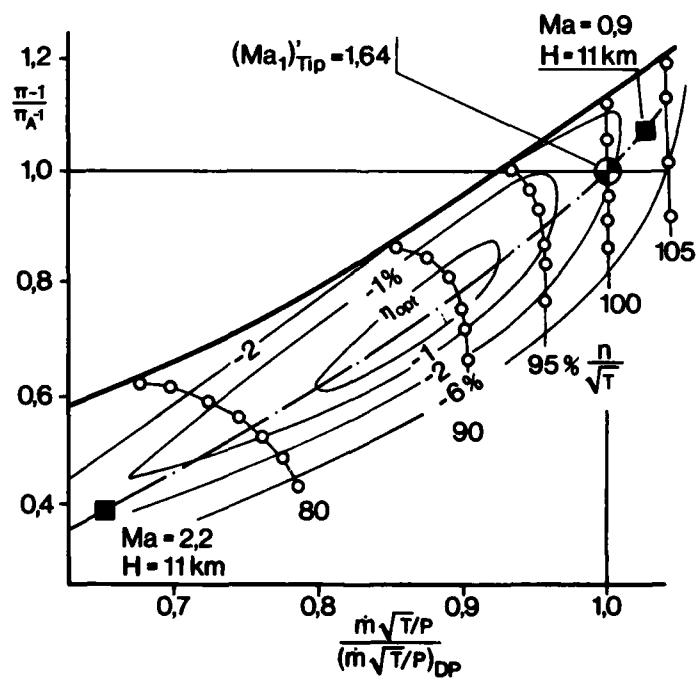
Fig. 16   Three-stage low pressure compressor performance characteristics
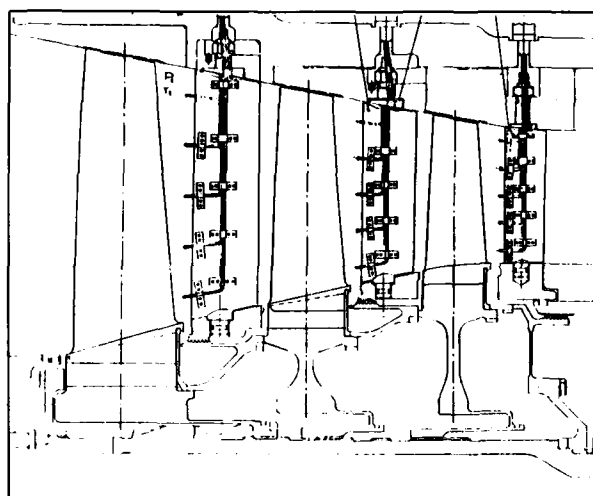
Totalpressure and-temperature probes   Totalpressure tubes on a vane
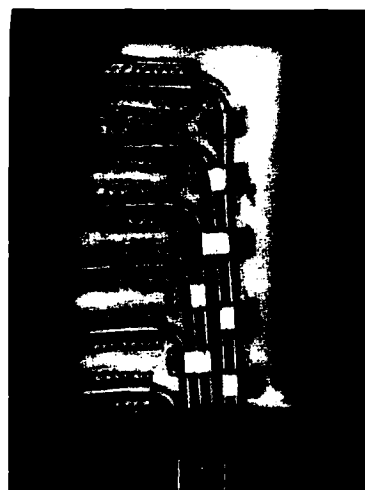
Fig. 17   Duct-Flow-Analysis
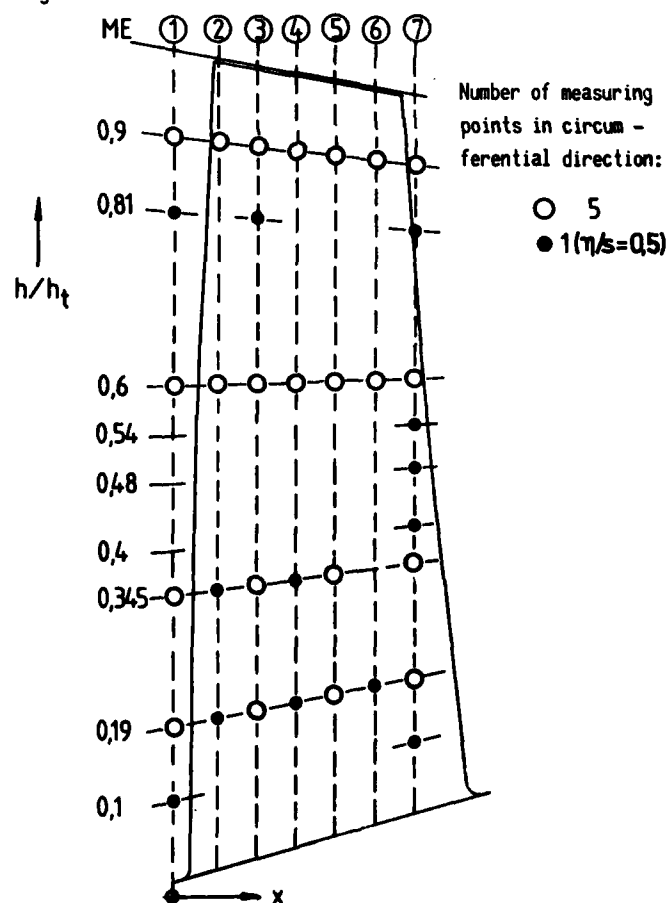
Fig. 18   Laser-2-Focus measuring positions of rotor 1 (MTU-1 profile)
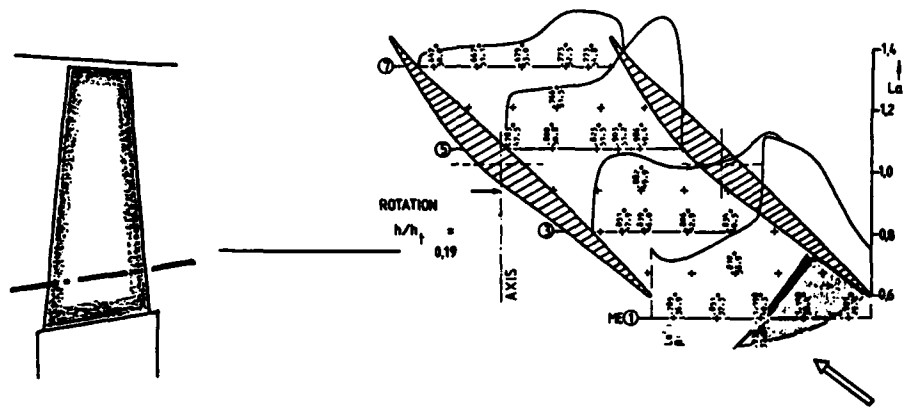
Fig. 19   Near hub blade-to-blade Laser-2-Focus measurements
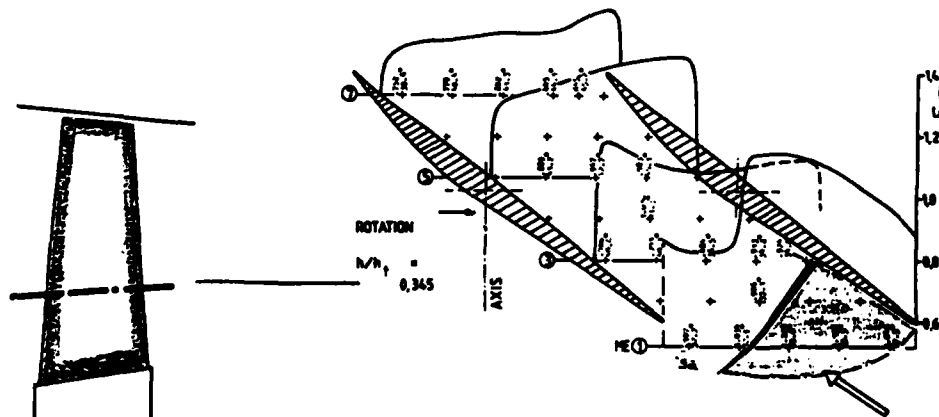
Fig. 20   Hub-mid blade-to-blade Laser-2-Focus measurements
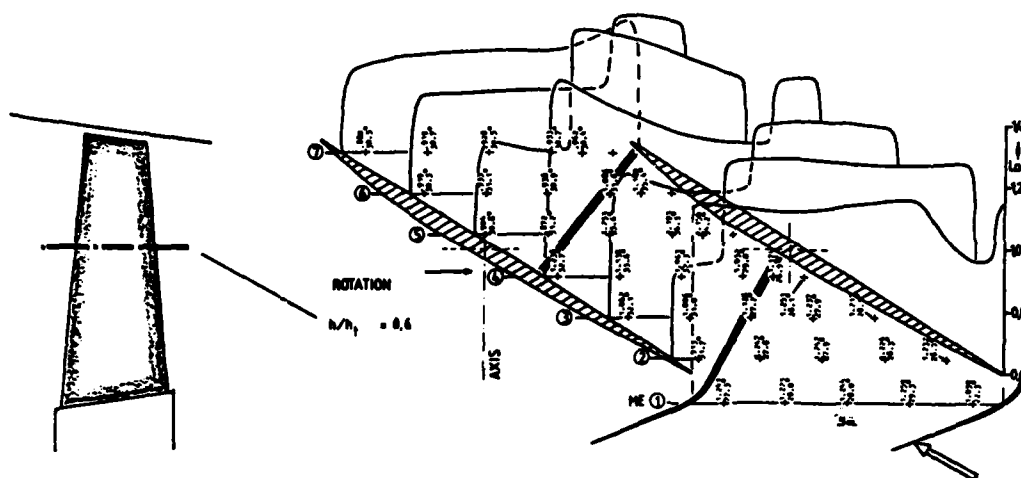
Fig. 21 Near mid blade-to-blade Laser-2-Focus measurements
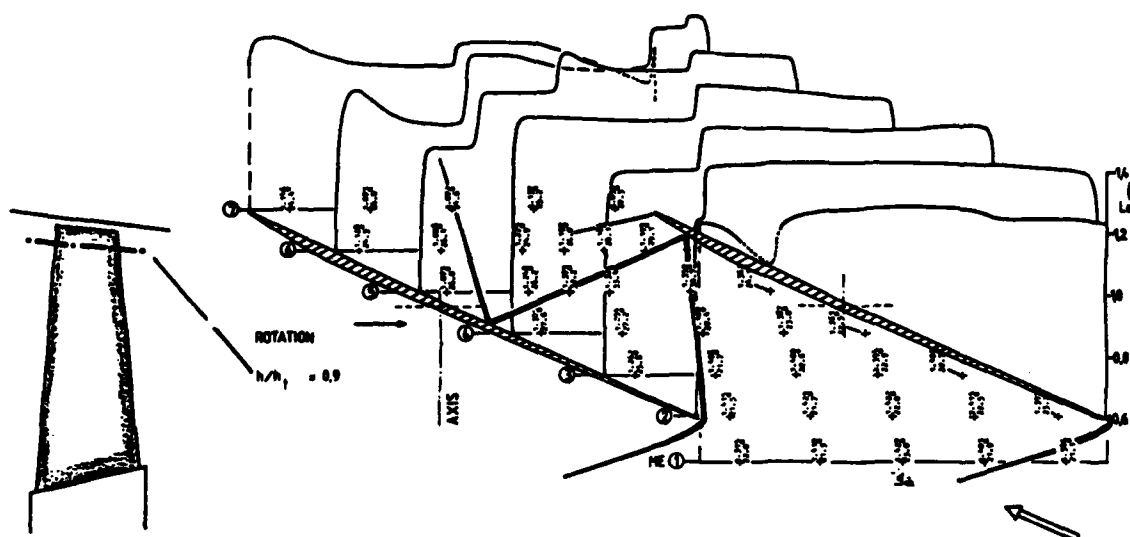
Fig. 22 Near tip blade-to-blade Laser-2-Focus measurements
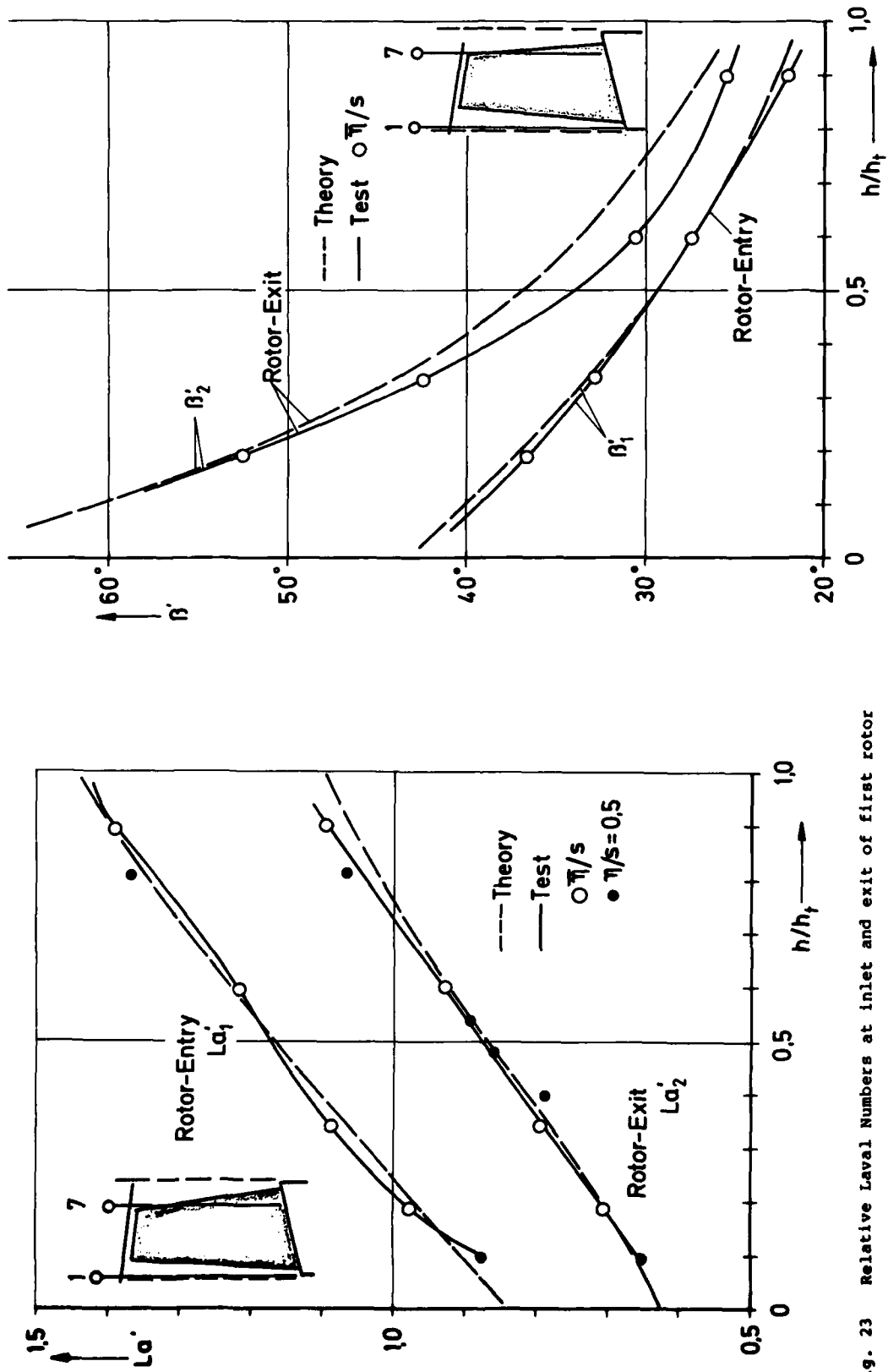
Fig. 23   Relative Laval Numbers at inlet and exit of first rotor
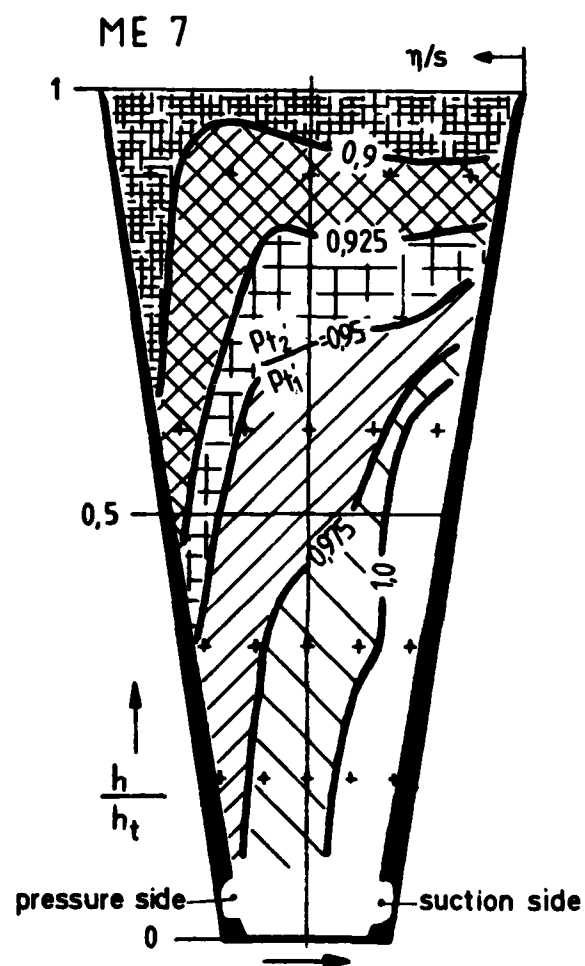
Fig. 25   Relative total pressure distribution at exit of first rotor

DISCUSSION

Karadimas

    (1) Have the presented profiles been defined by an inverse method or by geometrical direct methods?

    (2) Are the profiles, optimised at a design point for minimum losses, also adequate for off-design operating conditions? It is interesting to know if that is true, particularly near the stall line and in the low speed region.

Author's Reply

    (1) The presented profiles were designed by a geometrical method.

    (2) At the time the presented profiles were designed we were not able to calculate any off-design losses and also today this may be difficult. So the stringent point of your question cannot be answered, whether a profile not uniquely optimized for a single operation point can do better with regard to the whole range of operation. On the other hand, cascade tests of the presented profiles show no special misbehaviour at the high incidence side of the working range at supersonic inlet velocities, compared to other MCA profile tests.

    For subsonic inlet velocities, cascade measurements showed a sufficient working range for the MTU 1 profile type compared with DCA profiles, whereas for both other profile types (MTU-2, MTU-3) no subsonic tests are available.

W.J.Calvert, UK

The measured shock patterns, particularly near the blade tip (Fig.22), are significantly different from the pattern assumed in the design model (Fig.3). Would you comment on this difference?

Author's Reply

The shock wave pattern depends on the design point back pressure, which is fixed by the through flow calculation. In the case of the tip region, the exit Mach number is about 1 and higher (and not subsonic). Therefore, the optimal cascade configuration as described in the paper can only be rendered in the region with subsonic exit condition (mid-span region).

Wennerstrom

Is there a value of relative inlet Mach number above which you would consider introducing negative camber rather than a straight suction surface?

Author's Reply

As the cascade results have shown, there is no clear tendency for straight or convex supersonic part in the considered Ma-number region. But if the inlet Mach number is further increased $(Ma_1 > 1.6)$ we would consider also the use of a negative camber supersonic part as a physically possible method to reduce supersonic losses. But care has to be taken with regard to off-design behaviour.

Van den Braembussche, Be

About Fig.25, are these measurements taken at the same conditions as previous figures and could you comment on the fact that for the tip region (transonic) there are higher losses on pressure side than on the suction side? This is not expected from the shock patterns of the previous figures.

Author's Reply

The results shown on Fig.25 concerning the relative total pressure distribution at exit of first rotor are evaluated from the measurements which also had been used for the previous figures (i.e. at same conditions).

The losses on the pressure side are produced by friction losses, shock losses and shock/boundary layer interaction losses. According to the actual shock configuration higher losses can be produced on pressure side than on suction side. This is a non-usual result compared to subsonic cascade tests.

On the other hand one has also to consider the uncertainties of such evaluations:

— measuring plane (7) is not exactly located at blade trailing edge over the whole blade height.

— L2F measurements do not give information on total pressure. Therefore total temperature has been evaluated from measured angle and velocity using Euler's equation and the static pressure measured at tip and hub exit of first rotor.

It is necessary to continue these investigations with respect to the discussed problems.

FLOW TRAJECTORIES, MIXING AND ENTROPY FLUXES
IN A TURBINE CASCADE

John Moore
Professor of Mechanical Engineering
Virginia Polytechnic Institute and State University
Blacksburg, Virginia, 24061
USA

ADP0003076

SUMMARY

Flow in a turbine cascade studied by Langston, et al. at United Technologies Research Center is considered. Measurements have been made in a geometrically similar cascade with an axial chord of 235/mm (compared with the 281/mm used by Langston et al.) and the same span/chord and pitch/chord ratios. The present five-blade cascade has an exit Reynolds number based on axial chord of 0.8×10^5 compared with the value of 10×10^5 for the four-blade cascade of Langston et al. (100,000) (500,000)

Measurements of total pressure and flow direction downstream of the cascade complement the results of Langston et al. which showed the flow development only within the cascade. The downstream flow is important, however, as approximately 50 % of the losses occur downstream of the trailing edge. Regions of high-loss fluid are found and the origin of fluid in these regions is traced using the ethylene injection technique with a flame ionisation detector. From a computational standpoint, there is interest not only in the location of the ethylene at the downstream plane but also in the concentration levels and the diffusion rates. From a practical standpoint, the most significant result from the present tests is that the highest entropy fluxes downstream of this cascade (at x/c = 1.4) occur near midspan in a high-loss core and not near the end walls.

NOMENCLATURE

c	blade axial chord	β	mean camber line angle, measured from y axis
c_f	skin friction coefficient	δ^*	displacement thickness of boundary layer
C_{pt}	total pressure loss coefficient, Eq. 3	δ_3	mean kinetic energy thickness of boundary layer
$\overline{C}_{ptA}$	pitch-integrated entropy flux, Eq. 6	δ_{99}	boundary layer thickness
$\overline{C}_{ptB}$	pitch-wise-mass-averaged entropy, Eq. 8	θ	momentum thickness of boundary layer
$\overline{C}_{ptC}$	span-integrated entropy flux, Eq. 9	ρ	density
$\overline{C}_{ptD}$	span-wise-mass-averaged entropy, Eq. 11	ϕ	flow angle, Fig. 2
		ψ	flow angle, Fig. 2
H_{12}	$\equiv \delta^*/\theta$, shape factor		
I,J	indices for grid matrix, Fig. 6	**Subscript**	
P_t	total pressure	o	stagnation
s	entropy	1	free stream at inlet
T	temperature	2	downstream
u,v,w	velocity components, Fig. 2		
U	free-stream velocity	**Overbar**	
$\sqrt{\overline{u'^2}}/U$	measure of turbulence intensity	$-$	average
V_n	velocity component normal to measuring plane, Fig. 2	$=$	mass average
x,y,z	cartesian coordinates, Fig. 1	**Abbreviation**	
ΔY	blade pitch	ppm	parts per million by volume
ΔZ	blade span (measured from bottom wall)		

INTRODUCTION

One of the most extensively documented turbine cascade flows in the literature is that reported by Langston et al. [1-3] at the United Technologies Research Center. Sufficient detail is given about the inlet flow and the flow development within the blade passages for the computational fluid dynamicist to use this flow as a test case for the development of flow calculation methods [4-6]. Yet, even with this cascade flow, there are still questions about some aspects of the flow and about the sources of the losses. It is convenient therefore for a flow modeller to have his own cascade so that he can perform his own tests to answer questions of interest to him. For this reason, a five-blade replica of the Langston cascade [1] was built at VPI&SU [7].

This paper describes the results of measurements made in this VPI&SU low-speed turbine cascade to answer such questions as:
(a) How does the flow develop downstream of the trailing edge where more than half of the losses are created ?
(b) How are the losses distributed at a measurement plane 40 % of an axial chord downstream of the trailing edge (x/c = 1.4) ?
(c) What paths does fluid from the horseshoe vortices take in passing through the cascade ?
(d) Where does fluid need to enter the cascade in order to leave with low losses (at x/c = 1.4) ?

There are three sections. First, the cascade geometry and inlet flow are described. Questions (a) and (b) are then addressed as measurements of the downstream flow development and loss distributions are presented. In the last section, measurements of flow trajectories using an ethylene detection technique allow answers to questions (c) and (d) to be suggested.

It may interest flow modellers to know that the materials and equipment costs incurred in building the VPI&SU cascade and in purchasing and commissioning the flame ionisation detection system for ethylene were less than $4000.

5-BLADE REPLICA OF LANGSTON TURBINE CASCADE

Langston Blade and Cascade Geometries

The Langston blade geometry is that of a reaction-turbine rotor section; the airfoil mean camber line angles are $\beta_1 = 43.99°$ and $\beta_2 = 25.98°$, respectively, giving a nominal turning angle of 110° and a velocity ratio of approximately 1.6. In the tests reported by Langston et al. [1,2], the inlet air angle was 44.7°, close to zero incidence.

The blade camber line is close to being a double parabolic arc; and, based on the length of the camber line, the maximum blade thickness is approximately 16.7 % and the leading and trailing edge radii are approximately 3.8 % and 2.1 %, respectively. The trailing edge is quite thick, presumably to accommodate cooling-air passages in the actual turbine.

The aspect ratio (span/axial chord) of the Langston cascade is low, 0.9888. But the pitch/axial chord ratio is large, 0.9555, giving the Zweifel loading parameter [8] a value of 1.124. The axial chord is 281.3 mm.

VPI&SU Cascade Geometry

The ratio of the radii of the leading and trailing edges of the Langston blade is approximately 0.56. This suggested the possibility of using one inch diameter stock for the leading edge and 9/16 inch diameter stock for the trailing edge of the scale model. With the cascade geometry and blade angles of Langston et al., the corresponding axial chord length is then 235.2 mm. The 5-blade cascade, shown in Fig. 1, was constructed to this scale with a pitch of 224.8 mm and a span of 234.4 mm. The ratio of pitch/axial chord is 0.956, the same as used by Langston, and the ratio of span/axial chord is 0.997, approximately 1 % larger. More details of the VPI&SU cascade are given in references 7 and 9.

Reynolds Number and Trip Wires

The Reynolds number for this cascade, based on the blade axial chord and an exit velocity of 37.5 m/s, is 5.8×10^5. This is sufficiently low that the location of natural transition from a laminar to a turbulent boundary layer along the blade profile could significantly affect the profile losses. With the present method of blade construction, however, there are joints between the cylindrical leading-edge pieces and the plexiglas side walls. These joints are filled with plasticene and smoothed, but it is quite likely that they would influence transition, perhaps in a random manner. For this reason, a 0.020 inch diameter trip wire was epoxied to the plexiglas side walls on the pressure and suction surfaces of all the blades, approximately 3 mm downstream of the joints.

Upstream Boundary Layer

The inlet flow to the cascade was defined by performing boundary layer traverses with a hot-wire anemometer 400 mm upstream of the leading edges of the middle blade and of the adjacent blade. The boundary layer profiles were then integrated numerically to obtain the integral parameters displacement thickness δ^*, momentum thickness θ, kinetic energy thickness δ_3, and shape factor $H_{12} = \delta^*/\theta$. The values obtained are presented in Table 1. In addition, a measure of the turbulence intensity was obtained from the mean and root-mean-square values of the linearized hot wire signal, and the wall shear stress was measured using a Preston tube. These results, together with the freestream velocity $U_1 = 23.5 \pm 0.4$ m/s. obtained with a Pitot probe, define the inlet flow conditions for the present tests.

This inlet flow, with a boundary layer thickness of 35-40 mm compared with a span of 235.2 mm, was chosen to correspond approximately with the Langston flow with a thick inlet boundary layer, 33 mm compared with a span of 281.3 mm. It should be noted however that the ratio of inlet displacement thickness to span for the present tests, which was approximately 0.023, was nearly twice the value of 0.0134 in the Langston test.

Table 1. Results of Boundary Layer Measurements 400 mm Upstream of the Cascade (see Fig. 1)

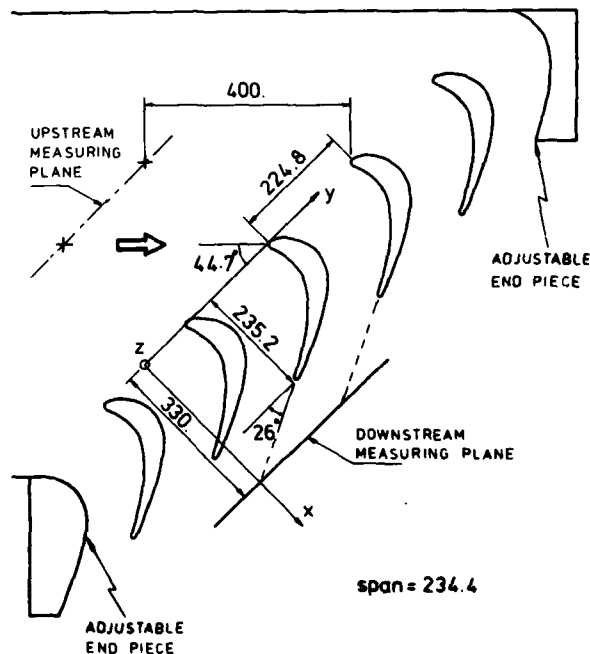|	Upstream of Middle Blade	Upstream of Adjacent Blade
δ_{99}	35. mm	40. mm
δ^*	5.03 mm	5.71 mm
θ	3.75 mm	4.25 mm
δ_3	6.71 mm	7.58 mm
H_{12}	1.34	1.34
c_f	0.0028	0.0027
$(\sqrt{\overline{u'^2}}/U)_{free\ stream}$	0.71 %	0.71 %

Figure 1. Cascade geometry and measurement planes. Linear dimensions in mm.

DOWNSTREAM FLOW DEVELOPMENT

Five-Hole Probe Measurements

Five-hole probe measurements were made at the slot downstream of the cascade at $x/c = 1.4$, as shown in Fig. 1. The results are presented and analysed using the two planes depicted in Fig. 2. The measurement plane is parallel to the plane containing the trailing edges of the blades; and a fictitious cross-sectional plane for the projection of secondary velocities and other data is defined to be perpendicular to the direction of the mean camber line at the trailing edges. Data taken in the measurement plane downstream of the cascade are projected onto this cross-sectional plane.

A nominal flow direction downstream of the blade row is defined in the direction of the mean camber line at the trailing edges of the blades ($\beta_2 = 26°$). The velocity component in this direction, which is defined to be the primary flow direction, is termed u. Thus secondary flow velocity components v and w are defined, which are contained within the cross-sectional plane. In the analysis of the five-hole probe data these three velocity components were calculated together with the component V_n, normal to the measuring plane, see Fig. 2. The flow angles, ψ and ϕ, connected with the velocity components are also shown in Fig. 2.

Averaged Properties

The mass-averaged total pressure loss coefficient is defined as

$$\overline{C_{pt}} \equiv \frac{\displaystyle\int_0^{\Delta Y} \int_{\Delta Z/2}^{\Delta Z} \rho V_n C_{pt} \, dz dy}{\displaystyle\int_0^{\Delta Y} \int_{\Delta Z/2}^{\Delta Z} \rho V_n \, dz dy} \quad , \tag{1}$$

and the average normal velocity as

$$\overline{V_n} \equiv \frac{2}{\Delta Y \Delta Z} \int_0^{\Delta Y} \int_{\Delta Z/2}^{\Delta Z} V_n \, dz dy \tag{2}$$

where

$$C_{pt} \equiv \frac{P_{t1} - P_t}{\frac{1}{2} \rho U_1^2} \quad . \tag{3}$$

Figure 2. Representation of downstream velocities using components v and w orthogonal to the velocity component u in the direction of the mean camber line at the trailing edge. V_n - velocity component normal to measuring plane.

The integrations are performed in the measuring plane over one blade pitch, from $y = 0$ to ΔY, and for the upper half of the plane from $z = \Delta Z/2$ at midspan to $z = \Delta Z$ at the upper end wall.

The results were:

$$(\overline{C_{pt}})_{x/c=-1.2} \quad 0.064 \pm 0.004$$

$$(\overline{C_{pt}})_{x/c=1.4} \quad 0.38 \pm 0.03$$

$$(\overline{V_n})_{x/c=1.4} \quad 14.33 \pm 0.15 \text{ m/s.}$$

The net increase in $\overline{C_{pt}} = 0.32$ may be compared with a value of $0.31-0.04 = 0.27$ reported by Langston, et al. for their plane 12, also at $x/c = 1.4$. The difference in the two results may be partly explained by the lower Reynolds number (based on axial chord and exit velocity) of the present cascade tests, Re = 5.8×10^5 compared with the Langston cascade tests of Re = 10×10^5. It would be expected that the lower Reynolds number would result in a higher loss. Also, in the present cascade, the trip wires applied shortly downstream of the leading edges of the blades will probably have shifted the point of transition, between a laminar and a turbulent boundary layer, upstream. This would result in a higher skin friction around the blade than for the case of natural transition without trip wires and consequently in higher losses, compared to the result obtained by Langston, et al. Considering these two factors, the agreement between the losses measured in the present cascade and those measured by Langston, et al. is reasonable.

Contour Plots and Secondary Flow Plots

Figure 3 shows contours of constant C_{pt} projected on the cross-sectional plane shown in Fig. 2 as seen by an observer looking upstream. The corresponding view of the secondary flow velocities is seen in Fig. 4. The highest values for C_{pt} appear in the end-wall boundary layer and reach a value of approximately 2.7 at the wall. Values of C_{pt} greater than 1.0 also occur in the midspan region, which will be termed the "high-loss core" (for this measurement plane); this region has a significant area with C_{pt} greater than 0.5. A region of moderate loss (0.1 < C_{pt} < 0.5) extends from the high-loss core to the end wall in a location roughly downstream of the trailing edge. This represents fluid in the blade wake, which is bounded on both sides by relatively low loss fluid (C_{pt} < 0.1). The low-loss region extends from the edge of the end-wall boundary layer, where there is a large "low-loss core," to midspan where it appears as a thin sheet between the high-loss core and the wake from the adjacent blade.
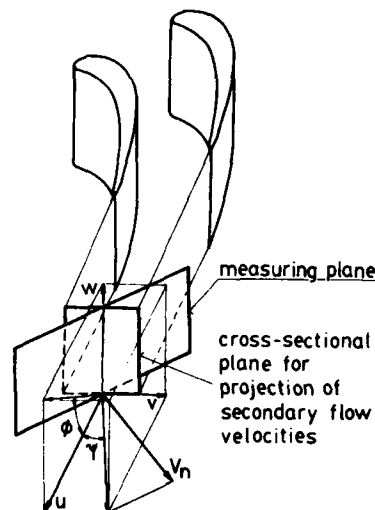
The secondary flow patterns in Fig. 4 are dominated by the passage vortex which developed in the blade row upstream and, at this measurement plane, is centered near the peak value of C_{pt} (≈ 1.3) in the high-loss core. Seen in the cross-sectional plane at $x/c = 1.4$, the passage vortex has a core of solid body rotation with a diameter of the order of 10% of the span and streamwise vorticity of approximately 2000 rad/s; the maximum secondary velocities are of the order of 10 m/s in the passage vortex and these may be compared with streamwise velocities of about 37.5 m/s.

Contours of Normal Velocity

Contours of constant normal velocity, V_n, are shown in Fig. 5. The values for these contours may be compared with the average normal velocity, $\overline{V}_n = 14.3$ m/s. Large normal velocities occur near midspan; these are associated with the passage vortex observed in Fig. 4. The velocities shown at the end wall are not exactly zero because of the presence of the slot, which influenced the five-hole probe measurements close to the wall.

Figure 3. Contours of total pressure loss coefficient C_{pt} at $x/c = 1.4$. Results projected in the cross-sectional plane; —— projections downstream of blades in direction of mean camber lines at trailing edges; suction – downstream of middle blade; pressure – downstream of adjacent blade.
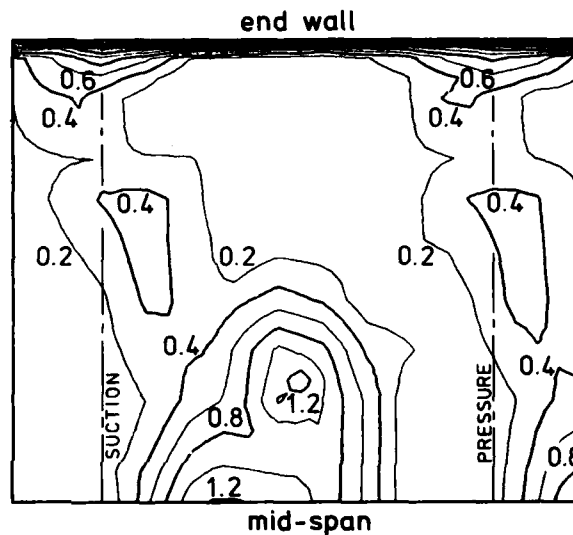
Figure 4. Secondary flow vectors in the cross-sectional plane at $x/c = 1.4$. —— Projections downstream of blades in direction of mean camber lines at trailing edges; suction – downstream of middle blade; pressure – downstream of adjacent blade.
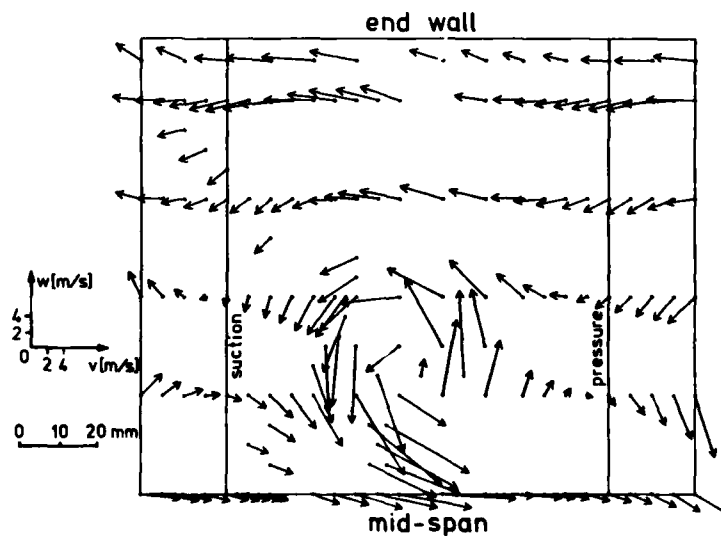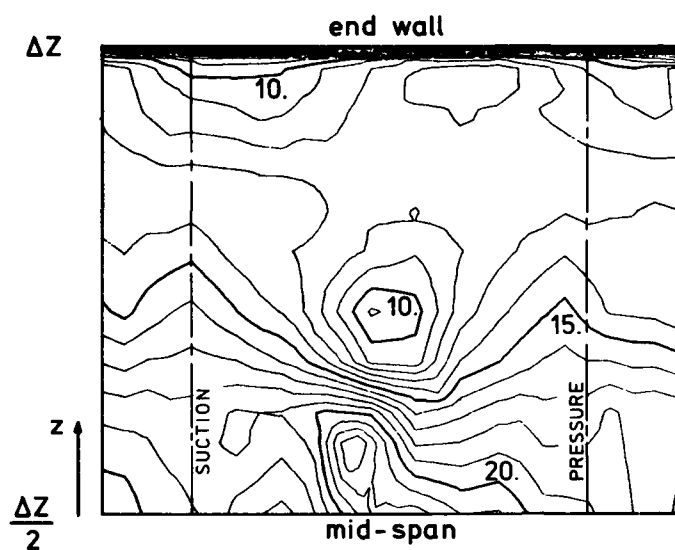
Figure 5. Contours of velocity
normal to the measuring plane
(V_n, m/s) at x/c = 1.4, here
presented in the cross-sectional
plane (see Fig. 2).
ΔZ - blade span.
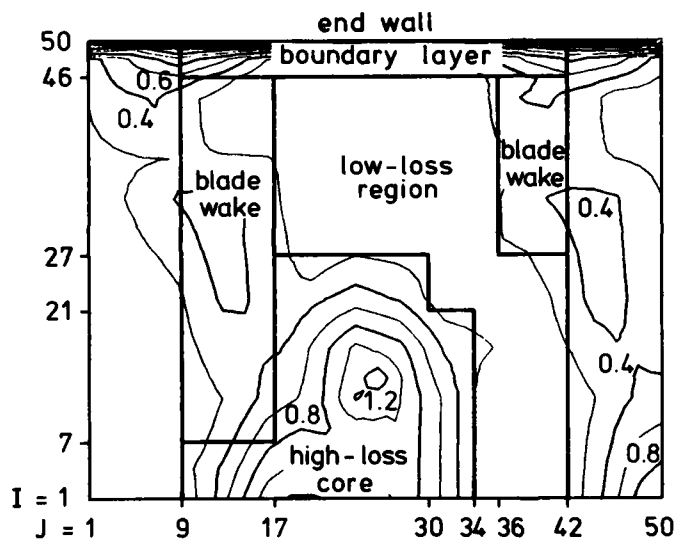
Figure 6. Areas chosen for
numerical integration of total
pressure losses at x/c = 1.4, see
Table 2. I, J - indices of the
50 x 50 grid matrix used to
define the areas.
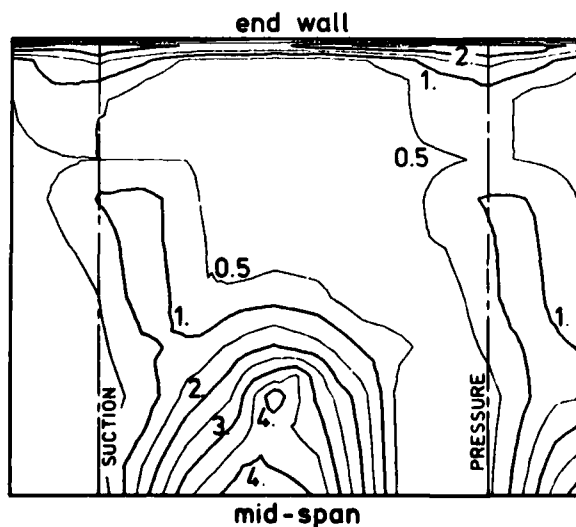
Figure 7. Contours of normalized
entropy flux (area average = 1.0,
see Eq. 5) at x/c = 1.4.

AD-A139 749   PROCEEDINGS OF THE CONFERENCE ON VISCOUS EFFECTS IN   2/4
                TURBOMACHINES HELD AT..(U) ADVISORY GROUP FOR AEROSPACE
                RESEARCH AND DEVELOPMENT NEUILLY..   SEP 83 AGARD-CP-351

UNCLASSIFIED   F/G 20/4   NL
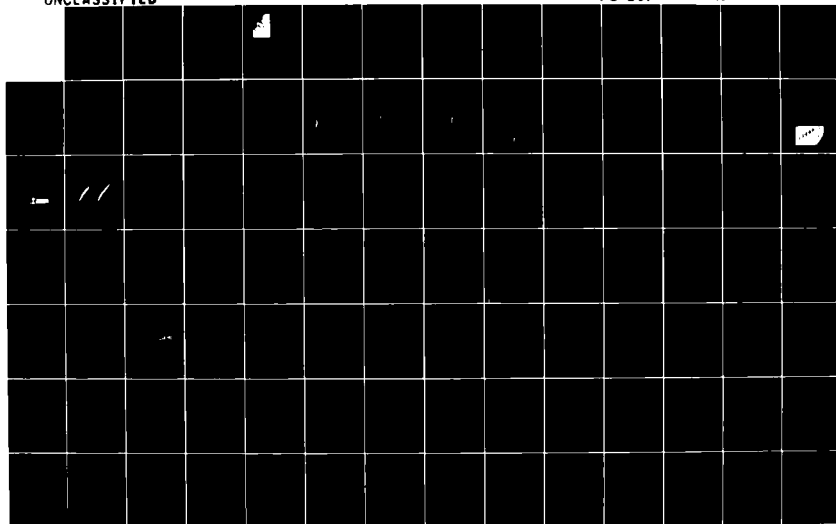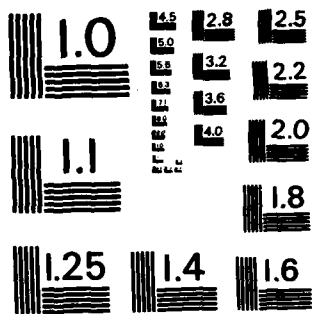
MICROCOPY RESOLUTION TEST CHART
NATIONAL BUREAU OF STANDARDS-1963-A

Contributions to the Overall Losses

In the discussion of the total pressure losses shown in Fig. 3, four areas were distinguished - the end-wall boundary layer, the high-loss core, the blade wake, and the low-loss region. These areas are shown in Fig. 6, which gives the selected values of the indices I and J of the 50 x 50 grid matrix used to define the areas. The contribution of each area to the mass-averaged total pressure loss coefficient was found by integrating the numerator of Eq. 1. The results are presented as percentages of contribution to the overall losses and are shown in Table 2.

Approximately 58 % of the losses are found in the high-loss core near midspan. By contrast the end-wall boundary layer at this plane gives only about 12 % which is really surprisingly small. The area attributed to the blade wake accounts for 21 % of the losses and the low-loss region contains 9 %.

Total Pressure Losses and Entropy Fluxes

For flow of an ideal gas with small changes in total pressure compared with the absolute total pressure at the inlet and with small changes in total temperature T_o, the mass-averaged entropy change is related to the mass-averaged total pressure loss coefficient by the approximation

$$\overline{\overline{s}}_2 - s_1 \simeq \frac{U_1^2}{2T_o} \overline{\overline{C}}_{pt} \qquad (4)$$

Table 2. Loss Contributions of Significant Regions to the Overall Losses at x/c = 1.4.

End-Wall Boundary Layer	12.0 %
High-Loss Core	58.6 %
Blade Wake	20.8 %
Low-Loss Region	8.6 %

For example, in the present test, $\overline{\overline{C}}_{pt} = 0.38$, $U_1 = 23.5$ m/s, and $T_o \simeq 298$ K, thus $\overline{\overline{s}}_2 - s_1 = 0.35$ J/kg K.

The mass-averaging of the total pressure losses in Eq. 2 may therefore be thought of as an integration of entropy fluxes, $\rho V_n(s - s_1)$, i.e.

$$\overline{\overline{C}}_{pt} \simeq \frac{2T_o}{U_1^2} \cdot \frac{\int_0^{\Delta Y} \int_{\Delta Z/2}^{\Delta Z} \rho V_n(s - s_1)\ dzdy}{\int_0^{\Delta Y} \int_{\Delta Z/2}^{\Delta Z} \rho V_n\ dzdy} \qquad (1a)$$

The contributions to the overall losses shown in Table 2 represent contributions to the total flux of entropy at this plane. It is interesting that the highest flux of entropy occurs near midspan in the high-loss core. This is confirmed in Fig. 7, where contours of normalized entropy flux, defined as

$$\frac{\rho V_n(s - s_1)}{\rho \overline{V}_n(\overline{\overline{s}} - s_1)} = \frac{\rho V_n C_{pt}}{\rho \overline{V}_n \overline{\overline{C}}_{pt}} , \qquad (5)$$

are shown. With this definition, the mean entropy flux is unity. In the high-loss core, values greater than four times the mean value are found, while in the end wall boundary layer the entropy fluxes rise to only 2.5 times the mean value before falling to zero at the wall.

Pitch-Averaged Losses

Further information about the distribution of entropy flux at the downstream measurement plane may be found by averaging the total pressure data in the pitch-wise direction. Two distributions in the spanwise direction are considered, the distribution of entropy flux or $\overline{C}_{ptA}$, and the distribution of pitch-wise-mass-averaged entropy of $\overline{C}_{ptB}$. These are defined as

$$\overline{C}_{ptA} \equiv \frac{\int_0^{\Delta Y} \rho V_n C_{pt}\ dy}{\frac{2}{\Delta Z}\int_0^{\Delta Y} \int_{\Delta Z/2}^{\Delta Z} \rho V_n\ dzdy} , \qquad (6)$$

such that

$$\overline{\overline{C}}_{pt} = \frac{2}{\Delta Z}\int_{\Delta Z/2}^{\Delta Z} \overline{C}_{ptA}\ dz , \qquad (7)$$

and

$$\overline{C}_{ptB} \equiv \frac{\int_0^{\Delta Y} \rho V_n C_{pt}\ dy}{\int_0^{\Delta Y} \rho V_n\ dy} . \qquad (8)$$

The spanwise distribution of entropy flux, represented as $\overline{C}_{ptA}$, is shown in Fig. 8. The distribution reaches a peak at midspan with higher levels than the maximum values recorded in the end-wall boundary layers. It may also be confirmed that the area under the curve yields $\overline{\overline{C}}_{pt} = 0.38$.

Pitch-wise-mass-averaged entropies, represented as $\overline{C}_{ptB}$, are shown in Fig. 9. The maximum values of entropy, corresponding to the maximum values of $C_{pt} = 2.7$, occur at the wall, while the minimum average entropies are found near the edge of the end-wall boundary layer. The entropies then rise to another maximum at midspan.
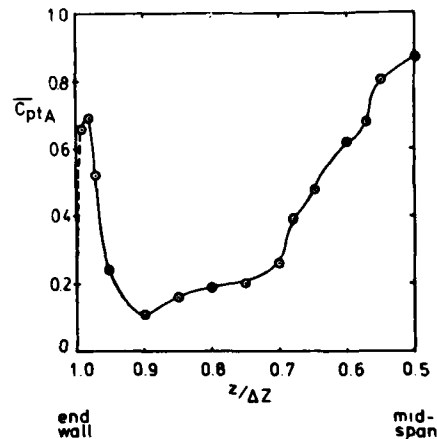

Figure 8. Spanwise distribution of entropy flux, represented as $\overline{C}_{ptA}$, at x/c = 1.4.

Pitchwise Distributions of Loss

The two corresponding distributions in the pitch-wise direction are the distribution of entropy flux or $\overline{C}_{ptC}$ and the distribution of span-wise-mass-averaged entropy or $\overline{\overline{C}}_{ptD}$. These are defined as

$$\overline{C}_{ptC} \equiv \frac{\int_{\Delta Z/2}^{\Delta Z} \rho V_n C_{pt}\, dz}{\frac{1}{\Delta Y} \int_0^{\Delta Y} \int_{\Delta Z/2}^{\Delta Z} \rho V_n\, dz\, dy} \quad , \tag{9}$$

such that

$$\overline{\overline{C}}_{pt} = \frac{1}{\Delta Y} \int_0^{\Delta Y} \overline{C}_{ptC}\, dy \quad , \tag{10}$$

and

$$\overline{C}_{ptD} \equiv \frac{\int_{\Delta Z/2}^{\Delta Z} \rho V_n C_{pt}\, dz}{\int_{\Delta Z/2}^{\Delta Z} \rho V_n\, dz} \quad . \tag{11}$$

These pitchwise distributions are shown in Fig. 10, and it can be seen that (at this plane) they are remarkably similar in both shape and magnitude. This similarity results from the small variation of the denominator of Eq. 11 (for $\overline{C}_{ptD}$) in the pitchwise direction; and this in turn is because the high and low values of normal velocity, V_n, both occur at the same pitchwise location, as seen in Fig. 5.

The significant cyclical variation in the losses in the blade-to-blade direction, shown in Fig. 10, results mostly from the residual low-loss fluid which stretches in the span-wise direction between the high-loss cores, as seen in Figs. 3 and 6.

MEASUREMENT OF FLOW TRAJECTORIES BY ETHYLENE DETECTION

In the last section, measurements of total pressure loss were described at an axial location 40 % of the axial chord downstream of the trailing edge. These results showed a large region of high-loss fluid near midspan and a low-loss region extending from midspan to the edge of the endwall boundary layer. In this section, the sources of fluid in these regions are traced by ethylene injection and detection [12]. Fluid from the horseshoe vortices is located at the blade exit and at the downstream measuring plane and the flow trajectories of this fluid through the cascade are inferred.

A Gowmac model 12-800 flame ionisation detector and model 40-700 electrometer were used as the basis of a detection system for ethylene. This system is described in references 13 and 14.

Tracing Horseshoe Vortex Flow

Figure 11 shows a flow visualization of the limiting streamlines on the end wall of the cascade. The visualization was achieved by rolling a mixture of diesel oil and titanium dioxide onto an aluminum sheet which was taped to the bottom wall; the thin lines on the picture were caused by the edges of the roller. The flow was then turned on for four minutes giving the picture shown. The middle blade of the picture is the middle blade of the five-blade cascade; the present studies were conducted in the flow between this blade and the adjacent blade on the suction side (i.e. the blade in the top right hand corner).

In Fig. 11, the separation of the end wall boundary layer and the formation of the horseshoe vortices near the blade leading edges are clearly defined by an accumulation of white titanium dioxide in a line which stretches across the passage to the suction side of the next blade. This almost straight line is associated with the pressure-side leg of the horseshoe vortex which reaches the suction side of the next blade at about midchord, just upstream of the throat. The other leg of the horseshoe vortex stretches around the leading edge and flows down the suction side where it is clearly seen in the end wall corner region until about the quarter chord position. At this point it appears to leave the end wall and move onto the suction surface.

The separation lines are also drawn on Fig. 12 which shows a top view of the test passage and sampling planes. The injection plane was at x/c = 0.09 just downstream of the leading edge and the two points P and S were chosen for injecting ethylene into the pressure-side and suction-side legs of the horseshoe vortex. The ethylene was injected at a rate of 150 cc/min through 3.1 mm diameter tubes located 2.0 % of the blade span (4.7 mm) from the top wall. Fig. 13 shows a cross-section of the injection plane viewed from downstream with the injection tubes drawn to scale. The injection was at a distance from the wall of approximately 12 % of the inlet boundary layer thickness.
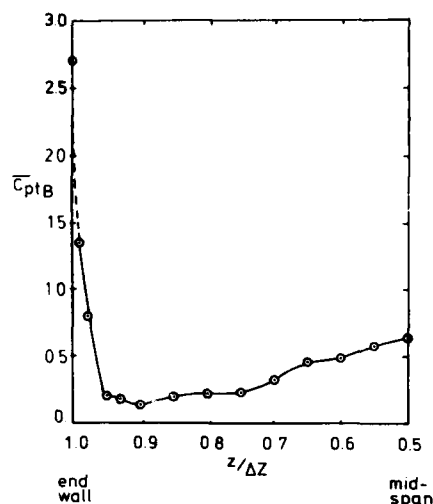
Figure 9. Pitch-wise-mass-averaged entropies, represented as $\overline{C}_{ptB}$, at x/c = 1.4.
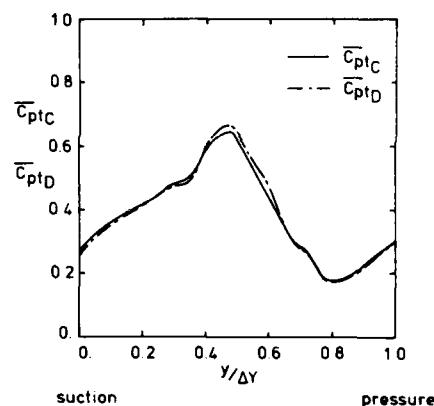
Figure 10. Distributions of entropy flux, represented as $\overline{C}_{ptC}$, and span-wise-mass-averaged entropy, represented as $\overline{C}_{ptD}$, in the pitchwise direction at x/c = 1.4.

Figure 11. Flow visualization of the limiting streamlines on the bottom wall of the cascade.

Figure 12. Top view of test passage showing ethylene injection and sampling planes. o - injection points for pressure-side (P) and suction-side (S) legs of horseshoe vortex. - - - likely path of fluid from point P; ───── likely path of fluid from point S.

Sampling at Downstream Measuring Plane

The flow was sampled isokinetically with a probe of 1.0 mm inside diameter which was traversed in the downstream measuring plane. The resulting concentration contours for points P and S are shown if Figs. 14a and 14b, respectively. These plots may be compared with the corresponding contour plot of total pressure loss shown in Fig. 3 and reproduced again in Fig. 15. The locations of the peak concentrations in Figs. 14a and 14b are marked as P and S in Fig. 15.

Figure 15 shows that the peak concentrations of ethylene from both legs of the horseshoe vortex are found in essentially the same location, at the downstream measuring plane, at a point corresponding very closely with the maximum total pressure loss (C_{pt} = 1.3) in the high-loss core. The maximum concentration of ethylene from the pressure-side leg of the horseshoe vortex is approximately 45 ppm while the peak from the suction-side leg is 25 ppm. The contours for the pressure-side leg in Fig. 14a are quite symmetrical about the peak with a reduction to one-half the peak concentration occurring at a radius of about 5 % of the span. The mixing is somewhat more complete for the suction-side leg and the distribution shows a tail at concentration levels below 10 ppm, as seen in Fig. 14b.

Sampling Near Trailing Edge

A seven-pronged rake was used for sampling just upstream of the blade exit at x/c = 0.96 (corresponding to plane 9 of Langston et al. [1]). This was constructed using 1.6 mm diameter tubing soldered in the configuration shown in Fig. 12. It was traversed vertically in the suction-side half of the passage. Figures 16a and b show the concentration contours at this plane for injection points P and S, respectively.

The contour shapes are quite different for the two injection points. Figure 16a shows the ethylene from the pressure-side leg of the horseshoe vortex in a relatively symmetrical distribution about a peak concentration of approximately 55 ppm. There is however a ridge of concentrations in excess of 20 ppm extending towards the suction side near midspan. This whole distribution is quite similar to the smoke
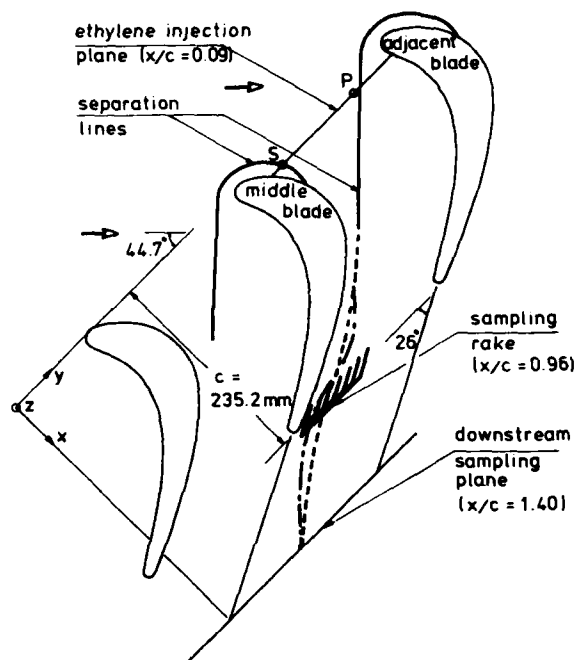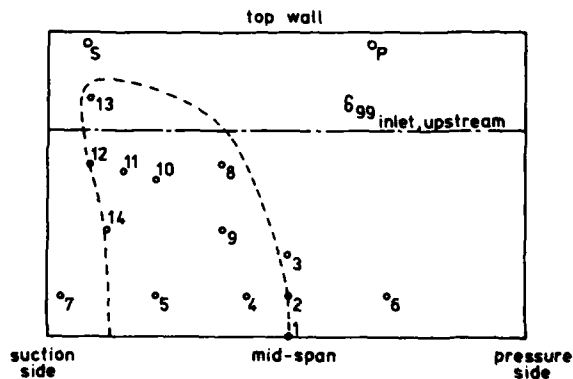
Figure 13. View of ethylene injection plane (x/c = 0.09) looking upstream. o - injection points for pressure-side (P) and suction-side (S) legs of horseshoe vortex. 1-14 - injection points for tracing low-loss fluid. - - - estimated locations of fluid with a downstream value of C_{pt} = 0.2.

top wall   top wall

injection   injection
at   at
point P   point S

suction / pressure   suction / pressure

bottom wall   bottom wall
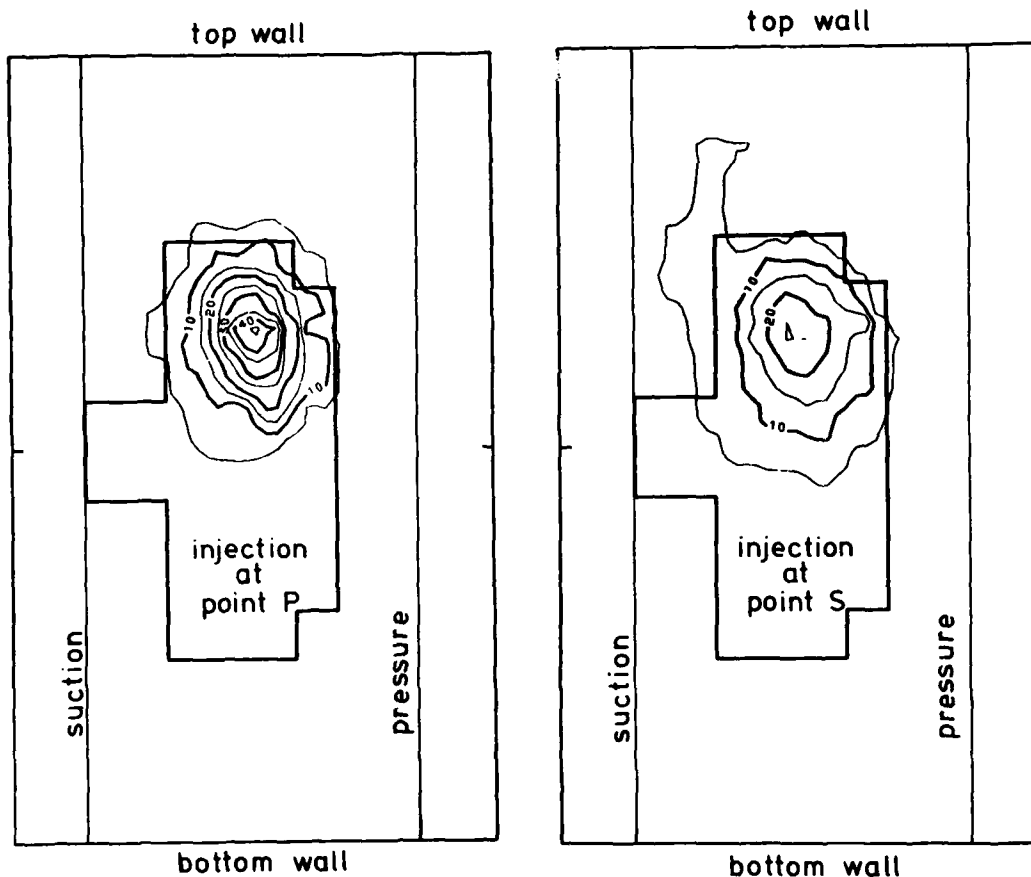
Figure 14a   **Figure 14b**

Figure 14. Ethylene concentration contours at downstream measuring plane (x/c = 1.4). Concentrations in ppm. Contours plotted in cross-sectional plane (see Fig. 2). Suction - downstream of middle blade; pressure - downstream of adjacent blade. ——— Outline of high-loss core (see Fig. 6).

end wall

mid-span
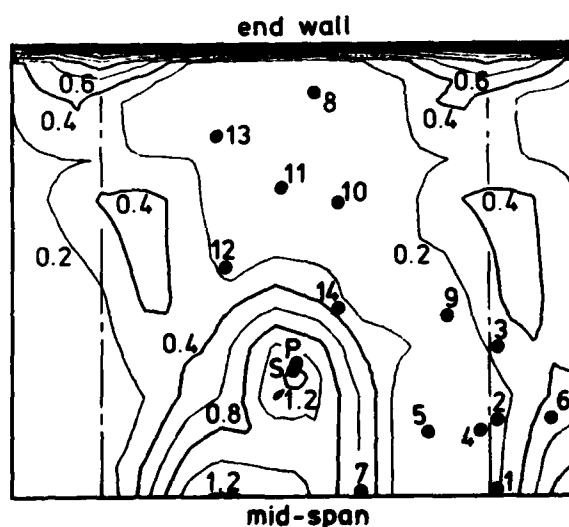
Figure 15. Contours of total pressure loss coefficient C_{pt} at the downstream measuring plane, x/c = 1.4. Results projected in the cross-sectional plane (see Fig. 2). • - locations of peak concentrations for injection at the points shown in Fig. 13.

trace obtained by Stanitz et al. and presented as Fig. 10 in reference 15. There they showed the formation of a passage vortex in a 90 degree rectangular elbow by injecting smoke on the plane wall at the elbow inlet. It appears therefore that fluid from point P is distributed throughout the passage vortex just as the smoke in Stanitz' duct marked his passage vortex.

By contrast, Fig. 16b shows an entirely different distribution of ethylene. Here there is a band of high concentrations, between 50 and 70 ppm, across the top. If the interpretation of the results in Fig. 16a is that fluid from the pressure-side leg of the horseshoe vortex locates the centre of the passage vortex at this plane, then the results in Fig. 16b indicate that fluid from the suction-side leg of the horseshoe vortex is being convected around the centre of the passage vortex. Indeed it is already starting another sweep around the centre. This could explain the band of high concentrations. In Fig. 12, we have drawn the likely paths of fluid from point P and S between the measured locations of maximum concentration. These paths are consistent with the picture of fluid from point S being convected around fluid from point P which marks the passage vortex. In this top view, the path of fluid from point S appears like a sine wave, oscillating about the path of fluid from point P.

top wall

injection
at
point P

suction
side

mid-span

pressure
side

Figure 16a

top wall

injection
at
point S

suction
side

mid-span

pressure
side

Figure 16b

top wall

injection
at
point S

suction
side

mid-span

pressure
side
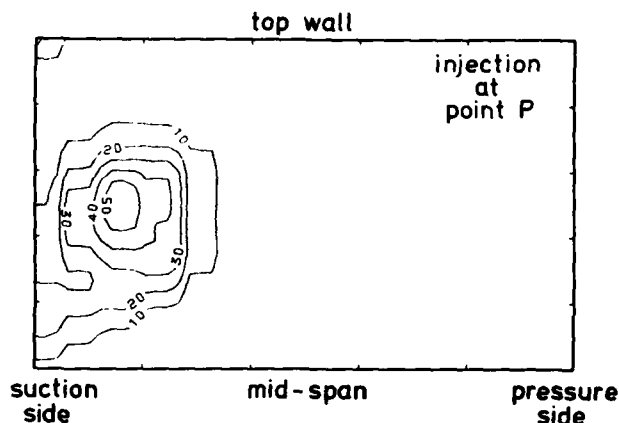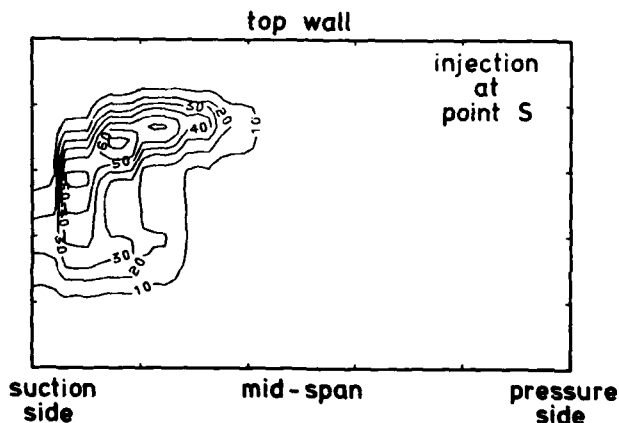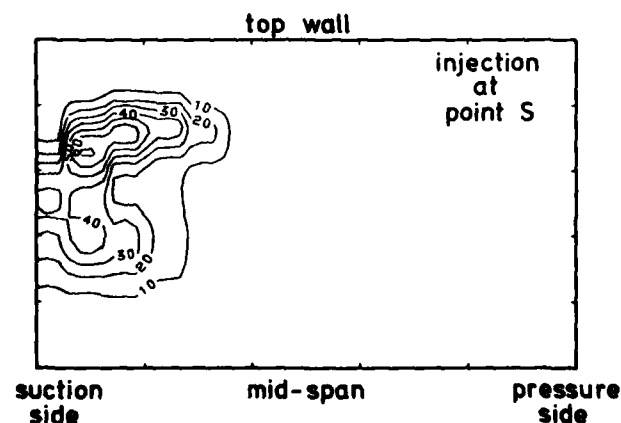
Figure 16c

Figure 16. Ethylene concentration contours near blade exit, x/c = 0.96. Concentrations in ppm. Injection probe diameters: Fig. 16a - 3.1 mm; Fig. 16b - 3.1 mm; Fig. 16c - 1.1 mm.

Consider the orientation of the rake in Fig. 12. A possible explanation of the band of high concentrations in Fig. 16b is that the path of fluid from point S actually takes it past several prongs of the rake each of which sees the same fluid with the same high concentration.

Comparison with Results of Marchal and Sieverding

Marchal and Sieverding [16] also investigated the path of the suction-side leg of the leading edge vortex through a cascade of turbine rotor blades. Using the light sheet technique, they were able to illuminate and photograph smoke patterns in a low Reynolds number flow (5-7 x 10^4, based on exit velocity and axial chord). These showed this counter vortex in the cascade outlet plane just ahead of the trailing edge; there, the counter vortex was on the midspan side of the passage vortex, clearly rotating in the opposite sense to the passage vortex.

In a second set of tests with a cascade of turbine nozzle blades, Marchal and Sieverding used a 5-hole probe to measure a flow of higher Reynolds number (1.9 x 10^5). Again the counter vortex was seen to move towards midspan along the suction surface of the blade; and downstream of the blade row, at x/c = 1.28, the vorticity remaining from the counter vortex appeared to combine with trailing shed vorticity in the blade wake.

Their results did not show the complete excursion of the counter vortex around the passage vortex or the subsequent mixing of the counter and passage vortices observed in the present tests.

Ethylene Concentrations as a Quantitative Measure of Turbulent Mixing

It is possible that the probe used to inject the ethylene into the horseshoe vortices at points P and S could have influenced the flow and mixing downstream. As a check, the 3.1 mm diameter injection tube at point S was replaced with a tube of 1.1 mm diameter, the concentration measurements near the trailing edge were repeated, and the concentration contours of Fig. 16c were obtained. Comparison of Figs. 16b and 16c shows little difference between the results; both figures show a band of high concentrations at the periphery of the passage vortex and both give a peak concentration of about 70 ppm; the shapes of the contours are remarkably similar. (It should be mentioned that the repeated measurements were made several months later by a different experimenter.)

Mixing Downstream of Blades

Some of the ethylene injected at point S has already diffused to the location of maximum concentration for point P by the blade exit. In Fig. 16b, we find the concentration at this location is 27 ppm. Let us therefore consider the change along a trajectory following the maximum concentration for point P downstream of the blade. Along this trajectory, the change for ethylene from point S is from 27 to 25 ppm, similar to the change for point P, from 55 to 45 ppm. But along a trajectory around the edge of the passage vortex the concentration of ethylene from point S falls from 70 to less than 25 ppm. It appears that fluid at the edges of the passage vortex

can mix out quite rapidly compared with fluid in its core. This explanation is consistent with the flow path of the fluid from point S shown in Fig. 3; this carries fluid from point S close to the blade surface at the trailing edge.

Tracing Fluid in the Low-Loss Region

In Fig. 6, a low-loss region was defined based on total pressure measurements at the downstream measuring plane. The total pressure contours are reproduced in Fig. 15 and the low-loss region is essentially that area with $C_{pt} < 0.2$. As discussed above, it consists of a large low-loss core near the end-wall boundary layer with a thin ridge extending to midspan between the high-loss core and the adjacent blade wake. In this section we attempt to find the sources of this fluid in the ethylene injection plane shown in Fig. 12.

To do this, we injected ethylene through a 2.4 mm diameter tube at the 14 locations shown numbered in Fig. 13. We then searched the downstream plane at $x/c = 1.4$ to find the peak concentrations; the locations of these are marked with the corresponding numbers in Fig. 15. We have also estimated with the dotted line in Fig. 13 the location in the injection plane of fluid with a downstream value of C_{pt} equal to 0.2. Thus the source of fluid in the low-loss region can be seen; it is found in the suction-side half of the passage at the blade inlet where it accounts for approximately 27 % of the flow area. This is consistent with the fact that fluid in the low-loss region represents about 36 % of the mass flow through the cascade.

CONCLUSIONS

A 5-blade replica of the Langston turbine cascade [1] has been used to gain further information about the flow development. The 5-hole probe measurements downstream of the cascade (at $x/c = 1.4$) complement the results of Langston et al. [1], who only described the flow within the blade passage. The downstream flow is important, however, as approximately 50 % of the losses for this cascade occur downstream of the trailing edge. The tracer-gas technique using ethylene and a flame ionisation detector shows the paths of fluid from horseshoe vortices through the cascade and shows where fluid with low losses downstream entered the blade row.

The present tests were performed with an exit Reynolds number based on axial chord of 5.8×10^5, compared with 10×10^5 for the Langston tests; the end-wall boundary layers at inlet were somewhat thicker ($\delta*/\Delta Z = 0.023$) than those used by Langston ($\delta*/\Delta Z = 0.0134$).

(i) The net increase in total pressure loss coefficient for the present cascade, between $x/c = -1.2$ (upstream) and $x/c = 1.4$ (downstream), was $\Delta C_{pt} = 0.32$. This is in reasonable agreement with the corresponding value of 0.27 reported by Langston et al.; the difference may be explained by the lower Reynolds number of the present tests and by our use of trip wires near the leading edges of the blades.

(ii) Downstream of the cascade, at $x/c = 1.4$, the distribution of total pressure losses showed
   (a) a high-loss core near midspan with values of C_{pt} greater than 1.0,
   (b) a low-loss region ($C_{pt} < 0.1$) extending from the edge of the end-wall boundary layer to midspan where it appeared as a thin sheet between the high-loss cores,
   (c) the blade wake, roughly downstream of the trailing edge and extending from the high-loss core to the end wall, with $0.1 < C_{pt} < 0.5$,
   (d) the end wall boundary layer with values of C_{pt} rising to about 2.7 at the wall.

(iii) The contributions of each of these four areas to the mass-averaged total pressure loss coefficient (at $x/c = 1.4$) were 58 % for the high-loss core, 21 % for the blade wake, 12 % for the end-wall boundary layer, and 9 % for the low-loss region.

(iv) The pitch-averaged losses were lowest at the edge of the end-wall boundary layer, due to a large "low-loss core," and then rose towards midspan. The entropy fluxes normal to the downstream measuring plane were higher at midspan than in the end-wall boundary layer.

(v) Over 65 % of the ethylene injected near the blade inlet at locations of horseshoe vortex flow was found downstream within the high-loss core. Flow from the pressure-side and suction-side legs of the horseshoe vortex appeared to be distributed around the location of maximum total pressure loss ($C_{pt} = 1.3$) in the high-loss core at the downstream plane.

(vi) Fluid from the pressure-side leg of the horseshoe vortex appeared to be distributed throughout the passage vortex at the blade exit. The distribution was similar to the distribution of smoke observed by Stanitz in a passage vortex in a rectangular elbow.

(vii) Ethylene injected at the location of the suction-side leg of the horseshoe vortex near the blade inlet was convected around the centre of the passage vortex. Fluid at the edges of the passage vortex seemed to mix more rapidly downstream of the trailing edge than fluid near its core.

(viii) Fluid with low losses ($C_{pt} < 0.2$) at the downstream plane represented about 36 % of the mass flow through the cascade. At the blade inlet this flow accounted for approximately 27 % of the flow area.

(ix) The observation that the size of the injection probes used for the counter vortex (3.1 mm and 1.1 mm diameter) did not measurably influence the ethylene concentrations at the blade exit has possible significance for flow modellers. It suggests that the ethylene concentrations presented here give a quantitative measure of the integrated effects of convection and turbulent mixing between the injection point and the sampling plane. This data may therefore be useful in testing three-dimensional turbulent flow calculation methods, especially in assessing turbulence models and numerical accuracy.

REFERENCES

1. Langston, L.S., Nice, M.L., and Hooper, R.M., "Three-Dimensional Flow Within a Turbine Cascade Passage," Trans. ASME, J. of Eng. for Power, Vol. 99, Jan. 1977, pp. 21-28.

2. Graziani, R.A., Blair, M.F., Taylor, J.R., and Mayle, R.E., "An Experimental Study of Endwall and Airfoil Surface Heat Transfer in a Large Scale Turbine Blade Cascade," Trans. ASME, J. of Eng. for Power, Vol. 102, April, 1980, pp. 257-267.

3. Langston, L.S., "Crossflow in a Turbine Cascade Passage," Trans. ASME, J. of Eng for Power, Vol. 102, Oct. 1980, pp. 866-874.

4. Barber, T.J., and Langston, L.S., "Three Dimensional Modelling of Cascade Flows," AIAA Paper No. 79-0047, Jan. 1979.

5. Sharma, O.P., and Graziani, R.A., "Influence of Endwall Flow on Airfoil Suction Surface Mid-Height Boundary Layer Development in a Turbine Cascade," ASME Paper No. 82-GT-127.

6. Hah, C., "A Navier-Stokes Analysis of Three-Dimensional Flow Inside Turbine Blade Rows at Design and Off-Design Conditions," ASME Paper No. 83-GT-40, to be published, Trans. ASME, J. of Eng. for Power.

7. Moore, J. and Ransmayr, A., "Flow in a Turbine Cascade. Part 1: Losses and Leading-Edge Effects," ASME Paper No. 83-GT-68, to be published, Trans. ASME, J. of Eng. for Power.

8. Horlock, J.H., Axial Flow Turbines, Krieger, New York, 1973.

9. Ransmayr, A., "The Influence of Leading-Edge Shape on the Overall Losses of a Turbine Cascade," M.S. Thesis, Virginia Polytechnic Institute and State University, Blacksburg, Virginia, August 1981.

10. Herzig, H.Z., Hansen, A.G., and Costello, G.R., "A Visualization Study of Secondary Flows in Cascades," NACA TN 2947, Feb. 1953.

11. Sjolander, S.A., "The Endwall Boundary Layer in an Annular Cascade of Turbine Nozzle Guide Vanes," M.E. Thesis, Carleton Univ., Ottawa, Ontario, Canada, 1975.

12. Denton, J.D., and Usui, S., "Use of a Tracer Gas Technique to Study Mixing in a Low Speed Turbine," ASME Paper No. 81-GT-86.

13. Smith, B.L., "Detection of Secondary Flow in a Turbine Cascade Using a Tracer Gas Technique," M.S. Thesis, Virginia Polytechnic Institute and State University, Blacksburg, Virginia, February 1983.

14. Moore, J. and Smith, B.L., "Flow in a Turbine Cascade. Part 2: Measurement of Flow Trajectories by Ethylene Detection," ASME Paper No. 83-GT-69, to be published, Trans. ASME, J. of Eng. for Power.

15. Stanitz, J.D., Osborne, W.M., and Mizisin, J., "An Experimental Investigation of Secondary Flow in an Accelerating, Rectangular Elbow with 90° of Turning," NACA TN 3015, Oct. 1953.

16. Marchal, Ph., and Sieverding, C.H., "Secondary Flows Within Turbomachinery Bladings," AGARD Conference Proceedings No. 214 on Secondary Flows in Turbomachines, The Hague, The Netherlands, March 1977.

DISCUSSION

R.Lewis, UK

If the entropy loss of 4.0 at the core of the vortex is twice that observable at the end wall after the cascade, where does the additional entropy rise come from, (Fig.7)? Is this loss core in fact not simply the consequence of the rolling up of low energy fluid admitted to the cascade from the annulus layer upstream, rather than an additional loss casued by the blade row?

Author's Reply

Entropy is produced, not lost, in this irreversible flow with friction. Figure 7 shows contours of entropy *flux* $(\rho V_n (s - s_1))$ normalized such that the area-averaged entropy flux is unity. Entropy flux is a measure of entropy flow per unit area and has the units $J/Km^2 s$; it is used here to show where the entropy is crossing the downstream measuring plane at $x/c = 1.4$.

At the downstream measuring plane, $x/c = 1.4$, the mass-averaged total pressure loss coefficient, $\overline{C}_{pt} = 0.38$. Table 2 gives the contribution due the high-loss core, at this plane as 58.6% or $\delta \overline{C}_{pt} = 0.223$. At the cascade inlet, $x/c = -1.2$, $\overline{C}_{pt} = 0.064$. Thus the losses in the high-loss core are 3.5 times the losses (relative to the inlet free stream) associated with the end-wall boundary layer at the cascade inlet. This is, of course, not surprising in view of the irreversibility due to friction, especially in the end-wall and suction-surface boundary layers, and mixing in the blade wake.

C.H.Sieverding, Be

Referring to Figure 6, I wonder whether the splitting of the total losses in various groups of losses should not be modified by taking into account (a) that due to the spanwise angle variation the blade wake is not normal to the end wall and (b) that the region qualified as "wake losses" should extend from the end wall to mid-span, which would somewhat reduce the percentage of the high loss core with respect to the total losses.

Author's Reply

In this turbulent flow, significant mixing occurs and distinct boundaries are not found between the flow regions. Fluid from one region mixes with fluid from adjacent regions. Choosing areas for numerical integration is therefore somewhat arbitrary. Our purpose here was to obtain answers to such questions as what proportions of the losses are found (at this plane) in the end-wall boundary layer and what proportions near midspan. A combination of ethylene concentration and total pressure loss measurements could be used to quantify the losses for particular fluid streams.

K.Papailiou, Gr

(1) I think that the two legs of the horseshoe vortex, having opposite vorticity, tend to cancel out. One, then, would like to know what is the ratio of the horseshoe vorticity with respect to the one associated with the passage vortex.

(2) If one mixes out the flow, starting from the trailing edge plane, and using momentum arguments, can one find that the losses have been doubled?

Author's Reply

In this turbulent cascade flow, vorticity is convected, stretched and diffused. The extensive data of Langston et al., upon which the results of Reference 1 are based, may provide quantitative answers.

At the exit of the cascade, with the inlet boundary layers reported here and by Langston [1], the suction-surface boundary layer and the passage vortex combine to cause a significant region of low momentum fluid on the suction side of the passage. *Complete* mixing of this flow with the relatively low-loss fluid on the pressure side of the passage can more than double the losses, starting from the trailing edge plane.

F.Leboeuf, Fr

Concerning the losses you measure at the downstream station, what should be the respective influences of the two legs of the horseshoe-vortex and of the passage vortex, which is associated with the deviation of the boundary layer on the end-wall?

Author's Reply

A measure of the weak influence of the horseshoe vortices on the overall losses of this cascade was obtained in References 7 and 9. There, an attempt was made to change the strength of the horseshoe vortices by changing the shape of the leading edges of the blades. This altered the overall losses by an amount which was considered to be within the experimental uncertainty of the measurements. Care should be taken in extrapolating this finding to other test conditions or other cascades.

Karadimas

In my experience, for an aspect ratio of one, I've never seen such high losses near the mid section. Are you sure that one part of those losses are not from a profile separation? Usually, for aspect ratio of one, the high losses are approximately in the 25% span region. Does your profile have a good velocity distribution?

Author's Reply

The loading factor was 1.12, so it's quite highly loaded. The boundary layer was attached in a two dimensional sense at the exit on the suction surface, but I think that there may well have been some three dimensional separation of the boundary layer on the suction surface associated with the roll-up of the passage vortex and associated with the boundary layer development near midspan. But the boundary layer velocity profile in the through flow direction was a well attached turbulent boundary layer.

METHODE DE COUPLAGE POUR LE CALCUL EN MODE INVERSE
DES ECOULEMENTS INTERNES TRANSSONIQUES AVEC ONDE DE CHOC

par

Georges MEAUZE et Jean DELERY

Office National d'Etudes et de Recherches Aérospatiales
B.P. n° 72 - 92322 CHATILLON (France)

Résumé

L'approche couplage fluide parfait-fluide visqueux est un substitut très économique à la résolution des équations de Navier-Stokes complètes, qui exige encore des temps de calcul très longs. La méthode proposée procède par couplage entre un domaine non visqueux, satisfaisant aux équations d'Euler, et des couches dissipatrices décrites par une formulation aux différences finies du type couche limite. Elle permet le calcul d'écoulements internes transsoniques avec chocs intenses et décollements étendus. La méthode est essentiellement basée sur un algorithme interactif Inverse-Inverse. Dans le cas présent, c'est la position du choc qui est fixée a priori. Le niveau de pression aval, ainsi que les pertes par effets dissipatifs, résultent du calcul interactif. Les applications présentées concernent à la fois des canaux symétriques et dissymétriques. La structure des champs calculés reflète fidèlement la réalité expérimentale, en dépit du caractère simpliste du modèle de turbulence utilisé jusqu'à présent.

Abstract

Viscid-inviscid coupling methods are a very economical substitute to the solving of the full time-averaged Navier-Stokes equations which still demands long computer time. The proposed method considers a coupling between an inviscid domain which satisfies the Euler equations and dissipative regions which are depicted by a finite difference boundary-layer type formulation. The method permits the calculation of transonic internal flows comprising strong shock waves and extented separations. The method is basically founded on an Inverse-Inverse interactive algorithm. In the present case, one fixes the shock wave location : the interactive calculation gives the recovery pressure level as well as the losses due to dissipative effects. The presented applications are relative both to symmetrical and unsymmetrical transonic channel flows. The computed flows fields faithfully reproduce experiments in spite of the rather crude turbulence model used up to now.

PRINCIPALES NOTATIONS UTILISEES

C_f : coefficient de frottement pariétal

F : fonction d'amortissement de VAN DRIEST

H : rapport d'épaisseurs $H = \delta^* / \theta$

H_i : paramètre de forme incompressible

ℓ : longueur de mélange de PRANDTL

M_e : nombre de Mach à la frontière de la couche limite

p : pression statique

u, v : composantes selon x et y de la vitesse dans la couche limite

x, y : coordonnées de la formulation couche limite, x est le long de la paroi, y est normale à la paroi

δ : épaisseur physique de la couche dissipative

δ^* : épaisseur de déplacement

θ : épaisseur de quantité de mouvement

ρ : masse spécifique

μ : viscosité moléculaire

τ : frottement tangentiel

ω : coefficient de relaxation

1 - INTRODUCTION

Les effets visqueux jouent souvent un rôle essentiel dans les écoulements, aussi bien supersoniques que transsoniques où, quasi-inévitablement, se forment des ondes de choc plus ou moins intenses. Les interactions fortes qui se produisent alors quand les chocs percutent une paroi, entraînent un épaississement rapide des couches limites et peuvent même provoquer leur décollement, si les sauts de pression dépassent un seuil critique. Ces phénomènes intéressent aussi bien l'aérodynamique externe que l'aérodynamique interne. Ils sont spécialement importants dans les écoulements de canal, où les interactions visqueuses limitent les performances effectives à des niveaux souvent très inférieurs aux valeurs théoriquement réalisables en fluide parfait.

Les calculs d'écoulements complexes, incluant plusieurs zones d'interaction visqueuse, peuvent maintenant être effectués en adoptant l'une ou l'autre des approches suivantes :

- la manière la plus rigoureuse de résoudre le problème est d'utiliser les équations de Navier-Stokes complètes avec modèle de turbulence. Toutefois une description réaliste du champ nécessite des maillages dont la densité conduit à des temps de calcul encore extrêmement longs, même en faisant appel à des techniques multi-domaines [1] ;

- les méthodes de couplage (ou d'interaction) visqueux-non visqueux, offrent des possibilités de calcul beaucoup plus économiques. En effet, elles profitent d'une double simplification en séparant l'écoulement en une partie non-visqueuse, régie par les équations d'Euler (ou encore plus simplement par l'équation du potentiel si le fluide est en outre irrotationnel), et en une partie visqueuse à laquelle sont appliquées des équations du type couche limite. L'approche couplage connaît actuellement de nombreux développements et est largement utilisée en aérodynamique externe où elle concurrence avantageusement les méthodes Navier-Stokes [2].

Dans le premier cas, l'objectif est de calculer l'écoulement correspondant à un point de fonctionnement donné, pour une géométrie imposée.

Dans la procédure inverse habituelle on recherche au contraire une géométrie optimale, en s'imposant tout ou partie de l'écoulement sous forme, par exemple, de répartitions de pression à satisfaire le long des parois du canal. Ces répartitions sont souvent choisies de manière à réaliser les recompressions maximales, compatibles avec l'absence de décollement des couches limites, c'est-à-dire entraînant des pertes minimales. Le point de fonctionnement résulte alors du calcul. Une telle méthode est utilisée classiquement pour définir des profils d'aubes [3].

Egalement, une technique du type inverse permet de contrôler les caractéristiques de l'écoulement correspondant à une configuration bien définie d'ondes de choc, par exemple à un régime "critique" où le choc principal est situé à l'entrée du diffuseur d'une prise d'air, ou du canal interaubes d'une grille de géométrie fixée.

Cette communication propose une telle procédure pour le calcul d'écoulements internes transsoniques avec ondes de choc. Son principe de base consiste à mettre en oeuvre des algorithmes de couplage spécialement adaptés au cas où la position d'une des zones d'interaction est choisie a priori. L'écoulement non-visqueux est calculé à partir des équations d'Euler ; les couches dissipatives sont modélisées par les équations de Prandtl, résolues ici par différences finies. La méthode proposée généralise le travail de CALVERT [4] qui utilisait notamment une méthode intégrale pour calculer les couches limites.

2 - PRESENTATION DE LA METHODE

2.1 - Remarques préliminaires

Rappelons que, dans l'approche couplage, l'écoulement considéré comme non visqueux et les couches dissipatives (couches limites et sillages) sont calculés tour à tour selon un cycle itératif qui doit être conduit jusqu'à ce que les deux domaines (non visqueux et visqueux) satisfassent à des conditions de compatibilité en tout point d'une surface de contrôle (Σ). Différentes surfaces (Σ) peuvent être adoptées. Sans entrer dans une discussion des problèmes de fond délicats, que pose le choix de (Σ), disons en résumé que le couplage est le plus souvent effectué :

- soit le long de la frontière δ de la couche visqueuse. Mais alors, si les équations de Prandtl (équations de la couche limite au premier ordre) sont utilisées pour calculer la zone dissipative, il se manifeste dès le transsonique ($M_e \gtrsim 1,3$ pour la plaque plane turbulente) des comportements "supercritiques" qui entraînent de graves difficultés de mise en oeuvre. Pour initialiser une interaction, il faut alors imaginer des "sauts" supercritique-subcritique totalement dépourvus de signification physique [5]. Pour cette raison, le couplage sur δ n'est plus guère utilisé ;

- soit le long de la surface de déplacement δ^* . C'est le choix le plus communément adopté, mais il conduit également à des problèmes de "criticité" qui sont toutefois reportés à des nombres de Mach plus élevés ($M_e \gtrsim 2$ pour la plaque plane turbulente) ;

- soit sur la surface du corps elle-même. L'écoulement non visqueux est alors prolongé jusqu'à la paroi où les effets visqueux se traduisent par une condition de vitesse de "transpiration" imposée qui se substitue à la condition de glissement classique. Le couplage à la paroi élimine totalement les comportements supercritiques [6]. Toutefois, il devient discutable en cas de décollements verticalement étendus.

La méthode interactive exposée ici utilise le couplage sur la surface de déplacement δ^*. L'équation de couplage exprime alors, pour le fluide parfait, la condition de glissement sur $\overline{\delta^*}$. Dans ce cas, (Σ) est donc une ligne de courant. Egalement, des grands décollements peuvent être représentés sans difficulté de principe. En revanche, les problèmes de criticité vont être rencontrés à partir de $M \simeq 2$, sauf adaptations spécifiques de la méthode de calcul de la couche limite, par prise en compte des gradients de pression normaux [7].

Avant d'aborder la présentation des algorithmes interactifs visqueux/non visqueux adoptés, il convient de préciser les méthodes utilisées pour calculer les parties non visqueuse et visqueuse de l'écoulement.

2.2 - Calcul de l'écoulement de fluide parfait

L'écoulement transsonique de fluide parfait est modélisé par les équations d'Euler dont l'emploi est indispensable pour calculer des écoulements internes bloqués, où des ondes de choc intenses sont susceptibles de se former. La méthode de résolution est du type pseudo-instationnaire, c'est-à-dire que l'enthalpie d'arrêt est supposée constante en permanence, condition qui n'est en réalité satisfaite que lorsque l'état stationnaire est atteint. On économise ainsi la résolution de l'équation de l'énergie ; en contre partie, la phase instationnaire du calcul est dépourvue de signification physique. La technique numérique est du type différences finies avec discrétisation dans le plan physique et utilisation d'un schéma prédicteur-correcteur de Mac Cormack (pour plus de détails, voir la réf. [8]). Dans sa version originale, la méthode procède en mode directe, c'est-à-dire qu'une condition de glissement est satisfaite sur les parois dont la forme est imposée. ELle a été étendue au mode inverse [9] de manière à calculer des écoulements satisfaisant à une loi de pression, imposée le long d'une frontière libre. Cette deuxième procédure permet de définir la géométrie des lignes de courant extrêmes d'un canal devant réaliser des répartitions de pression pariétale souhaitées. En fait, le calcul peut être conduit en mode inverse sur la totalité des parois ou en partie seulement avec passage d'un mode à l'autre.

La référence [9] donne une application de la procédure inverse à la reconstitution de l'écoulement de fluide parfait à l'intérieur d'un canal transsonique, où se produit une interaction choc-couche limite très intense, la donnée du calcul étant à répartition expérimentale de la pression pariétale. Les résultats obtenus reconstituent parfaitement le champ et en particulier l'effet de déplacement de la couche limite, largement décollée, est extrêmement bien reproduit. Une telle application prouve que le concept de déplacement demeure valable, même pour des décollements très importants, ce qui justifie le principe de couplage adopté ici.

2.3 - Calcul des couches limites

Il est maintenant bien connu que le calcul d'une couche limite en mode directe, cest-à-dire à pression imposée, devient instable à l'approche d'un point de décollement (ou de recollement). Ce comportement est lié à l'existence d'une singularité se manifestant, quand le frottement pariétal s'annule [10]. On évite toutefois ces difficultés par l'adoption d'une procédure inverse consistant à imposer une grandeur reflétant l'évolution de la couche limite : épaisseur de déplacement δ^* ou coefficient de frottement pariétal Cf par exemple. La loi de pression (ou de vitesse externe) devient alors le résultat du calcul.

La méthode utilisée ici procède par résolution des équations de couche limite locales, au moyen d'une technique de différences finies [11]. La formulation adoptée, inspirée de celle employée par CARTER [12], considère comme variables dépendantes, le rotationnel, et une fonction de courant, dite de "perturbation", qui représente le défaut de débit massique dû à la couche limite. Les équations sont discrétisées selon un schéma fortement implicite qui confère à la méthode une grande stabilité, même en cas de grand décollement. Le mode inverse peut procéder soit à δ^* soit à Cf imposé. Un calcul à Cf donné est très utile pour les applications du type "conception", où il s'agit, par exemple, de définir une compression $p(x)$ conduisant au ralentissement maximal que la couche limite peut supporter sans décoller. A partir de la loi $p(x)$ ainsi obtenue, la méthode de fluide parfait inverse brièvement décrite ci-dessus permet ensuite de déterminer la forme du canal qui réalisera cette compression. Pour les applications "couplage" où l'effet de déplacement joue un rôle primordial, c'est évidemment la version à δ^* donnée qui est utilisée.

Pour les applications présentes, l'intégration des équations locales est conduite selon une procédure de parabolisation complète dans le sens amont-aval. En cas de décollement, une telle façon de faire est en toute rigueur inexacte puisque, dans la zone de reflux, l'informaton se transmet de l'aval vers l'amont. En fait, l'erreur entraînée est très faible si les vitesses de retour demeurent modérées. La parabolisation est alors effectuée en supposant nul le terme de convection correspondant (approximation FLARE [13]).

Dans la version actuelle de la méthode, le frottement turbulent apparent est représenté par un modèle algébrique sous la forme [14] :

$$-\rho \overline{u'v'} = \mu_t \frac{\partial u}{\partial y}$$

avec

$$\mu_t = \rho \, F^2 \ell^2 \left| \frac{\partial u}{\partial y} \right|$$

La longueur de mélange ℓ est donnée par :

$$\ell = 0,085 \, \delta \, \tanh\left(4,82 \, y/\delta \right)$$

La fonction d'amortissement F est exprimée sous la forme :

$$F = 1 - exp\left[- \frac{1}{10,7\,\mu} \; \sqrt{\frac{|\tau|}{\rho}}\right]$$

où τ est le frottement <u>local total</u>, somme des contributions laminaire et turbulente. Entre autres avantages, l'introduction dans F du frottement total permet d'éviter la suppression complète de la composante turbulente qui se produirait au point de décollement avec la *formulation* originelle de VAN DRIEST où c'est le frottement pariétal qui figure dans F.

Il convient de souligner ici, que ce modèle algébrique a été proposé à l'origine pour calculer des couches limites soumises à des gradients de pression modérés. Il n'a donc pas la prétention de s'appliquer à des interactions très fortes, où la couche limite subit une déstabilisation extrêmement rapide sous l'effet d'un gradient de pression positif intense. Ce modèle a été surtout été choisi en raison de sa simplicité de mise en oeuvre, la présente communication étant davantage centrée sur le développement d'une méthode de calcul pratique que sur l'aspect modélisation physique des phénomènes. L'amélioration de ce second point fait l'objet des développements en cours.

2.4 - Algorithmes de couplage

Selon les domaines d'écoulement à calculer ou la nature des configurations à traiter, le couplage est effectué par l'une ou l'autre des procédures suivantes :

a) fluide parfait direct-couche limite directe

b) fluide parfait inverse-couche limite inverse

c) fluide parfait direct-couche .'mite inverse.

Nous allons maintenant examiner brièvement la nature de ces différents procédés, ainsi que les techniques numériques spécifiques à mettre en oeuvre pour assurer la convergence de l'algorithme de couplage.

2.4.1 - Couplage en mode Direct-Direct

Concernant ce mode, nous serons très brefs étant donné que son champ d'application est limité et qu'il ne soulève pas de problèmes particuliers. Il est utilisé pour calculer les écoulements avec interactions visqueuses dites "faibles", où il n'y a pas de risque de décollement de la couche limite, ce qui est le cas en amont de l'onde de choc où, pour toutes les configurations calculées, l'écoulement est accéléré. Dans ces conditions, les effets visqueux jouent un rôle *très faible et le calcul interactif* n'apporte qu'une correction minime à un champ qui serait purement non visqueux. La boucle de calcul est schématisée par le diagramme ci-dessous. La convergence du processus, traduite par l'invariance de la loi de pression pariétale $p(x)$, est extrêmement rapide : trois à quatre cycles itératifs suffisent.
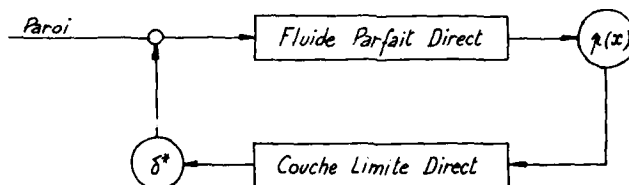
2.4.2 - Couplage en mode Inverse-Inverse

Cette technique est appliquée ici pour les situations où l'origine de l'interaction, c'est-à-dire le point où la pression pariétale se met à croître, est *fixée a priori*. Le cycle itératif est schématisé par le diagramme ci-dessous :
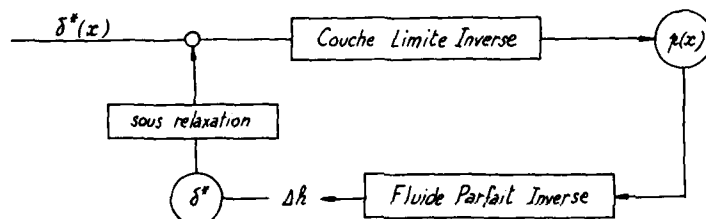
Partant d'une distribution donnée $\delta^*(x)$, le calcul de couche limite inverse fournit une répartition de pression $p(x)$. A partir de celle-ci, le calcul inverse de fluide parfait permet de déterminer le champ complet de l'écoulement et, en particulier, la géométrie de la ligne de courant sur laquelle est imposée la loi $p(x)$. L'écart Δh entre cette ligne et la paroi matérielle représente une nouvelle estimation de l'épaisseur de déplacement qui, après sous relaxation, est réinjectée dans le cycle itératif.

Dans le cas présent, la nécessité d'une sous relaxation s'explique clairement si l'on considère dans le plan (M_e , δ^*), (M_e est le nombre de Mach local à la frontière de la couche limite) les "courbes de réponse" respectives, du fluide parfait, et de la couche limite en un point du maillage de calcul situé sur la surface de déplacement $\delta^*(x)$ (voir fig. 1). Le point P d'intersection de ces deux courbes est l'image de l'état convergé visé. Désignons par m_{FP} (Fluide Parfait) et m_{CL} (Couche Limite) les pentes de chacune des courbes de réponse en P. Moyennant une linéarisation au voisinage de P, un raisonnement simple montre que l'itération de point fixe converge vers P, à condition que le coefficient de relaxation ω soit tel que :

$$\omega < \frac{2\,m_{FP}}{m_{FP} - m_{CL}}$$

On peut donc assurer la convergence de l'itération et l'optimiser en évaluant ω au moyen de la relation ci-dessus. Pour cela, à chaque cycle itératif, les pentes m_{FP} et m_{CL} sont estimées de la manière suivante.

Pour le fluide parfait, on suppose que l'écoulement dans le canal s'effectue par tranches planes. Alors, la conservation du débit conduit à la relation (théorème d'Hugoniot) :

$$m_{FP} = \frac{d\delta^*}{d\bar{M}_{FP}} = \frac{1 - \bar{M}_{FP}^2}{1 + \frac{\gamma-1}{2} \tilde{M}_{FP}^2} \cdot \frac{A - \delta^*}{\bar{M}_{FP}}$$

où A désigne la section droite locale du canal et $\bar{M}_{FP}$ le nombre de Mach moyen dans cette section.

La pente m_{CL} relative à la couche limite est évaluée à partir de l'équation intégrale de Von Karman où le frottement pariétal est négligé ; soit :

$$\frac{d\theta}{dx} + \theta \left(H + 2 - M_e^2 \right) \frac{1}{1 + m_e} \frac{1}{M_e} \frac{dM_e}{dx} = 0$$

θ représente l'épaisseur de quantité de mouvement et l'on a posé : $m_e = \frac{\gamma-1}{2} M_e^2$.

Adoptant la relation approchée $\frac{\delta^*}{\theta} = H = H_i + \alpha M_e^2$ où H_i est le paramètre de forme incompressible, il vient :

(1)
$$m_{CL} = \frac{d\delta^*}{dM_e} = \frac{\delta^*}{M_e} \left[\frac{2.\alpha M_e^2}{H} - \frac{1}{1 + m_e} \left(H + 2 - M_e^2 \right) \right]$$

La valeur de H est fournie par le calcul de couche limite, α étant pris égal à 0,4.

Il serait probablement préférable d'utiliser localement le coefficient de relaxation optimal adapté à chaque point de contrôle situé sur la surface de couplage. Toutefois, dans les applications présentées ci-après, la plus faible valeur trouvée pour ω a été appliquée à tous les points de calcul. Elle correspond d'ailleurs à la dernière station aval de la région subsonique.

Le cycle itératif de couplage "fort" est initialisé en se donnant une répartition $\delta^*(x)$ arbitraire depuis le point d'abscisse x_0 , choisi comme origine de l'interaction. L'état de l'écoulement en amont de x_0 résulte du couplage "faible", pratiqué selon la méthode Direct-Direct (voir paragraphe 2.4.1 ci-dessus). Il est évident que le processus itératif sera accéléré si l'on part d'un "prédicteur" $\delta^*(x)$ pas trop éloigné de la solution convergée. Pour cela, les corrélations expérimentales peuvent servir de guide [15]. Néanmoins, afin d'éprouver la robustesse de la méthode, un calcul a été effectué en partant d'une évolution $\delta^*(x)$ choisie volontairement peu réaliste. Les distributions successives de $\delta^*(x)$ tracées figure 2 montrent une convergence rapide des cycles itératifs. Ces résultats sont relatifs à la première des applications présentées paragraphe 3.2 ci-dessous.

2.4.3 - Couplage en mode Direct -Inverse

La méthode du type Inverse-Inverse est assez limitative en ce sens qu'elle ne permet de traiter qu'une seule interaction dont l'origine est fixée. C'est par exemple le cas d'un profil avec un choc à l'extrados ou celui d'un canal transsonique symétrique traversé par une seule onde de choc. Dans la réalité, bien sûr, les canaux interaubes sont dissymétriques et s'il est toujours possible de choisir l'origine de l'interaction sur une des parois, la position de l'interaction sur la paroi faisant face dépend de tout l'écoulement, c'est-à-dire de la solution elle-même. Son emplacement doit donc demeurer libre, il ne sera défini qu'à convergence du calcul.

La méthode permettant de calculer l'interaction dite "libre" est analogue, dans son principe, à celle utilisée pour les écoulements transsoniques autour de profils d'ailes [16]. Il s'agit d'une procédure Directe-Inverse dont l'algorithme d'itération est schématisé ci-dessous :
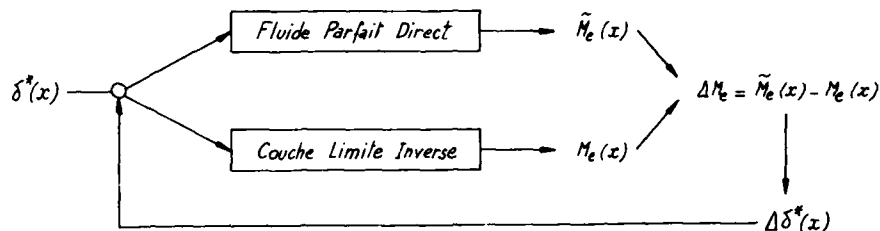
Partant d'une distribution $\delta^*(x)$, on effectue : un calcul de fluide parfait en mode direct, qui donne une répartition de nombre de Mach $\tilde{M}_e(x)$ sur la surface de déplacement et, parallèlement, un calcul de couche limite inverse conduisant à une loi $M_e(x)$ différente, sauf à convergence où $\tilde{M}_e(x) \equiv M_e(x)$. Procédant comme le fait CARTER [17], à partir de l'erreur $\Delta M_e = \tilde{M}_e(x) - M_e(x)$ une correction $\Delta \delta^*$ est évaluée au moyen de la formule 1 ci-dessus. L'expérience montre que le calcul converge sans relaxation, à condition toutefois d'opérer un lissage convenable de la nouvelle loi $\delta^*(x)$ obtenue, surtout dans la région correspondant à des nombres de Mach très légèrement supersoniques.

3 - APPLICATIONS DE LA METHODE ET COMPARAISONS A L'EXPERIENCE

3.1 - Conditions expérimentales

La méthode de couplage a été appliquée sur des configurations dont certaines ont fait l'objet d'expériences très détaillées [18]. Celles-ci ont été effectuées dans un canal transsonique bidimensionnel (soufflerie S8Ch de l'ONERA) représenté schématiquement figure 3. La soufflerie est alimentée en continu avec de l'air atmosphérique désséché, les conditions génératrices étant les suivantes : pression $P_i = 95$ k Pa, température $T_i = 300$ K. La veine d'essai a une envergure de 120 mm et une hauteur à l'entrée de 100 mm. Elle est équipée de blocs tuyère, interchangeables de manière à produire des écoulements légèrement supersoniques. Un deuxième col de section réglable, disposé en aval du canal, crée une onde de choc par effet de blocage. Il permet également d'isoler l'écoulement analysé des perturbations engendrées dans les canalisations aval. Les interactions choc-couche limite étudiées se produisent sur les parois haute et basse du canal, un peu avant la fin de la partie divergente supersonique, de manière à ce que l'onde de choc soit bien stable.

Les couches dissipatives en interaction ont été explorées très soigneusement au moyen d'un vélocimètre laser bidirectionnel. Il a été ainsi possible de déterminer les profils de vitesse de la couche limite avec une grande précision, même dans les zones décollées. Les répartitions de pression pariétale ont également été mesurées.

3.2 - Applications à des canaux symétriques

Quand le canal est symétrique, il suffit de calculer l'écoulement dans une des moitiés du canal. Le domaine de calcul est alors limité par la paroi sur laquelle l'interaction se produit et le plan de symétrie, qui se comporte comme une paroi sans couche limite, où une condition de glissement est appliquée. Pour toutes les configurations envisagées, un calcul est d'abord effectué pour le canal entièrement amorcé en supersonique. Les effets visqueux, qui se traduisent par une interaction du type "faible", sont pris en compte par la procédure Directe-Directe décrite plus haut (voir paragraphe 2.4.2 ci-dessus). Ce calcul fournit les conditions initiales à l'abscisse x_o choisie comme origine de l'interaction avec choc. Le processus est amorcé comme indiqué plus haut, le couplage utilisant alors le mode Inverse-Inverse.

La première interaction calculée a lieu dans une tuyère symétrique, conçue pour produire un écoulement supersonique uniforme de nombre de Mach nominal égal à 1,4. Le début de l'interaction est choisi à une abscisse où le nombre de Mach M_{e_o} à la frontière de la couche limite est égal à 1,28, ce qui est un peu en deçà de la limite expérimentale de décollement naissant en pied de choc [19]. Les lignes isobares du fluide parfait obtenues après convergence sont représentées figure 4. La répartition du nombre de Mach M_e est tracée figure 5 et celles des grandeurs relatives à la couche limite : δ^*, θ, Cf et H_i (paramètre de forme incompressible) figures 6a et 6b. Le calcul met en évidence un très léger décollement, qui est d'ailleurs à la limite de ce qui est expérimentalement décelable. Il n'y a pas pour ce cas de comparaison avec des mesures, les conditions initiales du calcul ne correspondant pas exactement à une configuration expérimentale.

Le deuxième exemple est relatif à une tuyère, toujours symétrique, dont le nombre de Mach nominal est de 1,6. L'interaction est initialisée à une station où $M_{e_o} = 1,44$ ce qui doit conduire à la formation d'un décollement franc. Ici, les conditions de calcul coïncident avec un cas analysé expérimentalement. La figure 7 donne le tracé des isobares de l'écoulement de fluide parfait et les figures 8 et 9 les distributions de M_e, δ^*, θ, Cf et H_i. L'évolution calculée de Cf confirme la formation d'un décollement assez étendu. Comme le montre la figure 8, le calcul conduit à une compression trop forte, conséquence de l'utilisation d'un modèle de turbulence trop "simpliste". Néanmoins, l'allure générale du phénomène est correctement reproduite par le calcul.

Le dernier exemple de canal symétrique, correspond à une interaction encore plus intense pour laquelle M_{ℓ_0} = 1,55. Elle se produit dans la même tuyère que l'exemple précédent. Les résultats de ce calcul sont donnés figures 10 à 12 (aucune expérience n'était disponible pour ce cas). On remarquera l'importance accrue de l'interaction, qui entraîne un large décollement de la couche limite. Le champ des isobares (voir fig. 10) met en évidence une "langue supersonique", incluse dans le champ aval subsonique. Ce phénomène est souvent observé dans les interactions choc-couche limite en transsonique élevé [20], sans que son caractère de généralité puisse être établi.

3.3 - Application à un canal dissymétrique

La paroi inférieure du canal comporte ici une "bosse" de 286 mm de long sur 12 mm d'épaisseur. La paroi supérieure est rectiligne. Les conditions expérimentales sont telles que, sur la paroi inférieure, le début de l'interaction se produit pour un nombre de Mach M_{ℓ_0} = 1,37. Il y a alors décollement de la couche limite avec formation d'une zone décollée très étendue, en raison du contour de la paroi.

Après l'étape préliminaire en mode Direct-Direct, le calcul est effectué en faisant coïncider l'origine de l'interaction sur la paroi inférieure avec l'expérience. Le mode Inverse-Inverse est utilisé le long de la paroi basse et le mode Direct-Inverse sur la paroi haute, où la zone d'interaction doit demeurer libre (voir paragraphe 2.4.3 ci-dessus). La figure 13 montre les distributions de pression sur les parois haute et basse, à l'initialisation du calcul, et après convergence. On notera le déplacement vers l'amont du début de l'interaction haute ainsi que la disparition des oscillations présentes au départ. La figure 14 donne le tracé des isobares du champ non visqueux. Les comparaisons théorie- expérience sont présentées figures 15 à 18. Le calcul conduit à une très bonne simulation de l'écoulement transsonique et des deux interactions dont il est le siège. L'accord quantitatif est raisonnable malgré l'inadaptation du modèle de turbulence utilisé ici. Celui-ci surestime les forces visqueuses (c'est-à-dire la tension de cisaillement turbulente), d'où une trop grande "raideur" de la couche limite ; ceci se traduit par une surestimation des recompressions, et une sous-estimation de l'épaississement et de la déstabilisation de la couche limite.

4 - CONCLUSION

L'approche couplage fluide parfait-fluide visqueux permet une prévision très réaliste des écoulements internes supersoniques et/ou transsoniques, sièges d'interactions visqueuses fortes. La méthode proposée procède par couplage entre un fluide non visqueux, satisfaisant les équations d'Euler, et des couches dissipatives décrites par les équations de Prandtl qui sont résolues ici selon un schéma aux différences finies. Les conditions de couplage sont exprimées sur la surface de déplacement. Des exemples d'écoulements transsoniques avec chocs intenses et décollements sont traités. La méthode est essentiellement basée sur un algorithme interactif en mode Inverse-Inverse qui permet de choisir l'origine de "l'interaction", c'est-à-dire en gros la position du choc. Le niveau de pression aval, ainsi que les pertes par effets dissipatifs résultent du calcul itératif. La méthode inclut également un algorithme Direct-Inverse (ou Semi-Inverse) pour traiter le cas général des canaux dissymétriques. En effet il n'est possible d'adopter le mode Inverse-Inverse que sur une seule paroi.

Les applications effectuées montrent que la méthode possède de bonnes qualités de convergence et constitue de ce fait un "outil" économique pour calculer des écoulements internes complexes comportant des interactions avec décollement étendu. La structure des champs calculés reflète fidèlement la réalité expérimentale ; néanmoins l'accord quantitatif n'est pas encore pleinement satisfaisant en raison du caractère trop rustique du modèle de turbulence utilisé dans la version actuelle de la méthode. La modélisation de la turbulence dans les interactions choc-couche limite est en fait un problème très complexe qui est encore loin d'être totalement résolu. Les études de base en cours, à l'ONERA en particulier [21], devraient toutefois permettre des progrès substantiels dans un proche avenir.

REFERENCES

[1] - CAMBIER L., GHAZZI W., VEUILLOT J.P. et VIVIAND H.
Une approche par domaines pour le calcul d'écoulements compressibles. 5ème Colloque International sur les Méthodes de Calcul Scientifique et Technique, INRIA, 1981, TP-ONERA n° 1981-143.

[2] - LE BALLEUR J.C.
Numerical viscid-inviscid interaction in steady and unsteady flows. 2nd Symposium on Numerical and Physical Aspects of Aerodynamics Flows, California State University, Long-Beach, 1983, à paraître chez Springer-Verlog.

[3] - LE FOLL J.
Inverse method for optimized blading calculations. Transonic flows in axial turbomachinery, V.K.I. Lecture Series 84, february 2-6 1976.

[4] - CALVERT W.J.
An inviscid-viscous interaction treatment to predict the blade-to-blade performance of axial compressors with leading edge normal shock waves. ASME Paper 82-GT-135, 1982.

[5] - CROCCO L.
Condiderations on the shock/boundary layer interaction. Proc. Centennial of Brooklyn Polyt. Inst., 1954.

[6] - LE BALLEUR J.C.
Couplage visqueux-non visqueux : analyse du problème incluant décollements et ondes de choc. La Recherche Aérospatiale n° 1977-6, pp. 349-358, 1977.

[7] – CARRIERE P., SIRIEIX M. et DELERY J.
Méthodes de calcul des écoulements turbulents décollés en supersonique. Progress in Aerospace Sciences, vol. 16, n° 4, pp. 385-429, 1975.

[8] – VIVIAND H. et VEUILLOT J.P.
Méthodes pseudo-instationnaires pour le calcul d'écoulements transsoniques. Publication ONERA n° 1978-4, 1978.

[9] – MEAUZE .G
Méthode de calcul inverse pseudo-instationnaire. La Recherche Aérospatiale n° 1980-1, pp. 23-30, 1980.

[10] – GOLDSTEIN S.
On laminar boundary layer flow near a position of separation. The Quaterly Journal of Mechanics and Applied Mathematics, vol. 1, part. 1, pp. 43-69, 1948.

[11] – DELERY J. et LE BALLEUR J.C.
Interaction et couplage entre écoulement de fluide parfait et écoulement visqueux. ONERA RSF n° 4/3073, 1980.

[12] – CARTER J.E.
On inverse solutions for laminar boundary layer flows with separation and reattachment. NASA TR R447, 1975.

[13] – REYHNER T.A. et FLUGGE-LOTZ I.
The interaction of a shock wave with a laminar boundary-layer. Int. Journal of Non-Linear Mech., vol. 3, n° 2, pp. 173-199, 1968.

[14] – MICHEL R., QUEMARD C. et DURANT R.
Application d'un schéma de longueur de mélange amélioré à l'étude des couches limites d'équilibre. ONERA NT 154, 1969.

[15] – SIRIEIX M. DELERY J. et STANEWSKY E.
High Reynolds number boundary-layer/shock wave interaction in transonic flows. Lecture Notes in Physics, vol. 148, pp. 149-214, Springer Verlag, 1981.

[16] – LE BALLEUR J.C.
Couplage visqueux-non visqueux : méthode numérique et application aux écoulements bidimensionnels transsoniques et supersoniques. La Recherche Aérospatiale n° 1978-2, pp. 67-76, 1978.

[17] – CARTER J.E.
A new boundary-layer interaction technique for separated flows. AIAA Paper n° 79-1450, 1979.

[18] – DELERY J.
Investigation of strong shock/turbulent boundary-layer interaction in 2-D transonic flows with emphasis on turbulence phenomena. AIAA Paper n° 81-1245, 1981 et AIAA Journal, vol. 21, n° 2, pp. 180-185, 1983.

[19] – DELERY J.
Some features of transonic shock wave/turbulent boundary-layer interaction. VKI LS 1980-8 on "Shock boundary-layer interaction in turbomachines", 1980.

[20] – SEDDON J.
The flow produced by interaction of a turbulent boundary-layer with a normal shock wave of strength sufficient to cause separation. ARC R & M 3502, 1967.

[21] – DELERY J. et VEUILLOT J.P.
Recherches expérimentales et théoriques sur la turbulence dans les interactions choc-couche limite en transsonique. Symposium IUTAM on "Structure of Complex Turbulent Shear Flows", IMST, Marseille, 1982.
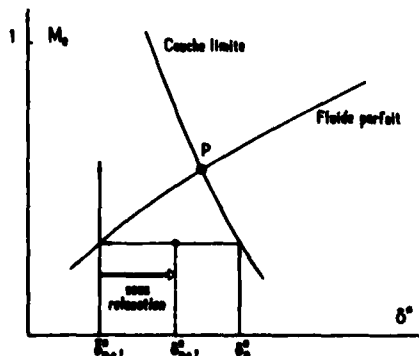
Fig. 1 — Image de l'itération de couplage inverse-inverse en un point du maillage.
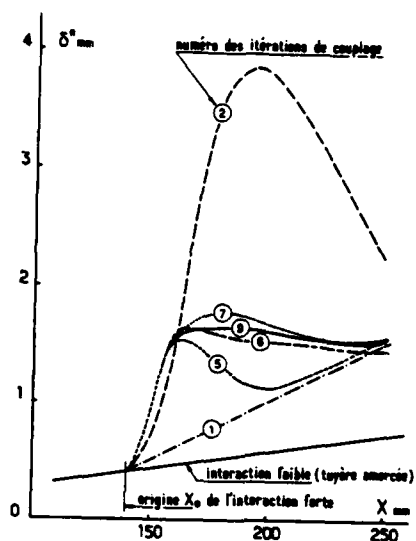
Fig. 2 — Evolution de la répartition δ*(X) au cours des itérations de couplage.

Fig. 3 — Interactions choc-couche limite dans un canal transsonique. Dispositif expérimental.
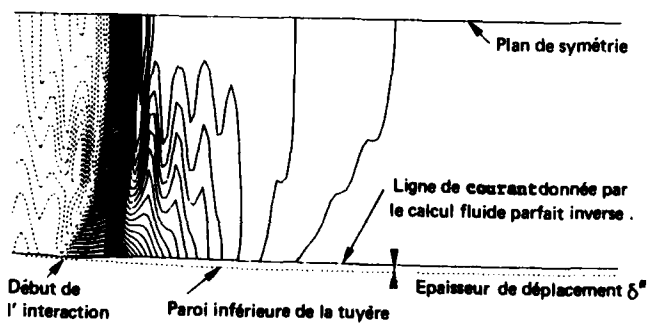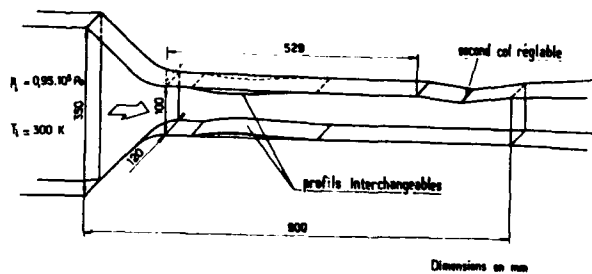
Fig. 4 -Champ des isobares . Cas M = 1,28.

Fig. 5 — Interaction à la paroi d'un canal symétrique. Cas M_{e_0} = 1,28. Nombre de Mach à la frontière de la couche limite.
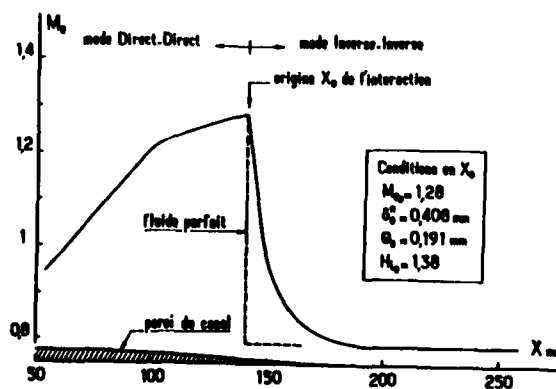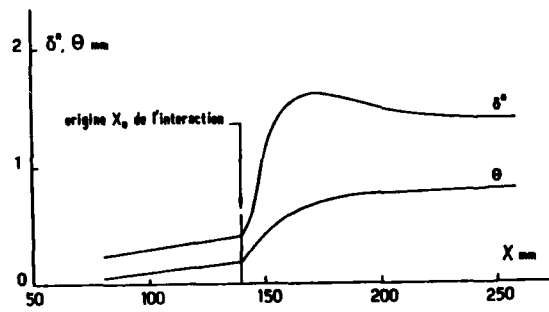
Fig. 6a — Interaction à la paroi d'un canal symétrique.
Cas $M_{e_0} = 1,28$. Epaisseurs de déplacement et de
quantité de mouvement.

Fig. 6b — Interaction à la paroi d'un canal symétrique.
Cas $M_{e_0} = 1,28$. Paramètre de forme et coefficient de
frottement pariétal.
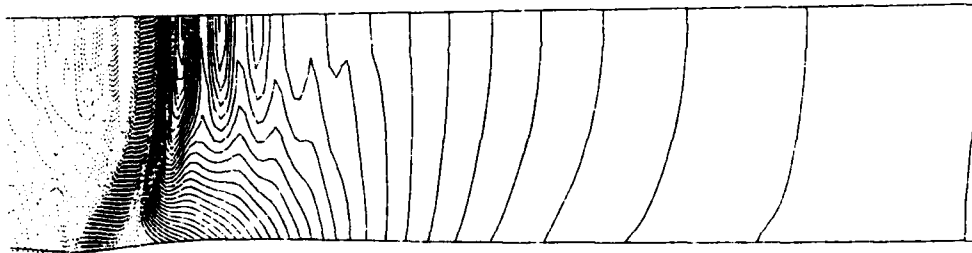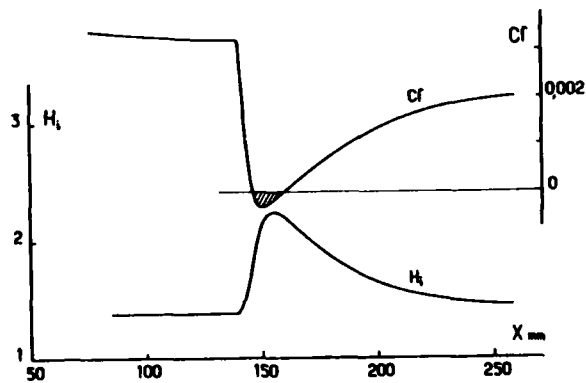
Fig. 7 -Champ des isobares . Cas $M_{e_0} = 1,44$.
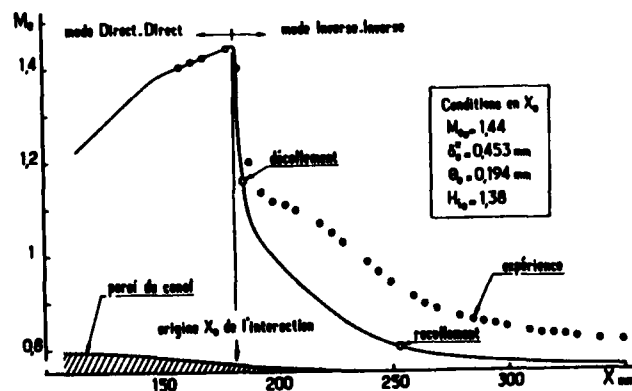
Fig. 8 — Interaction à la paroi d'un canal symétrique.
Cas $M_{e_0} = 1,44$. Nombre de Mach à la frontière de
la couche limite.
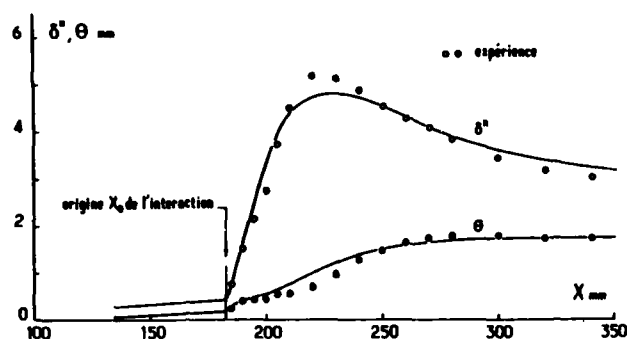
Fig. 9a — Interaction à la paroi d'un canal symétrique.
Cas M_{e_0} = 1,44. Epaisseurs de déplacement et de
quantité de mouvement.

Fig. 9b — Interaction à la paroi d'un canal symétrique.
Cas M_{e_0} = 1,44. Paramètre de forme et coefficient de
frottement pariétal.
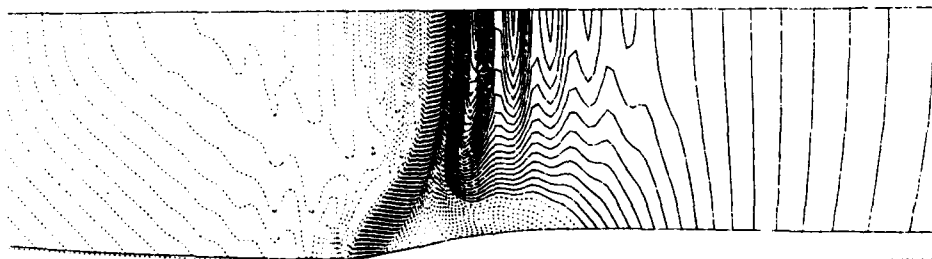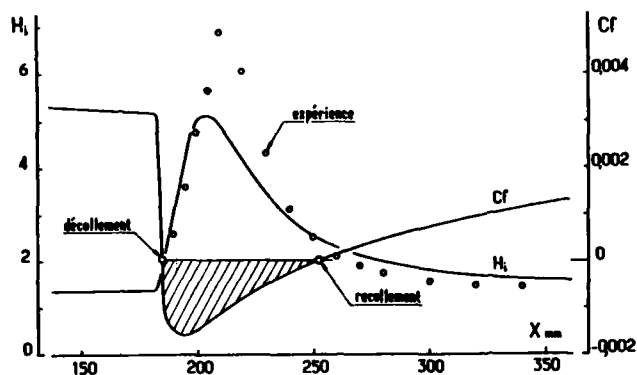
Fig. 10 –Champ des isobares. M = 1,55.
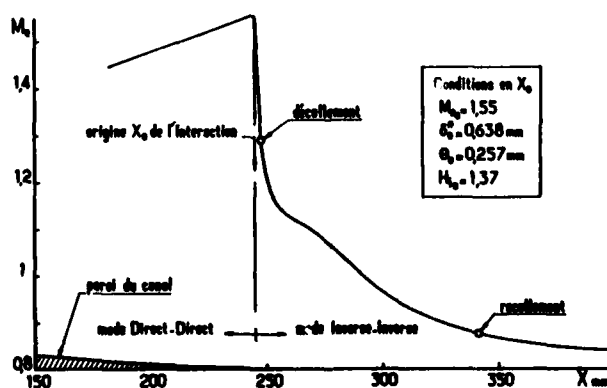
Fig. 11 — Interaction à la paroi d'un canal symétrique.
Cas M_{e_0} = 1,55. Nombre de Mach à la frontière de la
couche limite.
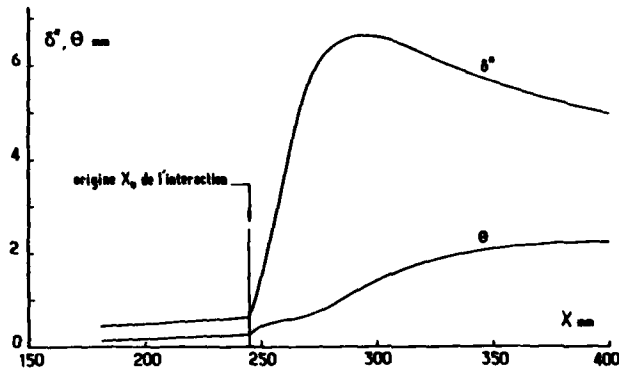
Fig. 12a — Interaction à la paroi d'un canal symétrique. Cas $M_{e_0} = 1,55$. Epaisseurs de déplacement et de quantité de mouvement.

Fig. 12b — Interaction à la paroi d'un canal symétrique. Cas $M_{e_0} = 1,55$. Paramètre de forme et coefficient de frottement pariétal.
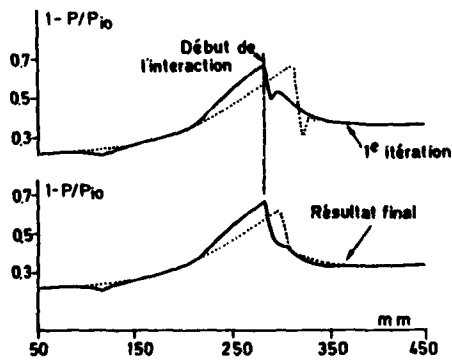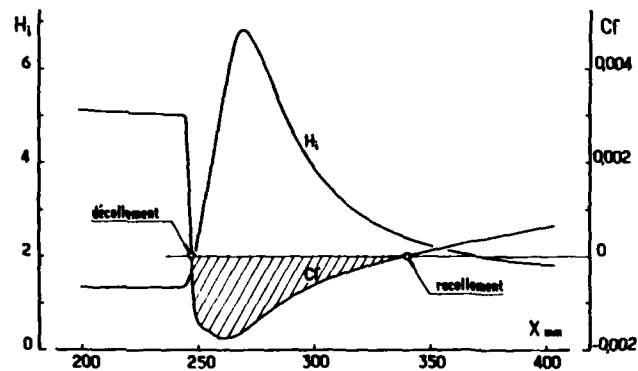
Fig. 13 — Canal dissymétrique. Répartition de pression sur les parois du canal à la 1ère itération et après convergence du calcul.
— paroi inférieure (mode inverse-inverse, début de l'interaction imposé).
— paroi supérieure (mode direct-inverse, interaction libre).

Fig. 14 — Canal dissymétrique. Champ d'isobares.
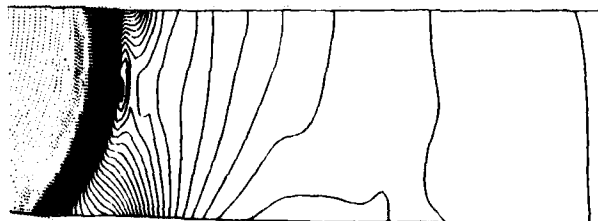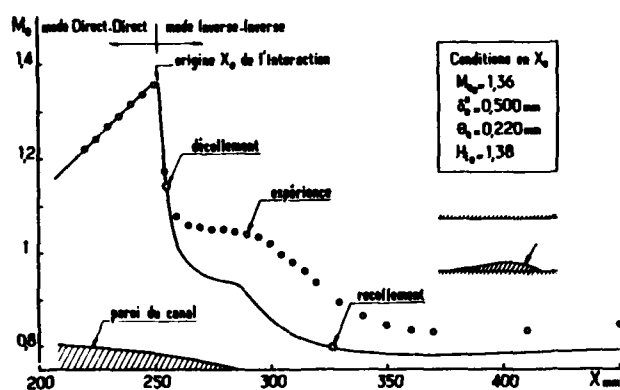
Fig. 15 — Interaction dans un canal dissymétrique. Paroi inférieure. Nombre de Mach à la frontière de la couche limite.

Fig. 16a — Interaction dans un canal dissymétrique. Paroi inférieure. Epaisseurs de déplacement et de quantité de mouvement.
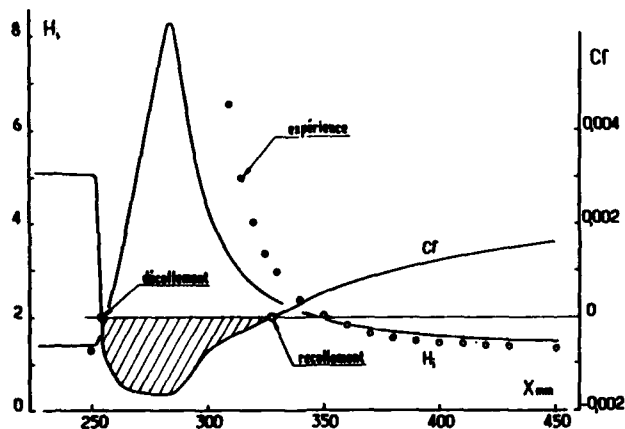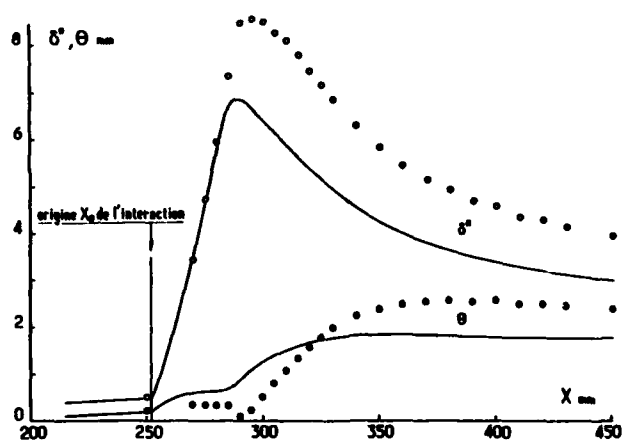
Fig. 16b — Interaction dans un canal dissymétrique. Paroi inférieure. Paramètre de forme et coefficient de frottement pariétal.

Fig. 17 — Interaction dans un canal dissymétrique. Paroi supérieure. Nombre de Mach à la frontière de la couche limite.
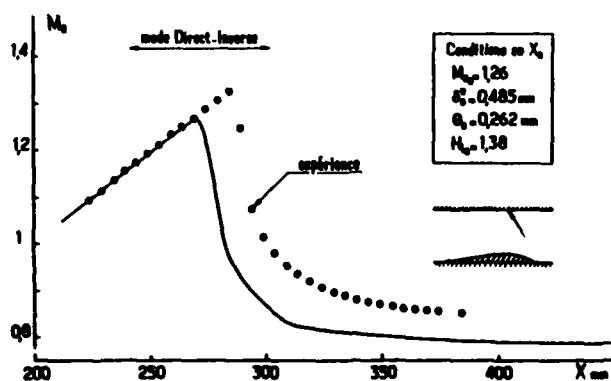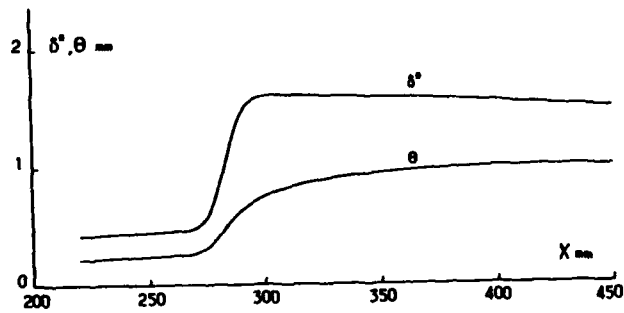
Fig. 18a — Interaction dans un canal dissymétrique. Paroi supérieure. Epaisseurs de déplacement et de quantité de mouvement.

Fig. 18b — Interaction dans un canal dissymétrique. Paroi supérieure. Paramètre de forme et coefficient de frottement pariétal.
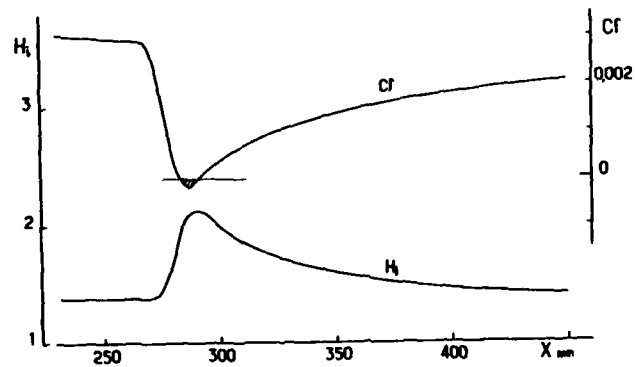
DISCUSSION

W.J.Calvert, UK

For the symmetrical calculation with $M_{eo} = 1.44$ (Fig.7-9), you attribute the discrepancy between the measured and predicted Mach numbers to the turbulence model in the viscous calculation. Since the calculated distribution of δ^* agrees well with the test data, surely the inviscid part of the calculation must also be somewhat in error.

Réponse d'Auteur

L'écoulement en aval de l'interaction étant transsonique, le niveau des pressions et des nombres de Mach est extrêmement sensible à une légère variation de la section offerte au fluide et donc de l'épaisseur de déplacement.

En particulier, comme le suggère M. Dunham, l'effet des couches limites pariétales et très important sur cette répartition de pression.

K.Papailiou, Gr

(1) The amount of aritificial viscosity influences the width of the calculated shock wave. Does this situation influence the final boundary layer calculation results?

(2) On which factor do you attribute the discrepancy between calculation and experiment? The luck of using Navier-Stokes equations or the turbulent model used?

Réponse d'Auteur

(1) Effectivement la viscosité artificielle a un effet sur l'épaisseur du choc, qui reste cependant modérée de l'ordre de 3 à 4 mailles. Par contre l'effet devient tout à fait négligeable au niveau de l'interaction avec la couche-limite grâce à l'étalement de la répartition de pression. Je rappelle en outre que d'une façon générale, la viscosité artificielle a un effet sur l'entropie presque exclusivement, et pratiquement aucun sur la pression statique.

(2) Je reste convaincu que les écarts avec l'expérience sont dus à la trop grande simplicité du schéma de turbulence utilisée et cela pour 3 raisons:

— les auteurs de la Réf. [1] ont effectués un calcul Navier Stokes avec le même schéma de turbulence, pour une configuration tout à fait analogue à la première présentée ici. Il apparait que les résultats sont tout à fait comparables et en particulier que le gradient de pression transversal dans la couche visqueuse et très faible.

— je rappelle un calcul présenté en [9] qui consiste à imposer la répartition de pression expérimentale au fluid parfait en mode inverse. L'évolution de l'épaisseur de déplacement que l'on en déduit est parfaitement comparable à celle mesurée.

— si l'on introduit comme donnée, la répartition de δ^* expérimentale pour le calcul de couche limite inverse on retrouve l'écart sur l'évolution de nombre de Mach; Si l'on effectue le même type de calcul avec un schéma de turbulence plus élaboré, l'écart diminue considérablement.

J.Dunham, UK

I wonder if the discrepancy between measurrd and calculated Mach numbers after the shock may perhaps be due to shock-induced separations on the *side* walls?

Réponse d'Auteur

Je suis tout à fait d'accord. Malheureusement les mesures effectuées ne permettent pas de chiffrer l'effet lié au développement des couches limites pariétales.

METHODE D'ANALYSE EXPERIMENTALE

DE L'INTERACTION CHOC-COUCHE LIMITE EN GRILLES D'AUBES

par

Antoine FOURMAUX

Office National d'Etudes et de Recherches Aérospatiales
29, avenue de la Division Leclerc
B.P. n° 72
92322 CHATILLON Cedex

RESUME

Dans les grilles d'aubes, la faible épaisseur physique des couches limites, due aux dimensions généralement réduites des maquettes, rend délicates les mesures permettant d'accéder aux grandeurs caractéristiques de la couche visqueuse. Afin d'avoir une estimation de l'effet de déplacement et d'évaluer l'importance de l'interaction entre les chocs et les couches limites, on utilise une méthode de calcul pseudo-instationnaire en mode inverse pour reconstituer par le calcul l'écoulement dans le canal inter-aubes à partir du relevé de la pression statique sur le profil.

On présente dans l'exposé le principe et les limites de cette méthode d'analyse, ainsi que des comparaisons entre les résultats du calcul et des mesures fines effectuées dans le canal. On aborde en outre l'aspect purement expérimental : techniques utilisées pour régler et contrôler l'écoulement, et techniques de mesure.

ABSTRACT

The small physical thickness of cascades boundary layers, due to the usually small dimensions of the test models, makes it difficult to measure the characteristic parameters of the viscous layer. In order to estimate the displacement effect and to evaluate the importance of the shock-boundary layer interactions, a time-marching computation method is used in inverse mode to reconstitute the flow in the channel from static pressure plot on the blade.

In the paper, the principle and the limits of this method of analysis are presented, as well as comparisons between the calculation results and detailed measurements carried out within the channel. Furthermore, the purely experimental aspect is taken up : techniques used to adjust and control the flow, and measurement techniques.

1 - INTRODUCTION

Des progrès considérables dans les recherches de profils optimisés destinés aux roues de compresseurs axiaux ont été rendus possibles ces dernières années par le développement des méthodes de calcul.

Mais le recours à l'expérience reste indispensable pour vérifier le bien-fondé des différentes approches utilisées, surtout lorsque l'on souhaite représenter par le calcul le comportement du fluide visqueux.

Afin d'établir des comparaisons significatives entre les résultats des calculs et les mesures, les méthodes expérimentales se sont donc vues contraintes de fournir des informations de plus en plus détaillées et délicates à obtenir.

A la fin d'une campagne d'essais, on se trouve devant un volume parfois important de données, dont il convient en premier lieu de vérifier la cohérence globale. Ensuite tout traitement d'une partie de ces données permettant de réduire les mesures nécessaires sera le bienvenu, car il permettra de diminuer à la fois la durée et le coût des campagnes ultérieures.

Cet article présente une méthode permettant de reconstituer l'écoulement dans un canal inter-aubes d'une grille supersonique à partir du simple relevé de la pression statique sur l'extrados et l'intrados du profil. Des comparaisons sont faites entre le champ de pression reconstitué et le champ de pression réel, exploré grâce à une sonde à 5 trous miniature. On verra aussi comment il est possible d'estimer l'effet de déplacement de la couche visqueuse et d'évaluer l'importance de l'interaction choc-couche limite.

2 - ASPECTS EXPERIMENTAUX DU PROBLEME

2.1 - Revue des principales difficultés expérimentales

Dès que l'on souhaite obtenir des informations très détaillées sur l'écoulement dans une grille d'aubes, des difficultés expérimentales apparaissent. Le centre de ces difficultés est la petite taille des maquettes couramment utilisées.

La taille de la maquette est pratiquement imposée par la soufflerie disponible : la puissance de l'installation détermine les dimensions de la veine d'essai, compte tenu des conditions génératrices de l'écoulement à réaliser. On doit noter également qu'un nombre d'aubes minimal est indispensable pour assurer correctement la périodicité de la grille.

Les conséquences sont de deux ordres :

- difficulté d'instrumentation des profils ;

les aubes de compresseurs, surtout en tête de pale, sont les plus minces possibles. L'épaisseur maximale d'un profil de grille est de quelques millimètres, alors que l'épaisseur aux bords d'attaque et de fuite est inférieure au millimètre. Des techniques nouvelles, comme l'usinage par électro-érosion, ont permis d'améliorer la réalisation et l'instrumentation des profils de grille. Toutefois les régions de bord d'attaque et de fuite restent trop minces pour être équipées de façon satisfaisante en prises de pression statique ;

- difficulté de mesure dans les canaux inter-aubes ;

le canal inter-aubes est exigu, et d'accès malaisé. Il est apparu nécessaire, pour y faire des mesures, de développer une instrumentation toujours mieux adaptée : sonde 5 trous miniature, et système de déplacement dans le volume à explorer. De plus, dans une grille supersonique, certaines zones de l'écoulement sont transsoniques, et la sonde doit avoir une bonne réponse aux alentours de $M = 1$.

2.2 - Présentation de la grille et des conditions d'essais

La grille étudiée (fig. 1) est composée de 6 aubes ayant les caractéristiques suivantes :

. corde $C = 122,2$ mm

. épaisseurs : bord d'attaque   0,7 mm
                    bord de fuite   1,0 mm
                    maximale   3,6 mm

. encombrement axial $Cx = 72,5$ mm
. envergure $1 = 100,0$ mm
. angle d'adaptation (angle entre
  la normale au front de grille et
  la direction de l'écoulement)   60°

Le pas de la grille vaut 58 mm (pas relatif : 0,475).
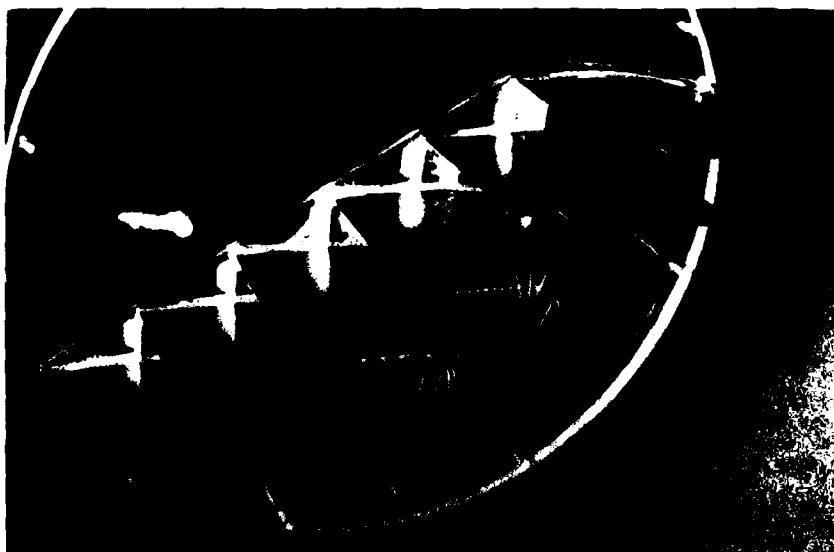
Fig. 1 - Vue de la grille.

Les essais ont eu lieu dans la soufflerie de grille plane de l'ONERA à Chalais-Meudon, décrite pour l'essentiel en [1]. Par rapport à cette référence, quelques modifications visant à améliorer la périodicité de l'écoulement et le contrôle des couches limites latérales ont été effectuées sur l'installation.

<u>Conditions d'essais</u> :

écoulement générateur : M_o = 1,5
$\quad\quad\quad\quad\quad\quad\quad\quad p_{io}$ = 80 000 Pa
$\quad\quad\quad\quad\quad\quad\quad\quad T_{io}$ = 300 K

Rapport de pression statique p_2/p_o = 2,04 pour l'essai détaillé présenté ici. Le taux de convergence amont-aval des nappes de courant est obtenu naturellement à partir du décollement des couches limites des parois latérales de la soufflerie. Ce décollement est contrôlé par un dispositif d'aspiration, et la mesure des sillages permet de s'assurer que le taux de convergence est constant sur une partie suffisante de l'envergure. Ici, le taux de convergence $\tau = \rho_1 V_1/\rho_2 V_2$ vaut 0,80 (indice 1 écoulement amont,
$\quad\quad\quad$ indice 2 écoulement aval moyen).

2.3 - <u>Mesures effectuées</u>

Pour cet essai, où le maximum d'informations était souhaité, les mesures suivantes ont été faites :

- mesures de la pression statique sur l'extrados et l'intrados des profils équipés (intrados : 20 prises, extrados : 19 prises), *pour plusieurs positions en envergure*, autour du plan médian de la veine ;

- mesure à la sonde miniature 5 trous $\emptyset$ 1,5 mm (fig. 2) ;

  . contrôle du nombre de Mach à l'amont de la grille,
  . mesure du sillage suivant l'envergure : contrôle de la périodicité et du taux de convergence,
  . mesure dans le canal (fig. 3) :
    7 axes d'exploration parallèles au front de grille,
    2 axes d'exploration inclinés de 30° par rapport au front de grille.

De plus, une visualisation par enduit visqueux sur l'extrados et l'intrados a été réalisée.
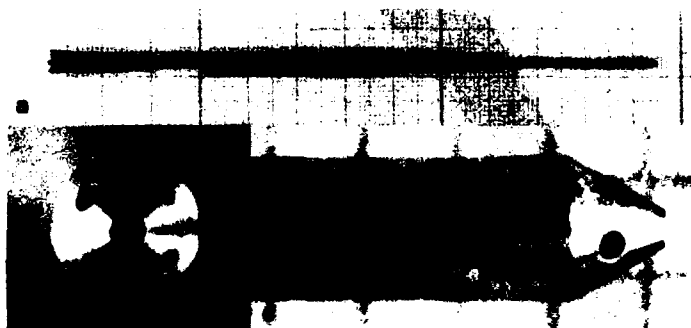
Fig. 2 – *Sonde 5 trous.*
  a) Vue générale
  b) Détail du nez, vue de face
  c) Détail du nez, vue latérale.

$Cx = 72,5\,mm$

	x/Cx		$z_h\,(mm)$
1	0,255	8	-17
2	0,410	9	-24
3	0,537		
4	0,604		
5	0,680		
6	0,795		
7	0,890		
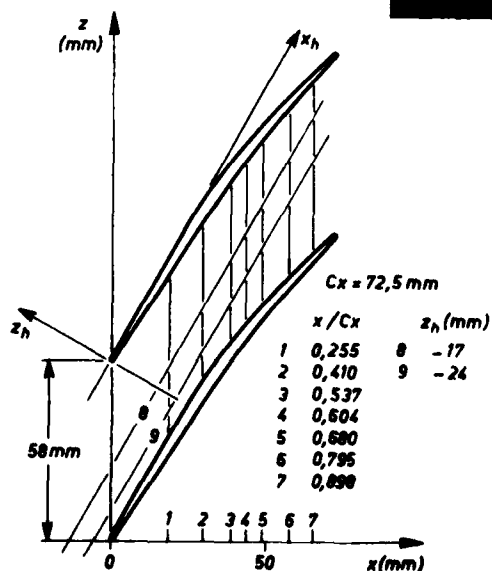
Fig. 3 – *Axes d'exploration (sonde 5 trous).*

3 - PRESENTATION DE LA METHODE UTILISEE

Le principe de base est le suivant : on connaît la répartition de la pression statique sur les parois d'un canal inter-aubes (extrados d'une aube, intrados de l'aube supérieure), et on impose cette répartition comme donnée d'un calcul de fluide parfait, ou, en d'autres termes, on cherche le canal qui, en fluide parfait, donnerait la répartition expérimentale de pression sur les parois.

Pour cela on utilise un programme de calcul résolvant les équations d'Euler par une méthode pseudo-instationnaire inverse [2] [3]. Au début du calcul, les frontières du maillage dans le canal (fig. 4a) sont naturellement l'extrados et l'intrados de l'aube, et la répartition $\uparrow(x/c_x)$ est imposée sur celles-ci (fig. 5).

Au cours du calcul le maillage se déforme (fig. 4b) et on admet, dans la version employée, que la pression se conserve sur des droites parallèles au front de grille, ou, autrement dit, on suppose que $\partial\uparrow/\partial\zeta = 0$ entre la frontière de départ (extrados ou intrados) et la frontière finale (simulant l'effet de déplacement des couches visqueuses). Cette approximation est valable quand le déplacement est relativement faible, ou quand le gradient $\partial\uparrow/\partial\sigma$ est faible (σ étant l'abscisse curviligne du profil ; un décollement isobare correspond à $\partial\uparrow/\partial\sigma = 0$, par exemple). Une meilleure approximation consisterait à supposer que c'est suivant la normale au profil que la pression statique se conserve. Ce point précis a d'ailleurs été développé dans les versions ultérieures du programme de calcul.

Ce schéma conserve évidemment le débit passant dans la grille et la différence entre les "parois" issues du calcul inverse et les parois réelles du canal représente l'épaisseur de déplacement dû aux couches visqueuses, décollées ou non. Par contre, la quantité de mouvement du fluide réel ne peut pas être restituée par le calcul inverse.

4a   **4b**
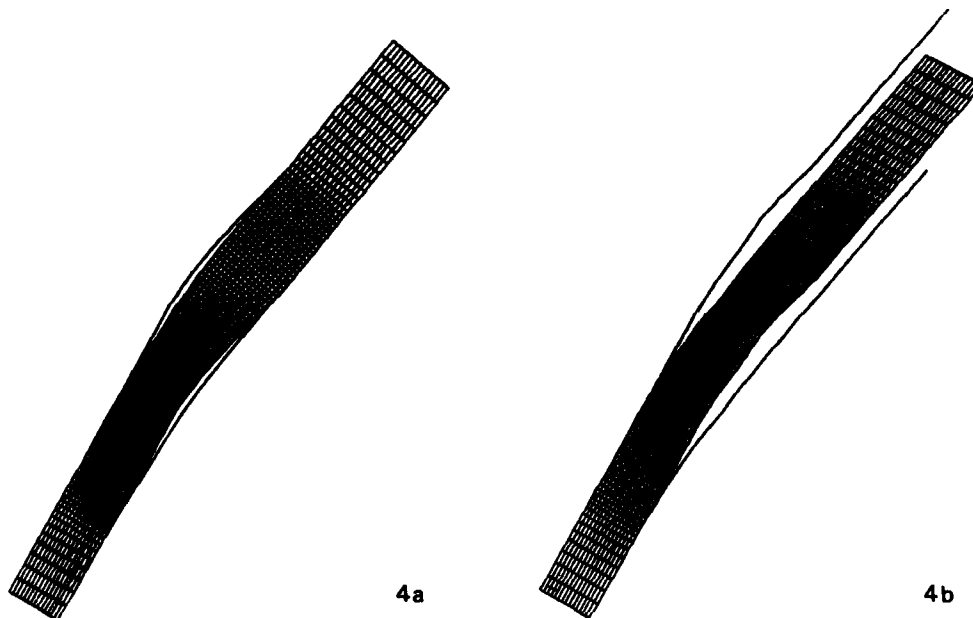
Fig. 4 — (a) Maillage initial
(b) Maillage final.
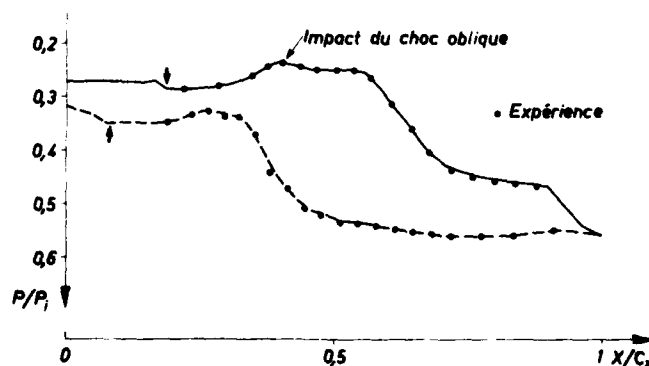
Fig. 5 — Répartition de pression sur l'aube.

Pour mener ce calcul au mieux, quelques aménagements se sont révélés nécessaires :

a) traitement au bord d'attaque ;

en réalité dans la grille il existe un choc de bord d'attaque, détaché et courbe. Il n'est pas possible de prendre en compte ce genre de choc dans le programme de calcul de canal en fluide parfait. Aussi on utilise l'artifice suivant : l'aube est légèrement allongée pour que le choc oblique obtenu de cette façon ait le même point d'impact sur l'extrados que le choc de bord d'attaque réel (fig. 6) ;

b) traitement au bord de fuite ;

dans la région du bord de fuite, la minceur du profil ne permet pas d'implanter de prises de pression statique. La répartition de pression à partir de la dernière prise jusqu'au bord de fuite, ainsi que le niveau de pression à l'aval de la grille sont extrapolés à partir des mesures de sillage proche.
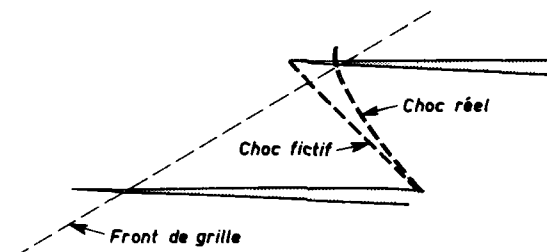
Fig. 6 — Traitement au bord d'attaque.

La donnée de la pression pour le calcul est représentée figure 5. On note sur cette figure les flèches indiquant les abscisses à partir desquelles la pression est effectivement imposée (avant ces points, la géométrie du canal est respectée) ;

c) Évolution de la convergence des nappes de courant à travers la grille ;

le taux de convergence $\tau = \rho_1 V_1 / \rho_2 V_2$ est obtenu par l'intégration aval sur un pas du débit passant dans la grille. Par contre son évolution dans le canal n'est pas mesurée : on est donc contraint d'introduire dans le calcul une loi arbitraire. Les expériences ont confirmé que la partie amont supersonique de l'écoulement est très sensiblement bidimensionnelle ($\tau = 1$) et que c'est donc à partir du choc que l'effet de convergence se fait sentir. D'autre part, les mesures de sillage indiquent que le taux de convergence n'évolue pratiquement pas selon l'axe x, à l'aval de la grille.

Plusieurs calculs ont été menés pour évaluer l'influence de ce paramètre : ils ont montré que l'allure générale du champ des isobares est assez peu modifiée.

4 - RESULTATS

4.1 - Reconstitution du champ de pression

Les figures 4a et 4b montrent l'évolution du maillage au cours du calcul.

Figure 4a : maillage de départ, et géométrie du profil.
Figure 4b : maillage après convergence du calcul.

La figure 7 représente le champ des isobares dans le canal interaubes. On peut constater aisément que le choc principal de recompression provoque le décollement de la couche limite avec la formation d'un λ aussi bien à l'extrados qu'à l'intrados ; ce λ est plus accentué à l'extrados où le nombre de Mach à l'amont du choc est plus élevé.

4.2 - Comparaison entre le calcul inverse et les sondages dans le canal

Il est possible, à partir des résultats du calcul, de tracer les évolutions de la pression statique sur les différents axes d'exploration de la sonde et de les comparer aux mesures expérimentales (fig. 8). Cette comparaison est tout à fait satisfaisante, sauf dans la partie amont du canal.

Dans cette région, le désaccord a probablement pour origine le traitement au bord d'attaque : le choc réel, perçu par la sonde engendre un écoulement différent de l'écoulement calculé où il y a un choc oblique de faible intensité.

Il faut aussi remarquer que le calcul inverse reflète les résultats d'un seul essai, tandis que chacune des explorations provient d'un autre essai. La reproductibilité de l'écoulement est généralement bien assurée, mais il peut arriver qu'une légère dérive des réglages (vannage, aspiration, tuyère...) induise des modifications minimes de l'écoulement.

Compte tenu de cette remarque, on voit (fig. 8c, d, e, h, i) que la position expérimentale du choc est bien restituée par le calcul, ainsi que certains détails de l'écoulement, telle la légère réaccélération après le choc (fig. 8d, i en particulier).
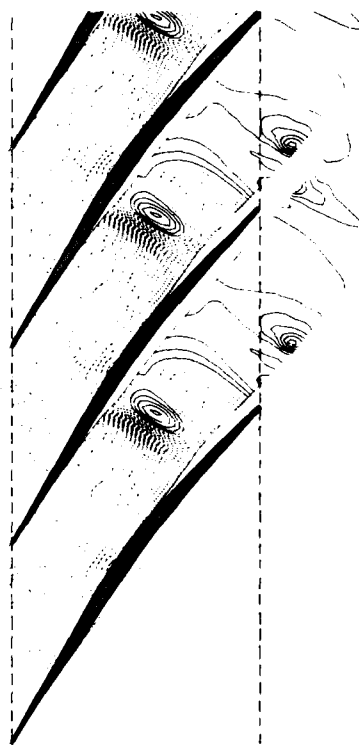
Fig. 7 — Reconstitution de l'écoulement (isobares).

D'autres comparaisons apparaissent sur les figures 9a et 9b. On y a reporté les mesures faites en x/c_x = 0,795 et 0,898, c'est-à-dire dans la partie aval du canal, près du bord de fuite. La chute de la pression d'arrêt P_{i1}/P_{i0} , associée à la stabilisation de la pression statique, indique clairement la présence de couches visqueuses dont l'épaisseur de déplacement δ^* est importante. Dans le calcul inverse, la différence entre le profil de l'aube et la frontière finale du maillage doit correspondre au δ^* . La détermination de δ^* à partir de l'expérience est imprécise à cause du nombre réduit de points de mesure dans la zone visqueuse, mais il est facile de constater que, qualitativement l'effet de déplacement est bien rendu par le calcul.

L'ensemble de ces résultats montre donc que la connaissance précise de la répartition expérimentale de pression sur les parois du canal permet de reconstituer très convenablement le champ des isobares dans le canal même. En outre, une estimation de l'épaisseur de déplacement peut être obtenue ; par contre pour évaluer les autres caractéristiques globales de la couche visqueuse, et par là remonter aux pertes, il faudrait faire appel à un calcul de couche limite en mode inverse (dont la donnée est δ^*). On obtiendrait alors une évolution de l'épaisseur de quantité de mouvement dépendant des conditions initiales qu'il faudrait ajuster pour assurer la compatibilité entre la répartition de pression expérimentale et la répartition de vitesse issue du calcul de couche limite.

4.3 - Cohérence globale des résultats

Le calcul inverse peut être considéré comme un mode de traitement de données de soufflerie. Ces données -pression statique sur des parois- sont plutôt fiables. Un bon accord entre les résultats du calcul et les mesures faites à la sonde prouve que l'ensemble des résultats est cohérent, et montre en particulier le bon fonctionnement de la sonde dans le domaine délicat des écoulements transsoniques. Ce dernier point est important car à l'aval de la grille, là ou il n'y a pas de recoupement possible, la mesure des sillages se fait aussi en écoulement transsonique.

5 - CONCLUSION

La simple connaissance de la répartition expérimentale de la pression statique sur un profil de grille plane de compresseur axial, associée à quelques mesures de sillage, a permis de reconstituer le champ de pression dans le canal inter-aubes. Pour cela on a utilisé une méthode inverse de calcul de fluide parfait : la pression imposée sur les frontières du domaine de calcul provoque le déplacement de ces dernières et donne une bonne estimation de l'effet de déplacement dû aux décollements des couches limites.

La comparaison entre les résultats du calcul inverse et des mesures fines dans le canal inter-aubes montre un accord satisfaisant compte tenu des aménagements nécessaires à la mise en oeuvre du calcul.

Enfin la cohérence globale des résultats obtenus dans ce cas où les couches limites sont d'épaisseur très importante est intéressante, car elle tend à justifier l'approximation fluide parfait-fluide visqueux pour le calcul de l'écoulement en grille d'aubes avec interaction choc-couche limite.

REFERENCES

[1] - G. MEAUZE
La soufflerie de grille plane supersonique de l'ONERA à Chalais-Meudon, ONERA TP 1409.

[2] - H. VIVIAND et J.P. VEUILLOT
Méthodes pseudo-instationnaires pour le calcul d'écoulements transsoniques, Publication ONERA
1978-4.

[3] - G. MEAUZE
Méthode de calcul aérodynamique inverse pseudo-instationnaire, la Recherche Aérospatiale
n° 1980-1.
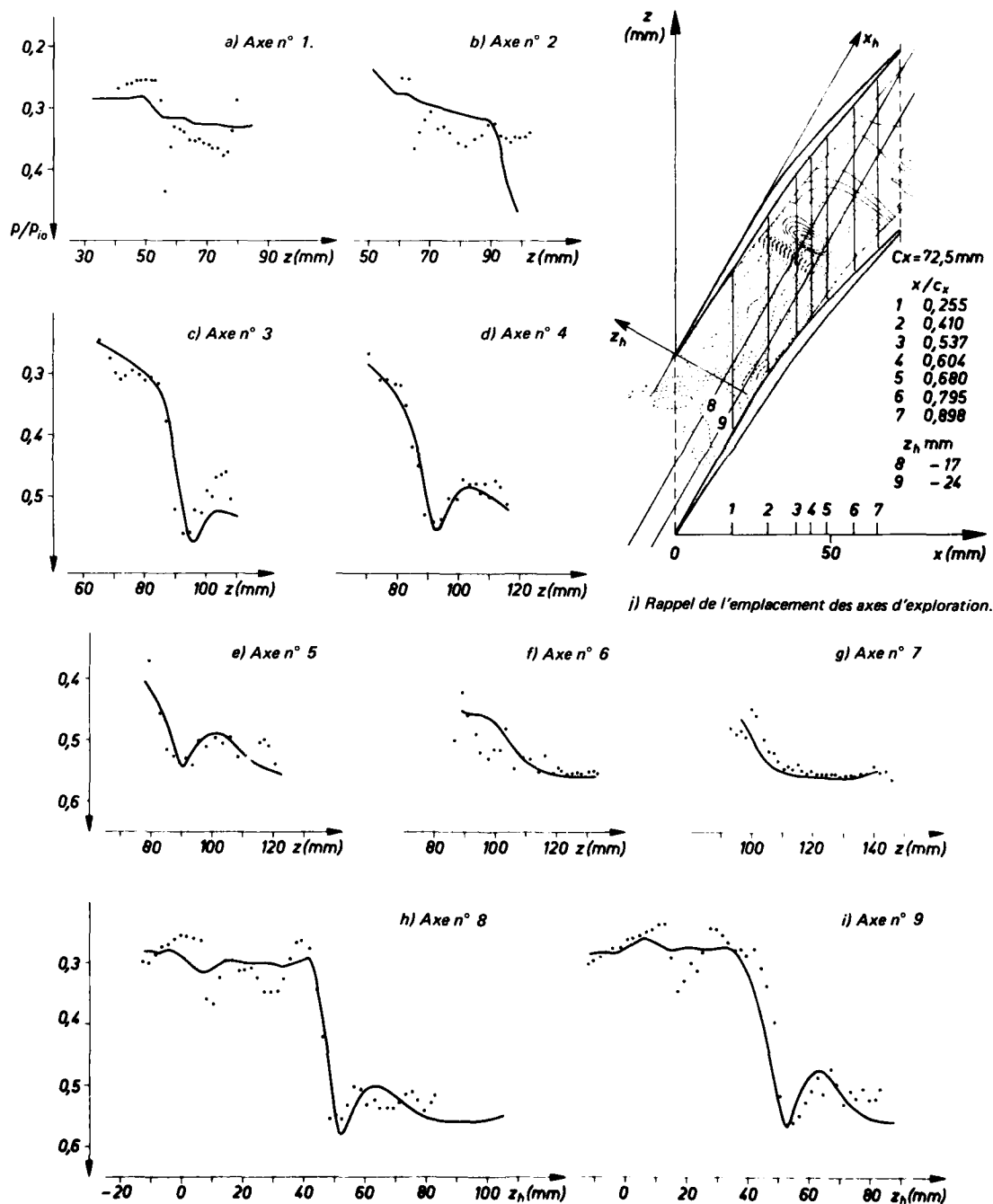
Fig. 8 — Comparaison calcul-expérience dans le canal.

a) $x/c_x = 0,795$

P_{i2}/P_{io}

P_2/P_{io}

• Mesures pression
statique paroi

b) $x/c_x = 0,898.$

P_{i2}/P_{io}

P_2/P_{io}

• Mesures pression
statique paroi
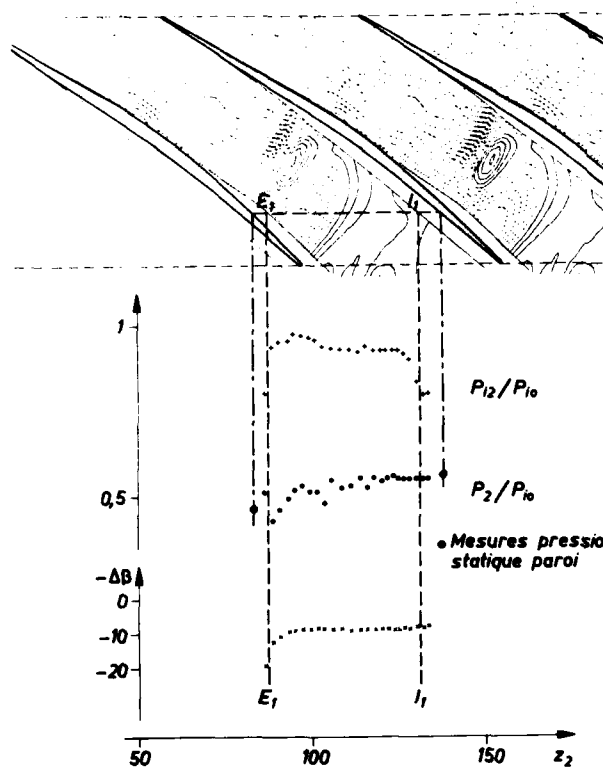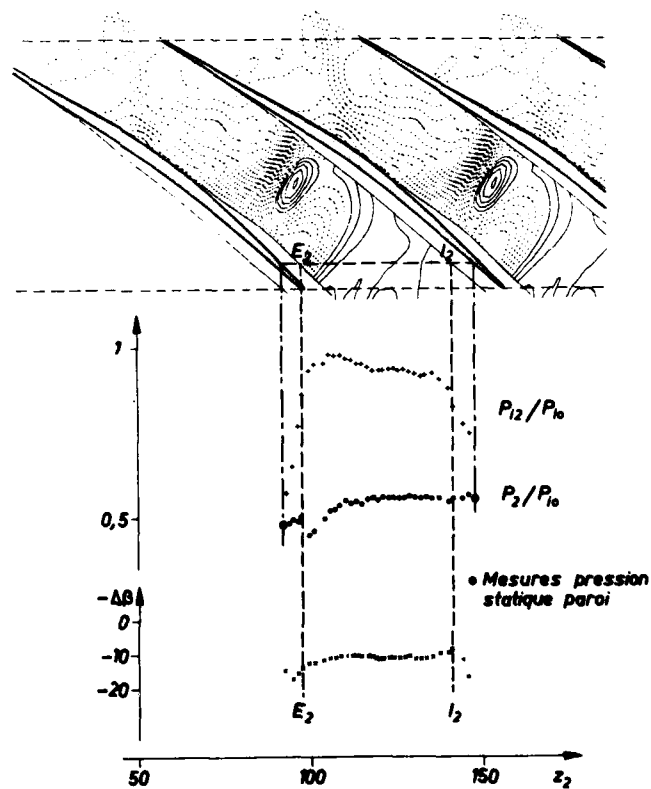
Fig. 9 — Effet de déplacement.

DISCUSSION

W.J.Calvert, UK

    (1) The separation of the boundary layer on the pressure surface is calculated to be the same as/or worse than the separation on the suction surface. Does this situation surprise you and do boundary layer calculations support it?

    (2) Was the condition show $(P_2/P_a = 2.04)$ the optimum operating condition for this cascade?

Réponse d'Auteur

    (1) Les résultats de ce calcul donnent une estimation du déplacement dû à la couche limite. Néanmoins, on ne peut pas prétendre obtenir la précision nécessaire pour effectuer correctement des calculs de couche limite en mode inverse, où la donnée serait cette estimation de l'épaisseur de déplacement.

    (2) Tout d'abord cette grille n'a pas été conçue pour être performante (D'ailleurs ses performances sont très modestes). Ensuite, le rapport de pression de 2,04 a été choisi pour distinguer sur l'extrados l'impact du choc oblique et l'impact du choc principal de recompression. Ce n'est pas le point "optimal" que l'on a obtenue pour une contrepression plus élevée.

C.H.Sieverding, Be

You should be congratulated for your effort in miniaturizing your five-hole probe. I wonder, however, whether in your particular application a three-hole probe would not have been more appropriate in view of the higher blockage effect of the five-hole probe. The angle in a plane normal to the blade surface will be anyway in error when the probe approaches the blade surface.

Réponse d'Auteur

Il est certain qu'une sonde trois-trous de même encombrement vertical que notre sonde à 5 trous donnerait un effet de blocage moindre. Néanmoins, dans de nombreuses régions explorées, les informations données par la sonde 5 trous étaient nécessaires, ou du moins utiles, et nous avons jugé préférable de faire l'ensemble des mesures avec la même sonde, étalonnée finement dans un domaine vaste de vitesse et d'angles.

D'autre part les problèmes liés à la proximité de la paroi auraient effectivement été les mêmes avec une sonde 3 trous qu'avec une sonde 5 trous.

COMPRESSOR AND TURBINE BLADE BOUNDARY LAYER SEPARATION

by

M. J. Werle
Manager, Gas Dynamics and Thermophysics
United Technologies Research Center
Silver Lane
East Hartford, CT 06108, U.S.A.

SUMMARY

Numerous sites on compressor and turbine blades are susceptible to the phenomenon of boundary layer separation. In such situations it is found that the boundary layer is incapable of negotiating a local adverse pressure gradient, which is subsequently relieved as it breaks away from the surface and induces a strong interaction with the inviscid stream. Since losses and heating due to such occurrences can be significant, a need continues to exist for efficient, and reliable prediction techniques for this class of problems. A review will be presented of the results of a multiyear, multiphase program aimed at developing and assessing finite difference techniques for a wide range of separation induced problems. Results will be given for leading edge bubbles, transonic shock induced separations, cove side bubbles, and trailing-edge induced wake bubbles. Both the analytical technique and collaborating experimental studies will be discussed and directions for future research identified.

INTRODUCTION

The overall problem area addressed here is that of small bubble boundary layer separation as it occurs on gas turbine compressor and turbine blades. These occur at numerous sites of local adverse pressure gradient and are generally unavoidable, undesirable, and unpredictable. Figure 1 presents a schematic of the principle potential blade separation sites - these being: (1) the leading edge overspeed region which often promotes premature boundary layer transition; (2) suction surface shock wave impingements that weaken the boundary layer's ability to overcome the trailing edge pressure rise; (3) the off-design cove region pressure rise that promotes separation and high reattachment heating on turbine blades; and (4) the blunt trailing edge induced wake recirculation that contributes to blade loss and turning deviation. These separations are unavoidable in the sense that other design needs take precedence (e.g., trailing edge bluntness for structural integrity), undesirable in the sense that they almost certainly lead to increases in loss and heating, and unpredictable in that, to date, no fully reliable and practical means has emerged to account for the extent and impact of such events. The problem of describing and predicting separation has, of course, been the subject of intense study by so many investigators that it is impossible to provide a complete historical perspective. Numerous conferences (Refs. 1 through 4, for example) have been focused entirely on this problem, and progress has definitely been made since Prandtl's initial interest in the area. Amid wide divergence of opinions and approaches, there does emerge a rather general picture which will be taken as the starting point for the present paper. It now appears that, for the small separation bubble regime of interest here, the physics can be represented by a multi-tiered interacting viscous layer approach. The principle ingredients of such an interaction theory involve a turning and separating bottom tier of flow represented by boundary layer like equations strongly disturbing the local inviscid flow structure through a displacement thickness surge which in turn communicates a mild disturbance to the global inviscid flow structure. Such an approach includes the asymptotic rational laminar and turbulent triple deck models (see Refs. 5 through 9, for example) as well as the reasonable (as distinguished from rational) interacting boundary layer models (see Refs. 10 through 16, for example). Within this framework, there are several remaining issues to be resolved: first, there remain strong questions about just what role normal pressure gradients play in the viscous region of separating turbulent boundary layers; second, it is not yet fully clear how flow detachment modifies the local turbulence model; third, a model has not yet emerged for satisfactorily representing and solving cases with transition in a separation bubble; fourth, the trailing edge separation bubble provides an anamolous situation, especially with respect to wake closure; and finally, there still remains a question as to the appropriateness of the displacement interaction concept for turbulent separated flows. Given the significant impact separated flow has on all aerodynamic configurations in general, and turbomachinery blade components in particular, the United Technologies Research Center launched a program four years ago with the goal to clarify these issues and provide reliable prediction techniques for the small separation bubble problem. A comprehensive combined analytical/experimental

program is underway to systematically address the five main issues presented above - using benchmark data sets to guide and assess advanced interacting viscous layer models and their solution techniques. Results to date of this study will be presented here, principally showing that (1) strong evidence exists that the interacting displacement concept can be generalized to a wide range of applications, including those where normal pressure gradients are significant, (2) transition in the shear layer can be accommodated straightforwardly, (3) trailing edge separation and wake closure provide an interesting flow structure that can be addressed by the present approach.

ANALYTICAL/EXPERIMENTAL APPROACH

The overall approach employed here focuses on the most prevalent aspect of all the separation bubble problems described above - that of their smallness. They appear to have the common structure of small chordwise lengths and width, thin viscous shear layers, turbulence, and relatively local (but additive) impact on the overall blade flow field. Thus, a basis is provided for comprehending all such elements within a local viscous interaction concept wherein the global inviscidly dominated flow over a blade element is locally perturbed by its interaction with a thin viscous layer. Within this structure, each such separation site can be addressed separately for its special features and a combined analytical/experimental program focused on refining the appropriate aspects of each model element.

Theoretical Model

Using this framework, the interaction process is thus taken as depicted in Figure 2 as containing an inviscid far-field that senses a small perturbation, an incoming thin viscous boundary layer that undergoes a strong interaction over a relatively short chord length, and a well behaved downstream classical viscous layer. Our interest here is in strong interaction regions in which the viscous flow influences the near field of the inviscid flow through rapid displacement thickness growth. Thus the approach falls quite naturally into a multi-scale (multi-layered?) configuration wherein a thin viscous layer interacts strongly with a local inviscid structure, which itself communicates weakly with the basic airfoil inviscid flow field.

The viscous region itself is taken to be represented by a thin layer generalization of the boundary layer equations to accommodate two critical aspects of the problem. First, a shear layer coordinate system as depicted in Figure 3 is introduced to relieve untenable constraints inherent to surface coordinates (see Ref. 10 for further discussion) and second, allowance is made for variations of the streamwise pressure gradient across the viscous layer as induced by the convective process. This latter issue is of fundamental importance to a wide class of flows, especially those involving transonic shock waves which penetrate deeply into a viscous layer as depicted in Figure 4 (see Ref. 3 for further discussion of this approach).

Within this framework, a very general representation of the viscous flow can be presented for the adiabatic case in terms of a turbulent version of the Levy-Lees dependent variables ξ, η (see Ref. 10) as

Continuity:

$$V_\eta + F + 2\xi F_\xi = 0 \tag{1}$$

Momentum:

$$(\ell F_\eta)_\eta - V F_\eta + \beta (\theta P - F^2) - 2\xi F F_\xi = 0 \tag{2}$$

Boundary Conditions:

$$F(\xi,0) = V(\xi,0) = 0 \tag{3a}$$

$$F \rightarrow F_i(\xi,\eta) \text{ as } \eta \rightarrow \infty \tag{3b}$$

where F and V are transformed versions of the longitudinal and normal velocities respectively, θ is the static enthalpy, ℓ is a kinematic and/or eddy viscosity function, and $F_i(\xi,\eta)$ is the inviscid longitudinal velocity component.* Here, β is the classical boundary layer pressure gradient parameter written as

$$\beta \equiv \frac{2\xi}{U_e} \frac{dU_e}{d\xi} \tag{4a}$$

___
*In Ref. 9, Davis introduced yet a simpler version of Eq. (2) that could have a significant impact on future developments in computational techniques for this problem.

and P is a function defined to account for inviscidly induced pressure gradients effects across the viscous layer. This is defined as

$$P \equiv \frac{\partial P_i(s,n)}{\partial s} \Big/ \frac{\partial P_i(s,0)}{\partial s} \qquad (4b)$$

The coordinates ξ and n are defined in terms of the longitudinal and normal shear layer distances of Figure 3 as

$$\xi \equiv \int_0^s \rho_e \mu_{e_T} U_e \, ds \qquad (5a)$$

$$n \equiv \frac{\tilde{R}_e^{1/2}}{s^{1/2}} \int_{-t}^n \frac{\rho}{\rho_e} \, dn \qquad (5b)$$

where $\tilde{R}_e$ is a running turbulent Reynolds number defined in terms of the relevant dimensional boundary layer edge values as

$$\tilde{R}_e \equiv \frac{\rho_e^* \, U_e^* \, L_{ref}^*}{\bar{\mu}_T^*} \qquad (5c)$$

with the relevant viscosity being a running average value defined as

$$\bar{\mu}_T^* \equiv \frac{\int_0^{s^*} \mu_T^* \, \rho_e^* \, U_e^* \, ds^*}{\rho_e^* \, U_e^* \, s^*} \qquad (5d)$$

and μ_T^* is a turbulent eddy viscosity level related to the edge value of the fluid viscosity as

$$\mu_T^* = (1 + e) \, \mu_e^* \qquad (5e)$$

and e is directly related to a well defined wake like eddy viscosity level (see Ref. 10 for detailed discussion). The use of this transformation is a turbulent generalization of the Blasius laminar flat plate variable that serves to virtually freeze *lateral growth* of the boundary layer. Its origin is embedded in similarity concepts and it comprehends Prandtl's coordinates for self similar turbulent wakes (see Ref. 17 for discussion).

Interaction effects are accounted for through the displacement thickness growth — here generalized to account for variations in the inviscid flow *structure in the overlap* region between the viscous layer and local perturbed inviscid field. Thus, as discussed in Refs. 14 and 15, the displacement thickness, δ^*, is defined as

$$\int_{\delta^*}^\infty \rho_i \mu_i \, dn = \int_0^\infty \rho_v \mu_v \, dn \qquad (6)$$

where the subscript i designates the inviscid flow above the displacement surface and the v subscript designates the viscous flow solution. The interacting inviscid flow is taken merely as that flowing past the original body plus the displacement thickness (i.e., the displacement body of Figures 2, 3 and 4).

Although, the principle focus of the current effort is the representation of strong interaction effects, these cannot be totally accounted for without proper addressing of weak interaction effects. Account can be made of such effects by merely modifying the base flow field within which strong interaction occurs. Thus (as discussed in Ref. 16) the general inviscid flow field representation can be written as a base flow plus a small local perturbation so that, for example, the local velocity may be written as

$$U_e = U_{e_b} + U_{e_\ell} \qquad (7)$$

where U_{eb} includes the basic inviscid flow up to a representative weak interaction level, while U_{el} includes local perturbation effect. Thus, for example, in subsonic closed bubble configurations Vatsa and Carter (Ref. 16) found that once a proper base flow with weak interaction effects was established, they were able to provide a very accurate representation of the perturbation field with a Cauchy integral representation. Extension of this concept for transonic or supersonic applications appears quite straightforward.

Results of application of the above analytical representation to several separation bubble flows is presented in the next section of this paper.

Experimental Study

The overall interaction model contains several elements that yet require guidance from definitive experimental studies. The most important of these is the displacement concept itself, which while seemingly complete and attractive from an analytical standpoint, yet requires extensive experimental verification and assessment across the range of controlling parameters relevant to turbomachinery application. To achieve this, the data base must include accurate measurement of the local velocity field and provide a high degree of profile resolution. These are of critical concern if the degree of importance of lateral variation of inviscid properties and the validity of the displacement concept are to be established. Additionally, concern must be given the proper representation of the transition and turbulence effects in separated regions - a area where the accuracy of measurement of the time variant aspects of the flow structure is of crucial concern. Finally, the issue of three dimensional contamination of two dimensional experiments is of fundamental importance due to its ability to completely neutralize the utility of benchmark data bases for assessment of state-of-the-art two dimensional analytical models.

In an attempt to address these issues, an experimental program has been established at UTRC aimed at providing (1) high resolution using large scale, (2) high accuracy and turbulence information through laser velocimeter techniques, and (3) representative two dimensionality through use of active endwall flow control. Detail results of several such experimental programs are presented below.

RESULTS

Both experimental and theoretical results have been obtained demonstrating a broad range of capabilities and applications. Four specific areas have been addressed; that of spearation at leading edges, transonic shock-wave roots, trailing edges, and the blade cove side.

Analytical Studies

The first case considered is that of leading edge separation. For this case the flow detaches from the surface in the leading edge over-speed/recompression region in a laminar state. The resulting free shear layer is unstable and undergoes rapid transition to a turbulent state - which, in turn, promotes a rapid reattachment to the surface in a region of adverse pressure gradient. Carter and Vatsa (Ref. 16) have applied their finite difference viscous interaction scheme to this problem and results of a comparison with the experimental data of Gaster (Ref. 18) are given in Figure 5. Here the pressure distribution is seen to be very accurately predicted when an instantaneous transition is triggered at s=1.0 with both the experimental separation and reattachment positions equally well predicted. These results clearly show that the interacting boundary layer approach is fully capable of representing this complicated flow phenomenon to within the limits of the transition model. Additional (see Ref. 16) numerical studies were performed to assess the sensitivity of the analytical model to the choice of transition site and length, with good evidence given to support use of an instantaneous transition model and leading to the conclusion that further research should now be focused on defining a basis for setting the transition site.

As a demonstration of the generality of this approach, solutions have also been obtained for transitional flow separation in a diffuser channel (Ref. 19). These results are presented in Figure 6, where the computed displacement thickness growth along the flat wall of an 8% diffuser wall for an inlet velocity of 40 ft/sec and an initial laminar boundary layer thickness of approximately 1/2 inch. The undisturbed inviscid flow was first determined using the procedure of Caspar et al (Ref. 20) with the inviscid/viscous perturbation solution obtained thereafter. For this case, the transition site was set at x=2.25 ft with the converged solution having separation at x=1.93 followed by rapid growth in δ^* up to transition where δ^* starts to diminish rapidly toward reattachment at x=2.35 ft. A family of numerical experiments were performed to ascertain the influence of the transition site location on the stability

and convergence properties of the technique. Whereas the flow structure, and in particular, the separation length was found to be extremely sensitive to the transition model, no hint of numerical instabilities were encountered. At this time an experimental program has been initiated to obtain a data base for assessing the accuracy of the results and for establishing a basis for predicting the transition site location.

For the case of transonic flow, the test case studied here was that of flow over a circular-arc bump placed on a flat plate in a $M_\infty = 0.875$ airstream. For this case, Bachalo and Johnson (Ref. 21) have provided the experimental data base using a large radius axisymmetric model to eliminate end effects. As shown in Fig. 7 separation was observed at x=0.65 just aft of the shock while reattachment occurred on the flat portion of the model at x=1.13. For this case solutions were obtained by Carter (Ref. 22) for the first order interacting viscous layer equations coupled to a transonic full potential technique. The sensitivity of their solutions to the details of the turbulence model is shown in Figure 7 where variations in the constant, δ, of the outer region turbulence model are seen to produce a significant influence on the pressure level in the separation region. Also shown in Figure 7 are the results of a second numerical study wherein the inviscid pressure level generated by the flow over the displacement surface was computed. The excellent comparison of these results with the experimentally measured pressures in Figure 7, clearly provide strong evidence that even in this complicated flow where the shockwave deeply penetrates the boundary layer (as depicted in Figure 4) the displacement-interaction concept is still valid. It is only necessary now to accommodate such effects in the viscous layer equations as outlined above and in Ref. 15.

For the case of trailing edge flows, one of the principle questions raised in the past 5 years concerns the applicability of the interacting thin viscous layer concept to the separation case. Chow and Melnik (Ref. 23), Brown and Stewartson (Ref. 24) and Stewartson (Ref. 25) and others have studied this flow and found well behaved interacting flow structure up to the case where zero shear friction (stall?) just appears at the trailing edge point. Unfortunately, numerical complications prevented "post-stall" studies and the postulate was put forward that perhaps this signaled the occurrence of a break-down of the applicability of the interaction structure. Smith (Ref. 26) has revisited this issue in an intense analytical and numerical study focused on clarification of this critically important issue. The vehicle employed was the laminar triple-deck theory, a formally rational asymptotic model contained within the interacting boundary layer equations. Smith's (Ref. 26) results give strong evidence that this approach is not limited by a "stall" singularity. Figure 8 shows the computed stream-lines for one such case wherein a family of separated trailing edge solutions were obtained starting with the symmetric case of Werle and Verdon (Ref. 29) and preceeding systematically to the unsymmetric case by collapsing the underside of the airfoil toward the upper half. The most notable feature of these solutions was the extremely abrupt streamline turning that accompanied wake closure at the trailing edge point. Smith gave strong numerical and analytical evidence to support this structure and provides insight as to why several pervious numerical studies have had difficulty passing the "trailing-edge stall" point. Most importantly, through this clarification, Smith has shown that the interacting boundary layer structure does not encounter a catastrophic termination at "stall" and thus its application to separated trailing edge flows violates no known fundamental theorems. Subsequently, Verdon and Vatsa (Ref. 27) have provided a compre-hensive analytical model for lifting trailing edge flows using interacting boundary layer concepts and have presented laminar solutions up to and including separation with wake curvature influences accounted for.

Separation of flow off relatively blunt trailing edge geometries is of concern to the turbomachinery community where structural considerations prevail and rounded trailing edge thicknesses on the order of the incoming boundary layer thickness are quite common. For this problem, a series of studies have been conducted by Werle, Verdon and Vatsa (Refs. 11, 27-29) aimed at developing and assessing a viable analyt-ical/numerical approach to this class of problems. For this case, the shear layer coordinate concept presented in Figure 3 plays a critical role as does the application of the turbulent version of the Levy-Lees coordinates discussed earlier. Using these and, where appropriate, a modified version of the turbulence model presented by Cebeci, et. al. (Ref. 30), a series of trailing edge geometries have been studied, the most severe of which is that of flow off a circular trailing edge with an inlet turbulent boundary layer as thick as the trailing edge. Comparisons of the analytical displace-ment surface predictions of Verdon and Vatsa (Ref. 27) with the recent data of Paterson (see Ref. 31) are given in Figure 9. Here the vertical scale has been greatly expanded for clarity causing a rather unavoidable distortion of the circular trailing edge geometry to a steep ellipse. These results clearly show the rather global effect caused by the dramatic necking-down of the displacement body as it fills in the void in the

near wake region aft of the body. Although the comparisons of Figure 9 are encouraging, it was found in Ref. 27 that the pressure distribution comparisons were not as good - displaying a hypersensitivity to subtle variations in the displacement surface shape. Research continues on improvement of the analytical technique with present attention being focused on enhancements to the turbulence model for such small separation bubbles.

A thrust has also been initiated to provide a fundamental analytical basis for representing the stall flow phenomenon. To this end, Smith (Ref. 26) has postulated a systematic process wherein the small bubble configuration could grow to the massive situation typical of stall (see Figure 10) as the angle of attack is increased. In Ref. 32, convincing evidence is presented by Smith concerning final closure of his inter-acting viscous layer concept introduced in Ref. 33. The isolated airfoil problem is approached as the infinite gap limit of the cascade flow structure of Figure 11 - the advantage being that the cascade provides a formally correct model at all finite cascade gap spacings. A critical element of this model is the discovery of the important role played by algebraically decaying boundary layer solutions in the recirculation/reinges-tion process. It is shown there that a complete model for the massive separation case can be formulated in terms of interacting viscous layers between large inviscid irrota-tional and rotational regions.

Experimental Studies

A large effort has been initiated to provide benchmark data sets for trailing edge flows typical of those encountered in turbomachinery applications. Here the major difference from external aerodynamic configurations is the degree of bluntness - with compressor and turbine environments both employing boundary layer to thickness ratio's of order one. Thus, information is needed for understanding and modeling flows in which separation occurs into a wake bubble where the ratio of the incoming boundary layer thickness to trailing edge thickness varies from approximately 0.5 (turbines) up to 2 or more (compressors) - a regime for which very little data is available. A program has been established at UTRC for a systematic study of this problem area with initial efforts focused on the flow off a circular trailing edge. Paterson (Refs. 31 and 34) presents the first such results employing the test configurations typified by that of Figure 12. Here a thick symmetric flat plate model was placed in a symmetric open jet wind tunnel to first produce a turbulent boundary layer trailing edge thickness to plate thickness ratio of 1.5, thus providing a large scale simulation wherein fine spatial resolution can be assured. The program has included detailed surface flow visualization, measurement of surface pressures, flowfield total and static pressure probing, extensive hot wire and laser velocimetry definition of mean and fluctuating velocity fields, and in the case of the turbine blade program (Ref. 34) surface heat transfer studies. Results are shown in Figures 13-15 for the case of symmetric flow with an incoming boundary layer thickness to the plate thickness ratio of 1.5 and a velocity of approximately 100 ft/sec. Paterson encountered large scale periodic unsteadiness in the near wake region due to unsymmetric vortex shedding at a Strouhal frequency of 0.18. This caused difficulty in measuring the centerline pressure level so that the wake levels shown in Figure 13 must be considered tentative at this time. This issue is discussed in more detail in Ref. 34 where studies were conducted in an effort to establish error bounds for such massively fluctuating flow fields - indicating levels of up to 10% error in the near wake regions. Nonetheless, a meaningful mean flow struc-ture was otherwise definable for assessment of the analytical models based on the time averaged governing equations. Of immediate interest in the pressure distribution of Figure 13 was the rather large region over which the trailing edge flow had significant impact. Not surprisingly, it was found that the upstream plate surface pressure began to depart significantly from its flat plate value 6-7 plate thickness's upstream whereas the downstream extent was approximately 2-3 plate thicknesses for an overall region of interest on the order of 10 plate thicknesses. The attendant displacement body shape was shown in Figure 9 to have undergone a rapid large reduction across the trailing edge region (approximately 60%) therein promoting the global disturbance to the surface pres-sure levels. The pressure is seen to drop monitonically along the surface up to the trailing edge circle juncture point, whereafter it starts to rise in anticipation of the trailing edge stagnation point. This adverse pressure environment precipitates quick separation at an azimuth angle of approximately 76° with a subsequent pressure plateau up to the trailing edge point. The pressure drops rapidly aft of the trailing edge to a minimum value at x/t=0.4 with a subsequent rise back to the freestream state. As indicated in Figure 14, the wake bubble itself is approximately one thickness long and on the order of 1/2 thickness wide with the total viscous layer undergoing some degree of deflection out to y/t of 1.0 for the entire region. The velocity profiles in the strong interaction separation region were found to display a subscale structure not

unlike that postulated in triple deck asymptotic theories for laminar separation. This structure is clearly seen in Figure 15 where the velocity profiles in the separation region of Figure 14 are presented on a common axis system. Note that the flow above the height of the original surface, undergoes very little change in the axial direction acting more like a rotational inviscid region, while the majority of the viscous induced profile alterations absorbed occur in the lower portion of the layer as flow entrainment serves to fill in the bottom of the layer. Such mean flow behavior gives considerable encouragement to analytical modeling thrusts. Additional studies of such trailing edge flows are continuing (Ref. 34) with emphasis on establising benchmark data bases for developing and assessing analytical techniques for representing the aerodynamics and heat transfer characteristics of such flows.

The second class of problems being addressed in the experimental program is that of surface separations as depicted in Figure 1, with programs focused on the leading edge, shock wave induced, and cove type separation bubbles currently underway at UTRC. Initial emphasis has been placed on cove type bubbles where the boundary layer is turbulent through the entire low speed interaction region. For this case the UTRC Boundary Layer Wind Tunnel previously used extensively for attached boundary layer studies (Refs. 35-36) has been configured to produce a two dimensional separation bubble on a flat surface (see Patrick and Paterson, Ref. 37 for details). Figure 16 presents a schematic of this closed circuit wind tunnel which has a test section approximately 9 feet long, 34 inches wide and 12 inches high. The flow is continuously filtered (to allow use of LV seeding), cooled (to maintain constant stagnation conditions) and its turbulence level controlled (using inlet screens and square-bar grids) for delivery to the test section. For the current study, a region of controlled diffusion followed by a region of acceleration was used to generate a closed separation bubble on the upper test plate - making extensive use of boundary layer bleed slots to keep the flow attached on the diffuser and side walls. Data acquired along the tunnel centerline plane provide an accurate benchmark data base for assessment of codes that solve the two dimensional time averaged governing equations. Extensive flow visualization (e.g., three dimensional tuft arrays and smoke) was employed to establish the level of centerline two dimensionality. Additionally, off centerline surface pressures and field values of transverse velocities were measured, both giving strong evidence that the measured field represented a benchmark two dimensional test case.

The resulting smoke streamline traces and attendant surface pressure levels are shown in Figure 17. Here it is seen that the separation bubble length is approximately 20 inches with a height of 3 inches. The impact of boundary layer bleed employed to maintain forward flow at the upper wall is evident, and it is anticipated that calculations will be performed using an outer streamline shape that enters the field at a height of 4 inches. Note that while a significant degree of turbulence was observed in these tests, none the less, clearly discernable time averaged streamlines where quite distinctive and well defined. The only exception to this was near reattachment, where as indicated by the dashed lines near the 40 inch station, the exact flow structure was difficult to define. The surface pressure distribution under the separation bubble is also given in Figure 17 (see Ref. 37 for other flow quantities) where it is seen that a distinctive plateau occurs over the entire length of the bubble, with the expected rise in pressure through reattachment before the flow accelerates to its downstream state. These pressure measurements in addition to their companion mean and fluctuating velocity fields are now being employed for assessing analytical models of separation phenomenon.

CONDLUDING REMARKS

The overall problem being addressed is that of separated flow in an effort to better understand the fundamental mechanisms controlling this phenomenon and ultimately improve the design analysis of turbomachinery components. To this end a combined analytical and experimental program has been conducted to extend and refine the interacting boundary layer concept for use in a wide class of blade type separated flows. From these results it was concluded that virtually all such effects as mid-bubble transition, shock wave penetration, trailing edge separation, and blunt base effects can be comprehended within such an analytical framework. Initiation of a program to establish benchmark experimental data bases for guiding and assessing such modeling has begun and will play a major role in the next critical phase of effort.

REFERENCES

1. "Viscous Interaction Phenomena in Supersonic and Hypersonic Flow", Symposium held at Aerospace Research Laboratories, Wright Patterson Air Force Base, Ohio, University of Dayton Press, Dayton, Ohio, 1970.

2. "Flow Separation", AGARD Conference Proceeding, CP-168, May 1975.

3. "AGARD Conference on Computation of Viscous-Inviscid Interactions", AGARD Conference Proceedings, CP-291, October 1980.

4. "Symposium and Physical Aspects of Aerodynamic Flows", California State University, Long Beach California, 19-21 January, 1981, Springer-Verlag, 1982.

5. Brown, S. N. and Stewartson, K., "Laminar Separation", <u>Annual Review of Fluid Mechanics</u>, Vol. 1, pp. 45-72, 1969.

6. Stewartson, K., "Some Recent Studies in Triple Deck Theory", appearing in <u>Numerical and Physical Aspects of Aerodynamic Flows</u>, pp. 129-144, Springer-Verlag, New York, 1982.

7. Smith, F. T., "Laminar Flow Over a Small Hump on a Flat Plate" <u>Journal of Fluid Mechanics</u>", Vol. 57, pp. 803-824, 1973.

8. Napolitano, M., Werle, M. J., and Davis R. T., "A Numerical Technique for the Triple-Deck Problem", <u>AIAA Journal</u>, Vol. 17, pp. 699-705, July 1979.

9. Davis, R. T., and Werle, M. J., "Progress on Interacting Boundary-Layer Computation at High Reynolds Number", appearing in <u>Numerical and Physical Aspects of Aerodynamic Flows</u>, pp. 187-210, Springer-Verlag, New York, 1982.

10. Vatsa, V. N., Werle, M. J., and Verdon, J. M., "Viscid/Inviscid Interaction at Laminar and Turbulent Symmetric Trailing Edges", AIAA Paper 82-0165, January 1982, Orlando Florida.

11. Vatsa, V. N., and Verdon, J. M., "Viscous/Inviscid Interaction Analysis of Asymmetric Trailing Edge Flows", presented at Second Symposium Numerical and Physical Aspects of Aerodynamic Flows, California State University, Long Beach, CA, 17-20, January 1983.

12. Melnik, R. E., Chow, R., and Mead, H. R., "Theory of Viscous Transonic Flow Over Airfoils at High Reynolds Number", AIAA Paper 77-680, June 1977.

13. Carter, J. E., "Viscous-Inviscid Interaction Analysis of Transonic Turbulent Separated Flow", AIAA Paper 81-1241, June 1981.

14. LeBalleur, J. C., "Strong Matching Method for Computing Transonic Viscous Flows Including Wakes and Separations" La Recherche Aerospaticle, No. 1981-3, 1981.

15. Carter, J. E., and Vatsa, V. N., "Analysis of Separated Boundary Layer Flows", presented at the Eighth International Conference on Numerical Methods in Fluid Dynamics, Aachen, Germany, June 28-July 2, 1982.

16. Vatsa, V. N., and Carter J. E., "Analysis of Airfoil Leading Edge Separation Bubble", AIAA Paper 83-0300, January 1982.

17. Schlichting, H., <u>Boundary Layer Theory</u>, McGraw Hill, New York, 1962.

18. Gaster, M., "The Structure and Behavior of Laminar Separation Bubbles", AGARD Conference Proceeding 4, pp. 819-854, 1966.

19. Vatsa, V. N., and Carter, J. E., "Transitional Separation and Reattachment in a Diffuser Duct", private communication, September 1982.

20. Caspar, J. R., Hobbs, D. E., and Davis, R. L., "Calculation of Two-Dimensional Potential Cascade Flow Using Finite Area Methods", <u>AIAA Journal</u>, Vol. 18, pp. 103-109, January 1980.

21. Bachelo, W. D., and Johnson, D. A., "An Investigation of Transonic Turbulent Boundary Separation Generated on an Axisymmetric Flow Model", AIAA Paper 79-1479, July 1979.

22. Carter, J. E., "Viscous-Inviscid Interaction Analysis of Transonic Turbulent Separated Flow", AIAA Paper 81-1241, presented at the 14th Fluid and Plasma Dynamics Conference, Palo alto, CA, June 23-25, 1981.

23.   Chow, R., and Melnik, R. E., "Numerical Solution of the Triple Deck Equation for Laminar Trailing-Edge Stall", Proceedings of the 5th International Conference on Numerical Methods in Fluid Dynamics", Lecture Notes in Physics #59 Springer, 1976, pp. 135-144.

24.   Brown, S. N., and Stewartson, K., "Trailing-Edge Stall", J. Fluid Mechanics, Vol. 42, Part 3, pp. 561-584, 1970.

25.   Stewartson, K., "D'Alembert's Paradox", SIAM Review, Vol. 23, pp. 308-340, 1981.

26.   Smith, F. T., "Interacting Flow Theory and Trailing Edge Separation-Stall", United Technologies Research Center Report UTRC82-13, Silver Lane, East Hartford, CT, May 1982.

27.   Verdon, J. M., and Vatsa, V. N., "Viscous/Inviscid Interaction Analysis of Thin-airfoil Trailing-Edge Flows", United Technologies Research Center Report R82-915793-4, December 1982.

28.   Vatsa, V. N., Werle, M. J., and Verdon, J. M., "Analysis of Laminar and Turbulent Symmetric Blunt Trailing-Edge Flows", United Technologies Research Center Report R81-914865-5, April 1981.

29.   Werle, M. J., and Verdon, J. M., "Viscid/Inviscid Interaction Analysis for Symmetric Trailing Edges", United Technologies Research Center Report R79-914493-5, January 1980.

30.   Cebeci, T., Thiele, F., Williams, P. G., and Stewartson, K., "On the Calculation of Symmetric Wakes -1, Two Dimensional Flow", Numerical Heat Transfer, Vol. 2, pp. 35-60, 1979.

31.   Paterson, R. W., and Weigold, H. D., "Experimental Investigation of a Simulated Compressor Airfoil Trailing Edge Flowfields", Pratt & Whitney Aircraft Group Government Products Division Report FR-15859, West Palm Beach Florida, October 1982.

32.   Smith, F. T., "Large-Scale Separation and Wake Closure/Reattachment - The Cascade Problem", United Technologies Research Center Report UTRC82-15, April 1983.

33.   Smith, F. T., "Laminar Flow of an Incompressible Fluid Streaming Past a Bluff Body, the Separation, Reattachment, Eddy Properties and Drag", Journal of Fluid Mechanics, Vol. 92, Part 1, pp. 171-205, 1979.

34.   Paterson, R. W., and Blair, M. F., "Benchmark Experimental on a Simulated Turbine Blade Trailing Edge Flowfield", United Technologies Research Center Report in preparation.

35.   Blair, M. F., and Werle, M. J., "The Influence of Freestream Turbulated Boundary Layer", United Technologies Research Center Report R80-914388-12, September 1980.

36.   Blair, M. F., and Edwards, D. E., "The Effects of Free-Stream Turbulence on the Turbulence Structure and Heat Transfer in Zero Pressure Gradient Boundary-Layers", United Technologies Research Center Report R82-915634-2, November 1982.

37.   Patrick, W. P., and Paterson, R. W., "Benchmark Experiments on Low Speed Turbulent Boundary Layer Separation and Reattachment", United Technologies Research Center Report, Contractor's Report to NASA, in preparation.

ACKNOWLEDGEMENTS

Figure 1 Blade Separation Sites
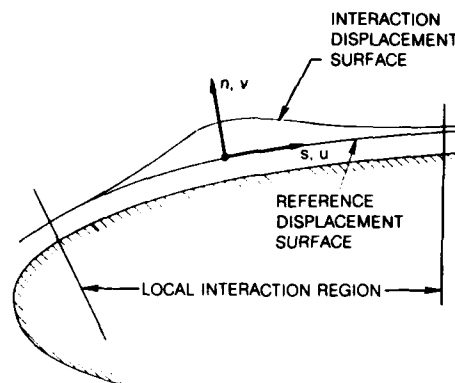
Figure 2 Localized Interaction Region Model
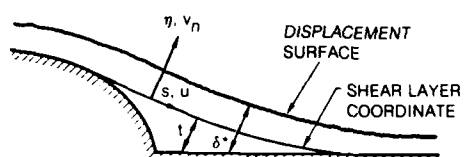
Figure 3 Shear Layer Coordinate System
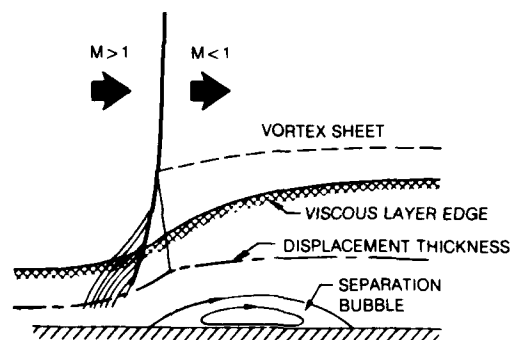
Figure 4 Transonic/Shock-Wave/Boundary Layer Interaction Model
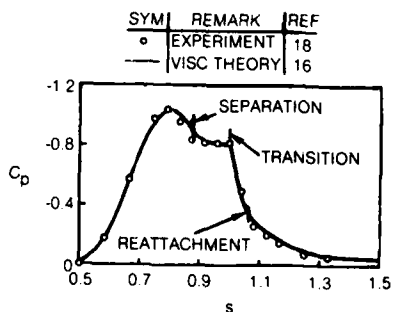
Figure 5 Transitional Separation
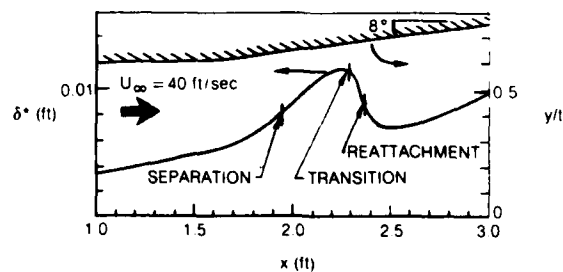
Figure 6 Channel Flow Transitional Separation Bubble

SYM	REMARK	REF
o	EXP. DATA	21
——	IBL, $\delta = 0.0034$	22
----	IBL, $\delta = 0.0158$	22
••••	INV. DISP. PRES.	22
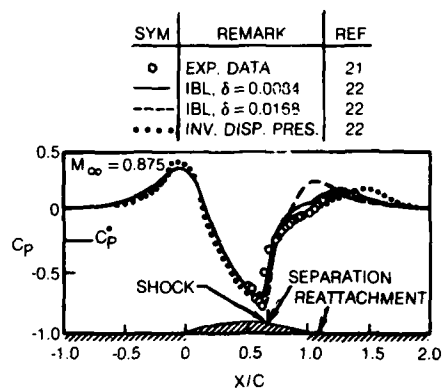
Figure 7 SWBL Interaction Surface Pressure
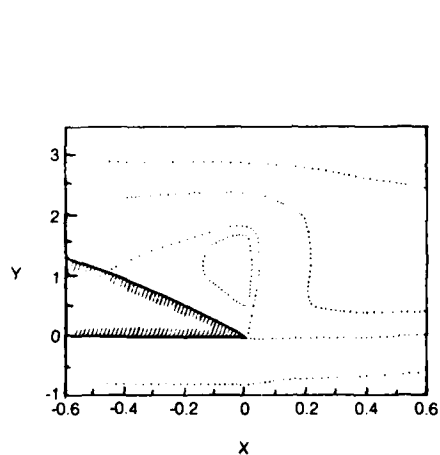
Figure 8 Triple-Deck Trailing Edge Separation Predictions

SYM	REWARD	REF
o	EXPERIMENT	31
——	THEORY	27
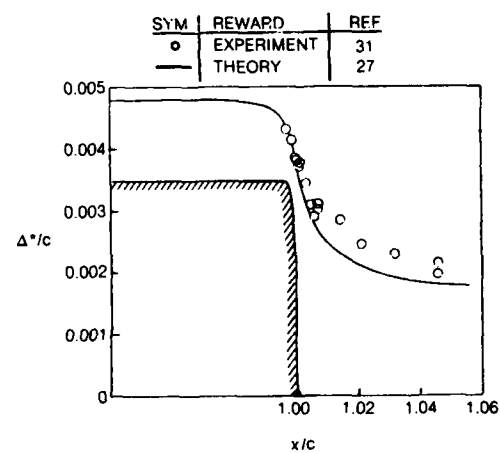
Figure 9 Blunt Trailing Edge Displacement Distribution
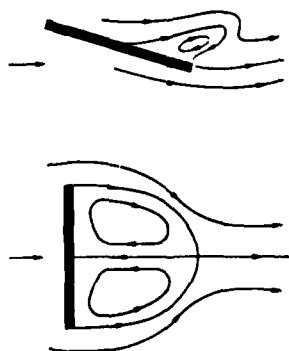
Figure 10 Near-Wake Flow Structure Evolution
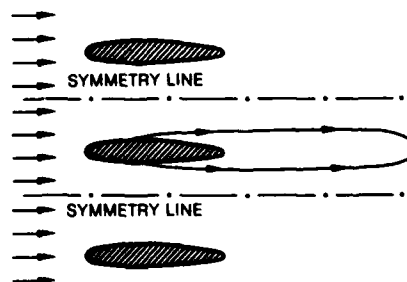
Figure 11 Stall Flow Structure
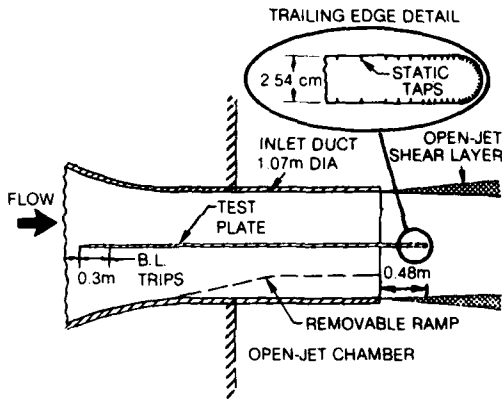
Figure 12 Blunt Trailing Edge Experimental Set-up
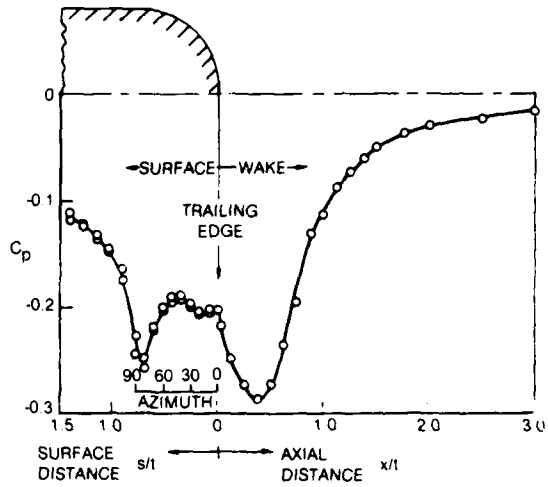
Figure 13 Blunt Trailing Edge Pressure Distributions
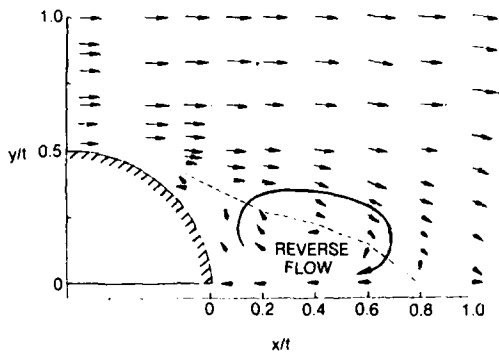
Figure 14 Blunt Trailing Edge Velocity Vectors
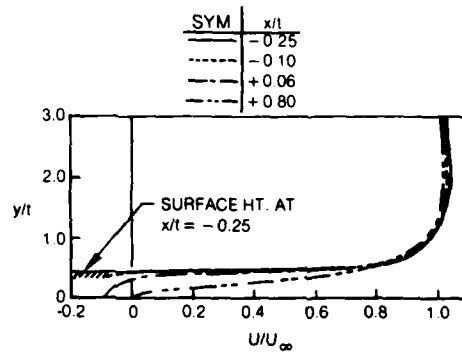
Figure 15 Blunt Trailing Edge Near Wake Velocity Profiles
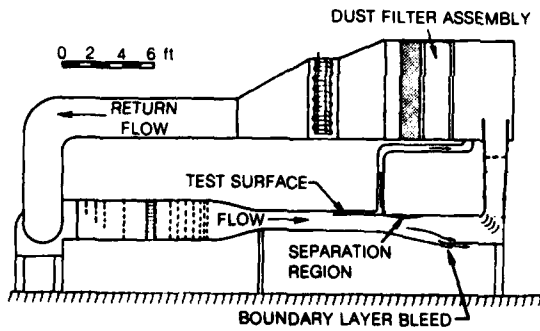
Figure 16 Surface Separation Experimental Set-up
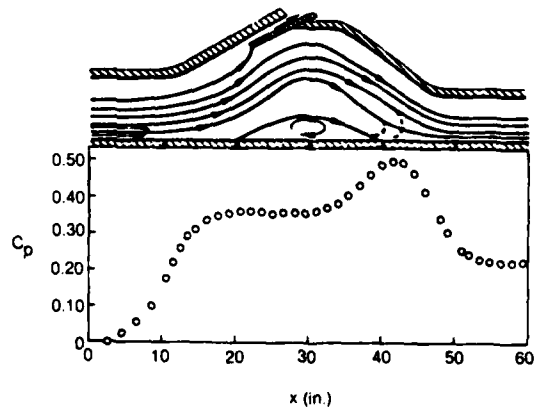
Figure 17 Surface Separation Pressure and Streamlines

DISCUSSION

K.Papailiou, Gr
(1) Are you using as S-direction the real flow direction or the inviscid flow one?

(2) Is the normal static pressure distribution of the inviscid flow different from the viscous one in other than the turbulent normal fluctuation terms?

(3) What is the importance of the curvature terms in the equations?

Author's Reply
(1) The S-direction used in these coordinates attempts to align as closely as possible with the true (vs inviscid) flow direction.

(2) The normal pressure variation identified in this work is that due to convective terms – not the turbulent normal fluctuation terms.

(3) For the high Reynolds numbers of interest in turbomachinery, the curvature effects do not appear to be significant.

THE DEVELOPMENT OF UNSTEADY BOUNDARY LAYERS ON THE ROTOR OF AN AXIAL-FLOW TURBINE

H.P. Hodson
Whittle Laboratory
Department of Engineering
University of Cambridge, U.K.

SUMMARY

The aerodynamic efficiency of an axial-flow turbine is significantly less than that predicted by measurements made on equivalent cascades which operate with steady inflow. This difference is strongly dependent upon the rotor-stator axial spacing. An experimental investigation has therefore been conducted into the effects of rotor-stator interactions upon the efficiency of a large scale, low speed turbine. A comparison is made between the performance of the mid-span section of the rotor blades and of a rectilinear cascade of identical geometry. Both wind tunnels were operated at a Reynolds number of 3.15 x 10^5

This paper presents measurements of the blade surface boundary layers and their associated profile losses. The profile loss of the turbine rotor at mid-span was approximately 50 percent higher than that of the rectilinear cascade. The mean velocity profiles of the boundary layers indicate that this difference is mainly due to the higher growth rate of the suction surface boundary layer on the turbine rotor. The time-resolved boundary layer measurements indicate that the increased growth rate is caused by the interaction of the wakes of the upstream nozzle row with the blade surface boundary layers. This results in a localized transition of the otherwise laminar boundary layers. The boundary layers thus alternate between characteristically laminar and turbulent states during one wake passing cycle.

NOMENCLATURE

A	Calibration constant	ω	Frequency
C	Chord	$\bar{\omega}$	Reduced frequency parameter
E	Voltage	Δ	Amplitude of
H	Shape factor		
h	Enthalpy	**Subscripts**	
k	Calibration constant	0	Stagnation
n	Calibration constant	1	Inlet
p	Static pressure	2	Exit
p_0	Stagnation pressure	∞	Free stream
r	Radius	m	Mean
Re	Reynolds Number	ps	Pressure surface
rms	Root-mean-square	s	Stator
s	Surface distance	ss	Suction surface
t	Time	turb	Turbulent
u,U	Velocity	x	Axial
U_m	Mean blade velocity	y	Tangential
x	Axial distance	**Superscripts**	
y	Tangential distance, distance from surface	$^-$	Mean
Y_c	Profile loss coefficient	$\sim$	Phase locked average
δ_{99}	99% boundary layer thickness	$'$	Random component
δ^*	Boundary layer displacement thickness	$*$	Isentropic
θ	Boundary layer momentum thickness, angle		

INTRODUCTION

It is well known that rotor-stator interactions result in a loss of aerodynamic efficiency in axial flow turbines. One of the first studies of this was carried out by Lopatitskii et al [1]. They found that, depending upon the blade geometry and Reynolds number, the rotor profile loss in a single-stage machine was between two and four times greater than that for the same cascade operating with steady inlet conditions. They also showed that the increased profile loss was largely responsible for the "lost" efficiency. Kirillov et al [2] found that the most important parameter in determining the profile loss was the ratio of the maximum velocity deficit in the wake to the convection speed of the wake. The results of references [1], [2] and [3] show that the increase in profile loss was greatest for the low Reynolds Number, high reaction designs.

Because the loss of efficiency is mainly caused by an increase in the rotor profile loss, this paper is concerned with the development of rotor blade surface boundary layers. The ideas presented are essentially two-dimensional, but it is acknowledged that secondary flow and tip leakage effects will contribute to the loss of efficiency.

The development of a boundary layer under the influence of an unsteady outer stream was first analysed by Lighthill [4], who considered the response of a two dimensional laminar boundary layer to a purely time dependent oscillation of low amplitude in the free stream. Hill and Stenning [5] found by experiment that a laminar boundary layer, of the type analysed by Lighthill, behaves linearly even for quite large amplitudes of the free stream oscillations. Karlsson [6] showed that the same was true for turbulent boundary layers. Patel considered the influence of a convected disturbance on laminar[7] and turbulent [8] boundary layers. Again, the change in mean values, when compared with those for a steady outer stream, showed no change. Despard and Miller [9], however, found that the mean separation point will move upstream of the steady state position as a result of unsteadiness in the outer flow. Therefore, where separation does exist, the unsteadiness may result in either a more severe gross separation as in reference [10] or, should reattachment occur, a greater length of the blade surface being covered by a turbulent boundary layer [11]. This does not, of course, explain the results of many investigators.

The linear behaviour of conventional, unsteady, laminar and turbulent layers suggests that the mechanism for the increased loss lies elsewhere. Obremski and Fejer [12] found that the transition Reynolds number for a boundary layer subject to an oscillating outer stream was dependent upon an unsteady Reynolds number which was based upon the amplitude and frequency of the oscillation. Obremski and Morkovin [13] provide a quasi-steady stability model in an attempt to expalin the results of reference [12]. Walker [14] found that the transition occurred on the stator blade of an axial flow compressor, much earlier than he would have expected. The transition was unsteady, and was coupled to the passage of the rotor wakes over the blade surface. Walker presented a stability model, based upon that of reference [13], to explain his observations. In doing so, he assumed that the dominant factor in the process was the fluctuations of the mean velocity.

It is well known that free-stream turbulence reduces the Reynolds number for transition. Presumably with this in mind, Pfeil et al [15] rotated a cascade of cylindrical bars in front of a flat plate boundary layer, thus simulating the effect of rotor wakes upon stator blade boundary layers. They found that the Reynolds number for transition was much lower than that predicted by the measurements of reference [12]. The transition was unsteady, the boundary layer being turbulent in the vicinity of the wakes and laminar between them. The authors of reference [15] conclude that the stochastic fluctuations within the wake are probably the cause of the differences between their own observations and those of reference [12].

Evans [16], like Walker [14], found that the stator blade boundary layer of an axial flow compressor oscillated between a characteristically laminar and turbulent condition in sympathy with the passing of the rotor wakes. Larguier et al [17] used surface mounted thermal anemometers to demonstrate the existence of unsteady transition of the type found by Evans [16] and Dring et al [18] have reported similar results for the rotor of an axial flow turbine. Unfortunately, none of these publications make a comparison with measurements made on the same cascade operating with steady inflow, so the magnitude of the effect of the unsteady transition process is unknown.

EXPERIMENTAL FACILITIES

Two of the wind tunnels at the Whittle Laboratory of Cambridge University were used for the experiments in this paper. The first is a low speed, single-stage axial-flow turbine. The results from this will be compared with those from a linear cascade wind tunnel with a blade geometry identical to that of the mid-span of the turbine rotor.

The scale of both wind tunnels makes them particularly suitable for making detailed flow measurements, including boundary layer traverses. The flow is incompressible and both wind tunnels were operated at a Reynolds number of 3.15×10^5 (based upon rotor mid-span exit conditions).

Linear Cascade

The steady state operation of the rotor mid-span was determined using a linear cascade of identical geometry. The cascade is shown in Figure 1. The seven blades have an aspect ratio of 3.0 and the centre blade was provided with static pressure tappings at its mid-span.

A traverse mechanism was fitted with a 3-hole cobra probe at one half of an axial chord downstream of the exit plane of the cascade. The inlet total pressure was measured using a conventional pitot tube.

The turbulence level at inlet to the cascade was 0.5 percent.

Single Stage Axial Flow Turbine

The Cambridge No. 2 rotating cascade wind tunnel (see Figure 2), in the configuration of a single stage turbine, was first investigated by Hunter [19] who reported on the secondary flow in the turbine as well as establishing the operating point. In a subsequent investigation, Denton and Usui [20] used a tracer gas technique in the turbine to determine the directions of fluid migration both at the mid-span and near the end walls.

The turbine was designed to be a free-vortex machine with zero swirl at the exit. Although a 50 percent reaction design of this type is conservative, the uniform and axial velocity at inlet to the stage [19] requires that the pressure gradients satisfy the

conditions of radial equilibrium with no curvature in the meridional plane. References [19] and [20] have shown this to be the case.

The stage consists of 36 stator blades followed by 51 rotor blades, with aspect ratios of 1.5 and 2.0 respectively. The hub/tip ratio is 0.7. The thickness distributions of the blades are given in reference [21]. They are fitted to parabolic camber lines with maximum thicknesses at 40 percent chord. The measurements described in this paper were all performed at the design condition of zero exit swirl. Further information can be found in Table I.

The importance of the reduced frequency parameter $\bar{\omega}$ is well known in connection with the development of unsteady boundary layers (see, for example, references [4] - [9]). In the case of axial-flow turbomachines, it is useful to define an "average" reduced frequency parameter

$$\bar{\omega} = \frac{\omega C_x}{U_x} \qquad (1)$$

which, on substitution of the appropriate values for the Cambridge Turbine (see Table I), is equal to 8.9 at the passing frequency of the stator blades. The flow over the turbine rotor blades is, therefore, unsteady in the true sense (i.e. $\bar{\omega} \gg 1$) at a reduced frequency which is typical of those found in modern axial turbines.

Fast Response Instrumentation

The blade-surface boundary layers of both the linear cascade and the turbine rotor were traversed with a hot-wire anemometer. DISA 55P15 boundary layer probes were used to make the measurements.

The hot wires were calibrated in a low turbulence wind tunnel. A least-squares-error criterion was used to decide upon the best fit for the general form of King's law

$$E^2 - A^2 = ku^n \qquad (2)$$

through the calibration points.

When a heated element is positioned close to a solid surface, an increase in heat transfer occurs. Equation (2) should therefore be modified when traversing boundary layers. In view of its simplicity, the "still air" correction technique of Cox [22] was employed. This involved the measurement of the heat transfer from the wire to the blade-surface in still air at the various locations encountered in the experiment. Equation (2) was then altered to give

$$E^2 - A^2 - [E_0^2(y) - E_0^2(\infty)] = ku^n \qquad (3)$$

where the constants A, k and n have the same values as in equation (2) and the term in the square brackets represents the increased heat transfer.

The rotor-relative stagnation pressure loss was measured using a fast response pitot supplied by Gaeltec Ltd., of the U.K. The pitot's sensor consisted of a small length of 1.5 mm bore steel tubing inside which a strain-gauge type pressure transducer was mounted. The cut-off frequency of the sensor was greater than 10 kHz. A reference pressure, for the rear of the diaphragm, was provided by a conventional pitot which was located upstream of the rotor blades at the same radius as the fast response pitot. Allowance was made for the non-linear response of the conventional pitot by measuring the voltage offset with the fast response pitot exposed to the same flow as the conventional pitot, upstream of the rotor blades. Centrifugal loading of the diaphragm was also taken into account by this method.

In order to determine the mass averaged loss coefficient, it is necessary to measure the rotor-relative exit velocity distribution. This was achieved using a two-dimensional adaptation of the single sensor technique of Whitfield et al [23]. The radial velocity was known to be small [20]. A DISA 45 degree hot wire sensor (type 55P12) was positioned so that the probe support axis was approximately aligned with the mean flow direction as shown in Figure 3. The corrected cosine law of Champagne et al [24] was then used to describe the response of the wire to changes in the flow direction.

In making the fast response measurements on the turbine rotor, phase-locked averaging [25] over 100 revolutions was used to enhance the periodic variations within the signals. If θ_j denotes the rotor position corresponding to the jth point in the nth sample of data, the nth raw signal

$$u(j,n); \quad j = 1,J \qquad (4)$$

can be represented as the sum of the ensembled mean

$$\tilde{u}(j) = \sum_{n=1}^{100} u(j,n) \qquad (5)$$

and the random component $u'(j,n)$, viz,

$$u(j,n) = \tilde{u}(j) + u'(j,n) \qquad (6)$$

The time mean of the signal is then given by

$$\bar{u} = \frac{\sum\limits_{j=1}^{J} \tilde{u}(j)}{J} \tag{7}$$

The ensembled root mean square

$$\sqrt{\tilde{u}'^2(j)} = \sqrt{\frac{\sum\limits_{n=1}^{100} (u(j,n) - \tilde{u}(j))^2}{N}} \tag{8}$$

is particularly useful since it can be used to identify regions of the flow where random fluctuations are present. The mean root-mean-square

$$\sqrt{\overline{\tilde{u}'^2}} = \sqrt{\frac{\sum\limits_{j=1}^{J} \tilde{u}'^2(j)}{J}} \tag{9}$$

is also useful in this respect.

Rotor-Relative Traverse Mechanism

The computer-controlled mechanism is shown in Figure 4. It provides movement, with a resolution of 1.8 μm, in a circumferential direction over two and a half blade passages, both within and downstream of the rotating blade row. Information is transferred between the rotating and stationary frames of reference in the form of electrical signals via a high quality 24-way slip ring unit.

It should be noted that the traverse mechanism provides movement in the circumferential direction only. This direction is not, in general, perpendicular to the blade surface. Therefore, as a probe traverses a blade surface boundary layer, it will have a component of displacement parallel to the surface. As a consequence, an error will be introduced into the measurements if the free-stream velocity and/or the boundary layer profiles are not constant over the surface length of the traverse. On the suction surface, this error was apparently negligible and the boundary layer profiles are therefore presented "as measured" with the exception that the distances have been corrected so that they are normal to the blade surface. On the pressure surface, the high velocity gradients near the trailing edge required that the error be corrected. This is discussed in the appropriate section.

RESULTS AND DISCUSSIONS

Linear Cascade

The non-dimensional isentropic blade-surface velocity, as defined by

$$U^* = \sqrt{\frac{P_{01} - p}{P_{01} - p_2}} \tag{10}$$

is plotted against the distance along the blade surfaces in Figure 5. This shows that the blade is aft loaded, with continuous acceleration on the pressure surface and only a small amount of diffusion at the rear of the suction surface.

Figure 6 presents the distributions of the displacement thickness δ^*, the momentum thickness θ, and the shape factor H, for the suction surface boundary layer. Some of the velocity profiles are shown in Figure 7. The results show that over the leading half of the suction surface, the boundary layer is quite thin with a shape factor which is typical of an accelerated laminar boundary layer. As the boundary layer encounters the constant pressure region, the rate of growth increases and the shape factor approaches the value for the Blasius profile, i.e. H = 2.59. Beyond the pressure plateau, the unfavourable pressure gradient is severe enough to cause the laminar boundary layer to separate at 78 percent of the surface distance. The separated layer does not reattach (see Figure 7). Instead, the free shear layer was found to contain an instability which coupled with the pressure surface boundary layer fluid to form a laminar vortex street with a Strouhal Number, based upon trailing edge thickness and the mean exit velocity, of 0.25.

Figure 8 presents the integral thicknesses for the pressure surface boundary layer. This shows that as a result of the continuous acceleration, the integral thicknesses remain virtually constant, with the shape factor being typical of a laminar boundary layer which has developed under the influence of a favourable pressure gradient.

The results of the blade-surface static pressure measurements were used as input data for the boundary layer prediction scheme of Cebeci and Carr [26]. Figure 6 shows the suction surface predictions superimposed upon the measured values. The agreement is excellent except in the region of the separation, where the analysis was provided with relatively few data points in a region of rapidly changing boundary layer parameters. The prediction does not extend beyond the point of separation because of the singularity which then exists in the boundary layer equations. Figure 8 shows the pressure surface predictions. The reason for the poor prediction on the pressure surface is not understood although the hot-wire output signals and surface-flow visualisation [27]showed that Görtler

vortices, one of the causes of discrepancies between measured and predicted boundary layers, did not exist.

The mass-flow weighted loss coefficient, as defined by

$$Y_c = \frac{U_x(P_{01} - P_{02})}{\bar{U}_x(P_{01} - p_2)} \qquad (11)$$

is plotted in Figure 9 for the linear cascade. Although only one blade pitch is shown, the periodicity of the cascade was excellent, with only the first and last of the seven blades showing any evidence of end effects. The plot shows that the wake is asymmetric, being much broader on the suction side. This is presumably a result of the separation which occurs on the suction surface.

The mass-averaged loss coefficient of the linear cascade was equal to 0.0180. This compares, very favourably, with the value of 0.0182 which was calculated using the measured momentum losses at the trailing edges of the blade surfaces and equation (12).

$$\bar{Y}_c = \left[\left(\frac{2.\theta.U^2}{p.\cos(\alpha)} \right)_{ss} + \left(\frac{2.\theta.U^2}{p.\cos(\alpha)} \right)_{ps} \right] \cdot \frac{1}{U_2^2} \qquad (12)$$

The low profile loss of these blades is a direct result of the large areas of favourable pressure gradients, the low Mach and Reynolds numbers and the small amount of suction surface diffusion.

Turbine Rotor

The rotor-stator axial clearance was equal to 75 percent of the stator axial chord. At this separation, the level of unsteadiness in the rotor inflow which is due to potential interactions of the rotating and stationary blade rows will be insignificant when compared with the unsteadiness which is generated by the relative motion of the stator wakes.

The stator wakes were traversed by mounting the fast response pitot and hot-wires on the rotor. The traverse plane was located at 43 percent of the stator axial chord downstream of the stator trailing edges. It is assumed that the potential influence of the rotor blades does not extend as far upstream as the traverse plane. The results of the traverse are presented in Table II. They show that there is an incidence variation of approximately 7.5 degrees and a velocity deficit in the wake which is equal to 10.5 percent of the mean velocity in the rotating frame of reference.

The free-stream velocities, adjacent to the blade surface, were measured during the blade-surface boundary layer traverses. The mean values are shown in Figure 10, superimposed upon the linear cascade velocity distribution. These measurements confirm that the inviscid flow at the rotor mid-span radius is two dimensional.

The blade surface boundary layers have been traversed using a hot-wire anemometer. The discussion and conclusions presented are essentially two dimensional since it is known [28] that radial migration is negligible within the suction surface boundary layer and that only a small amount of radial outflow occurs on the pressure surface.

Suction Surface Boundary Layer

The time-averaged values of the boundary layer integral parameters δ^*, θ and H have been calculated from the time averaged velocity profiles. They are presented, for the suction surface, in Figure 11.

Initially, the momentum and displacement thicknesses of the suction surface boundary layer are more typical of the laminar rather than the turbulent values. However, beyond the start of the pressure plateu, the momentum loss increases at a higher rate than in either the laminar or the turbulent layers. At the trailing edge, the momentum thickness is approximately 60 percent greater than that of the laminar boundary layer on the linear cascade. There is no separation.

The shape factor is, perhaps, the best single indicator of the state of the boundary layer. Figure 11 shows that over much of the blade surface, the shape factor has a value which is mid-way between the limits of the laminar and fully turbulent boundary layers. In fact, the shape factor indicates that the boundary-layer is becoming increasingly laminar between 25 and 50%s and that between 55 and 80%s, it undergoes "transition" so that the shape factor at the trailing edge is typical of a fully turbulent boundary layer in a decelerating flow. It is assumed that the "transition" process begins soon after peak suction. If this is so, the continued increase in shape factor beyond this point must be attributed to the effect of the small deceleration which occurs in this region.

Figure 12 shows the time averaged velocity and rms profiles of several of the blade surface boundary layers. The velocity profiles clearly show the effects of the initially favourable pressure gradient and the transition to a more turbulent form following peak suction. The increasingly turbulent form of the boundary layers is also reflected in the rms profiles. These show that the boundary layer at 55% has a higher turbulent content than that which occurs at 25%s, although neither of these profiles are as full as those normally associated with a turbulent boundary layer. On the other hand, the rms

profiles at 82 and 96%s are much more representative of those normally associated with a
turbulent boundary layer although the reduction in turbulent content between 82 and 96%s
is not consistent with the occurrence of the surface diffusion. It should, perhaps,
be pointed out that the rms is only a measure of the local turbulence intensity. It is
not equal to it. This is because the hot-wire sensors had a sensitivity to span-wise
velocity fluctuations which was much less than their sensitivity to streamwise or
surface-normal fluctuations.

Figure 13 presents the profiles of the amplitude and the phase lag (relative to the
free-stream) for the velocity fluctuations which occur at the blade passing frequency.
The amplitude profiles show that the position of maximum amplitude is located within the
boundary layer and that the maximum level is typically 2 to 5 times greater than that
which occurs in the free-stream. This relative increase in the magnitude of the velocity
fluctuations is much greater than the 8 percent increase which usually occurs in unsteady
fully laminar (e.g. Hill and Stenning [5]) or fully turbulent boundary layers (e.g.
Karlsson [6]). Closer to the surface, there is a minimum in the amplitude profiles.
The phase profiles of Figure 13 show that in most of the boundary layer, the velocity
fluctuations lag those in the free stream, in some cases, by up to 180 degrees. However,
close to the surface, there is usually a rapid phase advance which is coincident with
the amplitude minimum.

Using the velocity and rms traces of Figure 14, it is possible to explain the
observations made in the above paragraph concerning the phase and amplitude profiles of
the boundary layer which occurs at 55%s. The velocity traces clearly show the increasing
amplitude and phase lag in the upper half of the boundary layer. They also show that
between 25 and 10% δ_{99}, the velocity signal becomes inverted. The start of this inversion
can be seen in the velocity trace at 25% δ_{99}, where the peaks have become folded back.
This inversion of the velocity signal is coincident with the rapid phase advance and
amplitude minimum which has already been noted in Figure 13.

Figure 14 also shows that the turbulent fluctuations which are generated within the
boundary layer affect the rms levels at $y = \delta_{99}$. At 75% δ_{99}, the rms fluctuations have
further increased and at 50 and 25% δ_{99}, the rms wave-form is squarer with double peaks.
At 10% δ_{99} the wave form is less square and the double peaks are less pronounced. The
reason for this occurrence of the double peaks in the rms signals is not fully understood.
However, it is known that in fully turbulent, unsteady boundary layers (e.g. Cousteix et
al [29],the local rms will fluctuate at the same frequency as the mean velocity. Therefore,
it is possible that as a result of the large amplitude of the velocity fluctuations, there
will be an additional periodic production of turbulence which is out of phase with the
free-stream induced turbulence. Such a production could result in the observed
distortion of the rms wave-form.

In Figure 14, it can also be seen that in the upper half of the boundary layer, the
velocity and rms fluctuations are in antiphase whereas very close to the wall, they are
in phase. The change in the relative phase of the velocity and the rms fluctuations
is very similar to that observed by Pfeil et al [15] in time-dependent transitional boundary
layers. The change results from an oscillation of the boundary layer between
characteristically laminar and turbulent profiles, as illustrated in Figure 15.

The relatively large amplitudes of the velocity fluctuations within the boundary layer
at 55%s are due, only in part, to the oscillatory changes of state. It has already been
noted that the free-stream velocity and the rms are in anti-phase. Therefore, if it is
assumed that the change of state is controlled by the changing levels of the free stream
turbulence, it is probable that the periodic velocity fluctuations near the free-stream will
be in phase with those generated by a change of state. As a result, they will enhance
those variations.

In addition to the velocity and rms traces, Figure 14, also presents the velocity
profiles at four equally spaced time levels within the cycle of the free-stream oscillation.
The profiles shown represent an average for the 12 periods shown in the adjacent velocity
traces. These "instantaneous" profiles show that the boundary layer is truly unsteady,
that is, that the profiles do not resemble the quasi-steady profiles in Figure 15. Indeed
the increased phase lag of the velocity fluctuations is clearly evident. This large phase
lag is thought to be caused by inertial effects, since it is known [28] that on the
suction surface, the free-stream velocity fluctuations are much more significant than the
static pressure fluctuations.

Figure 16 presents the unsteady velocity and rms traces for the boundary layer at
96%s. The velocity traces show that the large phase shift and the amplitude minimum which
occur in the outer portion of the boundary layer (Figure 13) are a result of a gradual
inversion of the velocity signal. The velocity trace at 75% δ_{99} clearly shows the double
peaks which are associated with this inversion. As a result of the inversion, the velocity
and the rms fluctuations are in phase with each other within the main body of the boundary
layer. Very close to the wall, however, the velocity trace appears to be about to invert
again.

Figure 16 also shows a set of instantaneous velocity profiles for the boundary layer
which occurs at 96%s. A comparison of these profiles with those of Figure 14 shows that
the boundary layer at 96%s is much more unsteady, in the true sense, than the boundary
layer at 55%s. This is most surprising, because, as the time-averaged results of Figure 11
indicate, this boundary layer is supposed to be fully turbulent. It therefore appears that
the boundary layer "remembers" its unsteady history much better than its time-averaged

development and that because of this, there is an oscillatory motion of a large portion of the boundary layer fluid, relative to the mean boundary layer motion and parallel to the surface, over the entire length of the suction surface.

Pressure Surface Boundary Layer

It has been noted that the traverse mechanism only provided curcumferential movement and that because of this, the pressure surface traverse results are not presented in the "as measured" form.   Instead, the pressure surface boundary layer profiles have been determined by spatial interpolation between the various traverse planes.   This method was successful, largely because the integral parameters δ^*,θ and H and the velocity gradient are almost constant over the length of the surface.

The calculated values of δ^*,θ and H are shown in Figure 17 for the pressure surface boundary layer.   The data points indicate the approximate positions of the traverses. The linear cascade (laminar) results are also shown.   The predicted, fully turbulent, shape factors are shown to assist the interpretation of the results, because even though the predicted values of δ^* and θ will be in error, the shape factor will be approximately correct.

The results indicate that the rotor pressure surface boundary layer is transitional, and that relaminaraization is gradually taking place.   Full "transition", such as that which occurs on the suction surface, does not take place.   This is presumably because the levels of unsteadiness (periodic and random) are much lower in the free-stream (see Figure 18) and because there is a continuous acceleration of the boundary layer over the entire length of the surface.

Figure 17 shows that the measured values of the displacement and momentum thicknesses are almost the same as those on the linear cascade.   In particular, the total momentum losses are identical, which means that the pressure surface makes no contribution to the increase in profile loss which is associated with the wake generated unsteadiness. This is a little surprising because the boundary layer is known to be transitional.   It is therefore thought that the small increase in momentum loss, which should accompany a partial change of state, is offset by a thinning of the boundary layer.   This would be caused either by three dimensional effects, or by the mixing of the boundary layer fluid with the wake fluid and its subsequent migration away from the pressure surface (see below)

A typical set of results for the pressure surface boundary layer is shown in Figure 18.   Unlike the velocity profiles, which have been determined by interpolation , the rms and velocity traces are presented "as measured".   The free-stream fluctuations are smaller than those which occur on the suction surface.   These traces also show that in the free stream, the periodic fluctuations of the velocity and the turbulence in phase with each other.   The outer portion of the boundary layer is therefore subjected to two opposing, unsteady shear forces.   These are periodic variations of the turbulent and the mean shear stresses.   The latter tends to increase the velocity in the boundary layer at the same time as the former tries to reduce it.   The net result is that the fluctuations within the boundary layer are proportionately much less than those which occur on the suction surface.

Figure 18 also shows that the velocity wave-form becomes distorted near the surface. This distortion must, in part, be due to the cancellation effect which has just been described, but it must also be due to the fact that on the pressure surface, the pressure fluctuations are not insignificant when compared to the free stream velocity fluctuations [28], which means that near the wall, the pressure fluctuations will tend to dominate the flow, thereby resulting in the complex periodic wave forms of Figure 18.

Rotor-Relative Exit Flow

The rotor-relative exit flow was determined by traversing at one half of the rotor axial chord downstream of the rotor trailing edges.   This is the same location as that used for the exit traverse of the linear cascade.

The mass flow averaged rotor-relative loss coefficient is given in Table III together with various predicted values.   The agreement between the measured loss and that obtained using the measured momentum losses of blade surface boundary layers is excellent, which suggests that there is very little mixing loss as the stator wakes are convected through the rotor blade row.   A comparison of these results with those from the linear cascade shows that the profile loss of the rotor is approximately 50 percent greater than that of the linear cascade.   The boundary layer results have shown that this increase is due to the transitional and turbulent nature of the suction surface boundary layer.

The mass-flow weighted exit-profile of the rotor-relative loss coefficient is shown in Figure 19.   A comparison of this profile with that of the linear cascade shows that the rotor wake is more symmetrical, narrower and deeper than that of the linear cascade. These differences are a result of the differences in wake structure (there is no separation) and total loss.

Figure 19 also shows that the profile loss of the rotor is not zero between the wakes. Instead, it is positive on the suction side of the wake and negative on the pressure side. This can be explained using the model of Meyer [30].   If the stator wakes are considered to be "negative" jets superimposed on the free stream (see Figure 20), then it is obvious that migration of the stator wake fluid occurs, relative to the free-stream fluid, in a

direction which is aligned with the centre line of the wake. This will occur even when a stator wake has been cut by a rotor blade and as a result, high loss fluid will tend to accumulate on the suction surface. Adachi and Murakami [31] have observed a similar phenomena in an axial-flow compressor.

The expected time-histories of the velocities at positions on the blade surfaces which have experienced the passage of a wake are also shown in Figure 20. The similarity between these traces and the free-stream velocity traces of Figures 14, 16 and 18 is self evident although, in contrast to the model, the pressure surface fluctuations are less than those on the suction surface, presumably because the turbine rotor is not a flat plate.

It is possible that as the wake migrates towards the suction surface, it entrains the pressure-surface boundary layer fluid, thereby reducing the thickness of the boundary layer on that surface. Similarly, the suction surface boundary layer would be thickened. It is impossible to determine the extent to which this happens but in view of the small pitchwise gradient of the loss coefficient and the radial out-flow which is known to occur in the pressure surface boundary layer [28], it is thought that this entrainment is not responsible for the small amount of thinning which has occurred.

CONCLUSIONS

The aerodynamic performance of the mid-span section of a turbine rotor has been compared with that of an equivalent linear cascade operating with steady inflow. The profile loss of the rotor was found to be 50 percent greater than that of the linear cascade. This increase is a result of differences in the blade surface boundary layers.

On the linear cascade, the blade-surface boundary layers were laminar, with a separation point located near the rear of the suction surface.

Over the majority of the rotor suction surface, the boundary layer oscillates between characteristically laminar and turbulent states in sympathy with the passage of the stator wakes. As a result of this oscillatory change of state and because the free-stream velocity is in anti-phase with the fluctuations of free-stream turbulence, the levels of the velocity fluctuations within the boundary layer are much greater than those found in conventional laminar [5] or turbulent [6] unsteady boundary layers. Towards the rear of the rotor suction surface, the boundary layer becomes mainly turbulent, but even here, there are extremely large velocity fluctuations. As a result of the increased momentum transfer which occurs in the transitional boundary layer, there is no separation.

On the pressure surface of the rotor, the boundary layer is also transitional, but because of the reduced levels of unsteadiness and the favourable acceleration over the entire surface, this boundary layer was much less unsteady and the changes of state were less well defined. Full transition did not take place.

Early transition, induced by sinusoidal variations of the free-stream velocity has been observed by, for example, Obremski and Fejer [12]. However, the transition Reynolds number, predicted by their results for the turbine rotor, is much greater than the chord-based Reynolds number. Pfeil et al [15], whose results are similar to those presented here, made a similar observation. This suggests that the unsteady transitional behaviour is caused by the periodic variations of the free stream turbulence, which were absent from the work of Obremski and Fejer. It is, however, quite probable that the amplification of the velocity fluctuations induced by the free-stream turbulence is dependent upon the amplitude and frequency of the mean velocity fluctuations, as well as the local pressure gradient, in the manner observed by Obremski and Fejer.

The results of references [1], [2] and [3] show that the "lost" efficiency is greatest in machines of high reaction and low Reynolds number. Such designs favour the presence of laminar boundary layers over a large portion of the blade surfaces. It is not surprising, therefore, that these blades show the greatest increase in profile loss as a result of wake induced transition.

ACKNOWLEDGMENT

REFERENCES

1. Lopatitskii, A.O., et al., "Energy Losses in the Transient State of an Incident Flow on the Moving Blades of Turbine Stages", Energomashinostroenie, Vol.15, Aug. 1969.

2. Kirillov, I.I., Laskin, A.S., and Shpenzer, G.G., "Influence of Unsteadiness of the Flow on _ .iciency of Turbine Stages", Teploenergetika, 1970, Vol. 17, No. 10, pp 21-23.

3. Yurinskiy, V.T., and Shestachenko, I. Ya., "Losses in an Impulse Turbine Cascade in an Unsteady Flow", Fluid Mechanics - Soviet Research, Vol. 3, No. 1, Jan. 1974, pp 22-27.

4. Lighthill, M.J., "The Response of Laminar Skin Friction and Heat Transfer to Fluctuations in the Stream Velocity", Proc. R. Soc., 224A, 1954.

5. Hill, P.G., and Stenning, A.H., "Laminar Boundary Layers in Oscillating Flow", A.S.M.E. Jnl. Basic Eng., Vol. 82, 1960.

6. Karlsson, S.K.F., "An Unsteady Turbulent Boundary Layer", J.F.M., Vol. 5, No. 4, 1959, pp 622-636.

7. Patel, M.H., "On Laminar Boundary Layers in Oscillatory Flow", Proc. R. Soc., 347A, 1975.

8. Patel, M.H., "On Turbulent Boundary Layers in Oscillatory Flow", Proc. R. Soc., 353A, 1977.

9. Despard, R.A., and Miller, J.A., "Separation of Oscillatory Laminar Boundary Layers", J.F.M., Vol. 47, No. 1, 1971, pp 21-23.

10. Samoilovich, G.S., Yablokov, V.G., and Rabotarev, V.G., "Profile Losses with Unsteady Flow through Impulse Cascades of Moving Blades", Teploenergetika, Vol. 24, No.2, 1977, pp 40-42.

11. Miller, J.A. and Fejer, A.A., "Transition Phenomena in Oscillating Boundary Layer Flows", J.F.M., Vol. 18, No. 3, 1964. pp 438-449

12. Obremski, H.J., and Fejer, A.A., "Transition in Oscillatory Boundary Layer Flows", J.F.M., Vol. 29, No. 1, 1967, pp 93 - 111.

13. Obremski, H.J., and Morkovin, M.V., "Application of a Quasi-Steady Stability Model to Periodic Boundary Layer Flows", A.I.A.A. Jnl., Vol. 7, 1969, pp 1298-1301.

14. Walker, G.J., "The Unsteady Nature of Boundary Layer Transition on an Axial-Flow Compressor Blade", A.S.M.E., Paper 74-GT-135, 1974.

15. Pfeil, H., Herbst, R., and Schröder, T., "Investigation of the Laminar-Turbulent Transition of Boundary Layers disturbed by Wakes", A.S.M.E. Paper 82-GT-124, 1982.

16. Evans, R.L., "Boundary layer development on an axial-flow compressor stator blade" A.S.M.E. Journal of Engineering for Power, Vol. 100, April, 1978, pp 287-293.

17. Larguier, R., and de Sievers, A., "Unsteady Flow Measurements in Turbomachines", Paper presented to Supersonic Tunnel Association, Toronto, Sept. 1975.

18. Dring, R.P., Joslyn, H.D., Hardin, L.W., and Wagner, J.H., "Turbine Rotor-Stator Interaction", A.S.M.E. Paper 82-GT-3, 1982.

19. Hunter, I.H., "Endwall Boundary Layer Flows and Losses in an Axial Turbine Stage", A.S.M.E., Jnl. of Eng. for Power, Vol. 104, Jan 1982, pp 184-193.

20. Denton, J.D., and Usui, S., "Use of a Tracer Gas Technique to Study Mixing in a low-speed Turbine", A.S.M.E. paper 81-GT-86, 1981.

21. Smith, D.J.T., and Johnson, S.H., "Investigations on an experimental single-stage turbine of conservative design", A.R.C., R. & M. No. 3541, Jan. 1967.

22. Cox, R.N., "Wall Neighbourhood Measurements in Turbulent Boundary Layers using a Hot-Wire anemometer", A.R.C., Report 19101, Feb 1957.

23. Whitfield, C.E., Kelly, J.C., and Barry, B. "A three dimensional analysis of rotor wakes", Aero. Quart., Nov. 1972, pp 285-300.

24. Champagne, F.H., Sleicher, C.A., and Wehrman, O.H., "Turbulence measurements with inclined hot-wires, Part I", J.F.M., Vol. 28, 1967, p. 153.

25. Gostelow, J.P., "A new approach to the experimental study of turbomachinery flow phenomena", A.S.M.E. paper No. 76-GT-47, 1976.

26. Cebeci, T., and Carr, W.C., "A Computer Program for Calculating Laminar and Turbulent Boundary Layers for Two Dimensional Time-Dependent Flows", NASA TM-78470, Mar. 1978.

27. Hodson, H.P., "Boundary Layer and Loss Measurements on the Rotor of an Axial-Flow Turbine", presented at ASME Gas Turbine Conference, March, 1983.

28. Hodson, H.P. "Unsteady Boundary Layers on an Axial-Flow Turbine Rotor Blade", Ph.D. Thesis, Cambridge University, 1983.

29. Cousteix, J., Desopper, A., and Houdeville, R., "Structure and Development of a Turbulent Boundary Layer in an Oscillatory External Flow", presented at Symp. Turbulent Shear Flows, Penn. State Univ., April 1977.

30. Meyer, R.X., "The Effect of Wakes on the Transient Pressure and Velocity Distributions in Turbomachines", A.S.M.E. Jnl., Basic Eng.,Oct 1958, pp 1544-1552.

31. Adachi, T., and Murakami, Y., "Three Dimensional Velocity Distribution between Stator Blades and Unsteady Force due to Passing Wakes", J.S.M.E., Vol. 22, No. 170, Aug. 1979, pp 1074-1082.

TABLE I   Physical Description

	Stator	Rotor
Reynolds Number	4.20×10^5	3.15×10^5
Speed (r.p.m)	-	530
Axial Velocity (m/s)	17.95	-
Stage Loading, $\Delta h_0/U_m^2$	-	1.0
Flow Coefficient U_x/U_m	-	0.495
Inlet Angle (deg)	0.0	0.0
Exit Angle (deg)	65.0	~ 65.0
Stagger (deg)	44.5	~ 44.5
Chord (mm)	152.4	114.5
Pitch-Chord ratio	0.742	0.697
Aspect ratio	1.5	2.0
Blade number	36	51
Mean Radius (metre)	0.647	0.647

TABLE II   Stator Wake Parameters at 43% Cx_s-Downstream of the Stator Trailing Edges

Loss Coefficient	0.0140	
δ^*/pitch	0.0080	
θ/pitch	0.0071	Absolute Frame of Reference
$H = \delta^*/\theta$	1.27	
$(U_{max} - U_{min})/\bar{U}$	0.021	

Mean Incidence (deg)	2.1	
Maximum/Minimum Incidence (deg)	+ 4.0/ - 3.5	
$(U_{max} - U_{min})/\bar{U}$	0.105	
$\sqrt{\widetilde{U^2}}/\bar{U}$	0.041	Rotor-Relative Frame of Reference
$\sqrt{\widetilde{U^2}_{max}}/\bar{U}$	0.095	
$\bar{U}/\bar{U}_2$	0.447	

TABLE III   Loss Coefficients, $\bar{\zeta}$

Linear Cascade, Measured Direct	0.0180
Linear Cascade, Measured Boundary Layers	0.0182
Turbine Rotor, Measured Direct	0.0270
Turbine Rotor, Measured Boundary Layers	0.0260
Turbine Rotor, Predicted Turbulent Suction Surface + Measured Pressure Surface	0.0297
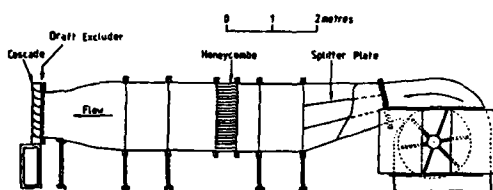
FIGURE 1.   SCHEMATIC DIAGRAM OF THE
            LINEAR CASCADE
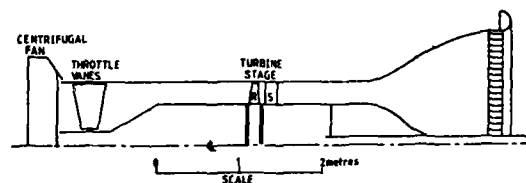
FIGURE 2.   SCHEMATIC DIAGRAM OF THE
            SINGLE STAGE TURBINE
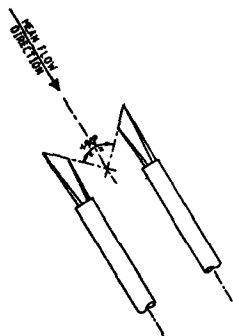
FIGURE 3.   ORIENTATION OF 45 DEGREE
            HOT-WIRE WITH RESPECT TO THE MEAN
            FLOW

FIGURE 4.   ROTOR TRAVERSE MECHANISM
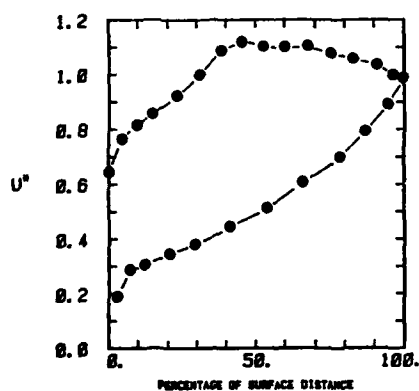
FIGURE 5   NON-DIMENSIONAL ISENTROPIC SURFACE VELOCITIES
           FOR THE LINEAR CASCADE
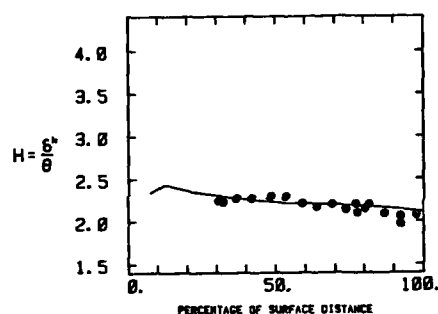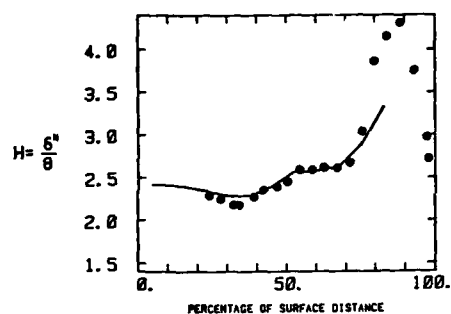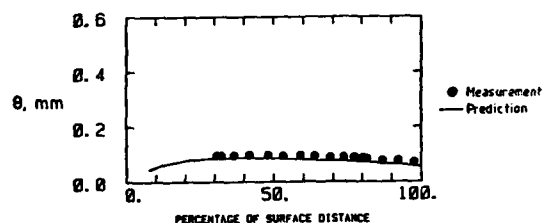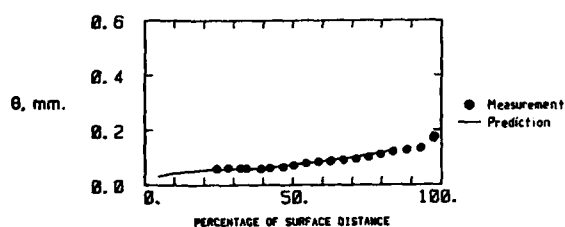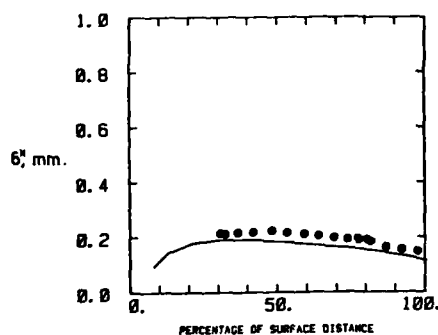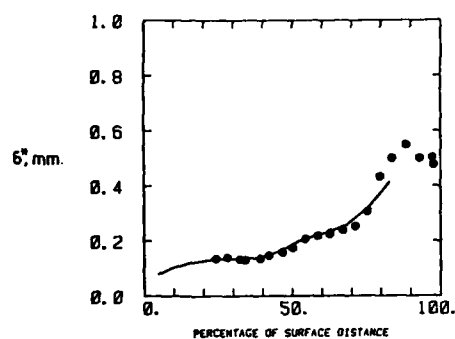
FIGURE 6   INTEGRAL PARAMETERS FOR THE
SUCTION SURFACE BOUNDARY
LAYER OF THE LINEAR CASCADE

FIGURE 8   INTEGRAL PARAMETERS FOR THE
PRESSURE SURFACE BOUNDARY LAYER OF
THE LINEAR CASCADE
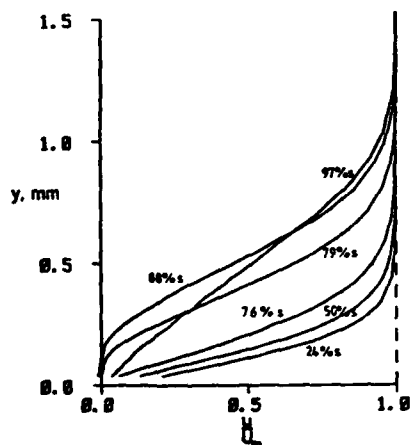
FIGURE 7   VELOCITY PROFILES FOR THE
SUCTION SURFACE BOUNDARY LAYER
OF THE LINEAR CASCADE
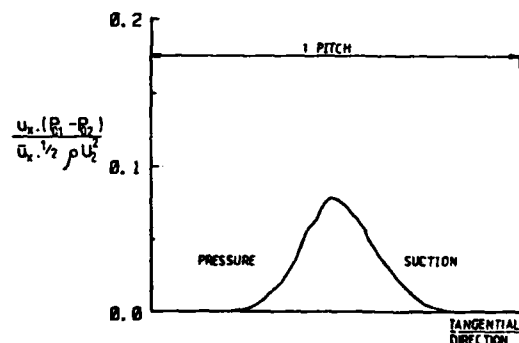
FIGURE 9   PROFILE LOSS FOR THE LINEAR
CASCADE
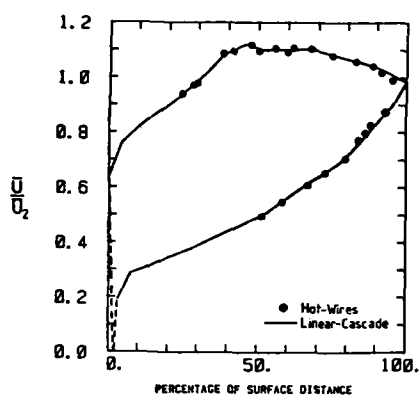
FIGURE 10   BLADE-SURFACE VELOCITY
DISTRIBUTIONS

KEY

● Turbine Rotor

— Turbulent
    Prediction

--- Linear Cascade,
    Laminar

FIGURE 12   TIME-AVERAGED VELOCITY AND RMS
PROFILES FOR THE ROTOR SUCTION-
SURFACE BOUNDARY-LAYER

FIGURE 11   TIME-AVERAGED INTEGRAL
PARAMETERS FOR THE ROTOR SUCTION
-SURFACE BOUNDARY-LAYER
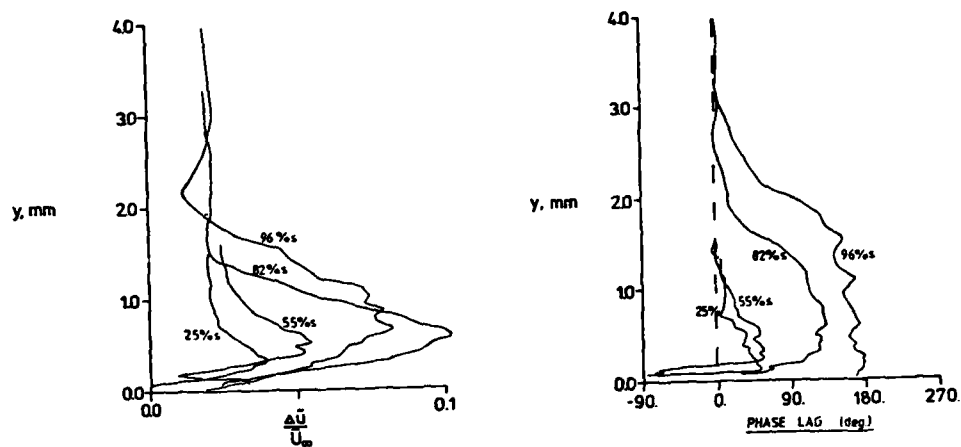
FIGURE 13   AMPLITUDE AND PHASE PROFILES (AT BLADE-PASSING FREQUENCY) FOR
THE ROTOR SUCTION-SURFACE BOUNDARY-LAYER
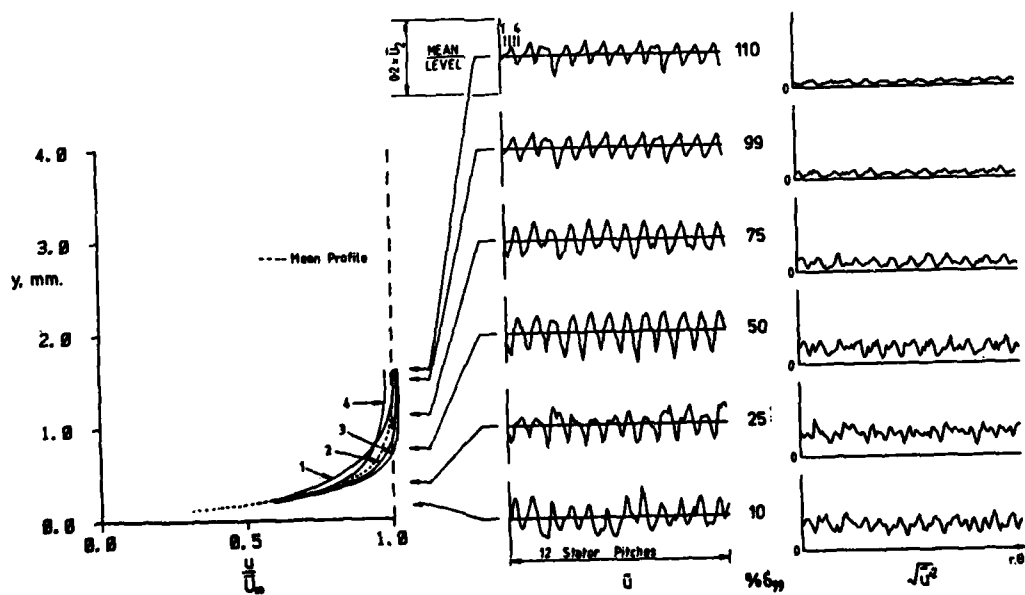
FIGURE 14   UNSTEADY VELOCITY PROFILES AND PHASE-LOCKED AVERAGES OF THE VELOCITY
AND THE RMS FOR THE ROTOR SUCTION-SURFACE BOUNDARY-LAYER AT 55%s
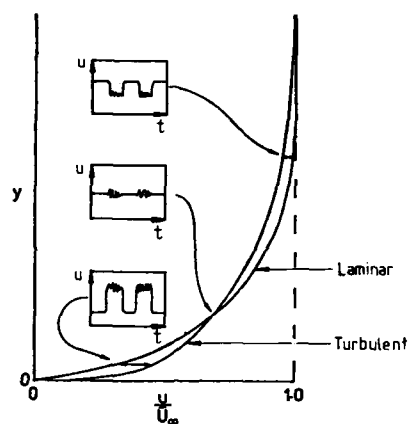
FIGURE 15   SCHEMATIC REPRESENTATION OF UNSTEADY TRANSITION (PFEIL ET AL [15])
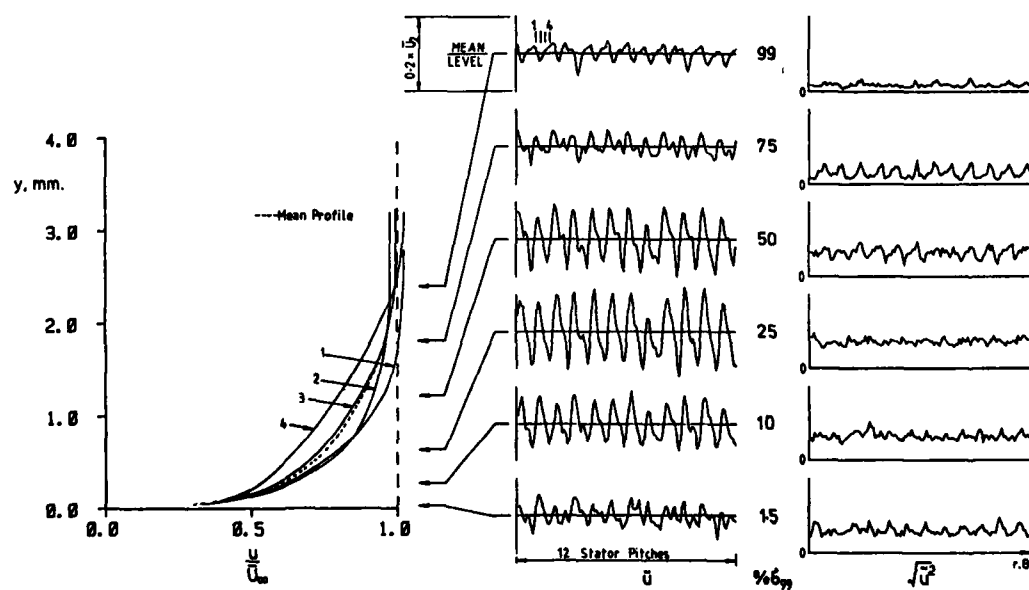
FIGURE 16   UNSTEADY VELOCITY PROFILES AND PHASE-LOCKED AVERAGES OF THE VELOCITY AND
THE RMS FOR THE ROTOR SUCTION-SURFACE BOUNDARY-LAYER AT 96%s
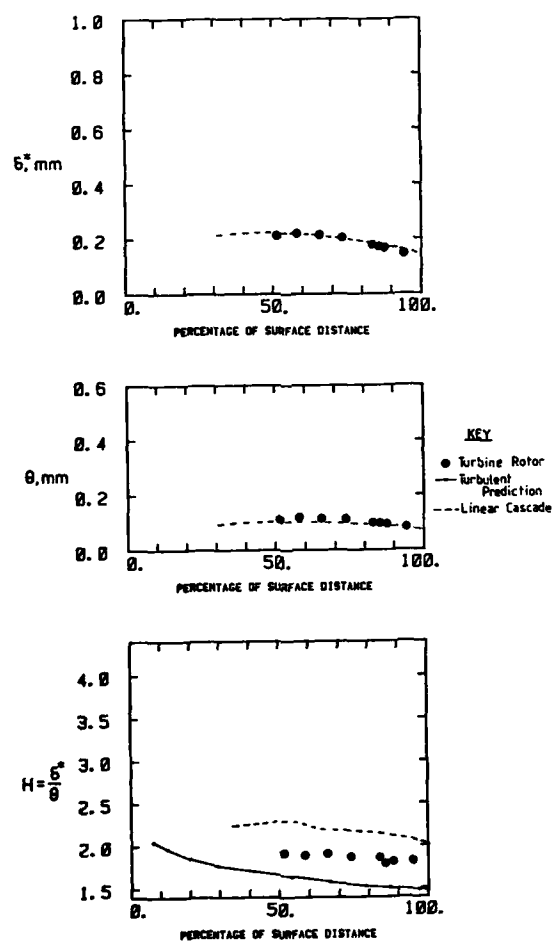
FIGURE 17   TIME-AVERAGED INTEGRAL PARAMETERS FOR THE ROTOR PRESSURE-SURFACE
BOUNDARY-LAYER
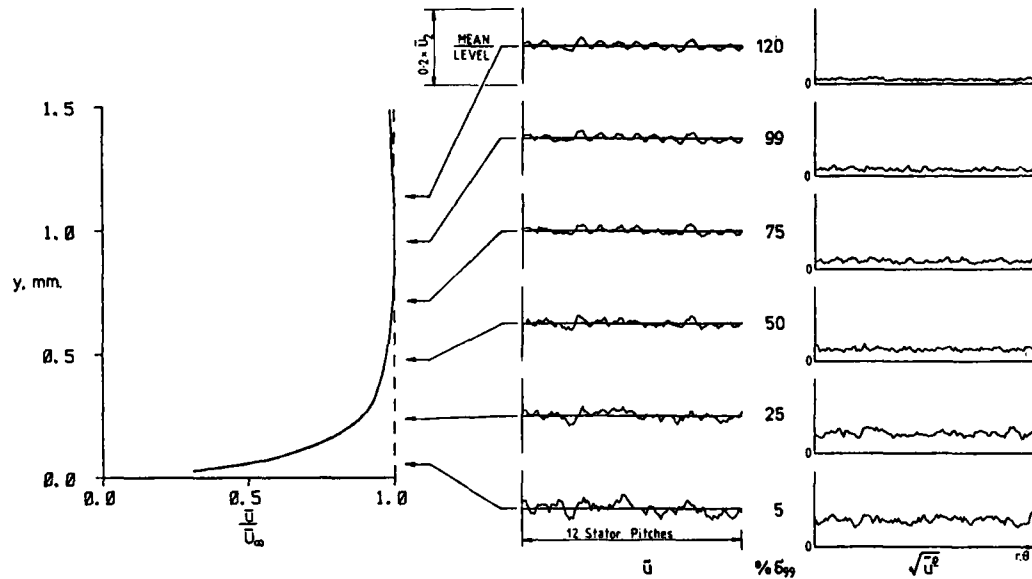
FIGURE 18 TIME-AVERAGED VELOCITY PROFILE AND PHASE-LOCKED AVERAGES OF THE
VELOCITY AND THE RMS FOR THE ROTOR PRESSURE-SURFACE BOUNDARY-LAYER
AT 88%s
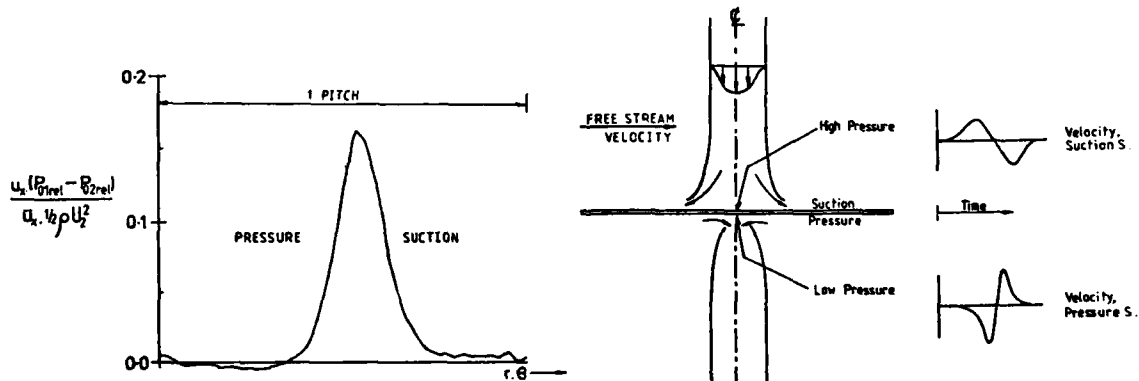
FIGURE 19 ROTOR-RELATIVE LOSS
COEFFICIENT

FIGURE 20 WAKE DISTORTION ON A TURBINE
ROTOR BLADE (MEYER [29])

DISCUSSION

G.Winterfeld, Ge

If one compares Fig.16 (for the suction side) with Fig.18 (for the pressure side) there is only a very small effect of the unsteady flow on the hot wire signal at the pressure side. One would expect that the passing wakes are registered on the pressure side with a similar intensity as on the suction side. Could the author please comment?

Author's Reply

There are several reasons as to why the suction surface boundary layers are more unsteady than those of the pressure surface. Firstly, the amplitude of the free-stream velocity and pressure fluctuations are much less on the pressure surface than on the suction surface. Secondly, the relative phases of the fluctuations in the free-stream turbulence intensity and velocity are such that on the suction surface, the boundary layer unsteadiness is enhanced, while on the pressure surface, it is suppressed.

AERODYNAMIC COMPUTATION METHOD OF AIRFOIL CASCADES SUBJECTED TO VISCOUS FLOW

by

P. Psarudakis
Istituto di Macchine, Università di Pisa
Via Diotisalvi 2
56100 Pisa – Italy

SUMMARY

A computational method for the determination of aerodynamic characteristics of airfoil cascades subjected to viscous flow is presented. Such method is based on the determination of the flux perturbation directly due to the local continuous stream velocity over every single cascade airfoil. Particular attention is given to the development of a method suitable to decrease automatical computation time and, at the same time, to make possible versatile application to physical phenomena simulation. Various comparisons with theoretical and experimental values carried out by other authors confirm the validity of the present method.

LIST OF SYMBOLS

C_p pressure coefficient based on the inlet flow characteristics

C_f $= \tau / \frac{1}{2} \rho U_e^2$, skin friction coefficient

d airfoils spacing along the cascade Y axis

H $= \delta^* / \theta$, shape factor

H^* $= (\delta - \delta^*)/\theta$, *Head shape factor*

I_j^0 , I_j^1 influence coefficients of the j-th segment vorticity (expression 2)

k streamline curvature

ℓ_t airfoil total contour length

N polygonal segments number

p static pressure

P^0 total pressure

q source density

Q_j source intensity on the j-th polygonal node

s curvilinear coordinate

u , U internal, external to boundary layer or wake, velocity component parallel to polygonal segment or main streamline

w induced complex conjugate velocity

W potential, or asymptotic complex conjugate velocity

β angle between cascade Y axis and $|W|$ velocity

γ vortex density

Γ_j vortex intensity on the j-th polygonal node

δ boundary layer or wake thickness

$\delta^* = \int_0^\delta (1 - \frac{u}{U_e}) \, dn$, displacement thickness

$\theta = \int_0^\delta \frac{u}{U_e} (1 - \frac{u}{U_e}) \, dn$, momentum thickness

ν flow kinematic viscosity

ρ flow density

ζ $= X + iY$, complex coordinate (fig. 3)

ζ_v $= (P_1^0 - P_2^0)/\frac{1}{2} \rho |W_1|^2$, total pressure loss coefficient

ω relaxation factor to displacement thickness definition (expressione 20)

Subscripts

0   indisturbate asymptotic flow

1   cascade asymptotic inlet flow

2   cascade asymptotic outlet flow

2P   cascade asymptotic outlet potential flow

j   polygonal node or segment number

e   on the boundary layer or wake edge

SEP   separation point

TE   trailing edge

TOT   total

w   wake

1 - INTRODUCTION

Over the past several years with the continuous increase of computers speed and storage capacity many new methods to be applied in automatical turbomachine calculations have been developed. Many of them are referred to inviscid, potential, flow (see, i.e., References [1 - 5]) and may be used in design and/or study of: a) profile aerodynamic characteristics; b) number of blades; c) peripheral speed; d) limits of noise; e) number of staggers; etc..

However for operating range, performance and optimization of machines, informations are required on: a) Reynolds number effect; b) pressure losses; c) efficiency; d) stalling incidences, etc..
Therefore in an effort to define such further requirements, methods which try to resolve the full Navier-Stokes equations have also been developed (see, i.e., References [6 - 8]). In the present time such methods need very large computing time and therefore they may be very expensive. For this reason, developments are increasing to improve methods which, making use of empirical relations of the existing boundary layer phenomena around airfoil (see, i.e., References [9, 10]), correct, by iterative processes, the previous inviscid calculation (see, i.e. References [11 - 16]).

Because it is approximately possible: a) correlate three and two-dimensional flow characteristics [17]; b) transform by conformal mapping a radial cascade to a rectilinear cascade; c) lead compressible flow field mathematical representations to incompressible flow field mathematical representations |3|, in this paper the rectilinear cascades in incompressible viscous flow are considered.

The effects of the flow viscosity are considered after determination of the flux streamlines perturbation, due to the boundary layer existing around every single cascade's airfoil.

In the development of the present method particular attention has been paid to: a) decrease automatical computation time; b) be possible to apply such method without limitations to geometrical cascade characteristics; c) use the computer program to further simulation studies of physical phenomena.

2 - INVISCID SOLUTION

It is known that in potential flow, the local flux velocity on the airfoils contour may be represented by continuous distributed vorticity $\gamma(s)$, fig. 1.
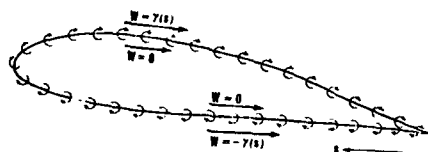
Fig. 1 - Inviscid representation of the local flow velocity on the airfoil contour.

Here the method developed by the author in Ref. [1] is considered.
Following this method each cascade's airfoil contour is approximate by N consecutive segments. The first and the last of such segments contain the airfoil trailing edge. The numbering of the segments is in a clockwise versus, fig. 2.

On every j-th segment a linear variation of the vorticity between the values Γ_j and Γ_{j+1} that assumes on the segment nodes is considered.

Therefore in the complex plane $\zeta = X + iY$ of the cascade, fig. 3, it results that the complex conjugate velocity, induced by the cascade infinite segments j in a point ζ, is

$$\Delta w_j(\zeta) = -\frac{1}{2\pi i}\left[\Gamma_j\left(I_j^0 - I_j^1\right) + \Gamma_{j+1} I_j^1\right] \qquad (1)$$

with

$$\left.\begin{array}{l} I_j^0 = \dfrac{|\sigma|}{\sigma}\ell n\,\dfrac{sh(\pi\dfrac{\zeta - \zeta_j}{d})}{sh(\pi\dfrac{\zeta - \zeta_{j+1}}{d})} \\[4ex] I_j^1 = \pi\,\dfrac{|\sigma|}{d}\displaystyle\int_0^1 \hat{s}\,cth(\pi\,\dfrac{\zeta - \zeta_j - \sigma\hat{s}}{d})\,d\hat{s} \end{array}\right\} \qquad (2)$$

and

$$\sigma = \zeta_{j+1} - \zeta_j \qquad (3)$$

Fig. 2 - Geometrical schematization of each cascade's airfoil.

Being β_0 the direction angle of the indisturbated velocity $|W_0|$, fig. 7, in every point ζ its complex

conjugate value is

$$W_o = - i \, |W_o| \, \exp(i \, \beta_o) \qquad (4)$$

Assuming that in the middle point of each i-th airfoil segment, the velocity

$$|W_i| = | W_o + \sum_{j=1}^{N} \Delta w_j | \qquad (5)$$

is parellel to these N segments and by the Kutta condition expressed by

$$\Gamma_1 + \Gamma_{N+1} = 0 \qquad (6)$$

the Γ_j vorticity values are defined.

Therefore the local flow velocity on each cascade's airfoil contour is immediately known and it is possible to calculate the flow characteristics on every point of the considered cascade.

$\zeta = X + i Y$

Fig. 3 —Cascade plane and reference axis.

3 - VISCOUS EFFECT

In the present method the viscous effects are computed using the Prandtl stationary boundary layer siplified equations and boundary layer integral methods.

As known, from the airfoil stagnation point, along the upper and lower surface, respectively, the boundary layer may be: a) laminar stable; b) laminar instable; c) transitional from laminar to turbulent; d) turbulent; e) separated from the airfoil contour. Behind the airfoil it forms the viscous wake.

Here the above structures of the boundary layer are represented as follows:

3.1 - Laminar boundary layer

The velocity profile in the laminar boundary layer is that of van Karman, Pohlhausen.

The momentum thickness is computed by Walz method; so it is

$$\theta^2(s) = \frac{0.470 \, \nu}{U_e^6(s)} \int_{s_o}^{s} U_e^5 (\xi) \, d \xi \qquad (7)$$

with s_o the stagnation point position.

The approximate test to verify when the laminar boundary layer is stable or instable is due to Schlichting [9] and it is represented in fig. 4.

3.2 - Transition

The transition phenomenon from laminar to turbulent boundary layer is very complex and depends on many parameters.

By any way, following also a Schlichting simple method, this transition is assumed to exist when the difference between the Reynolds number based on the momentum thickness, R_θ , and that based on the momentum thickness at the instability point, $(R_\theta)_{inst}$, in relation to

$$m = \frac{1}{s - s_{inst}} \int_{s_{inst}}^{s} \frac{\theta^2}{\nu} \frac{dU_e}{ds} ds \qquad (8)$$

results in the upper side of the curve in fig. 5.

Fig. 4 - Laminar instability criterion.
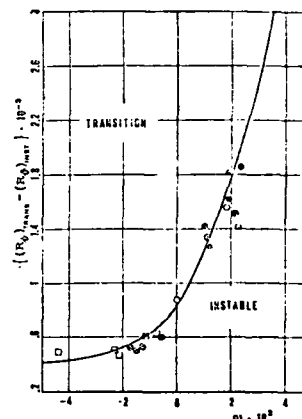
Fig. 5 - Transition criterion.

As known at the transition point the displacement thickness decrease. Here its value is computed assuming the momentum thickness continuity and the boundary layer thickness equilibrium.

3.3 - Turbulent boundary layer

After Smith [10] who has examinate 5 turbulent boundary layer methods, the better is that of Truckendrodt (see also pages 574 - 579 of Ref. [9]).

After Scholz [3] one of the best engineering turbulent boundary layer is that of Head's entrainment method [18]. This method has also been applied to interference airfoils [12].

Therefore the turbulent boundary layer is assumed to be represented by the integral momentum equation and Head's entrainment equation which, respectively, are

$$\left. \begin{aligned} \frac{d\theta}{ds} &= \frac{C_f}{2} - (2 + H) \frac{\theta}{U_e} \frac{dU_e}{ds} \\[2mm] \frac{d(\theta H^*)}{ds} &= F(H^*) - \frac{\theta H^*}{U_e} \frac{dU_e}{ds} \end{aligned} \right\} \qquad (9)$$

with

$$\left. \begin{aligned} H^* &= \frac{\delta - \delta^*}{\theta} = 3.3 + 1.535 \, (H - 0.7)^{-2.715} \\[2mm] F(H^*) &= 0.0306 \, (H^* - 3)^{-0.653} \end{aligned} \right\} \qquad (10)$$

and with

$$\left. \begin{aligned} C_f &= 0.246 \cdot 10^{-0.678\,H} \, R_\theta^{\,-0.268} \\[2mm] R_\theta &= U_e \, \theta \, / \, \nu \end{aligned} \right\} \qquad (11)$$

the Ludwieg - Tillman relation of the local skin-friction coefficient.

3.4 - Separation and wake

Laminar separation is assumed to occur when during the laminar boundary layer computation results $C_f = 0$.

By experimental investigations of other authors it is known (see, i.e., [19, 20]) that if the Reynolds number is greater than a critical value, following a laminar separation the boundary layer may reattach immediately or after a separated flow region, that is a bubble, and continue to flow downstream as turbulent.

Here this phenomenon has also been applied, considering coincident the laminar separation and the reattach_d points.

In turbulent boundary layer the separation point is more difficult to be fixed. Many authors correlate such point to the shape factor value, H. In this paper it is assumed the criterion of Simpson [21]. Following this criterion it is

$$H_{SEP} = 2 H^*/(H^* - 1) \qquad (12)$$

Therefore with the assumed Head relation between H^* and H , equation (10 - a), results

$$H_{SEP} \simeq 2.8 \qquad (13)$$

From the separated point to the trailing edge, the shape factor, H , is assumed to be frozen at the costant value H_{SEP}. In this case it is also assumed $C_f = 0$. So, because it is known that the pressure remain constant in the flow separated region, from the equation (9 - a) results

$$\theta(s) = \theta_{SEP} \qquad (14)$$

At the trailing edge the boundary layers coming from the upper and lower airfoil surfaces, are mixed and flow donwnstream as a viscous wake.

In the present method, the wakes of the cascade airfoil are modeled by the same turbulent boundary layer representation of Head.

4 - INVISCID FLOW PERTURBATION DUE TO VISCOUS EFFECTS

The effect of the boundary layer displacement thickness, δ^*, around the cascade airfoils is perturbing the inviscid flow which exists if this boundary layer is assent.

At least there are two simple methods of defining, iteratively, the perturbed inviscid flow: the displacement surface method and the surface transpiration method.

In the first method the airfoil countour and, some times, its wake thickness are changed by summing the displacement thickness which results from the previous inviscid calculation. So that the inviscid calculation is repeated to this new fictitious contour.

In the second method, along the airfoil contour and its wake mean streamline, a normal velocity is assumed to give the displacement thickness perturbation effect to the inviscid flow around the real contour.

Many numerical applications of other authors to isolate and interference airfoils (see, i.e. [14 - 16]) confirm the quasi - insensibility of the obtained results with the first or with the second method used. But in automatical calculation the second method needs much less computing time. Therefore the above second method is here used.

Because a distributed normal velocity to a discontinuity contour is identical to a sources distribution along this contour, on the cascade airfoil surfaces and wakes a continuous distribution of sources q(s) , is joint to the γ(s) vorticity (see fig. 1) as it is illustrate in fig. 6.
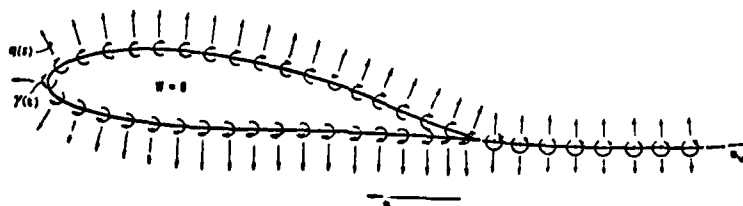
Fig. 6 - Viscid representation of the local flow velocity on the
airfoil contour and wake.

Following therefore the schematization made for the inviscid solution, on every j-th segment it is assumed a linear variation of the sources between the values Q_j and Q_{j+1} that they assume on the segment nodes.

The intensity of the sources on the j-th polygonal node, fig. 2, is

$$Q_j = d(U_e \, \delta^*)_j / ds \tag{14}$$

where U_e is the component of the flow velocity, parallel to the airfoil contour and on its boundary layer edge.

With this distribution of sources the incremental complex conjugate velocity, induced by the cascade segments j in a point ζ, fig. 3, is

$$\Delta w_j^* (\zeta) = \frac{1}{2\pi} \left[Q_j (I_j^0 - I_j^1) + Q_{j+1} I_j^1 \right] \tag{15}$$

with the I_j^0 and I_j^1 expressed by the (2).

Consequently the (5) is modified to the

$$|W_i| = |W_o + \sum_{j=1}^{N} \Delta w_j + \sum_{j=1}^{N} \Delta w_j^* | \tag{16}$$

Besides, the wake mean streamline of each cascade's airfoil is assumed to flow from the airfoil trailing edge and it is represented by consecutive linear segments.
On each of these segments, linear distributions of vortices and sources, as on the airfoil contour, are considered.

The source intensities

$$q_w(s_w) = d (U_e \, \delta^*)_w / ds_w \tag{17}$$

represent the viscous wake displacement thickness effects.

The vortex intensities

$$\gamma_w(s_w) = - k_w \, U_{ew} \, (\delta_w^* + \theta_w) \tag{18}$$

with k_w the wake mean streamline curvature, represent the viscous curvature effects.

For the imposition (6) and because at the trailing edge k_w may be very high, along each airfoil contour it is distributed the incremental vorticity

$$\Delta\gamma(s) = \left[1 - 2\sqrt{\frac{s}{\ell_t}} + \frac{s}{\ell_t} \right] \Delta\Gamma_\ell + \left[2 - 2\sqrt{1 - \frac{s}{\ell_t}} - \frac{s}{\ell_t} \right] \Delta\Gamma_u \tag{19}$$

with ℓ_t the total length airfoil contour and with the quantities $\Delta\Gamma_\ell$ and $\Delta\Gamma_u$ to verify: the equation (18) at the airfoil trailing edges and the imposition that the pressures on the upper and lower boundary edges at the airfoil trailing edges are the same.

Therefore the above distributions induce a velocity which is summed to that in equation (16).

5 - COMPUTING ALGORITHM

An iterative procedure of the inviscid flow perturbation due to the viscous effects is applied to provide the convergence of the boundary layer displacement thickness as follow:

a) the inviscid potential flow solution is obtained;

b) the strealines flowing from the cascade airfoil trailing edges are defined;

c) by means of the boundary layer solution, described in the preceding pages, the displacement thickness is computed;

d) the sources along the airfoil surfaces and the sources and vortices along the wakes are defined;

e) the unknown $\Delta\Gamma_\ell$ and $\Delta\Gamma_u$ are computed and the incremental vorticity expresed by the relation (19) is considered;

f) the unknown vortex intensities Γ_j are computed assuming the local flow in the middle of each j-th segment to have on this a normal component equal to $(Q_j + Q_{j+1})/2$;

g) the above procedure is repeated from voice c), until a prescripted convergence of the displacement thickness δ^* is reached.

To accelerate the convergence it has been found useful the relaxation to the displacement thickness

$$\delta^* = \omega\,\delta^*_{new} + (1 - \omega)\,\delta^*_{old}$$
$$\text{with } \omega \leqslant 1 \tag{20}$$

Further, to decrease the computing time the following expedients have been used:

a) the system of the N+1 linear equations Γ_j is solved inverting the influence matrix only the first time by standard Gauss - Jordan method;

b) the numerical integration of equation (2 - b) is provided by simple trapezoidal rule. During this integration when the induced point belongs to the inducent segment, the equation (2 - b) is substituted by the relation [1]

$$I^1_i = 2\varepsilon\frac{|\sigma|}{\sigma}\left\{\left(\frac{\pi\varepsilon\sigma}{3\,d}\right)^2\left[\left(\frac{\pi\varepsilon\sigma}{5\,d}\right)^2 - 1\right] - 1\right\} - 2\frac{\pi\,|\sigma|}{d}\int_\varepsilon^{1/2}\chi\,\mathrm{cth}(\frac{\pi\sigma}{d})\,d\chi$$
$$\text{with } 0 < \varepsilon \leqslant 10^{-2} \tag{21}$$

c) the numerical integration of the differential equations system (9) is obtained by the first order Euler predictor - corrector technique;

d) in the δ^* calculation, far from the flow separated points, the velocities U_e are assumed to be those on the airfoil surfaces;

e) the curvature effects of the airfoil surfaces are neglected.

6 - CASCADE AERODYNAMIC CHARACTERISTICS

When the convergence is reached the flow field in the cascade airfoils is everywhere known.

In the infinite upstream and in the infinite downstream of the cascade, the complex conjugate velocities result

$$W_1 = W_o + \frac{\Gamma_{TOT}}{2\,d\,i} - \frac{Q_{TOT}}{2\,d}$$
$$W_{2P} = W_o - \frac{\Gamma_{TOT}}{2\,d\,i} + \frac{Q_{TOT}}{2\,d} \tag{22}$$

with Γ_{TOT} and Q_{TOT} the integrals of the vortices and sources along the airfoil contour and wake.

Far downstream the flow is completely mixed. Therefore it results [3, 22, 23]

$$\beta_2 = \mathrm{ctg}^{-1}\left\{\frac{1 - A_w - B_w}{(1 - A_w)^2}\,\mathrm{ctg}\,\beta_{2P}\right\}$$

$$|W_2| = |W_1|\,\sin\beta_1\sqrt{1 + \mathrm{ctg}^2\beta_2}$$

$$C_{p2} = 1 - \left[\frac{\sin\beta_1}{\sin\beta_{2P}}\frac{1}{1 - A_w}\right]^2 + 2\sin^2\beta_1\left[\frac{1 - A_w - B_w}{(1 - A_w)^2} - 1\right]$$

$$\zeta_v = \frac{P^o_1 - P^o_2}{\frac{1}{2}\rho|W_1|^2} = 1 - \left[\frac{|W_2|}{|W_1|}\right]^2 - C_{p2} \tag{23}$$

12-8

with

$$A_w = (\delta_w^*)_{TE} / (d \sin \beta_{2P})$$

$$B_w = (\theta_w)_{TE} / (d \sin \beta_{2P}) \qquad (24)$$

and β_1, β_{2P} and β_2 the angles represented in fig. 7.
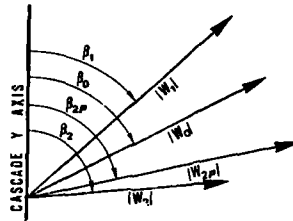
Fig. 7 - Asymptotical flow directions.

The pressure coefficient along the airfoil contours is calculated by the relation

$$C_p = \frac{p(s) - p_1}{\frac{1}{2} \rho |W_1|^2} = 1 - \left[\frac{|W_e|}{|W_1|}\right]^2 \qquad (25)$$

The forces and moments on each airfoil are obtained integrating the (25) on the airfoil contour.

7 - APPLICATIONS AND RESULTS COMPARISON

In fig. 8 there are presented three inviscid solutions obtained by the method of Ref. [1] which is the the base of the present developed one. Those solutions where reached describing the cascade airfoils by N = 50 segments. As can be seen, those inviscid solutions are better than an other theoretical one but do not agree very well with the experimental values near the airfoil trailing edges where the boundary layers are thick.

Applicating the present method to the same cascade NACA 8410 airfoils, with the same schematization, N = 50 and the wake main streamline descripted by 15 straight elements, in figures, respectively, 9, 10 and 11 it may be denoted: the importance of a better simulation of the cascade in a real viscous flow and the present method accuracy.
In such figures and the following there are also represented the main cascade characteristics which may be computed by this method. Unfortunately it has not been possible a comparison of the boundary layer obtained characteristics and so the accuracy of the method has been conducted only through comparisons of the predicted pressure coefficient values along the cascade airfoil contours.

At least, in fig. 12 it is represented the solution of the above cascade airfoils in separated flow near the trailing edges. The comparison of those obtained results with experimental values continuous to be satisfactory.

In figures 13 and 14 there are illustrated the obtained results of a cascade NACA 0010 airfoils. The comparison of such results with experimental values confirm, again, the validity of the present method.

The above results are obtained with a program written in FORTRAN IV for an IBM 360/168 series machine.

The convergence is reached after less than 4 cycles.

The running times are: 1.67 seconds for the beginning of the calculations; 8.43 seconds for each iterative cycle and 18.97 seconds for the computing cascade characteristics.

8 - CONCLUSIONS

The present method is an efficient computable one, specially for attached flow, which provides in short computing time, many cascade airfoil characteristics in incompressible viscous flow.

The computing algorithm allows to modify or substitute any single computing step method without chang
ing the main program philosophy structure. Therefor it is possible to use this program for better or fur-
ther cascade airfoils physical phenomena simulation.

The ratio computing time / number of cases to study, decreases as this number of cases, that is the
considered cascade airfoils operational conditions, increase.

Although the results of the local pressure coefficients along the airfoil contours reasonably agree
with the experimental ones and confirm the method validity, they may be more optimizated. Also, further
comparisons between the obtained results and the experimental values of the airfoils' boundary layer and
wake characteristics, may be useful for optimizing the boundary layer integral methods.

9 - REFERENCES

[1] Psarudakis P.: "Metodo di calcolo aerodinamico bidimensionale di schiere di profili a flusso incom-
primibile", 37° Congresso Nazionale della Associazione Termotecnica Italiana. Padova, September 27 -
October 1, 1982 - Italy.

[2] Akay H. U. - Ecer A.: "Finite - Element Analysis of Transonic Flows in Highly Staggered Cascades",
AIAA J., Vol. 20, No. 3, March 1982.

[3] Scholz N.: "Aerodynamics of Cascades", AGARD - AG - 220, 1977.

[4] Schlichting H.: "Berechnung der reibungslosen inkompressiblen Strömung für ein vorgegebeness ebenes
Schaufelgitter", VDI - Forschungsheft 447, Vol. 21, 1955.

[5] Hansen A. G. - Johner P. L.: "A Numerical Procedure for Designing Blades with Prescribed Velocity
Distribution in Incompressible Potential Flow", NACA TN 2101, 1950.

[6] Taylor C. - Hood P.:"A Numerical Solution of the Navier - Stokes equations using the finite element
technique", Computer and Fluid, 1, 73 - 100, 1973.

[7] Peyret R. - Viviand H.: "Computation of Viscous Compressible Flows Based on the Navier - Stokes
Equations", AGARD - AG - 212, 1975.

[8] Brune G. W. - Rubbert P. E. - Forester _. K.: "The Analysis of Flow Fields with Separation by Numer-
ical Matching", AGARD - CP - 168, 1975.

[9] Schlichting H.: "Boundary Layer Theory", 6 - th ed., New York, McGraw - Hill, 1968.

[10] Smith D. J. L. : "Turbulent Boundary Layer Theory and its Application to Blade Profile Design",
A.R.C., C.P., No. 868, 1966.

[11] Gilmer B. R. - Bristow D. R.: "Analysis of Stalled Airfoils by Simultaneous Perturbations to Viscous
and Inviscid Equations", AIAA J., Vol. 20, No. 9, September 1982.

[12] Seebohm T. - Newman B. G.: "A Numerical Method for Calculating Viscous Flow Round Multiple - Section
Airfoils", The Aeronautical Quarterly, Vol. XXVI, August 1975.

[13] Arieli R. - Murphy J. D.: " Pseudo - Direct Solution to the Boundary - Layer Equations for Separated
Flow", AIAA J., Vol. 18, No. 8, August 1980.

[14] "Computation of Viscous - Inviscid Interactions", AGARD - CP - 291, 1981.

[15] Bhateley I. C. - Bradley R. C.: "A Simplified Mathematical Model For the Analysis of Multi - Element
Airfoils Near Stall", AGARD - CP - 102, 1972.

[16] Jacob K. - Steinbach D.: "A Method for Prediction of Lift for Multi - Element Airfoil Systems with
Separation", AGARD - CP - 143, 1974.

[17] Wu Chung - Hua: "A General Theory of Three - Dimensional Flow in Subsonic and Supersonic Turboma-
chines of Axial -, Radial -, and Mixed - Flow Types", NACA TN 2604.

[18] Head M. R.: "Entrainment in the Turbulent Boundary Layer", A.R.C., R.M. 3152, 1958.

[19] Dunham J.: "Predictions of Boundary Layer Transition on Turbomachinery Blades", AGARD - AG - 164,
1972.

[20] Seyb N. J.: "The Role of Boundary Layers in Axial Flow Turbomachines and Prediction of Their Ef-
fects", AGARD - AG - 164, 1972.

[21] Simpson R. L.: "Characteristics of a Separating Incompressible Turbulent Boundary Layer", AGARD - CP
- 168, 1975.

[22] Lieblein S. - Roundebush W. H.: "Theoretical Loss Relations for Low - Speed Two - Dimensional Cascade
Flow", NACA TN 3662, 1956.

[23] Lieblein S. - Roundebush W. H.: "Low - Speed Wake Characteristics of Two - Dimensional Cascade and
Isolated Airfoil Sections", NACA TN 3771, 1956.
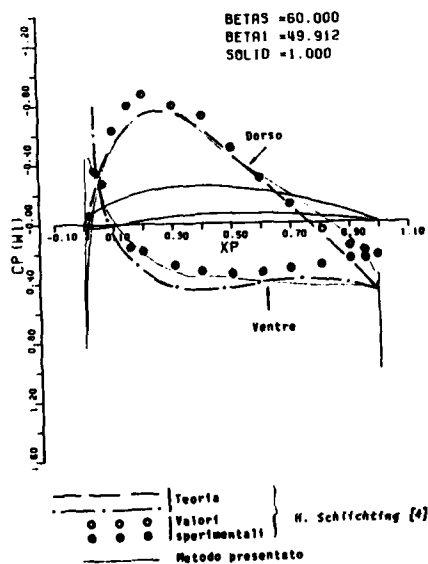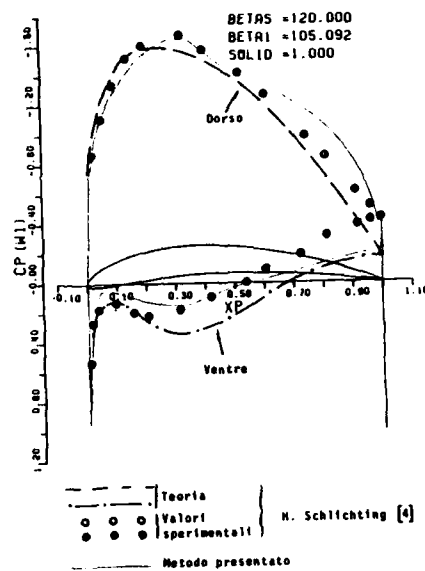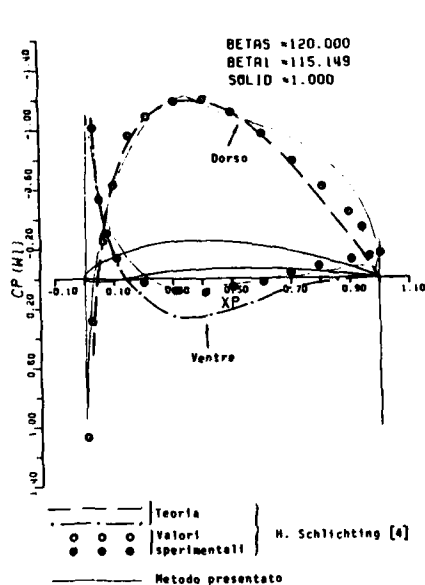
Fig. 8 - Inviscid solutions of cascades NACA 8410 airfoil, taken from Ref. [1].
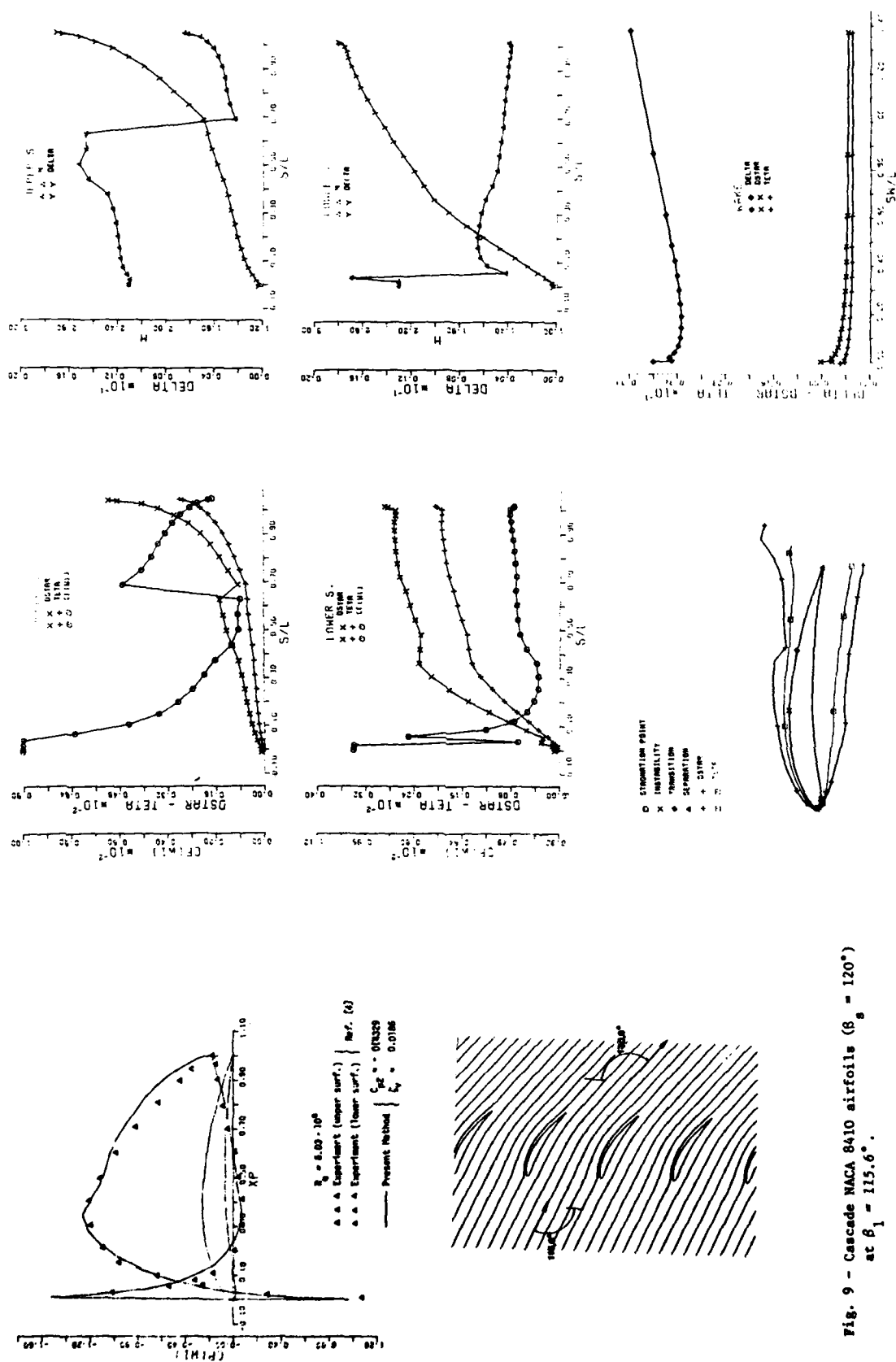
Fig. 9 — Cascade NACA 8410 airfoils ($\beta_s = 120°$) at $\beta_1 = 115.6°$.
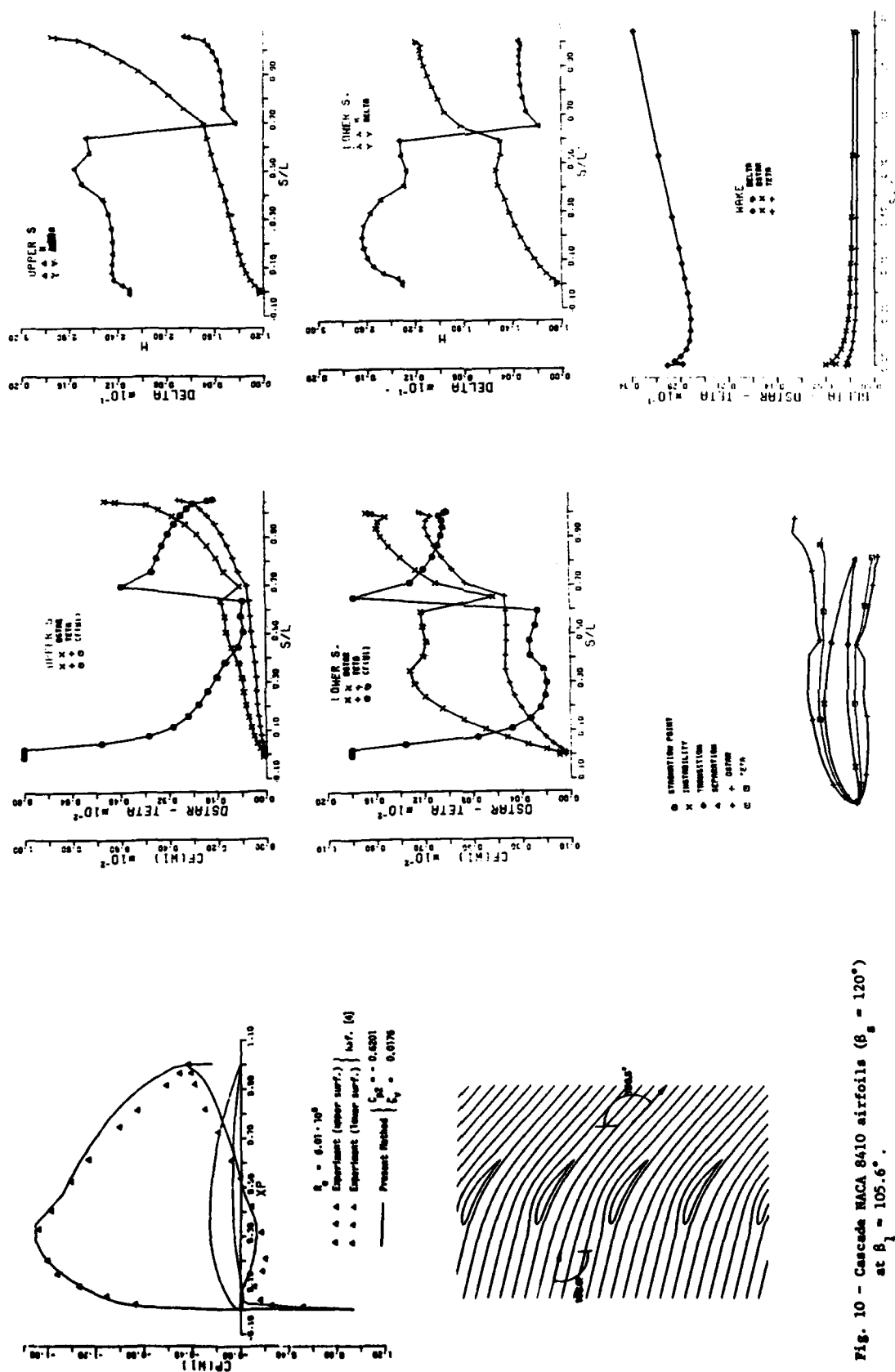
Fig. 10 — Cascade NACA 8410 airfoils ($\beta_s = 120°$) at $\beta_1 = 105.6°$.
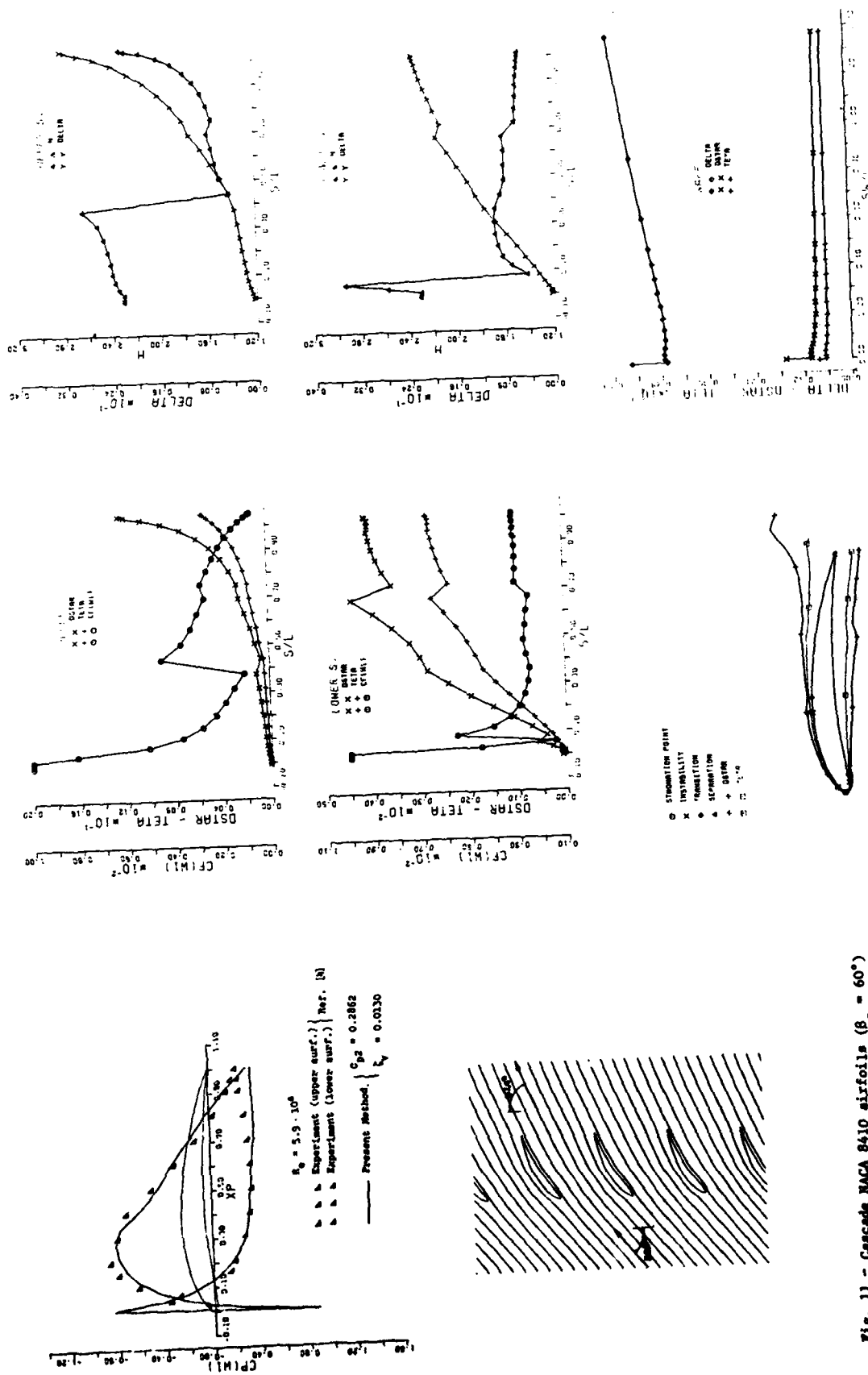
Fig. 11 - Cascade NACA 8410 airfoils ($\beta_g = 60°$) at $\beta_1 = 50.6°$.
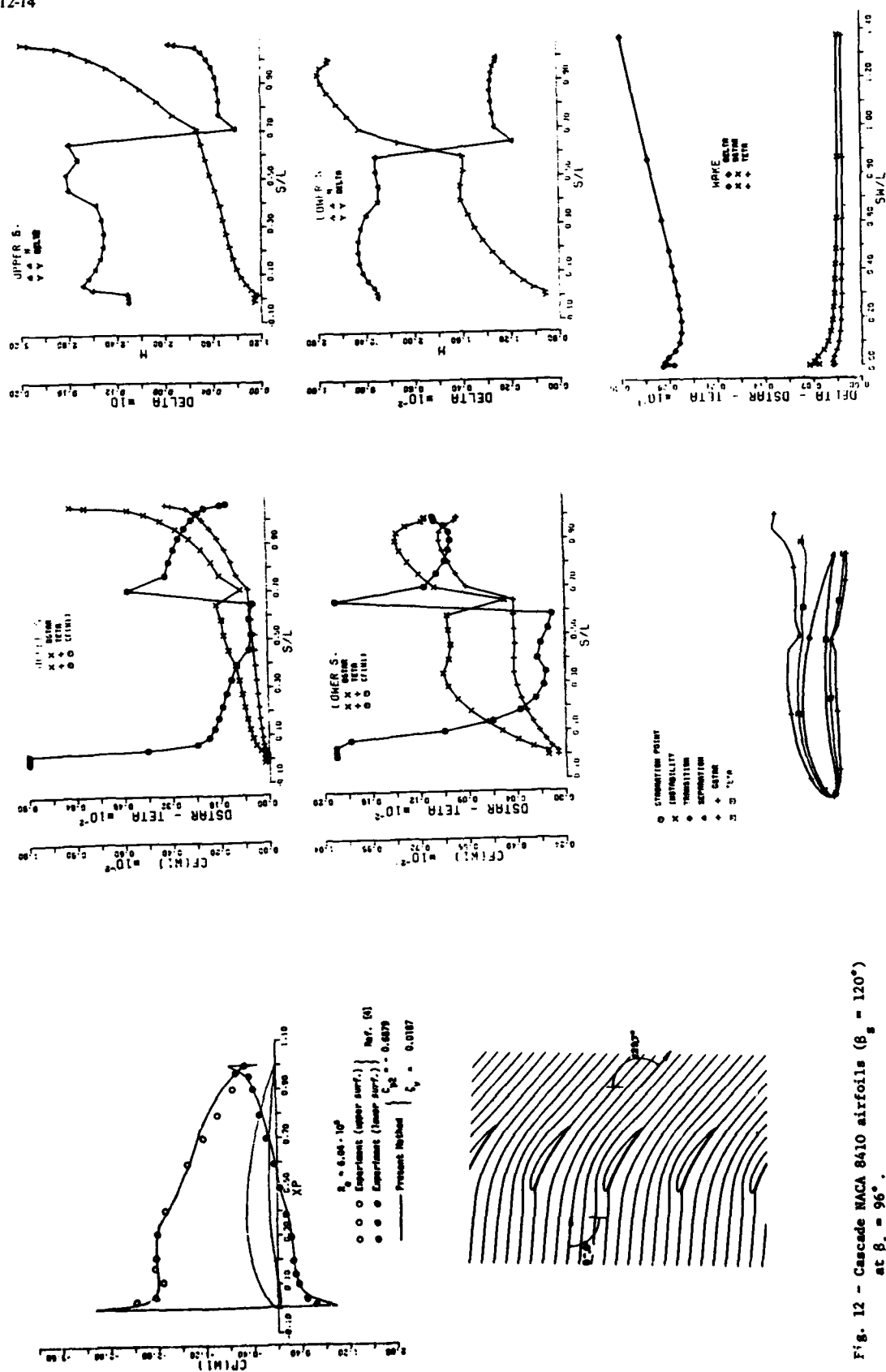
Fig. 12 — Cascade NACA 8410 airfoils ($\beta_g = 120°$) at $\beta_1 = 96°$.
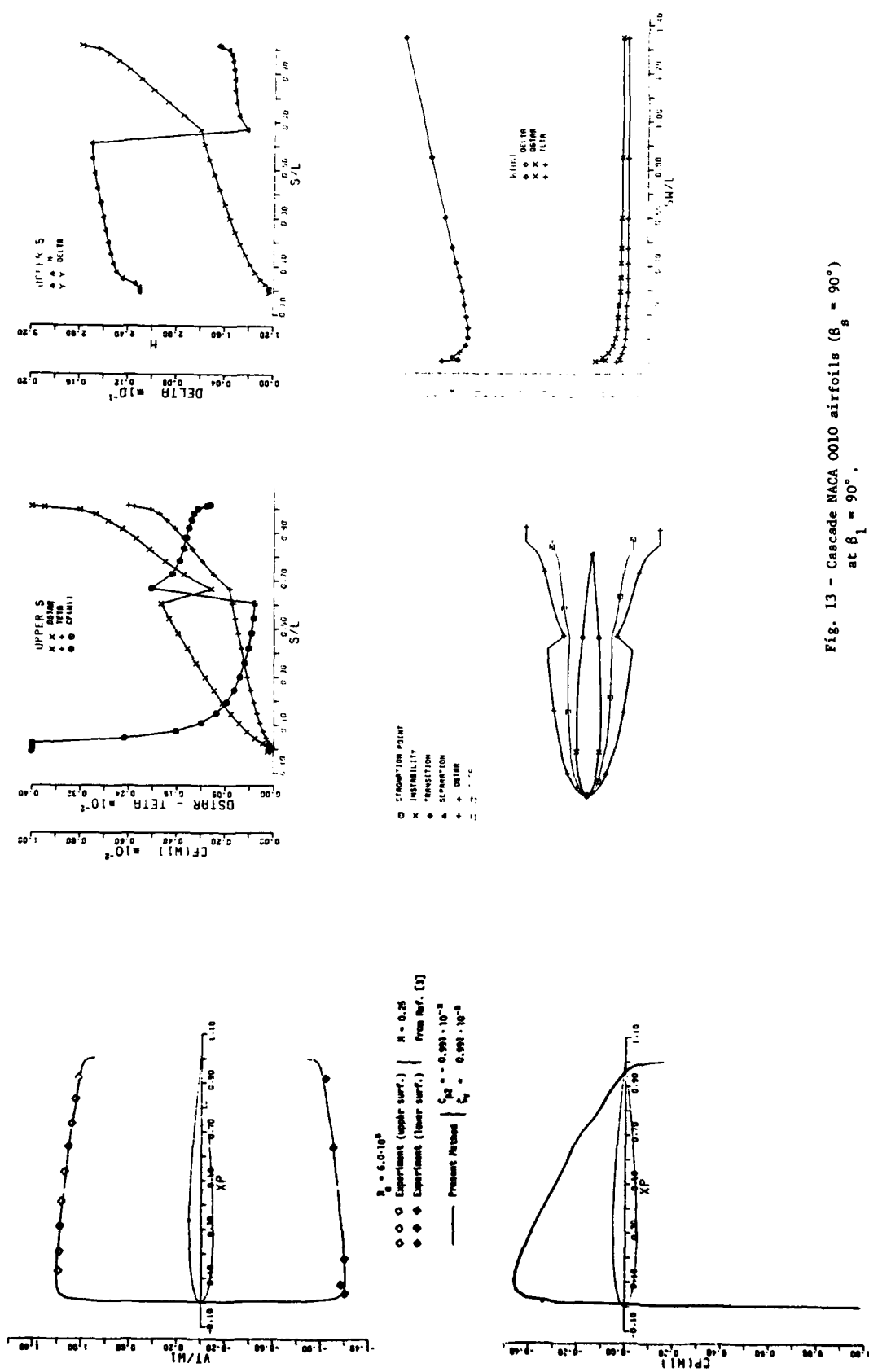
Fig. 13 - Cascade NACA 0010 airfoils (β_g = 90°)
at β_1 = 90°.
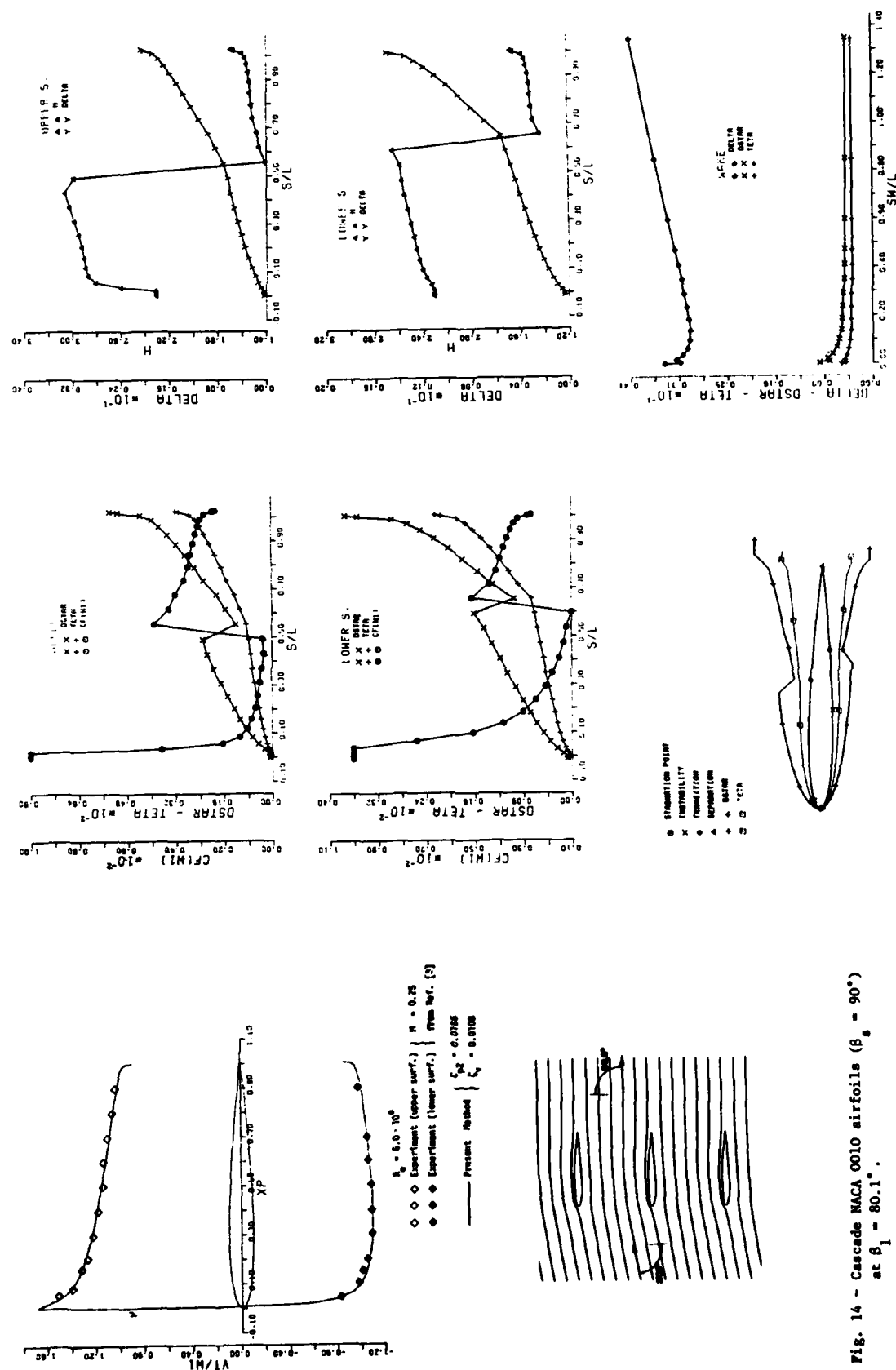
Fig. 14 - Cascade NACA 0010 airfoils ($\beta_s = 90°$) at $\beta_1 = 80.1°$.

DISCUSSION

Ph.Ramette, Fr

To what extent can the curvature of the airfoils be neglected, especially in the case of turbine airfoils for which the curvature is important?

Author's Reply

The airfoil curvature is high near the airfoil leading edge. In that region the boundary layer is very thin. Therefore, along the airfoil contour its curvature effect may be neglected.

At the trailing edge of the cascade airfoils the wake curvatures are very high and at the same time the boundary layer at that point is also high. So the wake curvature of the cascade airfoils cannot be neglected. This is the reason for using the incremental vorticity represented by Equation (19) of my paper.

Also, as it is written in my paper, the computing algorithm allows the modification or substitution of any single computing step method without changing the main program philosophy structure. Therefore, it is possible to see the airfoil curvature effect on the development boundary layer and on the pressure coefficient, which, as shown in the paper, agree well with the experimental values, even though the effect of the airfoil contour curvature has been neglected.

H-J.Lichtfuss, Ge

You have shown some remarkable agreement between computation and experiment. My question is: Have you also calculated the overall loss and the outlet flow angle and have you compared them to experimental values?

Author's Reply

Yes. In all my calculations and in all the results I illustrated in my paper, you can find the values of the outlet flow angle, β_2, and the total-pressure-loss coefficient, ζ_v. I have not been able to make as good comparisons as those values made to the pressure coefficients. I only can say that the total-pressure-loss coefficients agree with some results presented by Schlichting and Scholz in References, respectively [9] and [3] of my paper.

NUMERICAL SIMULATION OF STALLING FLOWS
BY AN INTEGRAL EQUATION METHOD

by

R. I. Lewis

Professor of Fluid Mechanics and Thermodynamics
Department of Mechanical Engineering
University of Newcastle Upon Tyne

and

D.T.C.Porthouse

Research Officer
Department of Mechanical Engineering
University of Newcastle Upon Tyne

SUMMARY

An integral equation method is presented for solution of the Navier Stokes equations for stalling aerofoil, cascade or bluff body flows. Vorticity created at the aerofoil or body surface at each time step of a numerical procedure, is diffused into the mainstream and convected by the local velocity vector. Viscous diffusion is simulated by a model akin to Brownian motion whereby all shed vorticity elements are given random displacements at each time step. Solutions are shown for boundary layers, bluff bodies, aerofoils and a first attempt at a cascade.

Notation

C	Circulation	v_s	Surface velocity
C_L	Lift coefficient	$w_\infty, \hat{w}_\infty$	Velocity (and vector velocity) at infinity
C_D	Drag coefficient		
i	Integer	x, y	Cartesian coordinates
$\hat{i}$	Unit vector	$\gamma(s)$	Surface vorticity
j	Integer	$\Delta\Gamma_N$	Free vorticity element shed at Nth time step
$K(s_n, s_m)$	Coupling coefficient of surface vorticity element	Γ	Point vortex
ℓ	Aerofoil chord	ϵ	Small distance
$L(N, m)$	Coupling coefficient of free vorticity element shed at Nth time step	θ	Profile slope, polar coordinate
		ν	Kinematic viscosity
M, n	Integers	ρ	Density
M_i	Random number	$\hat{\omega}$	Vorticity vector
N, n	Integers		
N_i	Random number		
p	Static pressure, probability function	**Suffixes**	
p_o	Stagnation pressure	a	At time t
P	Probability function	b	At time t + Δt
P_i	Random number	i	
$\hat{q}$	Velocity vector	j	Integers
Q_i	Random number	n	
r, θ	Polar coordinates	o	Stagnation conditions
Re	Reynolds Number	p	Sharp edged separation point
s	Distance along a surface	t	At time t
t	Time	∞	At infinity
Δt	Finite time step		
u, v	Velocity components in (x,y) plane		
$U(s_m, s_n)$, $V(s_m, s_n)$	Velocity components at s_m due to a unit vortex at s_n		
u_{aN}, v_{aN}	Drift velocity components.		
$\hat{v}_a, \hat{v}_b$	Drift velocity vectors		

1.0   Introduction

Since the early days of aviation it has been well understood that vortex motions exercise a crucial influence upon the behaviour of aerofoils or other rotor-dynamic devices. Traditionally vortex motions within the boundary layers have been regarded as fundamentally different in origin and nature from vortex motions associated with the fluid machine taken as a whole including, for example, bound vorticity giving rise to lift and trailing vorticity systems associated with form drag. In the last two decades these separate branches of study have advanced possibly to their individual limits and as far as it may be reasonable to take them, bearing in mind that in reality we may not be entitled in many cases to consider them in isolation. As will appear from this paper, all vortex motions originate from the same source.

During this same period, encouraged by rapid developments in computing, many research workers have therefore applied themselves to the numerical analysis of complete flows by appealing directly to the Navier Stokes equations which in vector form may be expressed

$$\frac{\partial \hat{q}}{\partial t} + \hat{q}.\nabla\hat{q} = - \frac{\nabla p}{\rho} + \nu\nabla^2\hat{q} \qquad (1)$$

Reading from left to right we are reminded that unsteadiness and convections in the flow are inextricably bound up with pressure gradients and shear stresses brought about through viscosity. A form more suitable to the present application is as follows.

$$\frac{\partial \hat{q}}{\partial t} - \hat{q} \times \hat{\omega} = - \frac{\nabla p_o}{\rho} + \nu\nabla^2\hat{q} \qquad (2)$$

Most attempts to solve these equations have grown from the first generation computer finite difference or other field mesh schemes, suitable for treating flows within closed regions such as ducts. Only recently have there been major attempts to solve the Navier Stokes equations for predominantly external flows with particular interest in separated flow regimes. In most of these studies of bluff body or stalling flows viscous diffusion has been ignored, requiring therefore human specification of the separation point locations and criteria. Furthermore, so far as the authors are aware, work in this field has been limited to bodies of restricted shape, such as circular cylinders, flat plates and wedges, for which simple classical models can be devised. Mair and Maull[1] reported on much of this work as surveyed in 1971 by 'Euromech 17' in relation to vortex shedding from bluff bodies. Bearman and Graham[2] more recently reported on 'Euromech 119' which updated this review to 1979. Notable too are the contributions of Chorin[3][4] who developed almost identical techniques to Porthouse[5] for simulation of viscous diffusion, a method similar to Brownian motion which will be explained here in Appendix I.

Lewis[6] established an integral equation method for inviscid separated flows past bodies of two-dimensional but otherwise arbitrary shape, reviewed in section (2.0). The major special contributions of this and the authors' subsequent work as compared with other workers have been (a) to avoid the restrictions of classical boundary modelling and to maintain the maximum generality possible and (b) to account for all terms in the Navier Stokes equations including both the unsteady and viscous terms. In other words, a direct simulation of real (but two-dimensional) flows for arbitrary body shapes has been attempted. As explained in reference (7) and section (4.2), a further important step in our work has been the abandonment of all separation criterion to permit the flow to determine this directly. Although the computations, which will be illustrated later in the paper, are convincing qualitatively and accurate to the first order quantitively, the authors at this stage claim only to have laid the foundations of a generalised method. The future, to a large extent, lies with further refinement but, more important than that, with the development of computers and high speed graphical presentation.

2.0   The production of vorticity

The dichotomy between boundary layer and "potential" flows mentioned in the Introduction as a device for simplifying complex flows, leads to confusion regarding the origin and nature of vorticity in fluid flows. For example classical potential flow modelling requires the invention of the concept of bound vorticity which in reality is impossible on a non-rotating body, since the surface velocity in a real flow is zero at all points. Also it is commonly believed that boundary layer vorticity is generated by viscous shear stresses whereas in reality it is created by the mainstream or potential flow, the action of viscosity being merely that of diffusion of the vorticity.

These points, which are fundamental to the present method, are best illustrated by consideration of an inviscid potential flow in more detail. Martensen's[8] surface vorticity method offers the most direct model of potential flows since it describes precisely the real fluid mechanisms involved as illustrated by Figure (1). As we know, the real flow close to a wall consists of a vorticity (boundary) layer sandwiched between the surface and the outer flow. In passing through this region along ss' the local velocity changes from zero immediately adjacent to the wall to the value vs of the potential flow at the edge of the layer, Figure (1)a. The surface vorticity inviscid potential flow method, Figure (1)b, adopts a direct simulation of this in which the boundary layer is reduced to an infinitely thin vorticity sheet of strength γ(s) in contact with the wall. In these circumstances the velocity along ss' changes discontinuously from zero at the wall to the value vs = γ(s) just outside the vorticity sheet.

(a) Boundary layer in a real flow

(b) Surface vorticity model

(c) Vorticity element

FIGURE 1.   Surface Vorticity Modelling
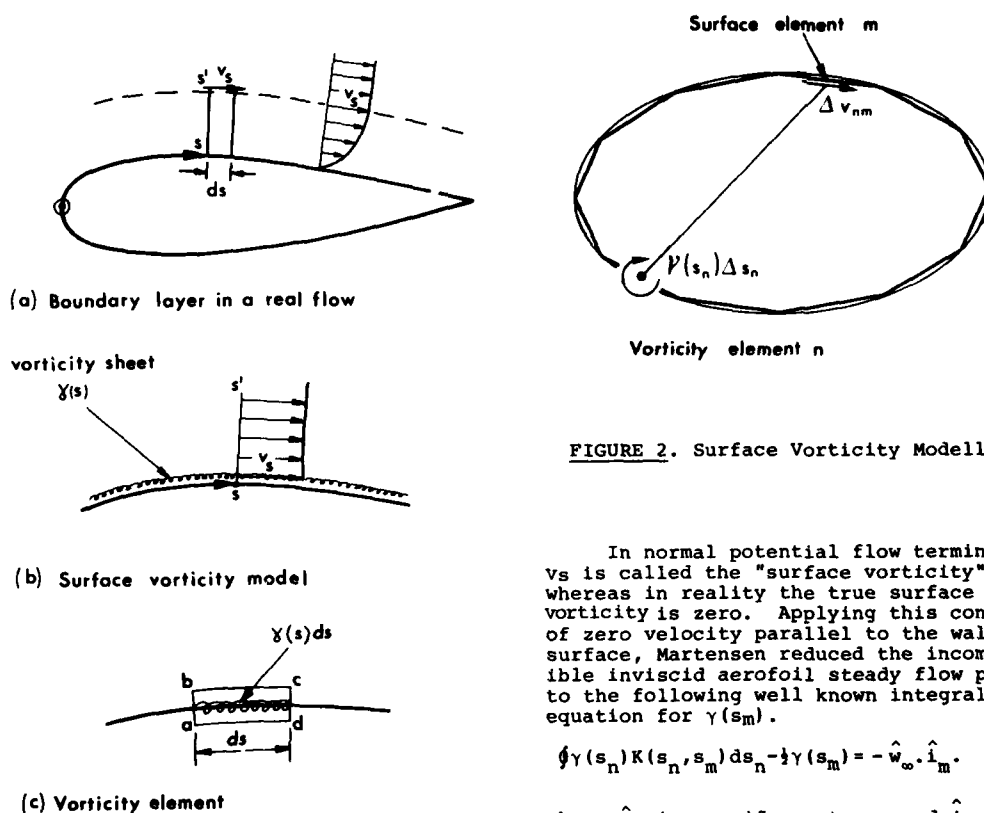
FIGURE 2. Surface Vorticity Modelling

In normal potential flow terminology Vs is called the "surface vorticity" whereas in reality the true surface vorticity is zero. Applying this condition of zero velocity parallel to the wall surface, Martensen reduced the incompressible inviscid aerofoil steady flow problem to the following well known integral equation for $\gamma(s_m)$.

$$\oint \gamma(s_n) K(s_n,s_m) ds_n - \tfrac{1}{2}\gamma(s_m) = -\hat{w}_\infty \cdot \hat{i}_m. \qquad (3)$$

where $\hat{w}_\infty$ is a uniform stream and $\hat{i}_m$ is a unit vector parallel to the surface at s_m.

$K(s_n,s_m)$ is a coupling coefficient which represents the surface velocity induced at s_m due to a unit vortex located at s_n and is given by

$$K(s_n,s_m) = \frac{1}{2\pi}\left\{\frac{-(x_m-x_n)(dy_m/ds)+(y_m-y_n)(dx_m/ds)}{(x_m-x_n)^2 + (y_m-y_n)^2}\right\} \qquad (4)$$

Fortunately equation (3) is readily soluble as a set of linear equations by the introduction of the trapezoidal rule, whereupon we have

$$\sum_{n=1}^{M} \gamma(s_n) K(s_n,s_m)\Delta s_n = - w_\infty\left\{\frac{dx_m}{ds}\cos\alpha_\infty + \frac{dy_m}{ds}\sin\alpha_\infty\right\} \qquad (5)$$

As illustrated by Figure (2), this is achieved by dividing the body profile into M discrete elements of length Δs_n and treating the flow as that induced by discrete vortex elements of strength $\gamma(s_n)\Delta s_n$ located at the centre of each element. The coupling coefficient $K(s_m,s_m)$, which represents the velocity parallel to the wall at m due to element m has the special form, as shown by Lewis[6],

$$K(s_m,s_m) = - \tfrac{1}{2} + \frac{\Delta s_m}{4\pi r_m} \qquad (6)$$

where the local profile radius of curvature r_m may be evaluated from the slopes of neighbouring elements as follows.

$$\frac{1}{r_m} = \frac{\Delta\theta_m}{\Delta s_m} = - \frac{1}{2\Delta s_m}\left\{\frac{dy_{m-1}}{dx} - \frac{dy_{m+1}}{dx}\right\} \qquad (7)$$

Without further elaboration of the subsequent numerical reduction procedures, sufficient has been said to illustrate this powerful numerical method which directly simulates vorticity production in potential flows. In steady flow v_s and thus $\gamma(s)$ is bound to the surface. In reality however the surface vorticity sheet drifts along the surface like the real boundary layer, but in this case with velocity $\gamma(s)/2$. Since

$\gamma(s)$ varies with s it is thus clear that a mechanism exists, even in the absence of viscosity, for the production or destruction of vorticity along the body surface. This mechanism is revealed if we establish the rate of vorticity creation at s as follows. If we define $d\gamma$ as the net vorticity per unit length created at point s in time dt, then the net vorticity flux through abcd, Figure (1)c, will be

$$d\gamma ds = \{\tfrac{1}{2}(v_s+dv_s)(\gamma(s)+d\gamma(s))-\tfrac{1}{2}v_s\gamma(s)\}dt$$

Bearing in mind that $v_s = \gamma(s)$ we have finally a vorticity production equation

$$\frac{d\gamma}{dt} = \frac{d}{ds}\{\frac{v_s^2}{2}\} - \frac{1}{\rho}\frac{dp}{ds} \tag{8}$$

Thus we see that the local pressure gradient in a potential flow causes vorticity to be either created (falling pressure) or destroyed (rising pressure). In a real flow the same principle is true when applied to the bulk vorticity of the boundary layer in the strip ds. Viscosity then fulfills the function of vorticity diffusion resulting in a continuous redistribution of the vorticity created by the pressure gradients of the outer flow. Additional to this are the equally important convective motions within the viscous shear layer which also redistribute the vorticity and in some circumstances may lead to instability of the strong shear layers and ultimately to turbulent flow.

3.0 Brief outline of the numerical method for separated flows

Before proceeding with further analytical details, it would be helpful to indicate the general computing scheme adopted here for simulating bluff body or stalling flows. With reference to Figure (3) and equation (2), the strategy is to march forward in a series of small time steps Δt satisfying various terms of the Navier Stokes equations in sequence for each time step.

(i) Potential flow calculation

(ii) Vorticity shedding

(iii) Convection of all vorticity elements

(iv) Diffusion

(v) Calculation of body forces and surface pressure

(vi) Advance by time Δt
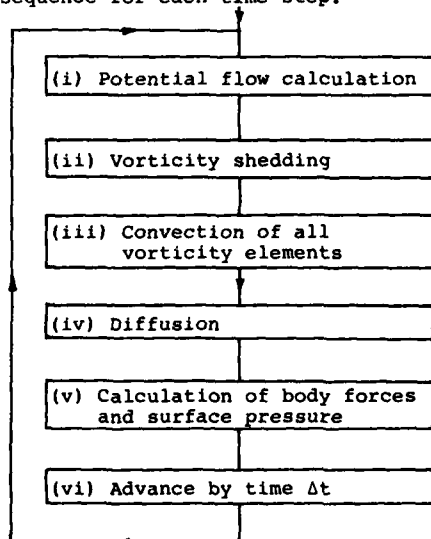
FIGURE 3. General Computational Scheme
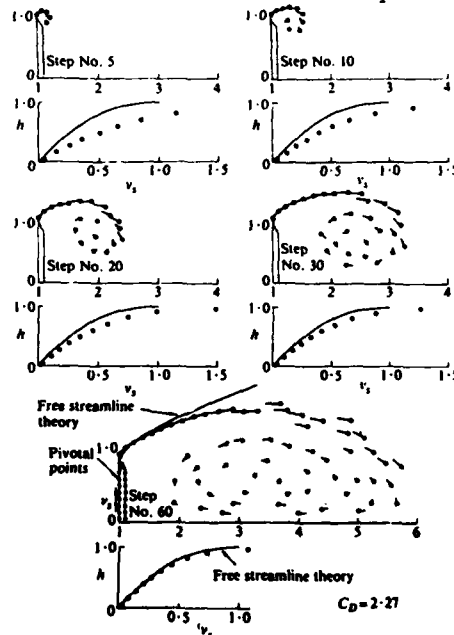
FIGURE 4. Separation from sharp-edged plate

An early example of the application of this procedure, excluding viscous diffusion, to the flow past a sharp edged plate, is given in Figure (4). By reflecting the flow below the x axis, symmetry was enforced, preventing the establishment of a vortex street. In this instance one vorticity element was shed from the sharp edge of the plate for each time step with a magnitude dependent upon the surface vorticity created close to the edge during the preceding potential flow calculation at step (i) of the computational sequence. During step (iii) each vorticity element in the field was allowed to drift with the local convective velocity, contributions to which are made by (a) the uniform stream (b) the surface vorticity on the plate and (c) all vortices already released into the flow. In Figure (4) the drift paths of each vortex are indicated in magnitude and direction by the tails which are in fact streak lines. Due to the recirculating flow to the rear of the plate the bounding streamline of the separated flow regime does not compare too closely to that of a free streamline flow apart from the region close to the plate. On the other hand the velocity on the up-stream face of the plate, which is reasonably protected from the wake effects, does progress with time towards a distribution which is in quite good agreement with free streamline theory. The predicted drag coefficient after 60 time steps was 2.27 which may be compared with an experimental value of 1.98 given by Hoerner[8].

Three particular defects were inherent in this early work as follows:

(i)   Due to the enforced symmetry and lack of viscous diffusion, no mechanisms were available for stabilising the total vorticity content of the wake which increases indefinitely. In later work, without enforced symmetry, wakes were found to break down into vortex streets thus enabling vorticity to escape downstream. Further vorticity leakage arises from viscous diffusion.
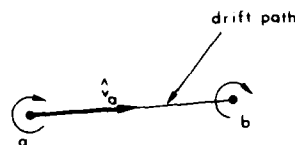
(a) drift path by forward difference a to b

(ii) The convection process adopted here involved forward marching over time step Δt from a to b, Figure (5)a, following the convection velocity $\hat{v}_a$ applicable at point a. This leads to errors which were later eliminated by means of a central differencing approach illustrated in Figure (5)b. The convection velocities $\hat{v}_b$ are recalculated for the new locations b. A revised drift path is then adopted based upon the vector average drift velocity $(\hat{v}_a + \hat{v}_b)/2$ resulting in an improved estimate of the final vortex element location at point c.

$$ac = \frac{1}{2}(\hat{v}_a + \hat{v}_b)\Delta t$$
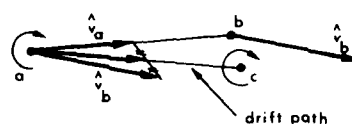
(b) drift path by central difference a to c

FIGURE 5. Vortex Convection Schemes

(iii) Due to (ii) above and the errors of the discretisation, it is inevitable that some vorticity elements will accidentally be drawn excessively close to or even across the solid boundaries. This gives rise to serious numerical errors but means for dealing with this problem have been developed which are outlined in Appendix II.

4.0   The dispersion of vorticity

The vorticity produced at the body surface is dispersed in three ways, namely (i) separation from sharp corners, (ii) convection and (iii) viscous diffusion. The joint actions of convection and viscous diffusion can of course give rise in certain circumstances to separations from smooth surfaces too. Models for separation more generally will therefore be dealt with in the following sections (4.1) and (4.2). In sections (4.3) and (4.4) we shall summarise the equations required to compute the convective and viscous diffusion motions.

4.1   Vorticity sheet separation

Separation from a sharp corner is the easiest situation to handle, Figure 6(a), since one may make the very reasonable assumption that the vorticity element p just prior to the separation point is projected into space in the local surface direction at its surface drift velocity $\gamma(p)/2$. The solution depicted in Figure (4) was computed on this basis, all the free vorticity elements having been initially projected from the separation point.

The main defect of this model as it stands is its inability to provide for other possible separations, for example from the wall (x axis) just prior to the rear stagnation point or from the rear surface of the plate. This problem was highlighted when the case of flow past a circular cylinder was first considered, Figure (6)b. In this situation there is no clear separation point and it was initially decided to fix one artificially at location A at the ends of the transverse diameter. Even with this assumption there remains the problem of selecting a trajectory for the separating vortex, since the path of the convective flow is far less certain for smooth surface separations. The final practice adopted in this phase of the work is to offset the separated element, which will be of strength

$$\Delta \Gamma = \gamma(s_p)\frac{v_p}{2}\Delta t = \frac{1}{2}\{\gamma(s_p)\}^2 \Delta t \tag{9}$$

by a small distance ε. Unless the corrections proposed in Appendix II are introduced, serious errors in the Martensen potential flow solution will occur if $\varepsilon < \Delta s_p$. The same is true for any free vorticity element which may later draw close to the surface. To avoid this in early phases of the work, an envelope was prescribed around the surface, Figure (6)b. Any vorticity element which strayed within this envelope was artificially

(a) Sharp edge separation

(b) Smooth surface separation

(c) Leading edge separation

(d) Full surface separation
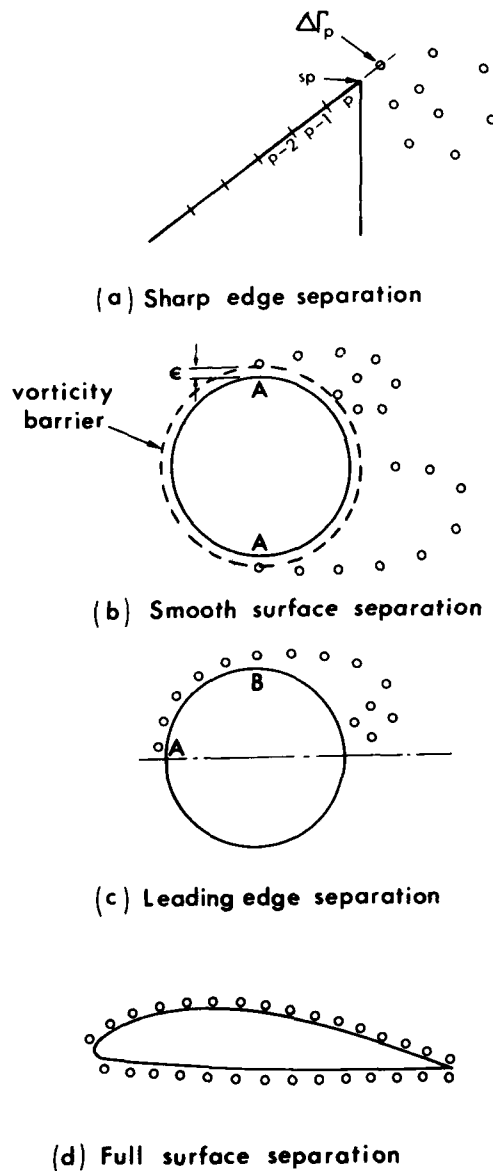
FIGURE 6.   Separation Models

FIGURE 7.   Vortex street predictions for Re = 20,000

placed just onto it before repeating the next potential flow calculation. On this basis very reasonable predictions of von Karman vortex streets were made(5), one of which is illustrated in Figure (7). Even with fixed separation points a plausible vortex street was established with reasonable C_D and C_L predictions and with a Strouhal Number here of 0.23±0.01 at Re = 20,000.

4.2   A direct simulation of vorticity shedding

In proceeding later to the calculation of stalling aerofoils, on the other hand, there was no way of determining or guessing the location of separation points and the authors sought a method for the numerical simulation to determine them automatically. A clue came from an earlier computer experiment, Figure (6)c, in which the separation point of a circular cylinder accidentally moved to the first pivotal point at the nose of the cylinder. The useful outcome of this accident was the observation that the shed vortex sheet as it developed tended to remain fairly close to the surface (A to B) until it reached the vicinity of the expected separation point B, whereupon the sheet naturally detached itself from the surface.

Arguing from this, the realisation dawned that Martensen's surface vorticity sheet is not in reality bound to the surface but is free to drift with the flow. In other words all vorticity in a fluid is free once created. Putting this notion to the test, the authors immediately moved over to a totally different scheme for vorticity shedding applicable to all bodies which directly simulates the real flow. This technique is illustrated in Figure (6)d. After the potential flow calculation at time t, all

vorticity elements $\gamma(s)\Delta s$ are shed into the fluid by displacing each element normal to the surface by a small distance ϵ. The value for ϵ, which can be argued from the viscous diffusion theory of section (4.4) is given by

$$\epsilon = \left[\frac{4\nu\Delta t}{3}\right]^{\frac{1}{2}} \tag{10}$$

In considering boundary layer growth, Chorin[4] made a similar assumption to this and boundary layer calculations by Porthouse[5], mentioned in section (4.4) were likewise based on a similar premise. Body separation flow problems have however not been treated this way to the best of the authors' knowledge. This represents a major step forward in the simulation method since in effect the procedure directly simulates the growth in time of the body boundary layer in which vorticity is created, shed, diffused and convected from every body surface element for each time step. Unfortunately the computer storage and execution times required to cope with this scheme put the method almost out of reach of a time sharing mainframe computer. However with the advent of 16 and 32 bit single user computers during the next few years and with the aid of vector processors it should be possible to investigate problems with greater resolution and with rapid turnover times.

4.3 Convection velocities

The potential flow as described by eqn.(3) is inadequate for the separated flow regimes illustrated above and we must add in the additional influence of all vortices shed during the preceding time steps, whereupon we obtain

$$\sum_{n=1}^{M} \gamma(s_n)K(s_n,s_m)\Delta s_n = - w_\infty\{\frac{dx_m}{ds}\cos\alpha_\infty + \frac{dy_m}{ds}\sin\alpha_\infty\} + \sum_{N=1}^{Z} \Delta\Gamma_N L(N,m) \tag{11}$$

$\Delta\Gamma_N$ is the vorticity element shed at the Nth time step and $L(N,m)$ is a coupling coefficient identical in form to equ.(4), which determines the interference velocity at body point m due to a unit vortex located at the position of Γ_N.

Since the additional free vortex terms on the r.h.s. of this equation change for each time step, the recommended procedure for solution of the equations is matrix inversion. The l.h.s. matrix may be evaluated once and for all at the outset of a computation. Furthermore the solution for the uniform stream may also be evaluated once and for all. At each subsequent time step all that remains is multiplication of the inverted matrix with the new right hand side terms due to $\Delta\Gamma_N$.

In addition to the convective influence of $\Delta\Gamma_N$ at the body surface, each shed vorticity element is free to drift under the collective convective influence of all vorticity elements and uniform streams in the flow.

Now the velocity components u,v at m due to a unit clockwise vortex located at n are given by

$$u = U(s_m,s_n) = \frac{(y_m-y_n)}{2\pi\{(x_m-x_n)^2+(y_m-y_n)^2\}}$$

$$v = V(s_m,s_n) = \frac{-(x_m-x_n)}{2\pi\{(x_m-x_n)^2+(y_m-y_n)^2\}} \tag{12}$$

Thus the convection velocity components of vorticity element $\Delta\Gamma_N$ will be compounded as follows

$$u_{aN} = \sum_{n=1}^{M} \gamma(s_n)\Delta s_n U(s_m,s_n) + \sum_{\substack{n=1\\n\neq m}}^{Z} \Delta\Gamma_N U(s_m,s_n) + U_\infty$$

$$v_{aN} = \sum_{n=1}^{M} \gamma(s_n)\Delta s_n V(s_m,s_n) + \sum_{\substack{n=1\\n\neq m}}^{Z} \Delta\Gamma_n V(s_m,s_n) + V_\infty \tag{13}$$

During the convection calculation, equs.(13) must be evaluated for each vortex in turn, after which the revised locations at time $t + \Delta t$ are calculable. Following the simplified forward difference scheme of Figure (5)a, from

$$x_b = x_a + u_{aN}\Delta t$$

$$y_b = y_a + v_{aN}\Delta t \tag{14}$$

If the convective velocities u_{bN}, v_{bN} are now recalculated from equs.(13), following the central difference model of Figure (5)b we then have the more accurate estimate of the free vortex location at time $t + \Delta t$ from

$$x_c = x_a + \tfrac{1}{2}(u_{aN} + u_{bN})\Delta t$$

$$y_c = x_a + \tfrac{1}{2}(v_{aN} + v_{bN})\Delta t \tag{15}$$

4.4 Vorticity transfer through viscous diffusion

A full exposition of the theory of viscous diffusion is given in Appendix I and only a brief outline of principle and application will be given here. Our reference point is the classical solution for a diffusing point vortex. As proved in the Appendix, if the vortex is replaced by a large number of vortex elements (say 100) all initially located at the origin of the (r,θ) plane, the diffusion of vorticity during time Δt may be accurately modelled if each element is subjected to r,θ displacements given by

$$r = \{4\nu\Delta t \ln(1/N_i)\}^{\tfrac{1}{2}}$$

$$\theta = 2\pi M_i \tag{16}$$

N_i and M_i are random numbers in the range 0 - 1. After a given time step Δt this process can be repeated for further time steps by shaking each individual element without further subdivision. In the limit of an infinite number of elements this model, which is similar to Brownian motion, approaches the exact solution for two-dimensional viscous diffusion.

If applied to a wall shear layer, for example a Blasius boundary layer, Figure (8), this model produces reasonable results bearing in mind the sparseness of vorticity elements enforced by practical computational constraints. The laminar low Reynold's number solution shown in Figure (8) is among the better results obtained so far due to the relatively low convection. At higher Reynold's numbers considerable reduction in time step Δt and thus increase in the number of vorticity elements is required to maintain similar resolution of the flow. In principle however, given sufficient computing speed and capacity, it ought to be possible to resolve the diffusion/convection processes for a complete body with fair representation of the surface boundary layers as well as adequate prediction of the far flow.

FIGURE 8. Simulation of a Blasius Boundary Layer for Re = 500

The application of this method to stalling or bluff body flows is quite simple. Following convection, each vorticity element is given a so-called "random walk" according to equations (16). If an element accidentally walks across a solid boundary, the normal treatment is to assign it strength zero or remove it from the field. A very simple technique has been devised to detect whether each vortex lies within or without the body and this is outlined in Appendix II. Many examples of this method have been given elsewhere in refs.5-7. The aim in the concluding section (6.0) of this paper will be to explore its application in some detail to the behaviour of a well known aerofoil taken through a wide range of angles of attack. With this in mind it is necessary to elaborate in the next section on the calculation of CL and CD which presents special problems in time dependent and viscous separated flow.

5.0 Calculation of surface pressure, lift and drag

The Navier Stokes equation (1) may be expressed in the alternative form

$$\frac{\nabla p_o}{\rho} = (\hat{q} - \nu\nabla)x\hat{\omega} - \frac{\partial \hat{q}}{\partial t} \tag{17}$$

In this compact form the local gradient of stagnation pressure is seen to derive from two sources, one due to the combined effect of convection and diffusion upon the transport of vorticity and the other due to local unsteady flow.

To focus attention on the first of these, we can identify $(\hat{q} - \nu\nabla)$ as a flux operator which is equivalent to a velocity vector $\hat{v}$ normal to both $\hat{\omega}$ and the local gradient of stagnation pressure ∇p_O. $\hat{v}$ is compounded of both convection and diffusion velocities which will generally lie in different directions. The Navier Stokes equation may thus be written yet more succinctly.

$$\frac{\nabla p_O}{\rho} = \hat{v} \times \hat{\omega} - \frac{\partial\hat{q}}{\partial t} \qquad (18)$$

The convective inputs into $\hat{v}$ can include both free and forced motions (e.g., a moving turbine blade row might be a typical forcing motion). The diffusive components could include viscous diffusion in a continuous medium as here, pseudo-Brownian motion as an equivalent model for discretised vorticity as adopted in this numerical scheme, or even Brownian motion itself (e.g., tiny insects experience buffeting due to Brownian motion in addition to viscous drag). All that is required to determine ∇p_O is to evaluate the terms on the right hand side of equation (18) during time dt.

(a) time t

(b) time t + Δt

If we apply this to our numerical scheme a procedure quickly emerges. Thus very close to the body surface due to the predominating influence of viscosity, the flux velocity $\hat{v}$ will be normal to the surface. For a given surface element Δs, Figure (9)a, the term $\hat{v} \times \hat{\omega}$ then represents the normal v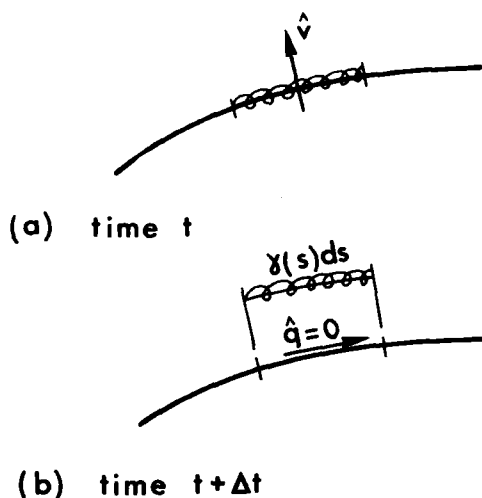elocity flux emanating from the body surface. Since the surface vorticity per unit length is $\gamma(s)$, we could express a numerical equivalent to $\hat{v} \times \hat{\omega}$ for the time step Δt as follows

$$\hat{v} \times \hat{\omega} \equiv - \frac{\Delta(\gamma(s)\Delta s)}{\Delta t} \qquad (19)$$

Now the numerical procedure adopted involves shedding the whole of the surface vorticity $\gamma(s)\Delta s$ into the fluid, Figure (9)b, during time Δt and thus the Navier Stokes equation (18) applied to surface element Δs becomes

$$\frac{\Delta p_O}{\rho} = - \frac{\gamma(s)\Delta s}{\Delta t} \qquad (20)$$

FIGURE 9.   Shedding of a vortex element

We take note that $\hat{q}$ is now zero on the body surface so that the term $\partial q/\partial t$ vanishes. This observation also leads directly to the pressure gradient Δp along the surface since equation (20) reduces to

$$\frac{\Delta p}{\rho} = - \frac{\gamma(s)\Delta s}{\Delta t} \qquad (21)$$

which agrees with equation (8).

Beginning at the leading edge the pressure at s' could thus be integrated through

$$p' = \int_O^s \frac{\partial p}{\partial s}\, ds$$

or in numerical form

$$p_n - p_{\ell e} = - \frac{\rho}{\Delta t} \sum_{i=1}^{n} \gamma(s_i)\Delta s_i \qquad (22)$$

Unfortunately the simplicity of this result is marred by a problem which arises during the random walk, since vorticity elements may in some cases diffuse back into the aerofoil. These must also be accounted for if we wish to ensure the "closure" of the pressure distribution

$$\oint \frac{\partial p}{\partial s}\, ds = 0 \qquad (23)$$

As explained in Appendix II any such element which strays inside the body will invalidate the Martensen analysis which requires zero internal circulation. Such vortices are therefore snuffed out. However Kelvin's circulation theorem must be obeyed and therefore the "bound" circulation of the contour is incremented by the strength of this vortex element. It should be mentioned that this condition forms one equation of the Martensen analysis which takes the form

$$\sum_{n=1}^{M} \gamma(s_n) \, s_m = \sum_{i=1}^{N} \Delta\Gamma_i + \sum_{j=1}^{S} \Delta\dot{\Gamma}_j \qquad\qquad (24)$$

where $\Delta\Gamma_i$ are the N shed vortex elements remaining in the field and $\Delta\dot{\Gamma}_j$ are vortex elements which have been snuffed out.

The procedure described in Appendix II for checking whether each free vortex element lies either inside or outside the body also reveals the particular surface element crossed by those that stray inside. Such surface elements have their pressure gradients modified according to

$$\Delta p_n := \Delta p_n^{\cdot} + \rho\frac{\Delta\Gamma_p}{\Delta t} \qquad\qquad (25)$$

Another problem mentioned in Appendix II arises when a vortex element drifts so close to the surface that its coupling coefficient L(N,n) is in serious error. A technique is explained whereby its influence at this surface location is adjusted to satisfy Kelvin's theorem, a procedure which makes such elements "civilised" in their interaction with the contour and one which has been a trade secret of this work,removing what was previously a major difficulty in the use of vortex singularities.

Finally, having determined the static pressure distribution we are in a position to evaluate lift and drag coefficients from the formulae

$$C_L = \frac{1}{\frac{1}{2}\rho\omega_{\infty}^2\ell} \oint p\sin\theta ds$$

$$\qquad\qquad (26)$$

$$C_D = \frac{1}{\frac{1}{2}\rho\omega_{\infty}^2\ell} \oint p\cos\theta ds$$

where ℓ is a leading dimension of the body such as aerofoil chord and θ is the local profile slope.

6.0   The Stalling of Aerofoils and Cascades

The computer program to simulate flow separation from bluff bodies has been run with aerofoil NACA 0012 at a range of angles of attack. The Reynolds Number based upon chord and mainstream flow speed was 100,000. Figures (10) and (11) show the types of flow obtained at different angles of attack. For each angle, the variation of lift and drag with time has been obtained. A particular difficulty is that the Brownian motion of the vorticity, used to simulate diffusion, has an associated uncertainty principle which may be expressed

$$\frac{\text{sampling}}{\text{time}} \times \frac{\text{error in}}{\text{pressure}} = \text{constant}$$

Thus the curves appear "noisy" when plotted at short time intervals, but since the relation between pressure and vortex flux is linear, it is permissible to average the flux over longer times to reduce the noise in the lift and drag variations. Figures (12) and (13) show some results with lift and drag evaluated every tenth time step. From these time-dependent results, average values of lift and drag may then be estimated. Figures (14) and (15) show the predicted variation of lift and drag with angle of attack, together with experimental results from Critzos, Heyson and Boswinkle.
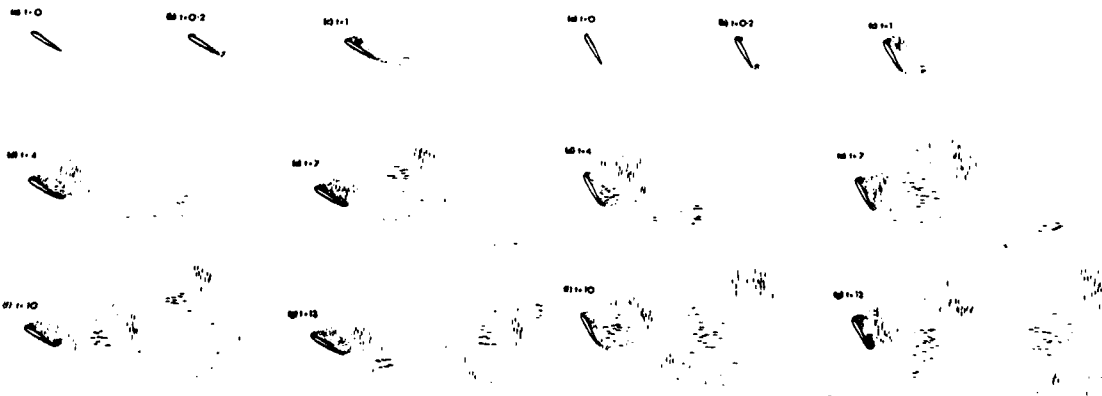
FIGURE 10.   Aerofoil NACA 0012 at 30°
angle of attack

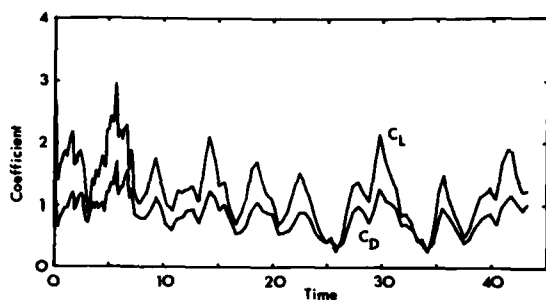FIGURE 11.   Aerofoil NACA 0012 at 60°
angle of attack

FIGURE 12. Time variation of lift and drag at 30° angle of attack
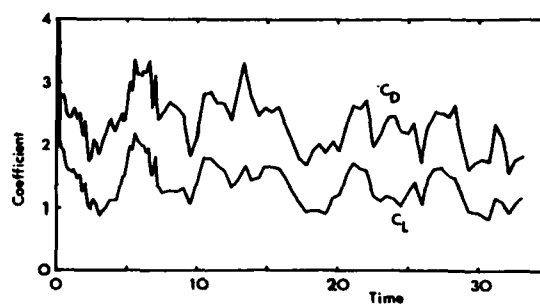

FIGURE 13. Time variation of lift and drag at 60° angle of attack
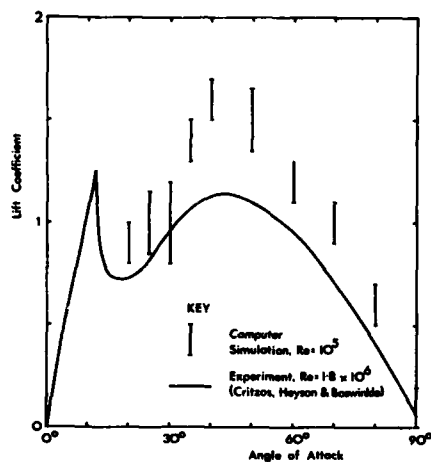

FIGURE 14. Predicted lift for aerofoil NACA 0012 at a range of angles of attack
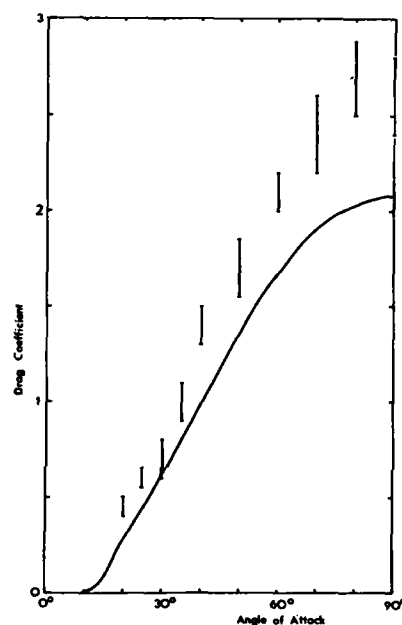
FIGURE 15. Predicted drag for aerofoil NACA 0012
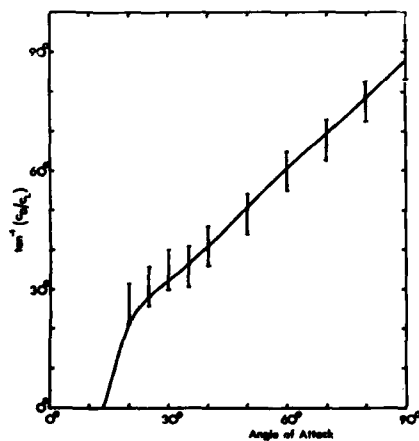
FIGURE 16. Angle of resulting force
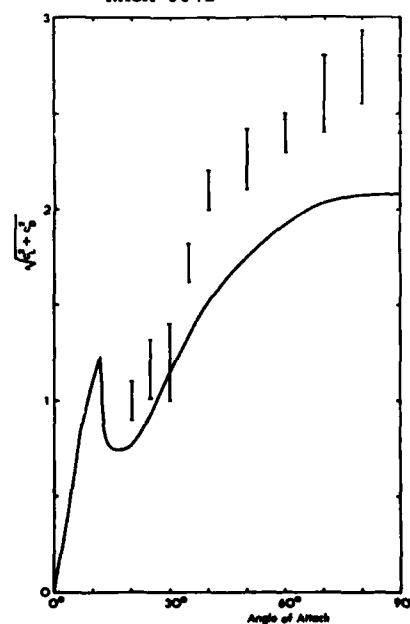
FIGURE 17. Magnitude of resulting force

Due to restrictions imposed by computing resources, data have been computed at 5° intervals up to 40° but at 10° intervals thereafter. Since it is not possible to compute each angle of attack for as long a time as one might desire, there is an error associated with the estimated values of lift and drag, which is indicated on the graphs. The direction of the force acting on the aerofoil is shown in Figure (16), and roughly speaking, this force acts normal to the chord of the aerofoil. The magnitude of the force

$$(C_L{}^2 + C_D{}^2)^{\frac{1}{2}}$$

is shown in Figure (17). This is the most revealing graph, and it must be commented that though the general trend is the same, there is still some difference between theory and experiment which cannot be wholly attributed to the differing Reynolds Numbers.

Porthouse and Lewis[5] explain boundary layer flow separation in terms of the piling up of vorticity. This is indeed seen in the stalling aerofoil simulations, so the phenomenology of flow separation is certainly being reproduced here. Vorticity also separates at the trailing edge, and in the unstalled case, this gives rise to the Kutta-Joukowski condition. (Note that in this computer program, the aerofoil is just another polygon, and no special assumptions are made about the "trailing edge"). At high angles of attack, the two streams of vorticity from the leading and trailing edges interact to form an irregular vortex street which is similar to observations from high speed cinematography (Goldstein, Dover edition, Plate 9).

However, we are attempting to simulate two very different scales of motion with just one method. Chorin proposed the random vortex method as the method best able to do this by virtue of its phenomenology, and indeed it does reproduce flow separation remarkably well. Nevertheless, because of the relatively coarse discretisation, we could hardly expect the method running on existing computers to predict the precise stalling angle for each Reynolds Number.
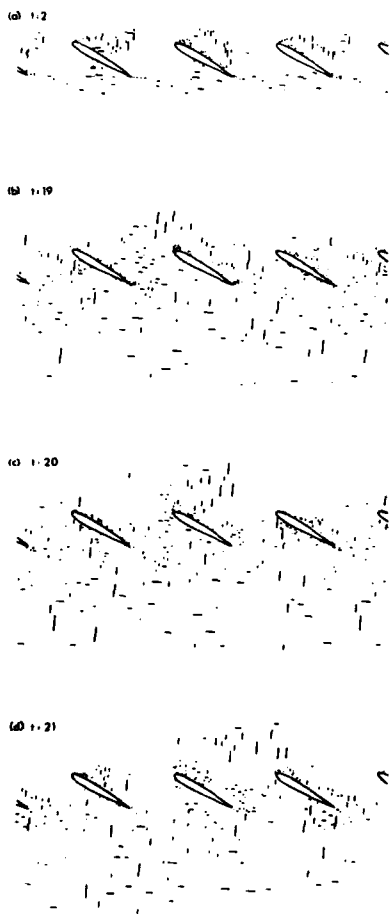
A vortex-in-cell method, as proposed by Christiansen, may do better, since it is possible to use about 10,000 vortices, and the errors due to their random motion will be reduced. However, it is also possible that we have already reached the limit of what can be done with a two-dimensional theory, and that although the method is qualitatively good, quantitative discrepancies between experiment and the computer simulations could be due to three-dimensional effects. The flow behind the aerofoil is turbulent, and the stretching of vortex filaments may be a dominant mechanism in the flow, but no two-dimensional method is able to simulate this.

Despite these reservations, it is still profitable to explore a variety of problems with this method. For example Figure (18) shows a three-bladed rotor which has been unwrapped onto the cascade plane. Initially, with the high angle of attack chosen here, all three blades stall in the same way. Another feature of Chorin's method is that the flow is continually being provoked into instability by the random motion of the vortices, and so eventually the stalling of the blades takes on a very different form. A large vortex, or soliton, moves along the cascade upstream of it. This vortex must lose some vorticity through the blade passages, but it is replenished as it passes each blade. We are looking at a possible mechanism for rotating stall, although the angle of attack here is large. Rotating stall is usually associated with the first stage of instability as a compressor is throttled. Unfortunately available computer time and capacity has limited this study to the case of deep stall only. Investigations of the cascade at different angles of attack and with more than three blades must await the acquisition of more powerful computing facilities.

FIGURE 18. Stalled flow through
a three-bladed rotor

APPENDIX I

Simulation of viscous diffusion

The viscous diffusion of a vortex of initial strength Γ located at the origin of the (r,θ) plane is described by the equation

$$\frac{\partial \omega}{\partial t} = \nu \left\{ \frac{\partial^2 \omega}{\partial r^2} + \frac{1}{r} \frac{\partial \omega}{\partial r} \right\} \qquad \text{A1}$$

which has the solution

$$\omega(r,t) = \frac{\Gamma}{4\pi\nu t} e^{-(r^2/4\nu t)} \qquad \text{A2}$$

The form of this solution over several time steps is illustrated in Figure A1.
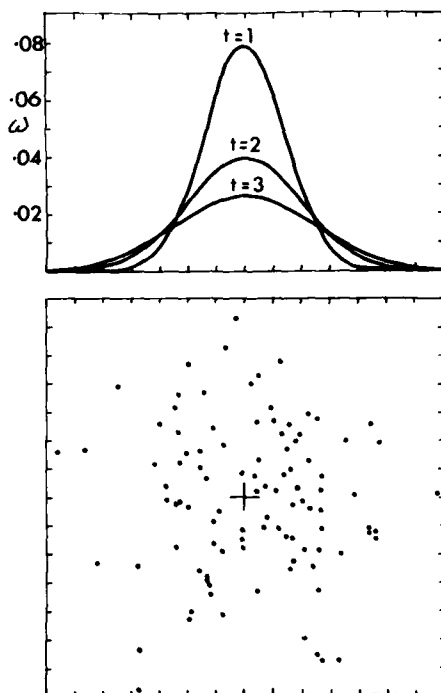
FIGURE A1. Diffusion of a point vortex
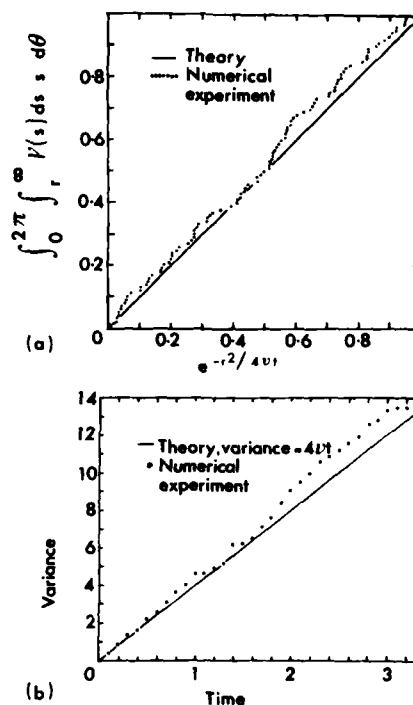
FIGURE A2. Diffusion of a point vortex

To arrive at a suitable numerical simulation of this well known flow we could begin by treating the vortex as a collection of say 100 elements each of strength 0.01 all free to move independently but initially all located at the origin. After time t the requirement of the simulation would be that the elements are scattered throughout the (r,θ) plane, Figure A1, in such a way that the density distribution agrees with equation A2. Thus the scattering technique should result in a uniform distribution circumferentially but a radial distribution which is dense near to the origin, falling away as r increases.

The clue to the achievement of this is then to regard equation A2 as a vorticity density distribution curve which must be delivered by the simulation process. Put another way we could say that after time t the probability of finding a vorticity element in the region $(r,r+\Delta r)$ and $(\theta,\theta+\Delta\theta)$ is given by

$$p = \frac{1}{4\pi\nu t} e^{-(r^2/4\nu t)} \Delta r r \Delta \theta \qquad \text{A3}$$

To proceed further, equation A3 may be integrated over the ranges $\theta = 0$ to 2π and radius $= 0$ to r, resulting in

$$P = 1 - e^{-(r^2/4\nu t)} \qquad \text{A4}$$

In this form P gives us the probability that our vorticity elements lie somewhere within the circle of radius r. At this point we should observe that equation A4 agrees with the normal distribution curve of statistical theory. The value of P is, therefore, equally likely to be anywhere in the interval (0,1) and could be selected by a random number generator for example. The radial location of each of the vorticity elements can thus be obtained if we invert equation A4 into

$$r_i = \{4 \nu t \ln (\frac{1}{P_i})\}^{\frac{1}{2}}$$ A5

The required procedure is thus to give a random number P_i in the range (0,1) to each element of the vortex. The elements are then displaced radially by the corresponding value of r_i. Circumferential displacements can be arranged by selecting a second set of random numbers Q_i in the range (0,1) whereupon for the ith element

$$\theta_i = 2 \pi Q_i$$ A6

The excellent agreement of this simulation with the exact solution is illustrated by Figure A2 in which vortex strength with radius r and variance versus time are compared.

Although it would be desirable to break all shed vorticity elements of a stalling or bluff body flow into a large number of sub-elements, in practice computing speed and capacity rules this out. Thus the practice of the authors is to apply equations A5 and A6 to each element in its entirety, once shed, at every time step. On average that individual element will then diffuse correctly when taken with all other elements over a period of time.

APPENDIX II

Drift of a vortex element close to a surface

The circulation C around a body contour due to an external vortex, Figure B1, is zero, namely

$$C = \oint \hat{q}.\hat{i}ds = 0$$ B1

On the other hand if a vortex element $\Delta\Gamma$ were accidentally to drift inside the body due either to numerical errors in the convection process or to the random walk diffusion process, the circulation around the body contour would become

$$C = \oint \hat{q}.\hat{i}ds = \Delta\Gamma_N$$ B2

Thus we have a simple device to check the location of each vortex if we express this in numerical form, namely

$$C = \Delta\Gamma_N \sum_{p=1}^{M} L(N,p)$$ B3

In this expression L(N,p) is given by equation (4) where N represents the (x,y) location of the vortex element and p the location of the surface vorticity elements.

If C is zero the vortex element lies outside the body. If non zero the element may lie inside and C should equal $\Delta\Gamma$.

However if a vortex element draws into close proximity ϵ to the body, the coupling coefficient which represents the surface velocity due to $\Delta\Gamma_N$ at the nearest body point p will be in error. Thus as $\epsilon/\Delta s_p \to 0$ so $L(N,p) \to \infty$. Thus for situations in which say $\epsilon/\Delta s_p < 1.0$ the Martensen solution will be subject to errors due to "leakage flux", since there would be an implied internal circulation due to this numerical defect. The Martensen method is very sensitive to this type of numerical error which can be eliminated by insisting that C is made equal to zero. This can be accomplished artificially by replacing the coupling coefficient L(N,p) by the value

$$L(N,p) = C - \sum_{\substack{n=1 \\ n \neq p}}^{M} L(N,n)$$ B4

The computing sequence is as follows:

FIGURE B1. Circulation due to a vorticity element close to a surface

(a)   Evaluate C.

(b)   If $|C|>\frac{1}{2}|d\Gamma_N|$ the vortex element is inside the body and should be snuffed out.

(c)   If $|C|<\frac{1}{2}|d\Gamma_N|$ the vortex element is outside the body and $K(N,p)$ must be evaluated by equation B4.

REFERENCES

1.   Mair,W.A.,   Bluff bodies and vortex shedding - a report on Euromech 17.
      Maull,D.   J.Fluid Mech. 45, 1971, p.209.

2.   Bearman,P.W.,   Vortex shedding from bluff bodies in oscillatory flow - a
      Graham,J.M.R.   report on Euromech 119.
                        Dept.of Aeronautics, Imperial College, 1979.

3.   Chorin,A.J.   Numerical study of slightly viscous flow.
                        J.Fluid Mech. 57, 1973, pp.785-796.

4.   Chorin,A.J.   Vortex sheet approximation of boundary layers.
                        J.Comp.Phys. 27, 1978, pp.428-442.

5.   Porthouse,D.T.C., Simulation of viscous diffusion for extension of the surface
      Lewis,R.I.   vorticity method to boundary layer and separated flows.
                        J.Mech.Eng.Sci. Vol.23, No.3, 1981.

6.   Lewis,R.I.   Surface vorticity modelling of separated flows from two-
                        dimensional bluff bodies of arbitrary shape.
                        J.Mech.Eng.Sci. Vol.23, No.1, 1981, pp.1-12.

7.   Lewis,R.I.,   Recent advances in the simulation of real fluid flows.
      Porthouse,D.T.C. Submitted to the North East Coast Institution of Engineers
                        and Shipbuilders.

8.   Hoerner,S.F.   Fluid dynamic drag.
                        (S.F.Hoerner), 1965.

9.   Critzos,C.C.,   Aerodynamic characteristics of NACA 0012 airfoil section.
      Heyson,H.H.,   NACA Technical Note 3361, 1954.
      Boswinkle,R.W.Jr.

10.   Goldstein,S.   Modern developments in fluid dynamics, II.
                        Dover (New York), 1957.

11.   Christiansen,J.P. Numerical simulation of hydrodynamics by the method of
                        point vortices.
                        J.Comp.Phys., 13, pp.363-379, 1973.
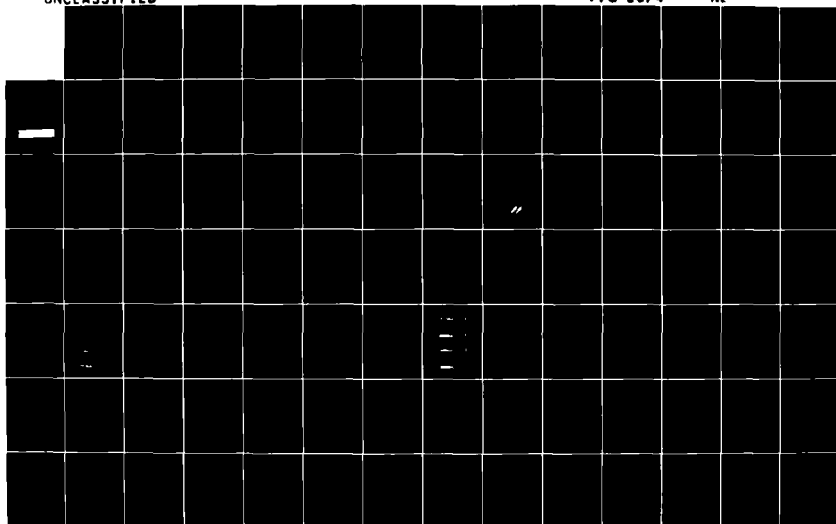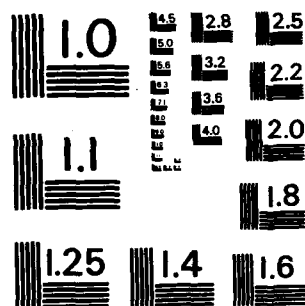
MICROCOPY RESOLUTION TEST CHART

NATIONAL BUREAU OF STANDARDS-1963-A

DISCUSSION

F.Leboeuf, Fr

    (1) Do you allow the vorticities to collapse together?

    (2) How do you define the strength of the vortices which are shed at the wall?

Author's Reply

Vortices are allowed to recombine if they come into close proximity. This occurs occasionally during the diffusion process. They are also recombined after travelling some distance downstream in the wake in order to reduce the amount of data carried in arrays or on file.

The strength of vortices shed from the wall must be that given by the preceding Martensen calculation.

Martinon

Since you use a random process, you have to reach statistical convergence. Are your present results very sensitive to the number of vortices you follow, and would there be an optimum (compromise between statistical error and computational time) number?

Author's Reply

The question of the appropriate number of vortices is an important one which needs more attention. The boundary layer calculation, shown in Figure 8, containing 500 vortices, is probably near to the best compromise between accuracy and density. Ideally we should undertake controlled studies to determine this matter but these must await availability of more suitable computing resources. With the resources available to us we have tried to push ahead through a variety of cases which would stretch both the method and ourselves in developing the model during the four and a half years since this project began.

C.H.Sieverding, Be

    (1) The Strouhal number of the flow behind a cylinder varies with the Reynolds number. Is your method able to calculate this Strouhal number—Reynolds number relation, and would you please comment on the difference of the vortex shedding process from cylinders for laminar and turbulent boundary layers.

    (2) M. Dyment from the Institute of Fluid Mechanics in Lille has made very detailed measurements of the vortex frequency in the near wake region. He shows that the Strouhal number varies significantly in this region with increasing downstream distance up to a distance of approximately the diameter of the cylinder through successive collapsing of the vortices to vortex structures of bigger dimensions. Is your method able to predict such a behaviour?

Author's Reply

Yes, the method, having a viscous diffusion model, can deliver Strouhal number versus Reynolds number. At high Reynolds number, each newly shed separation vortex sheet is more likely to undergo a Kelvin-Helmholtz instability before it would otherwise roll up into a von Kármán vortex. At low Reynolds number, diffusion of the shed vorticity shear layer damps down the Kelvin-Helmholtz instability tendency so that a full von Kármán vortex street is set up with periodicity, the case illustrated in the paper.

I am unfamiliar with Dyment's work and will need to follow this up. I would be grateful for more information on this problem. It is possible that the third dimension of flow is involved in these cases.

K.Papailiou, Gr

Can you, with your calculation, arrive at a steady state (of course, for the parts of the flow that we know should achieve a steady state)?

Author's Reply

In principle, yes. For example, we have calculated the NACA 0012 airfoil below stall since submission of the text of this paper. Due to the discretisations inherent in this method and the shedding of discrete vortices rather than distributed vorticity, the solutions are subject to "noise". If the number of elements could be substantially increased we could obtain better results for unstalled flows. At present the method handles wake flows better than it copes with flows dominated by viscous effects, due to insufficient resolution.

Heinemann

Applying a singularity method like the one of Martensen to calculate cascade blade surface pressure distributions and cascade data may sometimes lead to results which do not agree reasonably well with experiments. This may be due to the fact that the real physical flow behaviour is not taken into account for the computation, i.e. most of all the vortex shedding from the trailing edges. Therefore, I would like to know whether you are able to use the shedding frequency as an input value for such a surface pressure distribution calculation.

Author's Reply

The standard Martensen method is, of course, a pure potential flow model. As such, it is a good and versatile one. Like all potential flow methods though, it suffers from certain restrictions, notably simplistic trailing edge modelling. This contribution to the discussion and some others have indicated the need now to focus more attention upon models of the *real* trailing edge flow in what we think are installed, steady state aerofoil or cascade flows. Dr Werle's steady flow calculations implied the presence of a vortex core hanging on to the suction surface trailing edge region. Our film seems to suggest that such a vortex builds up and detaches in a periodic manner. Dr Dunker's L.D. plots imply periodicity in a "steady state" transonic rotor wake. Can it be that even installed blade rows can produce measurably periodic wakes, even with very thin trailing edges?

In direct response to the questioner's last point, I think that it would be possible to modify the standard Martensen to shed upper and lower surface vorticity sheets in real time steps, abandoning the usual Wilkinson type of Kutta condition. This would be well worth exploring to see whether the above questionings of periodic wakes have foundation.

C.L.Ball, US

Bypassing the issue of computational time, would you comment on the potential of this method for calculating the stalling characteristics of compressor type blade rows to include three dimensional effects and transonic flows?

– It is my understanding from your discussion that the method allows for rotating stall to develop naturally. Is this correct?

– Since the method was developed primarily for windmills, is the blade solidity limited to low values?

Author's Reply

The method is ripe for analysis of two-dimensional stalling behaviour of cascades. There is no problem here other than computing capacity and speed of execution. Figure 18 illustrates typical output. In this case up to 3 hours of IBM 370 c.p.u. time was required. For the future, this work demands a dedicated mini-computer with good graphics and probably video output for recording results. Three-dimensional and transonic flows are not possible by this method. In principle, three-dimensional flow is possible although there is no formulation as yet and computer requirements exceed facilities that are available. I do not think that transonic flows will ever be treated by surface singularities.

You are correct in your assumption that the method calculates rotating stall naturally. There is no human interference with these calculations. Blade solidity and profile are completely arbitrary.

Ph.Ramette, Fr

For a separated flow, how do you calculate the separation line?

Author's Reply

The separated vortex sheet is completely self generating and determines its own shape. We have tried to account for all known fluid influences in the theory, namely, potential flow (creating vorticity at the boundary), viscous diffusion, and vorticity convection. All vorticity in the flow is *free* to convect and diffuse. Separations, therefore, determine themselves according to the known laws of *two-dimensional* nature.

The authors wish to express their thanks for a very helpful probing discussion.

CALCULS DE COUCHE LIMITE TRIDIMENSIONNELLE DANS UN COMPRESSEUR

par

B. AUPOIX et J. COUSTEIX

ONERA/CERT
2 avenue E. Belin
31055 TOULOUSE Cedex (FRANCE)

RESUME

L'étude des équations de transport pour les tensions turbulentes en repère tournant ou sur paroi courbe a permis de mettre en évidence deux types d'effets : d'une part, une stabilisation ou déstabilisation de la turbulence due à la courbure longitudinale ou à la composante du vecteur rotation parallèle à la paroi ; d'autre part, un effet tridimensionnel quand la composante du vecteur rotation est normale à la paroi.

L'effet stabilisant ou déstabilisant, ainsi que celui de la turbulence extérieure, ont été introduits dans un schéma de longueur de mélange qui a ensuite été employé pour construire des familles de profils de vitesse de couche limite en similitude. L'analyse de ces familles de profils a fourni les relations de fermeture pour une méthode intégrale de calcul de couches limites tridimensionnelles.

SYMBOLES

$a_1 = \dfrac{-\overline{uv}}{1/2\, q^2} \approx 0,15$ "constante" expérimentale

$C_f = \dfrac{\tau_p}{1/2\, \rho_e\, U_e^2}$ coefficient de frottement pariétal

$H = \dfrac{\delta_1}{\theta_{11}}$; $H^{*} = \dfrac{\delta - \delta_1}{\theta_{11}}$ paramètres de forme

ℓ longueur de mélange

p fluctuation de pression

$\hat{p}$ pression instantanée

$\dfrac{1}{2}\, q^2 = \dfrac{1}{2}\, (\overline{u^2} + \overline{v^2} + \overline{w^2})$ énergie cinétique de turbulence

R rayon de courbure de la paroi

R nombre de Richardson $\dfrac{U/R}{\partial U/\partial y}$, $\dfrac{-2\omega}{\partial U/\partial y}$

$\hat{U}$, U vitesse instantanée, vitesse moyenne

U, V, W composantes du vecteur vitesse

$\overline{u^2}\ \overline{v^2}\ \overline{w^2}\ \overline{uv}\ \overline{uw}\ \overline{vw}$ tensions turbulentes

$U_\tau = (\dfrac{\tau_p}{\rho})^{1/2}$ vitesse de frottement

$\dfrac{\partial \vec{V}}{\partial y}$: $(\dfrac{\partial U}{\partial y} , \dfrac{\partial W}{\partial y})$ "vecteur" gradient de vitesse

$x\ y\ z$ coordonnées (y selon la normale à la paroi)

δ épaisseur de couche limite

$\delta_1 = \displaystyle\int_o^\infty \dfrac{\rho_e\, U_e - \rho U}{\rho_e\, U_e}\, dy$ épaisseur de déplacement longitudinale

$\theta_{11} = \displaystyle\int_o^\infty \dfrac{\rho U}{\rho_e\, U_e}\, (\dfrac{U_e - U}{U_e})\, dy$ épaisseur de quantité de mouvement longitudinale

ε taux de dissipation de l'énergie cinétique de turbulence

$\eta = y/\delta$

ν viscosité cinématique

ρ	masse volumique
$\tau = (-\overline{uv}, -\overline{vw})$	"vecteur" tension turbulente
$\chi = 0,41$	constante de KARMAN
Ω, ω_i	module et composantes du vecteur rotation
X_e	valeur de X à la frontière extérieure de la couche limite
X_p	valeur de X à la paroi
$\tilde{X}$	valeur instantanée de X
$\overline{X}$	moyenne d'ensemble de X

INTRODUCTION

L'accroissement des performances des compresseurs s'accompagne d'un accroissement de la charge aérodynamique des aubages. Les gradients de pression importants le long des aubes peuvent conduire au décollement des couches limites pariétales. Ce décollement doit cependant être évité car il entraîne d'importantes pertes de rendement. C'est pourquoi il est nécessaire de disposer de méthodes de calcul de couche limite permettant de prédire finement l'évolution de la couche limite sur l'aubage et son décollement éventuel.

Deux types de méthodes sont couramment utilisées pour prédire le développement d'une couche limite. Les méthodes locales résolvent les équations de couche limite (équations de continuité, de quantité de mouvement...) sur un maillage à l'intérieur de la couche limite. Les méthodes globales utilisent les équations de couche limite intégrées depuis la paroi jusqu'à la frontière extérieure de la couche limite. Les méthodes locales donnent une description plus fine de la couche limite. Par contre, elles sont lourdes à mettre en oeuvre et coûteuses en temps. Les méthodes intégrales sont plus simples à mettre en oeuvre, rapides et précises mais les relations de fermeture utilisées doivent être revues lorsqu'un nouveau phénomène (courbure de paroi, rotation ...) doit être pris en compte.

Une méthode intégrale a été choisie à cause de son coût faible pour une précision raisonnable. Cette méthode, d'abord développée en bidimensionnel /Réf. 1/ puis en tridimensionnel /Réf. 2/ pour les ailes d'avions a été étendue aux cas des compresseurs caractérisés par des taux de turbulence extérieure élevés, des courbures de paroi importantes et des effets de rotation.

Les principes de base des méthodes intégrales de calcul de couche limite tridimensionnelle sont brièvement rappelés dans la première partie de cet exposé. La prise en compte des effets de la turbulence extérieure, de la courbure de paroi et de la rotation est étudiée dans la dernière partie. La troisième partie donne une description succincte des possibilités du code de calcul ainsi que des exemples de résultats.

Le cas des couches limites turbulentes sera plus particulièrement étudié dans cet exposé. Les problèmes de couches limites laminaires sont abordés dans la référence /3/.

PRESENTATION DE LA METHODE INTEGRALE

Un profil de vitesse de couche limite tridimensionnelle peut être décomposé, comme le montre la figure ci-contre, en un profil de vitesse longitudinale U dans la direction de l'écoulement extérieur et un profil de vitesse transversale W dans la direction perpendiculaire à l'écoulement extérieur.
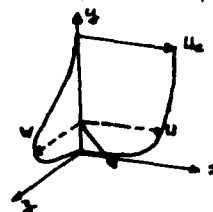
Pour un fluide incompressible, sans transfert de chaleur, l'écoulement dans la couche limite peut alors être décrit par trois équations : l'équation de continuité et les équations de quantité de mouvement selon les directions x et z.

L'intégration de ces équations depuis la paroi jusqu'à la frontière extérieure de la couche limite donne un système de trois équations globales dans lesquelles les nouvelles inconnues sont des grandeurs caractéristiques du profil de couche limite telles que le coefficient de frottement ou les épaisseurs intégrales de déplacement et de quantité de mouvement. Ces équations s'écrivent, à titre d'exemple, pour une couche limite bidimensionnelle incompressible :

(continuité) : $C_E = \dfrac{d\delta}{dX} - \dfrac{V_a}{U_e} = \dfrac{1}{U_e} \dfrac{d}{dX}(U_e(\delta - \delta_1))$

(quantité de mouvement) : $\dfrac{C_f}{2} = \dfrac{d\theta_{11}}{dX} + \theta_{11}\dfrac{H + 2}{U_e} \cdot \dfrac{dU_e}{dX}$

Lors de l'intégration, l'information sur la forme du profil de vitesse a été perdue. Comme le montre l'exemple simple ci-dessus, le nombre d'inconnues est alors supérieur au nombre d'équations.

Pour fermer le système, on a donc besoin de relations auxiliaires entre les diverses inconnues, c'est-à-dire que l'information sur la forme du profil de vitesse doit être réintroduite.

Une solution possible pour obtenir des relations de fermeture est d'utiliser des formes connues pour le profil de vitesse comme, par exemple, la loi de COLES ou encore des lois expérimentales comme la relation de LUDWIEG-TILLMAN. Cependant, avec cette démarche, la prise en compte de nouveaux phénomènes (turbulence extérieure, courbure de paroi, rotation ...) demande un grand nombre d'expériences fines pour établir de nouvelles formes de profils et relations de fermeture.

L'originalité de la méthode proposée réside dans l'utilisation de familles de profils de vitesse de couches limites en similitude. Ces familles de profils sont bien représentatives des profils de vitesse rencontrés même pour les couches limites hors d'équilibre. De plus, elles présentent l'avantage de pouvoir être généralisées pour prendre en compte de nouveaux effets tels que la turbulence extérieure, la courbure de paroi, la rotation ...

Les solutions de similitude pour le profil de vitesse sont analogues dans leur principe aux solutions de FALKNER et SKAN obtenues en laminaire. L'hypothèse de similitude consiste à supposer que les profils de vitesse longitudinale et transversale qui sont a priori fonction de x, y et z peuvent être exprimés sous forme réduite comme fonction d'une seule variable $\eta = y/\delta$ où δ est une longueur caractéristique, par exemple l'épaisseur de couche limite. Dans le cas d'une couche limite laminaire, l'hypothèse de similitude porte directement sur le profil de vitesse, soit $U/U_e = f(\eta)$. Dans le cas d'une couche limite turbulente, seule la région extérieure est en similitude. L'hypothèse de similitude porte alors sur la vitesse déficitaire soit : $(U_e - U)/U_\tau = f(\eta)$.

Avec cette hypothèse de similitude, les équations de quantité de mouvement qui étaient des équations aux dérivées partielles deviennent des équations différentielles ordinaires. Une hypothèse de faible écoulement transversal permet, de plus, de découpler l'écoulement longitudinal de l'écoulement transversal, c'est-à-dire que le profil longitudinal de vitesse se comporte comme un profil bidimensionnel.

Le profil de vitesse longitudinale est alors obtenu comme solution d'une équation différentielle ordinaire ; il ne dépend que de η et du gradient de pression longitudinal mis sous forme adimensionnelle. Le profil de vitesse transversal est ensuite obtenu à l'aide du système d'équations différentielles ; il dépend de η, du profil de vitesse longitudinale et du gradient de pression transversal mis sous forme réduite, soit encore de la courbure de la ligne de courant extérieure.

Dans le cas des couches limites turbulentes, un modèle de turbulence est nécessaire pour représenter les tensions de Reynolds dans les équations de quantité de mouvement. Un schéma de longueur de mélange a été choisi pour sa simplicité et sa commodité de mise en oeuvre. Ce schéma de longueur de mélange peut être modifié pour prendre en compte les effets de la turbulence extérieure, de la courbure de paroi ou de la rotation sur la turbulence au sein de la couche limite.

Les familles de profils de vitesse longitudinale et transversale ainsi obtenues comme solutions des équations de similitude peuvent être analysées pour obtenir les relations auxiliaires nécessaires à la fermeture du système des trois équations intégrales. Dans le cas présenté précédemment d'une couche limite bidimensionnelle incompressible, le système est fermé à l'aide de trois relations qui permettent le calcul du coefficient de frottement C_f, du coefficient d'entraînement C_E et du paramètre de forme $H^* = (\delta - \delta_2^*)/\theta_{11}$ en fonction d'une grandeur caractéristique de la forme du profil de vitesse. Dans le cas laminaire où l'hypothèse de similitude porte sur le profil de vitesse U/U_e, cette grandeur caractéristique sera le paramètre de forme H défini par :

$$H = \frac{\delta_1}{\theta_{11}} = \frac{\int_0^1 (1 - U/U_e)\, d\eta}{\int_0^1 \frac{U}{U_e}(1 - U/U_e)\, d\eta} \, .$$

Dans le cas turbulent où l'hypothèse de similitude porte sur le profil de vitesse déficitaire, cette grandeur sera le paramètre de forme G défini par :

$$G = \frac{\int_0^1 \left(\frac{U_e - U}{U_\tau}\right)^2 d\eta}{\int_0^1 \left(\frac{U_e - U}{U_\tau}\right) d\eta}$$

EXTENSION DE LA METHODE INTEGRALE AUX CAS DE COMPRESSEURS

Cette méthode intégrale a d'abord été développée pour des applications de type profil d'aile. L'extension au cas du compresseur demande de prendre en compte trois nouveaux phénomènes : le fort taux de turbulence à l'extérieur de la couche limite, les effets de courbure de paroi et la rotation. Le problème des flux de chaleur à la paroi, plus spécifique aux turbines, n'a pas été abordé ici.

I - INFLUENCE DE LA TURBULENCE EXTERIEURE

Dans le cas d'une couche limite laminaire, la turbulence extérieure favorise la transition. Dans le cas d'une couche limite turbulente, la turbulence extérieure apporte de l'énergie au mouvement turbulent par une augmentation de l'effet d'entraînement de l'écoulement extérieur dans la couche limite. La zone proche de la paroi étant ainsi mieux alimentée en énergie, le coefficient de frottement pariétal augmente et l'apparition du décollement est retardée.

L'effet de la turbulence extérieure sur la couche limite turbulente a déjà été étudié par ARNAL et al. /Réf. 4/ dans le cas bidimensionnel. Il a été montré que le schéma classique de longueur de mélange :

$$- \overline{uv} = \ell^2 \left(\frac{\partial U}{\partial y}\right)^2$$

$$\ell = 0,085 \, \delta \, th \left(\frac{x}{0,085} \cdot \frac{y}{\delta}\right) \qquad x = 0,41$$

pouvait être étendu sous la forme :

$$- \overline{uv} = th \left(\frac{0,085 \, \delta}{(a_1 \, q_e^2)^{1/2}} \, \frac{\partial U}{\partial y}\right) \, \ell^2 \left(\frac{\partial U}{\partial y}\right)^2 \qquad a_1 = 0,15$$

où $1/2 \, q_e^2$ est l'énergie cinétique de la turbulence extérieure.

L'analyse des familles de profils de vitesse obtenues avec cette version modifiée du schéma de longueur de mélange a montré que la forme des profils de vitesse était inchangée en présence de turbulence extérieure. Seule l'évolution selon x de l'épaisseur δ de couche limite était modifiée. Les relations de fermeture ne faisant intervenir que la forme du profil de vitesse (coefficient de frottement, paramètre de forme H^x, ...) restent donc inchangées. Seul l'entraînement de fluide sain par la couche limite :

$$C_E = \frac{\partial \delta}{\partial x} - \frac{V_e}{U_e}$$

a été modifié. L'entraînement augmente avec le taux de turbulence extérieure.

Dans le cas tridimensionnel, le profil de vitesse longitudinale étant inchangé en présence de turbulence extérieure, le profil de vitesse transversale le sera aussi. On n'observe alors pas de modification des relations de fermeture autre que la modification de l'entraînement.

II - INFLUENCE DE LA COURBURE DE PAROI

II.1. Observations expérimentales

Qualitativement, les effets de courbure de paroi sont souvent expliqués en utilisant la notion de déplacement virtuel d'un élément fluide. On suppose qu'un tel élément est déplacé normalement à la paroi en conservant son moment angulaire (le fluide est supposé sans frottement). Dans le cas de la paroi convexe, le gradient de pression existant tend à renvoyer l'élément à sa position initiale : l'écoulement est stable. Au contraire, dans le cas de la paroi concave, l'élément tend à s'éloigner de plus en plus de sa position initiale : l'écoulement est instable.
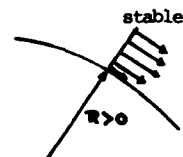
Pour une couche limite laminaire, les effets de courbure sont en général faibles et n'entraînent pas de modifications très importantes. Toutefois, on notera que dans le cas d'une paroi concave, la transition peut être favorisée par l'apparition de tourbillons de TAYLOR-GÖRTLER.

Pour une couche limite turbulente, la stabilisation de l'écoulement sur paroi convexe diminue l'agitation turbulente. Les régions proches de la paroi sont alors moins bien alimentées en énergie et plus sensibles à un gradient de pression adverse. La couche limite décolle alors plus facilement. A l'opposé, sur une paroi concave, l'agitation turbulente est augmentée et le décollement est retardé.

La courbure de paroi modifie peu l'évolution d'une couche limite laminaire et n'influe que sur sa transition. Par contre, le mouvement turbulent est amplifié ou amorti par la courbure, si bien que l'évolution d'une couche limite turbulente dépend beaucoup plus de la courbure de la paroi.

II.2. Influence de la courbure de paroi sur la turbulence

L'étude de l'influence de la courbure de paroi sur la turbulence a été faite dans le cas bidimensionnel par COUSTEIX et HOUDEVILLE /Réf. 5/ et étendue au cas tridimensionnel par AUPOIX et COUSTEIX /Réf. 3/.

La méthode employée consiste à utiliser les équations de transport pour les tensions turbulentes. Ces équations étant modélisées dans un repère curviligne, une hypothèse d'équilibre permet de se ramener à un système linéaire pour les tensions turbulentes. En se plaçant dans un repère lié aux lignes de courant extérieures et en appelant R_x et R_z les rayons de courbure de la paroi dans la direction de la ligne de courant extérieure

et de sa normale, les tensions turbulentes s'écrivent sous la forme :

$$- \overline{uv} = \frac{1}{2} q^2 \; a_1{}^* \; (R_x)$$

$$- \overline{vw} = \frac{1}{2} q^2 \; a_1{}^* \; (R_x) \; T \; (R_x, \; R_z) \frac{\frac{\partial W}{\partial y}}{\frac{\partial U}{\partial y}}$$

où $\quad R_x = \dfrac{\frac{U}{R_x}}{\frac{\partial U}{\partial y}} \quad$ et $\quad R_z \simeq \dfrac{\frac{W}{R_z}}{\frac{\partial W}{\partial y}} \quad$ sont des nombres de Richardson

caractéristiques des effets de courbure et T une fonction voisine de l'unité. La courbure modifie surtout le rapport $\frac{\tau}{1/2 \; q^2} \simeq \frac{- \overline{uv}}{1/2 \; q^2}$ dans le cas d'un faible écoulement transversal.

Cette modification peut être répercutée au niveau d'un schéma de longueur de mélange qui devient, dans le cas d'un faible écoulement transversal :

$$- \overline{uv} = f \; \ell^2 \; (\frac{\partial U}{\partial y})^2$$

$$- \overline{vw} = f \; \ell^2 \; \frac{\partial U}{\partial y} \cdot \frac{\partial W}{\partial y}$$

avec $\quad f \simeq (1 - \alpha \, R_x) \qquad \alpha \simeq 10,25$

où R_x est le nombre de Richardson formé avec le rayon de courbure de la paroi dans la direction des lignes de courant extérieures.

II.3. Application aux solutions de similitude

Les profils de vitesse de couche limite en similitude sur paroi courbe sont quasiment identiques aux profils obtenus sur paroi plane. On observe une très légère modification de la relation de fermeture donnant le coefficient de frottement pariétal C_f. Comme dans le cas de la turbulence extérieure, l'effet de stabilisation ou de déstabilisation de la turbulence par la courbure se traduit par une modification du taux de croissance de l'é-paisseur de couche limite ou encore de l'entraînement. Quand la turbulence est stabilisée par une paroi convexe, l'entraînement diminue ; quand la turbulence est déstabilisée par une paroi concave, l'entraînement augmente.

III - INFLUENCE DE LA ROTATION DE REPERE

III.1. Observations expérimentales

Pour qu'une couche limite bidimensionnelle soumise à une rotation reste bidimensionnelle, il faut et il suffit que le *vecteur rotation soit normal au plan de l'écoulement.*

La rotation a alors deux effets. La force d'inertie centrifuge correspond à une modification de la loi de vitesse extérieure si le rayon de giration est grand devant l'épaisseur de la couche limite. La force de CORIOLIS joue un rôle analogue au gradient de pression normal dans le cas d'une couche limite sur paroi courbe et stabilise ($\omega < 0$) ou déstabilise ($\omega > 0$) l'écoulement.

Dans le cas d'une couche limite tridimensionnelle, les effets de la rotation sont plus compliqués car les trois composantes du vecteur rotation sont à prendre en compte. Un cas simple intéressant est celui où le vecteur rotation est normal à la paroi. Les forces de CORIOLIS jouent alors le rôle d'un gradient de pression transversal qui incurve les lignes de courant extérieures et induit des effets tridimensionnels dans la couche limite.

Une certaine analogie peut être faite entre les effets de rotation et de courbure. Dans le cas bidimensionnel, la rotation ω_3 est analogue à la courbure longitudinale de la paroi qui stabilise ou déstabilise l'écoulement. Dans le cas tridimensionnel, la rotation ω_2 est analogue à la courbure des lignes de courant extérieures qui donne lieu à des effets tridimensionnels.

III.2. Influence de la rotation de paroi sur la turbulence

Les effets de la rotation sur la turbulence ont été étudiés par COUSTEIX et AUPOIX /Réf. 6/, à l'aide des équations de transport pour les tensions turbulentes.

En exprimant les composantes du vecteur rotation sous la forme de nombres de Richardson:

$$R_i = - \frac{2\omega_i}{\left[(\frac{\partial U}{\partial y})^2 + (\frac{\partial W}{\partial y})^2 \right]^{1/2}}$$
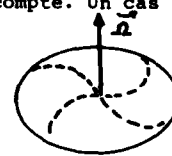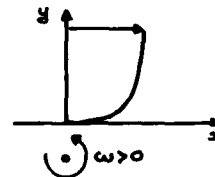
les tensions turbulentes s'écrivent, avec l'hypothèse de faible écoulement transversal :

$$- \overline{uv} = \frac{1}{2} q^2 \ (C_\mu - C_{\mu 1} \ R_3)^{1/2}$$

$$- \overline{vw} = \frac{1}{2} q \ (C_\mu - C_{\mu 1} \ R_3)^{1/2} \ . \ \left[(1 + A \ R_3) \frac{\frac{\partial W}{\partial y}}{\frac{\partial U}{\partial Y}} + B \ R_2 - A \ R_1 \right]$$

où $C_\mu = (2a_1)^2$, $C_{\mu 1}$, A et B sont des constantes.

Dans le cas d'une couche limite bidimensionnelle, l'écoulement est stabilisé pour ω_3 négatif de façon analogue à l'écoulement sur une paroi convexe et déstabilisé pour ω_3 positif de façon analogue à l'écoulement sur une paroi concave.

Dans le cas d'une couche limite tridimensionnelle, les effets sont plus compliqués car les différentes composantes du vecteur rotation sont à prendre en compte. L'effet stabilisant ou déstabilisant de la composante du vecteur rotation normale à l'écoulement longitudinal est identique au cas bidimensionnel. Dans le cas particulier où le vecteur rotation est normal à la paroi, les relations :

$$- \overline{uv} = \frac{1}{2} q^2 \ C_\mu^{1/2}$$

$$- \overline{vw} = \frac{1}{2} q^2 \ C_\mu^{1/2} \ (B \ R_2 + \frac{\frac{\partial W}{\partial y}}{\frac{\partial U}{\partial y}})$$

indiquent que les "vecteurs" tension turbulente ($- \overline{uv}, - \overline{vw}$) et cisaillement ($\frac{\partial U}{\partial y}, \frac{\partial W}{\partial y}$) ne sont plus alignés. Cet effet de non-alignement est déjà connu expérimentalement dans les couches limites tridimensionnelles sur paroi fixe /Réf. 7/ et a déjà été pris en compte dans des modèles de turbulence /Réf. 8, 9/ et des relations de fermeture pour l'écoulement transversal /Réf. 9/. Cet effet semble directement lié à la courbure des lignes de courant, courbure qui est analogue à la rotation ω_2 et produit les effets tridimensionnels.

Pour les applications aux turbomachines, les nombres de Richardson restent d'ordinaire de l'ordre du pour cent. En première approximation, seuls ces deux effets sont retenus :

- La composante du vecteur rotation normale à l'écoulement longitudinal stabilise ou déstabilise l'écoulement. La modification résultante du schéma de longueur de mélange est analogue à celle effectuée dans le cas sur paroi courbe.

- La composante du vecteur rotation normale à la paroi produit des effets tridimensionnels de façon analogue à la courbure des lignes de courant extérieures. Ces effets tridimensionnels se caractérisent par un désalignement entre la tension turbulente et le cisaillement, effet qui a déjà été pris en compte précédemment /Réf. 9/.

III.3. Application aux solutions de similitude

L'effet stabilisant ou déstabilisant de la composante du vecteur rotation normal à la paroi va, comme dans le cas de couches limites sur paroi courbe, se traduire par une légère modification de la loi pour le coefficient de frottement pariétal et surtout par la modification de l'entraînement.

Le non-alignement entre tension turbulente et cisaillement entraîne l'apparition de nouvelles familles de profils de vitesse transversale et donc de nouvelles lois pour les grandeurs caractéristiques de l'écoulement transversal.

Rappelons enfin que lorsque l'on considère les équations de quantité de mouvement dans un repère tournant, des termes supplémentaires apparaissent dus à la force de CORIOLIS. On retrouvera ces termes supplémentaires dans les équations intégrales de quantité de mouvement que l'on a à résoudre.

DESCRIPTION SUCCINCTE DU CODE DE CALCUL - EXEMPLES DE RESULTATS

I - *DESCRIPTION SUCCINCTE DU CODE DE CALCUL*

Le programme calcule le développement de couches limites laminaires et turbulentes compressibles (nombre de Mach < 5), sur paroi athermane.

Les équations intégrales de couche limite sont écrites dans un repère curviligne quelconque. Le repère lié aux lignes de courant extérieures n'est utilisé que pour l'exploitation des relations de fermeture tirées des solutions de similitude.

Les profils initiaux de couche limite peuvent être imposés ou calculés par le programme comme solutions de similitude le long d'une ligne de partage. La position du point de début de transition est calculée à l'aide du critère de GRANVILLE modifié prenant en compte l'histoire de la couche limite et le taux de turbulence extérieure /Réf.10/ pour l'écoulement longitudinal et du critère de BEASLEY /Réf. 11/ pour l'écoulement transversal. Au point de transition, ou en présence d'un bulbe de décollement, le calcul effectue une transition brutale et continue en turbulent. Le développement de la couche limite turbulente est alors

sensible aux rayons de courbure pariétaux, à la turbulence extérieure, à la rotation et au non-alignement choisi entre la tension turbulente et le cisaillement moyen.

II - EXEMPLES D'APPLICATION

Les performances du programme de calcul ont été évaluées par des comparaisons à l'expérience sur un ensemble de cas tests. Quelques-uns parmi les plus significatifs sont présentés ci-dessous.

II.1. Effet de la turbulence extérieure (couche limite bidimensionnelle turbulente)

Le diffuseur de 6° étudié par POZZORINI /Réf. 12/ constitue un bon cas d'étude des effets de la turbulence extérieure. Dans ce cas particulier, un programme a été récrit pour calculer à la fois l'écoulement de fluide sain au centre du diffuseur et les couches limites pariétales, en imposant la conservation du débit.

La comparaison porte sur les coefficients de pression à la paroi et les coefficients de frottement pariétaux qui permettent de localiser le point de décollement. Deux cas sont étudiés, l'un avec une faible turbulence extérieure, l'autre avec une turbulence extérieure importante. Dans les deux cas, l'accord calcul/expérience est très satisfaisant, sauf pour les faibles valeurs du C_f. Le diffuseur étant le même dans les deux cas, le fait que la turbulence extérieure augmente l'entraînement et retarde le décollement est mis en évidence dans cet exemple (figures 1 et 2).

II.2. Effet de la courbure de paroi (couche limite bidimensionnelle turbulente)

a) Expérience de SO et MELLOR /Réf. 13/

Ce premier exemple, étudié dans la référence /6/, concerne une couche limite bidimensionnelle turbulente se développant sur une paroi courbe. La couche limite se développe d'abord sur une plaque plane en gradient de pression nul, puis sur une paroi convexe en gradient de pression adverse. Au début de la partie courbe, le rapport de l'épaisseur de la couche limite au rayon de courbure de la paroi dépasse 10 %. A la fin de la partie courbe, la couche limite est presque décollée.

Deux calculs ont été effectués : l'un prend en compte l'effet de la courbure de paroi sur la turbulence ; l'autre non. La figure 3 compare les évolutions expérimentales et calculées du facteur de forme H, de l'épaisseur de quantité de mouvement longitudinale θ_{11} et du coefficient de frottement pariétal C_f. La nécessité de prendre en compte l'effet de la courbure de paroi sur la turbulence pour obtenir un bon accord calcul/expérience et une bonne prévision du décollement est bien mise en évidence sur la figure 3.

b) Cas d'une grille d'aube transsonique

Ce cas de grille d'aube transsonique a été étudié dans la référence /14/. Il s'agit d'une grille d'aube de compresseurs, utilisant le profil "115". La grille d'aube est placée comme indiqué sur la figure 4 dans un montage bidimensionnel permettant de varier l'angle d'attaque et le nombre de Mach. Le profil d'aube "115" est dessiné pour donner une déviation de 50° sans décollement.

Parmi l'ensemble des cas étudiés dans la référence /14/, nous ne présenterons que les deux cas de la figure 5 montrant l'apparition du décollement de la couche limite turbulente à M = 0,7 quand la déviation β augmente. On donne dans chaque cas l'évolution en fonction de l'abscisse curviligne de la vitesse extérieure, du paramètre de forme H et des épaisseurs longitudinales de déplacement δ_1 et de quantité de mouvement θ_{11}.

On retrouve la nécessité de prendre en compte les effets de la courbure de la paroi si l'on veut prédire correctement l'évolution de la couche limite et le décollement. Pour une déviation de 53°, le calcul prévoit le décollement de la couche limite un peu trop tôt ; le décollement est observé expérimentalement juste en amont de la deuxième station de mesure.

II.3. Couches limites turbulentes tridimensionnelles

a) Canal courbe supersonique

L'écoulement supersonique dans un canal courbe simulant le distributeur d'un diffuseur de compresseur centrifuge est étudié dans la référence /15/. Des mesures de pression pariétale très resserrées et de nombreux sondages de couche limite ont permis de connaître finement l'écoulement. Sur la figure 6, les résultats du calcul par la méthode intégrale sont comparés à l'expérience. Les épaisseurs de quantité de mouvement longitudinale et transversale sont prédites avec une bonne précision. Il en est de même pour la prédiction de la direction des lignes de courant pariétales.

b) Diffuseur tournant

Dans cet exemple théorique reporté dans la référence /16/, on s'intéresse à la couche limite sur un diffuseur tournant.

Lorsque le diffuseur est fixe, la position de la ligne de décollement dépend de l'angle d'entrée. Le décollement se rapproche de l'entrée lorsque l'angle d'entrée augmente (figure 7).

Pour un angle d'entrée donné, la figure 8 montre l'effet de la rotation du diffuseur. La vitesse de rotation est rapportée à la vitesse périphérique de l'écoulement à l'entrée du diffuseur. Lorsque la vitesse de rotation augmente, le décollement se produit plus loin de l'entrée puis la direction des lignes de courant s'inverse. Le décollement continue à s'éloigner de l'entrée. Aucun décollement n'a été trouvé pour $\Omega^* = \Omega \cdot r_o/V_{to} > 1$.

CONCLUSION

Une méthode intégrale de calcul de couche limite permet de calculer avec précision et à un faible coût, l'évolution de la couche limite tridimensionnelle dans un compresseur.

L'emploi de solutions de similitude comme familles de profils de vitesse permet de prendre en compte facilement les effets de la turbulence extérieure, la rotation ou la courbure de paroi.

L'utilisation d'un modèle de turbulence du type longueur de mélange déduit d'une étude des équations de transport des tensions de Reynolds met en évidence l'effet stabilisant ou déstabilisant de la courbure longitudinale et de la composante du vecteur rotation normale à l'écoulement longitudinal. La composante du vecteur rotation normale à la paroi crée d'autre part des effets tridimensionnels, tant par la modification des lois de vitesse extérieure que par son effet sur la turbulence.

Dans les cas tests considérés, la méthode intégrale donne des résultats corrects ; cependant, on manque de données sur des cas proches de la réalité où apparaissent à la fois les effets de courbure de paroi, de rotation, de turbulence extérieure sur des couches limites tridimensionnelles. Des expériences de couche limite tridimensionnelle en rotation fourniraient un défi intéressant pour les méthodes de calcul.

REFERENCES

/1/ MICHEL R., QUEMARD C., DURANT R. - "Application d'un schéma de longueur de mélange à l'étude des couches limites turbulentes d'équilibre" Note technique ONERA N° 154 (1969)

/2/ COUSTEIX J. - "Analyse théorique et moyens de prévision de la couche limite turbulente tridimensionnelle" Publication ONERA N° 157 (1974)

/3/ AUPOIX B., COUSTEIX J. - "Etude et développement d'une méthode intégrale de calcul de couche limite tridimensionnelle (laminaire-turbulent) adaptée aux compresseurs" Rapport interne

/4/ ARNAL D., COUSTEIX J., MICHEL R. - "Couche limite se développant avec gradient de pression positif dans un écoulement extérieur turbulent" La Recherche Aérospatiale N° 1976-1 (1976)

/5/ COUSTEIX J., HOUDEVILLE R. - "Méthode intégrale de calcul d'une couche limite turbulente sur une paroi courbée longitudinalement" La Recherche Aérospatiale N° 1977-1 pp. 1-13 (1977)

/6/ COUSTEIX J., AUPOIX B. - "Modélisation des équations aux tensions de Reynolds dans un repère en rotation" La Recherche Aérospatiale N° 1981-4 pp. 275-285 (1981)

/7/ ELSENAAR A., BOELSMA S.H. - "Measurements of the Reynolds stress tensor in a three-dimensional turbulent boundary layer under swept wing conditions" NLR TR 74095 U (1974)

/8/ ROTTA J.C. - "A family of turbulence models for three-dimensional thin shear layers" Symposium on Turbulent Shear Flows - PENNSYLVANIA State University - pp. 10.27-10.34 (1977)

/9/ COUSTEIX J., AUPOIX B. - "Three-dimensional boundary layers : turbulence modelisation and calculation methods" Second Symposium on Turbulent Shear Flows - Imperial College, LONDON - pp. 15.25-15.30 (1979)

/10/ ARNAL D., HABIBALLAH M., DELCOURT V. - "Synthèse sur les méthodes de calcul de la transition développées au DERAT" Rapport interne

/11/ BEASLEY J.A. - "Calculation of the laminar boundary layer and the prediction of transition on a sheared wing" ARC R & M 3787 (1973)

/12/ POZZORINI R. - "Das turbulente Strömungsfeld in einem langen Kreiskegel-Diffusor" Ph. D. Dissertation 5646, Eidgenössischen Technischen Hochschule ZURICH, Ed. Truninger AG, ZURICH (1976)

/13/ SO R.M.C., MELLOR G.L. - "An experimental investigation of turbulent boundary layer along curved surfaces" NASA CR 1940 (1972)

/14/ MEAUZE G. - "Transonic boundary layer on compressor stator blades as calculated and measured in wind tunnel" Fourth International Symposium on Air Breathing Engines ISABE ORLANDO (1 - 6 April 1979)

/15/ COUSTEIX J., MICHEL R. - "Analyse expérimentale et théorique des couches limites turbulentes tridimensionnelles dans un canal supersonique courbe" La Recherche Aérospatiale N° 1975-1 pp. 1-10 (1975)

/16/ MICHEL R. - "Méthode de calcul de la couche limite turbulente tridimensionnelle jusqu'à la séparation. Application à un cas simple de turbomachine" Groupe ad hoc AGARD sur les effets de couches limites dans les turbomachines - PARIS (18 - 21 avril 1972)
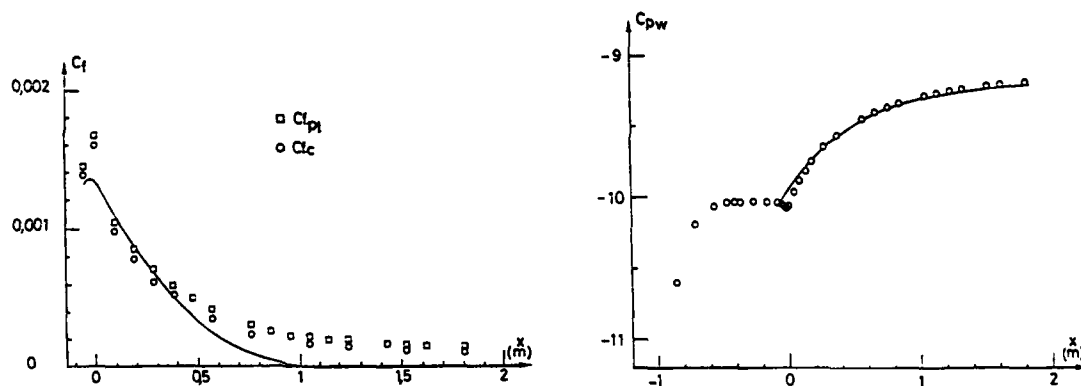
Figure 1 - Faible turbulence extérieure

Calcul dans un diffuseur conique - Expérience de POZZORINI
Evolution du coefficient de frottement parietal
Cf_{pt} : tube de PRESTON
Cf_c : loi de paroi
Evolution du coefficient de pression
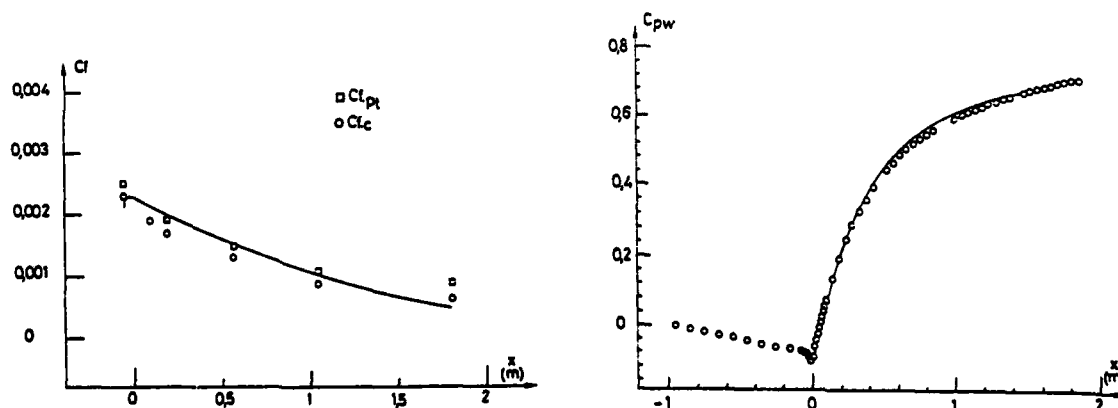
Figure 2 - Forte turbulence extérieure
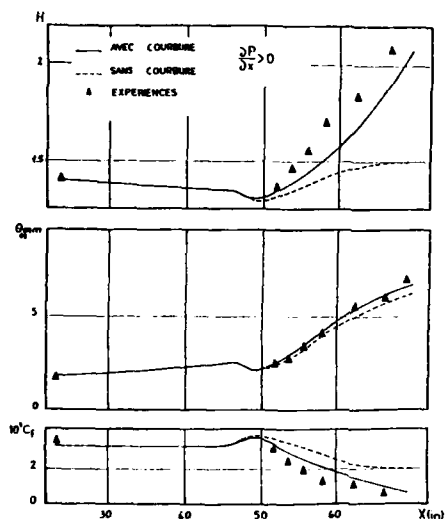
Figure 3 - Couche limite sur paroi courbe -
Expérience de SO et MELLOR
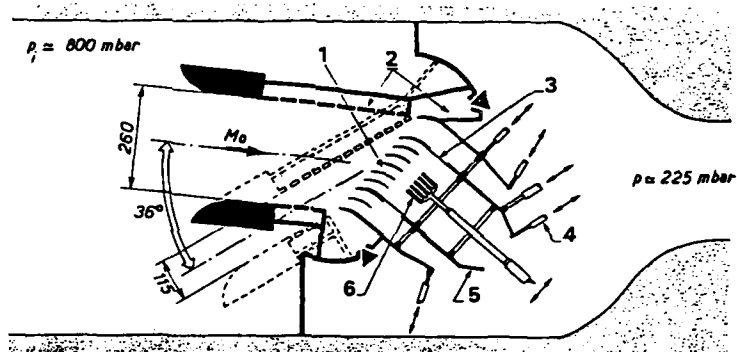
Figure 4 - Montage expérimental de grille d'aube transsonique
1 Canal interaube instrumenté - 2 Chambres d'aspiration -
3 Parois flexibles - 4 Vérins - 5 Col ajustable -
6 Peigne de pression

Figure 5 - Comparaison calcul - expérience sur la grille d'aubes
Expérience : ● écoulement non décollé   o écoulement décollé

(a)

(b)

$$\theta_{11} = \int_o^1 \frac{\rho U}{\rho_e U_e} \left(1 - \frac{U}{U_e}\right) \, d\eta$$

(c)
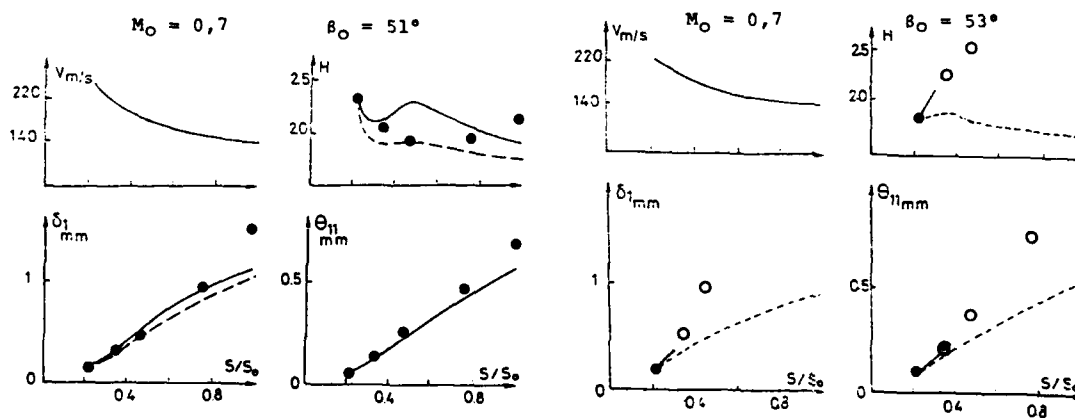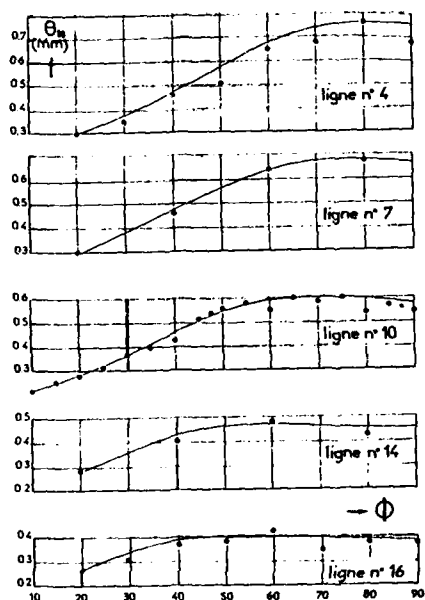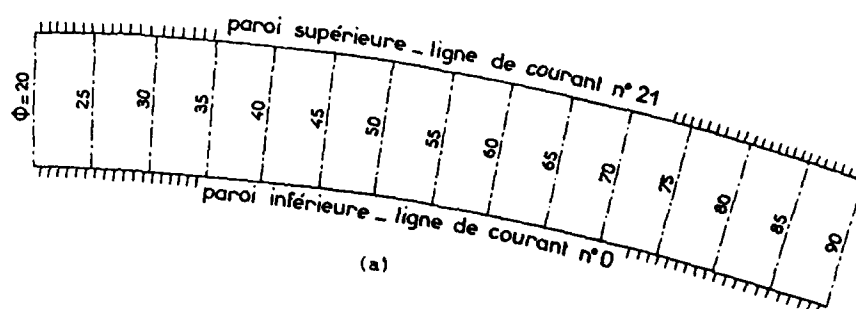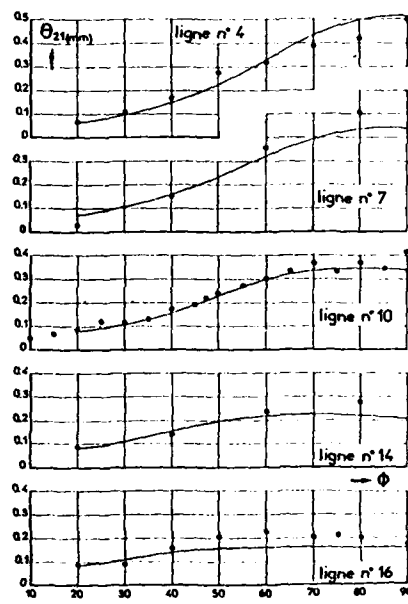
$$\theta_{21} = \int_o^1 - \frac{\rho U W}{\rho_e U_e^2} \, d\eta$$
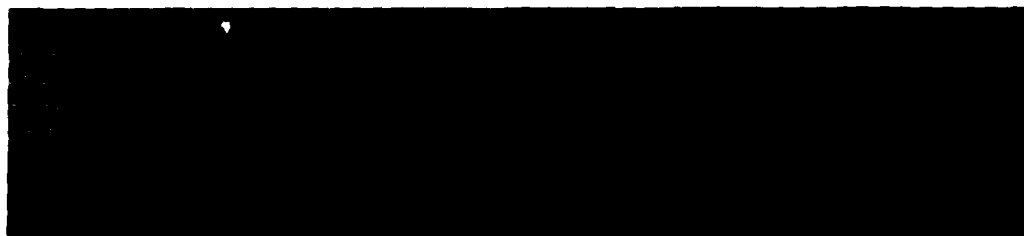
(d)

Figure 6 - Tuyère courbe supersonique

    (a) Configuration de la tuyère
    (b) Comparaison calcul-expérience. Evolution de θ_{11}
    (c) Comparaison calcul-expérience. Evolution de θ_{21}
    (d) Visualisation des lignes de courant pariétales
        et comparaison avec les lignes de courant pariétales
        calculées

Figure 7 - Couche limite tridimen-
sionnelle sur un diffu-
seur tournant. Influence
de l'angle d'entrée
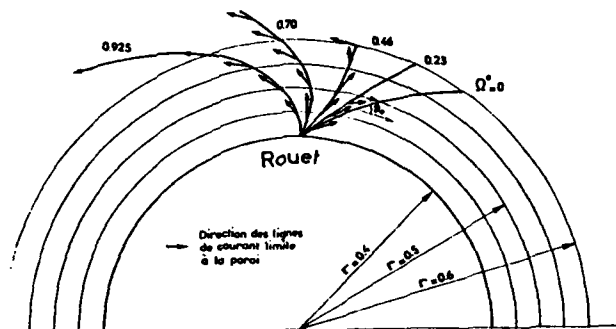
a) Lignes de courant des vitesses
relatives
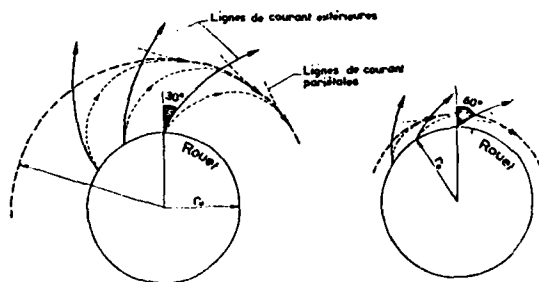
b) Accumulation des lignes de cou-
rant pariétales et décollement
radial

Figure 8 - Couche limite tridimension-
nelle sur un diffuseur tour-
nant. Influence de la vitesse
de rotation

a) Position du décollement radial

$$\Omega^{*} = 0 \qquad \Omega^{*} = \frac{\Omega r_{2}}{V I_{2}} = 0.5 \qquad \Omega^{*} = 1$$
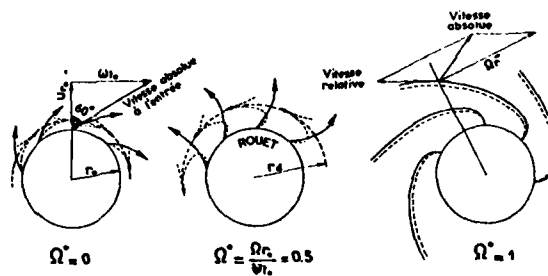
b) Evolution de l'épaisseur de couche
limite δ et de la déflection à la
paroi
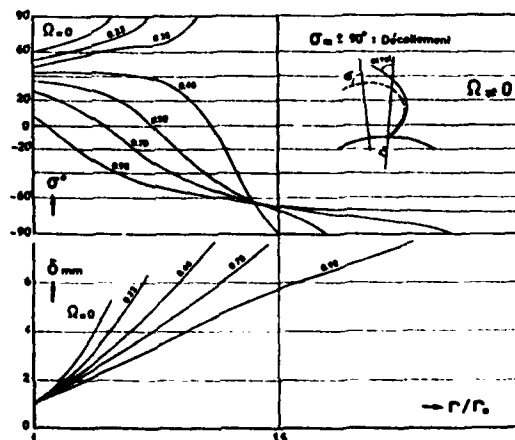
DISCUSSION

Ph.Ramette, Fr

    (1) Pourriez vous préciser comment le mod.:le de longueur de mélange a été modifié pour prendre en compte la turbulence extérieure?

    (2) Pouvez-vous appliquer votre modèle à des roues de compresseurs axiaux?

Réponse d'Auteur

    (1) Le modèle de longueur de mélange utilisé dans le cas avec turbulence extérieure est donné dans les références 3 et 4 et dans le papier écrit.

    (2) N'étant pas turbomachiniste, je ne connais pas d'expérience de grille en *rotation* suffisamment documentée pour fournir un cas test au code de calcul.

VISCOUS EFFECTS AND HEAT TRANSFER IN A CALCULATION METHOD FOR AXIALSYMMETRIC FLOW IN MULTISTAGE TURBOMACHINES USING THE STREAM FUNCTION

W. Sandel
Dipl. Ing.
Universität Stuttgart
Inst. für Luftfahrt-Antriebe
Pfaffenwaldring 6
7000 Stuttgart 8o

SUMMARY

A method is described for including viscous effects and heat transfer in a through-flow computation procedure based on the stream function approach for steady axialsymmetric flow. Viscous shear-stress and heat conduction relations are used within a coarse grid resolution due to storage and computation time limitations in multistage applications. Near the end walls an analytical function is used to model the dissipation rate. The approach allows for energy transport across streamlines.

LIST OF SYMBOLS

A	area
$\underline{c}$	velocity vector
c_m	velocity component within the meridional plane
c_r	radial velocity component
c_u	circumferential velocity component
c_z	axial velocity component
e	stands for h_t or i
f_u	circumferential viscous force component per unit mass
h_t	stagnation enthalpy per unit mass
i	rothalpy per unit mass
L	direction tangential to the streamlines
Ma	Mach number
N	direction normal to the stream surface or normal to c_m
n	direction normal to c_m within the meridional plane
$\dot{\underline{q}}$	heat flux vector
$\dot{Q}$	heat delivered per unit volume
r	radial direction
s	entropy per unit mass
T	temperature
V	volume
$\dot{W}$	mechanical work delivered per unit volume
z	axial direction
α	angle within meridional plane between z-axis and c_m
η	coefficient of viscosity
λ	coefficient of heat conduction
ρ	density
$\underline{\tau}$	stress tensor
ϕ	dissipation per unit volume
ψ	stream function
ω	rotor angular velocity
∇	Nabla operator
$(\ )^t$	transposed matrix

Subscribts:

abs	absolute
r	radial
rel	relative
u	circumferential
z	axial

INTRODUCTION

The internal flow in turbomachines is unsteady, three-dimensional, compressible, viscous and nonadiabatic. It is guided through a sequence of rotating and stationary passages. Since the numerical analysis in this generality is too complicated for available calculation methods, through-flow methods are built around simplified models of the turbomachine flow. Through-flow methods usually assume steady flow conditions and the three-dimensional flow is approximated by iterative coupling of two two-dimensional computations on the S1 - blade-to-blade stream surface and the S2 - hub-to-shroud stream surface /1/.

This paper deals with the computation of the flow on the meridional plane with the further assumption that the turbomachine flow be axialsymmetric. The S2-stream surface is used to introduce the turning effect of the blading.

In the through-flow calculation on the meridional plane viscous effects are often accounted for as total pressure loss, blockage and as change in blade turning. They are defined by empirical correlations and/or by end-wall boundary-layer computation methods /2,3,4,5/. Such an approach applies an entropy change on the streamline but usually assumes constant stagnation enthalpy or rothalpy along the streamline /6,7/. Therefore no transfer of energy is allowed across streamlines.

A different approach was investigated which is based on an attempt to couple viscous effects to the local flow properties by introducing shear stress and heat conduction relations into an existing computation procedure which employs the stream function in its mathematical formulation. Energy transport effects due to shear stress and heat conduction are considered by computing diffusive energy transport terms throughout the computational field. Losses are derived by using a dissipation function. With respect to future multistage applications with their high demand on computer storage only a rough computational grid resolution in cross-stream direction is presupposed. Strong curvatures in the velocity profiles near the end-walls are simulated by analytical velocity distributions which serve to model the dissipation rate.

VISCOUS EFFECTS

For a realistic computation of viscous flows one would like to solve the Navier-Stokes-equations together with a turbulence model. For the application in a through-flow method intended for multistage machines this approach has some drawbacks:

- The numerical solution for the Navier-Stokes-equations with a finite-difference method calls for high resolution in the discretized representation of the flow region. On the other hand, the scale of the whole region to be covered for a multistage computation is large in comparison to the scale of the necessary resolution of the physical events and the resulting very high number of grid points is uneconomical or even unfeasable with today's computers.

- The axialsymmetric model in itself introduces many simplifications; it would be unreasonable to apply a costly Navier-Stokes procedure that could not perform to its inherent capabilities because of the restrictions imposed on it by the axialsymmetric assumption.

For these reasons one must compromise on the modelling of viscosity. Common practise is to concentrate on the dissipation effect and to apply corrections to the computation of the predominantly inviscid flow by the introduction of total pressure losses and to account for the effect of reduced boundary-layer mass flow on the main flow by diminishing the passage cross-section area accordingly. Some of the losses, for example profile loss, have their origin in the cascade flow and/or are dependent of three-dimensional flow effects, for example secondary flow- and clearance flow-losses. These can be accounted for in a two-dimensional through-flow method only in a general way, as is usually done in the form of empirical loss correlations. The end-wall effects, although coupled with secondary flows, are related to velocity profile shapes which can be represented in the meridional plane and are therefore expected to be better suited for modelling. In addition to the dissipation effect the transport of mechanical energy by viscous shear stress is another aspect of viscosity in the wall region of the flow. In a compressor, for example, one has to assume that the low energy fluid particles in the wall region move against the increasing pressure through transfer of energy from the inner flow regions.

In the version of the through-flow method, which is described here, an attempt is made at modelling the viscous effects arising from velocity gradients within the axialsymmetric flow. These effects include dissipation as well as the cross-stream transport of mechanical energy through accounting for work done by shear stresses on neighbouring fluid particles. A model for the heat transfer arising from temperature gradients in the meridional plane is included.

THE BASIC STREAM FUNCTION METHOD

The basic through-flow method used to implement the expansion is characterized by the use of the stream function /8/. The mathematical formulation is a modification of Wu's principal equation. Similar equations are derived for rotor, stator and annular duct regions. A compressor,for example, is assembled by combining these subregions.
Due to the similar formulation the main computational variables , the stream function , the total energy term e and the entropy s can be solved in the same way for the different regions. Stator and annular duct regions are formulated in the absolute reference frame, the rotor region in a rotating system.

The stream function approach is in common use for through-flow computations. It ensures the conservation of mass flow and an easy application of the necessary boundary conditions for Ψ. Solved with a finite-difference relaxation method, it shows good convergence.

The circumferential velocity component in the annular duct region is derived from the angular momentum equation. For the region influenced by stator or rotor it is given through the S2-stream surface. The stream surfaces are currently assembled through radial stacking of plane cascade turning correlations in connection with an assumed linear deviation angle distribution for the streamline shape between leading and trailing edge of the blading. The turning depends on the inflow conditions to the blade regions and adjusts the stream surfaces with the ongoing iteration process.

EQUATIONS

If one derives the main equations starting with the shear stress relation in the momentum equation and introducing Fourier's heat conduction relation in the energy equation one obtains the following set of equations:

The principle equation for the stream function:

$$(1-Ma^{*2}) \frac{\partial^2 \Psi}{\partial L^2} + \frac{\partial^2 \Psi}{\partial N^2} = \text{right-hand side (RHS)} \qquad (1)$$

The formulation is projected on the meridional plane (for the annular duct region) or on the plane tangential to the stream surface (for the bladed region). L denotes the local direction of the streamline and N the direction normal to L either in the meridional plane (annular ducts) or in the plane tangential to the stream surface (bladed region).
See fig. 1 and fig. 2.

The Mach number depends on the respective region:

> annular duct: Ma^* is derived from meridional velocity
>
> stator: Ma^* is derived from absolute velocity
>
> rotor: Ma^* is derived from relative velocity

The right-hand side of the equation contains derivatives of stagnation enthalpy/rothalpy and entropy and in addition for the annular duct region derivatives of angular momentum or for the bladed region derivatives of the stream surface orientation and blockage factors.

The angular momentum equation used in annular ducts:

$$\rho \underline{c} \cdot \nabla (r c_{u,abs}) = r f_u \qquad (2)$$

The transport equations:

$$\rho \underline{c} \cdot \nabla e = \dot{Q} + \dot{W} \qquad (3)$$

$$\rho \underline{c} T \cdot \nabla s = \dot{Q} + \dot{\phi} \qquad (4)$$

The additional terms can be identified as:
- source of heat through dissipation $\dot{\phi}$
- supply of energy through work done by viscous forces on the moving fluid $\dot{W}$
- supply of heat through heat conduction $\dot{Q}$

The terms – dissipation, mechanical work done and heat conduction – are related to the computed flow and the end-wall boundary conditions through the shear stress definition following Newton's relation together with Stoke's assumption

$$\underline{\underline{\tau}} = \eta \, (\nabla \underline{c} + (\nabla \underline{c})^{t} - \frac{2}{3} \nabla \underline{c} \, \underline{\underline{I}} \,) \quad (5)$$

with

$$\dot{\phi} = \underline{\underline{\tau}} \cdots \nabla \underline{c} \quad (6)$$

$$\dot{w} = - \nabla \cdot (\, \underline{\underline{\tau}} \cdot \underline{c} \,) \quad (7)$$

and Fourier's law of heat conduction

$$\dot{\underline{q}} = - \lambda \nabla T \quad (8)$$

with

$$\dot{Q} = - \nabla \cdot \dot{\underline{q}} \quad (9)$$

Further, it is assumed that one can neglect the streamwise diffusive energy transport as opposed to the cross-stream transport. With the axialsymmetric model, diffusive transport in the circumferential direction is already precluded. The only diffusive energy transport direction taken into account is therefore the cross-stream direction. This "parabolization" of diffusive transport simplifies the solution algorithm but still contains the major effects.

Profile losses still must be introduced through correlations in the form of additions to the dissipation term, since they cannot be related to the meridional flow directly.

SOLUTION PROCEDURE

The solution follows a relaxation procedure. The stream function equation and transport equations are coupled through iterations. To linearize the set of nonlinear partial differential equations, the h_t / i and s values are assumed to be constant when computing the stream function and the ψ values are held constant while solving the transport equations on each iterative step. The stream function equation is solved with the finite difference method.

The range of applications for which this approach is intended can be described as a flow, where the viscous and heat conduction effects can be considered as corrections to an otherwise inviscid flow. It is not capable to provide solutions for strong viscous effects as in the case of flow separation. The dominance of convective energy transport must be ensured to get a stable iterative solution procedure.

Using less spatial resolution than the accurate describtion of the physical process actually requires means limiting oneself to the description of the effect of this process on a spatially averaged approximation of the real process. With the use of second order polynomials in the central difference scheme for the derivatives the stream function solution is not able to develop for example a thin boundary-layer velocity profile with the given coarse computational grid. It provides a velocity distribution which represents spatially averaged values for the mass flow. Therefore the values of h_t / i and s, which are used in the stream function equation and which the transport equations should deliver, must fit this averaged conception.

The method for the solution of the transport equations is built around the concept of energy and entropy fluxes. The convective component of the fluxes is described through ρ ce and ρ ca , according to the computational variables e and s. These convective fluxes are coupled to the averaged mass flow given by the stream function. The transport equations relate the convective energy transport to the diffusive energy transport and the dissipative energy sources. Diffusive transport is expressed through the derivatives of the velocity and temperature field in the flow. Since derivatives are defined for points in the field rather than for volumes it is difficult to express the proper averaged values to be used to correct the transported mean amount of energy / entropy. This is valid especially in the region close to the end-wall, where the velocity to be modelled

is rapidly changing in the direction normal to the wall.

A method working on control volumes (CV), the boundaries of which are defined through the computational grid, was found to be suited for the computation of the transport equations. Fluxes into the control volume as well as end-wall boundary conditions can be defined on the control volume faces, whereas dissipation is described throughout the volume. By adding these boundary energy / entropy fluxes to the mean energy flux, they are averaged over the whole control volume. Local conditions can thus be introduced with their effect on the mean convective energy flux. The use of a coarse grid, as a necessity for multi-stage computation, avoids at the same time low velocity flows. The mean mass flow through the control volume can be controlled by adjusting the volume size to be greater than the stability limit requires.

To apply the volume method, the transport equations must be recast via a conservative formulation

$$\nabla \cdot (\rho \underline{c} e) = -\nabla \cdot \underline{q} - \nabla \cdot (\underline{\underline{\tau}} \cdot \underline{c}) \tag{10}$$

$$\nabla \cdot (\rho \underline{c} s) = \frac{1}{T} (-\nabla \cdot \underline{\dot{q}} + \underline{\underline{\tau}} \cdot \cdot \nabla \underline{c}) \tag{11}$$

in an integral formulation

$$\oint_A \rho \underline{c} e \cdot d\underline{A} = -\oint_A \underline{\dot{q}} \cdot d\underline{A} - \oint_A (\underline{\underline{\tau}} \cdot \underline{c}) \cdot d\underline{A} \tag{12}$$

$$\oint_A \rho \underline{c} s \cdot d\underline{A} = \frac{1}{T} (-\oint_A \underline{\dot{q}} \cdot d\underline{A} + \int_V (\underline{\underline{\tau}} \cdot \cdot \nabla \underline{c}) dV \tag{13}$$

Under steady state conditions there cannot be any accumulation of energy / entropy inside the control volume. This fact is used to solve the transport equations. In the volume method the energy / entropy convection out of the control volume through the borderline b) in figure 3 is determined from the balance over all in- and outflowing or generated energy / entropy that contributes to the energy / entropy flows $\rho c e$ and $\rho c s$ through the volume. The sum of all energy / entropy fluxes disappears for steady flow conditions.

Considered fluxes are:

- Convective flux of total energy / entropy $\rho \underline{c} e$, $\rho \underline{c} s$ (which must be the main fluxes)

- Flux of mechanical energy over control volume faces through work done by viscous shear stress

$$(\underline{\underline{\tau}} \cdot \underline{c}) = - \frac{\eta}{c_m} \left\{ (c_z^2 - c_r^2) (\frac{\partial c_z}{\partial r} + \frac{\partial c_r}{\partial z}) + c_u (c_z \frac{\partial c_u}{\partial r} - c_r \frac{\partial c_u}{\partial z} - \frac{c_u c_z}{r}) + 2 c_z c_r (\frac{\partial c_r}{\partial r} - \frac{\partial c_z}{\partial z}) \right\} \tag{14}$$

- Flux of heat across control volume faces from heat conduction

$$\underline{\dot{q}} = - \frac{\lambda}{c_m} (-c_r \frac{\partial T}{\partial z} + c_z \frac{\partial T}{\partial r}) \tag{15}$$

- Heat source inside the control volume which represents the heat generation by dissipation

$$\dot{\phi} = \eta \left\{ \frac{4}{3} \left[\cos^2 \alpha (\frac{\partial c_r}{\partial n})^2 + (\frac{c_r}{r})^2 + \sin^2 \alpha (\frac{\partial c_z}{\partial n})^2 - \frac{c_r}{r} \cos \alpha \frac{\partial c_r}{\partial n} + \frac{c_r}{r} \sin \alpha \frac{\partial c_z}{\partial n} + \sin \alpha \cos \alpha \frac{\partial c_r}{\partial n} \frac{\partial c_z}{\partial n} \right] \right.$$
$$\left. + (\cos \alpha \frac{\partial c_u}{\partial n} - \frac{c_u}{r})^2 + \sin^2 \alpha (\frac{\partial c_u}{\partial n})^2 + (\cos \alpha \frac{\partial c_z}{\partial n} - \sin \alpha \frac{\partial c_r}{\partial n})^2 \right\} \tag{16}$$

Important for the determination of energy / entropy fluxes and the dissipation are the velocity derivatives normal to the flow. These are computed in the inner flow field by central differencing. While fluxes must be determined only at the volume boundaries without regard to the distribution throughout the volume, dissipation must be integrated over the control volume domain. Therefore an assumption on the shape of the velocity distribution over the control volume must be made. In the inner flow field constant velocity gradients were assumed throughout the control volume. At the end-walls, however, the no-slip wall condition must be observed, although it will not be reproduced in the velocity profile of the solution because of the coarse grid computation. An analytical velocity distribution function normal to the wall is established, which differs from the computed velocity profile, but which contains the no-slip wall boundary condition and is used only to model the dissipation rate near the wall. This velocity distibution function is introduced in the dissipation function and integrated analytically over control volume. The modelling of this velocity distribution is of great influence on the wall flow; further work must be done to find an improved model.

The transfer of mechanical energy across the end walls is set at zero according to the no-slip condition, as is the transfer of heat according to the condition of adiabatic walls.

The volume approach for the solution of the transport equations has several advantages over a finite difference procedure:

- Since the energy / entropy flux out of one control volume is identical to the flux into the adjacent control volume over the same boundary, energy / entropy fluxes are preserved.
- The equations are not formulated for a point in the field but over a small area or volume. This in itself provides the necessary averaging of h_t / i and s over the control volume or mesh spacing.
- The control volume approach does not assume a priori a certain shape for the distribution of the flow properties between its boundaries as the finite difference approach does between its mesh points (e.g. second order polynomials). Since the control volume approach uses only the integral of the dissipation inside the control volume, any suitable analytic function may be used which eases the way to model the wall boundary layers.
- It can be expected that, by adjusting the size of the control volume, the average mass flow through the control volume will be large enough to fullfill the stability condition of dominance of convective energy transport even in a wall element with imposed no-slip condition.

COMPUTED EXAMPLE

The velocity distribution function used for modelling of the dissipation is of the form: (see fig. 4)

$$c_x = c_{x1} + (c_{x2} - c_{x1})(e^{g_x(\frac{n - n_1}{n_2 - n_1})} - 1) / (e^{g_x} - 1)$$

where c_x = the modelled velocity component c_z, c_r, c_u

g_x = the function parameter for the velocity component

n = the coordinate normal to the meridional streamline

n_1 = endpoint of function interval at wall

n_2 = inner endpoint of function interval

Here 10% of the channel hight were chosen for the interval distance. The function parameter is defined by the velocity conditions at both ends of the analytical function interval. At the wall the velocity component c_{x1} is set at zero; at the inner endpoint, the velocity component c_{x2} is equal to the computed velocity. The function parameter g_x is derived for each component through the condition that the slope of the analytical velocity distribution equals the slope of the velocity in the computed field at the inner endpoint.

Figures 7, 8, 9 show an example for a computation of the flow through a 1-stage model compressor to demonstrate the feasibility of the described method. Other losses than the dissipation effect are not included.

Figures 5, 6 compare the radial distribution of the axial velocity component behind the stator and the stagnation pressure increase through the stage for the case of inviscid computation and for the dissipation model turned on.

The amount of diffusive energy transport in this test case is very small compared to the amount of dissipated energy at the wall, although the qualitative behaviour like supply of mechanical energy to the wall volume and the outflow of heat from the wall volume was shown in the printout. However, the test case is only a single stage compressor and the radial temperature profile is relatively flat due to the even radial distribution of energy supply through the rotor.

CONCLUSION

The method described here includes energy transport in cross-stream direction from viscous
effects and heat conduction as well as a dissipation model in a through-flow computation
based on the stream function formulation for S2-surfaces. The main features of the method
can be summarized as follows:

- use of coarse computational grid
- diffusive transport terms and dissipation terms "corrective" to a mainly convective
  flow situation (no recirculating flow effects)
- concept of energy / entropy fluxes
- spatially averaged derivation of energy / entropy values for the stream function
  equation
- diffusive transport of energy as work done by viscous forces on neighbouring fluid
  elements, and as heat conduction
- use of volume method and integral formulation of energy / entropy transport equations
- analytical integration to determine the dissipated energy in the wall control volume
  and use of velocity profile function near wall.

It has been indicated that shear stress and heat conduction relations can be introduced
in the stream function approach as long as they can be considered as "corrections" to an
otherwise inviscid flow. However, in order to aquire an applicable dissipation rate at
the end-walls, it is necessary that further progress be made toward a more realistic
velocity distribution model at the wall.

REFERENCES

1   Wu, Ch.H.   A General Theory of the Three Dimensional Flow in Subsonic
                             and Supersonic Turbomachines of Axial-,Radial-,and Mixed Flow

                             Type, NACA TN 2604, 1952

2   Grahl, K.G.   Über den Stand der Kennfeldrechnung mehrstufiger Axial-
                             verdichter,

                             Z. Flugwiss. Weltraumforsch. 1, Heft 1, 1977

3   Hüvel, B.   Berechnung der Strömung in Axialverdichtern mit einem
                             2 D-Verfahren unter Berücksichtigung der Seitenwandgrenz-
                             schicht- und Sekundärströmung,

                             Diss. Universität Stuttgart, 1980

4   Mellor, G.L./Wood,G.M.   An Axial Compressor End-Wall Boundary

                             Layer Theory, ASME 70-GT-80, 1971

5   Hirsch,Ch.   End-Wall Boundary Layers in Axial

                             Compressor, ASME 74-GT-72, 1974

6   Horlock, J.H.   On Entropy Production in Adiabatic Flow in Turbomachines

                             ASME 71-FE-3, 1971

7   Bosman, C./ Marsh, H.   An Improved Method for Calulating the Flow in Turboma-
                             chines, Including a Consistent Loss Model

                             J.Mech. Engg. Science Vol. 16, No 1, 1974

8   Hiebel, J.   Beitrag zur Nachrechnung von stationären Unter- und Über-
                             schallströmungen durch Turbomaschinen unter Berücksichti-
                             gung von Strömungsverlusten und Wärmeflüssen.

                             Diss. Universität Stuttgart, 1980

ACKNOWLEGEMENTS
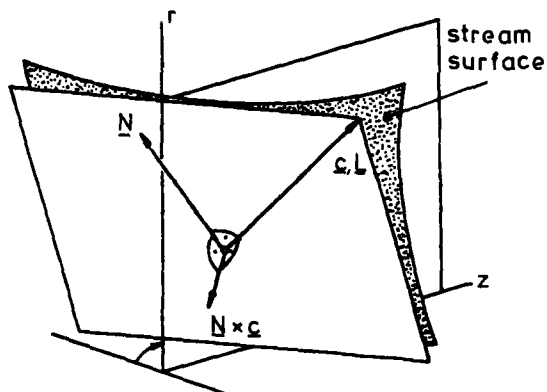
Fig. 1: Directions $\underline{L}$ and $\underline{N}$, rotor and stator
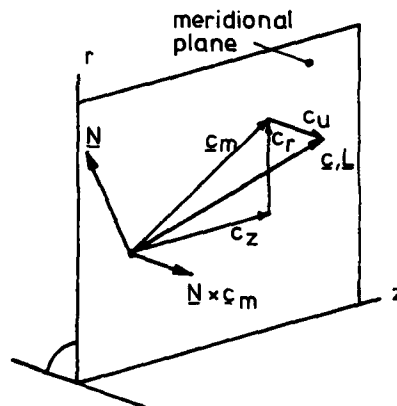
Fig.2: Directions $\underline{L}$ and $\underline{N}$, annular duct
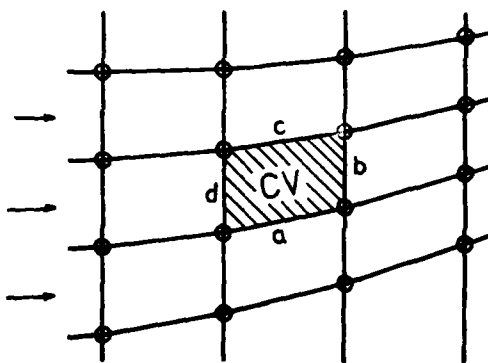
Fig.3: Computational grid and control volume
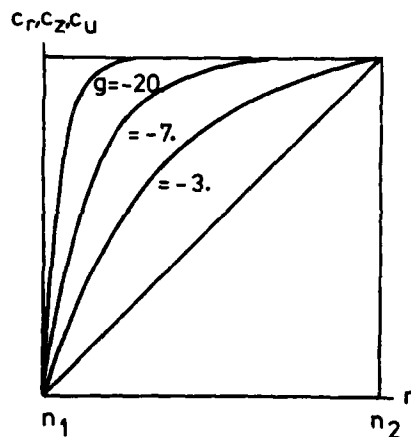
Fig.4: End-wall velocity distribution-function used for dissipation
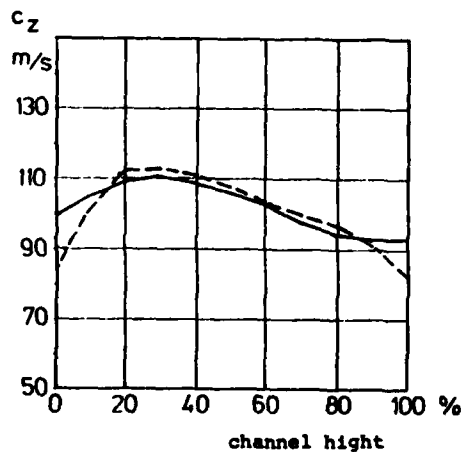
channel hight

Fig.5: Axial velocity component behind stator over relativ channel hight
————— inviscid
— — — dissipation included

channel hight

Fig.6: Stagnation pressure increase in stage over relativ channel hight
————— inviscid
— — — dissipation included

Fig.7: Computational grid for model compressor (11 x 41)
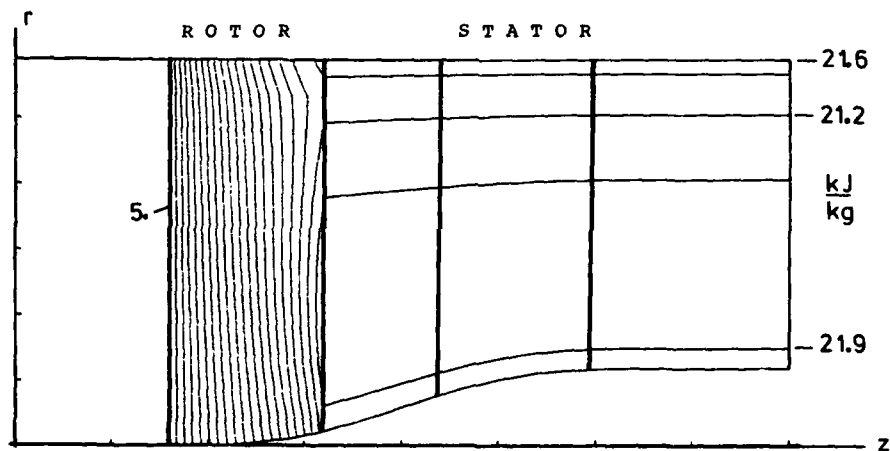
Fig.8: Contour plot for stagnation enthalpy distribution
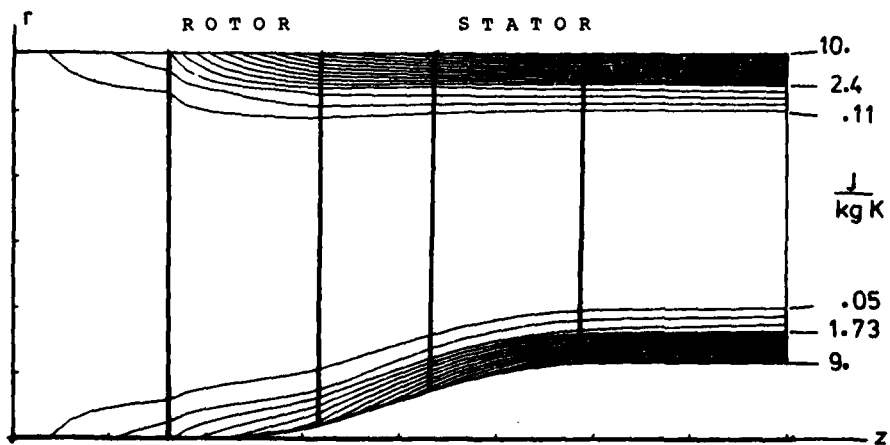
Fig.9: Contour plot for entropy distribution

DISCUSSION

Hamed

(1) Have you considered stream surface warpage that would be encountered, particularly in the region of high entropy production near the end wall?

(2) Is the drag force in the momentum equation consistent with the entropy production?

Author's Reply

(1) No.

(2) Yes, for the inner flow region; at the wall, however, where a sub-sonic velocity distribution is modelled and the stream function equation is solved for the mean flow of the grid points, there might be a discrepancy.

Ph.Ramette, Fr

In Figure 6 of your paper giving the stagnation pressure increase in the stage versus relative channel height, the inviscid solution shows an increase from 90 to 100%. Is this not surprising?

Author's Reply

No, the effect results from a bad stream surface layout for the rotor region. The outflow angle was given at three radial positions and interpolated in between. Close to the casing, a small change in turning angle results in a large change of supplied energy through the rotor, due to the relatively high blade speed at the tip.

F.Leboeuf, Fr

Did you make any comparison with a through-flow computation method which assumes a coupling with a secondary flow computation by an introduction of mass flow at the walls? If yes, did you find any modification of the static pressure field between the two methods?

Author's Reply

No.

EFFECTS OF A SKEWED INLET END WALL BOUNDARY LAYER
ON THE 3-D FLOW FIELD IN AN ANNULAR TURBINE CASCADE

by

E. Boletis, C.H. Sieverding, W. Van Hove,
von Karman Institute for Fluid Dynamics,
Chaussée de Waterloo, 72
B - 1640 Rhode Saint Genèse, Belgium

SUMMARY

The paper presents the results of an experimental investigation on the effect of a skewed inlet boundary layer on the flow field in a low speed, low aspect ratio, high turning annular turbine nozzle guide vane. Three test series, differing by their degree of inlet skew, were performed.

The flow was explored by means of double head four hole pressure probes in five axial planes from upstream to far downstream of the blade row. The results are presented in the form of contour plots and spanwise pitch-averaged distributions.

The axial evolution of the measured pitch-averaged spanwise flow angle distribution is compared with a three dimensional, inviscid, rotational flow calculation.

LIST OF SYMBOLS

C   chord

CP   local total pressure coefficient, $(P_{01,MS}-P_{0,\ell})/(P_{01,MS}-\bar{\bar{P}}_{s,2})$

$\overline{\overline{CP}}_0$ total pressure loss, $(P_{01,MS}-\bar{\bar{P}}_{02})/(P_{01,MS}-\bar{\bar{P}}_{s,2})$

CP_s local static pressure coefficient, $(P_{01,MS}-P_{s,\ell})/(P_{01,MS}-\bar{P}_{s,2})$

D   diameter

g   pitch

H   blade height

$H_{1,2}$ boundary layer form factor

O   throat

N   number of blades

P   pressure

R   radius

Re   Reynolds number, $Re = \dfrac{c \cdot V_1}{\nu}$

T   temperature

Tu   turbulence level, $Tu = \dfrac{\sqrt{v'^2_{ax}}}{V_{MS}}$

U   peripheral speed of the rotating hub end wall

V   velocity

v'   velocity fluctuation

w   velocity in the coordinate system rotating with the hub end wall

x,y   coordinates (see Fig. 3)

Y   radial distance from the hub end wall

β   flow angle in blade-to-blade plane

β'   blade angle (angle between tangent to camberline and axial direction)

γ   radial flow angle, $\gamma = \arctan\left[\dfrac{V_r}{V_{ax}}\right]$

δ   boundary layer thickness

δ*   boundary layer displacement thickness

θ   boundary layer momentum thickness

ν   kinematic viscosity

ω   angular velocity of the rotating hub end wall

Subscripts

1   upstream conditions, defined in plane $X/C_{ax} = -0.70$

2   downstream conditions, defined in plane $X/C_{ax} = 1.68$

atm   atmospheric conditions

ax   axial direction

H   hub

ℓ   local

MS   mid span

n   cross flow

o   total conditions

r   radial direction

s   static conditions, streamwise direction

T   tip

Superscripts

—   pitchwise mass averaged value or time averaged value

=   pitch- and spanwise mass averaged values

INTRODUCTION

Due to the complexity of the flow in a multistage machine, the researchers *were com-*
pelled to use simplified models to separate clearly the different effects of the numerous
geometric and aerodynamic parameters influencing the flow field. However, a continuous
effort has to be made to adapt the models step by step to the real flow field.

With respect to the subject matter "secondary flows in turbine bladings" we distin-
guish four different levels in approaching the real flow conditions in a multistage machine:

(1) Secondary flow in straight cascades.

(2) Flow in annular cascades reproducing correct radial pressure gradients.

(3) Flow in annular cascades with skewed inlet end wall boundary layer reproducing the
near end wall flow conditions which are due to the transition of the flow from a relative
(rotor) to a fixed frame (stator) and vice versa.

(4) Flow in annular cascades with inlet conditions generated by a preceding stage. Non
axisymmetric, unsteady inlet flow conditions are included automatically.

The present study is situated at the third level, with one restriction : the skewness
of the inlet flow is limited to the hub region and it can be expected that the effect of
a skewed tip end wall boundary layer might be not only quantitatively but also qualitatively
different from the effect of a skewed hub end wall boundary layer.

The occurrence of inlet skew at the entry of a stator is illustrated in figure 1. The
velocity flow field at the exit of a rotor blade row is transformed from the rotating
frame to the stationary coordinate system fixed with respect to the downstream stator.
This carry over of the velocities from the relative to the stationary frame causes signifi-
cant changes of the incidence angle to the next blade row. It is evident that the pressure
field in the stator passage is strongly influenced.

PREVIOUS WORK ON INLET SKEWNESS

A literature review shows that rather little work has been devoted so far to the
effect cf inlet skew. All investigations are experimental in nature and are carried out
at low speed.

Moore and Ricnardson (Ref. 1) studied the effect of inlet skew on the end wall boun-
dary layer evolution through a plane compressor cascade. The inlet skew was produced by
sucking off the end wall boundary layer far upstream of the cascade and injecting high
velocity air close to the end wall. The authors measured the flow field along the center
streamline to check the validity of different assumptions used in the solution of integ-
ral momentum equations applied to the flow in compressor blade passages.

It is important to notice that the natural inlet skew to compressor blades is opposite
to the skew which is experienced by the flow within the blade passage as a result of the
transverse pressure gradient, while for turbine cascades the inlet skew is reinforced by
the transverse pressure gradient inside the blade passage.

Carrick (Ref. 2) investigated the effect of inlet skew in a high turning plane tur-
bine cascade. The skewed inlet boundary layer was generated by moving a belt in front of
the cascade. The flow field was surveyed from upstream to downstream at a discrete number
of points. The results show an increase of secondary losses with skewness. The use of
three hole pressure probes did not allow the radial flow angle to be measured.

It seems that the first experiments in an annular turbine cascade are those reported
by Klein (Ref. 3). The experiments were carried out on a high turning steam turbine blade
with an aspect ratio of H/C = 1.45. The inlet skew was generated by a rotating hub end
wall with a rotational speed varying from zero to 2.7 times the free stream velocity. The
measurements included blade pressure distributions at various blade heights and a survey
of the inlet and outlet flow field with three dimensional pressure probes. The blade
pressure distributions are affected up to a depth corresponding to the physical inlet

boundary layer thickness, while the radial extension of the effect of inlet skew on the outlet flow field amounts to about twice the inlet boundary layer thickness. The losses with respect to the losses at zero skew increase from 5% at $U/V_{MS,1} = 1.$ to 20% at $U/V_{MS,1} = 2.$

Bindon (Ref. 4) studied the effect of inlet skew in a low turning ($\sim 45°$), low aspect ratio (H/C = 0.67) annular turbine cascade. Similar to Klein, Bindon generates the inlet skew by rotating the hub end wall ($U/V_{MS,1}$ = 0.0 and 1.0). The inlet and outlet flow field is surveyed with three hole pressure probes, but the measurements do not cover the whole blade span. This makes it difficult to evaluate the full impact of the inlet skew on the outlet flow field. Nevertheless, the measurements indicate that its influence is felt over a distance of more than three times the inlet boundary layer thickness. According-ing to the author the overall losses with inlet skew are smaller than without skew.

It appears that real progress in the understanding of the evolution of secondary flow in annular cascades, in the presence of a skewed inlet boundary layer, can only be obtained by exploring the complete flow field through the cascade with probes which can measure all three velocity components. This work has been undertaken in continuation of the work reported in reference 6 which presented a thorough study in an annular cascade with a collateral inlet boundary layer.

EXPERIMENTAL FACILITY - BLADE AND CASCADE GEOMETRY

The tests were carried out in the VKI open loop low speed turbine test rig. A full description of the experimental facility and the experimental procedure are given in reference 6. Figure 2 shows a sketch of the section.

The investigated guide vane has a constant profile over the blade height and is un-twisted (Fig. 3). The blade coordinates are given in reference 6. The most important geometrical characteristics of the nozzle row are summarized below :

- tip diameter, D_T	0.71 m	- pitch to chord ratio at hub, mid span and tip	0.705; 0.795; 0.885
- hub diameter, D_H	0.566 m		
- chord length, C	0.12 m	- inlet blade angle, β_1	-7°
- axial chord length, C_{ax}	0.087 m	- arc cos (O/g) at hub, mid span and tip (measured values)	69.0°; 67.8° 66.8°
- aspect ratio, H/C	0.6		
- number of blades, N	21		

NOTE : angles are given with respect to axial direction. The blade is stacked radially about point M (Fig. 3). The blade is made from araldite. A tripping wire of 0.2 mm $\emptyset$ is placed on the blade suction side at X/C = 0.35 (measured in chordwise direction).

MEASURING ACCURACY

The experimental accuracies associated with the four hole probes are as follows :

- radial position of probe	± 0.1 mm	- static pressure coefficient, CP_s	± 0.02
- axial and tangential position of probe	± 0.5 mm	- flow angle in blade-to-blade plane, β	± 0.8°
- total pressure coefficient, CP	± 0.01	- radial flow angle in streamwise direction	± 1°

Note that the measuring accuracy for the radial flow angle deteriorates for wall distances smaller than 2 mm.

TEST PROGRAM AND OVERALL TEST CONDITIONS

The test program consisted of three series of measurements characterized by different degrees of inlet skewness :

(1) Zero skew serving as baseline.

(2) Moderate skew : the peripheral velocity U of the rotating hub is of the same order of magnitude as the free stream velocity at mid span ($U/V_{MS,1}$ = 0.90).

(3) Large skew : the peripheral velocity U of the rotating hub is chosen equal to the peripheral speed of the rotor which is designed to form at a later date a complete stage with the subject stator ($U/V_{MS,1}$ = 2.25).

Based on the results in reference 6, five characteristic planes have been selected to survey the flow field : one upstream, two inside the passage and two downstream (see Fig 3).

In each plane 15 to 18 radial traverses were made, each full traverse from hub to tip containing 35 (from upstream to X/C_{ax} = 0.86) or 50 points (downstream planes).

The test conditions, common for the three experiments, are summarized below :

Upstream : X/C_{ax} = -0.70, mid span :

- total temperature, T_{01}	288°	- radial flow angle, γ_1	0°
- total pressure, P_{01}	P_{atm} + 70 mm H_2O	- velocity, V_1	12.5 m/s
- flow angle in blade-to-blade plane, β_1	0.7°	- Reynolds number, Re	$0.98*10^5$
		- turbulence, Tu	0.8%

The rotating hub extends from X/C_{ax} = -0.15 to X/C_{ax} = -4.16. The distance X/C_{ax} = -0.15 corresponds to about twice the distance of the end wall boundary layer saddle point from the blade leading edge. The axial distance between the rotating and the fixed stator hub is about 0.2 mm.

Downstream : X/C_{ax} = 1.68

- static pressure at hub for zero skew, P_{S2} (this pressure changes slightly with inlet skew)	P_{atm} -7 mm H_2O	- static pressure at tip (remains constant in all cases)	P_{atm} +16 mm H_2O

The inlet end wall boundary layer characteristics measured at X/C_{ax} = -0.70 are presented in the following table :

Hub end wall :

	$U/V_{MS,1}$ = 0		$U/V_{MS,1}$ = 0.9	$U/V_{MS,1}$ = 2.25
		Ref. 6		
δ_{ax}/h	0.12	0.11	0.16	0.20
δ^*_{ax}/h	0.017	0.017	0.019	0.025
θ_{ax}/h	0.010	0.010	0.015	0.020
$H_{12,ax}$	1.67	1.67	1.27	1.25
δ^*_n/h	0.	0.	0.018	0.068
θ_n/h	0.0	0.	0.004	0.033
$\overline{\overline{CP}}_0$	0.005		0.008	0.005

Tip end wall :

	$U/V_{MS,1}$ = 0		$U/V_{MS,1}$ = 0.9	$U/V_{MS,1}$ = 2.25
		Ref.6		
δ_{ax}/h	0.15	0.15	0.15	0.15
δ^*_{ax}/h	0.022	0.025	0.021	0.022
θ_{ax}/h	0.017	0.019	0.017	0.017
$H_{12,ax}$	1.29	1.33	1.29	1.29
δ^*_n/h	0.	0.	0.	0.
θ_n/h	0.	0.	0.	0.
$\overline{\overline{CP}}_0$	0.008		0.009	0.009

NOTE : The above $\overline{\overline{CP}}_0$ values are averaged over the half span distance. Integrating over the whole span, $\overline{\overline{CP}}_0$ would take the values 0.007, 0.009 and 0.007 respectively.

The upstream end wall boundary layer characteristics of reference 6 are included for comparison. Small differences exist at the tip end wall between the present values and those of reference 6.

The radial distribution of the mass-averaged inlet flow characteristics (velocity V, angle in blade-to-blade plane ß, radial flow angle γ and total pressure coefficient $\overline{\overline{CP}}_0$) are presented in figure 4. The flow angle in the blade-to-blade plane is indicated positive when pointing from pressure side to suction side. The radial flow angle γ is defined as the ratio of radial to axial velocity component :

γ = arctg (V_r/V_{ax}) It is positive when pointing from hub to tip.

DISCUSSION OF INLET FLOW CONDITIONS

The rotation of the hub end wall leads to an important modification of the end wall boundary layer characteristics. The increased flow path length of the boundary layer combined with the centrifuging effect of the swirling flow cause a significant increase of the radial extension of the boundary layer (Fig. 4), a tendency which was already observed by other investigators (Refs. 2,4,7). Near the end wall the swirl angle β takes values of $\sim 26°$ and $\sim 52°$ at $U/V_{MS,1} = 0.90$ and 2.25 respectively, while the maximum measured radial flow angle amounts to $\gamma = 10°$ at $U/V_{MS,1} = 2.25$ (Fig 4). (Note that the first recorded value of γ is at 2 mm wall distance. Closer to the wall the accuracy of the radial flow angle measurements diminishes considerably).

It is the usual practice to decompose skewed boundary layer profiles into a free stream and a cross flow direction (corresponding to axial and circumferential direction in the upstream measuring plane). The tests show (see table in preceding paragraph) that the shape factor of the velocity profile at the free stream direction decreases with skewness. The shape factor drops from $H_{12,ax} = 1.67$ (typical for profiles in transitional state) to $H_{12,ax} < 1.3$ corresponding to a turbulent layer. The displacement and momentum thicknesses in both axial and circumferential directions increase with skew. From the point of view of losses, the kinetic energy supplied to the boundary layer leads gradually to an increase of the total pressure near the wall such that the loss parameter $\overline{CP_0}$ takes negative values for $U/V_{MS,1} = 2.25$ (Fig 4). The pitch- and spanwise averaged value $\overline{CP_0}$ first increases with skew before dropping to the same value as at $U/V_{MS,1} = 0$. Similar tendencies are reported by Klein (Ref. 2).

The fact that the axial boundary layer thickness changes with skew could be considered as a drawback of the present study. However, tests in straight cascades carried out on nozzle blades (Refs. 2,9) indicate that the amount of secondary losses generated within the blading is largely independent of the inlet boundary layer thickness.

Attention must be drawn to the fact that the inlet measurement plane is situated at a distance equal to 70% of the axial blade chord from the leading edge plane while the rotating hub extends further downstream to a distance equal to 15% of the axial chord from the leading edge. This implies that the inlet characteristics as described before will still undergo some changes before entering the fixed frame of the stator.

The influence of the rotating motion of the hub end wall on the inlet flow field does not exceed 20% of the blade height. The tip end wall boundary layer does not undergo any changes. The velocity profile is turbulent with a shape factor $H_{12} = 1.29$.

EFFECT OF INLET SKEW ON CASCADE FLOW FIELD

Preliminary remarks

The generation and evolution of the secondary flow field in a turbine cascade depends on two factors :

(a) The characteristics of the inlet boundary layer and

(b) the transverse pressure gradient across the blade passage.

In the case of zero inlet skew, the transverse pressure gradient depends on the inlet boundary layer only to the extent to which the resulting passage vortex entails a local blade force deficit near the end wall. This dependence is of secondary importance compared to the direct effect exerted by the flow angle variation of a skewed inlet end wall boundary layer on the transverse pressure gradient. It seems to be appropriate to evaluate this incidence angle effect in a first approximation with a two dimensional blade flow calculation method (Ref. 8).

Figure 5 compares the blade pressure distribution at the outer edge of the inlet end wall boundary layer ($Y = 16$ mm, $\beta_1 = 0°$) with that at $Y = 1$ mm wall distance where the inlet flow angle amounts to $\beta_1 = 45°$. The effect of this incidence angle variation on the blade pressure distribution is, of course, greatest on the front part of the blade where a strong negative blade loading is observed. The incidence angle effect remains strong up to 50% of the axial blade chord and then disappears rapidly further downstream. The blade pressure distributions indicate that the incidence angle variation imposes not only a negative transverse pressure gradient in the entrance of the blade passage, but introduces also a radial pressure gradient (see Fig. 5). The latter counteracts the negative transverse pressure gradient but it is not clear which of them has a greater influence on the end wall cross flow.

EXPERIMENTAL RESULTS OF FLOW FIELD MEASUREMENTS

The effect of inlet skew on the cascade flow field is presented in figures 6,7,8 and 9. Each of these figures show a combination of contour plots of total pressure, static pressure, flow angle β (angle in the blade-to-blade plane) and radial flow angle γ.

The total and static pressure are shown in the form of pressure coefficients CP_0 and CP_S. Secondary velocity charts are not presented due to the difficulty of defining the appropriate reference streamwise direction at a given field point.

It should be mentioned that due to the high values of the flow angle β downstream of the cascade, $\beta = 60°$ to $75°$, the absolute value of the radial flow angle γ in the meridional

plane is considerably larger than the flow inclination measured in the streamwise direction. Hence, an error of one degree in the radial angle in the streamwise direction amounts to about $2° \rightarrow 3°$ error after projection into the meridional plane.

Flow inside the passage

The first measurement plane is positioned at $X/C_{ax} = 0.35$. This choice was made on the basis of previous measurements with a collateral inlet boundary layer which showed that the hitherto moderate effect of the passage vortex on the end wall boundary layer would start to become significant at this position. In the case of inlet skew the cascade pressure field acts more rapidly on the incoming flow which already exhibits a strongly modified flow structure in this plane (Fig. 6). The effect on the radial flow angle γ is particularly important for the case of large skew. The contour plots show an important downwash in the pressure-side end wall corner with angles up to $-8°$ and a corresponding upward motion at the suction side of the blade passage with γ values up to $14°$ (in the upstream measurement plane, at large skew, γ varied from $10°$ near the wall to zero in the free stream).

To evaluate the significance of the contour plots for the flow angle β one has to remember that the direction of the streamlines in the end wall region depends both on the incidence angle variation within the incoming end wall boundary layer and on the trans-verse pressure gradient across the blade passage which in turn depends on the inlet flow angle. The incidence angle effect can be looked at as being irrotational in character, while the effect of the transverse pressure gradient is rotational in character. The contour plots show a maximum flow angle at the wall of about $\beta_1 = 58°$ at $U/V_{MS,1} = 0.90$ and 2.25 compared to $\beta_1 = 48°$ at $U/V_{MS,1} = 0.0$.

As far as the total pressure contours are concerned, we observe a decrease of the concentration at low momentum material in the pressure side end wall corner and some radial migration towards mid span near the suction side. These features are, of course, closely related to the γ-angle and β-angle distribution.

The measured static pressure distribution shows only a moderate effect of the inlet skew. The blade pressure distribution in figure 5 shows in fact that the influence of inlet skew has already largely diminished in this measurement plane. Furthermore, the influence decreases naturally with increasing distance from the blade surface.

Proceeding further downstream to the measurement plane at $X/C_{ax} = 0.86$ one observes an impressive change in the distribution of the losses and the radial flow angle (Fig. 7). These changes are already important for zero skew but they are even stronger for the cases with inlet skew. At large skew, the low momentum material is concentrated along the suc-tion side with the particularity that this region contains two loss cores : one in the end wall suction side corner and the other at about 40% at the blade height.

The static pressure field is practically identical in all cases. The radial pressure gradient, which was negligibly small in the preceding measurement plane, takes here consi-derable proportions. Depending on the span and pitchwise position it reinforces or counter-acts the radial migration of low momentum boundary layer material.

The contour plots for the β flow angle are very similar with and without inlet skew except that the overturning at the hub is slightly more important with skew.

Outlet flow field

In the case of zero inlet skew the characteristic feature of the outlet flow field is the radial transport of low momentum boundary layer material through the wake from tip to hub (Figs. 8,9). This migration is confirmed by the radial flow angle distribution which takes values up to $-20°$ in the wake at mid-blade height.

With increasing inlet skew one observes a second strong radial motion of fluid in the opposite direction to that imposed by the radial pressure gradient at zero skew. The driving force behind this upwards flow motion is the strong lower passage vortex. The loss contour plots for moderate skew in plane $X/C_{ax} = 1.11$ (Fig. 8) show that the loss core which was found right at the hub at zero skew has moved to about 30% of the blade height. The outgrowth of the wake at this position is the direct continuation of the up-stream end wall boundary layer material which has moved inside the cascade onto the rear blade suction surface. The lifting of the loss core is underlined by a region with strong positive radial flow angles in the wake-hub end wall corner.

A further increase of the inlet skew to $U/V_{MS,1} = 2.25$ reinforces the tendencies observed before. The radial flow angle field is entirely dominated by two regions of almost equal size but opposite flow direction. The positive radial flow angle field does not only cause a further shift of the loss core to a higher radius but it contributes also to a lateral diffusion of the losses on the wake suction side. Both the β- and γ-angle distribution illustrate the presence of a strong hub passage vortex. A noteworthy feature is also the local decrease of the static pressure at the hub at mid distance between the wakes.

Proceeding further downstream to the plane at $X/C_{ax} = 1.68$ (Fig. 9) we observe roughly the same tendencies as at the preceding plane. The radial position of the loss core does not change with increasing downstream distance but the wake has spread out

considerably in the circumferential direction. The intensity of the radial flow motions has significantly diminished but it is noteworthy that the radial pressure gradient continues to impose a non-negligible inward flow in the wake region while the radial outward flow is reduced to a very small amount. The isobeta curves are interesting since they differ greatly at hub and tip, even in the case of zero skew : the flow conserves strong circumferential flow angle variations at the tip but almost none at the hub end wall.

SPANWISE DISTRIBUTION OF THE PITCH-AVERAGED FLOW ANGLE AND LOSSES

The axial evolution of the pitchwise averaged flow angle $\bar{\beta}$ is presented in figure 10. The spanwise distribution at zero skew shows the characteristic over/underturning behaviour of a flow under the influence of passage vortices. The axial evolution is, however, somewhat different at hub and tip which can be explained by a different strength of the vortices due to differences in the blade loading over the blade height. The influence of passage vortices is predominant, but there is also evidence of some other vortical motion. The best evidence for this is given in plane $X/C_{ax} = 1.11$ where the overturning tendency near the wall is interrupted to give way to a significant decrease of the flow angle. This points to the existence of a counter-rotating vortex, which possibly is the suction side end wall corner vortex.

Inlet skew modifies entirely the radial evolution of the flow angle $\bar{\beta}$. In the present experiments, inlet skew affects the $\bar{\beta}$-angle up to a distance between 60% and 80% of the blade height. Starting with an upstream skew angle of 26° and 53° respectively (corresponding to $U/V_{MS,1} = 0.90$ and 2.25) the amount of overturning right next to the hub end wall decreases in the downstream direction with respect to that for zero skew. This evolution is accompanied by a progressive increase of $\bar{\beta}$ in the region of maximum underturning of the zero skew curve, which leads finally at $X/C_{ax} = 1.68$ to an entire opposite radial evolution of β between zero and maximum inlet skew in the lower half of the blade passage. A strong suction side end wall corner vortex could explain for the case of inlet skew the radical change of the slope of the $\bar{\beta}$-curve at the hub. Figure 10 demonstrates also the influence of inlet skew on the spanwise position and extent of the characteristic underturning region associated with a passage vortex. Inlet skew causes a shift of the underturning region to a higher spanwise position, e.g., at $X/C_{ax} = 1.11$ the maximum underturning is situated respectively at $Y/H = 0.17$, 0.30, and 0.50 for $U/V_{MS,1} = 0.$, 0.9 and 2.25.

Figure 11 presents the spanwise total pressure loss distribution for the plane $X/C_{ax} = 1.68$. The loss coefficient $\overline{CP}_0$ refers the local (pitch-averaged) total pressure loss in the measurement plane to the upstream total pressure at mid span. In the case of a collateral inlet end wall boundary layer, $U/V_{MS,1} = 0$, the total loss includes the following individual loss contributions :

(a) profile loss;

(b) inlet end wall loss;

(c) boundary layer growth on the end wall inside the blade passage;

(d) end wall suction side corner loss;

(e) interference of end wall crossflow with main flow along blade suction surface and;

(f) downstream annulus loss.

The downstream spanwise loss distribution can be divided into several characteristic regions representing one or several of the above loss components. A major part of the high losses in the immediate proximity of the end walls are annulus losses generated downstream of the trailing edge plane. Since these losses are continuously growing with increasing downstream distance, it is difficult to define clearly the amount of secondary losses of a cascade. Next to the near end wall region we observe at zero inlet skew a high loss concentration between $Y/H = 0.05$ and 0.25 at the hub and between $Y/H = 0.95$ to 0.80 at the tip. This loss core includes losses (d) and (e), the major part of losses (b) and part of loss (c). If there were no radial pressure gradient, the loss between $Y/H = 0.25$ and 0.80 would present only profile losses. However, there exists a strong radial pressure gradient, causing part of the tip secondary losses to migrate towards the hub. Consequently, there does not exist a region of pure profile losses. The interpretation of the spanwise loss distribution is further complicated by the S-shape of the wake. This wake pattern is at least partially responsible for the local loss maximum at $Y/H = 0.60$.

Inlet skew affects the spanwise loss distribution in various ways :

(a) It causes additional losses due to the inlet angle variation within the inlet end wall boundary layer (this loss can be calculated as a local profile loss, but since its occurrence depends on the end wall boundary layer characteristics, it seems to be logical to consider it as part of the secondary losses);

(b) It strengthens the suction side end wall corner loss and;

(c) It contributes to an increased interference between end wall flow and main flow on the blade suction side. The radial displacement of the hub loss core, composed mainly of inlet loss, incidence angle loss, corner loss and interference loss, is particularly clearly demonstrated.

There is an important rise of the overall losses with skewness. These are $\overline{CP}_0 = 7.2\%$ at the collateral case, 10.2% with moderate skewness and 10.4% with large skewness. These values include the inlet end wall losses of 0.7%, 0.9% and 0.7% respectively. An increase

of the overall losses has also been reported in references 2 and 3, contrary to an over-all loss decrease reported by Bindon (Ref. 4).

COMPARISON WITH THREE DIMENSIONAL INVISCID, ROTATIONAL FLOW CALCULATION

The axial evolution of the pitch averaged spanwise flow angle distribution is com-pared for the case of large inlet skew with a three dimensional, inviscid, rotational flow calculation. The calculations were performed with a fully explicit time marching, corrected viscosity, finite volume method by Van Hove (Ref. 10). The method solves the Euler equations with respect to a cylindrical coordinate system fixed to the blade row. On the inflow boundary radial gradients of the flow can be introduced allowing the calcu-lation of rotational flow. On the outlet boundary a generalized radial equilibrium con-dition is used. The back pressure is imposed only at one radius and the radial outlet pressure distribution is part of the solution. The author demonstrated that his method was able to calculate fairly accurately the flow angle and static pressure distribution in an annular cascade with collateral inlet boundary layer (same cascade as in present investigation). This result allows two interpretations : either the flow angle is indeed little influenced by viscous effects or viscous effects were too small to show an impor-tant influence on the flow angle. The present case with inlet skew is a much more severe test case since viscous effects are much stronger than for zero inlet skew.

The computational domain (cascade plus upstream and downstream extension) is discre-tized by 65 orthogonal, 31 streamwise and 21 bladewise surfaces. The discretization is the same as in reference 10. The calculations were performed on a VAX 11/780 computer. The computing time per point and time step is 0.0024 s. The results presented in figure 12 were obtained after 4000 iterations. Inside the blade passage the flow angle distribution is very well predicted. However, the calculations are less satisfactory downstream of the cascade. In particular, the program does not predict the effect of what we believe is a corner vortex, which causes a reversal of the flow angle slope at the wall, as imposed by the passage vortex. The strength of this vortex depends on the degree of inlet skew.

CONCLUSIONS

Inlet skew amplifies all characteristic features associated with the usual end wall vortex system for a collateral inlet boundary layer. In particular it augments the con-centration of low momentum fluid in the suction side end wall corner and generates an important outward radial flow along the rear blade suction surface. Downstream of the cascade this counteracts the effect of the radial pressure gradient on the migration of low momentum boundary layer through the wake. The gradual shift of the maximum wake losses from the hub towards mid span with increasing skew underlines this feature.

A corner vortex of significant strength counteracts the effect of the passage vortex on the overturning near the end wall and at large skew the shape of the pitch averaged β-flow angle distribution in this region is completely changed.

The prediction of the spanwise β-angle distribution using a three dimensional, inviscid rotational flow calculation method is quite good inside the blade passage but less satis-factory downstream of the cascade due to the increasing influence of viscous effects with increasing inlet skew.

REFERENCES

1. MOORE, R.W. & RICHARDSON, D.L.: Skewed boundary layer flow near the endwalls of a compressor cascade. ASME Transactions, November 1957.

2. KLEIN, A.: Investigation of the entry boundary layer on the secondary flows in the blading of axial-flow turbines. BHRA T 1004, April 1969.

3. CARRICK, M.A.: Secondary flow and losses in turbine cascade with inlet skew. In: Secondary Flows in Turbomachinery, AGARD CP 214, 1977, paper 5.

4. BINDON, J.P.: Exit plane and suction surface flows in an annular turbine cascade with a skewed inlet boundary layer. Int. J. Heat & Fluid Flow, Vol. 2, No. 2, 1980, pp 57-66.

5. SJOLANDER, S.A.: The endwall boundary layer in an annular cascade of turbine nozzle guide vanes. Carleton Univ., TR ME/A 75-4, December 1975.

6. SIEVERDING, C.H.; VAN HOVE, W.; BOLETIS, E.: Experimental study of the three dimen-sional flow field in an annular turbine nozzle guide vane. Paper presented at the ASME 28th Int. Gas Turbine Conf., March 1983.

7. STEINHEUER, I.: Three dimensional boundary layers on rotating bodies and in corners. In: Recent Developments in Boundary Layer Research, AGARDograph 97, Part II, 1965, pp 567-611.

8. MARTENSEN, E.: Berechnung der Druckverteilung an Gitterprofilen in ebener Potential-strömung mit einer Fredholmschen Integralgleichung. Arch. Rat. Mech. & Analysis, Vol. 3, No. 3, 1959, p 235.

9. MARCHAL, Ph. & SIEVERDING, C.H.: Secondary flows within turbomachinery bladings. In: Secondary Flows in Turbomachines, AGARD CP 214, 1977, paper 11.

10. VAN HOVE, W.: Calculation of three dimensional, inviscid, rotational flow in axial turbine blade rows. Paper presented at the ASME 28th Int. Gas Turbine Conf., March 1983.
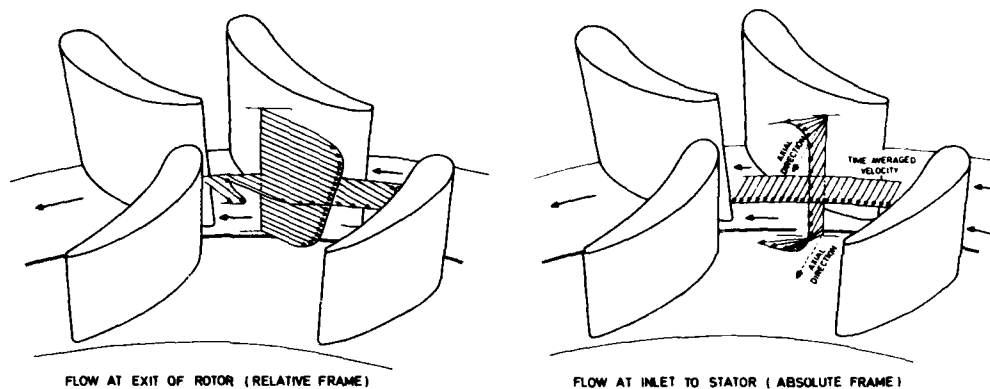
FIG. 1 - FLOW CONDITIONS BETWEEN TWO STAGES
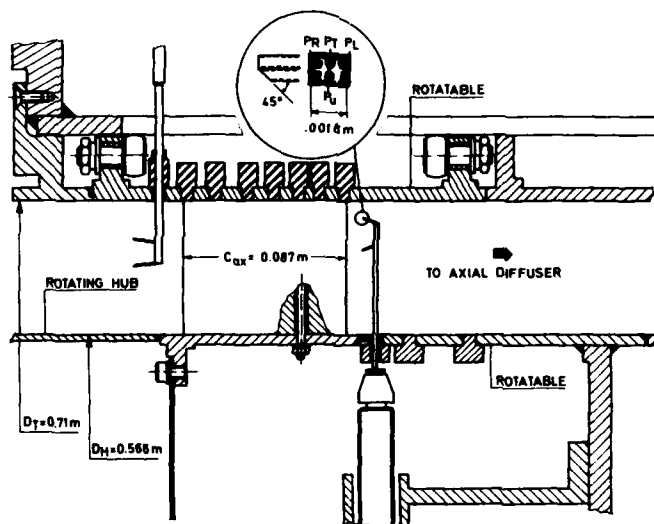
FIG. 2 - TEST SECTION
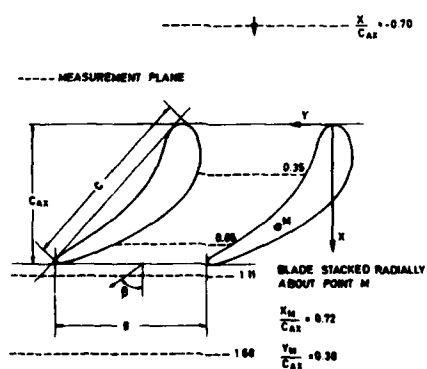
FIG. 3 - CASCADE GEOMETRY AT MID BLADE HEIGHT

MEASUREMENT PLANE X/C$_{AX}$ =- 0.70
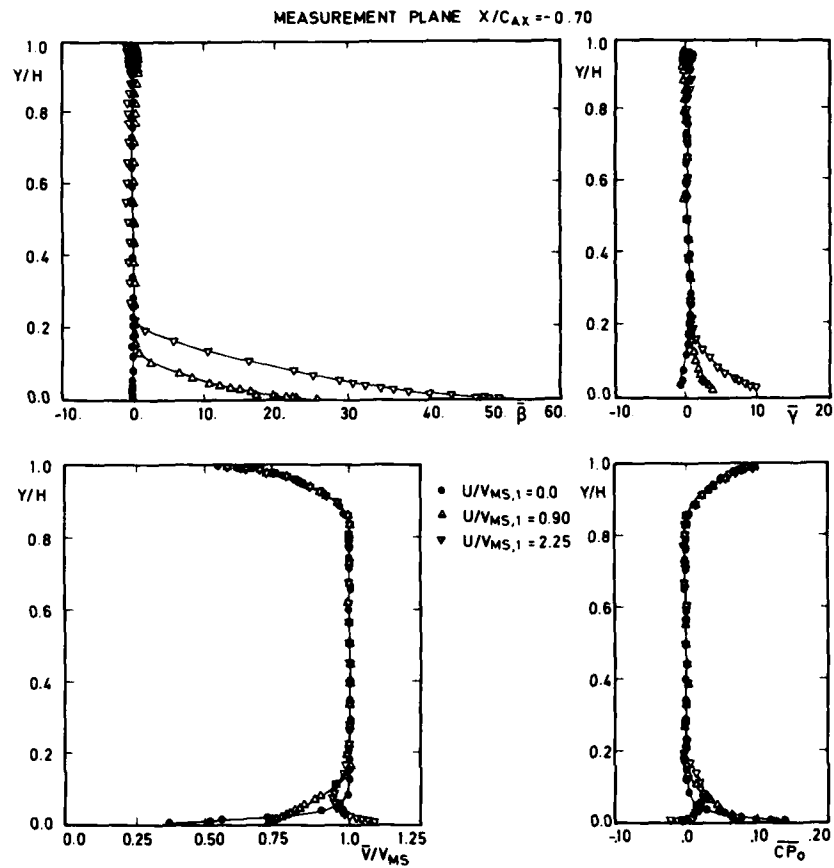
FIG. 4 - UPSTREAM FLOW CONDITIONS
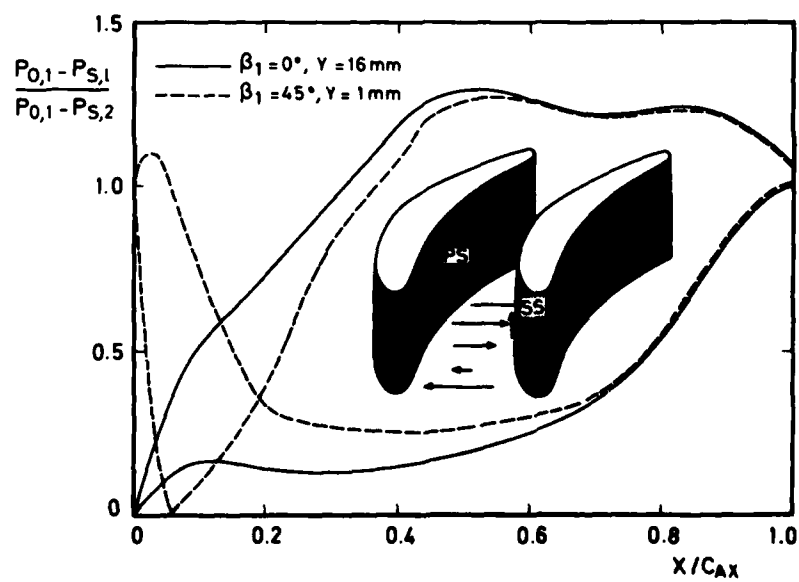
FIG. 5 - EFFECT OF INLET ANGLE VARIATION ON BLADE PRESSURE DISTRIBUTION
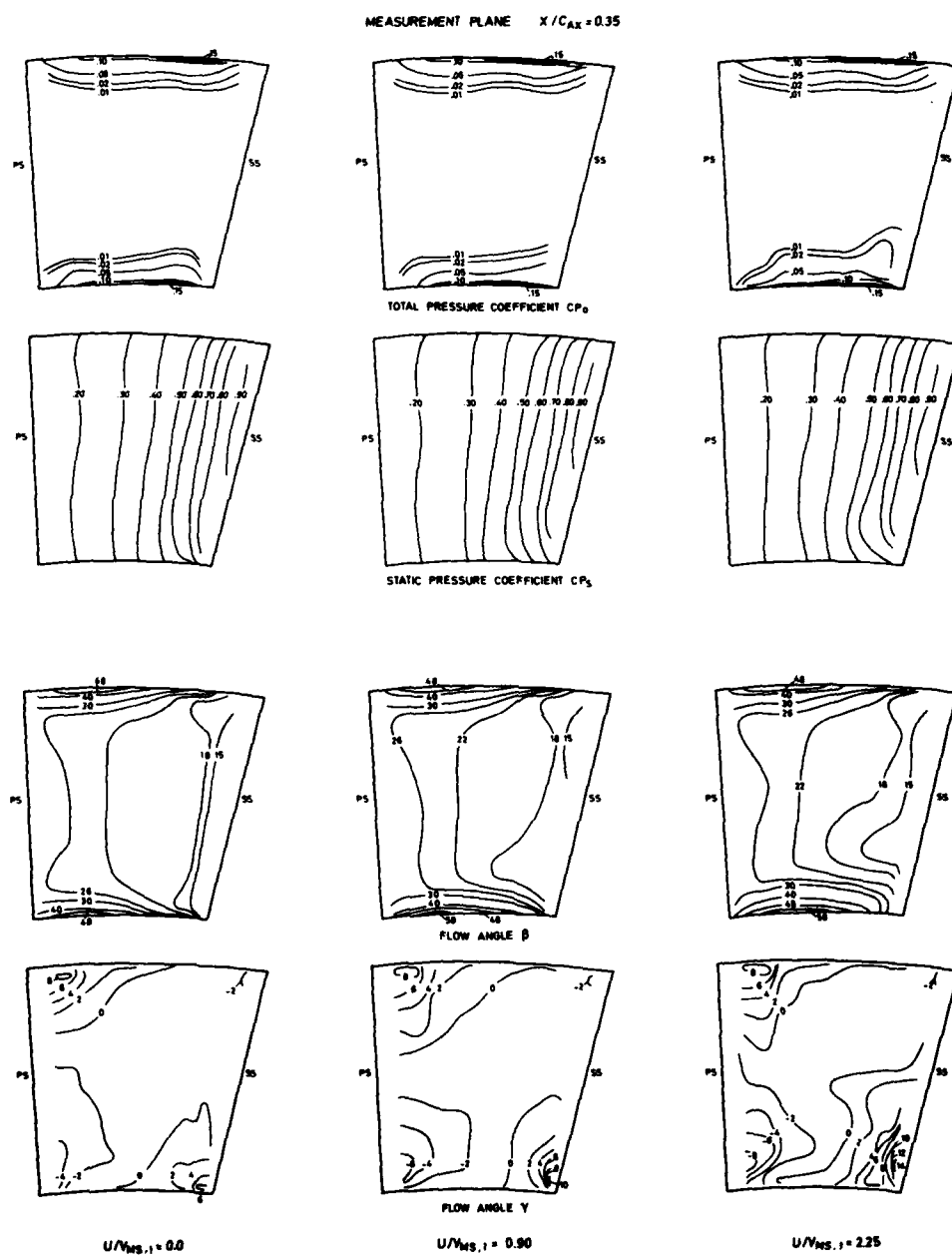
MEASUREMENT PLANE   X/C_AX = 0.35

TOTAL PRESSURE COEFFICIENT CP₀

STATIC PRESSURE COEFFICIENT CP_S

FLOW ANGLE β

FLOW ANGLE Y

U/V_HS,1 = 0.0   U/V_HS,1 = 0.90   U/V_HS,1 = 2.25

FIG. 6 - CONTOUR PLOTS OF TOTAL PRESSURE, STATIC PRESSURE, FLOW ANGLE β
AND RADIAL FLOW ANGLE IN THE MEASUREMENT PLANE X/C_AX = 0.35

MEASUREMENT PLANE   X/C$_{AX}$ = 0.86

TOTAL PRESSURE COEFFICIENT CP$_o$

STATIC PRESSURE COEFFICIENT CP$_s$

FLOW ANGLE β

FLOW ANGLE Y

U/V$_{MS,1}$ = 0.0   U/V$_{MS,1}$ = 0.90   U/V$_{MS,1}$ = 2.25

FIG. 7 - CONTOUR PLOTS OF TOTAL PRESSURE, STATIC PRESSURE, FLOW ANGLE β AND RADIAL FLOW ANGLE IN THE MEASUREMENT PLANE X/C$_{AX}$ = 0.86

MEASUREMENT PLANE X/C$_{AX}$ = 1.11

TOTAL PRESSURE COEFFICIENT CP$_0$

STATIC PRESSURE COEFFICIENT CP

FLOW ANGLE β

FLOW ANGLE Y

U/V$_{MS,1}$ = 0.0   U/V$_{MS,1}$ = 0.90   U/V$_{MS,1}$ = 2.25

FIG. 8 - CONTOUR PLOTS OF TOTAL PRESSURE, STATIC PRESSURE, FLOW ANGLE β AND RADIAL FLOW ANGLE IN THE MEASUREMENT PLANE X/C$_{AX}$ = 1.11

MEASUREMENT PLANE X/C_{AX} = 1.68

TOTAL PRESSURE COEFFICIENT CP₀

STATIC PRESSURE COEFFICIENT CPₛ

FLOW ANGLE β

FLOW ANGLE Y

$U/V_{MS,1}$ = 0.0 $U/V_{MS,1}$ = 0.90 $U/V_{MS,1}$ = 2.25
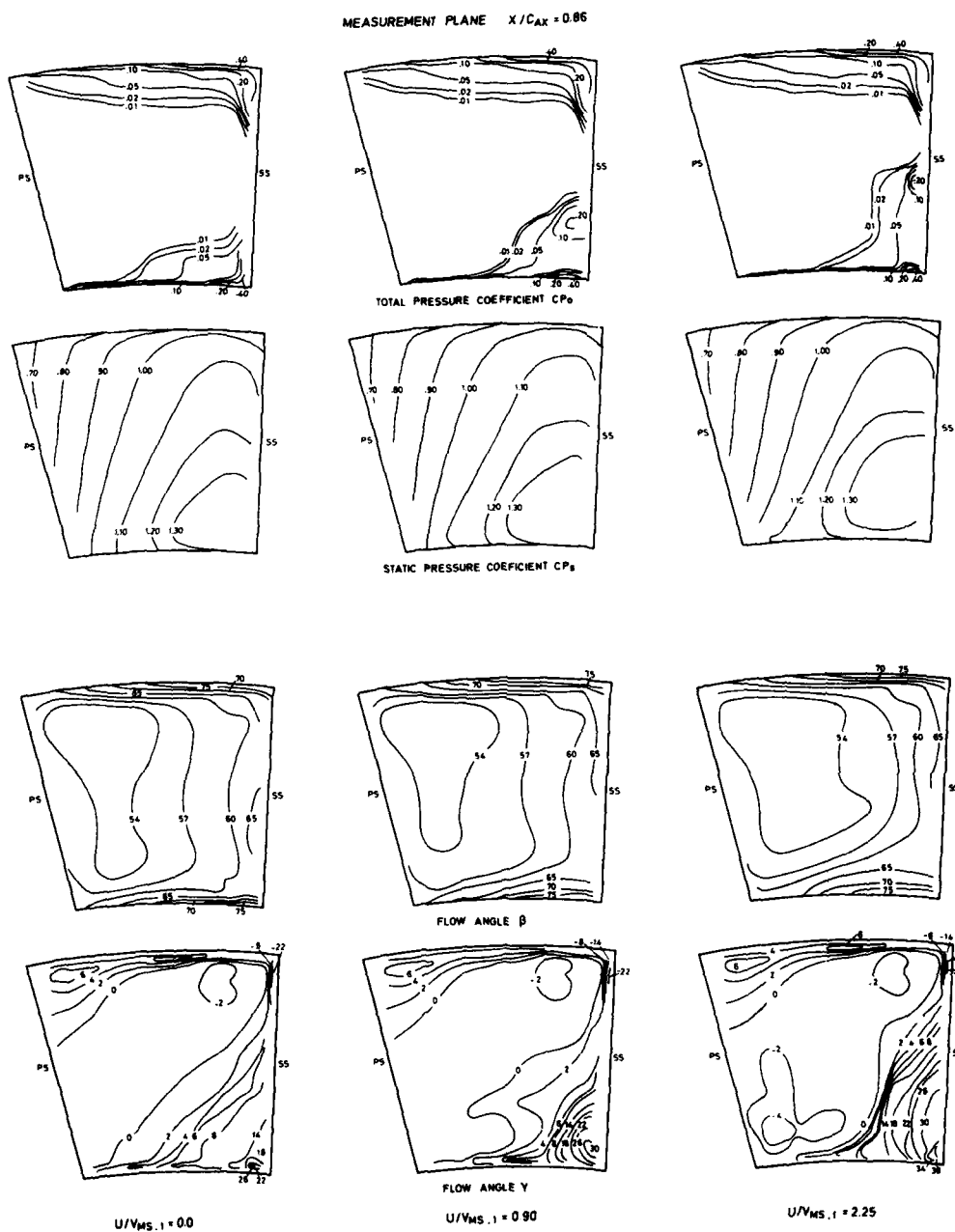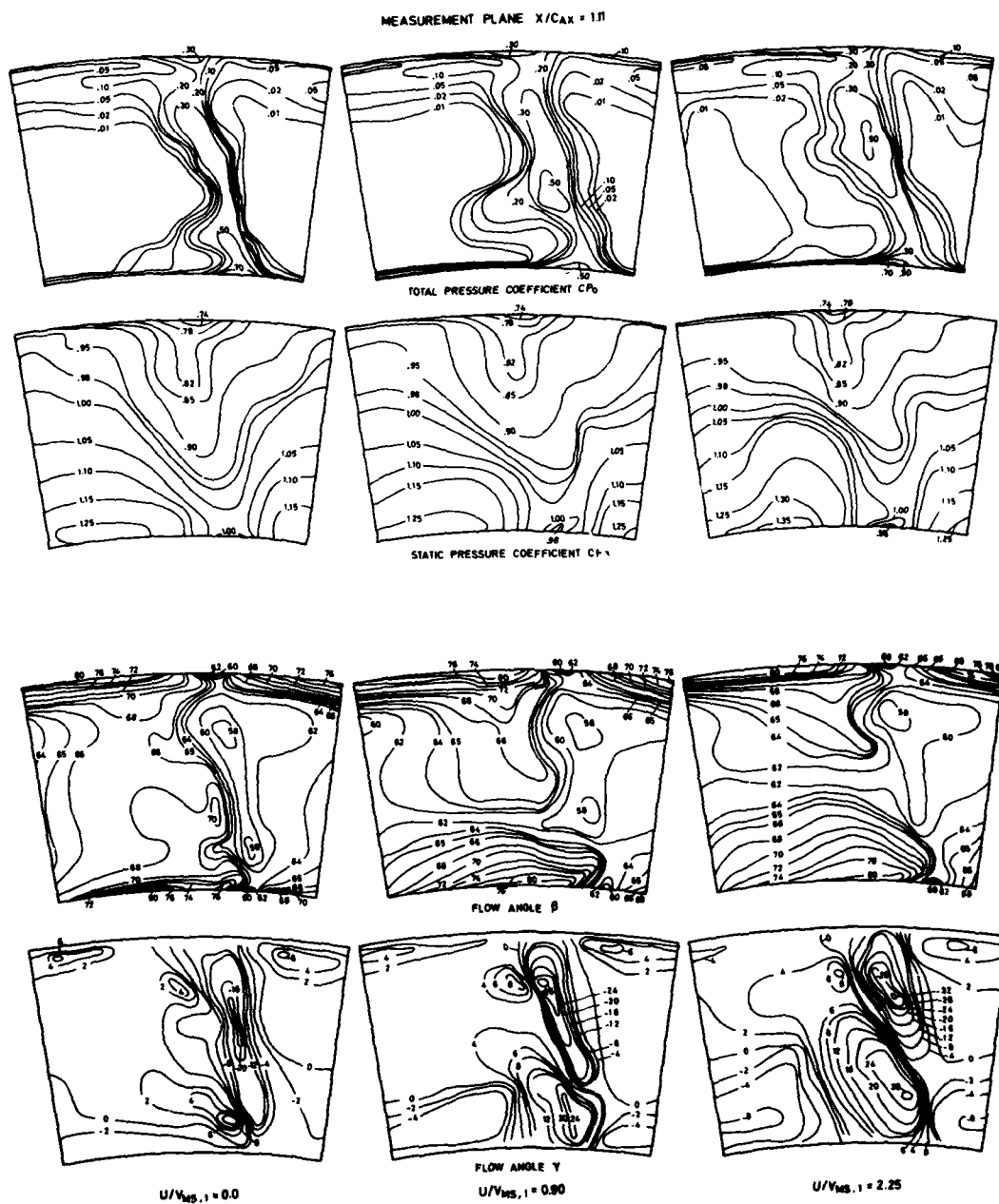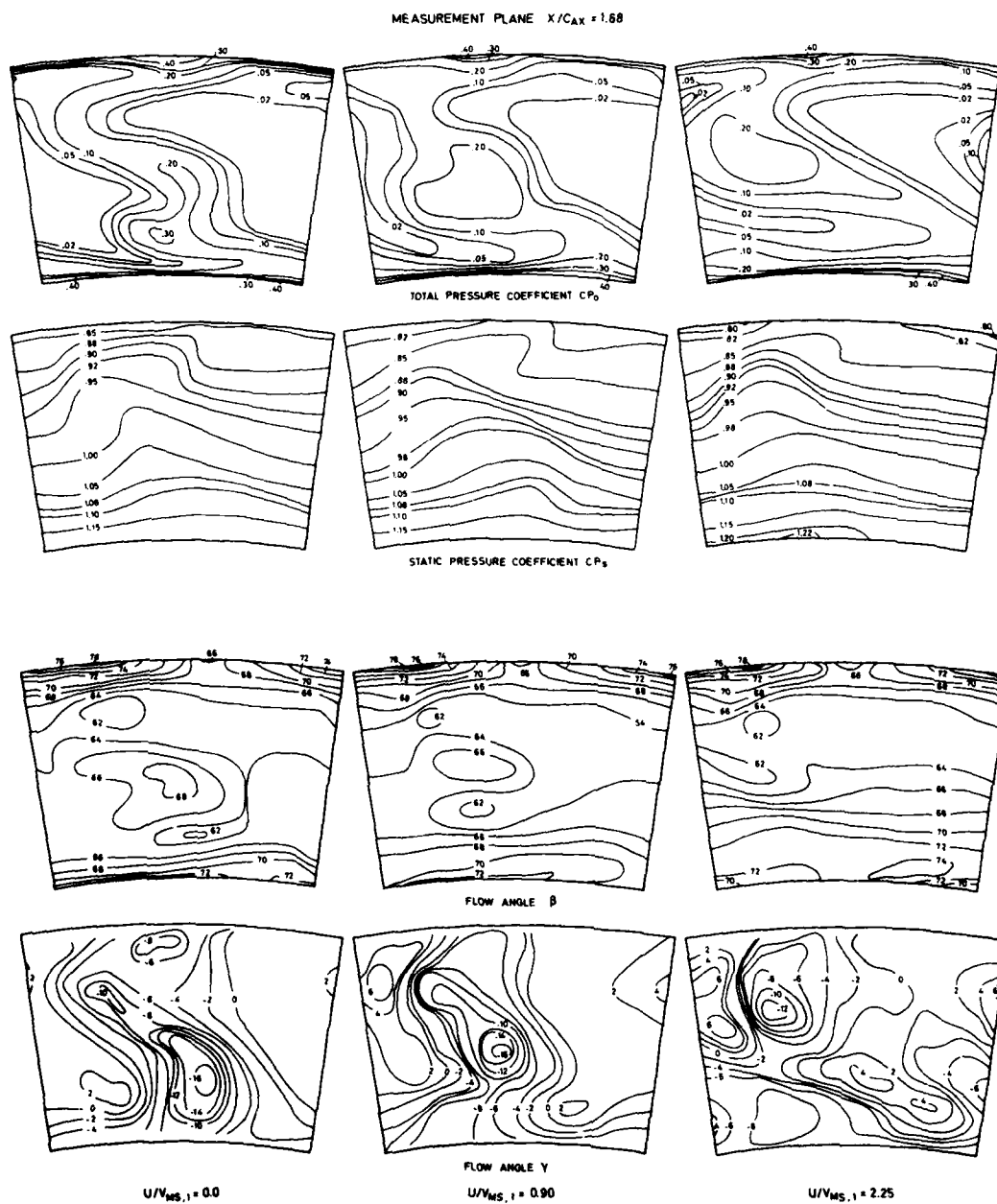
FIG. 9 - CONTOUR PLOTS OF TOTAL PRESSURE, STATIC PRESSURE, FLOW ANGLE β
AND RADIAL FLOW ANGLE IN THE MEASUREMENT PLANE X/C_{AX} = 1.68
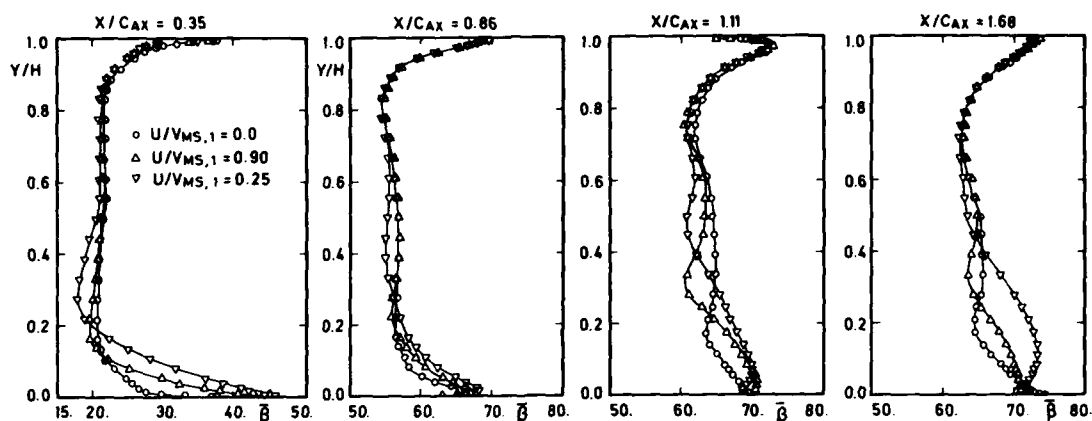
FIG. 10 - AXIAL EVOLUTION OF RADIAL DISTRIBUTION OF PITCHWISE AVERAGED FLOW ANGLE $\bar{\beta}$
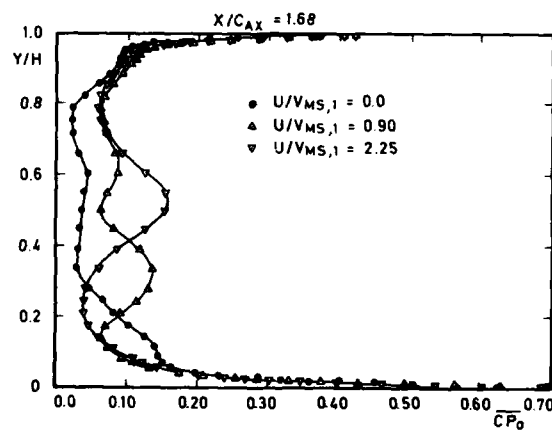
FIG. 11 - SPANWISE TOTAL PRESSURE LOSS DISTRIBUTION IN THE FAR DOWNSTREAM PLANE
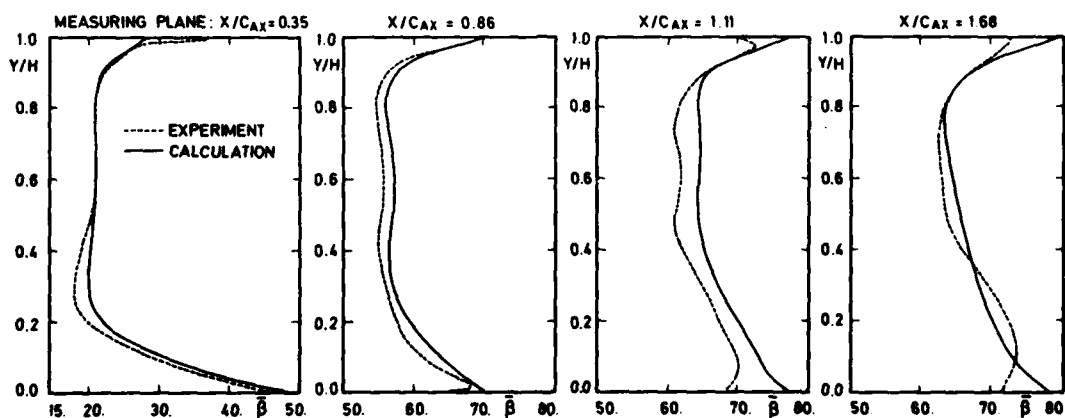
FIG. 12 - COMPARISON BETWEEN MEASURED AND CALCULATED AXIAL EVOLUTION OF RADIAL
DISTRIBUTION OF PITCHWISE AVERAGED FLOW ANGLE $\bar{\beta}$ ($U/V_{MS,1}$ = 2.25)

DISCUSSION

Gallus

A comment: Our measurements in a stage with an inlet Mach number around 0.2 to 0.4 with wall rotation U/V_{MS} up to approximately ± 0.9 showed very little influence of skewed boundary layers on the secondary flow in and behind the annular cascade. Measurements were done with hot wire and split film techniques.

Author's Reply

The influence of a skewed inlet end wall boundary layer on the 3-D field in a turbine cascade has been measured by different investigators with different cascade configurations and with relatively low turning to high turning blade geometries. This influence is also significant at $U/V_{MS,1} \cong 0.90$ as it can be seen from measurements included in References [2], [3] and [4].

SECONDARY FLOWS AND LOSSES IN A TURBINE CASCADE

by

D.G. Gregory-Smith   &   C.P. Graves
Department of Engineering   Gilbert Gilkes & Gordon Ltd.
University of Durham   Kendal
Durham, England   England

SUMMARY

In the design process for axial flow turbines, there is a need for relatively simple prediction techniques for the angle variations and losses produced by secondary flows. In order to improve the physical basis of such techniques, an investigation has been made of the flow in a cascade of large scale rotor blades of some 110° of turning. The aspect ratio (span/chord) was 1.77, and the inlet boundary layer on the end walls was varied around 0.2 of the span. The flow was traversed in great detail on ten planes using cobra-type probes with a computerised data recording and analysis system.

The results are presented graphically using contour and vector plots on various planes through the flow field. The horse-shoe vortex and passage vortex development are clearly seen, with the upstream boundary layer being shed downstream as a loss core. Another region of high loss is related to a counter vortex in the corner between the suction surface and the end wall. The results have also pitch averaged, and compared with predictions of angle and loss distribution.

Some traversing has also been carried out using hot wire anemometry. Regions of high turbulence intensity and shear stress have been identified, associated with the regions of high loss. Some indication is given of the mechanisms of loss production within the cascade.

The results of this work will aid modelling of secondary flows, and provide detailed data against which calculation methods may be tested.

1. INTRODUCTION

In the design process for axial flow turbines, the designer has to include estimates of the losses and variation of flow angle caused by secondary flows. The secondary flows arise from the turning of a sheared inlet flow, usually the end wall boundary layers on the hub and casing of the machine. In the past, use has been made of various empirical correlations for secondary loss such as those by Ainley and Mathieson (1) or Dunham (2) who reviewed a wide range of correlations. However, such correlations tend to be inaccurate and give no information on the radial distribution of the loss. More recently, methods have become available for the calculation of the three-dimensional flow field in a row of blades, for example the streamline curvature method of Stuart and Hetherington (3), the time marching method of Denton (4) and methods including a loss model, Moore and Moore (5) and Briley (6). However, these methods require considerable time and effort in preparing data and analysing the results; they may not satisfactorily model the flow; and they require a lot of computing time (a disadvantage which may be becoming less important with advances in computer technology). These methods are thus not suitable for use in the iterative process of design, and there is a need for relatively simple prediction techniques, which will give fairly reliable results. Gregory-Smith (7) has proposed a technique for predicting secondary flow angle and losses based on a physical appreciation of the flow within a blade row.

The complex patterns within a blade row caused by secondary flows have been studied by various workers. In the early days, Herzig et al (8) used flow visualisation to study the three-dimensional flows; Armstrong (9) used a large scale cascade to study secondary flows. A number of such studies are reviewed by Dunham (2). More recently, cascade studies have been made, measuring the flow within the blade row to gain detailed quantitative information, and some of these have been supplemented by flow visualisation studies; these include the work of Langston et al (10), Marshal and Sieverding (11), and Carrick (12). These and other workers have shown that a horse-shoe vortex forms around the leading edge of a blade; one leg of the vortex curls round onto and up the suction surface of the blade. The pressure side leg crosses the passage and usually meets the suction surface of the adjacent blade at about mid-chord. The sheared flow as it is turned causes a vortex in the blade passage, with overturning near the end wall and underturning further away. The pressure side leg of the horse-shoe vortex rotates in the same direction as the passage vortex and combines with it. A new highly skewed boundary layer forms on the end wall downstream of the pressure side leg of the horse-shoe vortex. The old upstream boundary layer is swept up by the passage vortex into a loss core which is shed downstream close to the suction surface and some distance from the end wall.

The method of Gregory-Smith (7) was based on this physical picture of the flow. The exit flow angle variation caused by the passage vortex was modelled using "classical" secondary flow theory, first suggested by Hawthorne (13). The loss was split into three components; the upstream boundary layer which is shed as the loss core, the new boundary layer formed on the end wall, and an "extra" secondary loss arising from the secondary flow interacting with the blade boundary layer.

In order to improve this relatively simple method, a detailed study of the flow in

a cascade of large scale rotor blades has been made. The objectives of the study were

(a) To provide detailed information for improving the prediction technique,

(b) To study the processes of loss generation by investigating the details of the turbulence as well as gaining mean velocity data,

(c) To increase the body of information on turbine secondary flows with data from a blade necessarily different from those of other workers.

2. APPARATUS

2.1 The Cascade

The linear cascade consisted of six blades set at exit from a low speed wind tunnel. The blades were cast from epoxy resin and fibre glass and set in a wooden frame. Table 1 gives relevant data for the blades, further information is given by Graves (18).

<div align="center">

TABLE 1

Flow inlet angle	42.75°
Blade exit angle	-67.5°
Axial chord	175.0 mm
Aspect ratio (span/chord)	1.77
Pitch	191.0 mm

</div>

In one end wall, slots were made for traversing at various axial positions, which are shown in Figure 1. The slots were filled in when not in use. The opposite end wall was made of perspex so that flow visualisation could be used. The traversing was done from the perspex end wall to mid-span, so that the flow was measured near the end wall which was not affected by the small discontinuities caused by the slots.

Upstream of the cascade there was some 2.5 metres of working section so that the wall boundary layer entering the cascade was fairly thick, about 100 mm. The boundary layer could be artificially thickened by inserting a triangular saw toothed fence half way along   the working section. It could also be made thinner by bleeding off some of the flow about 0.7 m   upstream of the blades.

2.2 Instrumentation : Pressure Probes

The flow was traversed with 3-hole and 5-hole cobra type pressure probes. The tips of the probes were made from 0.9 mm outside diameter hypodermic tubing. The 5-hole probe was used for most of the traversing and gave the flow direction in both yaw (the plane parallel to the end wall) and pitch (the plane perpendicular to the end wall). The 3-hole probe was used for traversing close to the end wall. The probe in use was mounted on a traverse gear which gave movement in both the tangential (along the cascade) and radial (perpendicular to the end wall) directions.

Both probes were calibrated for yaw angle and the 5-hole probe for pitch angle as well. The traversing technique was to set the probe approximately aligned with the flow for a given tangential position. The probe was then traversed radially and the difference in pressure for the two yaw holes was used to deduce the flow angle from the calibration map. For the 5-hole probe, the pitch angle was also deduced. The flow upstream of the cascade was monitored with a pitot-static probe.

Because of the large number of readings to be taken, the measurements were recorded by a data acquisition system. The pressures from the traverse probe and from the upstream monitoring probe were recorded, along with the radial and tangential position of the traverse gear. The system was controlled by a "Cifer" minicomputer which stored the readings on a "floppy" disc. The readings were transferred at a later stage to a mainframe computer for analysis.

2.3 Instrumentation : Blade Pressure Tappings

The two blades either side of the central passage were instrumented with pressure tappings. The tappings were made by a technique reported by Gregory-Smith and Marsh (14), whereby passages were cast under the blade surface, and sets of tappings at various radial positions were drilled into them. When taking readings, all the sets other than that required were sealed with thin tape. The passages were connected to an inclined multitube manometer and the readings were recorded by hand.

2.4 Instrumentation : Hot Wire Anemometry

The flow at inlet and exit of the cascade was also traversed using hot wire anemometry to gain turbulence information. Double traverses with two "X" hot wire probes were made, with one probe having its sensing plane parallel to the end wall (in the x-y plane) and the other with its sensing plane aligned with the flow direction and perpendicular to the end wall (in the x-z plane). The output signals from the two anemometer channels were linearised and the mean and root mean square of each signal obtained, together with the mean product of the two signals. Thus from each probe five voltages were obtained, which were fed into the data acquisition unit previously used for the pressure probes. From the ten voltages obtained for each traverse point, eight quantities were deduced giving

some redundancy which could be used to test the self-consistency of the results. The eight quantities were the three mean velocity components, the three Reynolds normal turbulent stresses and the Reynolds shear stresses in the x-y and x-z planes. The missing Reynolds shear stress is not so important when considering the mechanisms of loss generation, and so the extra complexity (e.g. using a triple-wire probe) was not felt to be justified.

2.5 Data Analysis and Presentation

In view of the complexity of the flow and the large amount of data to be collected, the method of presentation was important so that significant qualitative and quantitative features of the flow could be discerned. The minicomputer at the cascade ensured that the tunnel was run at a constant Reynolds number, and corrections were made to allow for variations in atmospheric temperature and pressure. For the pressure probes, the main-frame computer produced values of velocity magnitude and direction and values of total and static pressure. Similarly, from the hot wire probes, the mean velocity direction and magnitude and the Reynolds shear stresses were obtained; the turbulent kinetic energy was also calculated.

The traversing positions were arranged so that at each axial plane within the blade row, twelve tangential positions were taken, equally spaced across the blade passage. Upstream and downstream of the row, the tangential positions were extended to cover more than one blade pitch, with twelve spaced equally between lines drawn from the leading or trailing edges. Thus data could be presented on either axial planes, or planes parallel to the end wall or planes of constant fraction of passage width (quasi-streamline planes). The various quantities (velocity magnitude, yaw angle, total pressure, etc.) were presented as contour plots. The plotting routine used linear interpolation, and occasionally this has to be borne in mind when looking at the results. Also, velocity vector plots were presented on the various planes.

Some quantities (e.g. total pressure, flow angle, etc.) were mass meaned across the blade passage, giving a radial variation of the meaned quantity. Total pressure was also mass meaned over each axial plane.

3. EXPERIMENTS

Three sets of experiments were carried out.

(a) 5-hole and 3-hole pressure probe traverses of all 10 slots for the natural inlet boundary layer. The blade pressure tapping readings were also recorded.

(b) Pressure probe traverses at the inlet and exit only with the inlet boundary layer thickened. The traverses were repeated with the boundary layer made thinner.

(c) Hot wire anemometry traverses of the inlet and exit planes with the natural inlet boundary layer.

In this presentation of the results, some selection has had to be made in order to keep the number of diagrams to manageable proportions. For full details, see Graves (18).

4. RESULTS : PRESSURE PROBES, NATURAL BOUNDARY LAYER

4.1 Inlet Flow

The inlet boundary layer velocity profile is shown in Figure 2, which also shows the thick and thin profiles. The natural profile agrees fairly well with a 0.12 power law profile of thickness, δ = 115 mm. The displacement thickness, δ^* was 12.1 mm. Figure 3 shows the yaw angle at slot 1, just upstream of the blades. At mid-span, the variation due to the upstream potential effect of the blades is clearly seen. The static pressure and velocity magnitude plots indicate that the stagnation streamlines are at tangential positions 115 mm and -75 mm. The rapid angle change around these positions indicates the divergence of the flow. The effect of the horse-shoe vortex around the leading edge can be seen with the high yaw values near the wall on the suction side of the leading edge (decreasing tangential position value corresponds to moving across the blade passage from pressure surface to suction surface, see Figure 1). The low yaw angles associated with the pressure side leg of the horse-shoe vortex are not so clear because it is further from the traverse plane. Near the end wall the vortex also causes a negative pitch angle (flow towards the end wall) and a dip in total pressure contours, which are otherwise nearly parallel to the end wall at slot 1.

4.2 Flow Development Through the Cascade

Figures 4 to 10 show some of the total pressure loss contours and the secondary velocity vectors for the slots 2 to 7 through the cascade. The secondary velocity is here calculated as the vector sum of the radial component of velocity and the difference in tangential velocity from that given by the mid-span angle and local axial velocity. The 3-hole probe gives greater detail of the flow near the end wall, and its total pressure contours are shown beneath those for the 5-hole probe. It can be seen that the matching is fairly good, which is true for the other data not shown here.

At slot 2, Figure 4, the total pressure loss contours clearly show the two loss cores due to the legs of the horse-shoe vortex, the suction side leg on the left and the

pressure side leg from the adjacent blade on the right. Further away from the end wall, the total pressure contours are relatively undisturbed and parallel to the end wall, as they are at slot 1. The vector plot, Figure 5, shows the development of the passage vortex centred near the pressure surface with strong downward flows on the pressure surface and cross flows towards the suction surface. Even at this early stage the inlet boundary layer is starting to migrate towards the suction surface.

At slot 3, the effect of this migration is seen on the total pressure loss contours, Figure 6. The pressure side leg of the horse-shoe vortex has moved to about mid-pitch, with new fluid being brought down near the pressure surface. The suction side leg of the horse-shoe vortex does not show up, although there is a hint of it from the vector plots, Figure 7, in the suction surface corner with the end wall. The passage vortex is fairly centrally placed in the passage, although it does not coincide with the peak of the developing loss core shown by the contour plots.

At slots 4 and 5, (not shown), the loss core is further established due to the inlet boundary layer being swept towards the suction surface. Both the loss core and the passage vortex centre move across the passage, with the loss core a bit closer to the wall than is the vortex centre.

At slot 6, Figure 8, the loss core is seen to be detaching from the end wall, as the passage vortex starts to sweep it up the suction surface of the passage, with higher energy fluid being swept underneath it. A second loss peak is seen very close to the suction surface. The velocity vector plots, Figure 9, show flow leaving the surface at about the same distance from the end wall, about 30 mm. This may indicate the separation line caused by the suction side leg of the horse-shoe vortex, which has moved up the suction surface. This separation line has been observed by Langston et al (10), Marshal and Sieverding (11) and others. Thus at this point the losses produced by shear action upstream on the suction surface are being fed into the main passage flow. From the loss contours on the previous planes, it appears the same effect is present about 20 mm from the end wall at slot 5, about 10 mm at slot 4 and 5 mm at slot 3. Another significant point to note from the vector plots is the evidence of a separation line and a counter vortex which appear right in the corner of the suction surface and end wall. The 3-hole probe loss contours show a high loss region there. Again it appears there is a feeding into the main flow of loss produced upstream by the new boundary layer on the end wall.

These two new loss regions are more clearly seen at slot 7, Figure 10, while the loss core from the inlet boundary layer has moved further from the end wall. The vector plots show the separation line on the suction surface, now about 45 mm from the end wall, corresponding to the loss peak there as further loss is fed into the main passage flow. The counter vortex is also seen in the corner. The above description of the flow processes is also confirmed by the other data not presented here. Figure 11 shows the static pressure contours at slot 7, and it can be seen that there is a low static pressure region and this corresponds closely to the centre of the vortex. The static pressures recorded by the blade tappings are also shown, which tie up fairly well with the contours obtained from the cobra probes.

4.3 Flow Development Downstream of the Cascade

Figure 12 clearly shows the blade wakes at slot 8, which is 6 mm axially downstream of the trailing edge plane. However, it should be noted that the spacing of the tangential traverse positions was 15 mm, so that only one or two traverses are in the wake at mid-span. This explains why the left hand wake (one traverse) looks thinner than the right hand wake (two traverses), the contour plotting routine giving a linear variation between traverses, as seen by the even contour spacing. The loss core is clearly seen at about 55 mm from the end wall, and the second loss peak from the separation line on the suction surface at about 75 mm from the end wall. This loss peak has received suction surface boundary layer fluid which otherwise would have appeared in the wake beneath the loss core position. The loss region from the suction surface corner with the end wall is also seen, particularly on the 3-hole probe contours. The vector plots, Figure 13, show the passage vortex, with the shear of the vertical component of velocity across the wakes, which corresponds to the sheet of trailing shed and trailing filament vorticity of classical secondary flow theory. The remnant of the counter vortex in the corner is seen as an underturning cross flow with the separation line still evident at about -180 mm and +10 mm tangential position (zero is the tangential position of the trailing edge).

At slot 9, the loss core has continued to move away from the end wall, Figure 14, due to the flow field of the passage vortex. The two peaks are also clearly still visible. The coarse traverse does not show diffusion of the wake from slot 8 and slot 9. The continued feeding of loss from the new end wall boundary layer into the main flow is evident.

The last traverse plane, slot 10 is 49 mm axially downstream of the trailing edge, corresponding to 128 mm downstream in the direction of the mid-span flow angle. The blade wake diffusion is now evident on the loss contour plots, Figure 15, with the loss core centre some 80 mm from the end wall. The wake below the loss core is hardly discernible, since most of its low energy has been fed into the second loss peak by the separation line on the suction surface of the blade. The feeding of loss from the end wall is now seen as a large loss region, which is moving to the left of the line of the wake under the influence of the strong secondary flows. These are seen in the vector plots, Figure 16, where the flow is beginning to look fairly uniform in the tangential direction with most of the vertical components of velocity dissipated. However, the

separation line on the end wall still seems to persist (about -110 mm and -320 mm) with very low or negative overturning present.

Thus it seems likely that the feeding of the end wall boundary layer into the main flow will continue some distance downstream. The centre of the vortex (co-ordinates -260, 75) does not coincide with the loss peak originating from the upstream boundary layer (co-ordinates -270, 80) and so the loss core will continue to be convected differently relative to the vortex centre although the difference will be small.

Figure 17 shows the progression of the centre of the passage vortex as defined by the intersection of the zero pitch and zero cross flow lines, and the movement of the loss core peak around the vortex centre. The distances tangentially are measured from the suction surface or wake centre line, so that for slots 8, 9, 10 there is some uncertainty about the tangential position. The progression of the loss core around the vortex centre is very clearly illustrated, with an initial movement rapidly from pressure to suction surface and then convection out away from the end wall. The vortex is also convected by its own flowfield; this may be appreciated by considering the effect of the virtual vortex "reflected" in the end wall or suction surface.

4.4 Data on Planes Parallel to the End Wall

Presented here are only two of the vector plots of the velocity in a plane parallel to the end wall. Figure 18 shows the flow 1 mm from the end wall. Across the end wall, the separation line as indicated by a sudden change in velocity direction (and hence a radial velocity) is sketched in. This separation line is caused by the pressure side leg of the horse-shoe vortex. The counter vortex in the suction surface corner is clearly seen with underturning there as compared with the overturning elsewhere. The suction side leg of the horse-shoe vortex is not clearly seen except in its effects at slot 1. Behind the pressure side leg the very strong secondary flows are seen, with the flow angle even exceeding 90° to the axial near the separation line at slot 3.

At 60 mm, Figure 19, the flow at the early slots looks much like the expected potential flow, and the flow in the later slots can be seen to be underturning. However, the large component of velocity along the passage tends to obscure the relatively small underturning velocities.

4.5 Data on "Pseudo-Streamline" Planes

Figures 20 to 22 show velocity vector plots on the planes which are a constant fraction across the blade passage, pseudo-streamlines for two-dimensional flow. Figure 20 shows the flow near the pressure surface, with the strong downwards motion of the flow particularly early in the passage when the passage vortex is close to the pressure surface. The pressure side leg of the horse-shoe vortex appears to be between slots 1 and 2. The sudden upflow downstream of the trailing edge is caused by mixing with the strong upflow from the suction surface of the adjacent blade passage.

Figure 21 shows the plane near mid-pitch. The most noticeable feature is the horse-shoe vortex between slots 2 and 3, the upflow at slot 2 indicating the separation line. At the later positions the flow is slightly downwards near the wall, with a reduction in axial velocity.

Near the suction surface, Figure 22, the strong upward flow is seen, especially later on in the passage where the passage vortex has moved across to near the suction surface. The separation line from the suction side leg of the horse-shoe vortex is sketched in, and seems to be similar to the flow visualisation results of other workers.

4.6 Averaged Data Across Blade Pitch

The total pressure loss mass averaged across the blade pitch is shown for slots 7 to 10 in Figure 23. At slot 7, there is the clear peak due mainly to the loss core from the inlet boundary layer, and a rise close to the end wall. The outward convection of the loss core by the passage vortex moves the peak away from the end wall, and it also gets broader and less high. At the same time the loss near the end wall is seen to grow and forms a second peak as the new boundary layer loss is fed into the main flow. For slots 8 to 10, the wake loss is seen at mid-span.

The tangential velocity was similarly mass averaged to give the mean flow angle. This is plotted in Figure 24 as the difference from the mid-span value, representing the over- or under-turning of the mean flow. The position of maximum underturning moves away from the end wall, and also the underturning increases. The overturning near the end wall is most marked for slot 7, but the reduced flow angle from the corner counter vortex reduces the average overturning, leaving a peak at slot 10 some distance from the end wall.

5. INLET BOUNDARY LAYER VARIATION

The profiles of the thickened and thinned boundary layer profiles are shown in Figure 4 along with the natural profile. Table 2 compares the three boundary layers.

TABLE 2

Boundary Layer	Displacement Thickness, δ*	Total Pressure Loss Coefficient, Y	Nominal Thickness, δ
Thick	27.9 mm	0.175	180 mm
Natural	12.1 mm	0.085	115 mm
Thin	9.7 mm	0.053	100 mm

It can be seen that the effect of thickening has been much greater than the effect of thinning. Neither the thick nor thin profiles agree very well with a power law profile, both exhibiting points of inflexion. However, it was felt that the main effects on the flow in the cascade would not be greatly affected by having an unusual profile for the inlet boundary layer.

5.1 Flow Downstream of the Cascade

Figure 25 shows the total pressure loss contours at slot 8 for the thick inlet boundary layer. This may be compared with the corresponding diagrams for the thin boundary layer, Figure 26, and for the natural boundary layer, Figure 12. The main difference seen from the loss contours is the increasing size of the loss core as the boundary layer thickness increases.   Otherwise the contours look very similar, and in particular the loss region associated with the corner counter vortex looks almost identical for the three cases. The three vector plots again look similar with the centre of the passage vortex nearly at the same place, with the radial extent of the vortex being greater for the thicker boundary layer, and less for the thinner one. The corner counter vortex and its separation line appear for all three cases.

The diagrams at slot 10 (not shown here) show the same comparisons with those at slot 8. The loss core for the thicker boundary layer is larger, and the loss region near the wall as the end wall loss is fed into the mainstream look very similar. The extent of the secondary flows is greater for the thicker boundary layer.

Thus it would appear that for the range of boundary layer thickness investigated here, the overall flow pattern is not much affected by the inlet boundary layer thickness apart from the size of the loss core and extent of the vortex. In particular, the loss from the new end wall boundary layer and its introduction into the main flow is not affected by the inlet boundary layer thickness.

5.2 Averaged Data

Figure 27 shows the total pressure loss coefficient mass averaged across each of the slot planes. The continuous line for the natural boundary layer shows a fairly steady growth through the cascade, with a sudden jump at the trailing edge as the wake loss is included. The drop from slot 8 to slot 9 may be due to the inaccuracy in measuring the wake. The thick and thin boundary layers are shown at inlet and exit. It can be seen that the net increase in loss across the blade row is very similar for the three boundary layers.

6. TURBULENCE DATA

The flow at slot 1 was measured using the hot-wire anemometry. At mid-span, there is quite a high level of turbulence, a root mean square value of about 3%. The turbulence rises towards the wall steadily apart from a dip at 30 mm. The turbulence from 100 mm inwards is fairly isotropic, but near mid-span there appears a strong degree of anisotropy, with the component parallel to the end wall and perpendicular to the flow about twice the other two. These rather unusual features may be mainly due to a honeycomb flow straightener placed upstream of the working section. However, the low levels of turbulence usually found in a wind tunnel are not typical of those found in turbines, and so the high values here were felt to be acceptable.

The hot-wire anemometry gave mean velocity data which compared fairly well with that given by the cobra probes. However, a lot of care had to be taken to get reasonable results, especially by checking the calibration of the wires frequently because of dirt contamination.

The contours of turbulent kinetic energy at slot 8 are shown in Figure 28. The repeatability of the two wakes at mid-span is poor because of the relatively coarse traversing positions compared with the wake thickness (see section 4.3). However, nearer the wall, the repeatability is better. There is a region of high turbulent energy similar in appearance to the total pressure loss core. However, its peak value is on the side of the loss core and is nearly coincident with the passage vortex centre. There is also a hint of increased turbulence associated with the counter vortex from the passage corner. The values of the turbulent kinetic energy are very high when compared with the inlet flow. The contour values are normalised with reference to upstream flow, but when referenced to the local mean velocity, the peak turbulence intensity is about 30%. Thus some of the total pressure loss through the cascade appears as an increase in turbulent kinetic energy before being dissipated by viscous action.

The contours of shear stress (not shown here) give an indication of reversal of sign

across the loss core. However, the high values of turbulence present cast some doubt on
the quantitative accuracy of the results.

7.   LOSS AND ANGLE PREDICTIONS

The method proposed by Gregory-Smith (7) was used to predict the loss distribution
at the cascade exit, and also the angle variation, for the natural boundary layer at inlet.

Figure 29 shows the angle variation at slot 10 compared with the predicted angle
using the secondary flow theory. The underturning peak is not predicted well, and the
prediction gives very high overturning at the wall and does not follow the reduction in
overturning which is observed. This reduction cannot be predicted by the present theory,
since there is no allowance for the corner counter vortex which produces the reduction.
Usually an underturning peak is predicted by the theory (perhaps not in the correct place);
see for example, Gregory-Smith (7). However, here the inlet boundary layer is relatively
thick compared with the blade pitch, and the theory gives a much more spread out vortex
field. Hawthorne (13) illustrated this effect by comparing different boundary layer
thickness to pitch ratios for a 1/7th power law profile. The theory assumes no distortion
of Bernoulli surfaces (surfaces of constant total pressure) and this is clearly a very
poor assumption for this cascade.

The loss prediction is shown in Figure 30. The outer part with the loss core is
fairly well predicted, but there is an overprediction near the wall, although the overall
shape is about right. The loss core is underpredicted a little because the theory assumes
it to be made up only of the inlet boundary layer, whereas there is the additional loss
fed into it by the separation line on the suction surface. The main reason for the over-
prediction from the wall is the large over-estimate of the "extra" secondary loss, which
is related to the kinetic energy of the secondary flows as predicted by the theory. As
mentioned above, there is no allowance for the distortion of Bernoulli surfaces, and so
the secondary vorticity at exit is too high, giving a high value of secondary kinetic
energy.

8.   DISCUSSION

The results presented here are for a cascade of high turning, of fairly low aspect
ratio and with relatively thick inlet boundary layer, which has been varied. The broad
features of the flow are similar to those found by other workers. The horse-shoe vortex
has been observed with its associated separation lines, one on the suction surface and
the other crossing the passage to the corner of the adjacent blade. The establishment
of the passage vortex and the sweeping up of the upstream boundary layer into a loss core
are clearly seen. The way in which the vortex convects the loss core and also convects
itself has been demonstrated, and it is clear that the loss core and vortex centre do not
coincide, a distinction which is often not made.

In the cascade one element of loss is generated by the new boundary layer on the end
wall, which is highly skewed. Because the boundary layer is very thin, this process is
difficult to observe.   The loss appears downstream as it is fed into the main flow
through the separation line from the pressure side leg of the horse-shoe vortex and the
counter vortex formed in the corner of the end wall and suction surface. This process
seems to continue some distance downstream of the cascade. The counter vortex also gives
rise to a region of low overturning which depresses the exit mean flow angle near the wall.

A similar mechanism is seen to produce loss on the suction surface of the blade. The
boundary layer flow on the suction surface near the end wall is convected upwards, until
the separation line causes it to be fed into the mainstream giving a second loss peak near
the main loss core.

Thus it would appear that the three loss components at blade exit as suggested by
Gregory-Smith (7) are identified in this cascade. However, his simple modelling needs
some revision, as illustrated by the results of the comparison of predictions and
observations (Figures 29 and 30). There is obviously a need for an allowance for
Bernoulli surface distortion. Gregory-Smith (7) has suggested this may be done by using
streamline tracing as done by Glynn (15).

The variation of inlet boundary layer has shown little change of net increase in loss
across the cascade. This has also been observed by other workers, and the loss prediction
technique gives a similar trend, since the predicted end wall loss and "extra" secondary
loss will not vary much with inlet boundary layer.

The detailed traverse at slot 8 with the hot wire anemometer gives a picture of the
turbulence present, apart from some uncertainty in the blade wakes where closer traverse
positions would have been desirable. Very high levels of turbulence are associated with
the loss core, although not coincident in position.

Some workers have investigated the turbulent flow in turbine cascades. For instance,
Bailey (16) measured the turbulent flow in a turbine nozzle row and concluded that large
regions of the passage vortex had low turbulence compared with the inlet boundary layer.
The results here seem at variance with that conclusion, though it is possible the lower
acceleration and higher turning of this rotor blade compared with Bailey's nozzles are a
cause of the difference. Bailey measured the flow within the row, but at only three
positions across the passage. The turbulence here was fairly isotropic, which does not
agree with the observations of Taylor et al (17) who measured the secondary flows and

turbulence in a curved duct and found a degree of anisotropy at exit. However, the absence of a leading edge horse-shoe vortex in duct flows makes for cautious comparison with cascade flows. Further traversing within and downstream of the cascade will help to improve the picture of the flow with respect to turbulence quantities.

The mean flow data and the turbulence quantities at exit should provide an interesting test case for some of the fully three-dimensional calculation methods available. However, it is clear that the complex nature of the flow, and especially the effect of the horse-shoe vortex and its associated separation lines will be difficult to predict in detail.

9. CONCLUSIONS

(i) The secondary flows in a cascade of high turning rotor blades has been measured in great detail for mean flow quantities, with measurements at inlet and exit of the turbulence quantities.

(ii) The main features of the flow are the passage vortex and the loss core formed from the inlet boundary layer. The vortex convects itself and the loss core across the passage from pressure to suction surface, and then up the suction surface away from the end wall.

(iii) The horse-shoe vortex gives rise to two separation lines, one rising up the suction surface, and one which crosses the passage on the end wall and becomes associated with a counter vortex in the suction surface and end wall corner.

(iv) The surface separation lines are the means whereby loss formed by shear action close to the suction surface and end wall are fed into the main flow.

(v) The effect of varying inlet boundary layer thickness is small on the net increase in loss across the blade row.

(vi) Very high turbulence levels are associated with the regions of high loss, particularly with the loss core.

(vii) The data provide a test case for a single loss and angle prediction method, and indicate areas for development of the method. It will also provide data for other calculation methods, which will need to be fairly sophisticated if the complex details of the flow are to be predicted.

Further turbulence data from within the blade row are an objective for future work. Flow visualisation will also be performed to supplement the quantitative data. In a real turbine, a number of other factors may modify the flow, such as tip clearance and wall geometry, radial pressure gradients and blade row interference effects. Some of these may be investigated in cascade, but others can only be measured in real turbines.

ACKNOWLEDGEMENT

REFERENCES

1. Ainley, D.G. and Mathieson, G.C.R., A method of performance estimation of axial flow turbines, Aero. Research Council, R&M 2416, 1946

2. Dunham, J., A review of cascade data on secondary losses in turbines, J. Mech. Eng. Sci., vol 12, no 1, 1970, pp 48-59

3. Stuart, A.R. and Hetherington, R., The solution of the three variable duct flow equations, Fluid Mechanics, Acoustics and Design of Turbomachinery, NASA SP304, 1974, p 135

4. Denton, J.D., A time marching method for two and three dimensional blade to blade flows, Aero. Research Council, R&M 3775, 1974

5. Moore, J. and Moore, J.G., A calculation procedure for three dimensional viscous compressible duct flow, ASME J. Fluids Engineering, vol 101, 1979, p 415

6. Briley, W.R., Numerical methods for predicting three dimensional steady viscous flows in ducts, J. Computational Physics, vol 14, 1974, pp 8-28

7. Gregory-Smith, D.G., Secondary flows and losses in axial flow turbines, ASME J. Eng. Power, vol 104, no 4, 1982, pp 819-822

8. Herzig, H.Z., Hansen, A.G. and Costello, G.R., A visualisation study of secondary flows in cascades, NACA Report 1163, 1953

9. Armstrong, W.D., The secondary flows in a cascade of turbine blades, Aero. Research Council, R&M 2979, 1955

10. Langston, L.S., Nice, M.L. and Hooper, R.M., Three dimensional flow within a turbine cascade passage, ASME J. Eng. Power, vol 99, no 1, 1977, pp 21-28

11. Marshal, P. and Sieverding, C.H., Secondary flows within turbomachinery blading, AGARD-CP-214, The Hague, Paper 11, 1977

12. Carrick, H.B., Secondary flow and losses in turbine cascades with inlet skew, AGARD-CP-214, The Hague, Paper 9, 1977

13. Hawthorne, W.R., Some formulae for the calculation of secondary flows in cascades, Aero. Research Council, Report 17 519, 1955

14. Gregory-Smith, D.G. and Marsh, H., The manufacture of glass fibre rotor blades with pressure tappings, Aero. J., vol 75, no 723, 1971

15. Glynn, D.R., Calculation of secondary flow in cascades including effects of Bernoulli surface distortion, Int. J. Heat & Mass Transfer, vol 3, no 2, 1982, pp 73-80

16. Bailey, D.A., Study of mean and turbulent velocity fields in a large scale turbine vane passage, ASME J. Eng. Power, vol 102, 1980, pp 88-95

17. Taylor, A.M.K.P., Whitelaw, J.H. and Yianneskis, M., Curved ducts with strong secondary motion : velocity measurements of developing laminar and turbulent flow, ASME J. Fluids Engineering, vol 104, 1982, pp 350-359

18. Graves, C.P., Secondary flows and losses in gas turbines, Ph.D. thesis (in preparation), University of Durham
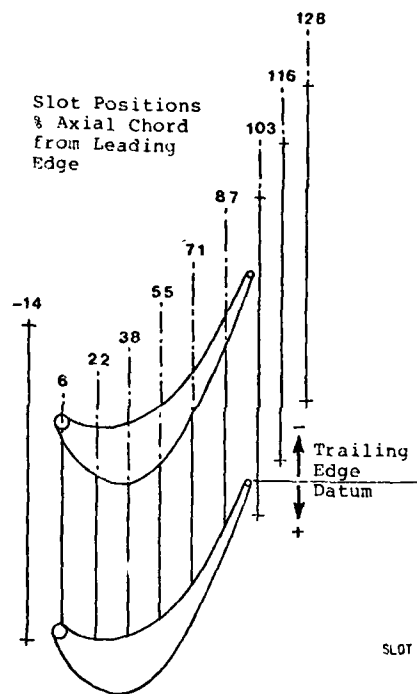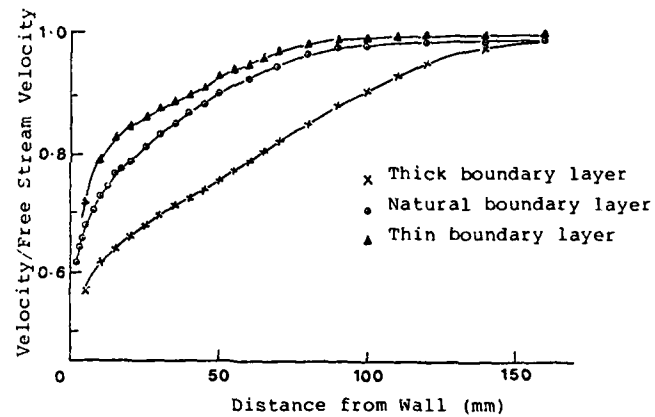
Figure 1: Cascade

Figure 2: Boundary Layer Velocity Profile

x Thick boundary layer

• Natural boundary layer

▲ Thin boundary layer

SLOT 1 YAW ANGLE CONTOURS (CONTOUR UNITS DEGREES)
NATURAL INLET BOUNDARY LAYER
X-AXIS TANGENTIAL CO-ORDINATE FROM TRAILING EDGE DATUM (MM)
Y-AXIS SPANWISE CO-ORDINATE FROM PERSPEX ENDWALL MM

Figure 3: Slot 1
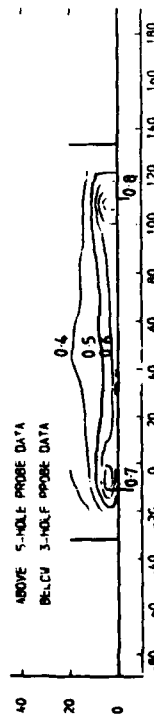
SLOT 2 VECTOR PLOT OF SECONDARY VELOCITIES (VT/SEC)-VT/CC)-VT'N,S)-VA/N,S,1)

NATURAL INLET BOUNDARY LAYER
X-AXIS TANGENTIAL CO-ORDINATE FROM TRAILING EDGE DATUM (MM)
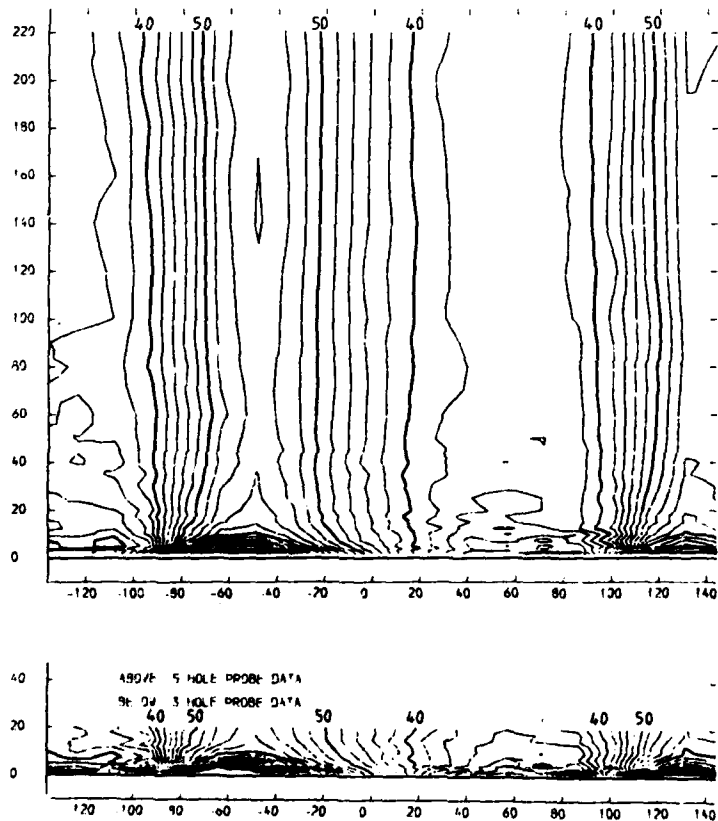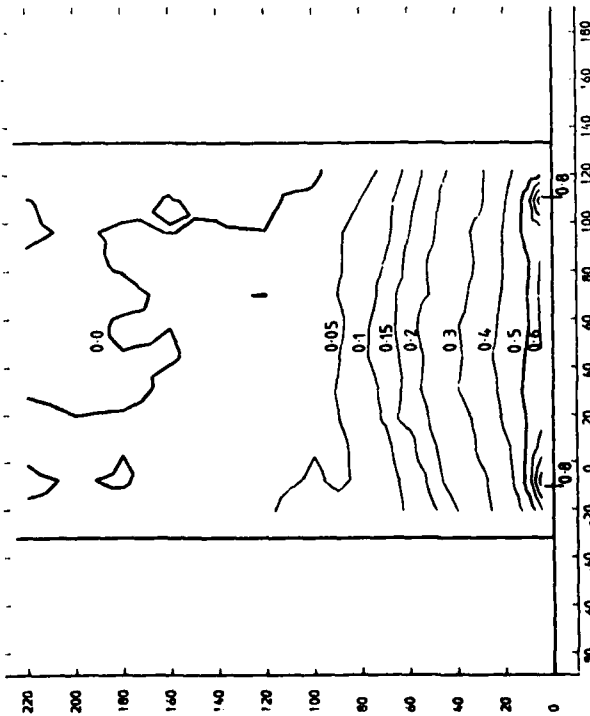Y-AXIS SPANWISE CO-ORDINATE FROM PERSPEX ENDWALL (MM)
VECTOR SCALE 20 METRES/SEC

Figure 5: Slot 2

SLOT 2 TOTAL PRESSURE LOSS COEFFICIENT ((PO1-POLOCAL)/(PO1-P1)) CONTOURS

NATURAL INLET BOUNDARY LAYER
X-AXIS TANGENTIAL CO-ORDINATE FROM TRAILING EDGE DATUM (MM)
Y-AXIS SPANWISE CO-ORDINATE FROM PERSPEX ENDWALL (MM)

ABOVE 5-HOLE PROBE DATA
BELOW 3-HOLE PROBE DATA

Figure 4: Slot 2

SLOT 3 VECTOR PLOT OF SECONDARY VELOCITIES (VT(SEC)=VT(LOC)-VT(M.S.)=VA(LOC) (VA(M.S.))
NATURAL INLET BOUNDARY LAYER
X-AXIS TANGENTIAL CO-ORDINATE FROM TRAILING EDGE DATUM (MM)
Y-AXIS SPANWISE CO-ORDINATE FROM PERSPEX ENDWALL (MM)
VECTOR SCALE 20 METRES SEC

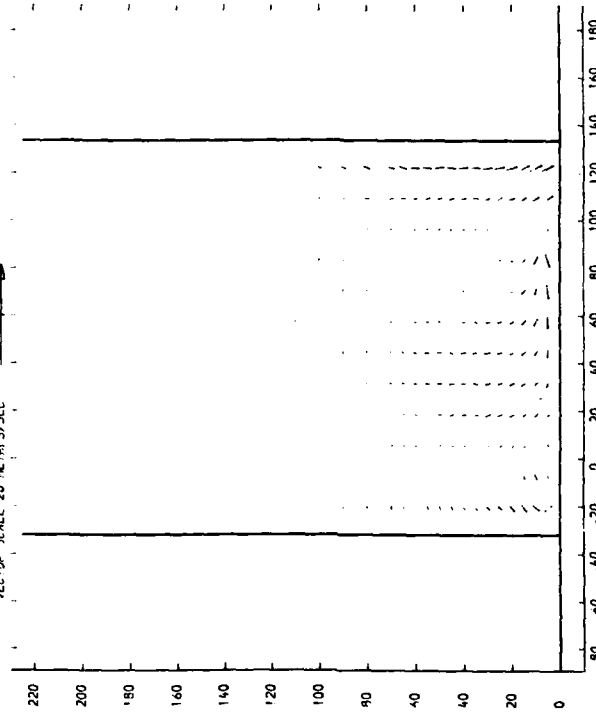Figure 7: Slot 3

SLOT 3 TOTAL PRESSURE LOSS COEFFICIENT ((PO1-POLOCAL) (PO1-P1)) CONTOURS
NATURAL INLET BOUNDARY LAYER
X-AXIS TANGENTIAL CO-ORDINATE FROM TRAILING EDGE DATUM (MM)
Y-AXIS SPANWISE CO-ORDINATE FROM PERSPEX ENDWALL (MM)

ABOVE S-HOLE PROBE DATA
BELOW 7-HOLE PROBE DATA

Figure 6: Slot 3

SLOT 6 VECTOR PLOT OF SECONDARY VELOCITIES (VT (SEC) =VT (LOC) -VT (M.S.) +VA (LOC)/VA (M.S.))
NATURAL INLET BOUNDARY LAYER
X-AXIS TANGENTIAL CO-ORDINATE FROM TRAILING EDGE DATUM (MM)
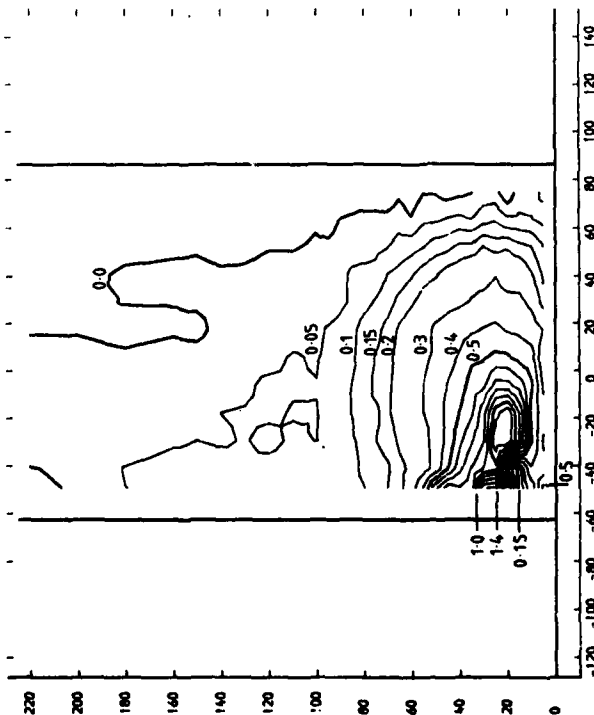Y-AXIS SPANWISE CO-ORDINATE FROM PERSPEX ENDWALL (MM)
VECTOR SCALE 20 METRES/SEC

Figure 9: Slot 6

SLOT 6 TOTAL PRESSURE LOSS COEFFICIENT ((PO1-POLOCAL) / (PO1-P1)) CONTOURS
NATURAL INLET BOUNDARY LAYER
X-AXIS TANGENTIAL CO-ORDINATE FROM TRAILING EDGE DATUM (MM)
Y-AXIS SPANWISE CO-ORDINATE FROM PERSPEX ENDWALL (MM)

ABOVE 5-HOLE PROBE DATA
BELOW 3-HOLE PROBE DATA

Figure 8: Slot 6

Figure 11: Slot 7 – Static Pressure

Figure 10: Slot 7

SLOT 8 VECTOR PLOT OF SECONDARY VELOCITIES (VT(SEC)=VT(LOC)-VT(X,5,.)+VA(LOC)/VA(M,5,.))

NATURAL INLET BOUNDARY LAYER
Y-AXIS TANGENTIAL CO-ORDINATE FROM TRAILING EDGE DATUM (MM)
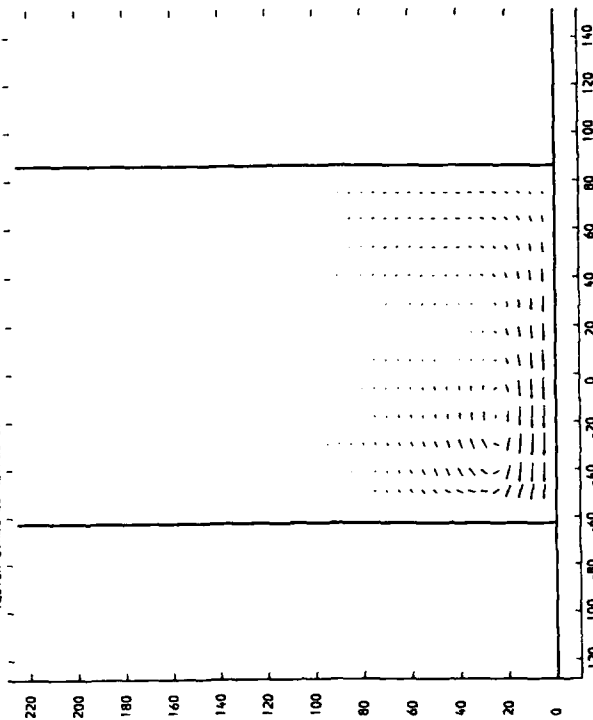Y-AXIS SPANWISE CO-ORDINATE FROM PERSPEX ENDWALL (MM)
VECTOR SCALE 20 METRES/SEC

Figure 13: Slot 8

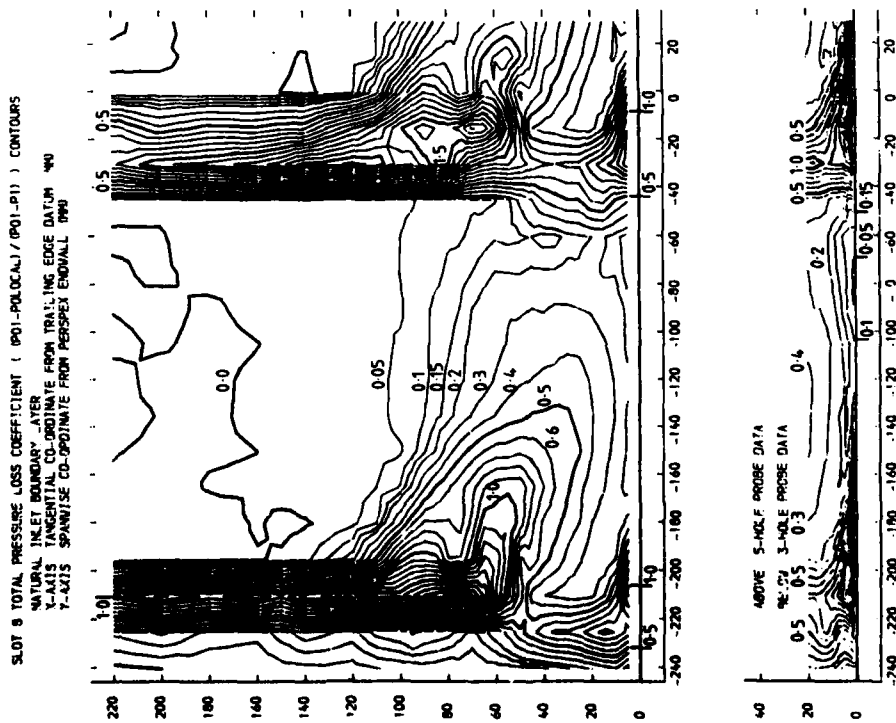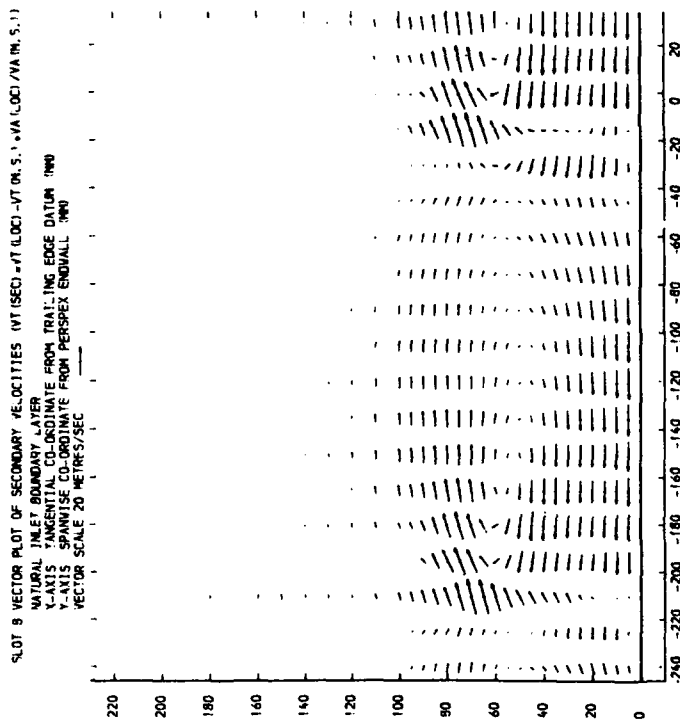SLOT 8 TOTAL PRESSURE LOSS COEFFICIENT ((PO1-POLOCAL)/(PO1-P1)) CONTOURS

NATURAL INLET BOUNDARY LAYER
Y-AXIS TANGENTIAL CO-ORDINATE FROM TRAILING EDGE DATUM (MM)
Y-AXIS SPANWISE CO-ORDINATE FROM PERSPEX ENDWALL (MM)

ABOVE 5-HOLE PROBE DATA
BELOW 3-HOLE PROBE DATA

Figure 12: Slot 8

SLOT 10 TOTAL PRESSURE LOSS COEFFICIENT ((PO1-POLOCAL) / (PO1-P1)) CONTOURS
NATURAL INLET BOUNDARY LAYER
Y-AXIS TANGENTIAL CO-ORDINATE FROM TRAILING EDGE DATUM (MM)
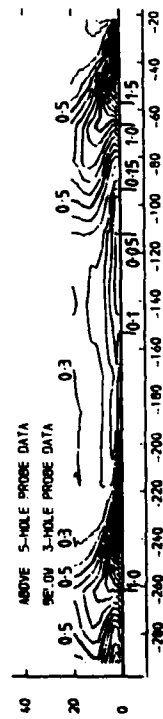Y-AXIS SPANWISE CO-ORDINATE FROM PERSPEX ENDWALL (MM)

ABOVE 5-HOLE PROBE DATA
BELOW 3-HOLE PROBE DATA

Figure 15: Slot 10

SLOT 9 TOTAL PRESSURE LOSS COEFFICIENT ((PO1-POLOCAL) / (PO1-P1)) CONTOURS
NATURAL INLET BOUNDARY LAYER
Y-AXIS TANGENTIAL CO-ORDINATE FROM TRAILING EDGE DATUM (MM)
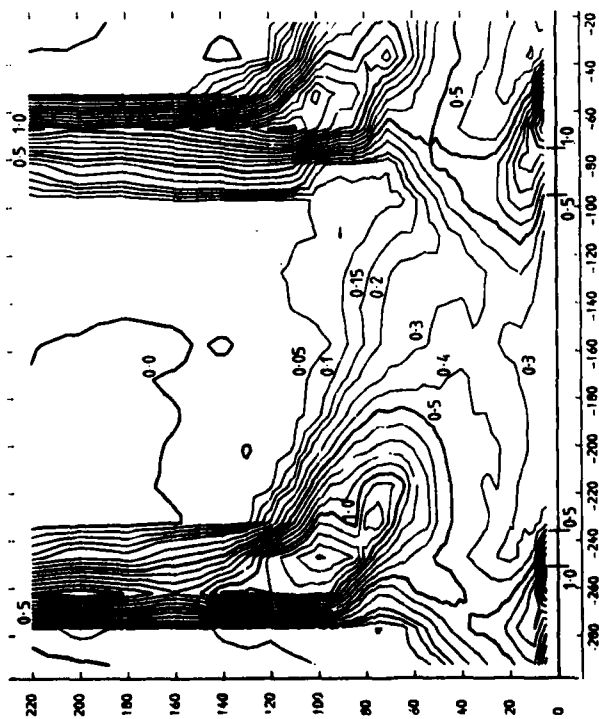Y-AXIS SPANWISE CO-ORDINATE FROM PERSPEX ENDWALL (MM)

ABOVE 5-HOLE PROBE DATA
BELOW 3-HOLE PROBE DATA

Figure 14: Slot 9

SLOT 10 VECTOR PLOT OF SECONDARY VELOCITIES (VT (SEC) =VT (LOC) -VT (M.S.) =VA (LOC) VA (M.S.))
NATURAL INLET BOUNDARY LAYER
X-AXIS TANGENTIAL CO-ORDINATE FROM TRAILING EDGE DATUM (MM)
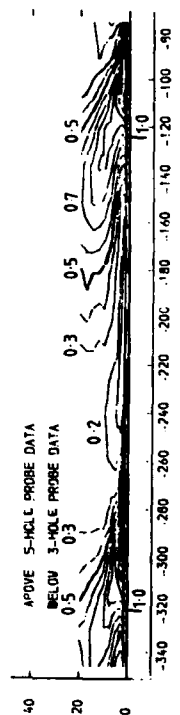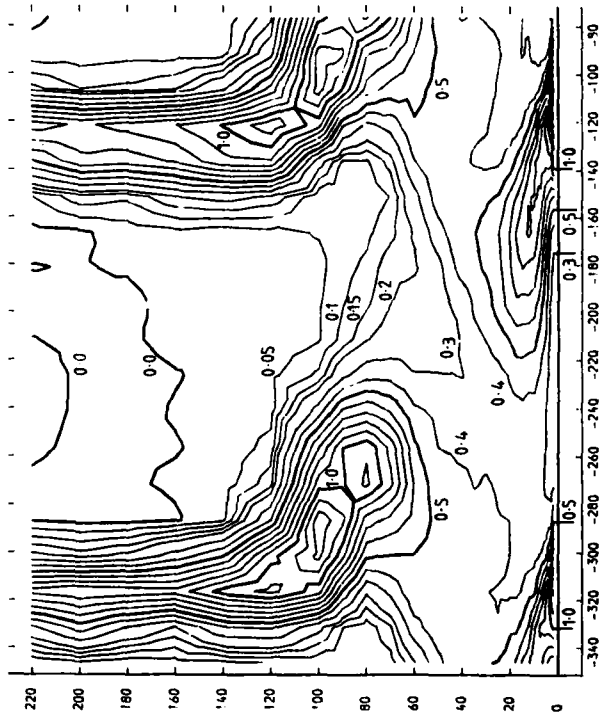Y-AXIS SPANWISE CO-ORDINATE FROM PERSPEX ENDWALL (MM)
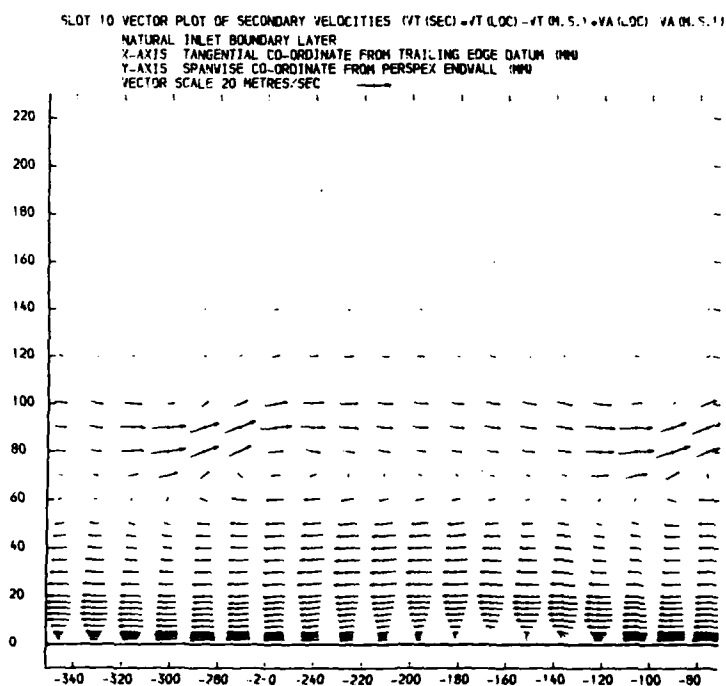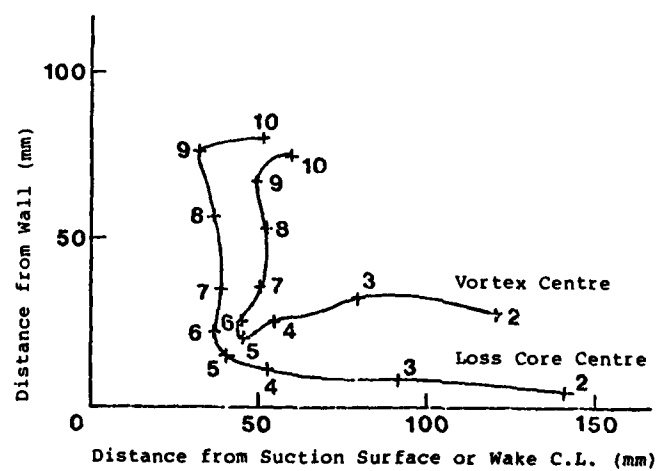VECTOR SCALE 20 METRES/SEC ——

Figure 16: Slot 10

Figure 17: Vortex and Loss Core Migration

PLOT ON PLANE 1.0 MM FROM PERSPEX ENDWALL (3-HOLE PROBE DATA)
VECTOR PLOT OF AXIAL AND TANGENTIAL VELOCITIES
X-AXIS   TANGENTIAL CO-ORDINATE FROM TRAILING EDGE DATUM (MM)
Y-AXIS   AXIAL CO-ORDINATE FROM TRAILING EDGE DATUM (MM)
VECTOR SCALE 40 METRES/SEC ——

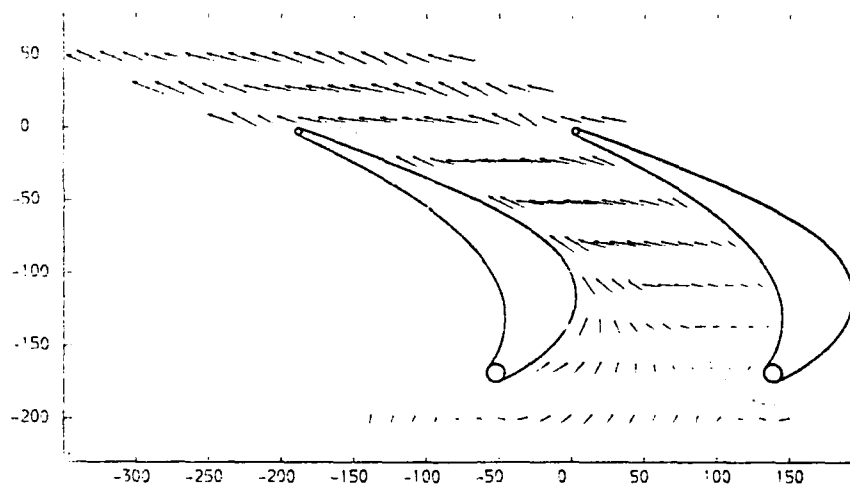Figure 18:   1.0 mm from End Wall

PLOT ON PLANE 60.0 MM FROM PERSPEX ENDWALL (5-HOLE PROBE DATA)
VECTOR PLOT OF AXIAL AND TANGENTIAL VELOCITIES
X-AXIS   TANGENTIAL CO-ORDINATE FROM TRAILING EDGE DATUM (MM)
Y-AXIS   AXIAL CO-ORDINATE FROM TRAILING EDGE DATUM (MM)

Figure 19:   60 mm from End Wall

Figure 20: Flow Near Pressure Surface

Figure 21: Flow at Mid-Pitch
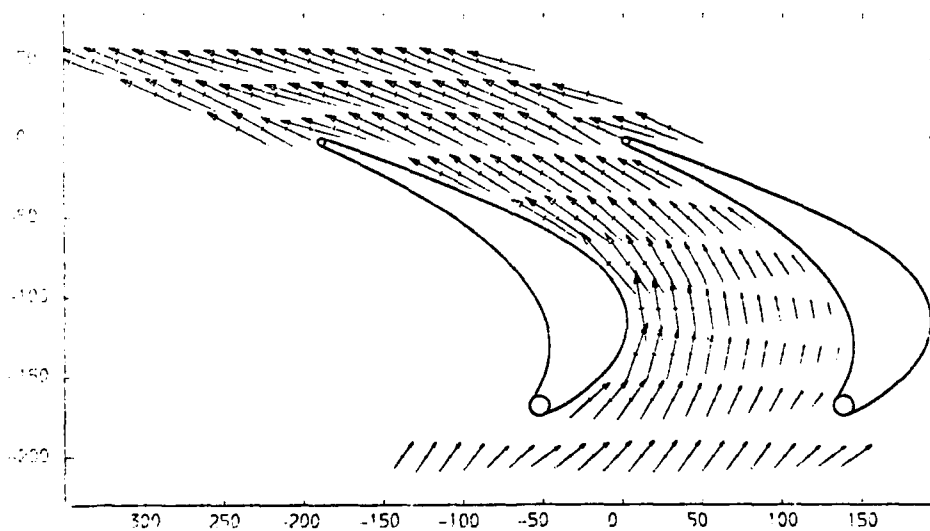
Figure 23: Pitch Averaged Loss Coefficient
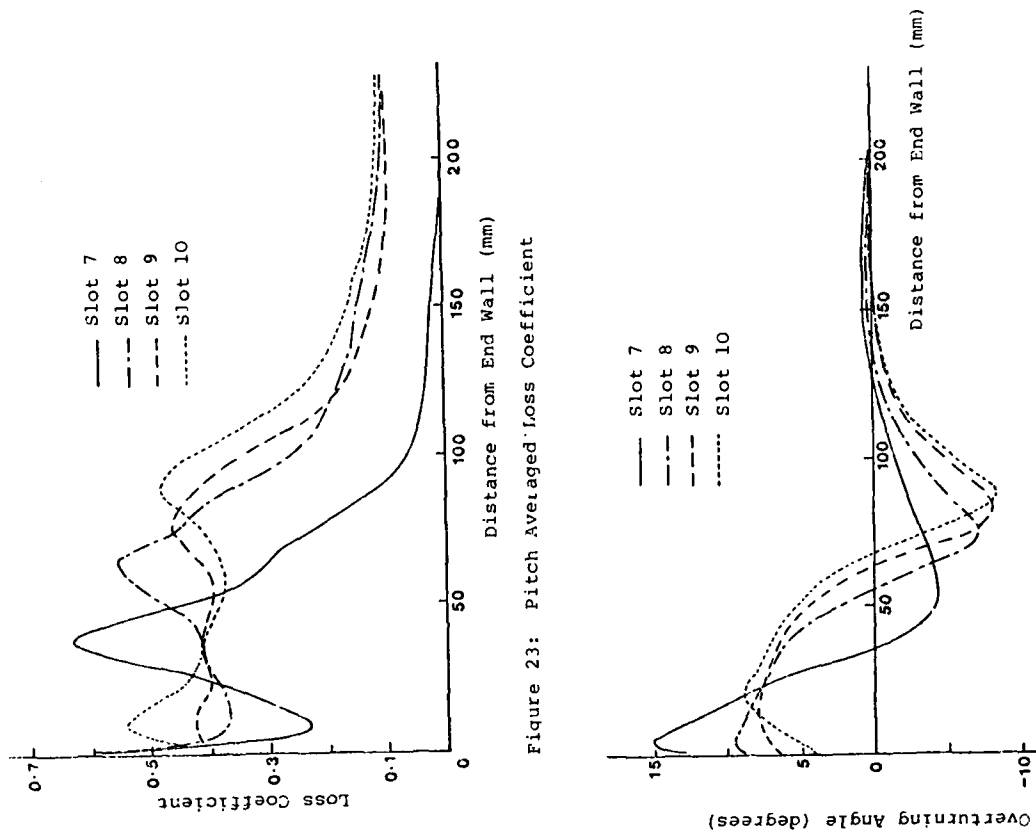
Figure 24: Pitch Averaged Flow Angle

PLOT APPROXIMATELY 6.7 Z OF BLADE PITCH LESS THICKNESS FROM SUCTION SURFACE
VECTOR PLOT OF AXIAL AND SPANWISE (RADIAL) VELOCITIES
X-AXIS AXIAL CO-ORDINATE FROM TRAILING EDGE DATUM (MM).
Y-AXIS SPANWISE CO-ORDINATE FROM PERSPEX ENDWALL (MM)
VECTOR SCALE 40 METRES/SEC

Figure 22: Flow Near Suction Surface
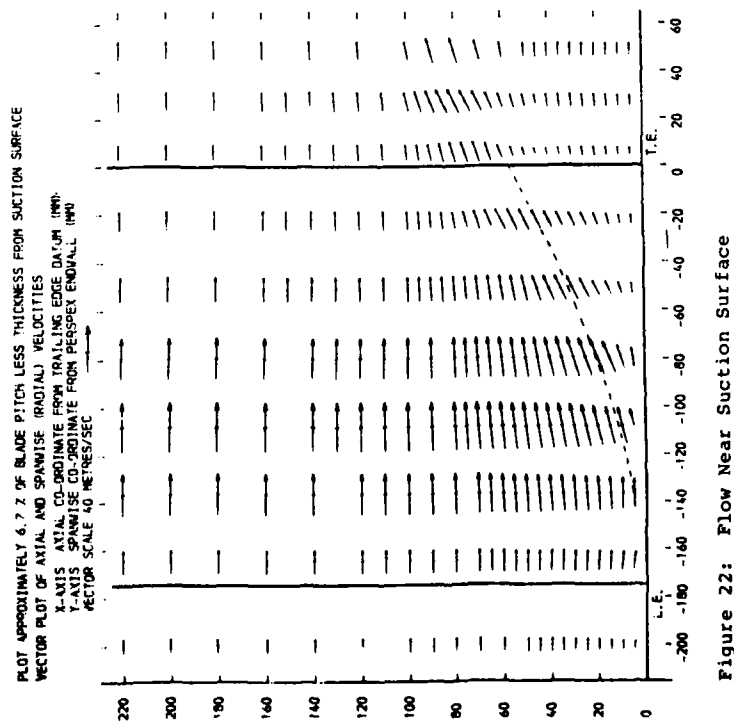
SLOT 8 TOTAL PRESSURE LOSS COEFFICIENT ((PO1-POLOCAL)/ (PO1-P1)) CONTOURS
THINNED INLET BOUNDARY LAYER
X-AXIS TANGENTIAL CO-ORDINATE FROM TRAILING EDGE DATUM (MM)
Y-AXIS SPANWISE CO-ORDINATE FROM PERSPE/ ENDWALL (MM)
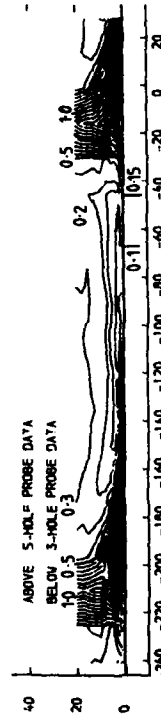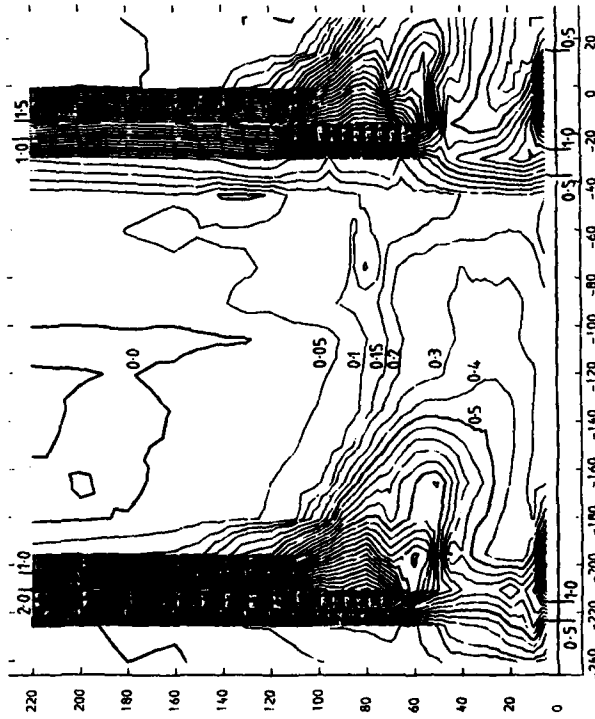
Figure 26: Slot 8 — Thin Boundary Layer

SLOT 8 TOTAL PRESSURE LOSS COEFFICIENT ((PO1-POLOCAL)/ (PO1-P1)) CONTOURS
THICKENED INLET BOUNDARY LAYER
Y-AXIS TANGENTIAL CO-ORDINATE FROM TRAILING EDGE DATUM (MM)
Y-AXIS SPANWISE CO-ORDINATE FROM PERSPEX ENDWALL (MM)

Figure 25: Slot 8 — Thick Boundary Layer

Figure 27: Loss Growth Through Cascade

SLOT 8 NORMALIZED TURBULENT KINETIC ENERGY CONTOURS

X-AXIS TANGENTIAL CO-ORDINATE FROM TRAILING EDGE DATUM (MM)
Y-AXIS SPANWISE CO-ORDINATE FROM PERSPEX ENDWALL (MM)
CONTOURS NORMALIZED USING UPSTREAM REFERENCE DYNAMIC HEAD
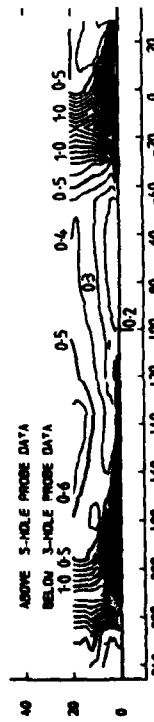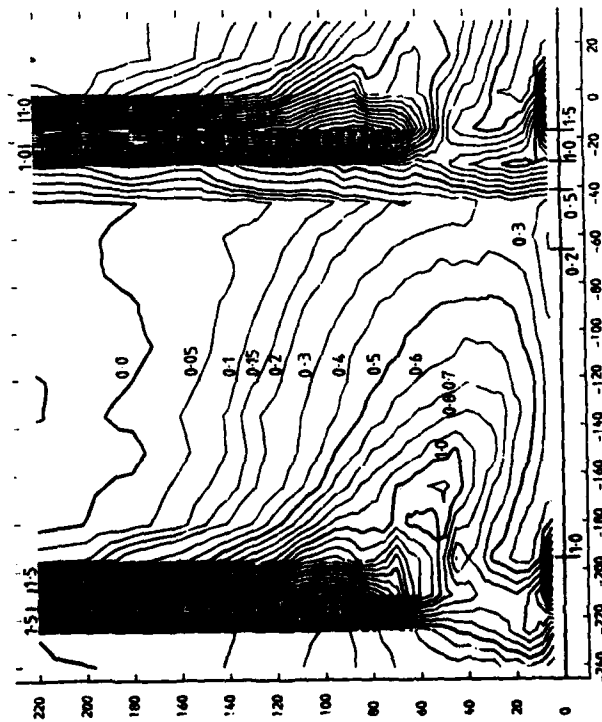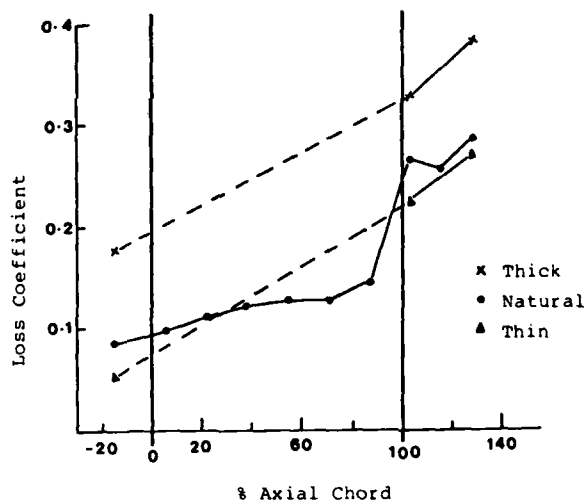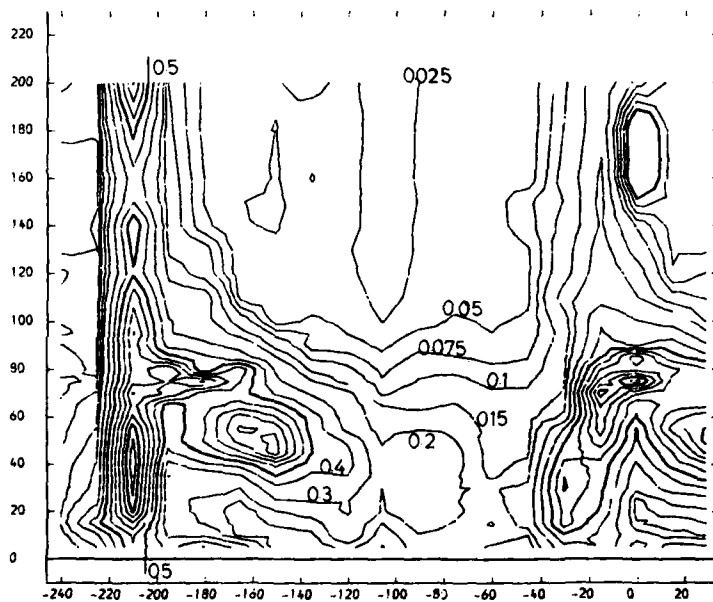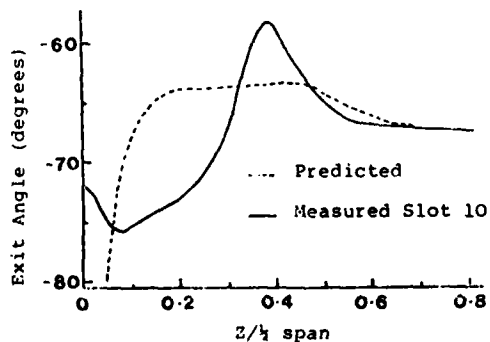

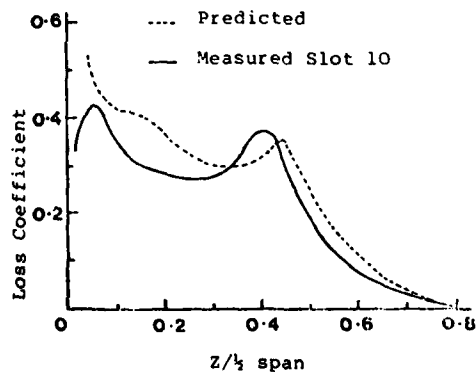Figure 28: Slot 8 - Turbulence

Figure 29: Exit Angle Comparison

Figure 30: Secondary Loss Comparison

DISCUSSION

K.Papailiou, Gr

When calculating the exit flow angle you used Hawthorne's theory to get the transverse velocity profile. What kind of longitudinal profile did you use?

Author's Reply

We used the mainstream longitudinal velocity, so we didn't reduce the longitudinal velocity to allow for the boundary layer. If we had done that, the overturning would have been even higher.

K.Papailiou, Gr

Many times in various comparisons it seems that the transverse velocity is well predicted by Hawthorne's calculation method, and my experience tends to give the same answer. Did you also plot transverse velocity rather than angle for comparison?

Author's Reply

I haven't done that, and it would be interesting to see whether the agreement is any better. I personally don't think it will be very much better. For this case, I think our problem is that we have such high turning, and the Hawthorne theory, as you know, assumes no distortion of the Bernoulli surfaces and, of course, here we have enormous distortion.

K.Papailiou, Gr

We have made this comparison on a similar cascade and got rather reasonable results. A second question: Did you mix out the losses from your exit plane to see how much more you get?

Author's Reply

No, we haven't done that.

B.Lakshminarayana

Do you have any detailed measurement upstream of the cascade? I am specifically looking for the presence of any flow separation upstream of the cascade near the leading edge. If you have detailed measurements, it would be useful to include them in this discussion, so that the data would be useful to computors. Please provide detailed velocity profiles and turbulence profiles (if you have them).

Author's Reply

We have measurements at the slot 1 position, i.e. 14% of axial chord upstream of the blades (see Figure 1). Figure 3 shows the yaw angle contours at slot 1, which show high turning of the flow around the leading edge near the end wall. This is also seen in Figure 18. Clearly close to the leading edge where the horseshoe vortex forms there is a separation line, and slot 1 appears to confirm that. However, we have no evidence of anything other than normal behaviour further upstream, although we have not traversed in detail.

Ph.Ramette, Fr

In Figure 8, which gives the losses in slot 6, we can see the passage vortex losses and the losses due to the horseshoe suction surface leg. In Figure 9, which gives the velocities in slot 6, we can see the passage vortex but not the horseshoe vortex. Could you comment about this?

Author's Reply

The vector plot of the secondary velocities is a good means of visualizing the general flow field, but small detail tends to get obscured. The suction surface leg of the horseshoe vortex is confined close to the suction surface, and it is also quite weak at slot 6 since its rotation is opposite to the strong passage vortex. Thus it is not visible in Figure 9, although its effect is shown on the loss contours of Figure 8, and its separation line can be picked out on the through-passage plot, Figure 22.

C.H.Sieverding, Be

Your results are much in line with the results of our experiments in straight cascades. In particular, I am glad to see that you also find that the center of the high loss core doesn't coincide with the center of the passage vortex. I would also like to comment on two points: (a) where, do you think, does the corner vortex start and (b) what are the main contributions to the high loss core?

Author's Reply

Answering the two points:

(a) Looking at Figure 18, it appears that the counter vortex starts when the separation line from the pressure side leg of the horseshoe vortex reaches the suction surface of the next blade, i.e. about slot 5. It is then that the high cross flow leaves the end wall close to the suction surface and the corner vortex is formed on the other side of the separation line.

(b) The high loss core is mainly composed of the original inlet boundary layer, which is convected around the passage forming the loss core, as our series of results show. However, there is also a smaller but significant contribution of loss which is formed by the shear action on the blade surface and which is then fed into the main flow by the separation line from the suction side leg of the horseshoe vortex.

BOUNDARY LAYER DEVELOPMENT ON ROTATING BODIES OF REVOLUTION

By

Lambros Lambropoulos, Student
Panagiotis Ktenidis, Scientific Collaborator
Kyriakos Papailiou, Professor

Laboratory of Thermal Turbomachines
Athens National Technical Univ.,
Athens, Greece.

Abstract

There are many practical cases in turbomachines, where the behaviour of the three-dimensional axisymetric rotating boundary layers must be known.

In this work the authors analyse existing experimental data concerning such rotating viscous flows. It is demonstrated how one may describe such cases in the rotational frame of reference, using simple boundary layer notions.

Boundary layer calculations are then performed in order to predict these flows. The theoretical and experimental results are found to be in a very good agreement.

List of Symbols

n	distance in the normal to the wall direction		
N	distance in the transverse direction		
R	radius		
s	distance in the longitudinal direction		
U=ωR	peripheral velocity		
V	absolute velocity		
W	relative velocity		
δ	boundary layer thickness		
$δ_1$	displacement thickness of the reduced velocity profile		
$δ_2$	momentum thickness of the reduced velocity profile		
ω	angular velocity		

Subscripts

e	external flow component
n	normal to the wall direction component
N	transverse direction component
s	longitudinal direction component
w	wall component

Superscripts

(~)	reduced component

Introduction

The general approximation, which consists in decomposing the flow into an inviscid and a viscous part (two zone model), along with Prandtl's approximation, has greatly helped the development of modern engineering calculations, which take into account the effects of viscosity.

Classical two or three-dimensional viscous calculations are based on the assumption that the external velocity, which results from an inviscid calculation, can be considered constant in magnitude and direction inside the viscous region. In addition, the viscous problem is formulated in deficit form in respect to the external inviscid flow.

Although not mentionned explicitly, most times, the separation of the flow field in two zones (inviscid and viscous) implies the existance of a reference direction and modulus in respect to which, knowing the deficit quantity, the reconstruction of the real flow field is possible. In the case of a turbulent flow, the external inviscid velocity vector is usually taken as reference for the mean velocity flow field and the direction of the external velocity is used to express the semi-empirical laws valid for the turbulent quantities.

In this sense we are talking about a privileged direction, while the above mentionned semi-empirical information is used to obtain closure for our formulation.

If the two zone model is adopted, the external flow is supposed to be described by the inviscid equations of Euler with boundary conditions such, that the viscous region manifests its presence through the blockage effects it produces. Such a description is valid in extreme cases such that of a shock/turbulent boundary layer interaction, which results into a severe boundary layer separation (see ref.(1)).

Several attractive simplifications result when adopting the two-zone model. The most important one is that, whether the nature of the flow is elliptic, hyperbolic or mixed, this will be considered only by the inviscid part of the solution. The viscous flow equations will be generally parabolic or, at the most, hyperbolic.

Looking at the two zone model from a different angle, we may see that it implies as well that the real flow is reconstructed by superposing two solutions, the inviscid and the viscous one. We may perform this superposition in a different way, as we do in practice. Following an established external flow, we may calculate step by step along each streamline the destruction of the mean kinetic energy (and the corresponding des-

truction of the total pressure) through the action of the viscous forces. This implies that the static pressure field is left untouched, if the flow is two-dimensional. This conclusion is not altered whether the calculation we perform constitutes an intermediate step in a number of iterations necessary to treat the viscous/inviscid interaction problem.

When the flow is three-dimensional, then the development of secondary vorticity is associated with the transformation of static pressure into kinetic energy and this must be taken into account for reconstructing the real static pressure flow field from the inviscid one.

Application of the two zone model in the case of shear flows, for which the Prandtl's approximation is not valid, necessitates certain precautions. For these flows the viscous layer extends so much in the normal to the wall direction, that the inviscid external velocity vector cannot be considered constant neither in magnitude nor in direction inside it. Such an application has been realized by necessity in the field of secondary flows. Mellor and Wood[2], were the first to consider the case of external flow field variations in the normal to the wall direction and give the notion of the reduced velocity profile. This notion, particularly useful, is explained in figure (1). Hawthorne[3] and Horlock[4], among others, contributed, indirectly, in clarifying the physical situation in the case of internal flows, where such a model was applied, by their work concerning the behaviour of the secondary vorticity and the associated velocity field.
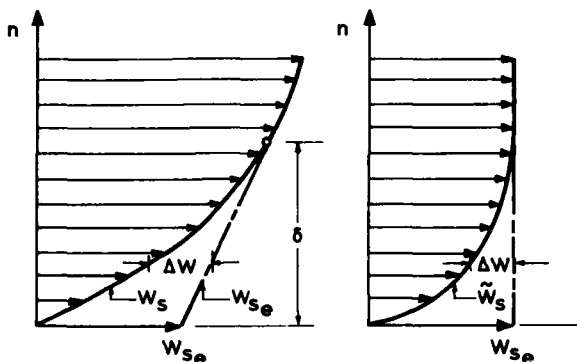
Fig.1   Schematic presentation of the way the reduced velocity profile is deduced. In the above figure:

$W_{s_e}(n)$ is the external velocity distribution

$W_s(n)$ is the real velocity distribution coinciding with the external one for $n > \delta$ (δ is the shear layer thickness)

n is the normal to the solid wall

$W_{s_{e_w}}$ is the value of W_{s_e} at the wall

$\Delta W = W_{s_e} - W_s$ is the velocity deficit inside the shear layer

$W_s(n) = W_{s_{e_w}} - \Delta W$ is the reduced velocity profile

Work that has been done in Lyon (refs(5) to (12)) has also supported the validity of the two-zone model in such cases. On the other hand, considerable information has been gathered for the rules of application of this model and a postulate has been put forth, which resumes these rules. This postulate may be expressed in the following way:

"We can decompose a flow region into an inviscid part and various viscous parts. The inviscid part, which may be rotational, can be described by Euler's equations, coupled with boundary conditions, where the blockage effects due to the various viscous layers have been taken into account. Each viscous layer must be considered and calculated separatelly along with the secondary vorticity that it itself creates. As reference for its calculation the external absolute or relative (according to the situation) velocity vector must be considered.

The work of the viscous forces destroys, with a good approximation, part of the mean kinetic energy".

Of course, inside the considered viscous shear layer for external flows with large velocity gradients this postulate must brake down. The limits of validity are not known, however, to-day, as it has been applied to cases for which only crude approximations were possible.

We have been mentionning the secondary flow field, for which calculations are performed assuming that this postulate is valid. The good results obtained in this way,

suggest that maybe more refined shear flow calculations may be based on the same as-
sumptions. This general idea along with the fact the one basic assumption cannot be
verified in the case of a secondary flow calculation is found at the origin of the
present work. This particular assumption concerns the reference system in respect to
which a developing shear layer must be considered and the reasons for which it may not
be tested using secondary flow experiments performed on stationary and rotating blade
rows are explained in references (6) and (7).

This question will be examined below for cases not so complicated as the ones
mentionned above. At the same time an important problem will be discussed, namely the
calculation of axisymmetric shear layers developing along rotating bodies of revolution,
as the one presented schematically in figure (2).
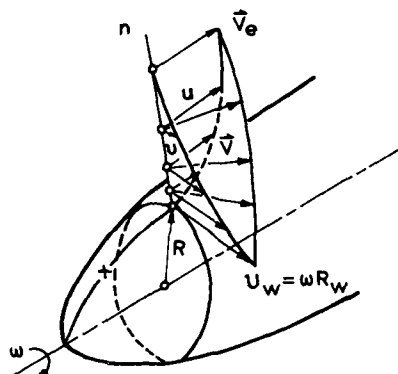
Fig.2   Schematic representation of the three-dimensional
         shear layer developing along a rotating body of
         revolution. The velocity vectors are presented in
         the absolute reference system.

These shear layers may be found in many turbomachinery applications as, for exam-
ple, along the rotating nacelles leading to the first rotating row of an axial or ra-
dial type turbomachine.

The analysis will be based on already existing experimental results and it will
be tried to apply the notions developed above. The present analysis will exclude the
case of the sudden shear applied to a layer developing along a stationary and then,
abruptly, on a rotating solid axisymmetric surface.

2.   Analysis of Cases of Rotating Viscous Layers

The experiments used in the present work are described mainly in references (13)
and (14). References (15),(16) and (17) were also considered. They concern essentially
two cases, which are presented schematically in figures (3a) and (3b). The first one
is cylindrical and the second one is conical. The internal solid boundary is rotating
around the axis of symmetry and we consider the three-dimensional boundary layer deve-
loping on it.
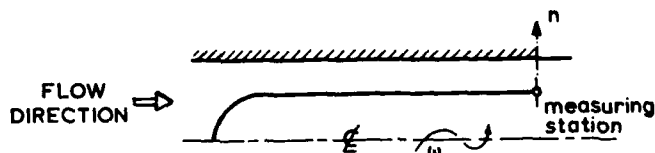
Fig.3a   First experimental case: Cylindrical body rotating
          in a channel.
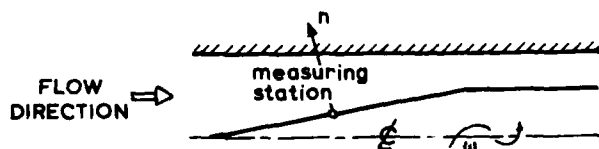
Fig.3b   Second experimental case:Conical body rotating
          in a channel.

After analysing the experiments, we came to the conclusion that, for a first approximation analysis, one could consider that the annulus height was large enough, so that secondary vorticity induced velocities outside of the wall boundary layer could be neglected. It was also possible to conclude that velocity profiles could be analysed taking into account that the external velocity in the absolute frame was axial and uniform for the cylindrical case.

The analysis of the experimental results, presented below, is based on the above mentionned two simplifying assumptions. Only the mean velocity field will be analysed in agreement with the measurements that were performed.

Typical velocity profiles described in the absolute system of reference for the cylindrical case, which will be considered first, are presented in figure (4). It can
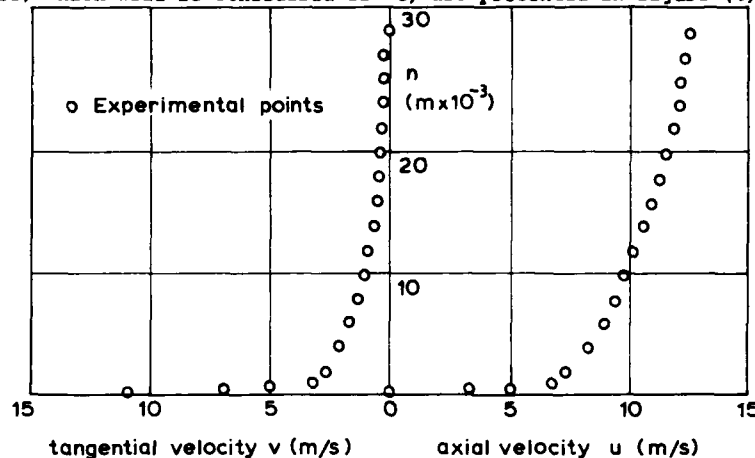
Fig.4· Velocity profiles in the absolute frame of reference .
Cylindrical case (ref.(13)).

be easily seen that the transverse velocity profile cannot be represented by any of the velocity profile families, which are known from boundary layer theory. Attempts to represent the longitudinal velocity profile by Coles' velocity profile family did not give acceptable results.

An attempt was, then, made to describe the velocity profile in the relative (rotating) frame of reference, in agreement with the assumptions used for secondary flow calculations. This reference system seems more natural to consider in our case, in view of the no slip condition at the solid wall upon the behaviour of a boundary layer. In the relative reference system, the reference velocity is the external relative one and it changes its magnitude and direction as we move away from the solid wall along a normal to it. A typical set of longitudinal and transverse velocity profiles in the new reference system is presented in figure (5). A first remark that can be made is that the

Fig.5   The longitudinal and transverse velocity profiles in the
relative frame of reference. Case of cylindrical rotating
body of revolution from ref.(13). Streamlined nose body.

   C   Relative longitudinal profile. Experiment

   ●   Relative transverse profile. Experiment

   —·—   Inviscid external velocity profile.

   ———   Analytical representation of the longitudinal
            experimental velocity profile using Coles' ve-
            locity profile family.

transverse velocity profile is non-existant. A second remark is that the <u>reduced</u> profile resulting from the longitudinal one can be very well described by the <u>Coles'</u> velocity profile family. The particular analytical velocity profile was specified from the experimental values of the displacement and momentum thicknesses δ_1 and δ_2 of the reduced velocity profile. The resulting analytical velocity profile has been transposed in the physical system and is presented, along with the experimental results, in figure (5).

This analysis suggests that the relative external velocity is the reference velocity for the rotating boundary layer. At the same time, the absence of a transverse velocity profile is easy to explain. Assuming that the rotating boundary layer has been essentially developed on the cylindrical part, we can remark that the external relative velocity doesn't change its direction along streamlines of the relative flow. The corresponding trajectories are spiral with constant angle. It is, thus, impossible to develop from primary vorticity a secondary vorticity and a transverse velocity profile associated to it.

Of course, this argument is not exact, especially near the wall where the effects of the boundary layer development along the initial rotating spherical part are felt. Observed deviations from a strictly nul transverse velocity profile near the solid wall in the analysis of the experimental results may be attributed to this cause as well as to the simplifying assumptions used for the reconstruction of the inviscid external flow.

We arrive, thus, at the conclusion that, not only our viscous shear layer must be considered in a relative reference system, but also that, for the cylindrical case, it may be considered as two dimensional.

In order to concretize this last statement, we have performed a two-dimensional boundary layer calculation along the spiral streamlines in the relative system, using the corresponding relative external velocity distribution at the wall as input. The calculations were performed using the integral boundary layer calculation method which was presented in reference (19). The comparison of the calculated integral quantities with the experimental ones, which correspond to the reduced velocity profile are presented in figure (6). The agreement is very good.
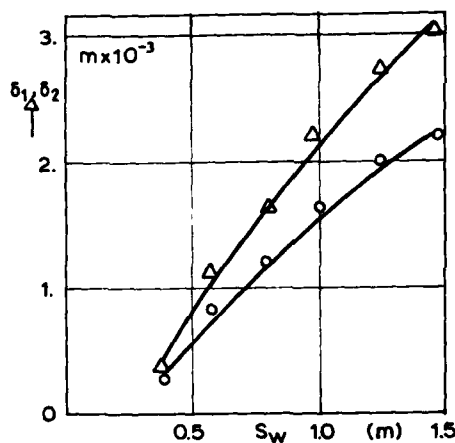
Fig.6a Comparison between theory and experiment. Cylindrical rotating body with hemisphere. Experimental results from ref.(13).
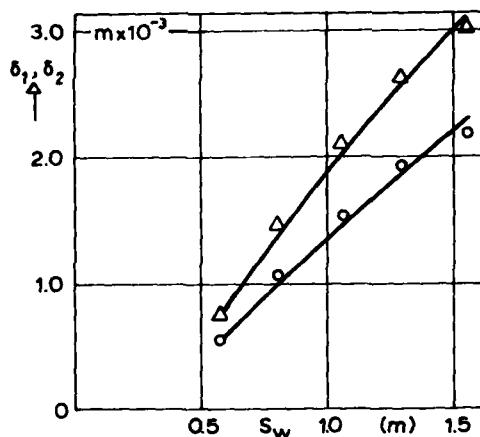
Fig.6b Comparison between theory and experiment. Cylindrical rotating body with streamlined nose. Experimental results from ref.(13).

O   Experimental values of momentum thickness δ_2

△   Experimental values of displacement thickness δ_1

———   Theoretical calculation results using method of ref.(13).

We may turn now to the case of the rotating cone. The same analysis in the relative system results in a longitudinal velocity profile, which can be accurately reproduced, as before, using Coles' velocity profile family. An example of this analysis is presented in figure (7). In this same figure the transverse velocity profile has been presented, which in non-zero for this case. This fact may be explained by the radius variation along relative streamlines. The relative external velocity changes, thus, not only in magnitude but also in direction. The corresponding turning of the primary vorticity creates, consequently, secondary vorticity or, in other words, a transverse velocity profile.
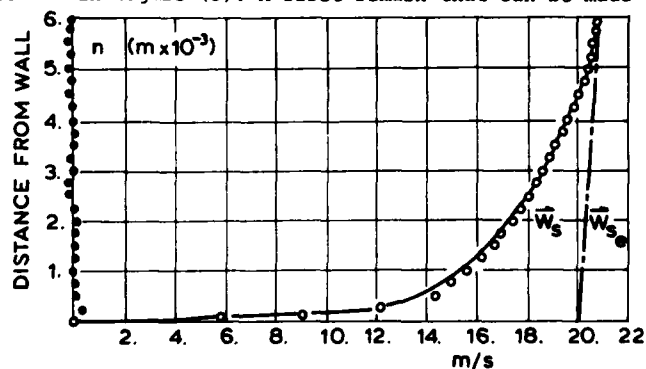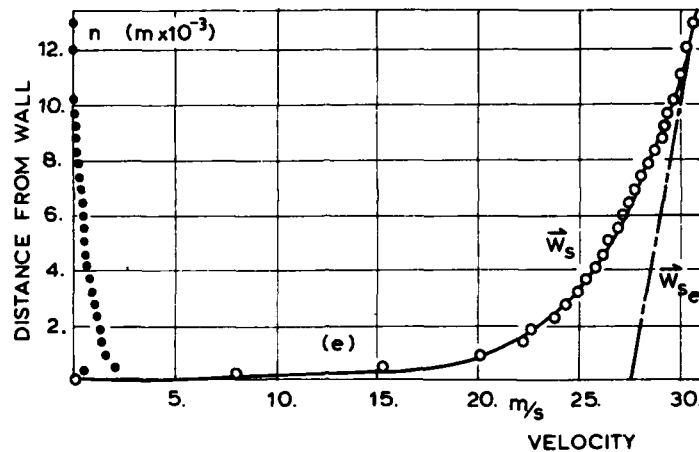
Fig.7 Longitudinal and transverse velocity profiles in the
relative frame of references. Case of conical rotating
body. Measurements from ref.(13).

- O   Relative longitudinal profile. Experiment
- ●   Relative transverse profile. Experiment
- —·—   Inviscid external velocity profile.
- ———   Analytical representation of the longitudinal
         experimental velocity profile using Coles' velo-
         city profile family.

Figure (8) presents such a profile in the same coordinate system that Johnston[18]
uses in order to obtain his triangular form. It can be seen that here, also, in spite of
the various approximations used in the present analysis concerning the external velo-
city field, the triangular form is evident.

Not having the possibility to perform a three-dimensional calculations, the present
analysis was stopped at this point.
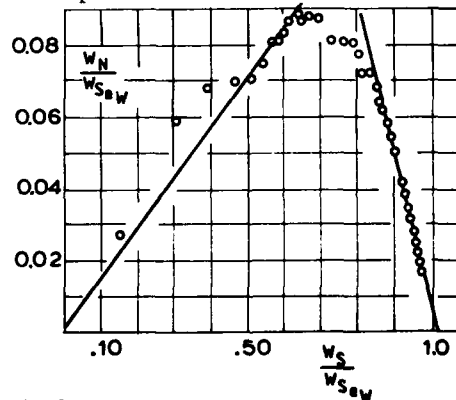
Fig.8 Triangular representation of the Trans-
verse velocity profile.

3.   Conclusions

An analysis of the behaviour of the mean velocity field was performed for boundary
layer developing on rotating bodies of revolution. Experimental results from cylindri-
cal and conical rotating bodies were examined.

It was concluded that the analysis ought to be performed in the rotating frame of
references and that, as reference for this viscous flow analysis, the relative external
velocity vector should be used.

If this was done, then, for the cases considered, the viscous velocity flow field
behaved in the same way as a classical two or three-dimensional boundary layer. Of
course, it is expected that Coriolis force effects will be present as far as the turbu-
lence behaviour is concerned.

References

1. G. Meauzé:"Méthode de Calcul Aérodynamique Inverse Pseudo-Instationaire" La Recherche Aerospatiale No 1980-1, pp 23-30, 1980.

2. G.L. Mellor, G.M.Wood:"An Axial Compressor End-Wall Boundary Layer Theory". ASME Paper No 70-GT-80. Transactions of the ASME, Journal of Basic Eng., June 1971, pp 300-316.

3. W.R. Hawthorne:"Rotational flow through cascades:The components of vorticity" Quart.Jr. of Mech. and Ap. Math. (VIII-3), 1955.

4. J.H. Horlock, B. Lakshminarayana:"Secondary flows:theory, experiment and application in turbomachinery aerodynamics", 1973.

5. K.D. Papailiou, R.Flot, J. Mathieu:"Secondary Flows in Compressor Blading" ASME Paper 76-GT-57, 1976. ASME Trans., Journal of Engg. for Power, Vol.99, pp 211-229, 1977.

6. G.Bois, F.Leboeuf, A.Comte, K.D. Papailiou:"Experimental Study of the Behaviour of Secondary Flows in a Transonic Compressor" AGARD CP-214, 1977.

7. A. Leboeuf, A.Comte, K.D. Papailiou:"Calculation Concerning the Secondary Flows in Compressor Bladings" AGARD CP-214, 1977.

8. G.Bois, A.Vouillarmet, J.Duchemin, K.D. Papailiou:"Analyse Experimentale de l' Ecoulement dans un Etage de Machine Centrifuge". Presenté au "Centrifugal Compressors, Flow Phenomena and Performance". AGARD Congress, 7-9 May, 1980.

9. A. Comte,G. Ohayon, K.D.Papailiou:"A Method for the Calculation of the Wall Layers Inside the Passage of a Compressor Cascade With and Without Tip Clearance". ASME Paper 81-GT-168, ASME Trans., Jr. of Engg. for Power, Vol.103/3, 1981.

10. F.Bario, F.Leboeuf,K.D. Papailiou:"Study of Secondary Flows in Blade Cascades of Turbomachines". ASME Paper 81-GR/GT-3. ASME Trans. Jr. of Engg. for Power pp 497-503, 1982.

11. F.Leboeuf, F.Bario, G.Bois,K.D. Papailiou:"Experimental Study and Theoretical Prediction of Secondary Flows in a Transonic Axial Flow Compressor". ASME Paper 82-GT-14.

12. K.D. Papailiou:"A Contribution to the Calculation of Secondary Flows in an Axial Flow Compressor". To be presented in the 6th International Symposium of Air Breathing Engines (ISABE), Paris, Juin 1983.

13. Y.Furuya, I.Nakamura:"Velocity Profiles in the Skewed Boundary Layers on Some Rotating Bodies in Axial Flow". Jr. of Applied Mechanics, Vol.37, March 1970, pp 17-24.

14. E.Arzoumanian, L.Fulachier, R.Dumas:"Experimental Investigation of the Three-Dimensional Boundary Layer on an Axially Rotated Cylinder" 2nd Intl. Symposium on Turbulent Shear Flows, July 2-4, 1979.

15. Chung Kyong-Cho, Kenneth N. Astill:"Momentum Integral Solution of Developping Flow in an Annulus with a Rotating Inner Cylinder" Tufts University. Unpublished Report.

16. I.Nakamura, S.Yamashita, Y. Furuya:"Experiments on Turbulence properties in the Thick Turbulent Boundary Layer on a Rotating Conical Body of Radius Decreasing towards downstream". 2nd Intl. Symposium on Turbulent Shear Flows, July 2-4, 1979.

17. O. Parr:" Untersuchungen der dreidimensionalen Grenzschicht an rotierenden Drehkorpern bei axialer Anstromung". Ingr.-Arch.32, 393-413,1963.

18. J.P. Johnston:"On the Three Dimensional Turbulent Boundary Layer Generated by Secondary Flow". Trans. ASME Series D., Jr. of Basic Engg., Vol.82, 1960, pp 233-248.

19. G. Assassa, K.D. Papailiou:"An Integral Method for the Calculation of the Separated Turbulent Boundary Layer". ASME Trans., Jr. of Fluids Engg., Vol. 101, pp 110-116, 1979.

END-WALL BOUNDARY LAYER CALCULATIONS IN
MULTISTAGE AXIAL COMPRESSORS

by

J. DE RUYCK   and   Ch. HIRSCH
Research ass.   Professor

VRIJE UNIVERSITEIT BRUSSEL
Dept. of Fluid Mechanics
Pleinlaan 2, 1050 BRUSSELS
BELGIUM

SUMMARY

A previously developed theory for the calculation of a three-dimensional boundary layer
along any curved axisymmetric wall surface is summarized. In addition, new defect force
correlations take into account the interactions between blades and end-wall boundary
layer flows, in particular tip clearance effects, relative motion and secondary losses
are included. Velocity profiles are reconstructed from the integral boundary layer
thicknesses by use of velocity profile models defined in the meridional and angular
directions.

The different aspects of the theory are tested systematically on various configurations.
It is shown that the overall behaviour of axial compressor boundary layers can be
simulated with the present method and that the defect force correlations are able to
simulate all the secondary flow effects.

SYMBOLS

b	boundary layer parameter	a	flow angle
c	absolute velocity component, chord	γ	stagger angle
E	entrainment rate	δ	physical boundary layer thickness
F	force defect thickness	δ^*	displacement thickness
f	blade force	ϵ_w	wall skewing angle
H	shape factor	η	efficiency
H^*	Head's shape factor	η_{bl}	boundary layer efficiency
h	annulus height	θ	momentum thickness
m	meridional coordinate	ν	defect force thickness
n	coordinate normal to the wall	ρ	density
P	power	σ	solidity
p	pressure	τ	shear stress
Q	volume flow	φ	mass flow coefficient c_m/U
r	radius	ω	angular speed
s	streamwise coordinate, pitch		
T	temperature	subscripts	
T^*	Eckert reference temperature		
t	transverse coordinate	k	kinematic
t	tip clearance	w	at the wall
U	wheel speed	m,n,u	in meridional coordinates
u	pitchwise coordinate	s,y,t	in streamline coordinates
W	velocity in the blade reference system		
w	relative velocity component		
y	coordinate normal to the wall		

INTRODUCTION

Three main components can be distinguished in the flow passing through a blade row. A
main component 'far' from blades and end-walls is in general considered as an inviscid
part of the flow.   The flows 'close' to the blade surfaces and to the end-walls are
subject to viscous effects since the presence of the blades and the end-walls both give
rise to boundary layers which moreover present a high three-dimensional character. A
direct consequence of the presence of boundary layers is a blockage effect which can rise
to 10 or even 20 % of the passage area. The three-dimensional character of the end-wall
boundary layers (EWBL) is moreover shown to have an influence on the energy exchange and
efficiency of the machine [1].

A current approach to solve for these three distinct parts of the flow consists in the
splitting of the complete flow into blade-to-blade flow and meridional through flow. The
meridional through flow is obtained by considering an averaged blade-to-blade flow in the
meridional plane. In this plane radial equilibrium is to be expressed and the EWBL are
to be taken into account. Because of the averaging of the blade-to-blade flow, the
through flow approach consists in an axisymmetric approach of the turbomachine flow.

The present paper illustrates a method for the determination of the EWBL effects.   This
is done through a three-dimensional integral boundary layer approach, where a special
attention is given to the blade-to-blade averaging procedure. Blade force variations
inside the EWBL are shown to have important effects and are taken into account in a

semi-empirical way. Since the present method is based on an integral boundary layer approach, it delivers integral boundary layer thicknesses only. Spanwise velocity profiles are however reconstructed from these integral parameters through the intro-duction of velocity profile models, allowing a complete through flow prediction, including the EWBL regions.

SUMMARY OF THE EWBL THEORY

The present method originates in Mellor and Wood's approach [2] where rigorous integral boundary layer equations were written for the end-wall boundary layers, including force defect *thicknesses*. In this work, simplified assumptions such as constant shape factor or skin friction were made and the equations were integrated from inlet to outlet of a blade row. This approach was extended by Hirsch [3] to include simple velocity profile models and further developed by the introduction of more sophisticated velocity profile models and improved correlations for the defect forces by De Ruyck and Hirsch [4]. Although the results presented in these papers were predicting correctly most of the phenomena associated with secondary flow and EWBL effects, detailed comparisons with experimental velocity profiles indicated some discrepancies, in particular in presence of tip clearances. An improved correlation for the force defect thicknesses has been introduced and discussed in the Ph. D. thesis of De Ruyck [5], where a detailed description of the whole theory is presented.

In the present section a summary is given of the equations which are used for all the applications. These equations are written in the meridional coordinate system m,n,u (fig 1). 'c' denotes an absolute velocity and 'w' a relative velocity component.

The boundary layer momentum and entrainment equations are

$$
\frac{d}{dm} \rho r c_m^2 \theta_{mm} + \rho r c_m \delta_m^* \frac{dc_m}{dm}
$$

$$
- \rho c_m^2 \frac{dr}{dm} (\delta_u^* tg\alpha + \theta_{uu}) = r \tau_m + r F_m \tag{1}
$$

$$
\frac{d}{dm} \rho r c_m^2 \theta_{um} + \rho r c_m \delta_m^* \frac{dc_u}{dm}
$$

$$
+ \rho c_m^2 \frac{dr}{dm} (\delta_m^* tg\alpha + \theta_{um}) = r \tau_u + r F_u \tag{2}
$$

$$
\frac{1}{\rho r c_m} \frac{d}{dm} \rho r c_m (\delta - \delta_m^*) = \frac{E(H_k^*)}{cos\alpha} \tag{3}
$$

Eqs 1 to 3 are written in the **absolute** reference system. All the variables are pitch-averaged. The boundary layer thicknesses in these equations are defined as

$$
\theta_{ij} = \int_o^\delta (\frac{\bar{w}_i}{\bar{w}_m} - \frac{w_i}{\bar{w}_m}) \frac{\rho w_j}{\bar{\rho} \bar{w}_m} dy \tag{4}
$$
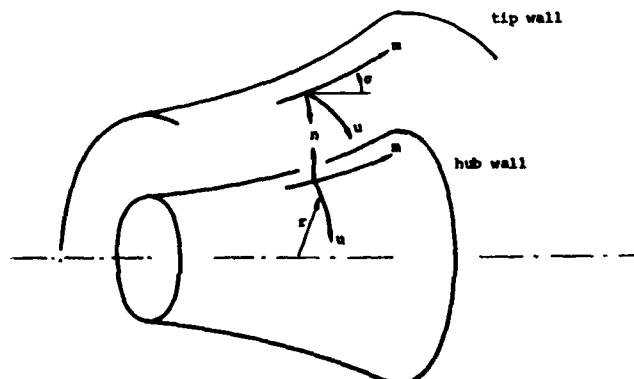
Figure 1 : Meridional coordinate system m,n,u

$$\delta_i^* = \int_o^\delta \left(\frac{\rho \hat{w}_i}{\rho \hat{w}_m} - \frac{\rho w_i}{\rho \hat{w}_m} \right) dy \tag{5}$$

These thicknesses are defined in the wall reference system. The velocities with an overhead carat ($\hat{\ }$) denote the 'outer' or 'inviscid' reference velocities. Corrections for variations of $\hat{w}$ with r are not considered in eqs 1 and 2. The velocity ratios are modelled through

$$\frac{w_m}{\hat{w}_m} = 1 - b\left(1 - \frac{y}{\delta}\right)^n \tag{6}$$

$$\frac{w_u - w_m tg\alpha}{\hat{w}_m} = (1-b) tg\epsilon_w' \left(1 - \frac{y}{\delta}\right)^n \tag{7}$$

where

$$b = \exp(-10n \ C_f^{.5} \ \cos\alpha^{-.134}) \tag{8}$$

$$tg\epsilon_w' = tg(\epsilon_w + \alpha) - tg\alpha \tag{9}$$

The density ratio is given by

$$\frac{\rho}{\hat{\rho}} = 1 - 2a\left(1 - \frac{w_m}{\hat{w}_m}\right) + (a+4a^2)\left(1 - \frac{w_m}{\hat{w}_m}\right)^2 \tag{10}$$

$$a = .89 \ \frac{\gamma - 1}{2} \ M^2 \tag{11}$$

The entrainment rate E is given by

$$E(H_k^*) = 0.0306 \ (H_k^* - 3.)^{0.653} \tag{12}$$

$$H_k^* = \frac{\delta - \delta_{mk}^*}{\theta_{mmk}} \tag{13}$$

The mainstream and cross flow shear stresses are obtained from

$$\tau_s = C_f \ \frac{\rho \hat{w}_s^2}{2} \tag{14}$$

$$\tau_t = \tau_s tg\epsilon_w \tag{15}$$

where

$$C_f = 0.246 \ Re_{\theta_{mm}}^{-0.268} \left(\frac{\hat{T}}{T^*} \right) \exp(-1.56 \ H_k) \tag{16}$$

$$H_k = \frac{\delta_{mk}^*}{\theta_{mmk}} \tag{17}$$

$$\frac{T^*}{T} = 1 + 0.72 \ a$$

The 'kinematic' thicknesses δ_{mk}^* and θ_{mmk} are defined as

$$\delta_{mk}^* = \int_o^\delta \left(1 - \frac{w_m}{\hat{w}_m}\right) dy \tag{18}$$

$$\theta_{mmk} = \int_o^\delta (1 - \frac{w_m}{\hat{w}_m}) \ \frac{w_m}{\hat{w}_m} \ dy \tag{19}$$

Eqs 4 to 19 are written in the wall reference system. The thicknesses θ_{mm}, θ_{um}, δ^*_m and δ^*_u and the parameters b and n have the same values in both absolute and relative systems whereas the wall skewing angles and θ_{uu} are related by the jump relations

$$(tg \ \epsilon'_w)^{abs} = (tg \ \epsilon'_w)^{rel} + \frac{1}{1-b} \ (tga^{rel} - tga^{abs})$$

$$\tag{20}$$

$$\theta_{uu}^{abs} = \theta_{uu}^{rel} + U \ \delta^*_u / \hat{c}_m$$

The blade mainstream defect force is found from

$$\frac{F_s}{\rho} = L \ \frac{\hat{w}_s^2}{2cos \ \gamma} \ \sigma \ C_L^2 \tag{21}$$

$$L \stackrel{\sim}{=} .01 \tag{22}$$

The tranverse lift defect is found from

$$\frac{F_t}{\rho} = - \frac{k}{s} \ w_s^2 \ \theta_{tm} \tag{23}$$

in absence of a tip clearance and from

$$\frac{F_t}{\rho} = \frac{t_c}{cos \ a} \ w_m \ \frac{dw_u}{dm} \ - \ \frac{k'}{s} \ w_s^2 \ \theta_{tm} \tag{24}$$

in presence of a tip clearance. The constants k and k' are given by

$$k \stackrel{\sim}{=} 3.$$
$$\tag{25}$$
$$k' \stackrel{\sim}{=} .5$$

The cross flow thickness is defined through

$$\theta_{tm} = - cosa \ \int_o^\delta \frac{w_t}{\hat{w}_s} \ \frac{w_m}{\hat{w}_s} \ dy$$

$$\tag{26}$$

$$\theta_{tm} = (\theta_{um} - \theta_{mm} tga) \ cos^2 a$$

Eqs 21 to 26 are written in the blade reference system.

The basic eqs 1, 2 and 3 are integrated in the meridional direction using a fourth order Runge-Kutta method (Merson) with as complementary relations eqs 4 to 26. The values for k, k' and L are obtained as the best overall values from a fit to the large number of applications discussed in the following.

EWBL EFFECTS ON THE OVERALL PERFORMANCE

The important impact of the end-wall boundary layers on the overall machine efficiency has been demonstrated in the early papers of Smith [1] and Mellor and Wood [2]. According to De Ruyck [5], the stage efficiency can be approached by

$$\eta = \hat{\eta} \ \eta_{bl} \tag{27}$$

where

$$\hat{\eta} = \frac{Q \overline{\Delta \hat{p}}_t}{\hat{P}}$$

$$\eta_{bl} = \frac{1 - \Delta \sum\limits_{h,t} \delta^{**}/h}{1 - \sum\limits_{h,t} (\nu - \delta_m^*)/h} \tag{28}$$

where $\quad Q = 2\pi r \hat{c}_m h$

$$\hat{P} = 2\pi \omega r^2 h \hat{f}_u \Delta m$$

The thicknesses δ^*, δ^{**} and ν are respectively the meridional displacement thickness, the absolute energy loss thickness and the angular defect force and they are defined as

$$r \hat{c}_m \delta_m^* = \int_0^\delta (\hat{c}_m - c_m) r dr \tag{29}$$

$$\Delta \hat{p}_t r \hat{c}_m \delta^{**} = \int_0^\delta (\hat{p}_t - p_t) c_m r dr \tag{30}$$

$$\hat{f}_u \nu = F_u = \int_0^\delta (\hat{f}_u - f_u) dr \tag{31}$$

$\Delta \hat{p}_t$ and $\hat{P}$ denote respectively the overall pressure increase and the input shaft power which would be found in absence of the EWBL. The energy thickness was in general not considered in efficiency corrections in the past, but in the authors opinion, the variation $\Delta \delta^{**}$ may not be neglected since an important reenergizing of the EWBL can occur in a rotor and the absolute value of δ^{**} may vary in an important way. It was found that $\Delta \delta^{**}$ may be of the same order of magnitude as $\nu - \delta_m^*$.

It is important to observe that ν and δ_m^* have the same value in both absolute and relative reference systems, but the energy thickness δ^{**} not. In an incompressible approach the absolute and relative energy thicknesses are related as follows

$$Ec_m \delta^{**}|_{rel} = Ec_m \delta^{**}|_{abs} - U \rho c_m^2 \theta_{um} \tag{32}$$

Hence, if the energy exchange occurs without extra loss in the EWBL, giving no increase in the energy loss thickness in the steady relative reference system, a variation in absolute energy thickness is found through eq 32. It was found that the three contributions δ^{**}, δ^* and ν are not independent and the efficiency decrease due to the EWBL directly depends on the energy loss only. The defect force thickness however has an important indirect effect on the efficiency, since non-zero defect forces can increase or even decrease the energy loss thickness, through the boundary layer momentum equations. It can be shown that in the absolute system

$$\Delta \delta^{**\text{underturned}} > \Delta \delta^{**\text{collateral}} > \Delta \delta^{**\text{overturned}} \tag{33}$$

It should finally be observed that the efficiency eq 27 is an approximation. A correct way to estimate the total efficiency is discussed in [5].

APPLICATIONS

The theory has been tested in its different aspects. The base boundary layer models were first tested through simple 2D boundary layers along flat plates and conical diffusers where strong adverse pressure gradients are present. Three-dimensional boundary layers are next considered in a radial angular diffuser. The force defect correlations are tested in cascades and single stage compressors where the tip clearance effects are emphasized. The details of all these tests can be found in [5] and the most interesting results are reported in the present paper. The theory is finally applied to a NASA two stage compressor [12].

The following test cases are considered

2D boundary layers with given pressure gradient

The boundary layer development in 2D flows is predicted using experimental pressure gradients as input. The theory is tested in presence of positive and negative pressure gradients. Two conical diffuser tests are considered where the flow is close to

separation, which can be considered as a severe test for the used model equations.

3D boundary layers in a radial vaneless diffuser

A radial diffuser with a 3D boundary layer at inlet is considered. A simple viscous-inviscid interaction algoritm is introduced in order to predict the diffuser blockage level as well as the meridional pressure gradient. The overall angular velocity is determined through radial equilibrium. 3D profiles, boundary layer thicknesses and external velocities are compared with experimental data.

Cascades of blade rows

The behaviour of the EWBL in a single compressor blade row is analysed. These tests allow the analysis of the defect force correlations in absence of a tip clearance. External pressure gradients are based on experimental data at inlet and outlet of the considered cascades.

Single stage compressors with variable tip clearance

Two test cases are considered in order to analyse the defect force assumptions in presence of a tip clearance. These tests are performed in experimental turbomachines, since such cascade data are not available. Even in the case of turbomachine flows, detailed data about the tip clearance flows are not profuse.

NASA two stage compressor

The method is finally applied to a low aspect ratio two-stage fan where detailed experiments are available.

STANFORD TURBULENT BOUNDARY LAYER TEST CASES [6]

The first elements which are tested are the 2D momentum conservation eq 1, complementary equations eqs 3, 12, 16 and the profile model equations 6 and 8. All the test flows are incompressible. Test flows with negative, constant and positive external pressure gradient are considered. For the experiments where the momentum balance is not satisfied in an experimental way, no good agreement can be expected between calculation and experiment. The input pressure gradients have therefore been determined from the experimental momentum thickness, shape factor and skin friction in such a way that the momentum balance is satisfied.

On figures 2 and 3 some results obtained with the Stanford Turbulent Boundary layer data are shown. Most of the Stanford data were analysed and the results obtained at the most downstream position are summarized on fig 2 and in table 1. The different markers in fig 2 discern the zero-pressure gradient, the negative and positive gradient and the diffuser tests. According to fig 2 the momentum thicknesses are correctly predicted for Reynolds numbers based on the momentum thickness from 1000 to 100,000. The shape factor presents some scatter. The friction coefficient is correctly predicted except for test case 3600 where an abrupt positive gradient is present. On fig 3 velocity profiles are compared at exit of two conical diffuser test cases. The experimental profiles are quite well predicted, although these profiles are close to separation.

RADIAL VANELESS DIFFUSER [7]

In the present application three-dimensional effects are introduced. The second momentum equation eq 2 and the cross flow velocity profile model eq 7 are verified.

Since the present method is based on an axisymmetric approach of a turbomachine flow simple 3D channel flows are not suited as test cases. Axisymmetric flows such as pipe flows or diffuser flows are to be considered. In the present section, the flow through a radial vaneless diffuser has been selected (Gardow [7]). The test diffuser is drafted on fig 4. A rotating screen was used at inlet of the diffuser in order to obtain a flow angle of about 45 degrees. Experimental data are available for all the boundary layer thicknesses, skewing angle, friction coefficient, external velocity and detailed 3D velocity profiles at several radii.

The experimental external velocities are not used as input for the boundary layer calculation but are predicted through radial equilibrium and continuity. The radial velocity is given as function of blockage through

$$\hat{c}_m = \frac{Q}{S(1-B)} \tag{34}$$

where B denotes the blockage. The pitchwise velocity is given by radial equilibrium through

$$r\hat{c}_u = cte \tag{35}$$

An iterative procedure is to be used since eq 34 depends on the blockage which is still unknown. The boundary layers are assumed to be identical at both walls of the radial diffuser.

The results are reported on figs 5 and 6. On fig 5 four momentum and two displacement thicknesses, the skin friction coefficient and the wall skewing angle are compared with the experimental data. A fair agreement is in general found. This figure illustrates the possibility to predict all the integral boundary layer thicknesses through the use of an integral boundary layer method with profile models. The reconstruction of all these thicknesses would not be possible without the use of velocity profile model equations.

Less agreement is found between the prediction and the experimental streamwise and displacement thicknesses for the most downstream data points. This is probably due to the confluence of the boundary layers, as reported by Gardow. The mainstream displacement thickness (and hence the shape factor) is somewhat underestimated. This is in contradiction with the good result for the radial velocity since both values contain the same information through eq 35. The experimental data are therefore not fully compatible which may be due to an asymmetry in both end-wall boundary layers (only one has been measured).

Calculated and experimental profiles at different radial positions are compared on fig 6. On this figure, the radius increases from the left to the right. The overestimation of the exit thickness appears on fig 6. The power of the profile shape is about one, which corresponds quite well with the quasi-linear shape of the outer profiles, in particular for the cross flow profiles.

The present test gives a fair result which is moreover obtained without any experimental input, since blockage level, cross flow intensity and external velocities are obtained through calculation. The calculation approaches the procedure which is used in real turbomachines where the radial equilibrium is performed in a less straightforward way.

SALVAGE CASCADE DATA [8]

In the previous applications the basic equations and velocity profile models have been tested in flows where no blade interactions and defect forces are present. These interaction terms are introduced in the present application where single cascades of compressor blades are considered.

A large amount of experimental cascade data have been compiled by Salvage and presented in a VKI report [8]. In these test cases, several solidities, blade camber, stagger and Reynolds numbers were considered. All inlet boundary layers can be considered as quite collateral. Experimental data are available at inlet and outlet of the cascades along the center streamline. It is to be accepted that these local data are representative for the pitch averaged data.

Results are summarised in table 2 and are shown on figures 7 to 9. Much scatter is present on these results which is to be explained by measurement incertainty and errors due to the poor knowledge of the experimental pressure gradient. Quite similar test cases sometimes give strongly different experimental results.

On fig 7 results are shown where zero defect forces were assumed. Although much scatter is present, the calculated data show a clear tendency to an underestimation of the exit boundary layer thickness. This underestimation is the most pronounced at the high thickness over chord ratios. The defect force equations 21 and 23 were used for figure 8 where the agreement between experiments and calculated data is improved when compared with figure 7. The increase in the predicted thicknesses is mainly due to the secondary loss, through the drag defect force eq 21.

On fig 9 calculated flow angle profiles are shown for some of the considered test cases. The outlet cross flows are overestimated in all cases when no defect forces are considered. A fair agreement is found for all the outlet flow profiles when eqs 21 and 23 are used for drag and lift defect forces. From fig 9 it appears how the cross flow intensity is restricted by the lift defect force through equation 23.

Although much scatter is present on the results, the importance of the defect force and the validity of the used assumptions is well illustrated in the present test cases.

CASCADE WITH 3D INLET BOUNDARY LAYER [9]

The inlet boundary layers in the Salvage cascade data can in general be considered as collateral. In the present application, a cascade is considered where a three-dimensional upstream boundary layer is present (Moore & Richardson [9]). Experimental thicknesses and velocity profiles are available at several chordwise positions along the centerline of the cascade flow. These data are not pitch averaged data and it is to be accepted that they are representative for the pitch averaged flow. On figure 10 experimental and calculated thicknesses and velocity profiles are compared. The blade leading and trailing edges are indicated by a mixed line.

Results with and without defect forces are shown. The cross flow profiles are well approached when using the defect force assumptions and the behaviour of the other thicknesses is improved when compared with the zero defect force assumption. In particular, the qualitative behaviour of the axial momentum thickness which first decreases and next increases is correctly predicted. This evolution is due mainly to the influence of the lift defect force eq 23.

SINGLE STAGE COMPRESSORS WITH VARIABLE TIP CLEARANCE

The last important topic which has not been analysed yet is the force defect assumption in presence of a tip clearance. The tip clearance force defect eq 24 is applied in the EWBL of two experimental single stage compressors.

Hunter and Cumpsty single rotor [10]

A single rotor tip boundary layer flow is considered. Two mass flow rates (φ = .55 and φ = .7) and four values of tip clearance are considered (t_c = 1, 3.1, 5.1 and 9.4 % chord). The external pressure gradient used as input is determined from the experimental velocities at inlet and outlet of the rotor tip.

On figure 11 calculated axial momentum, axial displacement and force defect thicknesses are compared with experiments. Since the absolute inlet cross flow is collateral, the force defect thickness gives an idea of the cross flow thickness θ_{um} since eq 31 for ν reduces to

$$\nu = \delta_m^* + \frac{\theta_{um}}{tg\alpha}\Big|_{outlet} \tag{36}$$

On figure 12, comparisons are made between calculated and experimental profiles of axial velocity, tangential force and relative flow angle.

A strong increase in thickness is found as the tip clearance is increased. A fair agreement is in general found for the calculated thicknesses. Less detailed agreement is found for the profile shapes, in particular at the highest mass flow rate (figure 12 lower figure). For these test cases, the more complex flow patterns can no more be approached by simple profile model equations such as those used in the present method.

The present test shows the important blade force variations in presence of a tip clearance. This effect is shown to be approached by the defect force equation eq 24. Less detailed agreement is however found for the detailed velocity profiles inside the EWBL. The present test has been used as a calibration for the value k' $\backsim$ .5.

Bettner and Elrod single stage compressor [11]

In the present test the EWBL through a single stage compressor has been measured at rotor tip. The stage consists of a rotor where the upstream boundary layer is two dimensional in the absolute reference system and a stator which restores the rotor outlet flow into the meridional direction. The results are reported on figures 13 and 14.

Two values of the tip clearance are considered at the design mass flow rate. The tip clearances are as large as the observed displacement thicknesses and the present test is therefore to be considered as severe.

On figure 13 calculated and experimental values of δ_m^*, θ_{ss}, δ_s^* and δ_t^* are compared. All the thicknesses are strongly underestimated at the exit of the rotor when no defect forces are assumed. When the lift and drag defect forces are added, a better agreement is found. At the high tip clearance value an overestimation in boundary layer thickness is found, indicating less reliability at such high clearance values, which are unprobable in practice however.

On figure 14 a comparison is made between calculated and experimental velocity profiles. No agreement is found for the angular velocity at exit of the rotor, but the agreement is improved as soon as the stator is entered. The agreement at stator exit is fair for this test configuration where the tip clearance has a small value (1.13 % span).

Although the qualitative behaviour of the EWBL is improved through the defect force assumptions, less agreement is found in the present test case. A better agreement can be found when the values of the coefficients k, k', and L are modified (eqs 22 and 25). These values were however obtained as the best overall values and are kept constant for all the present applications.

TWO STAGE COMPRESSOR [12]

Detailed experimental flow and pressure gradient distributions in all the stages of a multistage compressor are practically inexistant at the present time. Past applications of the EWBL theory in multi-stage compressors were therefore performed in connection with the prediction of the complete meridional compressor flow. Results of such applications were presented in the past [4]. The quality of the results obtained in these applications depends not only on the accuracy of the EWBL method, but also on the accuracy of the profile loss and the wall velocity field estimations.

Detailed experimental data in a two stage compressor were recently presented [12] and the present theory can be applied in this multistage machine without interference of other calculations. This NASA compressor is a highly loaded machine with a low aspect ratio in the first rotor.

The predicted boundary layer profiles are compared with the experimental data on figure 15. A good agreement is in general observed for the cross flow profiles, in particular at the rotor exits, whereas less agreement is observed in the mainstream direction. In reality, the disagreement is mainly present in the angular direction, as can be observed from figure 16 where the same results are projected in the meridional and angular directions. On this figure it can be seen how the angular velocity is overestimated in the neighbourhood of the rotor tip clearances.

As in the previous test cases, a finer agreement can be obtained when changing the values of k, k' and L, whereas the overall values given by eqs 22 and 25 were used in the present applications.

CONCLUSIONS

In the present work a detailed axial compressor end-wall boundary layer calculation method has been summarised. This theory is defined in a general meridional coordinate system. Boundary layer velocity profile models are used in order to predict detailed spanwise flow profiles in a compressor, including the end-wall regions. All the interaction effects between blades and end-wall boundary layers are taken into account through some relatively simple defect force assumptions.

The method has been applied to several types of boundary layer flows which range from simple two dimensional boundary layers to boundary layers in high speed and highly loaded turbomachines. The different aspects of the theory have been tested separately. All the boundary layer thicknesses, detailed velocity, blade force and flow angle profiles have been predicted and compared with experimental data. A fair agreement has in general been found and the used defect force assumptions improve the quality of the results, when compared with a zero-defect force approach. The defect force is shown to be a key element which can play a dominant role in the secondary flow and tip clearance effects.

The present work shows that it is possible to approach the complex turbomachine end-wall boundary layer flows through an integral boundary layer technique. Detailed data can be reconstructed through the modelling of the boundary layer profiles. Although all the details of the flow cannot be predicted accurately, the quality of the results can be sufficient for engineering purposes and the computer requirements for such an approach are small.

REFERENCES

[1] SMITH L.H., 1969, "Casing Boundary Layers in Multistage Axial Flow Compressors" Brown Boveri Symposium, Flow Research on Blading, Elsevier, 1969

[2] MELLOR G.M., WOOD G.L., 1971, "An Axial Compressor End-Wall Boundary Layer Theory" ASME Journal of Basic Engineering, Series d, Vol 93, 1971, pp 300-316

[3] HIRSCH C., 1974, "Flow Prediction in Axial Flow Compressors Including End-Wall Boundary Layers" ASME Journal of Engin. for Power, Vol 96, 1974, pp 413-426

[4] DE RUYCK J., HIRSCH CH., 1981, "Investigations of an Axial Compressor End-Wall Boundary Layer Prediction Method" ASME Journal of Eng. for Power, Vol 103, no 1, pp 20-33, 1981

[5] DE RUYCK J., 1982, "Computation of End-Wall Boundary Layers in Axial Compressors" Phd Thesis, Vrije Universiteit Brussel, Dept of Fluid Mechanics, 1982

[6] COLES D.E., HIRST E.A., 1968, "Computation of Turbulent Boundary Layers" Afosr - Ifp - Stanford Conference Proceedings, Volume 2, Compiled Data, Dept of Mech. Eng., Stanford Univ., California, 1968

[7] GARDOW E., 1958, "The Three Dimensional Turbulent Boundary Layer in a Free Vortex Diffuser" MIT Gas Turbine Lab. Report 42, 1958

[8] SALVAGE J.W., 1974, "Investigation of Secondary Flow Behaviour and End-Wall Boundary Layer Development Through Compressor Cascades" Von Karman Institute, Technical Note no 107, 1974

[9] MOORE R.W., RICHARDSON D.L., 1956, "Skewed Boundary Layer Flow Near the End-Walls of a Compressor Cascade" ASME Paper no 56-a-131, 1956

[10] HUNTER I.H., CUMPSTY N.A., 1982, "Casing Wall Boundary Layer Development Through an Isolated Compressor Rotor" ASME Paper Number 82-gt-18, 1982

[11] BETTNER J.L., ELROD C., 1982, "The Influence of Tip Clearance, Stage Loading, and Wall Roughness on Compressor Casing Boundary Layer Development" ASME Paper Number 82-gt-153, 1982

[12] GORRELL T., 1983, "Detailed Flow Measurements in the Casing Boundary Layer of a 427 Meter per Second Tip Speed Two Stage Fan" AVRADCOM, Lewis Research Center, report to be published.
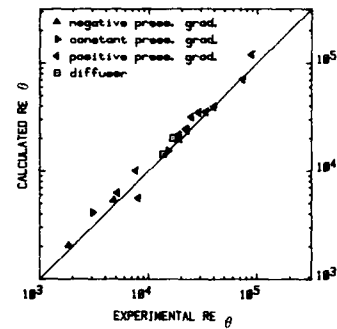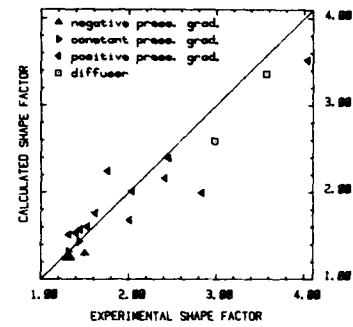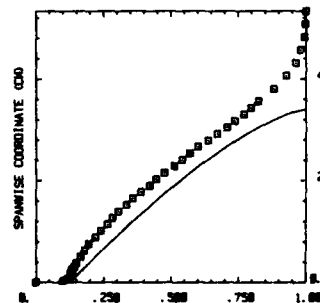
Stanford turbulent boundary layer data

Ident	Reø calc.	exp.	shape factor calc.	exp.	friction coefficient calc.	exp.
1100	35254.	33957.	1.76	1.62	.00096	.00117
1200	39627.	40150.	2.01	2.04	.00062	.00060
1300	5319.	4749.	1.24	1.34	.00357	.00338
1400	15374.	15152.	1.32	1.31	.00236	.00243
2100	71239.	74184.	1.99	2.84	.00055	.00012
2200	21686.	19075.	1.57	1.45	.00145	.00189
2300	34948.	29125.	2.24	1.76	.00045	.00088
2500	24641.	22187.	1.53	1.40	.00152	.00195
2900	120053.	89603.	2.16	2.41	.00037	.00023
3000	4144.	3042.	1.43	1.43	.00283	.00321
3100	2039.	1846.	1.29	1.50	.00423	.00392
3300	24003.	22679.	1.60	1.53	.00136	.00156
3500	31772.	24919.	2.39	2.46	.00037	.00018
3600	5629.	8045.	1.68	2.01	.00178	.00067
3800	10061.	7661.	3.52	4.04	.00009	.00002
4000	6271.	5149.	1.51	1.32	.00222	.00305
5000	14394.	13625.	2.59	2.98	.00033	.00018
5100	20235.	16654.	3.36	3.57	.00009	.00004
6300	19223.	18850.	1.24	1.28	.00252	.00253

Table 1 : Stanford Turbulent Boundary Layer data :
Calculated and experimental data at the most downstream position

Salvage cascade data

Test number	solidity	turning degrees	axial momentum thickness exp.	calc.	shape factor exp.	calc.
1	.67	-.8	1.56	1.07	1.52	1.31
2	.67	4.9	1.41	1.15	1.77	1.36
3	.67	7.6	1.69	1.28	1.68	1.37
4	.67	8.8	1.82	1.31	1.69	1.39
5	1.00	-.2	.90	.83	2.13	1.29
6	1.00	4.8	.83	.90	2.12	1.37
7	1.00	10.0	1.17	.93	1.90	1.44
8	1.00	16.6	1.19	1.16	1.85	1.56
9	2.00	9.5	1.21	.73	2.26	1.39
10	2.00	22.0	2.16	1.93	1.73	1.70
11	2.00	24.7	2.62	2.13	1.66	1.71
12	2.00	23.9	3.52	2.51	1.56	1.67
13	.99	8.0	1.84	2.26	1.90	1.56
14	1.00	17.1	2.93	2.55	1.61	1.65
15	2.00	29.4	3.76	2.78	1.58	1.72
16	1.99	27.5	.86	1.49	2.40	1.56
17	1.99	28.6	1.71	1.46	2.12	1.59
18	1.00	21.4	2.09	2.72	1.74	1.76
19	2.00	36.7	.89	1.27	2.31	1.69
20	1.00	23.9	3.17	2.82	1.73	1.88
21	.99	20.5	1.60	2.75	1.91	1.70
22	.99	14.7	1.36	1.88	1.92	1.49
23	1.00	19.5	2.86	3.31	1.85	1.49
24	1.00	13.2	2.39	2.36	1.90	1.32
25	1.00	11.4	1.13	1.49	1.95	1.35
26	1.00	21.1	2.38	2.34	1.75	1.58
27	1.99	30.2	.79	1.48	2.70	1.57
28	1.00	24.1	3.45	2.74	1.69	1.85
29	2.00	31.7	.86	1.16	2.39	1.48
30	1.00	19.4	1.40	1.81	2.02	1.52
31	2.00	35.3	.89	1.02	2.22	1.48
32	1.00	28.7	3.34	2.80	1.57	1.92
33	1.00	27.4	2.13	2.29	1.68	1.63
34	1.00	35.6	2.63	2.97	1.49	1.60
35	1.00	32.2	2.25	2.73	1.61	1.77
36	1.99	38.3	1.44	1.11	1.74	1.52
37	1.00	25.9	3.91	3.14	1.67	2.07
38	1.00	24.1	2.78	1.31	1.61	1.38
39	2.00	45.1	3.07	2.91	1.55	1.64
40	1.00	29.0	4.89	4.70	1.66	2.06
41	1.01	22.9	4.39	2.69	1.54	1.70
42	2.02	46.6	2.20	1.84	1.51	1.45
43	1.01	24.3	5.26	2.85	1.60	1.94
S 1	1.00	10.6	4.11	3.11	1.54	1.38
S 2	1.00	13.4	2.86	2.79	1.51	1.45
S 3	1.00	16.3	3.46	3.60	1.54	1.60
S 4	1.00	18.9	1.91	3.03	1.64	1.52
S 5	2.00	22.3	4.74	4.80	1.48	1.37
S 6	.99	20.3	3.33	4.14	1.52	1.51
S 7	1.98	36.0	1.40	2.41	1.87	1.49
S 8	1.98	27.8	1.30	2.14	2.37	1.45
S 9	1.00	17.9	4.92	2.68	1.57	1.28
S10	1.00	19.3	3.67	2.76	1.49	1.29
S11	2.00	31.7	1.49	1.70	1.81	1.33
V 1	1.00	28.1	3.04	3.06	1.52	1.41
V 2	1.99	43.3	2.52	4.86	1.65	1.43
V 3	2.02	43.9	3.05	2.37	1.47	1.36
V 4	.67	3.4	1.19	.76	1.64	1.47
V 5	.67	7.1	1.02	.77	1.59	1.55
V 6	1.00	3.4	.66	.58	2.36	1.41
V 7	1.00	7.1	.40	.69	2.21	1.49
V 8	1.00	12.5	1.26	.78	1.84	1.59
V 9	1.00	19.5	.94	1.19	1.90	1.77
V10	2.00	18.3	2.07	.94	2.06	1.72
V11	2.00	24.1	2.51	1.90	1.70	2.01
V12	2.00	25.4	1.69	1.39	1.87	2.03
V13	2.00	24.9	2.75	2.13	1.61	1.94
V14	1.99	33.5	1.69	1.35	1.96	2.25

Table 2 : Salvage Cascade data : calculated and experimental results

Figure 2 :
Stanford Turbulent Bound. Layer Data
Calculated and experimental data at
the most downstream position
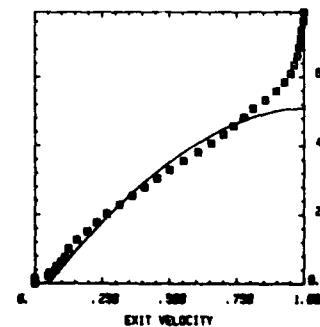
Figure 3 :
Stanford Turbulent Bound. Layer Data
Velocity profiles at downstream position
Conical diffuser test cases 5000, 5100
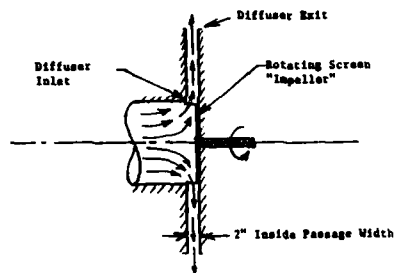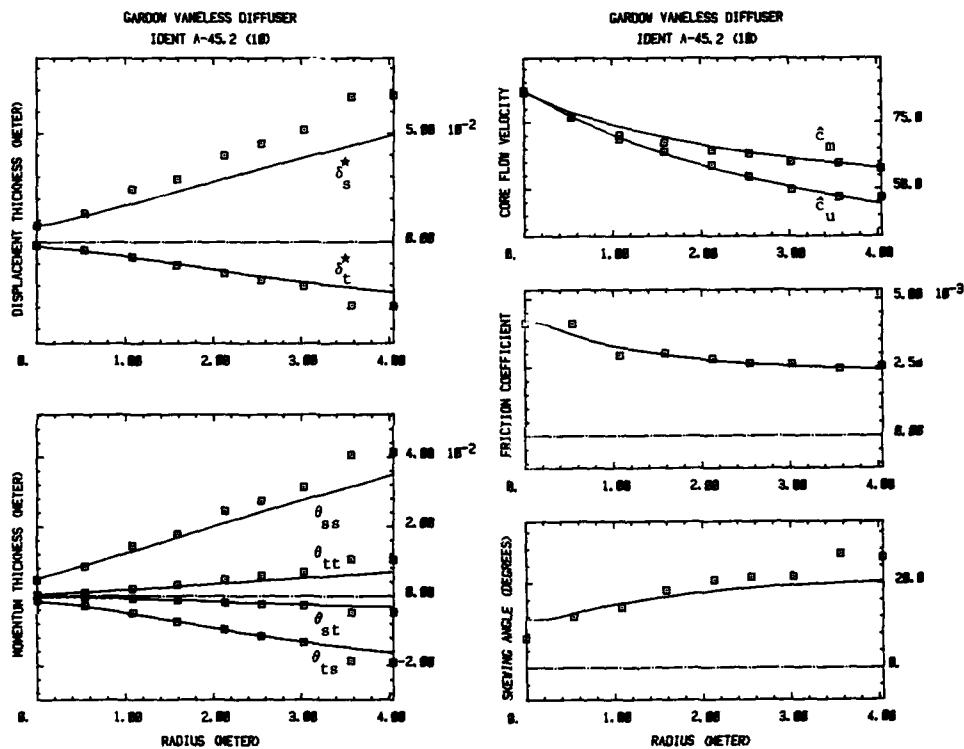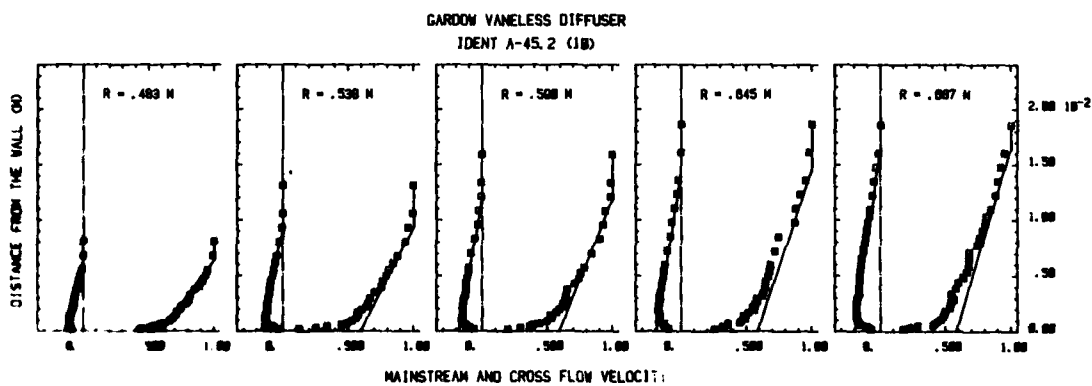
Figure 4 :   Gardow vaneless diffuser (ref 7)

Figure 5 :   Gardow vaneless diffuser (ref 7)
              Solid lines : calculated, symbols : experiment

Figure 6 :   Gardow vaneless diffuser (ref 7)
              Velocity profiles at several radii
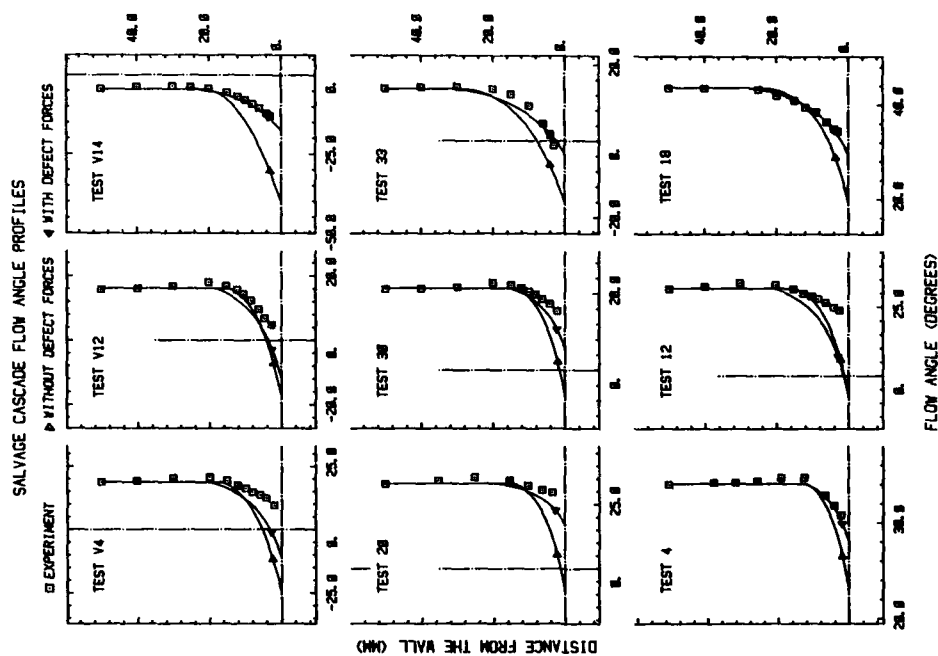   Solid lines : calculated, symbols : experiment

Figure 9 : Salvage cascade data (ref 8)
Calculated and experimental flow profiles at exit of the cascades
Solid lines : calculated, symbols : experiment
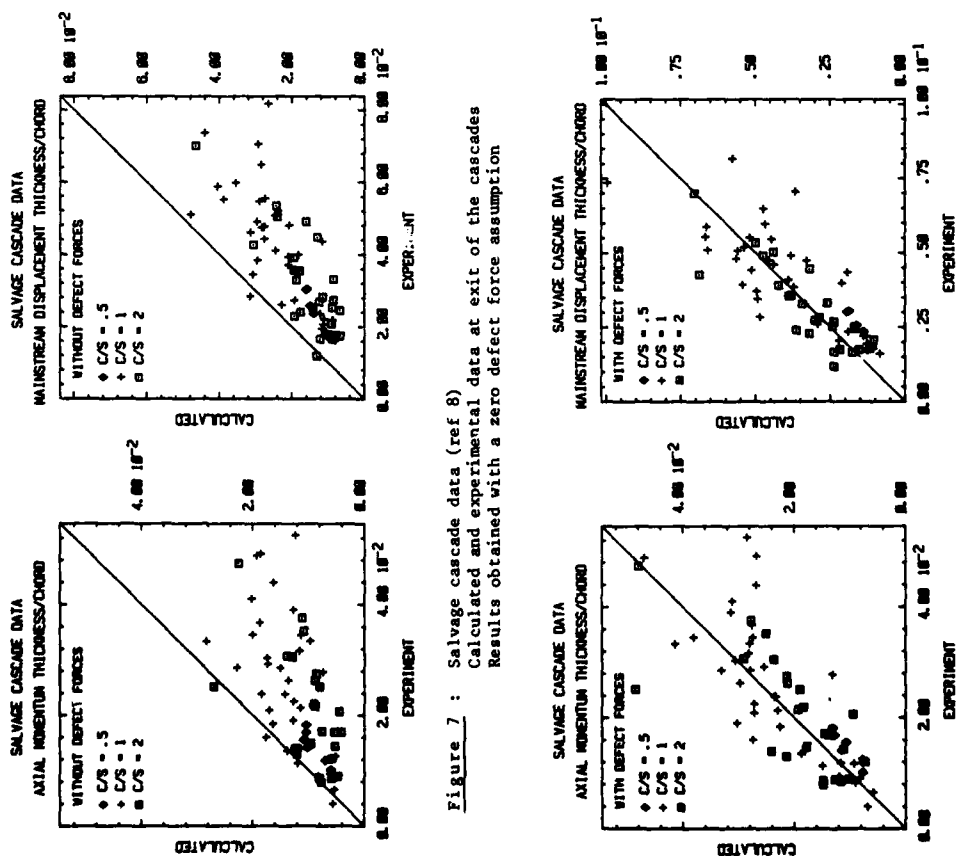Results with and without defect force assumptions

Figure 7 : Salvage cascade data (ref 8)
Calculated and experimental data at exit of the cascades
Results obtained with a zero defect force assumption

Figure 8 : Salvage cascade data (ref 8)
Calculated and experimental data at exit of the cascades
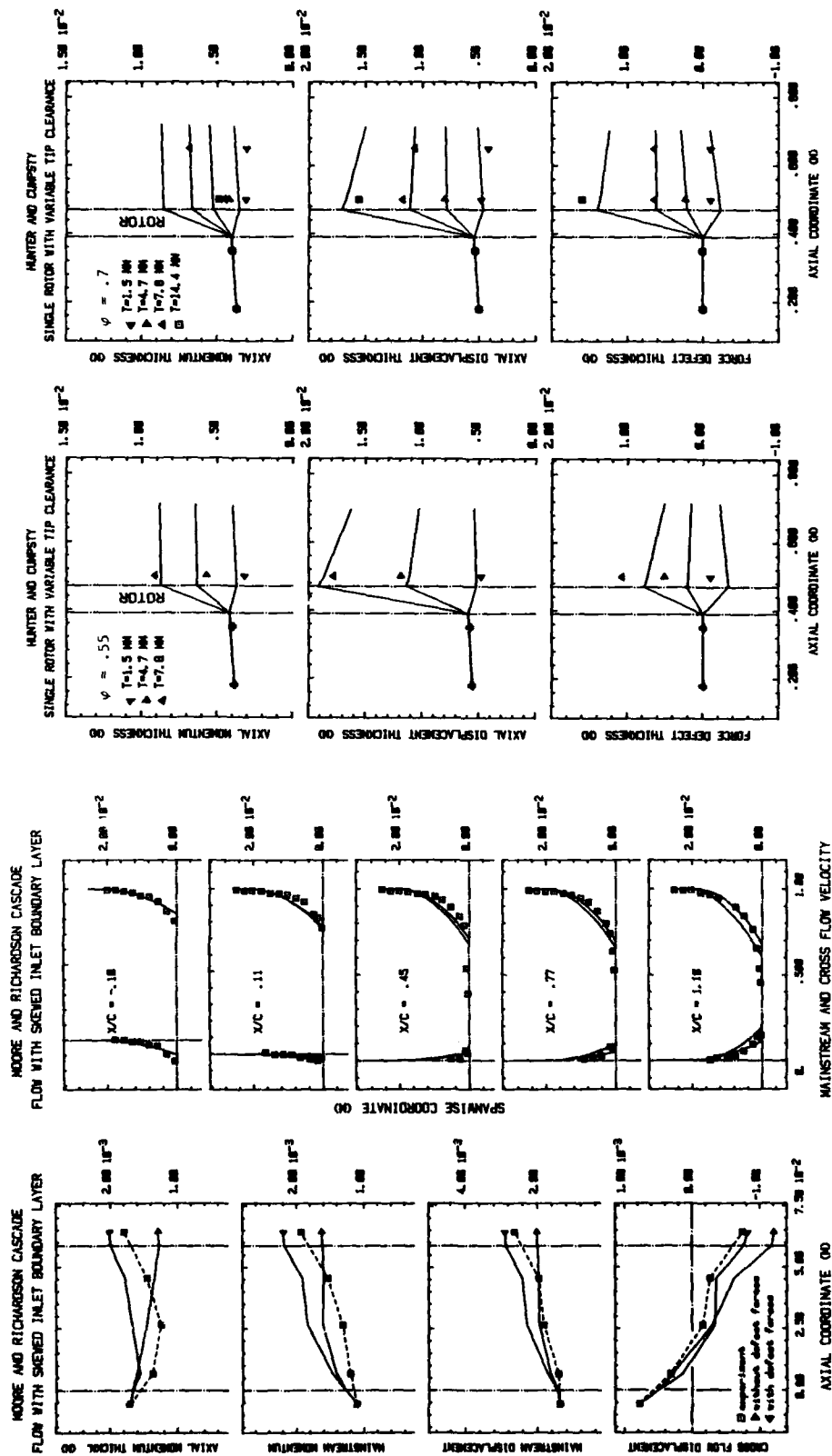Results obtained when using the defect force eqs 21 and 23

HUNTER AND CUMPSTY
SINGLE ROTOR WITH VARIABLE TIP CLEARANCE

$\varphi = .7$

T=1.5 MM
T=4.7 MM
T=7.8 MM
T=14.4 MM

ROTOR

AXIAL MOMENTUM THICKNESS (X)
AXIAL DISPLACEMENT THICKNESS (X)
FORCE DEFECT THICKNESS (X)

AXIAL COORDINATE (X)

HUNTER AND CUMPSTY
SINGLE ROTOR WITH VARIABLE TIP CLEARANCE

$\varphi = .55$

T=1.5 MM
T=4.7 MM
T=7.8 MM

ROTOR

AXIAL MOMENTUM THICKNESS (X)
AXIAL DISPLACEMENT THICKNESS (X)
FORCE DEFECT THICKNESS (X)

AXIAL COORDINATE (X)

Figure 11 : Hunter & Cumpsty single rotor with variable tip clearance (ref 10) Solid lines : calculated, symbols : experiment

MOORE AND RICHARDSON CASCADE
FLOW WITH SKEWED INLET BOUNDARY LAYER

X/C = -.18
X/C = .11
X/C = .45
X/C = .77
X/C = 1.18

SPANWISE COORDINATE (X)

MAINSTREAM AND CROSS FLOW VELOCITY

MOORE AND RICHARDSON CASCADE
FLOW WITH SKEWED INLET BOUNDARY LAYER

AXIAL MOMENTUM THICK. (X)
MAINSTREAM MOMENTUM
MAINSTREAM DISPLACEMENT
CROSS FLOW DISPLACEMENT

Experiment
without defect forces
with defect forces

AXIAL COORDINATE (X)

Figure 10 : Moore and Richardson cascade (ref 9) Solid lines : calculated, symbols : experiment Results with and without defect force assumptions
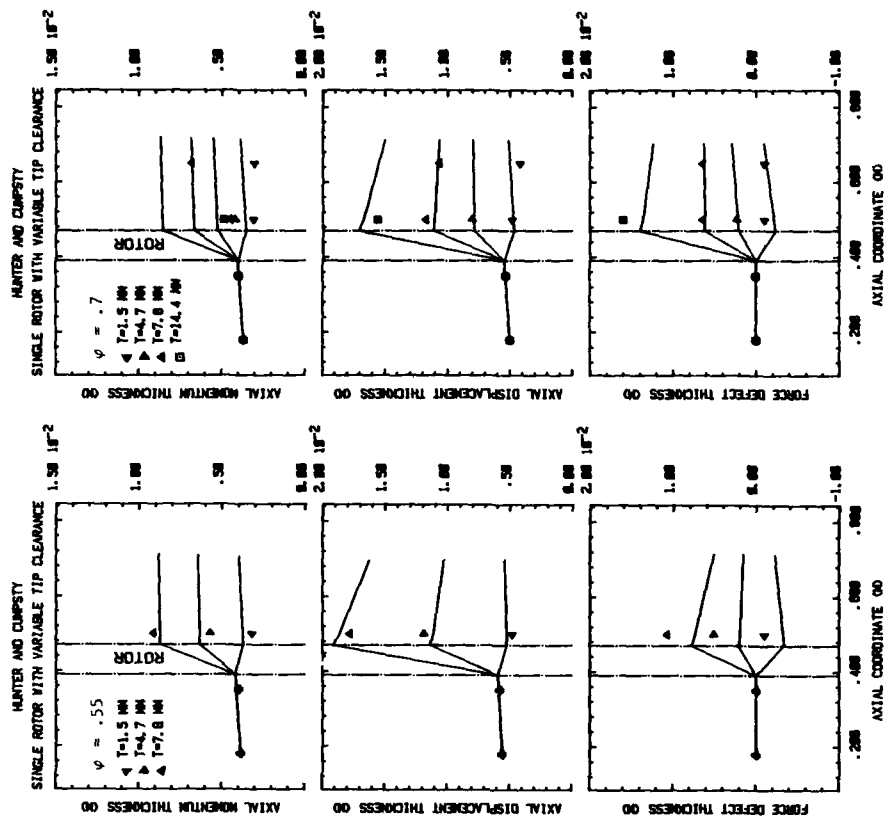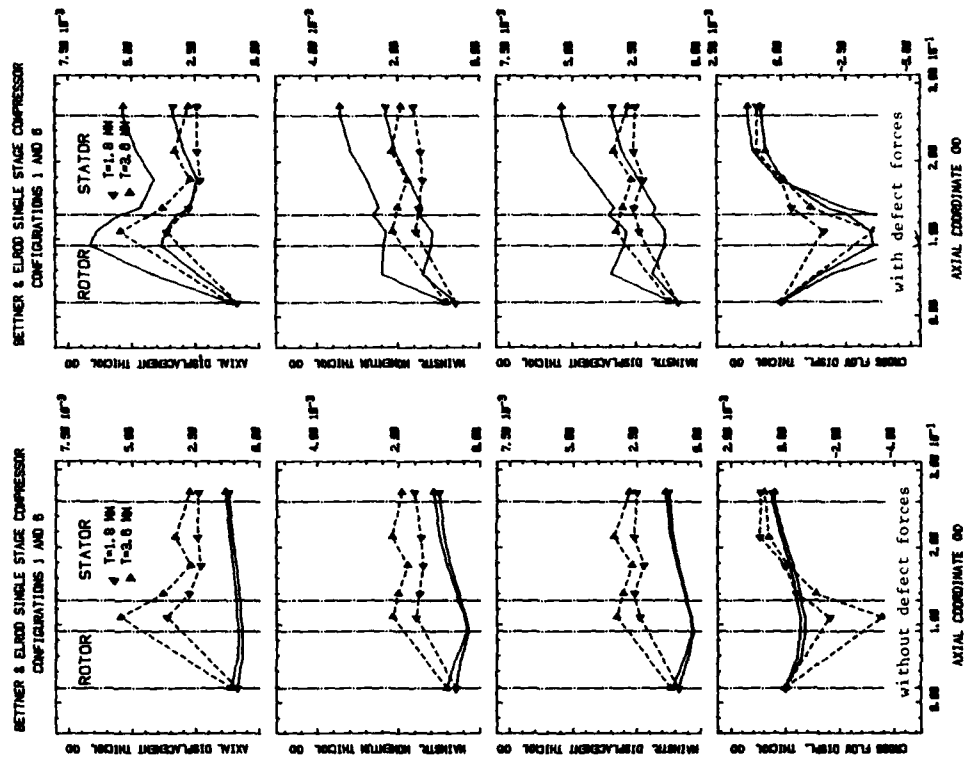
Figure 13 : Bettner & Elrod single stage compressor (ref 11)
Left side figures : results obtained with a zero defect force ass.
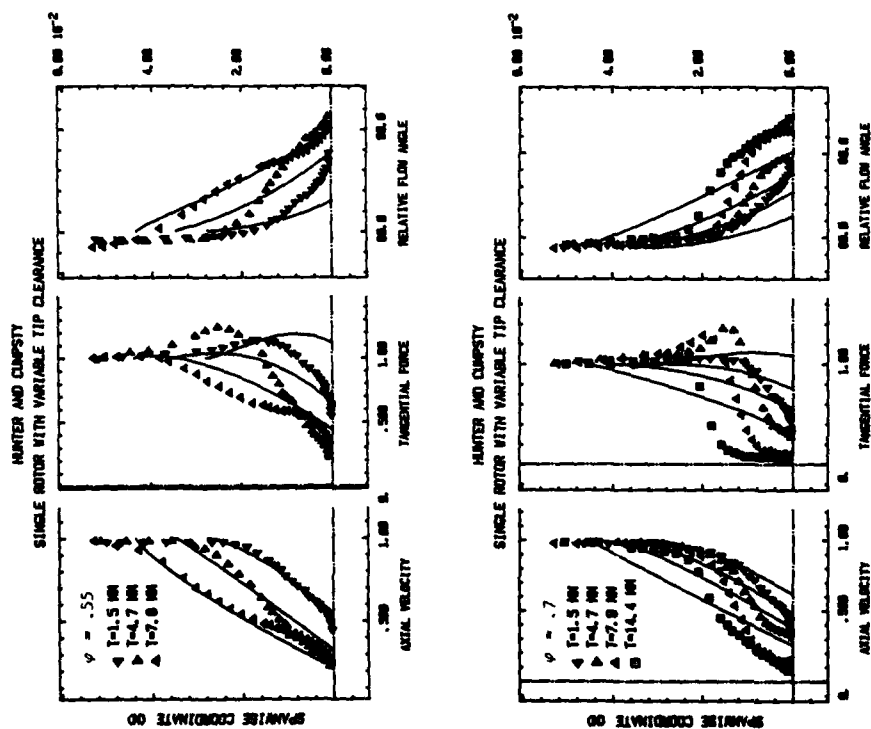Right side figures : results obtained with defect force eqs 21, 24

Figure 12 : Hunter & Cumpsty single rotor
with variable tip clearance (ref 10)
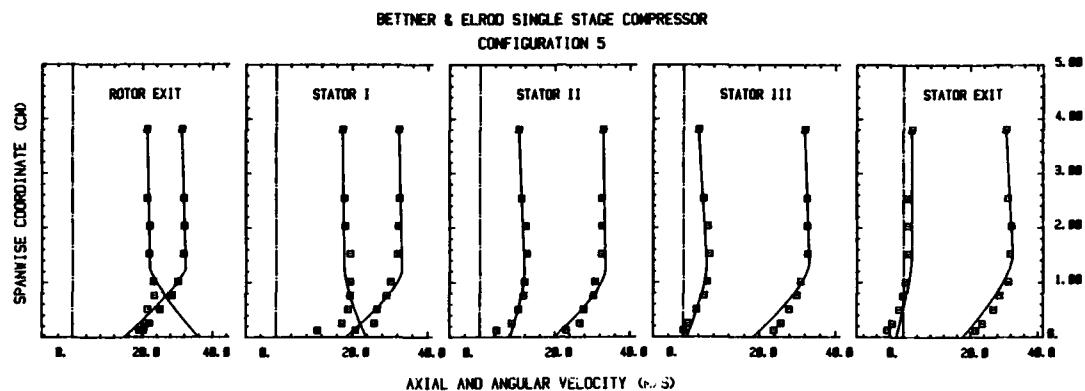Solid lines : calculated
Symbols : experiment

BETTNER & ELROD SINGLE STAGE COMPRESSOR
CONFIGURATION 5

SPANWISE COORDINATE (CM)

ROTOR EXIT   STATOR I   STATOR II   STATOR III   STATOR EXIT

AXIAL AND ANGULAR VELOCITY (M/S)

Figure 14 : Bettner & Elrod single stage compressor (ref 11)
Solid lines : calculated, symbols : experiment

NASA TWO STAGE AXIAL COMPRESSOR
TIP BOUNDARY LAYER PROFILES

DISTANCE FROM THE WALL (CM)

INLET   EXIT ROTOR 1   EXIT STATOR 1   EXIT ROTOR 2   EXIT STATOR 2

MAINSTREAM AND CROSS FLOW VELOCITY (M/S)
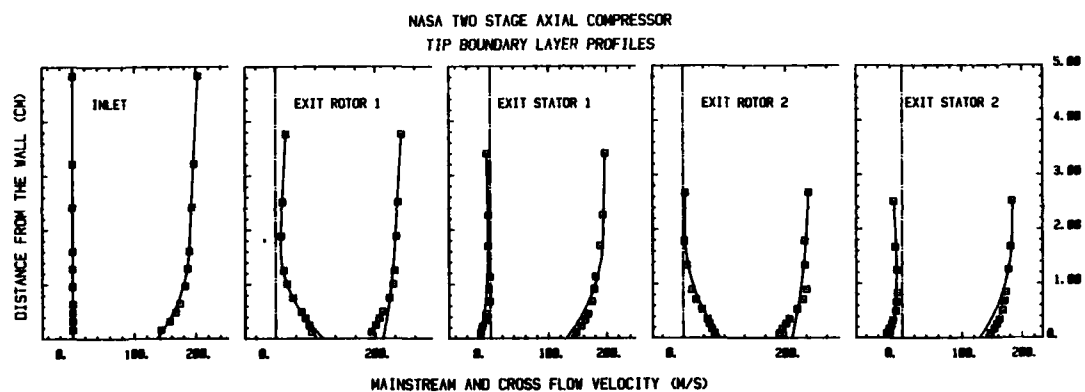
Figure 15 : NASA Two Stage Compressor (ref 12)
Mainstream and cross flow velocity profiles
Solid lines : calculated, symbols : experiment

NASA TWO STAGE AXIAL COMPRESSOR
TIP BOUNDARY LAYER PROFILES

DISTANCE FROM THE WALL (CM)

INLET   EXIT ROTOR 1   EXIT STATOR 1   EXIT ROTOR 2   EXIT STATOR 2

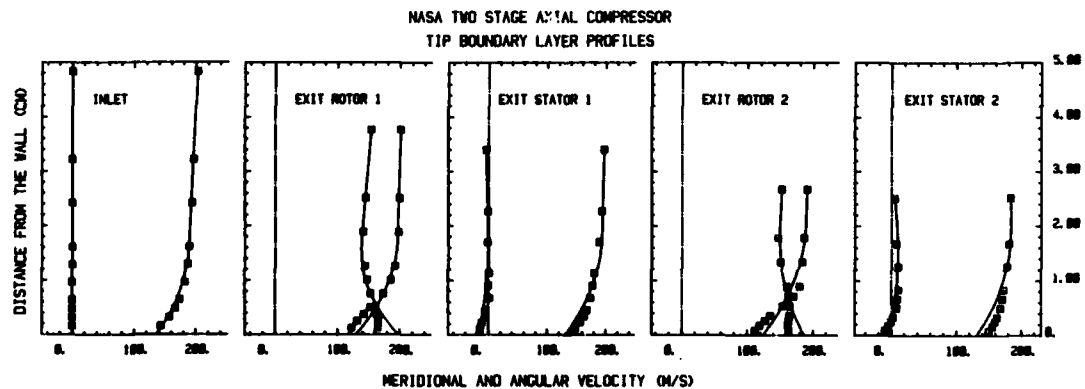MERIDIONAL AND ANGULAR VELOCITY (M/S)

Figure 16 : NASA two stage compressor (ref 12)
Meridional and angular velocity profiles
Solid lines : calculated, symbols : experiment

DISCUSSION

J.Dunham, UK

When you calculate a force, a defect force, you need the inlet angle and velocity and outlet angle and velocity to do that. When you have a multistage calculation or a calculation with more than one blade row, what inlet angle and velocity do you use for the blade rows after the first? Because obviously, if you've done the calculations through the first blade row you then have a velocity profile near the wall with rapidly changing inlet angle and velocity. Now, what values do you actually use to get the force defect?

Author's Reply

The reference we use is an estimation of the inviscid velocity profile near the wall.

Comment by K.Papailiou, Gr

A similar calculation method has been presented in the references cited below. In Reference (5), comparisons are made of two theoretical methods, the one we mention and Sockol's method (6) with experimental results coming from a highly compressor cascade (presented in Reference (2)). These results include defect force term measurements. It would be interesting to see how your prediction method compares with these experimental results, which are available from the Laboratoire de Mécanique des Fluides, Ecole Centrale de Lyon.

References

1. Leboeuf, F.
   Comte, A.
   Papailiou, K.
   Calculation Concerning the Secondary Flow in Compressor Bladings, AGARD CP 214, 1977.

2. Comte, A.
   Ohayon, G.
   Papailiou, K.
   A Method for the Calculation of the Wall Layers Inside the Passage of a Compressor Cascade with and without Tip Clearance, ASME Paper 81-GT-168. ASME Trans. Jr. of Engg. for Power, Vol.103/3, 1981.

3. Bario, F.
   Leboeuf, F.
   Papailiou, K.
   Study of Secondary Flows in Blade Cascades of Turbomachines. ASME Paper 81-GR/GT-3. ASME Trans. Jr. of Engg. for Power, pp.497-503, 1982.

4. Leboeuf, F.
   Bario, F.
   Bois, G.
   Papailiou, K.
   Experimental Study and Theoretical Prediction of Secondary Flows in a Transonic Axial Flow Compressor. ASME Paper 82-GT-14.

5. Papailiou, K.
   A Contribution to the Calculation of Secondary Flows in an Axial Flow Compressor. Sera présenté dans le 6ème International Symposium of Airbreathing Engines (ISABE), Paris, Juin 1983.

6. Sockol, P.M.
   End Wall Boundary Layer Prediction for Axial Compressors. AIAA Paper No.78-1139, 11th Fluid and Plasma Dynamics Conference. July 10-12, 1978.

ETUDES EXPERIMENTALES ET THEORIQUES DES COUCHES VISQUEUSES PARIETALES DANS UN COMPRESSEUR MONO-ETAGE TRANSSONIQUE

F. LEBOEUF[1], H. NAVIERE[2]
ECOLE CENTRALE DE LYON
Laboratoire de Mécanique des Fluides
36, Avenue Guy-de-Collongue
Boîte Postale 163
69131 ECULLY Cedex (France)

[1] Maître-Assistant, Ecole Centrale de Lyon
[2] Ingénieur CNAM, Ecole Centrale de Lyon

RESUME

Les objectifs de ce papier sont à deux niveaux : tout d'abord nous présentons des résultats expérimentaux obtenus sur un compresseur mono-étagé transsonique représentatif d'un étage de moteur aéronautique ; l'accent sera mis particulièrement sur les vecteurs vus par les aubages, en amont et en aval de ceux-ci, dans les zones du moyeu et du carter.

En parallèle une étude théorique de ces écoulements est présentée. Les principales caractéristiques de la méthode utilisée sont d'assurer un transfert cohérent de l'information lors des changements de repère, et une très bonne stabilité du calcul. Pour cela, les équations de transport de deux composantes de la vorticité secondaire sont utilisées simultanément avec les équations décrivant dans une forme intégrale une couche visqueuse tridimensionnelle, et avec une équation décrivant l'écoulement sain à la paroi. Une comparaison entre les résultats expérimentaux et théoriques permet d'apprécier la validité de la méthode.

SUMMARY

The objectives of this paper are two fold : first, we present experimental results obtained in a one-stage transonic axial flow compressor, which is a typical stage of an aeronautical motor ; we shall particularly point out the velocity vector in front of and downstream of the blades, near the hub and the tip of the machine.

A theoretical study of these flows will be also presented. The main characteristics of the method are that the transfer of information is properly realized while changing a frame of reference. Also a very good computational stability is obtained. In this method, two equations for the transport of two vorticity components are used in parallel with the equations which describe, in an integral form, the 3D viscous layer, and with an equation which describes the inviscid flow at the wall. A comparison between the experimental and theoretical results allows to appreciate the validity of the method.

LISTE DES SYMBOLES

b	Fraction du pas dans une direction θ, laissée libre à l'écoulement.
H_{12}	Facteur de forme : épaisseur de déplacement/épaisseur de quantité de mouvement.
h	Envergure
$\vec{1}$	Vecteur de base du repère
P_s	Pression statique
R	Rayon
(N,S,B)	Système de coordonnées curvilignes associé à l'écoulement sain (S selon $\vec{W}$, B normale à la paroi)
(θ,m,B)	Système de coordonnées curvilignes lié à la machine (m méridien, θ circonférentiel)
T	Température
V	Vitesse absolue
W	Vitesse relative
α	$\tan^{-1}(V_\theta/V_m)$
β	$\tan^{-1}(W_\theta/V_m)$
δ	Epaisseur de couche limite
ρ	Densité
Ω	Vorticité
$\vec{\omega}$	Vecteur rotation de la machine
μ	Viscosité

Indices Inférieurs

a	Condition relative à un repère absolu ou fixe
o	Condition d'arrêt
R	Condition relative à un repère tournant
S	Condition statique ou selon la direction S
V	Visqueux
H	Caractérise une fraction de Ω_N (associé aux conditions amont essentiellement,

Indices Supérieurs

ˆ	Ecoulement sain
'	Ecoulement secondaire
—	Valeur moyenne selon θ

1. INTRODUCTION

Le développement de machines de plus en plus poussées nécessite, à l'évidence, une connaissance accrue de l'écoulement dans ces machines ainsi que des moyens de prédictions de plus en plus performants. Nous nous intéressons particulièrement dans cet article au développement des écoulements visqueux dans les zones proches du moyeu et du carter d'un compresseur axial mono-étagé transsonique.

Dans ce domaine des compresseurs axiaux, différents auteurs ont présenté des résultats expérimentaux détaillés en particulier Lakshminarayana et son groupe, pour les zones proches des parois et pour un compresseur fonctionnant à de faibles nombres de Mach [1, 2, 3]. Un effort cohérent a été entrepris depuis plusieurs années à l'Ecole Centrale de Lyon sous l'égide de la DRET et de la SNECMA, pour l'étude expérimentale et théorique des phénomènes secondaires dans les turbomachines, et en particulier dans les compresseurs. [4, 5, 6, 7].

Dans un précédent papier [4], nous avons présenté des résultats expérimentaux détaillés obtenus sur un compresseur axial transsonique. L'intérêt d'utiliser une machine fonctionnant dans ce domaine de nombre de Mach est évidemment d'étudier des phénomènes plus réalistes pour certains industriels ; mais aussi de permettre une meilleure information sur les mécanismes assurant les transferts énergétiques entre les pâles et le fluide. En particulier, l'analyse de nos résultats à l'aval de la roue mobile a montré que les phénomènes secondaires, qui ont une origine visqueuse, avaient, par le biais des changements du repère mobile au repère fixe, contribué à l'augmentation de l'énergie utile dans la région du moyeu, sous l'effet des tourbillons secondaires engendrés. Alors que dans la région du carter, les effets de jeu conduisent en général à une diminution de l'énergie fournie au fluide.

Dans le présent papier, et sur le plan expérimental, nous nous intéresserons plus particulièrement à l'aspect cinématique des phénomènes secondaires dans ce compresseur, dans les régions du bord d'attaque et du bord de fuite des aubages.

Sur le plan théorique, le traitement des écoulements secondaires s'appuie souvent sur une hypothèse de type couche limite se développant sous les influences conjuguées d'un écoulement sain, et d'une vorticité secondaire, dont l'évolution peut être décrite principalement par le biais de mécanisme non visqueux. Cette notion de vorticité secondaire intervient plus ou moins implicitement dans les méthodes de calcul, telles celles de Mellor et Wood [12] ou de Hirsh [11]. Elle est utilisée explicitement dans la méthode de Comte, Ohayon et Papailiou [9]. Notre démarche s'appuie sur la méthode développée dans [9], et dont les équations sont développées dans le cas d'une machine centrifuge par Vouillarmet [6]. Nous en résumons brièvement ici les idées de base. Nous supposons l'existence d'une direction privilégiée notée S, généralement définie par l'écoulement sain local, selon laquelle les propriétés de l'écoulement cisaillé seront exprimées à l'aide de lois de similitude au niveau de la composante V_S du profil de vitesse. Dans les directions transversales (notée N et B), nous supposerons que les composantes de vitesses V_N et V_B sont associées principalement avec le développement d'une vorticité longitudinale Ω_S. En pratique la méthode de calcul est batie sur une moyenne des équations selon la direction circonférentielle θ, ce qui crée des termes dits de "fluctuations" qui traduisent la non-uniformité azimuthale. Puis une formulation déficitaire par rapport à l'écoulement sain local est utilisée avant d'introduire une intégration selon la normale à la paroi B de l'équation de conservation de la masse et de la composante de l'équation de quantité de mouvement selon la ligne de courbure moyenne de l'aubage (s'). Dans les méthodes décrites en [6] et [9], et utilisée en [4] ces deux équations sont résolues simultanément avec une équation de transport de la vorticité Ω_S.

Le deuxième objectif du présent papier est de présenter une nouvelle méthode qui permet de corriger l'hypothèse trop restrictive d'un écoulement de type couche limite selon s, décrite plus haut. Ceci assurera un traitement plus correct des transferts d'informations lors des changements de repère. Dans ce but une nouvelle formulation des équations de transports de la vorticité secondaire sera présentée. Enfin, une comparaison entre les résultats expérimentaux et théoriques sera donnée.

2. ETUDE EXPERIMENTALE DES PHENOMENES SECONDAIRES

Les expériences ont été réalisées sur le compresseur qui est donné schématiquement figure 1. Le compresseur a été testé sur le banc d'essai de compresseur haute-vitesse de l'Ecole Centrale de Lyon. Une description détaillée du banc et des moyens de mesures (sondes de pression stationnaires directionnelles) utilisés sont donnés en [4]. Dans la même référence, on trouvera des indications sur la méthode suivie afin d'assurer une bonne cohérence des mesures.

Le compresseur utilisé est légèrement différent de celui dont les résultats ont été présentés en [4]. La forme de la veine au niveau du moyeu du redresseur a en effet été modifiée afin de diminuer la charge sur la coupe de pied de cet aubage ; ceci a de légères conséquences sur l'écoulement dans la roue mobile.

Dans ce qui suit nous allons présenter les résultats expérimentaux obtenus dans les plans notés 3, 4 et 6 sur la figure 1. Dans les plans 3 et 6, les mesures moyennées en azimuth sont le résultat de l'exploration sur plus d'un pas en aval de l'aubage fixe qui précède. Notre propos est de définir les conditions cinématiques en amont et en aval de la roue mobile et du redresseur. L'objectif est aussi de vérifier la validité d'une hypothèse de type couche limite dans la direction de l'écoulement sain, et dans la région du bord d'attaque des aubages.

Dans ce but, nous présentons figures 2a, 3a, 4a, 5a, 6a, la composante de la vitesse moyennée selon θ et projetée selon la direction donnée par l'écoulement sain local pour la vitesse dans un repère fixe Vs (2a, 5a, 6a) et dans un repère mobile Ws (3a, 4a). Le vecteur vitesse complet peut être obtenu en utilisant les distributions d'angles moyen pour le vecteur vitesse absolu $\vec{V}$: α (figures 2b, 5b, 6b) et pour le vecteur vitesse relative $\vec{W}$: β (figures 3b, 4b), dans les positions axiales correspondantes. Sur ces figures les symboles ($\diamond$, $\triangle$) correspondent à des mesures réalisées respectivement avec une sonde cobra au moyeu, et cylindrique au carter, dans les mêmes positions azimuthales. Le trait pointillé décrit l'écoulement sain de référence. Le trait continu correspond aux résultats des calculs que nous décrirons dans la suite du texte.

L'écoulement entrant dans la roue directrice d'entrée (plan 1, figure 1) est du type couche limite bidimensionnelle au moyeu et au carter. Nous constatons que ce caractère semble effectivement conservé dans le plan 3 (figure 2a), si nous considérons Vs. A cette couche limite, il se superpose un effet tourbillonnaire (figure 2b) qui est issu au carter d'un tourbillon de passage Ω_{sp}, et au moyeu des effets conjugués de Ω_{sp} et d'un tourbillon de jeu Ω_{sj}. (Le détail de ces mesures peut être trouvé en référence [4]. En changeant de repère, (figures 3a et 3b), l'aspect de type "couche limite" n'est pas fondamentalement modifié au carter. Au moyeu, on pourrait considérer que le facteur de forme H_{12R} a fortement diminué par rapport à H_{12a} dans le repère absolu ; c'est cette remarque que nous avions utilisée en [4], avec l'hypothèse que l'épaisseur de couche limite δ était conservée dans les deux repères.

La répartition d'angle relatif β (figure 3b) dans le plan 3 peut donner lieu à deux interprétations différentes, quoique complémentaires. Nous pouvons considérer que l'aubage de la roue mobile ressent un écoulement sous une forte incidence aux parois ; ce qui interprété en utilisant un modèle d'écoulement sain se traduirait par des pertes élevées aux parois. Rappelons cependant que dans notre modèle, l'écoulement sain est responsable de la majeure partie du champ de pression statique Ps (effet d'équilibre radial) ; pour les compresseurs cette hypothèse est assez bien vérifiée ainsi que le montre la répartition de Ps dans le plan 3 (figure 8) ; notons que la valeur de Ps de l'écoulement sain donnée figure 8, correspond au trait pointillé donné figure 3b. Selon une autre hypothèse, l'augmentation de β_3 aux parois traduit des conditions aux limites particulières sur la vorticité secondaire Ω_s pour la roue mobile ; c'est cette deuxième idée que nous utiliserons dans la suite.

En aval de la roue mobile, Ws (figure 4a), a toujours un aspect de type couche limite au carter, ainsi qu'au moyeu. On notera cependant au moyeu, pour $0 < h < 0.15$, une croissance de la valeur expérimentale de Ws, qui résulte directement d'une augmentation de la température d'arrêt relative T_{OR}, par rapport à sa valeur T_{OR} dans l'écoulement sain. [4]. Ceci indique peut être des transferts parasites au travers de la paroi moyeu de la roue mobile. La répartition de β_4 montre de nouveau un écoulement tourbillonnaire qui se superpose donc à la couche limite (effet de tourbillon de passage en pied Ω_{sp}, effet de jeu Ω_{sj} + Ω_{sp} en tête).

Dans le repère absolu, si l'approche de type couche limite au carter ne semble pas introduire d'erreur remarquable a-priori, il est clair que cette situation est bouleversée au moyeu (figure 5a). La répartition observée pour V_S met donc en défaut l'approche classique de type couche limite qui est sensée décrire <u>intégralement</u> la composante V_S pour l'écoulement entrant dans le redresseur. En outre il semble que la répartition de V_S à l'aval (plan 6) du redresseur soit fortement influencée par l'état de non couche limite à l'amont (figure 6a). Il suffit d'observer que la zone de fort gradient $\partial V_S/\partial h$ au moyeu, que l'on serait tenté d'assimiler à une épaisseur δa de la nouvelle couche visqueuse, est de l'ordre de $\delta a = 0.07$ h alors que dans le repère relatif $\delta_R \sim 0.15$ h au plan 4. Afin de mieux apprécier l'origine des pertes de pression d'arrêt dans le plan 6, on donne figure 7 la répartition de la pression d'arrêt P_O, dans le plan azimuthal (R,θ) sur plus d'un pas inter-aubage du redresseur. Nous observons une forte concentration de pertes dans le sillage de l'aube du redresseur, ainsi qu'à proximité de l'extrados au moyeu.

En conclusion, nous devons donc remarquer que la composante V_S ou W_S de la vitesse, dans la direction de l'écoulement sain ne peut pas être uniquement décrite par une fermeture de type couche limite bidimensionnelle pour la zone du moyeu. Pour la zone du carter, cela reste qualitativement vrai, bien qu'il soit assez facile d'imaginer qu'une partie de l'information soit oubliée par l'utilisation unique d'une hypothèse de type couche limite selon s, également dans cette zone.

L'écart de V_S (ou W_S) par rapport à un profil de type couche limite, dans un nouveau repère, résulte directement de l'effet de la vorticité Ω_S existante dans le repère précédent, au travers du changement de repère.

Comme il est clair que le phénomène secondaire est principalement caractérisé par un effet du vecteur rotationnel $\vec{\Omega}'$ au travers de ces deux composantes Ω_N (pour V_S) ou de Ω_S (pour α), et que ce même vecteur $\vec{\Omega}'$ ne se modifie pas lors du changement de repère, il est donc nécessaire de prévoir dans la méthode de calcul, en plus du calcul de Ω_S et de l'aspect couche limite de V_S, un traitement particulier de la vorticité Ω_N qui n'est pas directement touchée par l'effet visqueux de type couche limite. Nous avons choisi de traiter cet "excès" de Ω_N en supposant que le champ de P_S n'est toujours pas perturbé directement dans l'écoulement. C'est-à-dire que le phénomène secondaire n'intervient au niveau de l'écoulement sain que par le biais d'une modification de la veine aux parois. Ceci constitue une approximation dont le degré d'importance reste cependant à préciser.

3. ETUDE THEORIQUE DES PHENOMENES SECONDAIRES

a) Nous allons dans ce qui suit détailler une méthode permettant d'assurer un transfert adéquat de l'information, associée aux phénomènes secondaires, lors d'un changement de repère dans une machine, et cela pour une méthode de calcul intégrale du type de celle décrite dans l'introduction de ce papier. Puis, nous donnerons deux équations de transport de la vorticité pour Ω_S puis Ω_N. Enfin une comparaison sera établie avec les résultats expérimentaux précédents. Soit $\vec{\Omega}_a$ et $\vec{\Omega}_R$ les vorticités rapportées à des repères absolu et relatif respectivement ; et soit $\vec{\omega}$ le vecteur rotation de la machine. Nous avons : $\vec{\Omega}_a = \vec{\Omega}_R - 2\vec{\omega}$ 　　　　　(1)

Soit $\vec{\Omega}$ et $\vec{\Omega}'$ les vecteurs rotationnels associés à l'écoulement sain, et secondaire respectivement.
Nous posons : $\vec{\Omega} = \vec{\Omega} + \vec{\Omega}'$ 　　　　　(2)

Dans ce qui suit seul $\vec{\Omega}'$ sera considéré. Nous supposerons que, dans un repère curviligne, lié à l'écoulement sain, nous aurons :

$$\vec{\Omega}'_a = (\Omega'_{Nv} + \Omega'_{NH})_a \, \hat{I}_{Na} + \Omega'_{b_a} \, \hat{I}_{Sa} + \Omega'_{b_a} \, \hat{I}_{B_a} \qquad (3a)$$

$$\vec{\Omega}'_R = (\Omega'_{Nv} + \Omega'_{NH})_R \, \hat{I}_{N_R} + \Omega'_{S_R} \, \hat{I}_{S_R} + \Omega'_{b_a} \, \hat{I}_{B_a} \qquad (3b)$$

Ω'_{Nv} représente la fraction de la composante Ω'_N qui peut être décrite par un profil de type couche limite uniquement.
Ω_{NH} représente donc le complément de Ω'_{Nv} dans Ω'_N. Il est clair que Ω'_{Nv} dépend directement de la fermeture utilisée pour le phénomène visqueux. Cependant, si on dispose d'une équation décrivant l'évolution de Ω_{NH} (ou Ω_N) de l'amont vers l'aval de la grille, on disposera alors d'une description plus réaliste de l'écoulement dans la machine.

Afin de définir Ω_{NH} et Ω_{Nv} dans le nouveau repère, il nous est nécessaire de formuler une hypothèse puisqu'une relation manque. Nous supposerons que $(\Omega_{Nv})_R$ dans le nouveau repère n'est lié qu'à $(\Omega_{Nv})_a$. Cette hypothèse sous-entend que l'effet turbulent dans le nouveau repère ne peut provenir, au bord d'attaque d'un aubage, que de l'effet turbulent dans l'ancien repère. Ce qui peut se justifier, au moins partiellement, en notant que le phénomène turbulent se caractérise d'une part par un mécanisme à mémoire, et d'autre part par un temps de réponse non négligeable face à des sollicitations imposées, dans le nouveau repère, par le champ de vitesse moyenne $\vec{W}$; ce dernier mécanisme doit cependant être modéré à proximité immédiate de la paroi, où on peut imaginer une réponse quasi-instantanée.

A l'aide de cette hypothèse, nous aurons alors, à partir de (3a - b) :

$$(\Omega'_{Nv})_R = (\Omega'_{Nv})_a \cdot \cos(\hat{\alpha} - \hat{\beta}) \tag{4a}$$

$$(\Omega'_{N_H})_R = (\Omega'_{N_H})_a \cdot \cos(\hat{\alpha} - \hat{\beta}) + (\Omega'_s)_a \sin(\hat{\alpha} - \hat{\beta}) \tag{4b}$$

$$(\Omega'_s)_R = (\Omega'_{Nv} + \Omega'_{N_H})_a \cdot \sin(\hat{\alpha} - \hat{\beta}) + (\Omega'_s)_a \cos(\hat{\alpha} - \hat{\beta}) \tag{4c}$$

$$(\Omega'_B)_R = (\Omega'_B)_a \tag{4d}$$

Les relations (4a - 4d) constituent donc un moyen de transférer l'information du repère absolu au repère relatif. L'étape suivante, dans le cas d'une méthode intégrale, consiste à ajuster (au sens des moindres carrés par exemple), les paramètres intervenant dans la loi analytique donnant W_s (δ, UT) afin de décrire au mieux le profil de vitesse associé à $(\Omega'_{Nv})_R$ (UT est une vitesse de frottement) ; cette étape ne pose pas en général de difficulté, si on note que d'après l'hypothèse précédente on a : $\delta_a = \delta_R$
Malgré tout, si $\cos(\hat{\alpha} - \hat{\beta}) < 0$, alors (Ω_{Nv}) change de signe dans le nouveau repère ; ceci signifie qu'un profil de couche limite associé à (Ω_{Nv}) peut engendrer un maximum de vitesse à la paroi dans le nouveau repère. Dans ce cas particulier, nous supposons alors que la zone de paroi, identifiée par l'étendue maximum de la zone log. dans V_s, est le siège d'une couche limite, pour laquelle la valeur du facteur de forme H_{12} est fixé arbitrairement à 1.4.

   b) Nous allons maintenant donner les équations permettant de décrire le développement de Ω_N et Ω_S. L'équation du vecteur tourbillon (équation de Navier-Stokes sur laquelle est appliquée l'opérateur ($\nabla\wedge$) rotationnel) s'écrit dans un repère tournant à la vitesse $\vec{\omega}$:

$$\frac{\partial \vec{\Omega}_R}{\partial t} + (\vec{W}.\nabla)\ \vec{\Omega}_R - (\vec{\Omega}_R \cdot \nabla)\ \vec{W} - \frac{\vec{\Omega}_R}{\rho}\ (\vec{\nabla}\rho.\vec{W})$$

$$= 2(\vec{\omega} \cdot \nabla)\ \vec{W} + 2\frac{\vec{\omega}}{\rho}\ (\vec{\nabla}\rho.\vec{W}) - \nabla(\frac{1}{\rho})\wedge \nabla\ P_s + \frac{\mu}{\rho}\ \nabla^2\vec{\Omega}_R \tag{6}$$

Nous avons uniquement négligé les effets des variations de μ et ρ dans le terme visqueux.

   Cette équation est tout d'abord projetée dans le repère curviligne $(\hat{I}_s,\ \hat{I}_b,\ \hat{I}_N)$ orthonormé, selon $\vec{I}_N$ et $\vec{I}_s$. Puis nous appliquons une moyenne selon θ, la direction circonférentielle. Il vient alors en négligeant les termes d'aubages, et les termes de fluctuations selon θ, et en notant $\overline{W}$ une vitesse moyenne en θ :

$$\frac{\rho\overline{W}_m}{b}\ \frac{\partial}{\partial m}\ (\frac{b}{\rho}\ \overline{\Omega}_{N_R}) + \frac{\rho\overline{W}_b}{b}\ \frac{\partial}{\partial B}\ (\frac{b}{\rho}\ \overline{\Omega}_{N_R})$$

$$+ (\overline{W}_N K_{Ns} - \frac{\cos\overline{\beta}}{b}\ \frac{\partial b\overline{W}_N}{\partial m})\ (\overline{\Omega}_{S_R} + 2\ \omega_s)$$

$$+ (\overline{W}_N K_{Nb} - \frac{1}{b}\ \frac{\partial b\overline{W}_N}{\partial B})\ (\overline{\Omega}_{bR} + 2\ \omega_b)$$

$$- (\overline{W}_s K_{Ns} + \overline{W}_b K_{Nb} - \frac{\sin\overline{\beta}}{b}\ \frac{\partial b\overline{W}_N}{\partial m})\ (\overline{\Omega}_{N_R} + 2\ \omega_N)$$

$$= 2\ \omega_N\ (\frac{\overline{W}_m}{b\rho}\ \frac{\partial b\rho}{\partial m} + \frac{\overline{W}_b}{b\rho}\ \frac{\partial b\rho}{\partial B}) + 2\ \omega_s\ (W_N K_{Ns} - W_s K_{s_N})$$

$$+ 2\ \omega_b\ (W_N K_{Nb} - W_b K_{b_N}) + [\nabla(\frac{1}{\rho})\wedge \nabla\ (P_s) + \frac{\mu}{\rho}\ \nabla^2\vec{\Omega}_R].\ \hat{I}_N \tag{7a}$$

Le terme visqueux est déterminé en supposant qu'il est créé par $(\overline{\Omega}_{Nv})$ et en posant :

$$\frac{\rho\overline{W}_m}{b}\ \frac{\partial}{\partial m}\ (\frac{b}{\rho}\ \overline{\Omega}_{Nv}) + \frac{\rho\overline{W}_b}{b}\ \frac{\partial}{\partial B}\ (\frac{b}{\rho}\ \overline{\Omega}_{Nv}) = (\frac{\mu}{\rho}\ \nabla^2\vec{\Omega}_R) \cdot \hat{I}_N \tag{7b}$$

Enfin le terme de pression est négligé.
Les termes de courbures K_{ij} sont donnés en fonction des métriques h_i par $K_{ij} = \frac{1}{h_i h_j}\ \frac{\partial h_i}{\partial Y_j}$
où Y_j est la coordonnée selon la direction j.
De même une équation pour Ω_{s_R} peut être obtenue en projettant (6) selon $\hat{I}_s$:

$$\frac{\rho\overline{W}_m}{b}\ \frac{\partial}{\partial m}\ (\frac{b}{\rho}\ \overline{\Omega}_{s_R}) + \frac{\rho\overline{W}_b}{b}\ \frac{\partial}{\partial B}\ (\frac{b}{\rho}\ \Omega_{s_R})$$

$$- (\frac{\cos\overline{\beta}}{b}\ \frac{\partial b\overline{W}_s}{\partial m} + K_{sb}\ \overline{W}_b + K_{sN}\ \overline{W}_N)\ (\overline{\Omega}_{sR} + 2\ \omega_s)$$

$$+ (\overline{W}_s\ K_{sb} - \frac{1}{b}\ \frac{\partial b W_s}{\partial B})\ (\overline{\Omega}_{bR} + 2\ \omega_b) \cdot$$

$$+ (\overline{W}_s K_{sN} + \frac{\sin\widehat{\overline{\beta}}}{b} \frac{\partial b\overline{W}_s}{\partial m}) \ (\overline{\Omega}_{NR} + 2 \ \omega_N)$$

$$= 2 \ \omega_s \ (\frac{\overline{W}_b}{b\rho} \frac{\partial b\rho}{\partial B} - \frac{W_N}{b\rho} \sin \widehat{\overline{\beta}} \ \frac{\partial b\rho}{\partial m})$$

$$+ 2 \ \omega_b \ (W_s K_{sb} - W_b K_{bs}) + 2 \ \omega_N \ (W_s K_{sN} - W_N K_{Ns})$$

$$+ [\nabla(\frac{1}{\rho}) \ _\Lambda \ \nabla \ (P_s) \ ] \ . \ \vec{I}_s + (\frac{\mu}{\rho} \nabla^2 \ \vec{\Omega}_R) \ . \ \vec{I}_s \qquad (8)$$

De même nous négligeons l'effet du terme de pression. L'effet du terme de dissipation est modélisé par un raccordement du profil transversal de vitesse $\overline{W}_N$ à zéro à la paroi, sur l'étendue de la zone log. de $\overline{W}_s$. Il est intéressant de comparer (8) avec l'équation habituellement utilisée pour le transport de Ω_s, (références [4], [5], [6], [8]), et qui est déduite des travaux de Lakshminarayana et Horlock [10] pour un repère de Fresnet. Dans ce cas, si le repère de Fresnet est assimilé au repère lié à l'écoulement sain, et en ne conservant que les termes essentiels, il vient :

$$\frac{d}{ds} \ (\frac{\overline{\Omega}'_{sR}}{\rho\overline{W}_s}) \ \simeq 2 \ \frac{\overline{\Omega}_{NR}'}{\rho\overline{W}_s} \ \frac{d\widehat{\overline{\beta}}}{ds} \qquad (9)$$

Dans l'équation (8), le transport de Ω_{sR} est assuré par les 2 premiers termes. L'allongement de Ω_{sR} sous l'effet de W_s est contenu dans $(\frac{\partial b\overline{W}_s}{\partial m} \ \overline{\Omega}_{sR})$; ceci décrit donc le premier membre de (9).
Nous avons en outre : $K_{sN} = - \frac{\partial\widehat{\overline{\beta}}}{\partial s}$

et $\qquad \overline{\Omega}_{bR} = - \frac{1}{bR} \frac{\partial bR\overline{W}_\theta}{\partial m} \ \sim \ - \ \overline{W}_s \ \frac{d \sin\widehat{\overline{\beta}}}{\partial m} \ \sim \ - \ \overline{W}_s \ \frac{\partial\widehat{\overline{\beta}}}{\partial s}$

$\qquad \overline{\Omega}_{NR} \ \sim \ - \frac{1}{b} \frac{\partial b\overline{W}_s}{\partial B}$

ce qui montre que le second membre de (9) peut être décrit par :

$$(- \frac{1}{b} \frac{\partial b\overline{W}_s}{\partial B}) \ \overline{\Omega}_{bR} + \overline{W}_s \ K_{sN} \ \ \overline{\Omega}_{NR} \ \sim \ - \ 2 \ \overline{\Omega}_{NR}' \ \overline{W}_s \ \frac{\partial\widehat{\overline{\beta}}}{\partial s}$$

sous certaines hypothèses. Ainsi (8) est à préférer à (9) puisque la production de $\overline{\Omega}_{sR}$ sous l'effet de $\frac{\partial W_s}{\partial B}$ est associée en réalité pour une part à la déflexion de l'écoulement sain $d\beta/ds$ et $\qquad \overline{\partial B}$ pour une autre part à la variation de $R\overline{V}_\theta$ selon m, et non pas à 2 $d\beta/ds$. La différence entre (8) et (9) pourrait être plus sensible dans les veines centrifuges.

c) L'application pratique d'une telle méthode consiste à résoudre simultanément les équations (7a - b), (8) et les deux équations intégrales décrivant la couche visqueuse sous une forme intégrale. Afin d'assurer la stabilité du calcul, nous avons trouvé nécessaire de joindre au système précédent une équation supplémentaire qui décrit le comportement de l'écoulement sain à la paroi sous l'influence des phénomènes secondaires. Cette équation traduit particulièrement l'effet des courbures engendrées par l'évolution du blocage pariétal associé à la couche visqueuse au niveau de l'écoulement sain ; en outre elle assure une conservation du débit global dans un plan de calcul. Nous ne décrirons pas cette équation ici, mais on pourra en avoir une idée à partir des travaux de Leballeur [13].

d) Pour appliquer cette méthode à notre cas expérimental, nous avons utilisé les valeurs expérimentales issues du plan 3 dans le repère absolu (figure 2a, 2b). Les résultats des calculs sont portés sur les figures 3 à 6 en traits continus. Nous constatons en général un accord assez satisfaisant, en particulier en aval du redresseur (figure 6).

4. CONCLUSION

Les résultats expérimentaux, décrits dans ce texte, montrent à l'évidence qu'une hypothèse de type couche limite n'est pas toujours applicable afin de modéliser dans la totalité la composante V_s du vecteur vitesse secondaire près des parois d'un compresseur. L'écart de V_s par rapport à un profil de type couche limite est associé soit à un effet de changement de repère simplement, soit à l'effet du changement de repère sur les composantes de la vorticité Ω_s et Ω_N du repère précédent.

Afin de permettre une description plus adéquate de l'écoulement dans une machine, nous avons séparé la composante Ω_N en une partie dont l'origine est associée uniquement au phénomène visqueux et turbulent, (Ω_{NV}) et une autre (Ω_{NH}), qui traduit plus spécifiquement l'influence de conditions amont au travers de l'action des aubages. Cette démarche s'inscrit cependant dans le cadre d'une approche de type couche limite puisque nous supposerons que les écoulements sain et secondaire inter-agissent par le biais d'une modification de la forme des parois sous l'effet du déficit de masse associé à l'écoulement visqueux. Aussi le champ de pression P_s est identifié à celui créé par l'écoulement sain.

Nous avons également donné deux équations de transport de la vorticité Ω_N et Ω_g, qui s'avèrent plus générales que celles utilisées habituellement dans ce type de méthode. Enfin, la comparaison des résultats du calcul et des expériences montre en général un accord assez satisfaisant qui pourra sans doute être amélioré grâce à une description plus fine du phénomène turbulent.

LISTE DES REFERENCES

[1] B. Lakshminarayana, M. Pouagare, R. Davino ; "Three dimensional flow field in the tip region of a compressor rotor passage. Part 1 : Mean velocity profiles and annulus wall boundary layer" - ASME Paper 82-GT-11, Londres 1982.

[2] B. Lakshminarayana, T.R. Govindan, B. Reynolds ; "Blade loading and rotation effects on a compressor rotor wake near end walls" - AIAA Journal, Vol. 21, n° 3, Mars 1983, p. 407-414.

[3] B. Lakshminarayana, A. Ravindranath ; "Interaction of compressor rotor blade wake with wall boundary layer/vortex in the end wall region" - ASME paper 81-GR/GT-1. Journal of Engineering for Power, Vol. 104, p. 467-478, April 1982.

[4] F. Leboeuf, F. Bario, G. Bois, K.D. Papailiou ; "Experimental study and theoretical prediction of secondary flows in a transonic axial flow compressor" - ASME paper 82-GT-14, Londres 1982.

[5] F. Bario, F. Leboeuf, K.D. Papailiou ; "Study of secondary flows in blade cascade of turbomachines" - ASME paper 81-GR/GT-4. Journal of Engineering for Power, Vol. 104, p. 497-509, April 1982.

[6] A. Vouillarmet ; "Contribution à l'étude et à la compréhension de l'écoulement visqueux dans un compresseur centrifuge" - Université Lyon I, Octobre 1979, Thèse de Docteur-Ingénieur.

[7] F. Leboeuf, A. Comte, K.D. Papailiou ; "Calculation concerning the secondary flows in compressor blading" - AGARD CP-214, La Haye, 1977.

[8] M. Pouagare, B. Lakshminarayana ; "Development of secondary flow and vorticity in curved ducts, cascades and rotors, including effects of viscosity and rotation" - Journal of Fluid Engineering, December 1982, Vol. 104, p. 505-512.

[9] A. Comte, G. Ohayon, K.D. Papailiou ; "A method for the calculation of the wall layers inside the passage of the wall layers inside the passage of a compressor cascade with and without tip clearance effects" - ASME paper 81-GT-168, Houston 1981.

[10] B. Lakshminarayana, J.H. Horlock ; "Generalized expressions for secondary vorticity using intrinsic coordinates" - J.F.M. Vol. 59, part 1, pp. 97-115, 1973.

[11] J. De Ruyck, C. Hirsch ; "Investigations of an axial compressor end-wall boundary layer prediction method" - ASME paper 80-GT-53, March 1980.

[12] G. Mellor, G. Wood ; "An axial end-wall boundary layer theory" - ASME paper 70-GT-80.

[13] J.C. Leballeur ; "Calcul des écoulements à forte intéraction visqueuse au moyen de méthodes de couplage" - ONERA TP n° 1980-121, ou AGARD-CP-291, (paper n° 1). (in Symposium AGARD/FDP on "Computation of viscous inviscid interactions", Colorado Springs, Octobre 1980).

REMERCIEMENTS

FIGURE 1   SCHEMA DU COMPRESSEUR

FIGURE 3B · BETA PLAN 3
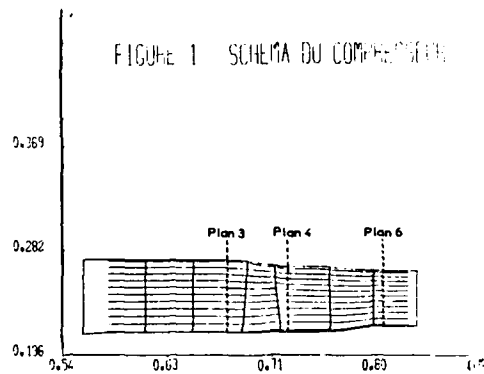
FIGURE 2A · VS PLAN 3
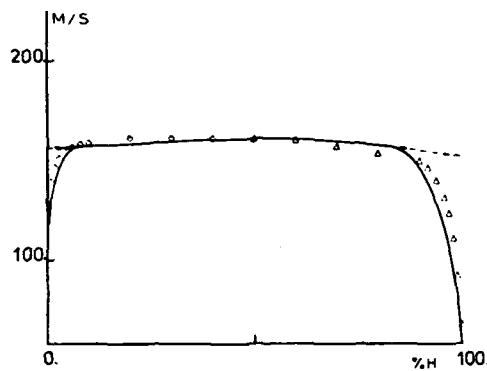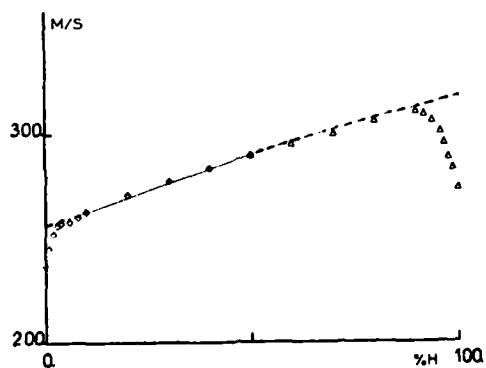
FIGURE 4A · VS PLAN 4

FIGURE 2B · ALPHA PLAN 3
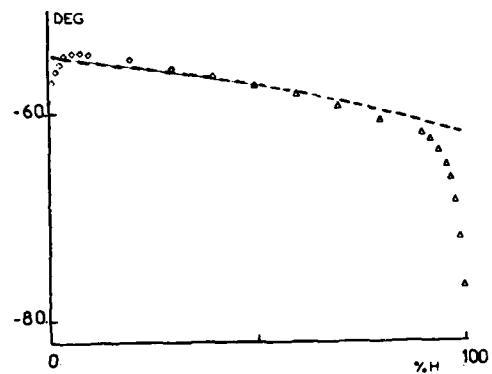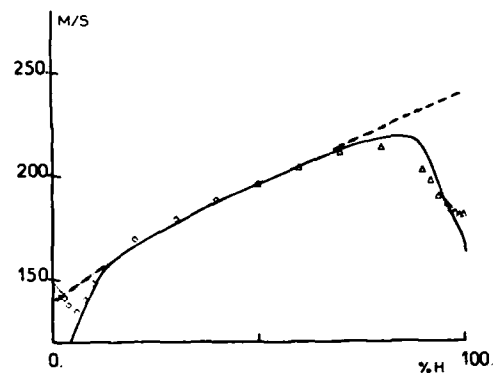
FIGURE 4B · BETA PLAN 4

FIGURE 3A · VS PLAN 3
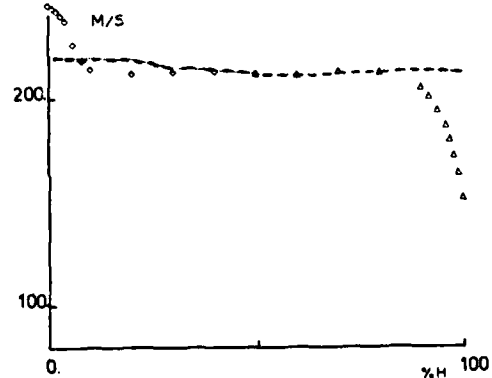
FIGURE 5A · VS PLAN 4

MICROCOPY RESOLUTION TEST CHART

NATIONAL BUREAU OF STANDARDS-1963-A

FIGURE 5B - ALPHA PLAN 4

FIGURE 6 - PS PLAN 3

FIGURE 6A - US PLAN 6

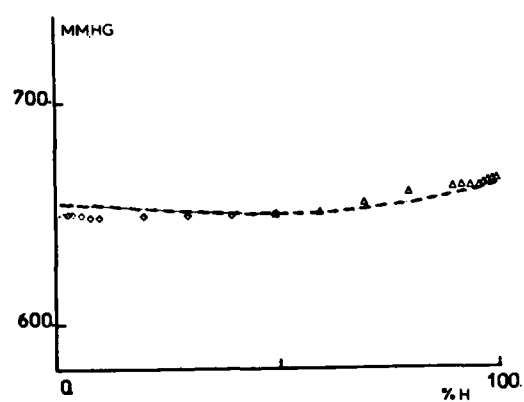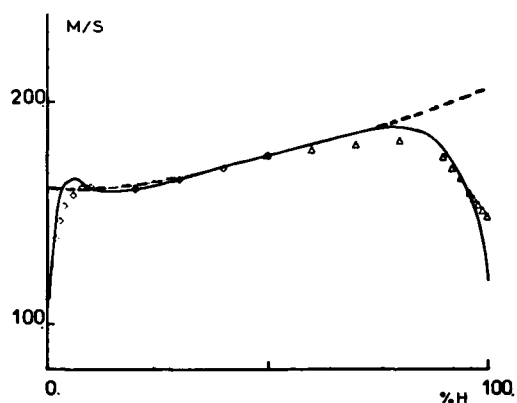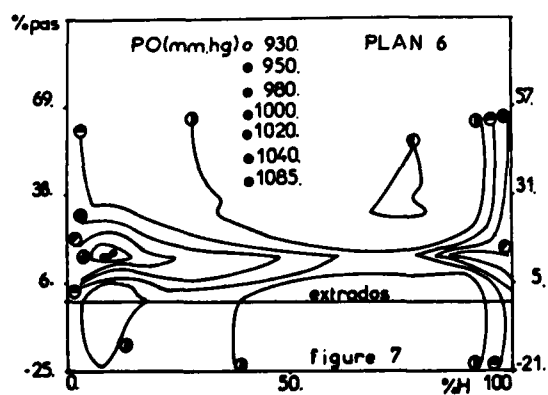
FIGURE 6B - ALPHA PLAN 6

figure 7

DISCUSSION

J.Chauvin, Fr

One could be a bit surprised to note that the zone of influence on angles is relatively small — it seems confined to the thickness of boundary layers. Now in your basic calculation for the through flow, have you used correlations taking into account the effects of secondary flow?

Author's Reply

No, in our calculation of through flow we only take into account the effects associated with the viscous flow. The scales on my plates may be a little bit misleading. There is an influence of the secondary phenomenon, an influence on the angle. It's not clearly illustrated here, I must admit. Nevertheless, in certain cases you can obtain one or two degrees. Generally speaking, we have observed that the secondary phenomena go up to possibly 25 to 30% of the vane height.

ANNULUS WALL BOUNDARY LAYER DEVELOPMENT IN A COMPRESSOR STAGE, INCLUDING THE EFFECTS OF TIP CLEARANCE [*]

B. Lakshminarayana, K. N. S. Murthy

and

M. Pouagare, and T. R. Govindan,

153 Hammond Building
Department of Aerospace Engineering
The Pennsylvania State University
University Park, PA 16802 U.S.A.

SUMMARY:

The end-wall boundary layer development in a compressor stage, including the inlet guide vane (IGV) passage and the rotor passage, was measured. The measurements upstream of the rotor and inside the IGV passage were carried out with a five-hole probe. The data (blade-to-blade) inside the rotor passage were measured using a three-sensor rotating hot-wire below the tip clearance region and a 'V' configuration probe inside the clearance region. The rotor exit measurements (blade-to-blade) were acquired with a laser doppler velocimeter. The velocity profiles and the integral properties are presented and interpreted in this paper. The boundary layer is comparatively well behaved up to the leading edge of the rotor, beyond which complex interactions result in very unconventional profiles. The momentum thicknesses decrease in the leakage flow region of the rotor. The momentum thicknesses and the limiting streamline angles predicted from a momentum integral technique agree well with the data up to the leading edge of the rotor.

LIST OF SYMBOLS

C_I	axial chord of the IGV blade at the tip
C_{pw}	wall pressure coefficient $(p - p_A)/\frac{1}{2} \rho V_{x_\infty}^2$
C_R	axial chord of the rotor at the tip
p	static pressure
R	r/r_w
r_w	annulus wall radius
r, θ, x	radial, tangential and axial coordinates (see Fig. 3)
S	blade spacing
s, n, r	streamwise, normal and radial coordinates (see Fig. 3)
t	tip clearance height
T_x, T_θ	axial and tangential turbulent intensities normalized by the local total velocity (relative velocity in the case of rotor).
V_s, V_n	streamwise and normal component of absolute velocities (Fig. 3) normalized by the free stream axial velocity at the IGV inlet
V_x, V_θ	axial and tangential absolute velocities normalized by the free stream axial velocity at the IGV inlet
W_x, W_θ	axial and relative tangential velocities (see Fig. 3) normalized by the free stream axial velocity at the IGV inlet
X	distance from IGV leading edge normalized by C_I
X_R	distance from rotor leading edge normalized by C_R
Y	tangential distance measured from the suction surface normalized by the blade spacing $(r\theta/S$, $\theta=0$ on the suction surface)
α_w	limiting (wall) streamline angle of the absolute flow
δ_s, δ_n, θ_{ss}, θ_{nn}, θ_{sn}, H_s	boundary layer integral parameters - thickness normalized by blade span (see equations 1 to 3)
δ	boundary layer thickness (distance from wall to the location where the maximum velocity occurs) normalized by r_w - see Fig. 12a
ψ	loading coefficient

[*] This is the revised version of the preprint. Figs. 12, 13, 18 and 19 and the corresponding text have been revised.

ν_T, ν_x	tangential and axial force defect thickness (eqs. 4 and 5) normalized by the blade span
ρ	density
ϵ	$\alpha_e - \alpha_w$

Subscripts

A, max	ambient and maximum value
e	edge of the boundary layer
∞, 1	upstream of IGV (free stream) and leading edge of the rotor
h, t	hub and tip

Superscript

――――	passage-averaged values

INTRODUCTION

The boundary layers that develop on casing and hub walls of compressor stages limit the pressure rise, efficiency, mechanical reliability and mass flow through the stage. In addition, they introduce considerable three-dimensionality and unsteadiness in the flow, and affect the stall and surge characteristics of the compressor. They have also been recognized as a source of noise in recent years. Previous attempts to analyze this flow were based on simplified flow models and momentum integral techniques (refs. 1-4) that neglect the complex interactions in the end-wall region of blade rows. The comparison between the measured and the predicted annulus-wall boundary layer (AWBL) growth are poor, or only qualitative in nature for the rotor end-wall boundary layer, but are quite good for the stator or IGV blade rows. The methods have not been tested for the AWBL inside a rotor passage. One of the objectives of this paper is to provide such data for the validity of these analyses as well as computer codes now under development.

The AWBL that develops on the casing of a turbomachinery stage (including through the inlet guide vane, rotor and stator) is three-dimensional and turbulent in nature. Furthermore, the complex interaction of the tip leakage flow and the blade boundary layer, and its transport towards the blade tip, in the AWBL near the rotor end-wall region produces an extremely complex flow field in the region. This region of the AWBL remains largely unexplored experimentally, it is beyond the scope of analytical methods, and is very difficult for computational methods. The measurements inside the rotor are complicated, since the measuring probe has to be rotated with the rotor. The measurement technique for the clearance region, which is small, is also complex and miniature probes combined with elaborate data processing procedures have to be employed in acquiring the data in this region. There is no data available at present for the AWBL growth inside the rotor blade and in the immediate vicinity of the trailing edge of the rotor in the downstream region.

A comprehensive program was started at The Pennsylvania State University to acquire such data in the end-wall region, using a rotating three-sensor hot-wire probe, laser doppler velocimeter, a five-hole pitot probe and a stationary "V" type hot-wire sensor. Most of the data presented in this paper is new, but some of the earlier data (refs. 5-7) has been reprocessed, replotted, or reinterpreted to provide a comprehensive and systematic presentation of the AWBL growth in a compressor stage. A tabulation of the new data and the earlier data used in this paper is given in the next section.

EXPERIMENTAL FACILITY, MEASUREMENT TECHNIQUE AND PROGRAM

The AWBL measurements are carried out in a single stage axial flow compressor facility in the Department of Aerospace Engineering, The Penn State University. A general description of the compressor stage is given by Smith [8], and a detailed discussion of the facility is given by Lakshminarayana [9]. Overall performance, radial distributions of flow properties at various axial locations of the stage (upstream and downstream of IGV, rotor, and stator) are presented in ref. 10. Good peak efficiencies are exhibited by the rotor. The hub/annulus wall diameter ratio of the facility is 0.5, with the diameter of the annulus wall equal to 0.9377 m. The inlet guide vane row, made up of 43 blades, is followed by the 21-bladed rotor. The rotor is driven by a 37 kw variable-speed motor through a belt and pulley system. The rotor is followed by a stator vane row of 25 blades. Downstream of the stator there is an axial flow fan with variable-blade setting for control of the pressure rise and mass flow of the facility. A schematic of the measurement locations is shown in Fig. 1. Operating conditions and rotor specifications are as follows: inlet velocity, $V_{x\infty}$, of 29 m/s; flow coefficient based on tip speed of 0.56; stage loading coefficient based on tip speed of 0.4864; rotor speed of 1066 rpm; tip clearance between 2 mm at the leading edge to 1.5 mm at the trailing edge. Blade element data at the tip of the rotor are NASA 65 series; chord of 15.41 cm; spacing of 14.12 cm; maximum thickness of 5.10 percent of the chord; stagger angle of 45.0 deg; and maximum camber height of 8

percent of the chord. The blade element details of the IGV and rotor are given in Table V of ref. 10.

The inlet guide vane has NACA 65-010 circular arc blades, with the following tip section specification; camber angle of 42.9°, stagger angle of 21°, chord of 10.91 cm; spacing of 6.82 cm, maximum thickness of 8.29 percent of the chord, the inlet flow is axial.

A tabulation of the measurement stations, the technique employed in the various regions and the type of data acquired, is shown in Table 1.

Table 1

Measurement Stations, Techniques and Data Summary
(Ref. to Fig. 1)

| | | | Measurement Technique | Data Available | | Remarks |
		X/C_I		Blade to Blade	Mean or Axisymmetric	
IGV PASSAGE →	1	-0.25	Five-Hole Probe	V_x, V_θ, V_r, α_w, C_{pw}	$\bar{V}_x$, $\bar{V}_\theta$, $\bar{V}_r$, $\bar{\alpha}_w$, $\bar{C}_{pw}$	Upstream of IGV
	2	0.25				
	3	0.52				
	4	0.81				
	5	0.98				(IGV TE, X/C=1.0)
	6	1.14	Five-Hole Probe		V_x, V_θ, α_w, C_{pw}	Downstream of IGV
	7	1.25				
	8	1.44				
	9	2.00				
	10	2.312				
	11	2.625				
	12	2.752				
ROTOR PASSAGE →	13	3.250	Rotating Three-Sensor Hot-Wire Probe Inside the Passage. In the clearance region "V" type of hot-wire probe.	V_s, V_n, V_r, W_θ, W_x, T_θ, T_z, T_r Reynolds Stress Blade Static Pressure	$\bar{V}_s$, $\bar{V}_n$, $\bar{V}_r$, $\bar{W}_\theta$	LE of the rotor, X/C = 3.25 Data in refs. 6, 7 11 & 12 reprocessed to derive AWBL characteristics Rotor TE, X/C = 4.323
	14	3.780				
	15	4.054				
	16	4.3107				
	17	4.3855	LDV Measurement 2.5 mm away from the wall; hot-wire measurements very close to the wall	V_s, V_n, W_θ, W_x	$\bar{V}_s$, $\bar{V}_n$, $\bar{W}_x$, $\bar{W}_\theta$	Hot-wire Data from refs. 7 & 12 for the wall region
	18	4.5105				
	19	5.0105				
	20	5.8230				

A miniature five-hole probe (1.65 mm diameter), described in refs. 5 and 10 was used for the AWBL measurement upstream of IGV, inside the IGV passage, and upstream of the rotor. A rotating three-sensor hot-wire probe was traversed across the passage of the rotor, at radii up to 4 percent of the blade span from the tip at the following radial locations;[*] R = 0.976, 0.968, 0.954, 0.940, 0.914 and 0.886, and axial stations; X_R = 0 (leading edge), 0.25, 0.5, 0.75, and 0.979 (trailing edge). Details of the measurement technique and data are given in ref. 6. The flow in the rotor tip clearance region was measured, up to about 1 mm (half way into the clearance) from the annulus wall, using a "V" type hot-wire sensor. These measurements were carried out from 6 to 11 radial locations inside the tip clearance region; at X_R = -0.012, 0.003, 0.50, 0.75, 0.979, inside the rotor passage; and at X_R = 1.055, 1.179, 1.44, 1.593, 1.731, at the exit of the passage. Details of the measurement technique used inside the tip clearance region and some of the processed data are given in refs. 7 and 12. The measurements down-stream of the rotor were acquired from a laser doppler velocimeter (LDV) at X_R = 1.058, 1.174, 1.640, 2.397. These measurements were combined with the measurements close to the wall (ref. 7) to provide composite profiles of velocity at the exit.

A single channel, dual-beam laser anemometer with on-axis backscatter light collection (TSI Model 9100-6) was used to make measurements in the end-wall region behind the rotor blade. The system operated with a Lexel 4W argon-ion laser tuned for the green line (514.5 mm). The transmitting optics consisted of a beamsplitter, a 3.75X beam expander,

---

[*]It should be noted that the radii in ref. 6 is normalized by the radius of the blade tip. These radii correspond to R = 0.980, 0.973, 0.959, 0.945, 0.918, and 0.819, respectively, of ref. 6.

and a 152 mm diameter front lens with a focal length of 762 mm. The half-angle of the intersecting beams was measured to be 3.12° and provided a probe volume diameter of 0.133 mm and a probe volume length of 2.50 mm, based on the $1/e^2$ intensity points. The receiving optics consisted of the 152 mm front lens, a field-stop unit, and a receiving assembly with a photomultiplier tube. The entire system moved on a three axes traverse table which also had facility to tilt the assembly so that the beams are projected radially to the rotor. A counter type signal processer (TSI Model 1995) interfaced with a HP 2100S computer provided an on-line data processing capability. An ensemble-averaging technique similar to that described by Powell, et al. [13] was used to average the velocity information. The flow was seeded with an atomized spray of mineral oil, and was injected into the flow 200 mm upstream of the rotor.

END-WALL SURFACE MEASUREMENTS

The wall static pressure and the limiting (wall) streamline angles were measured in the end-wall region. The former has a major influence on the development of the AWBL inside the IGV and the rotor blade passages. The limiting (wall) streamline angles and its deviation from the freestream flow angle denote the extent of three-dimensionality in the AWBL profiles. The limiting (wall) streamline angle was derived by the ammonia streak technique. In this technique, ammonia gas is injected into the boundary layer through static pressure holes in the casing, and a trace of the wall flow is obtained by the reaction of the ammonia on an ozalid paper pasted on the wall.

The limiting (wall) streamline angle (measured from the axial direction) at various axial locations is shown plotted in Fig. 2. Inside the IGV passages, the measured angles at mid-passage were chosen and are compared with the mean blade angle distribution. Between IGV and the rotor, the angle of the free stream is assumed to be the same as the IGV blade outlet angle. For most locations, the maximum, minimum and the average angles derived from the ammonia traces are shown. The deviation of the flow from the blade angle is considerable (10 to 20°) inside the IGV passage, and at the exit, but vanishes rapidly downstream. At X = 3, the differences are very small.

As the rotor is approached, the difference between the absolute flow angle (design - in the absence of tip clearance) and the limiting (wall) streamline angle increase considerably. Inside the passage, the difference between these two angles is as high as 70°. Since the "fan angle" of the ammonia traces was very large and the boundaries of the fan were faint, only the mean values are plotted at these locations. The data inside the passage should be interpreted as qualitative in nature. The boundary layers at these locations are highly three-dimensional, unsteady and have large skew angles. The mid-chord location inside the rotor has the maximum deviation of the limiting (wall) stream-line angle from the absolute flow angle, this is caused by the leakage flow. At X = 4 (which is at 0.75 rotor chord from the leading edge) and X = 4.3 (trailing edge), the deviations are still large (about 30°), further downstream the flow near the wall tends to align itself with the flow in the freestream (to within 10°), indicating that the three-dimensionality of the wall boundary layer has reduced substantially, beyond about half-a-chord downstream of the rotor trailing edge.

The wall static pressure distribution is also shown in Fig. 2. Inside the IGV passage, the wall static pressure along the mean streamline (mid-passage) is shown. Inside the rotor passage, the wall static pressures plotted are the average values derived from measurements using the static pressure taps and a Validyne pressure transducer. The wall static pressure inside the passage should be viewed as qualitative, as no attempt was made to measure it using a high-frequency response probe. The streamwise pressure gradient is large both inside the IGV passage (favorable) and the rotor passage (adverse). This should have a substantial effect on the boundary layer growth. The wall static pressures become nearly uniform at about one-third chord length downstream of the trailing edge of the rotor and the IGV.

ANNULUS WALL BOUNDARY LAYER DEVELOPMENT INSIDE AND AT THE EXIT OF THE ROTOR PASSAGE

The AWBL inside the blade passages is non-axisymmetric and highly complex, and develops under streamwise and crosswise pressure gradients. The qualitative nature of the AWBL inside the rotor passage is shown in Fig. 3. A complex profile (Fig. 3) results from the interaction of the leakage flow with the AWBL. The profile consists of a wall layer, leakage jet layer, the free shear layer, and the inviscid region. The characterization of the profile is extremely difficult. The momentum thickness and the displacement thickness is based on the edge velocity (such as A) discerned from the axial velocity profile derived from inviscid flow measurements.

The AWBL developing inside the IGV passage is presented in ref. 5 and will not be repeated here.

AWBL Velocity Profiles

The AWBL inside the rotor passage is presented at five axial stations inside the rotor (X_R = 0.0, 0.25, 0.5, 0.75 and 0.979) and at five tangential locations (Y = 0.05, 0.25, 0.5, 0.75 and 0.95), where Y is the tangential distance from the suction surface normalized by the blade spacing. The data up to R = 0.976 are from a three sensor rotating hot wire (refs. 6 and 11) and those beyond this radius, inside the tip clearance region, are from a stationary "V" configuration hot-wire sensor (refs. 7 and 12). The velocity profiles are presented in a boundary layer coordinate system (s, n, r) for the absolute

velocity and in the cylindrical coordinate system (r, θ, x) for the relative velocity. This enables a better understanding and interpretation of the AWBL growth through the rotor. In the s-n-r system (absolute flow), the "s" direction is aligned with the absolute freestream, away from the wall and blades, at R = 0.886. It should be noted that this is an arbitrary choice and does not imply that the boundary layer edge (which is very difficult to discern in view of the radially varying inviscid flow) is at R = 0.886. There is no "freestream" in the conventional sense (Fig. 3). The coordinate n is normal to s, and r is in the radial direction. The nature of streamlines, both relative and absolute, in the freestream as well as inside the AWBL in the blade clearance region is shown in Fig. 3. All velocity components are normalized by the axial velocity at the inlet to the guide vane $(V_{x\infty})$, of 29.68 m/sec.

As mentioned earlier, the measurements of the rotor exit flow were carried out with an LDV (with ensemble-averaging procedure to derive the blade-to-blade flow properties) up to the wall region ($\sim$2.5 mm), beyond which the measurement was carried out with a "V" configuration hot-wire probe traversed from the wall. The data was taken at X_R = 1.058, 1.174, 1.640 and 2.397. The blade location was identified from the rotor wake profile.

The streamwise (V_s), axial (W_x), and relative tangential (W_θ) velocity profile at various tangential locations and chordwise locations, X_R = 0.0, 0.25, 0.5, 0.75, 0.979, inside the passage are shown in Figs. 4, 5, 6, 7, and 8, respectively. At the leading edge location $(X_R = 0)$, the profiles at all tangential stations inside the blade passage are almost identical. A small discontinuity exists in the V_s and W_x profiles between the last point inside the tip clearance (R = 0.995) and the first point inside the passage (R = 0.976). This is because the fluid in the tip clearance region is not subjected to the same blade force as the fluid inside the passage. The magnitude of the normal velocity V_n (not shown) is found to be high in the annulus wall region, indicating three-dimensionality of the AWBL.

At the axial location X_R = 0.25 (Fig. 5), the measurements inside the tip clearance are not available. At this location, the AWBL growth differs in the tangential direction, with maximum growth occuring near the suction surface. The presence of a "wall jet" type of profile, with peak values close to the wall and higher than that in the freestream, appears at Y = 0.75 and 0.95 in the V_s and W_x profiles. This is caused by the "leakage jet" originating from the pressure side and has the same effect as that of "blowing" by a wall jet. The interaction between this leakage jet and the AWBL produces the effect mentioned. The peaks in the V_s and W_x profiles noticed at X_R = 0.25 near R = 0.976 at Y = 0.75 and 0.95 have increased and the effect has spread to most of the tangential locations at X_R = 0.5 (Fig. 6). As indicated in refs. 6 and 7, maximum leakage flow occurs in the mid-chord region. This effect is clearly seen at these locations. The normal velocities (V_n) are found to be high in this region. There is also considerable variation in V_n in the radial direction, resulting in large gradients of the normal velocity $(\partial V_n/dr)$ in the end-wall region. Data on the passage-averaged values of V_n are given in a later section.

The velocity profiles $(V_s$ and $W_x)$ are very unconventional inside the rotor passage, and it is clear that none of the assumptions (for profiles of crossflow and main flow components of velocity) made in most AWBL analysis are valid in this region. No appreciable growth in the boundary layer is observed between X_R = 0.25 and 0.5; but the AWBL is highly three-dimensional, with unconventional velocity profiles, and with substantial variation along the blade tangential direction. This seems to indicate that the analyses based on passage-averaged values or conventional velocity profiles are not valid in the prediction of rotor AWBL growth. The axial (W_x) velocity profile is similar to the V_s profiles, but the W_θ profiles show very sharp gradients near the wall. The AWBL velocity profiles at X_R = 0.75 are shown in Fig. 7. The AWBL has grown from X_R = 0.5 to X_R = 0.75. The severe velocity gradients (V_s, W_x) in the radial direction observed near the tip (R = 0.976) at X_R = 0.5 have now spread over a larger radial extent. This indicates that the leakage flow (and the jet) has now spread over a larger spanwise height. The peaks in the velocity profile have also moved downward along the blade span, and are present over the entire passage. The normal velocities (V_n) are found to be highest near the suction surface at this axial location, dropping to almost zero values as the pressure surface is approached. This would indicate that the effect observed may not have been caused entirely by the leakage flow at X_R = 0.75, but by the leakage flow occuring upstream as well. The relative velocity vector over the blade tip is inclined to the chordwise direction as shown in Fig. 3. Hence the leakage jet originating, for example, at X_R = 0.5 on the pressure surface will produce its effect further downstream on the suction side.

The velocity profiles at X_R = 0.979 (Fig. 8), near the trailing edge, show extremely complex profiles, never observed or measured before. At this location, the interaction of the leakage flow with the AWBL and the transport of the blade boundary layer to AWBL regions results in an extremely complicated profile and that is very difficult to interpret. The boundary layer growth is not substantial.

At all axial locations inside the rotor passage, the behavior of V_s and W_x profiles is similar; the only difference is that the gradients and defect in V_s near the wall are somewhat greater than those observed in the W_x profile. This can be explained on the basis that the magnitude of V_s includes a part of the absolute tangential velocity (V_θ) which has a much higher defect near the wall, as revealed by the W_θ profiles plotted.

The relative tangential velocity profiles near the leading edge locations, X_R = 0 (Fig. 4), X_R = 0.25 (Fig. 5), have the conventional shape, with the velocity near the

wall approaching the rotational speed of the rotor. Beyond $X_R = 0.25$ (Figs. 6-8) the profiles are distorted, especially near the pressure side. At $X_R = 0.5$ (Fig. 6) and at the location nearest to the pressure side ($Y = 0.95$), the flow is significantly overturned at $R \sim 0.976$ (inside the blade passage). The flow in the clearance region is underturned substantially. The flow underturning is caused by the leakage flow. The presence of overturning indicates that other phenomena influence the flow inside the passage. One possible explanation of the overturning at $R = 0.976$ is that the tip leakage flow (jet) has descended into the passage and started to roll. Another possible reason for the overturning is the presence of secondary flow.

The velocity profiles at $X_R = 1.058$ and 1.640 are shown in Figs. 9 and 10, respectively. It is clear from Fig. 9 that the boundary layer is still asymmetric, with substantial blade-to-blade variation at $X_R = 1.058$. Comparing the profiles of V_s at $X_R = 0.979$ (Fig. 8) and at $X_R = 1.058$, it is evident that the boundary layer has a much smoother profile at $X_R = 1.058$. The leakage jet, which had substantial effect up to $X_R = 0.979$, seems to have diffused and moved away from the tip. A distinct freestream can now be recognized at $X_R = 1.058$. The normal (V_n) velocity is found to have decreased substanially and is confined to a small region between $R = 1.0$ and 0.96. The velocity profiles at $X_R = 1.179$ and 1.640 are similar, hence only the data at the latter station are presented. The effect of leakage flow in the region $R = 0.975$ still persists at this location, but the boundary layer does not grow very rapidly. The crossflows are also found to be substantial in this region. The boundary layer profiles still vary across the passage, but the differences are small. The data at $X_R = 2.397$ indicate that the profiles are identical at all passage locations. The flow has become axisymmetric at this location. In view of this fact, only the average data are relevant and these are presented in the next section.

Vectorial Plot of Velocity

The absolute and relative velocity vectors at three typical locations inside the AWBL ($R = 0.968, 0.976, 0.997$, the last station being inside the clearance region) are shown in Fig. 11. At the leading edge ($X_R = 0$), the flow is collateral and the boundary layer is nearly two dimensional. As the flow proceeds downstream, its three-dimensionality increases. At all axial locations, the flow angle deviation between $R = 0.970$ and 0.976 is not large, but the absolute velocity vectors show substantial deviation in the clearance region, especially near the pressure surface. The absolute flow angles decrease dramatically (the flow is underturned) in the clearance region. The relative velocity vectors are closer to the tangential direction, also indicating the underturning of the flow. Inside the passage at $X_R = 0.75$ and 0.979, the flow is overturned at $R = 0.976$ (compared to that at $R = 0.970$ This effect is more prounounced near the suction side. This may be caused by the secondary flow, by the roll up of the leakage jet, or by the formation of a leakage vortex. The skewness of the AWBL decreases drastically as the flow leaves the trailing edge. Such drastic changes in the flow angles between $R = 0.976$ and 0.997 make the analysis of this flow and prediction of the AWBL in the rotor passage extremely complicated.

Integral Properties (Blade-to-Blade Variation)

The integral properties of the annulus wall boundary layer at all the axial locations inside and at the exit of the rotor passage and at nine tangential locations ($y = 0.05$, 0.15, 0.25, 0.375, 0.5, 0.625, 0.75, 0.85, 0.95) have been calculated. The method used is illustrated in Fig. 12a. The inviscid velocity $\bar{V}_x$ derived from the five-hole probe (Ref. 13) and the AWBL profile derived from the present measurement are shown plotted together in Fig. 12a. There is an overlapping region between the two measurements. These composite profiles are used to locate the edge of the boundary layer for integration purposes. At $X_R = 0$ and 0.5 it is clear that the edge is located at E. At other locations, ($X_R = 0.75$ & 0.979), distinction is not clear as the two profiles did not match well. Hence the edge was taken to be that obtained from the inviscid flow measurements (shown as E). For conventional boundary layers (outside the blade rows) the integration is carried out to the location where the velocity reaches 99% of the free-stream value (Fig. 3).

The integral properties are defined as follows

$$\delta_x = \frac{1}{R_t - R_h} \int_1^{1-\delta} (1 - \frac{V_x}{V_{xe}}) dR; \qquad \delta_s = \frac{1}{R_t - R_h} \int_1^{1-\delta} (1 - \frac{V_s}{V_{se}}) dR \qquad (1, 2)$$

$$\theta_{xx} = \frac{1}{R_t - R_h} \int_1^{1-\delta} (1 - \frac{V_x}{V_{xe}}) \frac{V_x}{V_{xe}} dR \qquad (3)$$

All the thicknesses are normalized by the blade span.

The blade-to-blade variation of θ_{xx} at various axial locations is shown in Fig. 12b. As the flow proceeds from $X_R = 0.0$ to $X_R = 0.5$, θ_{xx} diminishes near the pressure side of the blade surface and increases at all other locations, with a large increase occuring near the mid-passage. The decrease of θ_{xx} near the pressure surface is due to the tip leakage, which has a "blowing" effect on the wall boundary layer previously mentioned. As the flow proceeds towards the three-quarter chord point ($X_R = 0.75$), θ_{xx} decreases

from the mid-passage to the pressure surfaces, a beneficial effect caused by the leakage flow. As the flow proceeds towards the trailing edge, the momentum thickness reaches a negative value very near the pressure surface (caused by the leakage flow), while there is a general increase in θ_{xx} at all other locations. It is interesting to note that θ_{xx} increases near the mid-passage from $X_R = 0$ to 0.5, and decreases from $X_R = 0.5$ to 0.75. This again may have been caused by the leakage jet, which moves towards the center of the passage due to the blade motion. This high velocity jet would presumably mix out in the blade passage beyond $X_R = 0.75$, giving rise to an increase in θ_{xx} at most of the passage locations.

The blade-to-blade distribution of θ_{xx} downstream of the trailing edge is also shown in Fig. 12b. Appreciable decrease in the value of θ_{xx} is observed in the immediate vicinity of the trailing edge, as the flow leaves the passage. Beyond the trailing edge, the blade-to-blade distribution becomes more uniform with a general increase in the magnitude of θ_{xx} at the far downstream station.

The axial and tangential force defects are derived from the passage-averaged velocity profiles. The tangential force defect is defined as,

$$v_T = \frac{1}{R_t - R_h} \int_1^{1-\delta} \left[1 - \frac{(\overline{V}_x \overline{V}_\theta) - (\overline{V}_x \overline{V}_\theta)_1}{(\overline{V}_x \overline{V}_\theta) - (\overline{V}_x \overline{V}_\theta)_{1e}} \right] dR \qquad (4)$$

The axial force defect is defined as (ref. 15),

$$v_x = \frac{\rho}{P - P_1} \left[\overline{V}_x^2 \theta_{xx} - \overline{V}_{x1}^2 \theta_{xx1} + (\overline{V}_x - \overline{V}_{x1}) \overline{V}_x \overline{\delta}_x \right]_e \qquad (5)$$

where

$$\overline{\theta}_{xx} = \frac{1}{R_t - R_h} \int^{1-\delta} (1 - \frac{\overline{V}_x}{\overline{V}_{xe}}) \frac{\overline{V}_x}{\overline{V}_{xe}} \, dR, \quad \overline{\delta}_x = \frac{1}{R_t - R_h} \int_1^{1-\delta} (1 - \frac{\overline{V}_x}{\overline{V}_{xe}}) dR \qquad (6,7)$$

In the derivation of v_T and v_x, value of δ was derived as illustrated in Fig. 12a. The subscript 1 denotes inlet local values ($X_R = 0$), e denotes the local value at the edge of the AWBL and 1e the value at the rotor inlet at the edge of the AWBL. The tangential force defect thickness is normalized by the blade span, as in all other thickness distributions. The axial variation of v_T and v_x is given in Fig. 13. The value of v_T increases from the leading edge to $X = 0.75$. This is caused by the overall increase in the AWBL growth inside the passage. From $X_R = 0.75$ to 0.979, v_T decreases slightly, this may have been caused by the leakage which has a tendency to decrease the growth of the AWBL through the "blowing" effect. The value of v_T remains nearly constant beyond the blade trailing edge. Downstream values of v_T (≈ 0.02) are shown plotted in Fig. 13 and compared with the earlier data due to Smith [16] and Hunter [15]. The authors' data agree well with the earlier data taken downstream of single stage and multi-stage compressors.

The axial force defect thickness, v_x, shown plotted in Fig. 13, indicates that it increases from $z = 0.5$ to $z = 0.979$ and then decreases to almost zero value at the trailing edge.

Turbulence Intensities

The hub-to-tip variation of the turbulence intensities upstream of the IGV and upstream of the rotor ($X_R = -0.35$) is shown in Fig. 14. Upstream of the IGV the turbulence is found to be nearly isotropic and hence, only a plot of T_x is shown, its value is approximately 1% in the freestream. Upstream of the rotor ($X_R = -0.35$), the freestream values of T_x and T_θ are still close to 1% but in the endwall regions, a large increase in T_x and T_θ can be seen.

The turbulence intensities, T_x and T_θ, inside the rotor at mid-passage location ($Y = 0.5$) are shown in Fig. 15. At $X_R = 0.0$, T_x and T_θ values are approximately 3 to 4% at the lowest radius, $R = 0.866$. A significant increase in free-stream turbulence occurs when the flow enters the rotor passage. The maximum value of T_x has increased appreciably from its value upstream, while the increase in the maximum values of T_θ (near the annulus wall) is dramatic. This is mostly caused by the blade scraping effect. At the mid-chord location ($X_R = 0.5$), the maximum value of T_x and T_θ have more than doubled from their value at the leading edge. There is a substantial increase in the intensities away from the blade tip (inside the passage), with significant increase in the T_θ value. Beyond the mid-chord location ($X_R = 0.75, 0.979$), both intensities decrease in the AWBL region. This may have been caused by the diffusion of the leakage jet. The turbulence level increases again as the flow proceeds from $X_R = 0.979$ to $X_R = 1.058$. This is caused by the intense mixing of the various flows and the diffusion of the wake in this region.

ANNULUS WALL BOUNDARY LAYER DEVELOPMENT IN THE STAGE

The AWBL development in the entire stage, starting from upstream of IGV to downstream of the rotor is presented in this section. The absolute system (s,n) is chosen to present this data. The data inside the blade passages (IGV and rotor) and immediately downstream of the blade trailing edges are passage-averaged values. The streamwise velocity ($\bar{V}_s$) profile is shown in Fig. 16, from stations 1 through 20 whose locations are tabulated in Table 1. The AWBL development is rapid and profiles are well-behaved up to the IGV trailing edge (station 5), beyond which the growth rate decreases. As the rotor is approached (station 13), dramatic changes in the AWBL occur. The shear layer in the outer region remains unchanged, but the flow in the tip region undergoes a large change due to the scraping effect of the blade. The inner region is modified by this scraping effect. The effect of the leakage flow is evident from the dip in velocity profiles at stations 15 ($X_R = 0.75$) and 16 ($X_R = 0.979$). The transition into a well-behaved turbulent boundary layer occurs at station 19 and beyond. Comparing the velocity profile at inlet (station 12) with those at the exit (station 20), it becomes clear that the leakage flow effects are just as important as those due to the pressure gradient in the AWBL growth and shear gradients in the outer layer.

The normal velocity profiles inside the AWBL at various axial locations are shown in Fig. 17. It should be noted here that the choice of the location where V_n is zero is arbitrary and is located at R = 0.886. The distribution shows some unusual features. The normal velocity at station 1 (upstream of IGV) is zero everywhere indicating that the boundary layer is two-dimensional. The three-dimensionality in the AWBL increases as the flow goes through IGV, the normal velocity reaching very high values near the exit of the IGV. Beyond this station, the normal velocity profiles remain nearly unchanged till the rotor leading edge, even though the deviation between α_e and α_w decreases between the IGV exit and the rotor leading edge (Fig. 2). The plot in Fig. 2 does not allow for the variation in the value of α_e between IGV and rotor blade row. This seems to indicate that the three dimensionality in the AWBL is either frozen or decreases. The negative values of V_n (Fig. 17) indicate that the flow inside the AWBL is turned more than the freestream, commonly referred to as "overturning." Near the rotor (station 12), the boundary layer still retains its three-dimensional character.

The boundary layer becomes highly three dimensional as the flow enters the rotor (station 13). The overturning at the rotor leading edge is large away from the wall, but is reduced considerably as the wall is approached. The overturning is due to the secondary flow, but the large reduction in V_n near the tip is brought about by the leakage flow. Inside the passage (stations 14 and 15), overturning (or negative values of V_n) is observed for R < 0.98, but near the wall the normal velocity reverses its direction, resulting in an underturning. This is caused by the leakage flow. Large overturning away from the tip can be attributed to the inviscid effects (design) and the secondary flow. It may also be caused by the roll up of the leakage jet, and its movement towards the suction surface as explained in ref. 6. The magnitude of the crossflow decreases as the flow proceeds downstream of the rotor (stations 17 and 18), and the flow is overturned at all locations. Immediately downstream of the rotor (between stations 17 and 18), the flow tends to become more three-dimensional, and this is caused by the mixing of the rotor wake leakage flow and the radial transport of the blade boundary layer. The three-dimensionality decreases again as the flow progresses downstream.

Integral Properties (Passage-Averaged Values)

The integral properties of the boundary layer were computed from expressions similar to eqs. (1 - 3, 6 and 7), but the velocities used were the passage-averaged values given by:

$$\bar{V}_i = \int_0^1 v_i \, dy.$$

The integration of eqs. (1 - 3, 6 and 7) is carried up to the edge of the AWBL. The procedure used in locating the edge of the AWBL has been described earlier and is illustrated in Fig. 12a. The boundary layer thickness is derived from the axial velocity profile and is used for computing $\bar{\theta}_{xx}$, $\bar{\delta}_x$.

The boundary layer growth for the most part of the IGV passage is gradual (Fig. 18). There is a decrease in their values downstream of the IGV trailing edge. Downstream of the IGV, the boundary layer growth is small up to X = 2.8. The sudden increase in the values of $\bar{\theta}_{xx}$ near the leading edge of the rotor is probably caused by the scraping effects of the blade. The values of $\bar{\theta}_{xx}$ and $\bar{\delta}_x$ increase as the flow progresses through the rotor up to mid-chord, then decrease from $X_R = 0.5$ to 0.75. There is a drastic decrease in their values near the blade trailing edge. This may be attributed to the presence of leakage flow and its "blowing" effect in reducing the growth of the AWBL. The values of $\bar{\theta}_{xx}$ and $\bar{\delta}_x$ remain nearly constant downstream of the rotor.

The AWBL data from a multi-stage compressor (ref. 16) and a single-stage compressor (ref. 15) are shown plotted with the authors' data on Fig. 18. The authors' data is much lower than the multi-stage compressor which is as expected. But Hunter [15] has measured larger boundary layer growth than the authors, this is caused by the larger displacement thickness coming into Hunter's rotor due to longer than usual inlet in his facility. The values of $\bar{\delta}_x$ at the rotor entry of ref. 15 for thin boundary layer and at t/c = 1.0% is about 5 mm compared to a corresponding value of 2.30 mm in the authors' facility.

PREDICTION OF THE AWBL GROWTH

A momentum integral technique developed to predict the growth of the three-dimensional boundary layer on rotor blades [17] was modified to predict the growth of the AWBL from the inlet of the guide vane to the inlet of the rotor. The crossflow direction (n), in this case, was taken to be normal to the absolute freestream as shown in Fig. 3. In the case of the rotor boundary layer, for which the technique was originally developed, the crossflow direction was radial. The geometry of the IGV section was approximated by circular-arc camber lines for the guide vane, and a trailing straight section was used between the guide vane and the rotor inlet. Appropriate curvature terms were used in the momentum-integral equations. The measured wall pressure distribution (Fig. 2) was input to the calculation procedure. The computation was started with the measured value of the momentum thickness (Fig. 18) and a shape factor of 1.286. The predicted values of the momentum thickness are compared with the measured data in Fig. 19. The growth of the boundary layer is predicted reasonably well within the guide vane. The rapid growth of the boundary layer in the region of the trailing edge of the guide vane is not captured. The predictions of the growth of the boundary layer upstream of the leading edge of the rotor are satisfactory. The predictions are poor beyond the leading edge of the rotor. A more detailed definition of the pressure field in these regions and modelling of the blade scraping effect and leakage flow would be required. The predictions of the deviation (ϵ) between the limiting (wall) streamline angle (α_w) and the freestream angle (α_e) for the absolute flow, is compared with the measured data in Fig. 20. While the overall magnitudes of ϵ are predicted, the distribution is not. This is most probably due to approximating the guide vane shape by circular arcs. In this case, the maximum crossflow would be expected, and is predicted, at the trailing edge of the blade.

It is beyond the capability of most analysis (refs. 1-4) and the authors' technique to predict the AWBL growth in a rotor as the flow field associated with blade motion and leakage flow is extremely complex.

CONCLUDING REMARKS

It is evident from the data presented in this paper that the annulus wall boundary layer growth inside a rotor passage is complex, modified greatly by the leakage flow and the pressure gradient. The growth of the AWBL, as well as its velocity profiles are very unconventional with considerable three-dimensionality and skewness in the profile. Any attempt to model this flow as a simple superposition of leakage flow over the AWBL would be inadequate to capture all of the AWBL characteristics. The perturbations caused by the rotor, both mechanical (scraping) and aerodynamic, are highly complex and affect the growth of the AWBL substantially. The boundary layer profiles inside the rotor have the features of "wall layer," "wall jet," and "wake." A fresh approach is needed to adequately describe and analyze this flow. The momentum integral technique developed by the authors provides good predictions inside the IGV passage and up to the rotor leading edge, beyond which the deviations are large and the technique fails.

T. ooundary layer inside the passage is highly asymmetric with substantial variation in the blade-to-blade direction. The AWBL in between the blade rows tends towards two-dimensional, axisymmetric boundary layers.

ACKNOWLEDGMENT

REFERENCES

1. Mellor, G. L., and Wood, G. M., "An Axial Compressor End Wall Boundary Layer Theory," Trans. ASME, J. Basic Engineering, Vol. 93, 1971, pp. 300-316.

2. DeRuyck, J., and Hirsch, C., "Investigations of an Axial Compressor End-Wall Boundary Layer Prediction Method," J. Engineering for Power, Vol. 103, Jan. 1981, pp. 20-33.

3. Comte, A., Ohayon, G., and Papailiou, K. D., "A Method for the Calculation of the Wall Layers Inside the Passage of a Compressor Cascade With and Without Tip Clearance," J. Engineering for Power, Vol. 105, 1983.

4. Horlock, J. H., and Perkins, H. J., "Annulus Wall Boundary Layers in Turbomachines," AGARD AG 185, 1974.

5. Lakshminarayana, B. and Sitaram, N., "Wall Boundary Layer Development Near the Tip Region of an IGV of an Axial Flow Compressor," ASME Paper 83-GT-171.

6. Lakshminarayana, B., Pouagare, M., and Davino, R., "Three Dimensional Flow Field in the Tip Region of a Compressor Rotor Passage," Parts I and II, J. Engineering for Power, Vol. 104, pp. 760-781, Oct. 1982.

7. Pandya, A., Lakshminarayana, B., "Investigation of the Tip Clearance Flow Inside and at the Exit of a Compressor Rotor Passage," Parts I and II, J. Engineering for Power, Vol. 105, Jan. 1983, pp. 1-17.

8. Smith, L. H., "Three Dimensional Flow in an Axial Flow Turbomachinery," WADC Tech. Rept. 55-348, Vol. 2, Johns Hopkins University, Aug. 1955.

9. Lakshminarayana, B., "An Axial Flow Compressor Facility Designed for Flow Measurements in a Rotor Passage," ASME J. Fluids Engineering, Vol. 102, No. 4, Dec. 1980, pp. 402-411.

10. Sitaram, N. and Lakshminarayana, B., "End Wall Flow Characteristics and Overall Performance of an Axial Flow Compressor Stage," NASA CR 3671, 1983.

11. Davino, R., "Three Dimensional Mean Flow and Turbulence Characteristics in the Annulus Wall Region of an Axial Flow Compressor Rotor Blade Passage," M.S. Thesis, Dept. of Aerospace Engineering, The Pennsylvania State University, 1980.

12. Pandya, A., "Investigations of the Tip Clearance Flow Inside a Compressor Rotor Passage and at the Exit of the Rotor," M.S. Thesis, Dept. of Aerospace Engineering, The Pennsylvania State University, March 1982.

13. Powell, J. A., Strazisar, A. J., Seaholtz, R. G., "Efficient Laser Anemometry for Intra-Rotor Flow Mapping in Turbomachinery," J. Engineering for Power, Vol. 103, pp. 424-429, April 1981.

14. Pouagare, M., Murthy, K. N. S. and Lakshminarayana, B., "Three-Dimensional Flow Field Inside the Passage of a Low-Speed Axial Flow Compressor Rotor," AIAA Paper 82-1006, 1982.

15. Hunter, I. H. and Cumpsty, N. A., "Casing Wall Boundary Layer Through an Isolated Compressor Rotor, J. Engineering for Power, Vol. 104, pp. 805, October 1982.

16. Smith, L. H., "Casing Boundary Layers in Multistage Axial Flow Compressors," Flow Research on Blading, ed. L. S. Dzung, Elsevier, Amsterdam, 1970.

17. Lakshminarayana, B. and Govindan, T. R., "Analysis of Turbulent Boundary Layer on Cascade and Rotor Blades of Turbomachinery," AIAA Journal, Vol. 19, pp. 1333, 1981.
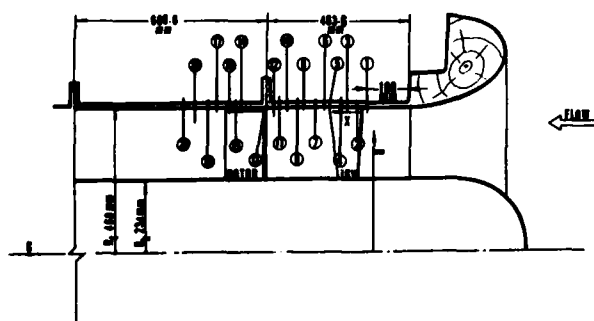
Fig. 1. The Schematic of the Blade Rows and the Measuring Stations
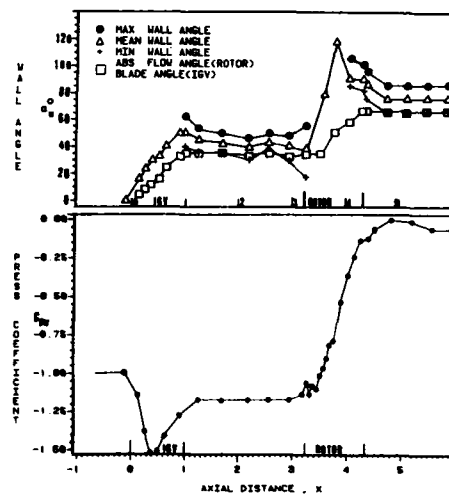
Fig. 2. Axial Variation of the Limiting (Wall) Streamline Angles and the Wall Static Pressure
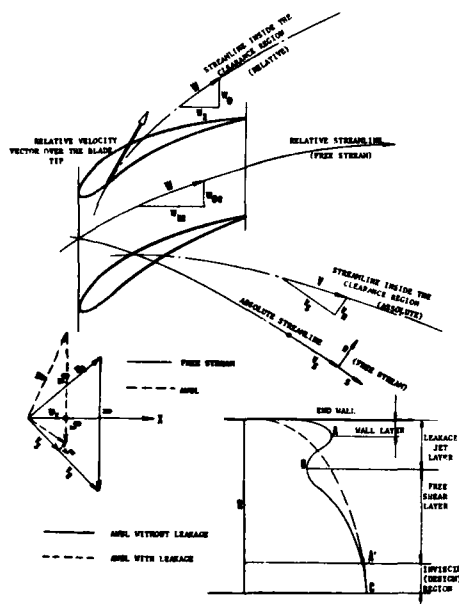
Fig. 3. Nature of Relative and
Absolute Flow Field and the
Velocity Profiles in the AWBL
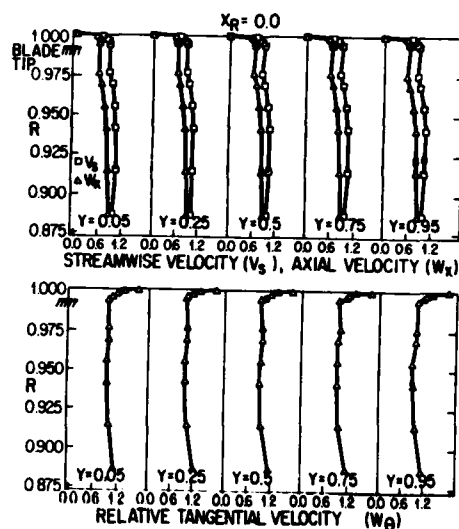
Fig. 4. Profiles of V_s, W_x, W_θ at the
Leading Edge $(X_R = 0)$
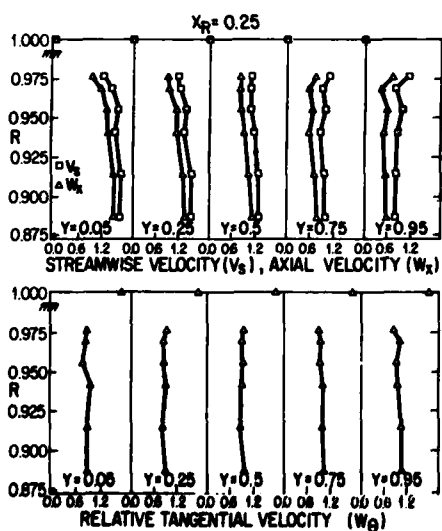
Fig. 5. Profiles of V_s, W_x, W_θ Inside
the Rotor Passage at $X_R = 0.25$
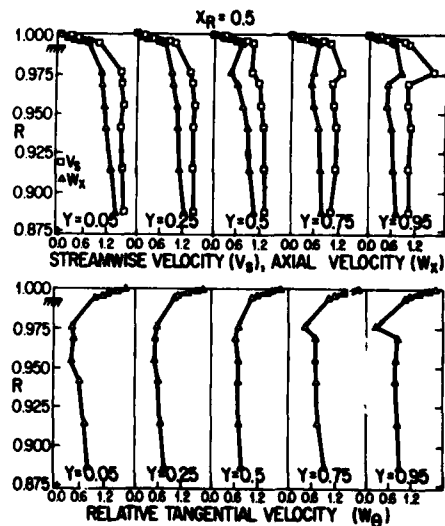
Fig. 6. Profiles of V_s, W_x, W_θ Inside
the Rotor Passage at $X_R = 0.5$
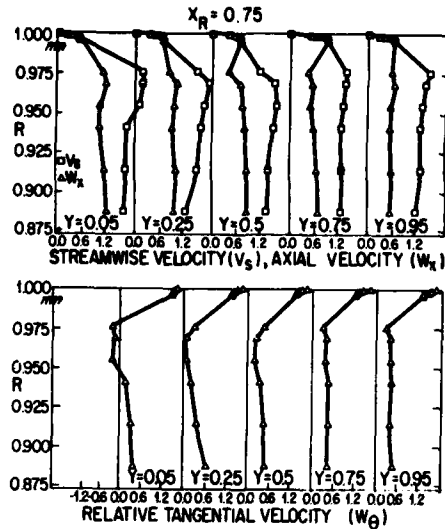
Fig. 7. Profiles of V_s, W_x, W_θ, Inside the Rotor Passage at $X_R = 0.75$
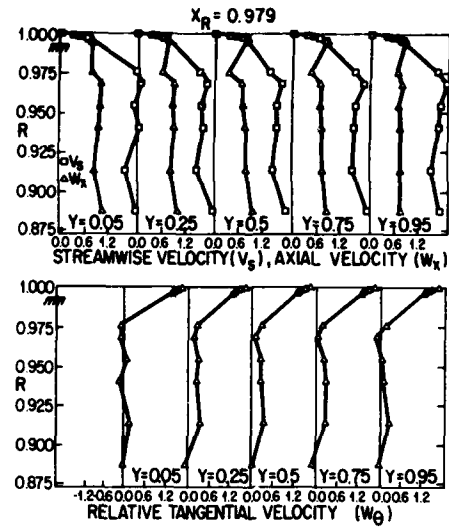
Fig. 8. Profiles of V_s, W_x, W_θ Inside the Rotor Passage at $X_R = 0.979$
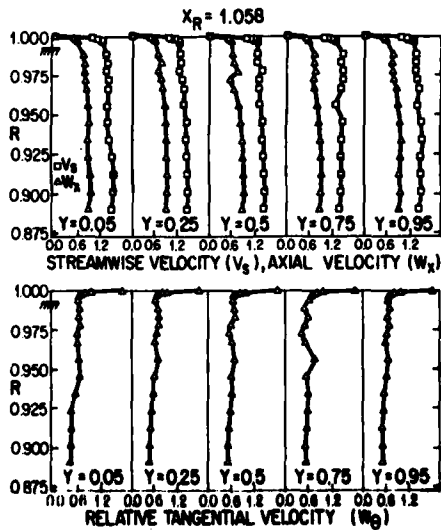
Fig. 9. Profiles of V_s, W_x, W_θ at the Exit of the Rotor Passage at $X_R = 1.058$
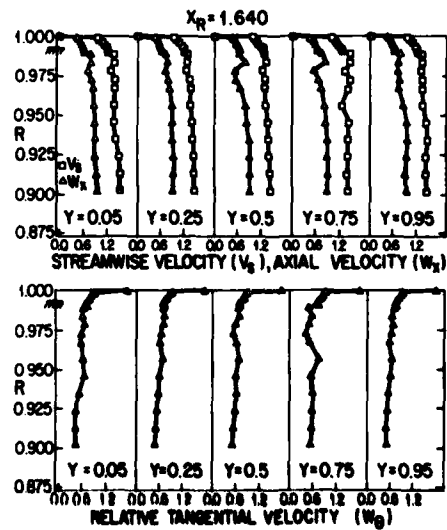
Fig. 10. Profiles of V_s, W_x, W_θ at the Exit of the Rotor Passage at $X_R = 1.640$
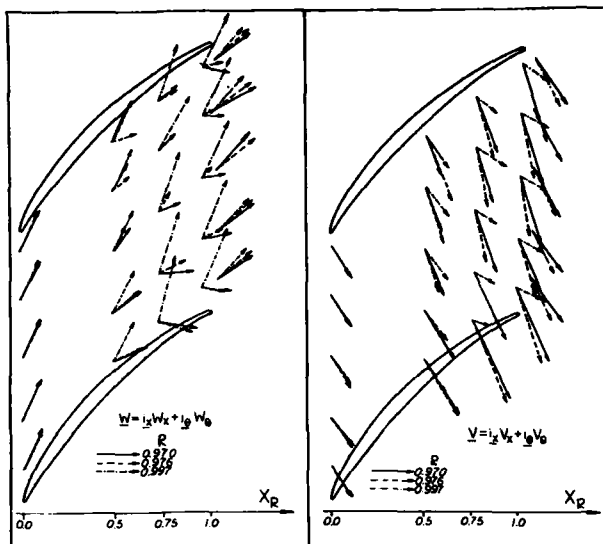
Fig. 11. Relative and Absolute Velocity Vectors Inside the Blade Passage (R=0.970, 0.976, 0.997)
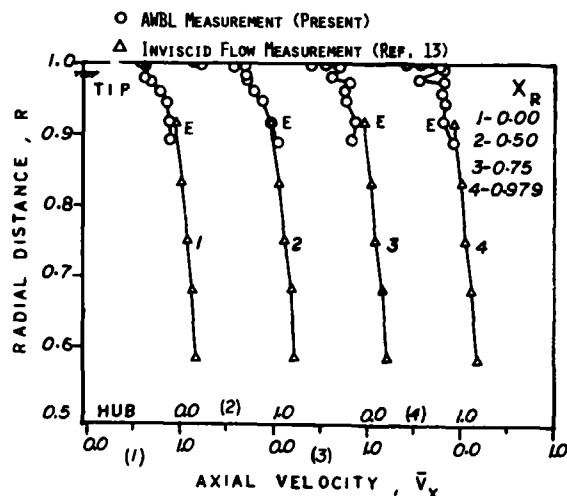
Fig. 12a. Radial Distribution of Passage-Averaged Axial Velocity ($\bar{V}_x$) and the Method of Locating Edge of the AWBL
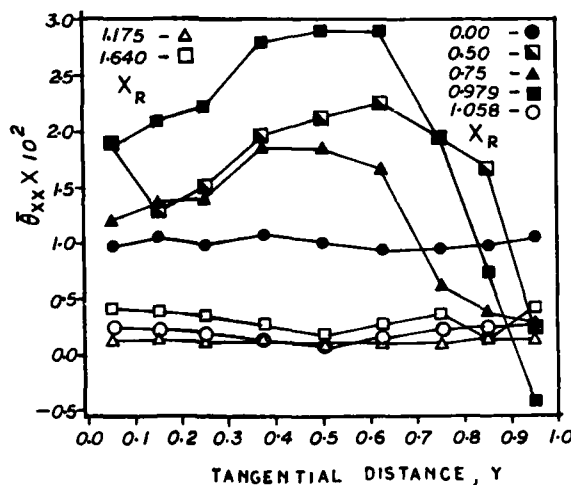
Fig. 12b. Blade-to-Blade Distribution of Momentum Thickness, $\bar{\theta}_{xx}$ Inside the Blade Passage and at the Exit of the Blade Passage
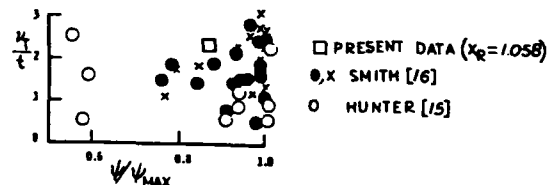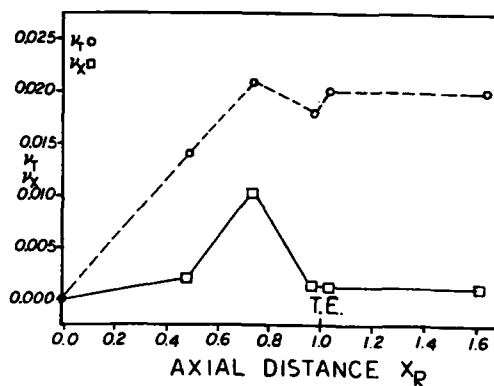
Fig. 13. Variation of the Force Defect Thicknesses (ν_T, ν_x)
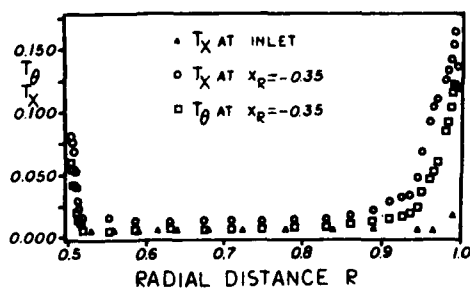
Fig. 14. Axial and Tangential Turbulence Intensity Profiles Upstream of IGV and at $X_R = -0.35$
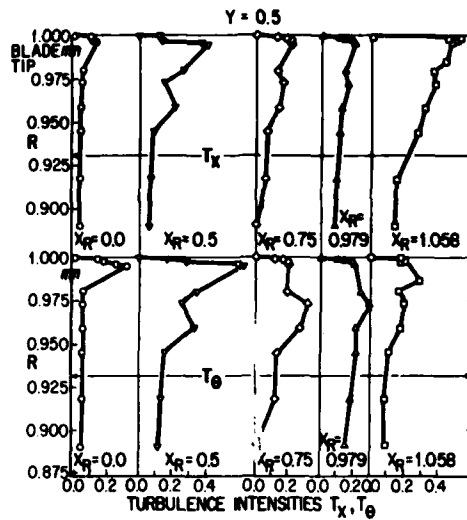
Fig. 15. Axial and Tangential Turbulence Intensity
Profiles at Mid-Passage and at Different
Axial Locations Inside the Rotor
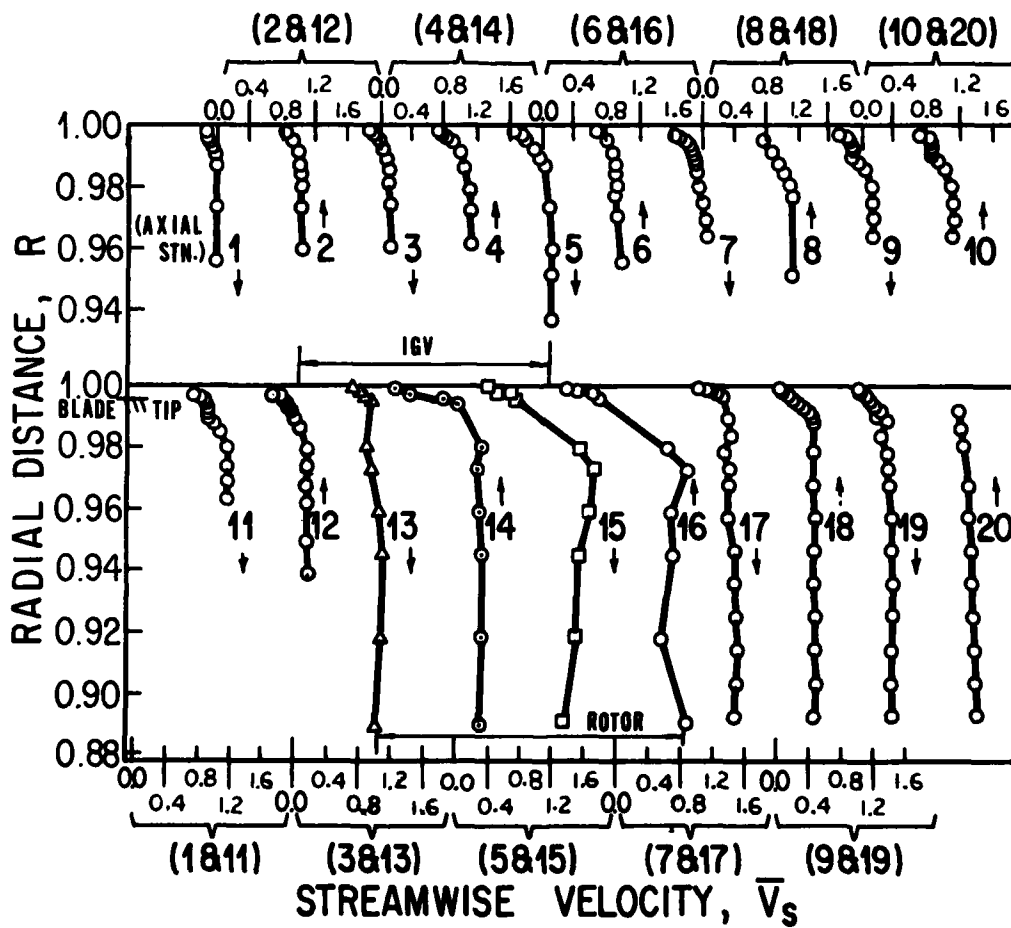
Fig. 16. AWBL Development in the Compressor Stage, $\overline{V}_s$ Profile
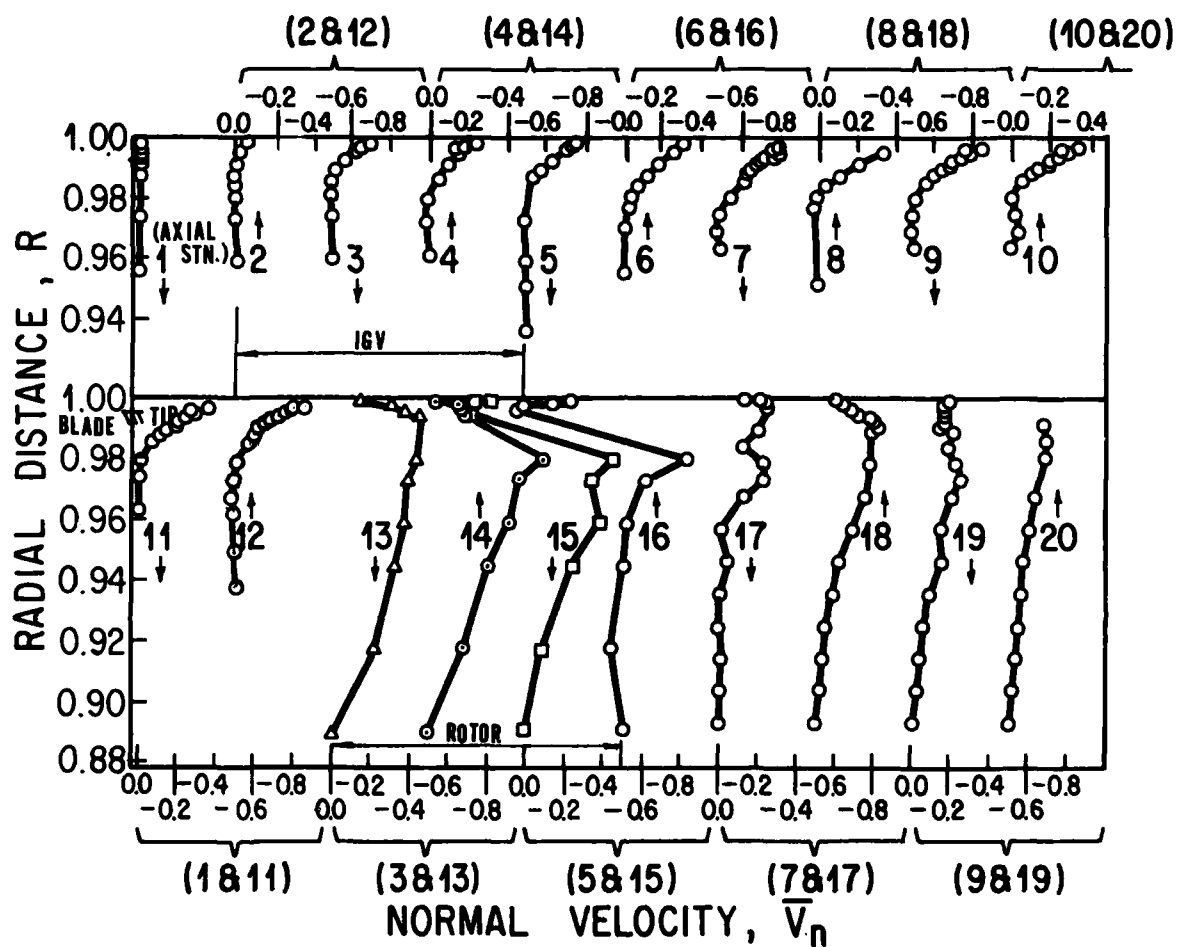
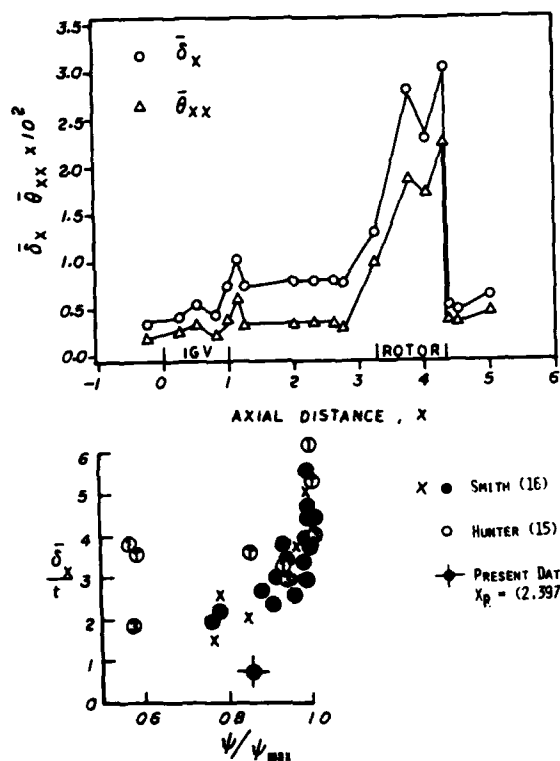Fig. 17. AWBL Development in the Compressor Stage, V_n Profile

Fig. 18. Axial Variation of the Passage-Averaged $\bar{\theta}_{ss}$, $\bar{\delta}_s$, $\bar{\delta}_x$ for the Stage and Comparison with Earlier Data
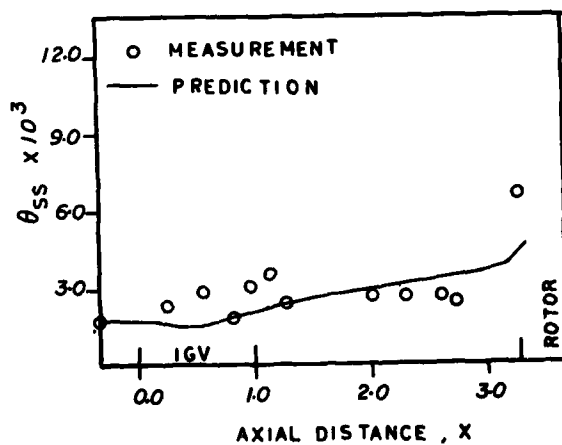

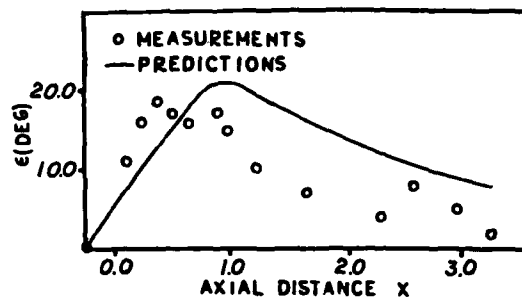Fig. 19. Predicted and Measured Values of Momentum Thickness, $\bar{\theta}_{ss}$

Fig. 20. Predicted and Measured Values of ϵ

DISCUSSION

J.G.Moore, US

Considering the large changes in static pressure and flow direction in the rotor tip region the streamwise momentum thickness (Fig.12) is an appropriate parameter for understanding the losses in annulus wall boundary layers. A more appropriate integral parameter might be based on total pressure or entropy.

Author's Reply

The message we were trying to convey in this paper is simply the growth of the annulus wall boundary layer in the tip region of a compressor. We did not seek to analyze the losses, and we do agree with the discusser that for the evaluation of the losses one needs to look at the total pressure or entropy. The momentum thickness as plotted in this paper was meant to study the development of the boundary layer growth which is expressed in terms of either the displacement or the momentum thickness. We are planning to measure the total pressure also and derive the losses in this region.

F.Leboeuf, Fr

I just want to make a comment on the use of a proper frame of reference in order to derive integral thicknesses, like for the momentum thickness. For instance, when using the axial or meridional direction, we have found in our compressor shown in page 20, and for particular operating point, that the axial momentum thickness could be negative. And this could create some problems if one searches to analyze such experimental results in terms of 'boundary layer' concepts, such as to try fitting the axial velocity with analytical profile.

Author's Reply

We do agree with the fact that in some cases the momentum thickness may become negative, and this has been noticed in our experimental data, especially near the blade surfaces (Figure 12b of the revised version). This is again closely tied in with the location of the edge of the boundary layer. If the edge of the boundary layer is not properly located by either analysis or the inviscid flow data, one could envision taking the edge far into the stream which will then include the contribution to the momentum thickness from the inviscid flow as well as the viscous flow, and that could show a negative thickness. We feel that the negative values of momentum thickness θ_{xx} observed results from the beneficial or blowing effect of the leakage flow on the annulus wall boundary layer.

K.Papailiou, Gr

(1) The results you have presented in integral form are given in the absolute system. It would be, maybe, instructive to give them for the rotor in the rotating frame.

(2) How have you analyzed the flow into two parts in order to calculate these integral quantities?

(3) Have you compared the three types of measurements (laser, hot wire and pneumatic) in order to see if they agree? Did you observe any non-stationary influence on the pneumatic probe measurements?

Author's Reply

Since this paper deals with the boundary layer development in the entire stage including the upstream of the IGV passage, exit of the IGV, exit of the rotor, inside the rotor, we thought it would be appropriate to stay with one convention, namely, the absolute system for the entire stage. The momentum thickness, θ_{xx} is common to both the coordinate systems. In the revised paper (present version), the emphasis is placed only on the behaviour of θ_{xx}.

The flow was analyzed by utilizing the inviscid data available from Reference 13. This inviscid data was matched with the anulus wall boundary layer data presented in the paper, as shown in Figure 12 a, and utilizing this, the inviscid region was recognized, and thus, locating the edge of the annulus wall boundary layer. There are some disadvantages in doing this, but in an extremely complicated flow such as this one, this is as good a method as we could devise.

Coming to the last point, we did measure the flow field far downstream of the rotor using the LDV, hot-wire as well as pneumatic probes. Since the flow was measured far downstream where it is steady, no non-stationary influences were felt, and all the three measurements agreed quite well in most of the regions.

END-WALL BOUNDARY LAYER MEASUREMENTS IN A TWO-STAGE FAN

Calvin L. Ball, Lonnie Reid, and James F. Schmidt
National Aeronautics and Space Administration
Lewis Research Center
21000 Brookpark Road
Cleveland, Ohio 44135
U.S.A.

SUMMARY

Detailed flow measurements made in the casing boundary layer of a two-stage transonic fan are summarized. These measurements were taken at stations upstream of the fan, between all blade rows, and downstream of the last blade row. At the design tip speed of 429 m/sec the fan achieved a peak efficiency of 0.846 at a pressure ratio of 2.471. The boundary layer data were obtained at three weight flows at the design speed: one near choke flow, one near peak efficiency, and one near stall. Conventional boundary layer parameters were calculated from the data measured at each measuring station for each of the three flows. A classical two-dimensional casing boundary layer was measured at the fan inlet and extended inward to approximately 15 percent of span. A highly three-dimensional boundary layer was measured at the exit of each blade row and extended inward to approximately 10 percent of span. The steep radial gradient of axial velocity noted at the exit of the rotors was reduced substantially as the flow passed through the stators. This reduced gradient is attributed to flow mixing. The amount of flow mixing was reflected in the radial redistribution of total temperature as the flow passed through the stators. The data also show overturning of the tip flow at the stator exits that is consistent with the expected effect of the secondary flow field. The blockage factors calculated from the measured data show an increase in blockage across the rotors and a decrease across the stators. For this fan the calculated blockages for the second stage were essentially the same as those for the first stage.

SYMBOLS

C_f	skin friction coefficient, eq. (B6)
C_p	specific heat at constant pressure, 1004 J/kg K
D	diffusion factor, eq. (A1)
H_c	axial compressible form factor, eq. (B4)
H_i	axial incompressible form factor, eq. (B5)
K	blockage allowance, $1 - K_b$
K_b	blockage factor, eq. (A11)
K_{des}	design blockage allowance, $K_2 + K_3$
K_{meas}	calculated blockage from measured data, $K_1 + K_2$
K_1	equivalent blockage allowance associated with design end-wall loss
K_2	design blockage to account for tempering of design end-wall loss gradient relative to actual (measured gradient)
K_3	blockage resulting from nonaxisymmetric flows, eq. (A12)
M	Mach number
N	rotative speed, rpm
P	total pressure, N/cm^2
p	static pressure, N/cm^2
Pr	Prandtl number, 0.71
R	universal gas constant
r	radius, cm
T	total temperature, K
t	static temperature, K
U	wheel speed, m/sec; boundary layer air velocity, m/sec

V	air velocity, m/sec
W	weight flow, kg/sec
$W(y/\delta)$	eq. (B12)
y	boundary layer distance from wall
z	axial distance referenced from rotor-blade-hub leading edge, cm
φ	relative air angle (angle between air velocity and axial direction), deg
γ	ratio of specific heats
δ	ratio of rotor-inlet total pressure to standard pressure of 10.13 N/cm^2; edge of boundary layer distance
δ^*	displacement thickness, eq. (B3)
η	efficiency
θ	ratio of rotor-inlet total temperature to standard temperature of 288.2 K; momentum thickness, eq. (B2)
μ	dynamic viscosity
ρ	density
Π	eq. (B10)
σ	solidity; ratio of chord to spacing
φ	flow coefficient, eq. (A7)
ψ_p	head-rise coefficient, eq. (A6)
ψ_T	temperature-rise coefficient, eq. (A9)

Subscripts:

ad	adiabatic (temperature rise)
aw	adiabatic wall condition
b	boundary layer
des	design
e	edge-of-boundary-layer condition
h	hub
inv	inviscid flow
LE	blade leading edge
meas	measured quantity
p	polytropic
ref	reference temperature condition
TE	blade trailing edge
t	tip
w	wall condition
x	boundary layer axial direction
z	boundary layer tangential direction
θ	flow tangential direction
τ	shear
0	plenum condition

Superscripts:

'   relative to blade

¯   average quantity

INTRODUCTION

The strong influence of end-wall flows on compressor performance is well rec-
ognized. The potential benefit of being able to model these flows in multistage axial-
flow compressors is evident by the large number of researchers who have treated various
aspects of the subject over the years. The results of some of this research are pre-
sented in references 1 to 13 and summarized by Hirsch and Denton in reference 14. This
modeling effort has treated, in addition to what might be considered the more classical
annulus end-wall boundary layer approach, the influence of the various secondary flows
on both the through-flow and tangential-flow radial gradients. The secondary-flow
effects that have been considered include the passage vortex, flows due to secondary
stresses, corner vortices, leakage flows, and the migration of the blade surface bound-
ary layers, which tend to accumulate in the end-wall regions. Koch and Smith in refer-
ence 15 present a method for calculating the design-point efficiency potential of a
multistage compressor that is based to a large extent on modeling the end-wall flows.
Adkins and Smith in reference 16 present an approximate method to account for spanwise
mixing in design through-flow calculation procedure. The spanwise mixing that occurs
in a multistage axial-flow compressor is recognized to have a strong influence on the
extent of the apparent end-wall boundary layer and thus on energy addition and losses.
The Adkins and Smith procedure takes into account main-stream non-free-vortex flows,
end-wall boundary layers, blade-end clearances, blade-end shrouding, and blade-surface
boundary layer and wake centrifugation on flow mixing.

The success of the various modeling efforts is highly dependent on adequate experi-
mental data for developing, extending, and validating the various features of the end-
wall flow models. The NASA Lewis Research Center has a strong interest in the modeling
of the end-wall flows in turbomachinery and in the validation of these models. The
objective of this study was to obtain detailed flow measurements in the casing boundary
layer of a two-stage transonic fan in order to expand on the somewhat limited experi-
mental data base available from high-speed, high-pressure-ratio multistage fans and
compressors for use in modeling and code verification.

The aerodynamic design along with the overall and blade-element performance of this
fan is presented in reference 17. Data from this fan were used as a test case by the
AGARD Propulsion and Energetics Panel, Working Group 12, for through-flow calculations
in axial turbomachines. The results of that effort are presented in reference 14.

The flow measurements made in the casing boundary layer of this fan are presented in
detail in reference 18 in both tabular and graphical forms. The data presented herein
include the radial distributions of various flow parameters along with calculated bound-
ary layer parameters based on the flow measurements. Data are presented for stations
upstream of the fan, between all blade rows, and downstream of the last blade row for
three weight flows at design speed: one near choke flow, one near peak efficiency, and
one near stall.

DeRuyck and Hirsch of the Department of Fluid Mechanics, Vrije Universiteit-Brussel,
Brussels, Belgium, calculated the boundary layer parameters for this fan by using their
end-wall boundary layer prediction method for multistage axial-flow compressors (ref.
13). Their calculations used as input the aerodynamic design for the two-stage fan to
include the running clearance for the blading and the flow points at which data were
obtained. Comparisons between measured and predicted velocities in the end-wall region
are presented by deRuyck and Hirsch in reference 19.

The experimental data were obtained from tests conducted in the multistage com-
pressor test facility at the Lewis Research Center, National Aeronautics and Space
Administration, Cleveland, Ohio, U.S.A.

APPARATUS AND PROCEDURE

Two-Stage Fan

The overall design parameters for the two-stage fan are presented in table I. Flow
blockage allowances are presented in table II. The flow path and axial locations of the
measuring stations are shown in figure 1. The two-stage fan assembly is shown in fig-
ure 2. One obvious feature of this fan is the unusually large axial spacing between
blade rows. It was configured this way to provide a fan representative of one designed
to minimize blade-row interaction noise. Figure 2 shows the fan with casing treatment
over the rotors. However, when taking the boundary layer data, solid inserts were
installed over the rotor tips.

The fan was originally designed with a first-stage rotor having an aspect ratio of
2.9 and incorporated a part-span damper to eliminate potential aeroelastic problems.
A number of damper configurations were tested in an attempt to maximize aerodynamic per-

formance and to maintain structural integrity. The results are reported in references 20 to 22. None of these configurations achieved the desired efficiency levels.

The first stage was redesigned to accommodate a rotor having an aspect ratio of 1.5, which eliminated the need for the dampers. The design and performance of the fan incorporating the low-aspect-ratio first-stage rotor are presented in reference 17. This modification resulted in a fan having excellent performance.

The fan with the low-aspect-ratio first-stage rotor was judged to be hub critical in terms of the blade elements that were controlling the stall line at the higher speeds. This judgment was in part based on the insensitivity (lack of movement) of the stall line to casing treatment. In addition the blade-element data indicated that the stall line was most likely being controlled by the flow in the hub region of the second stage (ref. 17).

The end-wall boundary layer measurements were obtained in the two-stage fan having the low-aspect-ratio first-stage rotor. Contrary to statements in reference 18, as noted earlier in this paper, circumferentially grooved casing treatment was not in-stalled over both rotors during the boundary layer surveys. The rotor-tip running clearances were estimated to be 0.04 cm at design speed. The stator design incorporated a full chordwise platform at the tip, therefore eliminating the clearances.

The design of the low-aspect-ratio first-stage rotor considered an inlet-tip bound-ary layer total pressure based on unreported boundary layer survey data obtained with the configuration reported in reference 21. This resulted in the first-stage-rotor blading having leading-edge end-wall bends. The computer program used in the design and described in reference 23 was unable to handle the measured steep total-pressure gradi-ent through the outer-wall boundary layer region. To alleviate this problem, the total-pressure distribution was tempered and combined with an end-wall blockage allowance of 0.01. It was expected that this modified accounting of the boundary layer would more closely aline the blade with the flow entering the rotor at the tip and result in reduced losses. At the other stations in the two-stage fan, the hub and casing boundary layers were accounted for by increasing the flow loss in the end-wall regions and adding a blockage allowance. The blockage allowances at the tip were 0.013 at the first-stage rotor exit, 0.018 at the first-stage stator inlet, and 0.020 at all other leading- and trailing-edge locations. Blockage allowances at the hub were the same as those at the tip. The combined hub and tip blockage allowance is given in table II.

The general level of blade loading is indicated by the design diffusion factors at the tip of the first- and second-stage rotors of 0.451 and 0.410, respectively, and the first- and second-stage stators of 0.472 and 0.464, respectively. The definition used in calculating the diffusion factors is given in appendix A.

Compressor Test Facility

The two-stage fan was tested in the multistage compressor facility, which is de-scribed in detail in reference 20. A schematic diagram of the facility is shown in fig-ure 3. Atmospheric air enters the test facility at an inlet located on the roof of the building and flows through the flow-measuring orifice, through the inlet butterfly throttle valves, and into the plenum chamber upstream of the test fan. The air then passes through the test fan into the collector and is exhausted either to the atmosphere or to an altitude exhaust system. Mass flow is controlled with a sleeve valve in the collector. For this series of tests the large inlet butterfly valve was positioned fully open to provide near atmospheric pressure at the inlet to the fan. The air was exhausted to the atmosphere.

Instrumentation

Radial surveys of the flow conditions between 1 and 30 percent of passage height from the casing were made at the fan inlet, behind each rotor, and behind the two stator-blade rows (fig. 1). Indicated values of total pressure, static pressure, total temperature, and flow angle were measured with combination probes (fig. 4). Wall static pressures were also recorded at each survey station. Each probe was alined in the streamwise direction with a null-balancing control system. The thermocouple material was Chromel-constantan. All pressures were measured with calibrated transducers. Two combination probes were used at the compressor inlet, behind each rotor, and behind the first-stage stator; four combination probes were used behind the second-stage stator. The circumferential locations of the probes and wall static taps at each measuring station are shown in figure 5. The probes behind the stators were circumferentially traversed one stator-blade passage clockwise from the nominal values shown. The fan mass flow was determined with a calibrated thin-plate orifice located in the inlet line. An electronic speed counter, in conjunction with a magnetic pickup, was used to measure rotative speed (rpm).

The validity of using the combination probe for obtaining boundary layer measure-ments was established by comparison with the survey probe and boundary layer rakes mea-surements reported in reference 24. These boundary layer rakes were used in conjunction with the combination probes when obtaining the unpublished inlet-casing boundary layer measurements used in the design of the low-aspect-ratio first stage and discussed earlier. Excellent agreement was obtained between the survey probe and the boundary

layer rakes to within 1 percent of span. This in part is attributed to the accuracy to which the probe can be positioned in the radial direction.

The errors in the data estimated from the inherent accuracy of the instrumentation and the recording systems are as follows:

Mass flow, kg/sec . . . . ±0.3

Rotative speed, rpm . . . . ±30

Flow angle, deg . . . . ±1

Temperature, K . . . . ±0.6

Total pressure (stations 1 and 2), N/cm^2 . . . . ±0.07

Total pressure (station 3), N/cm^2 . . . . ±0.10

Total pressure (stations 4 and 5), N/cm^2 . . . . ±0.17

Indicated static pressure (stations 1, 2, and 3), N/cm^2. . . . . ±0.07

Indicated static pressure (stations 4 and 5), N/cm^2. . . . . ±0.17

Radial position, cm . . . . ±0.003

Test Procedure

The data for the boundary layer surveys were taken at three mass flows ranging from maximum flow to near stall at design equivalent rotative speed. At each flow condition, data were recorded at 10 radial positions at each of the five measuring stations. At the fan-inlet and rotor-exit stations (stations 1, 2, and 4), radial distributions of total pressure, static pressure, total temperature, and flow angle were recorded. At each radial position behind the stators (stations 3 and 5) the combination probes were circumferentially traversed to 10 equally spaced locations across a stator-blade gap. Values of total pressure, static pressure, total temperature, and flow angle were recorded at each circumferential position.

Data Reduction

Redundant measurements at each measuring station were arithmetically averaged. Indicated total pressures and static pressures were corrected for streamline slope, and total temperatures were corrected for recovery based on Mach number, streamline slope, and pressure environment (ref. 25). The measured temperature was then adjusted to the streamline (radial position) of the pressure measurement. All data were corrected to standard-day conditions based on values at 30 percent of the passage height at the first-stage rotor inlet. At the stator exits, radial distributions of gap-averaged (axisymmetric) parameters were obtained as follows: the circumferential distributions of total temperature were mass averaged, total pressure was energy averaged, and flow angle was arithmetically averaged. Circumferential distributions of parameters were obtained as follows: the Mach number at each radial and circumferential position behind a stator was calculated from the measured total pressure at each radial and circumferential position and an arithmetically averaged static pressure at each radial position, absolute velocity was calculated from the Mach number and measured total temperature, and absolute velocity and measured flow angle were used to calculate axial and tangential velocity components.

Selection of Static Pressure

Total-pressure, total-temperature, and flow angle measurements were taken at 10 radial positions between 1 and 30 percent of passage height from the casing. To acquire static pressures for the boundary layer surveys, the side balancing holes on the combination probes (fig. 4) were manifolded to read an indicated static pressure. Figure 6 is a comparison of the measured static pressures at station 1 from the boundary layer surveys at a mass flow of 34.23 kg/sec and calculated static pressures from full-passage-height surveys at 34.27 kg/sec (ref. 17). At 30 percent of passage height the measured static pressure was lower than the calculated static pressure.

The calculated static pressures were determined by using design end-wall blockage values. It would appear that, if the blockage value were adjusted until the calculated value at 5 percent of passage height matched the wall static value, the calculated value at 30 percent of passage height would nearly equal the measured value as well.

Since the accuracy of the static-pressure measurement was uncertain near the casing, it was assumed that a linear distribution of static pressure between the wall static and the measurement at 30 percent of passage height could be used to reduce the boundary-layer survey data. However, all measured static pressures are available from reference 18.

Boundary Layer Calculation Procedure

The procedure used in calculating the end-wall boundary layer parameters from measured data was based on a concept originally presented by van Dyke (ref. 26) and referred to as "matched asymptotic expansion." It was extended to turbomachinery flows by Mellor and Wood (ref. 6) as a means of separating the core flow from the end-wall boundary layer flow and establishing the boundary layer edge. Ludwieg and Tillman's empirical relationship (ref. 27) was used to calculate a skin friction coefficient. A similar approach is used by deRuyck and Hirsch in their axial compressor end-wall boundary layer prediction method (ref. 13). Schmidt in evaluating the performance of a sonic inlet (ref. 24) also uses this basic procedure. A detailed description of the procedure is given in appendix B. A graphical description of the inviscid velocity profile and the boundary layer profile obtained from the measured velocity profile when applying this procedure is given in figure 7.

RESULTS AND DISCUSSION

The overall and stage performance of the two-stage fan is presented in figures 8 and 9. Figures 10 to 14 show the radial distributions of various flow parameters between 1 and 30 percent of passage height at each measuring station. Figure 15 presents radial and circumferential distributions of axial velocity at the stator exits. The data in these figures are presented in tabular form in reference 18. The calculated boundary layer parameters are presented in table III. The calculated blockage factors based on measured data are compared with design values in table IV.

Overall and Stage Performance

The overall performance of the two-stage fan with the low-aspect-ratio first-stage rotor is presented in figure 8. At the design tip speed of 429 m/sec the fan achieved a peak efficiency of 0.846 at a pressure ratio of 2.471. Arrows pointing to the design speed line indicate the locations where the boundary layer data were obtained. The stage performance is given in figure 9. The first stage achieved a peak efficiency of 0.870 at a pressure coefficient of 0.257 (pressure ratio = 1.655). The second stage achieved a peak efficiency of 0.842 at a pressure coefficient of 0.260 (pressure ratio = 1.494).

A detailed examination of the blade-element data for the fan indicates that the stall line near design flow was most likely controlled by the flow in the hub region of the second stage. Unreported test results obtained on the first stage operating as a single stage indicate a stall flow of 30.8 kg/sec, which was appreciably below that for the two stages. This is further evidence that the stall line was being controlled by the second stage.

Radial Distributions at Measuring Stations

The results presented in figures 10 to 14 are for design speed at three equivalent mass flows: 34.63 kg/sec (near choke), 34.23 kg/sec (near peak efficiency), and 34.01 kg/sec (near stall). The solid lines in the figures are design values and the symbols are measured values. The boundary layer edges calculated by the previously described procedure are noted in the figures.

First-stage rotor inlet (station 1). - The wall boundary layer at the fan inlet was the most clearly identifiable and is reflected in the defect in total pressure near the wall and the associated relatively steep gradient in axial velocity (fig. 10). Since the fan did not employ an inlet guide vane, the end-wall boundary layer flow at this location was collateral, and thus a classical two-dimensional boundary layer existed. The outer casing curvature at the fan inlet (fig. 1) tended to induce an axial velocity gradient over a greater portion of the blade span than that caused by the defect in total pressure.

Note that the calculated boundary-layer-edge location determined by applying the van Dyke-Mellor-Wood approach (appendix B) was at approximately 15 percent of span from the tip (fig. 10). Even through the plots show a nearly constant total pressure beyond 10 percent of span, the tabular data presented in reference 18 show that the total pressure decreased slightly from approximately the 15 percent spanwise location. This somewhat validates the procedure for separating the inviscid effects (in this case streamline curvature) from the viscous end-wall boundary layer effect in establishing a boundary-layer-edge location. This application provides some confidence for generally applying this procedure. However, it is recognized that validation of the procedure with the two-dimensional collateral boundary layer flow at the fan inlet does not represent a complete validation of the procedure with the three-dimensional skewed boundary layer flows at the other blade-row stations.

The axial velocity was higher than design over most of the outer 30 percent of the passage height (fig. 10). This velocity difference was due at least in part to the mass flow being higher than design. The measured velocity decreased rapidly from 5 percent of span to the outer wall, and this was consistent with the decrease in total pressure. The tempered total-pressure gradient used in the design at the rotor inlet resulted in a radial mismatch in relative flow angle and thus in incidence angle from design, as would

be expected. The comparison of design and measured total-pressure distributions through the end-wall region illustrates a design problem. The measured total-pressure profile reflects the real flow loss gradient, but the design total-pressure profile reflects the approximate loss gradients that can be accommodated in typical axisymmetric design calculations. The differences resulted in the need for an end-wall flow blockage correction and an unavoidable mismatch in relative flow angle and incidence angle from the design intent. This same reasoning, of course, applies at all blade-row inlet and outlet stations. A slight increase in total temperature was detected that is difficult to explain but often observed.

First- and second-stage rotor exits (stations 2 and 4). - Similar trends in the radial distribution of flow parameters existed at the first- and second-stage rotor exits (figs. 11 and 13). From approximately 10 percent of span to the outer wall the parameters deviated appreciably from free-stream values, reflecting the impact of the end-wall boundary layer on these parameters. The calculated boundary layer edge was in close proximity to the rapid falloff in velocity. For both rotor rows the penetration of the high-loss region (composed of end-wall boundary layer and associated secondary flows) into the free stream was approximately one-half that of the staggered spacing, a penetration parameter suggested by Smith (ref. 4).

As shown by the radial distributions of flow angles in figures 11 and 13, the boundary layer flow behind the rotors was a highly skewed, three-dimensional flow, in contrast to the two-dimensional end-wall boundary layer that existed at the first-stage rotor inlet. The data show axial velocities in the high-shear end-wall region that are appreciably lower than free-stream values and are consistent with the decay in total pressure near the wall. The lower axial velocities resulted in higher end-wall energy additions, as reflected in the tangential velocities and the temperature. This higher energy addition existed even though the relative flow angles reflected higher deviation angles and lower relative flow turning than free-stream values. The lower end-wall total pressure coupled with the high temperature reflected a low tip-region efficiency for the first stage. It was not as obvious for the second stage because of the radial gradients in flow parameters at both the rotor inlet and exit. However, close examination revealed the same to be true for the second stage. The much higher than design absolute flow angles in the end-wall region at the rotor exits reflected a higher than design incidence coming into the stators.

First- and second-stage stator exits (stations 3 and 5). - The trends in flow parameters behind the stators (figs. 12 and 14) were similar to those observed behind the rotors (figs. 11 and 13). However, the magnitude of the gradients was greatly reduced. The tempering of the end-wall gradients as the flow passed through the stator was particularly evident when comparing the axial velocity profiles between stations. The gradient in axial velocity near the wall at the stator-exit measuring stations (figs. 12 and 14) was much less than that at the rotor-exit measuring stations (figs. 11 and 13). From figures 12 and 13 it can be seen that the total-temperature profile leaving the first-stage rotor was redistributed as it passed through the following stator. Measured total temperatures near the wall at the stator exit were lower than the corresponding temperatures at the rotor exit. Conversely, total temperatures in the free-stream region were higher at the first-stage stator exit than at the first-stage rotor exit. This redistribution of total temperature is considered to be a result of mixing. It is reasoned that the mixing would increase with larger axial spacing between blades and thus could be greater for this fan than for fans with closely coupled blade rows. Note that the calculated boundary-layer-edge location was far inboard of the more noted falloff in axial velocity. This could also be a result of flow mixing. The plots of absolute flow angle show a 6° overturning of the flow near the casing (past the 0° design outlet flow angle) at the first-stage stator exit and a 4° overturning of the flow at the second-stage stator exit. This reflects the strength in the crossflow component from the pressure surface to the suction surface within the stator passage.

Circumferential Distributions at Stator Exit Stations

The radial and circumferential distributions of axial velocity behind the first- and second-stage stators (stations 3 and 5) are plotted in figure 16 for a mass flow of 34.23 kg/sec. For clarity, only 5 of the 10 radial positions at each station are plotted. The wakes behind both stators were less pronounced at 30 percent of the passage height than at 3 or 4 percent of the passage height. This reflects an increase in flow blockage caused by the nonaxisymmetric flow field near the walls. The wake also appeared to shift circumferentially toward the pressure side of the blade near the tip of both stators. This reflects the crossflow component from the pressure surface to the suction surface, which results in the overturning noted earlier. The axial velocity at the edge of the wake on the suction side of the blade was significantly lower than the corresponding velocity at the tip on the pressure side. This velocity imbalance existed at 1 and 2 percent of passage height and was nearly gone at 3 or 4 percent of passage height. The data indicate that the gap-average profile used in the boundary layer calculations did contain secondary flow effects and that the classical boundary layer parameters calculated from the measured data reflect the presence of this secondary flow field.

Boundary Layer Calculations

The boundary layer parameters calculated from the measured data are presented in table III. Only small differences are noted between the different flow points. This might be expected because of the relative closeness of the points, coupled with the fact that the fan did not appear to be tip critical, as discussed earlier. It is reasoned that only when the tip is critical would an increase in displacement thickness and flow blockage be expected for the tip when near stall. It is interesting that an incompressible form factor of 1.5 or less for all axial stations and flow points was calculated since it is generally accepted that an incompressible form factor in the range of 1.8 to 2.2 signals separation of a two-dimensional collateral boundary layer. This would appear to be additional evidence that the tip flow across the fan did not initiate stall.

The easiest parameter to examine in order to get a physical insight and appreciation for the boundary layer calculation is the blockage factor. With the blockage being one minus the blockage factor the conversion was made to compare measured blockages with design values in table IV. Before discussing the comparisons one must consider what constitutes the blockage calculated from the measured data and what the design blockage allowance represents. The radial distribution of axial velocity used to calculate an end-wall boundary layer is influenced by a number of factors. Two of these factors (fig. 16) are inviscid: streamline curvature in the meridional plane and varying energy levels of the streamlines along the blade span. The latter factor generally results from a radially varying work input from the rotor rows. Both of these factors can either increase or decrease the level of axial velocity in the end-wall region. Factors that are viscous are the radial distribution of flow losses and a blockage type of effect due to a nonaxisymmetric flow field. The radial distribution of losses includes the blade profile loss, shock loss, end-wall boundary layer loss, and secondary flow losses. The latter two loss sources are strongest in the end-wall flow region. The blockage effect due to nonaxisymmetric flows must be applied whenever circumferentially mass-averaged parameters, in particular total pressure, are used to compute the gap-averaged flow velocities. This accounts for the mass flow differences when flow, which is an area-averaged quantity, is computed from mass-averaged parameters. Hence the need to consider such a blockage when applying design procedures, through-flow analyses, some data analyses, etc., where pressures, temperatures, and angles used to compute the velocity field are, or are assumed to be, mass-averaged quantities. The nonaxisymmetric flow field and associated blockages are discussed in detail by Dring in references 28 and 29.

The difference between measured and design blockage allowances is shown in figure 17. Typically the design procedures partially account for the higher loss levels in the end-wall regions but cannot accommodate the very severe gradients through the end-wall boundary layer flows. Hence the need for an end-wall blockage exists. In most cases the spanwise blockages associated with nonaxisymmetric flows are unknown and are added to the end-wall blockage. As figure 17 shows, the measured blockage is the sum of the equivalent blockage associated with the design end-wall loss gradient K_1 and the design end-wall blockage allowance K_2. The design blockage allowance includes the design end-wall blockage allowance K_2 and the blockage associated with the non-axisymmetric flow field K_3.

The foregoing discussion delineates some of the flow physics in the compressor end-wall flow regions that necessitates the use of blockage factors in design and analysis procedures and points to the difficulty of extracting the needed parameters from measured data. Hence a comparison of the design and measured blockages is a subjective one at present. The comparisons for this fan are presented in table IV.

In general, the level of measured blockage agreed reasonably well with the design values. For the first-stage rotor the measured blockage was somewhat higher than design, and for the exit of the second stator it was somewhat lower than design. The measured blockages did reflect an increase through the rotors and a decrease through the stators. Also the measured blockage for the second stage was essentially the same as that for the first stage. This could be due in part to the flow mixing noted earlier.

It was recognized that meaningful blockage factors can be obtained from compressor end-wall experimental measurements only if the selection of the boundary layer thickness (edge) effectively accounts for all of the viscous flow effects and ignores the inviscid flow effects. The van Dyke procedure described in appendix B was selected for this study since it had these capabilities. Some judgment on the worthiness of the van Dyke-Mellor-Wood procedure can be made by applying it to the fan inlet flow. At the fan inlet the total-pressure distribution indicates the spanwise extent of the viscous effects, and the axial velocity distribution indicates that local streamline curvature effects are also present.

As noted previously the calculated boundary-layer-edge location determined by applying the van Dyke-Mellor-Wood approach (appendix B) is at approximately 15 percent of span from the tip (fig. 10). Even though the plots show a nearly constant total pressure beyond 10 percent of span, the tabular data presented in reference 18 show the total pressure to decrease, starting at approximately 15 percent of span. This somewhat validates the procedure for separating the inviscid effects (in this case streamline curvature) from the viscous end-wall boundary layer effect in establishing a boundary-layer-edge location. This application provides some confidence for generally applying this procedure. However, it is recognized that validation of the procedure with the two-dimensional, collateral boundary layer flow at the fan inlet does not represent a

complete validation of the procedure with the three-dimensional, skewed boundary layer flows at the other blade-row stations.

To provide an indication of the sensitivity of the boundary layer parameters to the selected boundary layer thickness (edge), the boundary layer parameters were calculated from the measured profiles by arbitrarily selecting the boundary layer edge at various spanwise locations along the measured velocity profile. This standard boundary layer procedure is illustrated in graphical form in figure 18 and the results of the calculations are shown in figure 19. The data presented in figure 19 are for the near-peak-efficiency flow point. Plots of axial and tangential momentum thickness and axial displacement thickness are presented as a function of spanwise location of the assumed boundary layer edge for each of the five axial locations. As can be noted from the figure, the magnitude of the calculated boundary layer parameters is a relatively strong function of the assumed boundary-layer-edge location. At stations behind the rotors the calculated boundary layer parameters tend to level off in the region where one might assume the boundary layer edge to be (figs. 11 and 13) and the edge value determined by the procedure presented in appendix B. However, at the first-stage rotor inlet and at the exits of each stator the boundary layer parameters continue to increase as the assumed boundary-layer-edge location is moved to larger percentages of the span. This is particularly true at station 1 and can be attributed to stronger streamline curvature effects at this station. In any case the data presented in figure 19 reflect the need for a sound procedure for establishing the boundary-layer-edge location in a flow field that includes both inviscid and viscous effects in terms of the governing factors controlling the velocity profiles. Although the van Dyke-Mellor-Wood procedure for selecting the end-wall boundary layer edge downstream of rotors and stators cannot be firmly established as valid from the data, it represents the consistent procedure needed to carry out an extended correlation of end-wall boundary layer parameters.

CONCLUDING REMARKS

The detailed boundary layer measurements obtained in the high-tip-speed, high-pressure-ratio two-stage fan extend the experimental data base for end-wall boundary layer modeling and code verification. Various factors that contribute to the flow blockage through a compressor were discussed. The blockage based on measured data was related to the blockage used in the design and analysis procedures.

Because specific design and performance features of this fan probably influenced the data, some care should be exercised in applying these results in general. These features included

1. Wide axial spacing between blade rows (to alleviate noise generation). This provided an unusually long flow path for enhanced flow mixing, which appeared to have a significant effect on end-wall gradients and blockage values.

2. High reaction stages (large static pressure rise across the rotors and low static pressure rise across the stators). This may have a significant influence on the trend of an increase in blockage across the rotors and a decrease across the stators.

3. Fan stall initiated in hub region of second stage. This probably was responsible for the nearly constant tip blockage over the flow range covered.

A need therefore exists to provide data to permit generalizing and quantifying the influence of the various design and performance features on the end-wall flows.

Two recent methods to calculate the factors directly or indirectly affecting flow blockages have recently been introduced. One is the method proposed by Adkins and Smith in reference 16 for calculating the spanwise mixing of the flow as it passes through a multistage compressor. This method can be applied directly to a design or analysis procedure. The second is an approach to calculating the spanwise distribution of blockage due to nonaxisymmetric flows proposed by Dring in references 28 and 29. This approach requires detailed gapwise measurements at the rotor-exit stations and at the stator-exit stations to obtain the pertinent data. Both of these methods must be supported by relevant experimental data.

Finally, the data presented reflect the need for improved design approaches (methods) to more accurately account for the significant departures in the flow parameters in the end-wall boundary layer region in relation to free-stream values. The results of a program conducted on a large low-speed compressor to address this need are summarized by Wisler in reference 30. Various designs incorporating end-wall bends into the stator blade rows to accommodate the highly skewed end-wall profiles were studied. The effects of these design concepts on efficiency and stall margins as well as on the local blade-surface velocity distributions were presented.

SUMMARY OF RESULTS

This report presents detailed measurements of the casing boundary layer in a 429-m/sec-tip-speed, two-stage fan. The fan achieved a peak adiabatic efficiency of 0.851 at a pressure ratio of 2.433 at design speed. The principal results from the measured data were as follows:

1. The measured radial distributions of flow parameters obtained in the casing boundary layer showed sharp departures from the free-stream values at all survey stations near the casing wall.

2. In this high-shear end-wall flow region at the rotor exit the following combination of flow conditions existed: low axial velocity, high energy addition, low pressure, low efficiency, high relative flow angles, and large deviation angles. The low absolute velocity measured at the rotor exits near the casing reflected a high incidence on the stator.

3. In the end-wall flow regions downstream of the stators, decreased gradients and increased spanwise penetration of the end-wall boundary layer (as compared with the rotor exit) indicated that some mixing occurred in the flow across stator rows. Significant overturning of flow close to the outer wall was evident.

4. Over the complete flow range at 100 percent of design speed the calculated casing boundary layer parameters showed only small variations with operating conditions. No indication of boundary layer separation was apparent during near-stall operation.

5. For this fan the tip annulus boundary layer and associated flow blockage increased across the rotors and decreased across the stators. The calculated blockages for the second stage based on measured data were essentially the same as those for the first stage.

APPENDIX A

EQUATIONS

Diffusion factor

$$D = 1 - \frac{V'_{TE}}{V'_{LE}} + \frac{(rV_\theta)_{TE} - (rV_\theta)_{LE}}{(r_{TE} + r_{LE})\sigma(V'_{LE})} \tag{A1}$$

Percent of passage height

$$\frac{(r_t - r)}{(r_t - r_h)} \, 100 \tag{A2}$$

Adiabatic (temperature rise) efficiency

$$\eta_{ad} = \frac{\left(\dfrac{P_{TE}}{P_{LE}}\right)^{(\gamma-1)/\gamma} - 1}{\dfrac{T_{TE}}{T_{LE}} - 1} \tag{A3}$$

Equivalent mass flow

$$W\sqrt{\theta}/\delta \tag{A4}$$

Equivalent rotative speed

$$N/\sqrt{\theta} \tag{A5}$$

Head-rise coefficient

$$P = \frac{C_p T_{LE}}{U^2_{tip}} \left[\left(\frac{P_{TE}}{P_{LE}}\right)^{(\gamma-1)\gamma} - 1 \right] \tag{A6}$$

Flow coefficient

$$\varphi = \frac{V_z}{(U_{tip})_{LE}} \tag{A7}$$

Polytropic efficiency

$$\eta_p = \frac{\ln \left(\frac{P_{TE}}{P_{LE}}\right)^{(\gamma-1)/\gamma}}{\ln \left(\frac{T_{TE}}{T_{LE}}\right)} \tag{A8}$$

Temperature-rise coefficient

$$\psi_T = \frac{C_p (T_{TE} - T_{LE})}{U_{tip}^2} \tag{A9}$$

Relative flow angle

$$\beta' = \arctan \left(\frac{V_\theta'}{V_z'}\right) \tag{A10}$$

Blockage factor

$$K_b = \frac{(r_t - \delta^*)^2 - (r_h + \delta_h^*)^2}{r_t^2 - r_h^2} + K_3 \tag{A11}$$

Blockage from nonaxisymmetric flows

$$K_3 = \frac{(\overline{V}_z)_{\text{based on area average}}}{(\overline{V}_z)_{\text{based on mass-averaged properties}}} \tag{A12}$$

APPENDIX B

BOUNDARY LAYER REDUCTION PROCEDURE

Devising a method for separating the inviscid rotational core flow from the end-wall boundary layer flow is complicated by the fact that the free stream (edge of the boundary layer) velocity is unknown. By using an approximate engineering approach, the following turbulent boundary layer data reduction program was developed.

From van Dyke's original concept (ref. 26) and as suggested for internal flows by Mellor and Wood (ref. 6), the measured velocity across an annular passage with total-pressure variation is given by

$$U_{meas} = U_b + U_{inv} - U_e \tag{B1}$$

where U_{meas} is the measured velocity profile, U_b is the boundary layer velocity profile, U_{inv} is the curve-fitted inviscid velocity profile, and U_e is the free-stream (edge of the boundary layer) velocity. A graphical description of the inviscid, measured, and calculated boundary layer velocity profiles is given in figure 7.

Assuming an initial value for U_e, the outer values of the inviscid velocity profile U_{inv} were curve fitted to the wall value U_e. With the measured velocity profile U_{meas} and an initially assumed U_e, the boundary layer velocity profile U_b was calculated from equation (B1). The boundary layer integrations were then performed to obtain the following momentum and displacement thicknesses:

$$\theta = \int_0^\delta \left(1 - \frac{U_b}{U_e}\right) \frac{\rho}{\rho_e} \frac{U_b}{U_e}\, dy \tag{B2}$$

$$\delta^* = \int_0^\delta \left(1 - \frac{\rho}{\rho_e} \frac{U_b}{U_e}\right) dy \tag{B3}$$

where θ is the momentum thickness, δ^* is the displacement thickness, y is the boundary layer distance from the wall, δ is the edge of the boundary layer distance, and ρ is the density.

The compressible form factor H_c and the incompressible form factor H_i are

$$H_c = \frac{\delta^*}{\theta} \tag{B4}$$

$$H_i = \left(H_c - Pr^{1/3}\gamma \frac{M_e^2}{2}\right)\Big/\left(1 + \frac{\gamma}{2} M_e^2\right) \tag{B5}$$

where Pr is the Prandtl number set at 0.71, γ is the ratio of specific heats, and M_e is the Mach number at the edge of the boundary layer.

With U_e, H_i, and θ already calculated, the skin friction coefficient C_f was calculated by using Ludwieg and Tillman's relationship from reference 27

$$\frac{C_f}{2} = 0.123 \left(e^{-1.561 \, H_i}\right) \left(\frac{\mu_{ref}}{\rho_e U_e \theta}\right) \left(\frac{t_e}{t_{ref}}\right) \tag{B6}$$

where μ_{ref} is the dynamic viscosity based on reference temperature and the reference temperature t_{ref} is

$$t_{ref} = t_e \left(1.0 + 0.72 \, Pr^{1/3} \frac{\gamma}{2} M_e^2\right) \tag{B7}$$

where t_e is the static temperature at the edge of the boundary layer.

From the already determined boundary layer parameters and Cole's law of the wake the shear velocity can be calculated. Cole's law of the wake is

$$\frac{U}{U_\tau} = \frac{1}{K_1} \ln\left(\frac{\rho U_\tau y}{\mu}\right) + C_1 + \frac{2\Pi(x)}{K_1} \, W\left(\frac{y}{\delta}\right) \tag{B8}$$

where $K_1 = 0.40$, $C_1 = 5.1$, U_τ is the local air velocity at each point in the boundary layer, $\Pi(x)$ is a parameter describing the velocity defect law, and $W(y/\delta)$ is a wavelike function describing the outer wake region of the boundary layer.

At the boundary layer edge $U = U_e$, and equation (B8) becomes

$$\frac{U_e}{U_\tau} = \frac{1}{(C_f/2)^{1/2}} = \frac{1}{K_1} \ln\left(\frac{\rho_e U_\tau \delta}{\mu_e}\right) + C_1 + \frac{2\Pi(x)}{K_1} \tag{B9}$$

Solving for $2\Pi(x)/K_1$ in equation (B9) gives

$$\frac{2\Pi(x)}{K_1} = \frac{1}{(C_f/2)^{1/2}} - C_1 - \frac{1}{K_1} \ln\left(\frac{\rho_e U_\tau \delta}{\mu_e}\right) \tag{B10}$$

Solving for U_τ in equation (B8) gives

$$U_\tau = \frac{U_n}{\frac{1}{K_1} \ln\left(\frac{\rho_n U_\tau y_n}{\mu_n}\right) + C_1 + \frac{2\Pi(x)}{K_1} W\left(\frac{y}{\delta}\right)} \tag{B11}$$

where

$$W\left(\frac{y}{\delta}\right) = 2 \sin^2\left(\frac{\Pi}{2} \frac{y}{\delta}\right) \tag{B12}$$

and n is the measured boundary layer point for evaluating U, y, ρ, and μ. Initially, the shear velocity U_τ was estimated from the shear stress equation as

$$U_\tau = U_e \left(\frac{C_f}{2}\right)^{1/2} \tag{B13}$$

Then equation (B11) was iterated for the correct U_τ. The iterated U_τ was obtained for

   n = 1 (first measured point)
   n = 2 (second measured point)

The U_τ's calculated by using the first and second points were then averaged to obtain the new U_τ. From this U_τ and equation (B13) a new U_e can be obtained

$$U_e = \frac{U_\tau}{(C_f/2)^{1/2}} \qquad (B14)$$

With this new U_e the complete iteration loop was repeated until the new U_e had negligible change from the old U_e.

REFERENCES

1. Railly, J. W.; and Howard, J. H. G.: Velocity Profile Development in Axial Flow Compressors. J. Mech. Eng. Sci., vol. 4, no. 2, Apr. 1962, pp. 166-176.

2. Cooke, J. A.; and Hall, M. G.: Boundary Layers in Three Dimensions. Progress in Aeronautical Sciences, vol. 2, A. Ferri, D. Kuchemann, and L. H. G. Sterne, eds., Pergamon Press, 1962, pp. 221-282.

3. Stratford, B. S.: The Use of Boundary Layer Techniques to Calculate the Blockage from the Annulus Boundary Layers in a Compressor. ASME Paper 67-WA/GT-7, 1967.

4. Smith, L. H.: Casing Boundary Layers in Multistage Axial Flow Compressors. Flow Research on Blading, L. S. Dzung, ed., Elsevier, 1970, pp. 275-304.

5. Horlock, J. H.: Boundary Layer Problems in Axial Turbomachines. Flow Research on Blading, L. S. Dzung, ed., Elsevier, 1970, pp. 322-371.

6. Mellor, G. L.; and Wood, G. M.: An Axial Compressor End-Wall Boundary Layer Theory. J. Basic Eng., vol. 93, 1971, pp. 300-316.

7. Marsh, H.; and Horlock, J. H.: Wall Boundary Layers in Turbomachines. J. Mech. Eng. Sci., vol. 14, no. 6, Dec. 1972, pp. 411-423.

8. Daneshyar, M.: Annulus Wall Boundary Layers in Turbomachines. Ph.D. Thesis, Cambridge University, 1973.

9. Horlock, J. H.; and Perkins, H. J.: Annulus Wall Boundary Layers in Turbomachines. AGARD AG-185, 1974.

10. Hirsch, C.: End-Wall Boundary Layers in Axial Compressors. ASME Paper 74-GT-72, Mar. 1974.

11. deRuyck, J.; Hirsch, C.; and Kool, P.: An Axial Compressor End-Wall Boundary Layer Calculation Method. J. Eng. Power, vol. 101, no. 2, Apr. 1979, pp. 233-249.

12. deRuyck, J.; Hirsch, C.; and Kool, P.: Investigation on Axial Compressor End-Wall Boundary Layer Calculations. Presented at the International Joint Gas Turbine Congress (Haifa, Israel), July 1979.

13. deRuyck, J.; and Hirsch, C.: Investigations on an Axial Compressor End-Wall Boundary Layer Prediction Method. J. Eng. Power, vol. 103, no. 1, Jan. 1981, pp. 20-33.

14. Hirsch, C.; and Denton, J. D., eds.: Through Flow Calculations in Axial Turbomachines. AGARD Advisory Report No. 175, Oct. 1981.

15. Koch, C. C.; and Smith, L. H., Jr.: Loss Sources and Magnitudes in Axial-Flow Compressors. ASME Paper 75-WA/GT-6, Nov. 1975.

16. Adkins, G. G., Jr.; and Smith, L. H., Jr.: Spanwise Mixing in Axial-Flow Turbomachines. ASME Paper 81-GT-57, Mar. 1981.

17. Urasek, D. C., Gorrell, W. T., and Cunnan, W. S.: Performance of a Two-Stage Fan Having Low-Aspect-Ratio First-Stage Rotor Blading. AVRADCOM TR-78-49, NASA TP-1493, Aug. 1979.

18. Gorrell, W. T.: Detailed Flow Measurements in Casing Boundary Layer of 427-Meter-Per-Second-Tip-Speed Two-Stage Fan with Casing Treatment. AVRADCOM TR-81-C-28, NASA TP-2052, Jan. 1983.

19. deRuyck, J.; and Hirsch, C.: End-Wall Boundary Layers in Multistage Axial Compressors. AGARD Paper 61-A-19, June 1983.

20. Cunnan, W. S.; Stevans, W.; and Urasek, D. C.: Design and Performance of a 427-Meter-per-Second-Tip-Speed Two-Stage Fan Having a 2.40 Pressure Ratio. NASA TP-1314, Oct. 1978.

21. Urasek, D. C.; Cunnan, W. S.; and Stevans, W.: Performance of Two-Stage Fan with *Larger Dampers on First-Stage Rotor.* NASA TP-1399, May 1979.

22. Gorrell, W. T.; and Urasek, D. C.: Performance of Two-Stage Fan with a First-Stage Rotor Redesigned to Account for the Presence of a Part-Span Damper. AVRADCOM TR-79-10, NASA TP-1483, Sept. 1979.

23. Ball, C. L.; Janetzke, D. C.; and Reid, L.: Performance of 1380-Foot-Per-Second-Tip-Speed Axial-Flow Compressor Rotor with Blade Tip Solidity of 1.1. NASA TM X-2449, Mar. 1972.

24. Schmidt, J. F.; and Ruggeri, R. S.: Performance and Boundary-Layer Evaluation of a Sonic Inlet. NASA TN D-8340, Nov. 1976.

25. Glawe, G. E.; Krause, L. N.; and Dudzinski, T. J.: A Small Combination Sensing Probe for Measurement of Temperature, Pressure, and Flow Direction. NASA TN D-4816, Oct. 1968.

26. van Dyke, M. D.: Perturbation Methods in Fluid Mechanics. Academic Press, 1964, pp. 81-97.

27. Sasman, P. K.; and Cresci, R. J.: Compressible Turbulence Boundary Layer with Pressure Gradient and Heat Transfer. AIAA J. vol. 4, no. 1, Jan. 1966, pp. 19-25.

28. Dring, R. P., Wagner, J. H., and Joslyn, H. D.: *Axial Compressor Middle Stage Secondary Flow Study.* NASA CR in preparation, 1983.

29. Dring, R. P.; Joslyn, H. D.; and Wagner, J. H.: Compressor Rotor Aerodynamics. AGARD Paper 61-A-24, June 1983.

30. Wisler, D. C.: Core Compressor Exit Stage Study, VI - Final Report. (GE-R81AEG-288, General Electric Co., NASA Contract NAS3-20070.) NASA CR-165553, Dec. 1981.

TABLE I. - OVERALL DESIGN PARAMETERS

(a) Two-stage fan

Fan total-pressure ratio	2.399
Fan total-temperature ratio	1.334
Fan adiabatic efficiency	0.849
Fan polytropic efficiency	0.866
Weight flow, kg/sec	33.248
Weight flow per unit frontal area, kg/sec m^2	162.381
Weight flow per unit annulus area, kg/sec m^2	189.016
Rotative speed, rpm	16042.800
Tip speed, m/sec	428.896

(b) First stage

Rotor total-pressure ratio	1.629
Stage total-pressure ratio	1.590
Rotor total-temperature ratio	1.167
Stage total-temperature ratio	1.167
Rotor adiabatic efficiency	0.896
Stage adiabatic efficiency	0.848
Rotor polytropic efficiency	0.903
Stage polytropic efficiency	0.857
Rotor head-rise coefficient	0.236
Stage head-rise coefficient	0.223
Flow coefficient	0.429

(c) Second stage

Rotor total-pressure ratio	1.537
Stage total-pressure ratio	1.509
Rotor total-temperature ratio	1.143
Stage total-temperature ratio	1.143
Rotor adiabatic efficiency	0.911
Stage adiabatic efficiency	0.870
Rotor polytropic efficiency	0.917
Stage polytropic efficiency	0.877
Rotor head-rise coefficient	0.269
Stage head-rise coefficient	0.256
Flow coefficient	0.464

TABLE II. - FAN DESIGN BLOCKAGE ALLOWANCES

	Inlet	Outlet
	Blockage, percent	
Rotor 1	2.0	2.6
Stator 1	3.6	4.0
Rotor 2	4.0	4.0
Stator 2	4.0	4.0

TABLE III. - MEASURED BOUNDARY LAYER PARAMETERS

Sta-tion	Edge velocity, U_e, m/sec	Mach number, M_e	Boundary layer edge, δ, cm	Axial momentum thickness, θ_x, cm	Axial displace-ment thickness, δ_x^*, cm	Tangential momentum thickness, θ_z, cm	Blockage factor, K_b	Axial incom-pressible form factor, H_i	Skin friction coefficient, $C_f/2$	Shear velocity, U_τ, m/sec
				Mass flow = 34.63 kg/sec (near choke)						
1	194.7	0.591	2.326	0.1375	0.2009	------	0.982	1.309	0.00246	9.66
2	204.0	.570	1.545	.1838	.3103	-0.0567	.967	1.530	.00147	7.815
3	182.7	.503	1.213	.1228	.1722	.0185	.980	1.290	.00259	9.296
4	178.8	.460	0.830	.1305	.2042	.02423	.972	1.460	.00183	7.650
5	176.1	.452	0.846	.0716	.0792	.02536	.986	1.300	.00299	9.638
				Mass flow = 34.23 kg/sec (near peak efficiency)						
1	193.6	0.586	2.362	0.1481	0.2164	------	0.980	1.31	0.00240	9.48
2	195.1	.540	1.219	.1585	.2524	-0.0460	.973	1.46	.00175	8.15
3	186.4	.509	1.515	.1049	.1484	.0093	.983	1.31	.00263	9.56
4	167.7	.424	0.671	.1067	.1631	.00393	.978	1.44	.00206	7.61
5	175.8	.444	1.073	.0607	.0856	.0257	.988	1.32	.00299	9.62
				Mass flow = 34.01 kg/sec (near stall)						
1	191.10.	0.579	2.131	0.1399	0.2036	------	0.982	1.31	0.00247	9.49
2	196.6	.547	2.042	.1750	.2886	-0.0472	.969	1.50	.00158	7.82
3	189.5	.518	1.853	.1085	.1539	-.00012	.982	1.30	.00258	9.63
4	177.8	.451	0.838	.1198	.1850	-.00005	.975	1.45	.00191	7.76
5	173.1	.437	0.844	.0604	.0826	.0295	.988	1.29	.00321	9.81

TABLE IV. - COMPARISON BETWEEN
DESIGN AND MEASURED BLOCKAGES

[Tip values at measuring station,
near peak efficiency.]

$[K_{meas} = K_1 + K_2; K_{des} = K_2 + K_3.]$

	Design	Measured
	Blockage, percent	
Rotor 1 inlet	1.0	2.0
Rotor 1 outlet	1.5	2.7
Stator 1 outlet	2.0	1.7
Rotor 2 outlet	2.0	2.2
Stator 2 outlet	2.0	1.2

Flow path coordinates

Axial distance, Z, cm	Radius, r, cm	
	Outer	Inner
-13.093	25.654	8.994
-8.016	25.654	8.903
-2.936	25.654	9.093
[a]-.203	25.651	9.543
2.144	25.570	10.160
4.684	25.128	10.973
7.224	24.681	11.565
[a]9.764	24.460	11.902
12.304	24.384	12.139
14.844		12.438
17.384		12.822
19.924		13.025
[a]20.803		13.038
22.464	24.328	13.152
25.004	23.993	13.627
27.544	23.655	14.371
[a]30.084	23.622	14.699
32.177		14.849
36.754		15.237
[a]38.850		15.240
42.784		15.240

Figure 1. - Flow path of two-stage low-aspect-ratio fan.

[a]Instrument survey plane.

Figure 2. - Two-stage fan with low-aspect-ratio, first-stage rotor.

C-76-3887

AIR INLET (ATMOSPHERE)

ATMOSPHERE EXHAUST

BUTTERFLY VALVE

ORIFICE PLATE

VANED ELBOWS

STRAIGHTENER SCREEN

ALTITUDE EXHAUST

WORK PLATFORM

COLLECTOR SLEEVE VALVE

BUTTERFLY VALVE

BUTTERFLY VALVE

TEST FAN

BUTTERFLY VALVE

REFRIGERATED AIR RISER

DRIVE MOTOR

GEARBOX (SPEED INCREASER)

PLENUM CHAMBER

STRAIGHTENER SCREEN
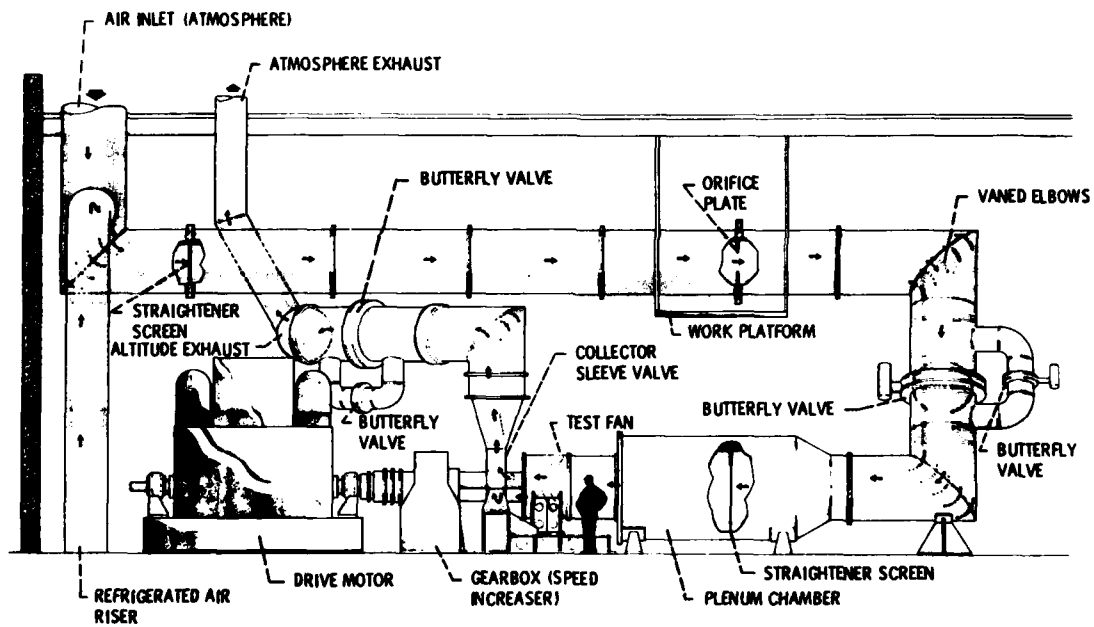
Figure 3. - Multistage compressor test facility.

TWO NULL BALANCING PRESSURE TAPS FOR FLOW-ANGLE AND STATIC-PRESSURE MEASUREMENTS

THERMOCOUPLE

TOTAL-PRESSURE TUBE (.051 cm diam)
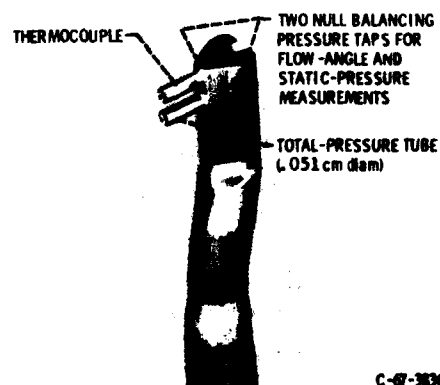
C-67-3036

Figure 4. - Combination total-pressure, static-pressure, total-temperature, and flow-angle probe (double barrel).
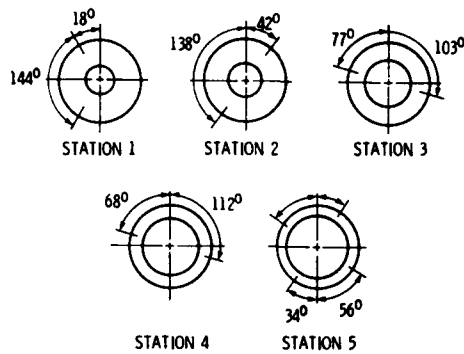
(a) Combination probes.
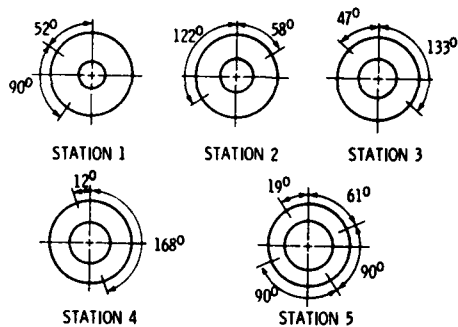
(b) Static-pressure taps.

Figure 5. – Circumferential locations of instrumentation at measuring stations (looking downstream).

Figure 6. – Comparison of measured and calculated static pressure at station 1.
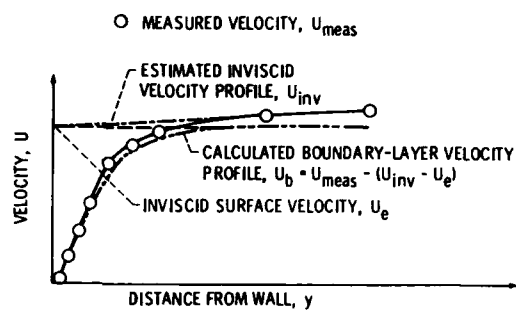
Figure 7. – Graphical description of inviscid, measured, and calculated velocity profiles.

Figure 8. – Overall performance of two-stage, low-aspect-ratio fan.
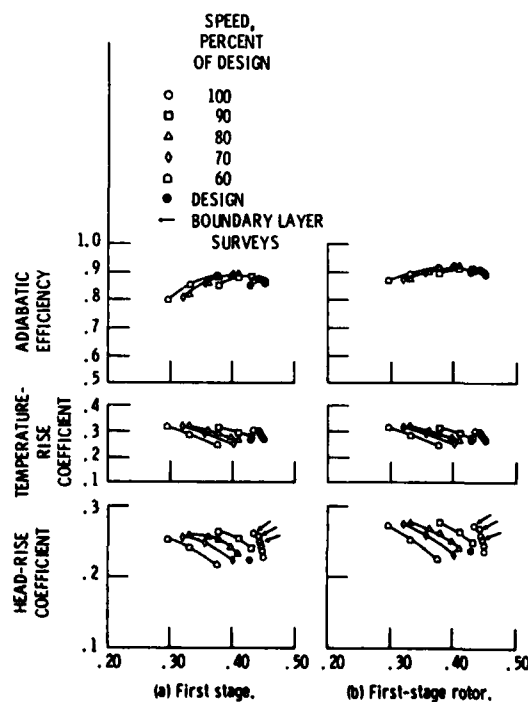
Figure 9. – Dimensionless overall performance.

SPEED,
PERCENT
OF DESIGN

○ 100
□ 90
△ 80
◇ 70
⬠ 60
● DESIGN
— BOUNDARY LAYER
SURVEYS

(c) Second stage. (d) Second-stage rotor.
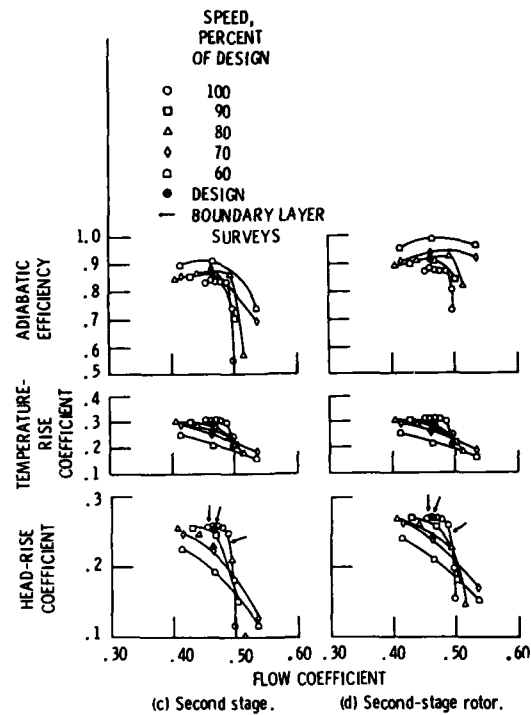
Figure 9. - Concluded.

EQUIVALENT FLOW,
kg/sec

□ 34.63 (CHOKE)
○ 34.23 (PEAK EFFICIENCY)
△ 34.01 (NEAR STALL)
— DESIGN

CALCULATED
BOUNDARY LAYER
EDGE
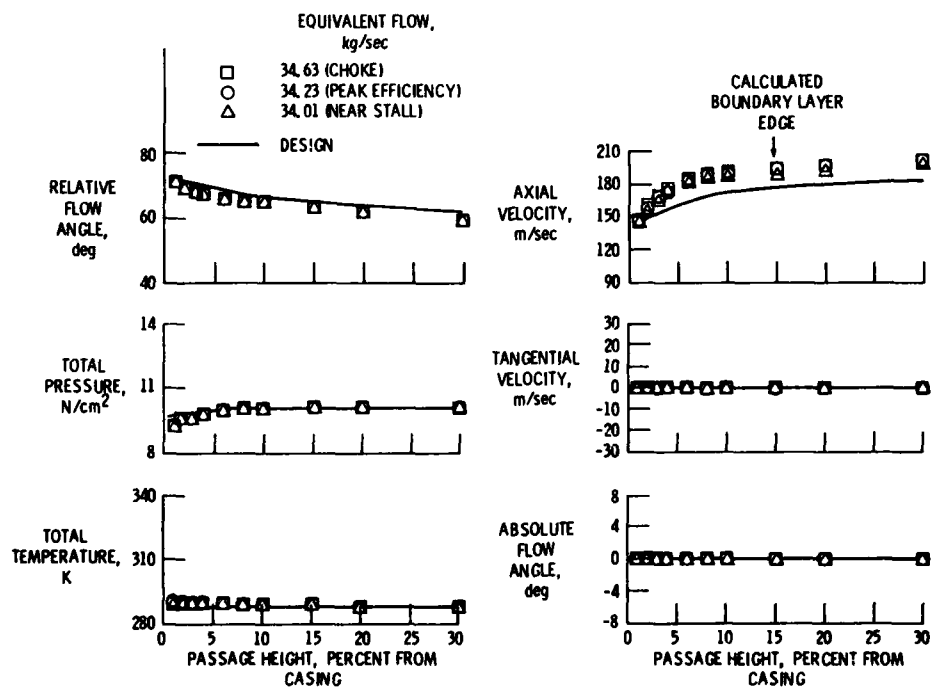
Figure 10. - Radial distributions at measuring station 1, first-stage rotor inlet.
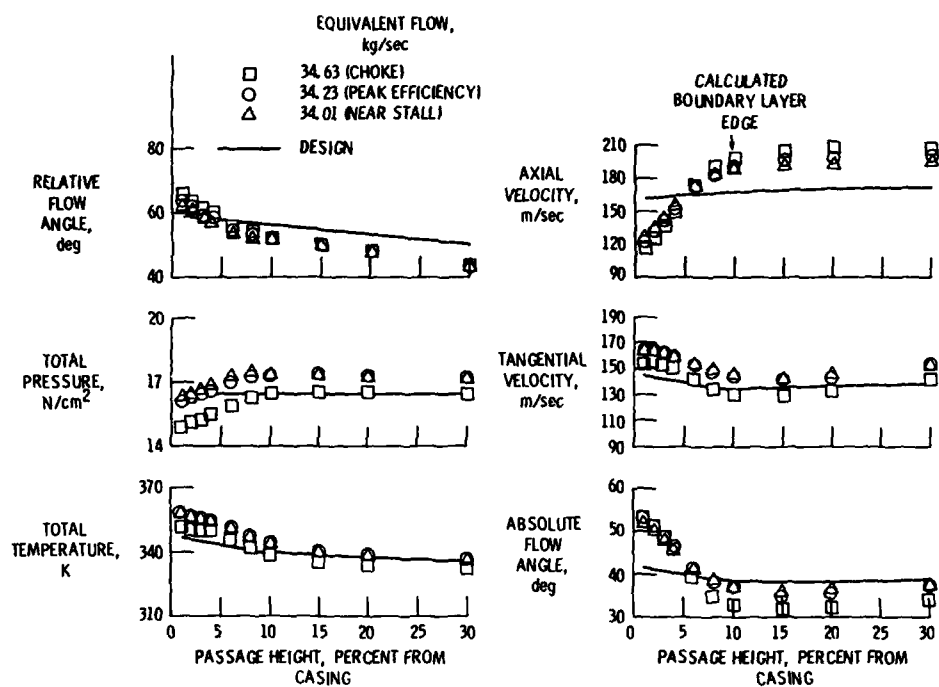
Figure 11. - Radial distributions at measuring station 2, first-stage rotor exit.
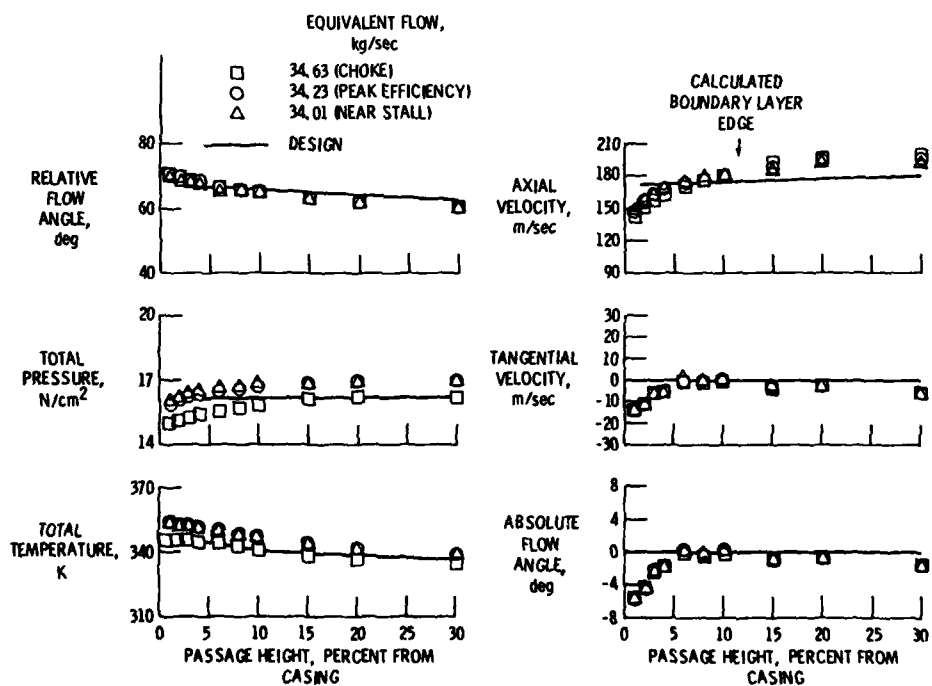
Figure 12. - Radial distributions at measuring station 3, first-stage stator exit.
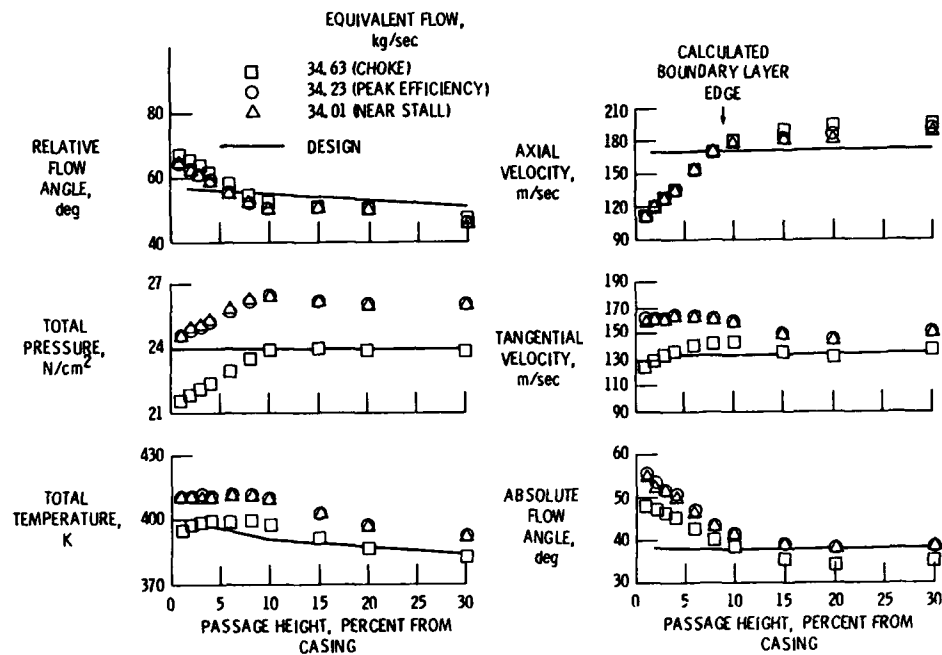
Figure 13. - Radial distributions at measuring station 4, second-stage rotor exit.
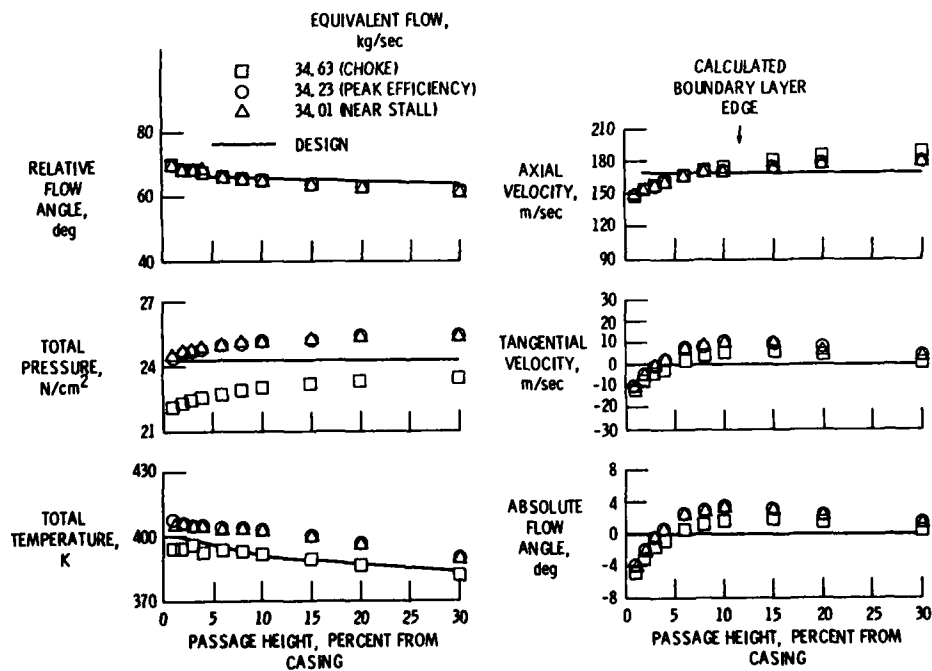
Figure 14. - Radial distributions at measuring station 5, second-stage stator exit.

Figure 16. - Factors affecting measured velocity profiles.

IDEALIZED, FREE-VORTEX PROFILE
STREAMLINE CURVATURE, +, INVISCID
RADIAL WORK GRADIENT, +, INVISCID
INVISCID VELOCITY PROFILE
END-WALL LOSS GRADIENT, -, VISCOUS
NONAXISYMMETRIC FLOWS, +, VISCOUS
MEASURED VELOCITY PROFILE

VELOCITY, U

DISTANCE FROM WALL, y

INVISCID VELOCITY PROFILE
K_1
DESIGN END-WALL LOSS
K_2 DESIGN VELOCITY PROFILE
K_3 DESIGN END-WALL BLOCKAGE
MEASURED VELOCITY PROFILE
NONAXISYMMETRIC FLOWS
AXISYMMETRIC (FULLY MIXED) VELOCITY PROFILE

VELOCITY, U

DISTANCE FROM WALL, y

Figure 17. - Comparison between design and measured blockage allowance. $K_{meas} = K_1 + K_2$, $K_{des} = K_2 + K_3$.

PASSAGE HEIGHT, PERCENT FROM CASING

○ 1
□ 2
◇ 3
△ 4
◁ 6
◁ 15
□ 30

220
200
180
160
140
120 PRESSURE SIDE   SUCTION SIDE
100

(a) First-stage stator exit.

200
180
160
140
120 PRESSURE SIDE   SUCTION SIDE
100
0   20   40   60   80   100
GAP, PERCENT OF TOTAL

(b) Second-stage stator exit.

AXIAL VELOCITY, m/sec

Figure 15. - Circumferential variation of axial velocity at stator exits. Mass flow, 34, 23 kg/sec.

MEASURED PROFILE

U_e

1. ASSUME MEASURED PROFILE EQUAL TO BOUNDARY LAYER PROFILE
2. CALCULATE BOUNDARY LAYER PARAMETERS AS A FUNCTION OF ASSUMED BOUNDARY LAYER EDGE LOCATION

VELOCITY, U

δ DISTANCE FROM WALL, y

Figure 18. - Standard method of calculating boundary layer parameters from measured data.
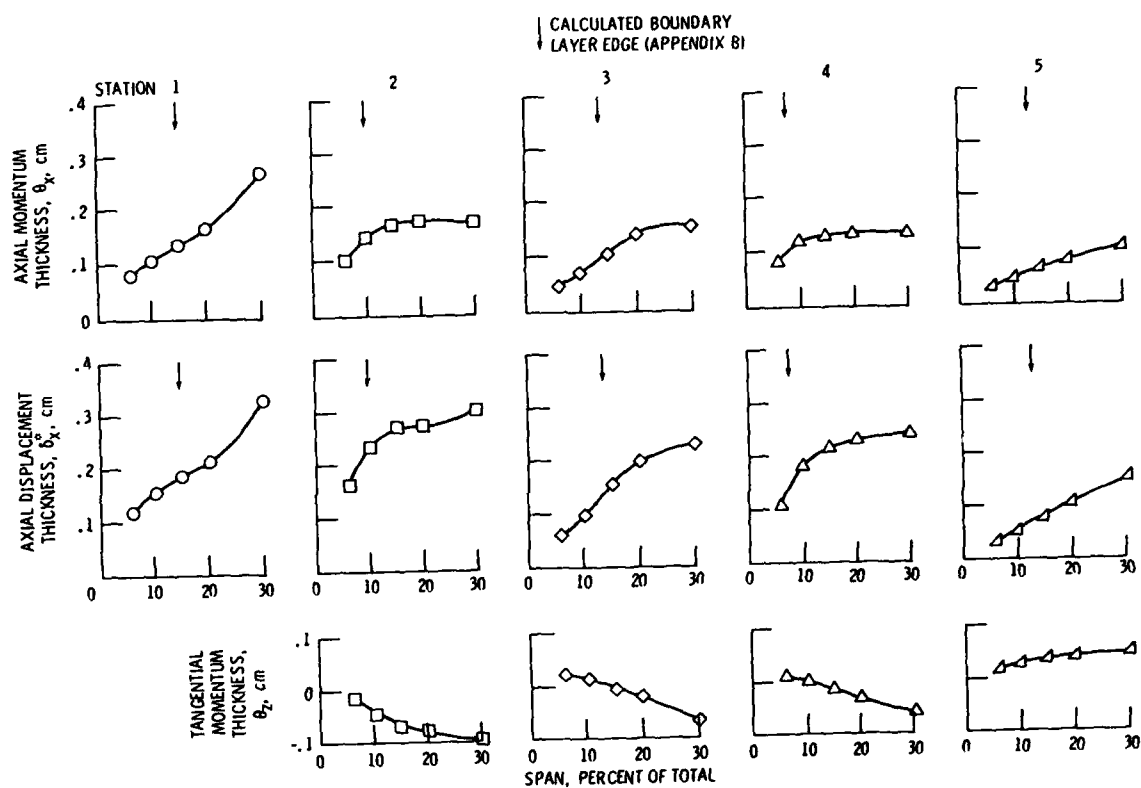
Figure 19. - Calculated boundary layer parameters from measured velocity profiles.

DISCUSSION

Gallus

I wonder why the wakes measured close to the wall (1% span) are larger than those at greater distances from the wall. This is contrary to our experience. Reasons are high turbulence and mixing out close to the walls.

Author's Reply

I feel that the most likely reasons for the wakes being larger near the walls than in the mainstream are due to: (1) the fact that the incidence in the tip region of the stators near the wall is higher than for the mainstream and therefore one would expect larger wakes near the wall than for the mainstream, (2) the fact that the stator tends to separate out the high momentum flow coming from the rotor (rotor wake flow). This low momentum flow tends to accumulate near the pressure surface and thus show up in the wake region of the stator. This fact may also affect the apparent size of the wake as a function of span, and (3) it is not clear where the rotor tip vortex shows up downstream of the stators, although there is some evidence that in some cases the tip vortex is showing up in the 'freestream" mid gap region.

E.E.Covert, US

The discussion by Fottner and Lakshminarayana is interesting and helpful in clarifying the basic physical processes near the hub. Nevertheless, my experience suggests the wake characteristics are dependent upon a number of details such as gap-chord ratio, blade trailing edge thickness, local momentum thickness, etc. Hence one may not want to discuss details too closely until one has also compared geometrical details as well.

Author's Reply

I agree with Professor Covert's comment. One must go cautiously when attempting to generalize results obtained from specific cases on such complex and detailed flow phenomena as that which exists within the end wall boundary layer of multistage compressors; specially questionning the existence and strength of the non-axisymmetric flow field noted within the end wall boundary layer behind the stators of the two-stage fan based on the fact that none was observed in any other machine. Detailed geometry and operating conditions must be compared before attempting to generalize results. Some reasons why one might expect to see the existence of the non-axisymmetric flow field behind the stators of the subject fan are given in the address to Prof. Fottner's question.

K.Papailiou, Gr

(1) Did you find any marked differences in the circumferential distributions for the near-design and near-stall points?

(2) The blockage distributions that you have shown are different from those usually produced by the Mellor and Wood method to which you referred. Could you comment on this point?

Author's Reply

(1) We did not see significant differences in the circumferential distributions of flow parameters behind the stators between the near-peak-efficiency point and the near-stall point. We attribute this to the fact that the tip elements for this fan do not seem to be controlling the stall line. Rather, the hub flow in the second stage appears to trigger stall. Therefore we would not expect a thickening of the tip boundary layer to the near-stall point. Also, the points are, in reality, relatively close.

(2) We feel that the reason that the blockage of the second stage is about the same as that of the first stage may be due to the large axial spacing and significant mixing of the flow. The trend from rotor to stator may be imparted by the high reaction design with most of the static pressure rise occurring in the rotor.

J. de Ruyck, Be

(1) In calculating the tangential momentum thickness how was the boundary layer location established, and

(2) How was the measured boundary layer profile extrapolated from the one percent span measuring location to the physical wall?

Author's Reply

In answer to the first question, the boundary layer edge location in the tangential direction was assumed to be the same as that established for the axial direction. The boundary layer edge location in the axial direction was established following the procedure presented in Appendix B. In calculating the tangential boundary layer parameters, no attempt was made to establish an inviscid profile based on the measured data as was done in establishing the axial boundary layer profile.

In answer to the second question, a spline fit of the data was used in conjunction with assuming the velocity to be zero at the physical wall. The resulting curve was examined to assure smoothness. It was noted that, in particular, the tangential boundary layer parameters were sensitive to the fairing between one percent of span and the wall.

Flow Measurements in the Stator Row of a Single-Stage Transonic Axial-Flow Compressor with
Controlled Diffusion Stator Blades

R.J. Dunker
DFVLR, Institut für Antriebstechnik,
5000 Köln 90, Postfach 90 60 58,
Federal Republic of Germany

AGARD
61st A Specialists' Meeting
of the
Propulsion & Energetics Panel
on
Viscous Effects in Turbomachines
Copenhagen
Denmark
1.-3. June 1983

Abstract

The time-dependent three-dimensional viscous flow downstream of the rotor in a single-stage
transonic axial-flow compressor without inlet guide vanes was measured and analysed at de-
sign and off-design operating conditions. Measurements were made between the blade rows and
within the stator row which had been recently redesigned using a controlled diffusion blade
design method.

Detailed measurements of the blade surface pressure distributions were performed in order
to investigate whether the favourable behaviour of controlled diffusion blades can be ob-
tained under the real flow conditions within a turbomachine, and not only under those con-
ditions in a cascade. These data, as well as laser-velocimetry data, indicate blade bound-
ary layer separation under some operating conditions.
The optical measurements were taken at different instantaneous rotor positions relative to
the stator. These results give some insight into the unsteady flow within the stator, e.g.
the development of the fluctuating velocity vectors, of the turbulence intensity, of the
rotor blade wakes, and of the stator blade boundary layers.

Nomenclature

c	absolute velocity
c	chord length
Ma, M	Mach number
t	blade pitch
Tnorm	turbulence intensity, normal to mean flow direction, $Tnorm = \sqrt{\overline{v'^2}}/c$
Tpar	turbulence intensity, parallel to mean flow direction, $Tpar = \sqrt{\overline{u'^2}}/c$
u_{tip}	circumferential velocity at rotor tip
β	relative flow angle
ω	total pressure loss coefficient
	$\omega = (p_{01} - p_{02})/(p_{01} - p_1)$

Introduction

Future aircraft engines must be smaller and lighter, and must operate with lower fuel con-
sumption than those of the present-generation.

Improvements in axial-flow compressor performance are necessary to meet this need. New
compressor designs will require:

- higher pressure ratios with at least no increase in the number of stages, and preferably
  with the same airflow as today's compressors but with fewer stages and a lower frontal
  area,

- and refined aerodynamics to improve the compressor efficiency.

The broad message apparent from these requirements is the necessity of a basic understanding of the flow phenomena involved. In particular, a detailed understanding of the flows within and between the blade rows is essential for further technological gains in axial-flow compressor aerodynamics. A deep insight into the fundamental aerodynamics involved makes possible the development of reliable flow models for analytical use and the successful application of new design concepts.

Within such R & D acitivities the stator blade row of an existing transonic axial compressor stage has been redesigned by applying a controlled diffusion blade design concept. This method, originating in single airfoil aerodynamics, is based on prescribed blade pressure or velocity distributions which are optimized with respect to blade boundary layer development. Cascade test results reveal a favourable flow behaviour with these new profiles, as well as a great potential for future application of the controlled diffusion concept.

The purpose of the present work is to investigate and analyze the flow phenomena in detail, and to determine the capabilities of the redesigned stator blade row under the real flow conditions within a turbomachine, i.e. unsteady three-dimensional viscous inlet flow to the stator as produced by a high-speed transonic rotor and associated with high positive and negative incidence angles.

In order to provide data for a somewhat qualitative comparison, detailed measurements of the stator blade surface pressure distributions were also performed in an equivalent linear cascade. It should be considered, however, that the measured static pressures on the blade surface represent mean values which could be significantly affected by an unsteady through-flow.

In recent years many experimental investigations concerning linear cascades and time-averaged compressor flows have been performed in order to gain more insight into the physical processes involved. Also some experience, although limited, has been gained with the unsteady effects of flows resulting from and within rotating blade rows, e.g. using high response pressure probes, rotating probes and hot wire anemometry.

A laser-two-focus-velocimeter (L2F) was used as a first step in measuring the unsteady flow-field downstream of the rotor within one stator blade passage. This nonintrusive measurement technique allows measurement of local flow velocity, direction, and turbulence components within or adjacent to rotating blade rows. The determination of density and pressure (static or total) is still rather difficult in this context and is therefore omitted in the present work.

In this presentation special emphasis is placed on the determination of the detailed internal stator aerodynamics and the stator rotor blade interaction. This has required the omission of many details of the measurement technique, with the attempt being made to present and discuss the more significant results which have been obtained so far.
However, before going into the details, a brief description is given of the transonic stage, its redesign , and some main test features.

Single-Stage Axial-Flow Compressor

The original machine was a single-stage axial-flow transonic compressor without inlet guide vanes, and was designed for a total pressure ratio of 1.51, a mass flow rate of 17.3 kg/s, and a rotational speed of 20,260 rpm.
The rotor inlet outside diameter is 400 mm with a hub-to-tip ratio of 0.5. Thus, the design rotor tip speed is 425 m/s with a maximum inlet relative Mach number of 1.37. All data are corrected so as to be representative of standard sea-level conditions at the rotor inlet.

The rotor consists of 28 MCA-profile blades, each with a tip chord length of 60 mm. The resulting blade solidities between 1.34 and 2.0 are considered typical. The original stator had 60 blades with NACA-65 profiles and circular arc camberlines.

The main aspects of the aerodynamic design and various investigations of the original stage using time-averaging measuring techniques are discussed in detail in References 1 through 4. Detailed optical measurements of the flow field within the transonic rotor have been performed by means of the L2F-anemometer and are documented in References 2 through 4.
In Reference 4 additional measurements of the unsteady total pressure downstream of the rotor between the blade rows using high response pressure probes are reported and combined with laser-velocimeter measurements.

The main features of the redesigned stator can be described as follows:
The number of blades was reduced from 60 to 31. The blade chord length was enlarged from 30 to 40 mm, resulting in a thicker blade profile to allow the installation of surface pressure taps. The positions of the blade leading edges were unchanged. The flowpath of the redesigned stage is shown in Fig. 1. The stator blades were designed using five sections parallel to the compressor axis. These sections at 10, 30, 50, 70,and 90 percent span are indicated in Fig. 1 by circled numbers. Basic design considerations, design flow parameters, geometric data, and blade element parameters are described in detail in a paper recently published [5]. In that report the inverse calculation method, test results from a linear cascade with equivalent stator blade sections (at 10, 50, and 90 percent span), and investigations concerning the overall performance of the new stage are discussed.
Therefore, only a short introductory selection is presented here.

In Fig. 2 are presented cascade test results for the stator mid-section at the design point condition with a comparison of the experimentally determined Mach number distribution and the design distribution.

The inverse calculation method requires the velocity triangle and the blade surface pressure distribution as input data for each blade section. The blade surface pressure distributions were prescribed on the basis of experience gained with former supercritical cascade designs. In Fig. 2 is shown the equivalent prescribed blade surface Mach number distribution for the stator mid-section (termed UKG 30.3) and some geometric and aerodynamic parameters. This figure illustrates the corresponding cascade airfoil shape resulting from the inverse cal-culation method.

The blade suction surface leading-edge region maintains a continous acceleration up to the peak Mach number at approximately 30 percent chord. This is in order to provide a favourable pressure gradient for keeping the boundary layer laminar. Diffusion from the peak Mach num-ber is controlled on the rear portion of the airfoil so as to keep the boundary layer shape-factor within the range of that for an unseparated turbulent boundary layer. The agreement between the experimentally determined Mach number distribution and the design distribution is quite satisfactory in spite of some deviation in the leading-edge region. Full details of the cascade test results are given in Reference 6.

In Fig. 3 is shown an example of the stator blade element performance within a turbomachine at 50 percent span. The total-pressure loss coefficient is plotted versus inlet flow angle for the redesigned airfoil at 85, 92.5, and 100 percent speed (triangles, rectangles and crosses, respectively). These data are compared with the results of the original NACA-65 blade section at 100 percent speed (open circles) and with the results for the correspond-ing cascade (dashed line with full dots). The cascade loss coefficient was interpolated to meet the inlet Mach number and AVDR values of the stage at design speed.

The comparison of the results for the original and redesigned blade profiles demonstrates a substantial reduction of the blade total-pressure loss between choke and design incidence for the redesigned (controlled diffusion) blade. In addition, the choke line is slightly shifted to higher incidence. Beyond the design incidence the flow losses increase consider-ably exceeding even the NACA-65 blade losses and resulting in a reduced stall margin.

The cascade results show a sharp increase in the flow losses near stall incidence, and thus resulting in a reduced stall margin as compared with the compressor results. 3-D and unstea-dy flow effects are believed to cause the more gradual increase in the losses near stall in the compressor cases. The unsteady effects can be shown using the results obtained from the laser-anemometer data. This will be discussed in a later section.

Examples of mid-span blade surface pressure distributions and laser-velocimetry data for the stator will be presented and discussed for 100 percent speed and some different mass flow rates:

- 17.58 kg/s, i.e. blade choking at high negative incidence with a time-averaged inlet flow angle of about 116 deg. (see Fig. 3).

- 17.3 kg/s, i.e. near the minimum loss conditions at an inlet flow angle of 121 deg..

- 15.35 kg/s, i.e. blade stall at high positive incidence at an inlet flow angle of 136 deg..

Blade Surface Pressure Distributions

The measurements of the blade surface pressure distributions were performed at design and off-design operating conditions for all five blade sections involved in the redesign pro-cess, i.e. 10, 30, 50, 70, and 90 percent span. In order to install as many surface press-ure taps as possible, the blade thickness and the blade chord length were enlarged. The re-sulting stator blades contained up to 14 taps on a given side from the leading edge to 60 percent chord.

In Figs. 4 through 7 related blade surface pressures versus percent chord are shown. The absolute values of the static pressures depend on the blade inlet total conditions which are essentially different for both the cascade and stage tests. Therefore, the absolute sta-tic pressure at 45 percent chord on the blade pressure side was selected as the reference value for comparing the distributions. Fig. 4 illustrates the pressure distribution for the stator mid-section with the compressor mass flow adjusted to the design value. The stage results (open circles) are compared to the cascade test results (triangles). The comparison is quite good except for the increased acceleration of the compressor stator flow near the leading edge on the suction surface. It is believed that due to unexpected changes in rotor throttling the actual stator inlet parameter values, particularly the in-let flow angle, might be different than the design values (based on the rotor performance in conjunction with the original stator). The data obtained using conventional time-avera-ging probes revealed a stator inlet flow angle change of about 4 deg. at the mid-section, i.e. in going from the original to the new stator. The design flow angle is 128.5 deg., whereas the actual flow angle value corresponding to design mass-flow is about 124.5 deg. (see Fig. 3).

In Fig. 5 is shown the pressure distribution corresponding to higher negative incidence (mass flow rate = 17.3 kg/s). These results are compared to the cascade results for the design condition. Here, too, no boundary layer separation can be noticed along the chord as far as the pressure taps are installed. Separation is not expected since this operating

point is associated with the near minimum loss condition for the mid-section (see Fig. 3).

In Fig. 6 are presented data for the stage near choking (mass flow rate = 17.58 kg/s).
Clearly, a typical distribution for high negative-incidence flow can be identified.

The pressure distribution corresponding to the near blade-stall condition at high positive
incidence (mass flow rate = 15.35 kg/s) is shown in Fig. 7. Here boundary layer separation
is indicated by the subsiding suction surface pressures at about 45 percent chord. Since
the measured static pressures within the stator row represent mean values, which are
undoubtedly affected by the unsteady through-flow, it is remarkable that this effect is
so clearly apparent. In additon, the laser-velocimetry data will prove the boundary layer
separation at this operating point.

Laser Measurements

The experimental work on the modified transonic compressor was extended by using a L2F-ane-
mometer to make nonintrusive measurements. These detailed measurements were performed down-
stream of the high speed rotor at locations between the blade rows, within the stator row
and behind the stator row. These locations were near to and within one single stator blade
passage which had been selected for the measurements.

The periodically varying absolute flow velocity vectors within the stator row were studied
at design speed for different operating conditions. These investigations were used to de-
termine the three-dimensional periodically unsteady flow field downstream of the rotor both
qualitatively and quantitatively. It should be emphasized that these flow processes occur
very rapidly due to the rotor passing frequency of approximately 10 KHz (rotor design speed
20,260 rpm).

The operating principles of the L2F-anemometer used is well documented in the literature
[7]. Only some special features are mentioned here concerning the application of the ane-
mometer to the study of rotor stator interactions.
An important point worth noting is that laser-velocimeter measurements are always performed
in the absolute system, even within rotating components.
The flow field within a distinct stator blade passage varies periodically at the rotor blade
passing frequency. The measurements downstream of the rotor were therefore made for differ-
ent rotor blade positions determined by equally dividing one rotor blade pitch into 16 inter-
vals. The data were obtained as each rotor blade passed the measurement region, and not on-
ly as the same rotor blade passed.
In order to cover a complete stator blade passage the window in the casing was staggered.
Each spatial location can be reached by displacing the velocimeter in a cartesian coordi-
nate system. The flow velocity and direction are evaluated only in a plane normal to the
laser-beams' axis. The flow component parallel to the laser axis cannot be determined with
this anemometer.

Examples of axial and circumferential measurement point locations for the stator mid-span
(open circles) are shown in Figs. 8 and 9. The relative position of the rotor blades with
respect to the stator measurement passage is also shown in these figures, with the rotor
in the first position. In order to simplify the displacement of the anemometer, the mea-
surement plane was made parallel to the compressor axis.
In Fig. 8 are shown the measurement locations for the case of near-stall operation (mass
flow rate = 15.35 kg/s). The region without measurement locations near the rear portion
of the suction surface is of particular interest. Here, no measurements were made because
of an excessive data acquisition time coupled with a relatively high uncertainty in the
results. For this operating condition blade boundary layer separation is indicated (see
Fig. 7).
In Fig. 9 is shown the distribution of measurement locations for measurements made near
the stage choke margin (mass flow rate = 17.58 kg/s).
Analog measurments as illustrated in Figs. 8 and 9 were made near hub and casing at 10 and
90 percent span, respectively, too.

It can now be appreciated that stator investigations of this kind pose a special problem.
Namely, the flows involved are three-dimensional and transient, i.e. the problem is actually
four-dimensional. A complex test procedure as well as special computer programs were re-
quired to achive compatible results, which were then combined to give a meaningful and
conclusive idea of the stator through-flow.
Only a brief selection of the many results obtained from this research effort can be pre-
sented in this paper. These results concern only the stator mid-span flow, but it is be-
lieved that some essential flow phenomena can be shown.

Some distributions of the turbulence intensity at mid-span are illustrated in Figs. 10
through 12. The data were obtained for a mass flow rate of 17.3 kg/s at design speed and
are presented for three rotor blade positions which differ by approximately one third of
the rotor blade pitch.
As mentioned before this operating point is associated with near minimum loss condition
for the mid-section.
Also, in the course of analysing the results it appeared that the turbulence intensity,
both parallel as well as normal to the temporary local main flow direction, was most appro-
priate for exhibiting the movement of rotor blade wakes through the stator blade passage.

A picture of the instantaneous stator through-flow at a particular rotor blade position is shown in Fig. 10. The rotor blade wakes are visible as areas of increased turbulence intensity. Between the wakes the turbulence intensity (Tpar) goes below 3 percent.
By viewing all three figures (Figs. 10, 11, and 12) in sequence it can be seen, that the rotor blade wakes move downstream through the stator blade passage with the progressive movement of the corresponding rotor blades. Simultaneously these "wake segments" become wider due to mixing and are rotated due to the mean velocity difference between the stator blade suction and pressure sides. In these examples there appears to be no shifting of rotor wake fluid towards the stator blade pressure side as the wakes move through the passage.

Similar "instantaneous" pictures for different stage operating conditions (same rotor position as in Fig. 11) are shown in Figs. 13 through 15, here again by means of the turbulence intensity parallel to the temporary local main flow direction.
The data presented in Fig. 13 were obtained at the near choke condition of the stage, where for the stator mid-section this corresponds to a high negative incidence angle (see Fig. 3). The data shown in Figs. 14 and 15 are for operating points with high positive-stator-incidence angles. Of particular interest are Figs. 13 and 15 in conjunction with the corresponding Figs. 7 and 8. The resulting blade turbulent boundary layer separation from increasing blade loading (Figs. 8 and 15) can be identified by the increase in turbulence intensity in both magnitude and extent near the suction surface from about 50 to 100 percent chord (compare Figs. 13 and 15). This boundary layer separation can also be clearly seen from Fig. 14.

Further remarkable phenomena are apparent in Figs. 10 through 15. In particular, the figures show well-defined regions of higher turbulence intensity within each rotor blade wake.
The regularity of these regions might indicate vortex like structures, possibly being shed periodically from the rotor blade or forming within the wake itself. A more detailed frequency analysis of this process, taking into account the applied measurement technique and procedure, indicates that the formation of these structures is possibly triggered from rotor stator blade interaction, i.e. the frequency of vortex shedding is "in-phase" with the stator blade passing frequency with respect to the rotor. A periodic unsteady flow can be viewed from either a relative or absolute frame of reference. For example, an observer on the (upstream) rotor feels a periodic influence from the (downstream) stator blades (if the axial flow velocity component is subsonic), whereas an observer within the stator feels the periodic unsteadiness from the rotor (upstream) blades. The former case (rotor frame of reference) can be only a potential flow effect, while the latter includes both potential and viscous flow effects.

Lastly, in Figs. 16 through 18 are illustrated the blade-to-blade distributions of the instantaneous absolute flow velocity (non-dimensionalized using the rotor tip speed) at three rotor positions (same positions as in Figs. 10 through 12). These experimental results pertain again to the stator mid-section and the near minimum-loss condition. No unusual flow behaviour can be observed in these figures. One can clearly identify the stagnation region ahead of the stator blades, the area of flow acceleration near the suction surface, the well known velocity decrease towards the pressure side, and the flow diffusion between the inlet and outlet of the stator blade row.

By examining Figs. 16 through 18 in sequence the variations in stator through-flow at progressive rotor positions can be seen. They can be particularly identified within the vicinity of the blade suction surface. The high frequency of these flow variations (approximately 10 KHz) does not produce an unregularly disturbed flow. It appears that the entire stator passage flow is dominated in a quasi-steady manner by the potential flow field induced by the stator blades.

An analogy to unsteady single airfoil aerodynamics seems to be appropriate. This can be proved by further analysis of the results. This analysis, however, is to be presented in another publication.

Summary

The stator row of an existing single-stage transonic axial-flow compressor was modified by applying a design method typically used for subsonic controlled diffusion blades. In order to verify the design concept both cascade and compressor stage tests were performed using conventional time-averaging probes.
Blade surface pressure distributions were measured at the five design sections of the stator for comparison with corresponding cascade results.

The test data show that the modified stator airfoils operated efficiently, over a wide range of aerodynamic conditions resulting in low losses, and that an attached suction surface boundary layer could be obtained. At high positive stator incidence angles a turbulent boundary layer separation could be observed.

Laser-velocimetry (L2F) measurements were performed in order to investigate rotor stator interaction effects and the flow diffusion within the stator row. The results for different operating conditions at design speed gave some insight into the unsteady stator through-flow behaviour, and in particular allowed, identification of the rotor blade wakes. These data might possibly form a reliable basis for a better empirical understanding of unsteady flow effects in turbomachines, e.g. the influence on stage efficiency of the number of blades and the axial spacing between blade rows.

23-6

References

1 Strinning, P.E., Dunker, R.J., "Aerodynamische Auslegung und Schaufelauslegung einer
   transsonischen Axialverdichterstufe", FVV-Forschungsbericht, Heft 178, 1975.

2 Dunker, R.J., Strinning, P.E., Weyer, H.B., "Experimental Study of the Flow Field within
   a Transonic Axial Compressor Rotor by Laser-Velocimetry and Comparison with Through-Flow
   Calculations", Trans. ASME, J. Eng. Power, Vol. 100, 1978.

3 McDonald, P.W., Bold, C.R., Dunker, R.J., Weyer, H.B., "A Comparison Between Measured
   and Computed Flow Fields in a Transonic Compressor Rotor", Trans. ASME, J. Eng. Power,
   Vol. 102, 1980.

4 Dunker, R.J., Hungenberg, H.G., "Transonic Axial Compressor Using Laser Anemometry and
   Unsteady Pressure Measurements", AIAA Journ., Vol. 18, No. 8, 1980.

5 Dunker, R.J, Rechter, H., Starken, H., Weyer, H.B., "Redesign and Performance Analysis
   of a Transonic Axial Compressor Stator and Equivalent Plane Cascades with Subsonic Con-
   trolled Diffusion Blades", ASME Gasturbine Conference, Phoenix, USA, ASME-Paper 83-GT-208,
   1983.

6 Rechter, H., Steinert, W., "Auslegung und experimentelle Untersuchung von Naben-, Mittel-
   und Gehäuseschnitt eines hochbelasteten Verdichterleitrades", DFVLR Interner Bericht IB
   325/7/1981, 1981.

7 Schodl, R., "A Laser-Two-Focus (L2F) Velocimeter for Automatic Flow Vector Measurements
   in the Rotating Components of Turbomachines", Trans. ASME, J. Fluids Eng., Vol. 102,
   No. 4, 1980.

Figures

Fig. 1:
Flow path geometry of stage
RO30-UKS and design stator
blade sections

flowpath transonic stage R 030 UKS

UKG 030.3
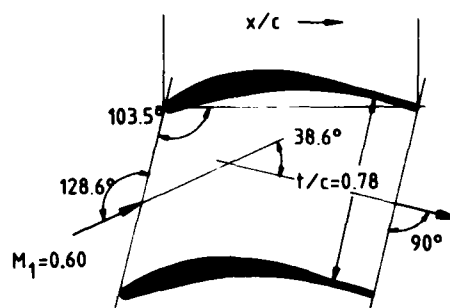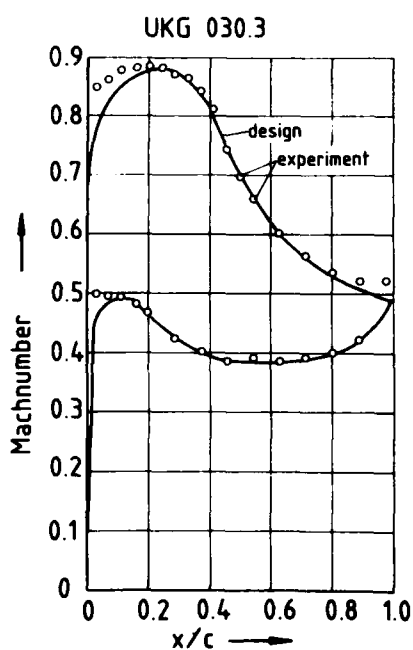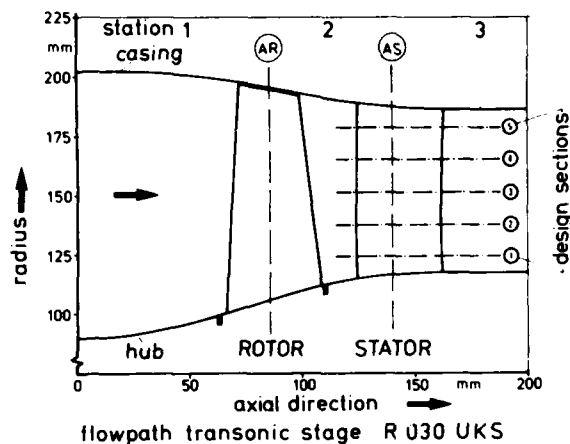
design
experiment

Fig. 2:
Prescribed surface Mach num-
ber distribution, results of
cascade design calculations,
and results of cascade tests
for stator blade mid-section

Fig. 3:
Total-pressure loss coeffi-
cient versus inlet flow an-
gle for stator blade mid-
section

STATOR SECTION:3
o—o   NACA-65 100% n_A
x—x   UKS 30.3   "
□ □   "   92,5% n_A
△ △   "   85%
CASCADE SECTION
←-→ UKG 30.3

β_1 ——   i=0°
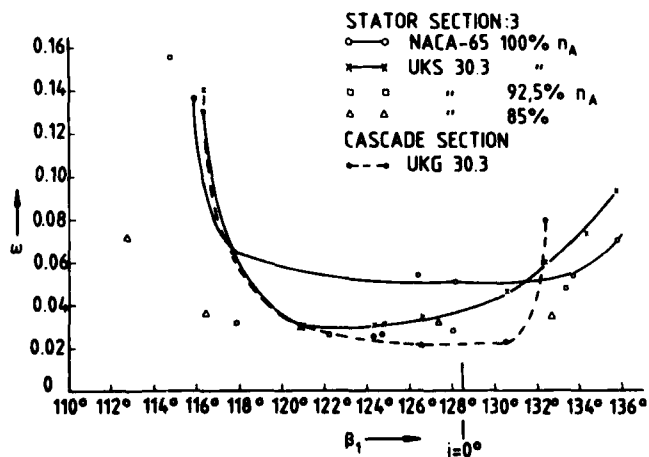
Fig. 4:
Blade surface pressure dis-
tribution versus chordlength
for stator blade mid-section
with reference static press-
ure at 45 percent chord for
cascade and stage tests
each, design mass flow:
17.15 kg/s

cascade UKG 030.3   stator section UKS 030.3
β₁=128.5°   blade height 50% (middle)
Ma₁=0.6005   n=100% n_A.n_A=20260Upm
                     ṁ_red=17.15 kg/s

rel. static pressure

pressure side

suction side

% chordlength

cascade UKG 030.3 stator section UKS030.3
β₁ = 128.5°   blade height 50%(middle)
M_o1 = 0.6005   n=100% n_D.n_D = 20260 rpm
                   ṁ_red = 17.3 kg/s

pressure side

suction side

rel. static pressure

% chordlength
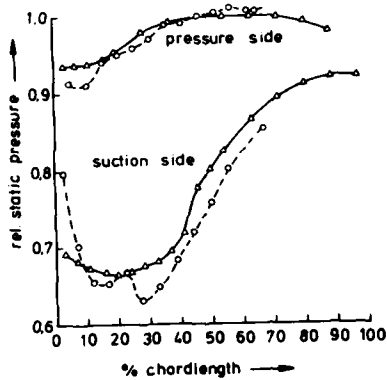
Fig. 5:
as fig. 4, but mass flow:
17.3 kg/s

stator section UKS 030.3
blade height 50% (middle)
n=100% n_D;n_D=20260 rpm
ṁ_red = 17.58kg/s

pressure side

suction side

rel. static pressure

% chordlength

Fig. 6:
as fig. 4, but mass flow:
17.58 kg/s

o= stator section UKS 030.3
blade height 50% (middle)
n=100% n_b : n_b=20260 rpm
$\dot{m}_{red}$ = 15.35 kg/s

Fig. 7:
as fig. 4, but mass flow:
15.35 kg/s

Fig. 8:
L2F-measuring positions
in one blade passage of
stator UKS for cartesian
section at 50 percent span;
mass flow: 15.35 kg/s,
near stage stall margin

Fig. 9:
as fig. 8; mass flow: 17.58
kg/s, near stage choke margin
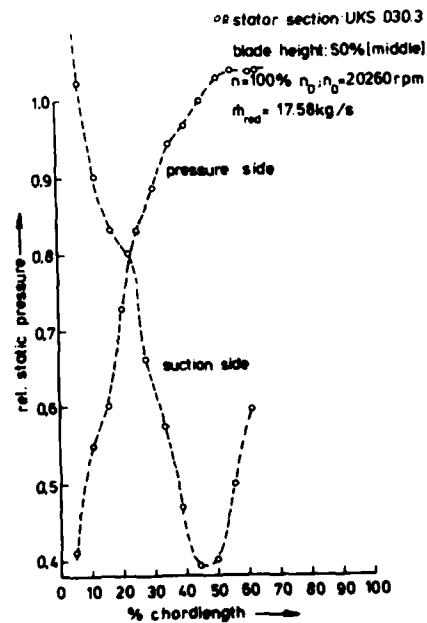
Fig. 10:
Distribution of turbulence in-
tensity parallel to local tem-
porary main flow direction
(Tpar) within one stator
blade passage; mass flow:
17.3 kg/s
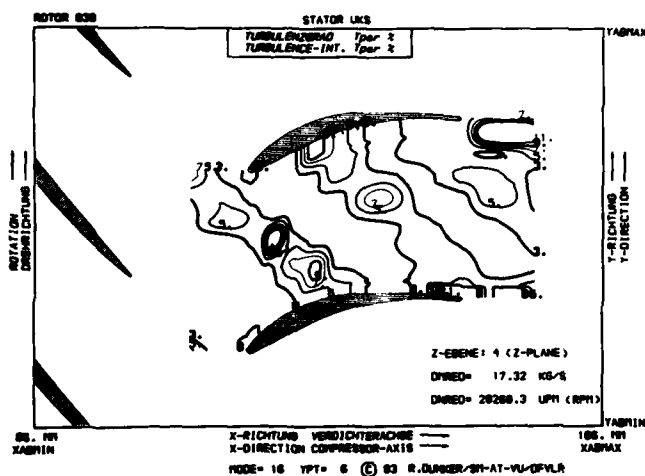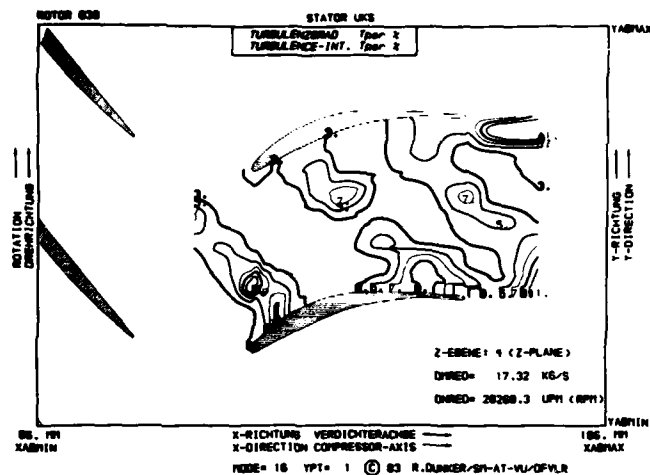
Fig. 11:
Distribution of turbulence in-
tensity (Tpar) as in fig. 10,
but at altered rotor blade
setting by 1/3 rotor blade
pitch

Fig. 12:
Distribution of turbulence
intensity (Tpar) as in fig.
10, but at altered rotor
blade setting by 2/3 rotor
blade pitch
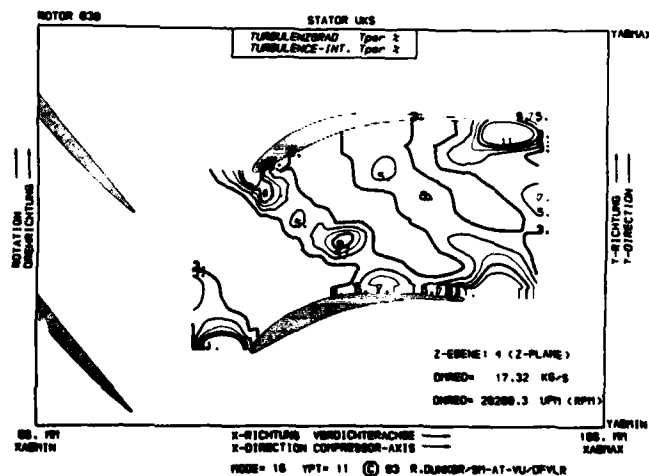
Fig. 13:
Distribution of turbulence
intensity (Tpar) as in fig.
11, but for a mass flow:
17.58 kg/s
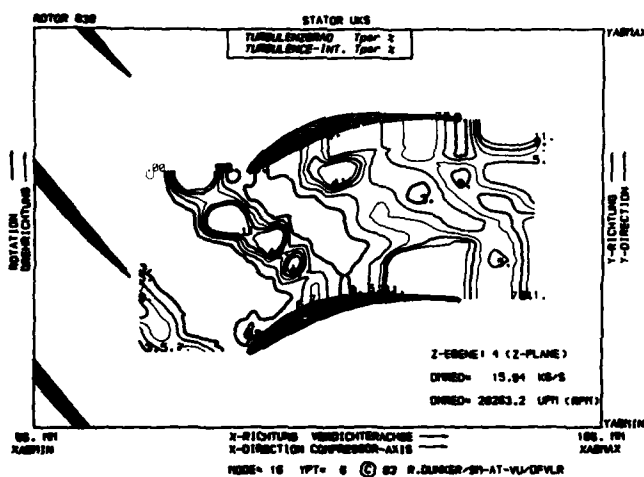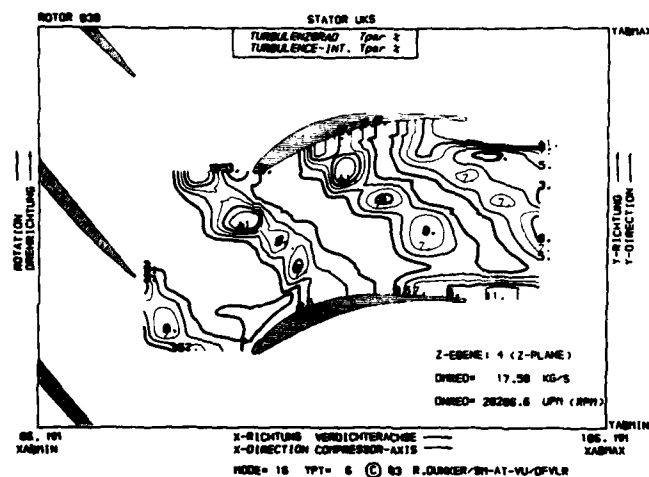
Fig. 14:
as fig. 13, but for a mass
flow: 15.93 kg/s

Fig. 15:
as fig. 13, but for a mass
flow: 15.35 kg/s
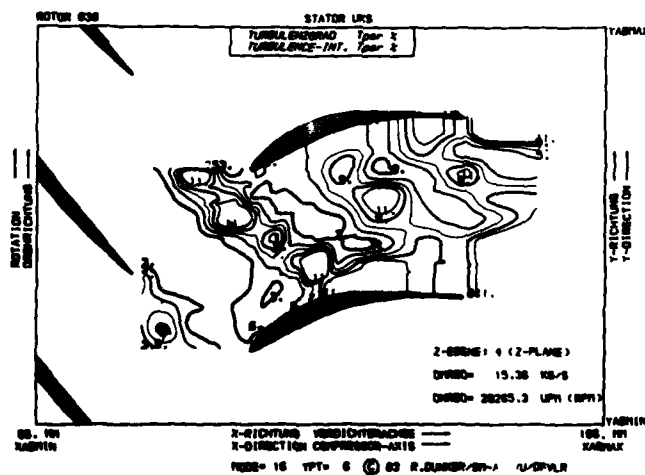
Fig. 16:
Distribution of absolute
velocity c (related to
rotor tip speed u_{tip}) with-
in one stator blade passage
as in fig. 10
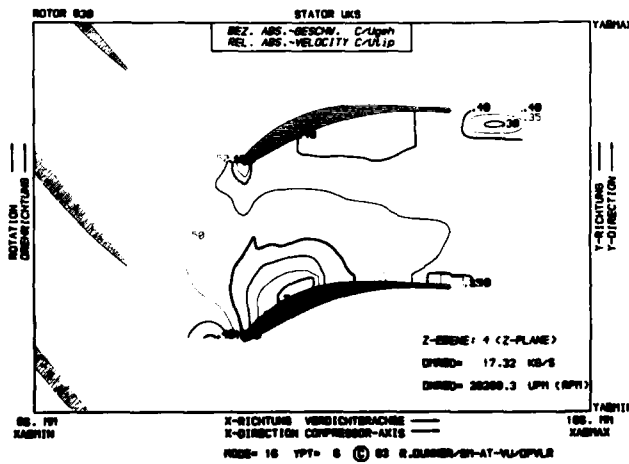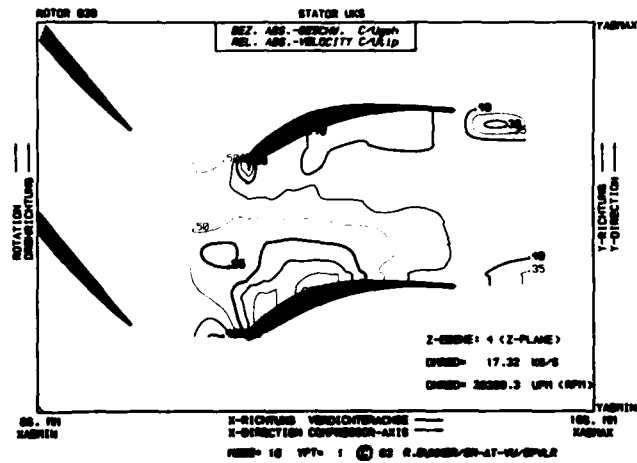
Fig. 17:
Distribution of absolute
velocity as in fig. 16,
but at altered rotor blade
setting by 1/3 rotor blade
pitch

Fig. 18:
Distribution of absolute
velocity as in fig. 16,
but at altered rotor blade
setting by 2/3 rotor blade
pitch
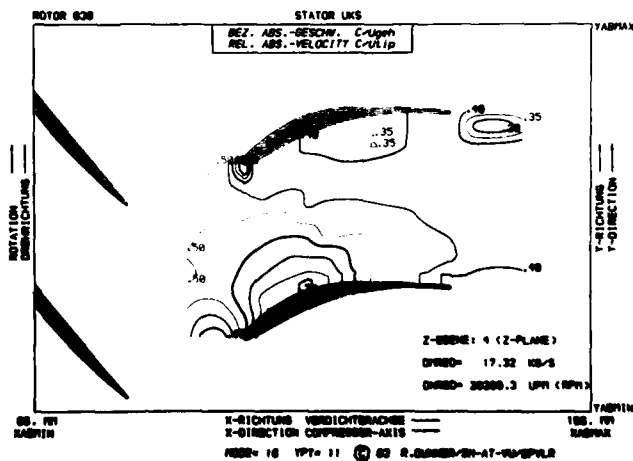
DISCUSSION

R.I.Lewis, UK

Needless to say, the vortex patterns in the last few figures can't be left without comments from me. It's very interesting to see these pictures that you described as pictures of turbulence intensity. I wonder whether they are that or whether they are, as you say, possibly vortex streets. Looking at them there are two points one could make: first of all, I think you could actually calculate the frequency of these little islands of turbulence, get a Strouhal number from it and compare that with the blade passing frequency. I don't know whether you have tried to do that. And then, secondly, from most of the figures you can see that the diffusion effect of the stator seems to diminish the intensity of these islands of vorticity, if that's what they are, as they pass through. I think that probably is what one would expect. If they were vortices there would be viscous diffusion going on and if the flow is decelerating, I think that probably would augment the spread of the vortex. If in fact it is a vortex shedding and it is not connected with the blade passing frequency, then it looks as if there's something there that should be investigated in a bit more detail. Maybe there is some other problem to do with trailing edge flows in your transonic rotor that really should be taken care of.

Author's Reply

I've been a little bit cautious. I said in my presentation "vortex-like structures". I'm not totally sure about that, if they are vorticities or vortexes. But, at the time, we thought a lot about that problem and at first we didn't believe those things when we made the measurement series or when we had such a lot of different operating conditions and always we saw these particular regions. Then we tried to understand why that happens and at first we asked our measurement technique, is it correct? And we came to the conclusion that it must be correct. If there is not something like a vortex, then there would be a random signal or a noise signal in our velocity distributions.

COMPRESSOR ROTOR AERODYNAMICS

Robert P. Dring, Manager Gas Turbine Technology
H. David Joslyn, Research Engineer
Joel H. Wagner, Research Engineer
United Technologies Research Center
East Hartford, Connecticut 06108 U.S.A.

SUMMARY

Although the numerical sophistication of multi-stage turbomachinery through-flow cal-culations has evolved to a very high level, the aerodynamic inputs of total pressure loss, deviation and blockage are subject to a high degree of empiricism. There is a need for detailed flow field data in a multi-stage environment in order to bring some discipline to this important aspect of turbomachinery design. This paper presents a survey of some of the initial results of an in-depth investigation of the aerodynamics of the second stage of a large scale two-stage axial compressor. The second stage rotor data will be compared with data obtained on an isolated rotor with very thin and then very thick inlet hub and tip boundary layers. The single and multi-stage rotor data presented here include surface flow visualization and rotating frame radial/circumferential traverse measurements presented in the form of fullspan contour plots of rotary total pressure. Also presented are the spanwise distributions of loss, deviation and blockage. Some implications of these results for through-flow analyses are discussed.

INTRODUCTION

The "through-flow" analysis in compressor (and turbine) design is a two-dimensional, axisymmetric calculation describing the spanwise variation of the flow at streamwise loca-tions both within and between blade rows from the inlet of the compressor to its discharge. The analysis is used both to determine rotor and stator metal angles for optimum design point performance (based on various criteria for optimum incidence and deviation) and to predict off-design performance and the approach to stall or choking. It is a fairly well recognized fact that the limiting feature in the accuracy of a through-flow analysis is not so much in the numerics but rather in the aerodynamic data that the analysis requires

as input. This observation has also been made in at least two prior AGARD reports (Refs. 1 and 2). Specifically, it was observed that there "was a lack of reliable and publicly available data especially for multi-stage compressors".

In recognition of this state of affairs, since 1977 the UTRC Large Scale Rotating Rig (LSRR) has been engaged in obtaining detailed data of high quality in the flows over iso-lated compressor rotors and in a multi-stage compressor environment. The objectives of this program include (1) gaining a better physical understanding and providing a basis for improved analytical models for the complex three-dimensional flows present in compressor blade rows, and (2) conducting detailed comparisons between measured and computed results both on a blade-to-blade basis and on a through-flow basis. To date this combined experi-mental and analytical program has included: (1) an isolated rotor with thin inlet boun-dary layers ($\delta \approx 5$ to 10% span) on the hub and casing (Refs. 3 and 4), (2) the same rotor with thick inlet boundary layers ($\delta \approx 37$% span) on the hub and casing (Ref. 5), and (3) a two stage compressor. Each one of these test programs includes a large amount of detailed, high quality data taken on the airfoils and in the flows downstream of the airfoils.

This paper presents a survey of some of the results obtained in these three test pro-grams. The data to be presented for each of the three rotor tests includes: surface flow visualization on the airfoil and on the endwall, rotating frame radial-circumferential traverse measurements presented in the form of fullspan contour plots of rotary total pres-sure, and spanwise distributions of mass averaged total pressure loss, inlet and exit flow angle and blockage. The results for the three rotors will be compared and their implica-tions so far as through-flow analyses are concerned will be discussed.

Of particular significance in this regard is the concept of blockage. Considering its pivotal role in compressor through-flow analysis, blockage has been the subject of remark-ably little discussion in the literature. The concept of blockage is an empirical attempt on the part of the compressor analyst to account for the difference in a through-flow ana-lysis between mass averaged quantities (such as work) and area averaged quantities (such as mass flow). Historically, blockage has been based on rough estimates reflecting past ex-perience and little or no direct physical measurement. It has been deduced analytically from previous compressor test results. Errors in estimated blockage are one of the primary reasons for compressors initially not achieving their design goals of flow, pressure rise and efficiency.

Because of the highly detailed nature of the results that can be obtained in both the rotating and stationary frames of reference in the UTRC LSRR blockage can be calculated directly from the data. The results clearly indicate the sites and magnitudes of the major

contributions to blockage (i.e., corner stall and casing boundary layer flow) and, as such, they provide a unique basis for an analytical explanation and representation of this phenomena.

EXPERIMENTAL FACILITY AND INSTRUMENTATION

The United Technologies Research Center Large Scale Rotating Rig (LSRR) is 5-ft (1.52 m) in diameter and can run at speeds up to 900 rpm. The inlet flow is from ambient room air and the flow through the facility is essentially incompressible. More detailed descriptions of the rig and its data acquisition system are available in Refs. 4 and 6.

The airfoil geometry and the aerodynamic test conditions for both the isolated compressor rotor and the two stage compressor rotor are summarized in Table I. The isolated rotor had a 6 inch (0.152 m) chord (B) and was tested both with thin inlet hub and casing boundary layers (δ_{hub} = 5% span and δ_{tip} = 10% span) and with thick inlet hub and casing boundary layers (δ_{hub} = δ_{tip} = 37% span). The results of these two test programs are presented in detail in Refs. 3 and 4 for the thin case and in Ref. 5 for the thick case. The absolute inlet flow in both cases was axial. The second stage rotor tested in the two stage compressor had a 4 inch (0.102 m) chord and its inlet conditions were determined by the flow leaving the first stage stator.

The present discussion is limited to the data taken when both rotors were being operated at their nominal design flow coefficients (ϕ). These are 0.85 for the isolated rotor and 0.51 for the two stage rotor. These flow coefficients are based on the area averaged C_x and the wheel speed at midspan (U_m). The flow coefficients that will be quoted for the isolated rotor with the thin inlet boundary layer will be based on midspan C_x at the inlet which is 2 percent greater than the area average. This is done in order to be consistent with all of the results presented in Refs. 3 and 4 where the inlet midspan C_x was used.

The major differences between the isolated and two stage rotors are in their nominal design flow coefficients (0.85 and 0.51), their stalling flow coefficients (approximately 0.6 and 0.44), their aspect ratios (1.0 and 1.5) and their tip clearance to chord ratios (0.016 and 0.039).

The technique used to obtain the airfoil and endwall surface flow visualization has been discussed and demonstrated previously in Refs. 3, 4, 5 and 6. In brief, it consisted of seeping a small amount of ammonia out of one of the airfoil surface static pressure taps. The ammonia caused a dark blue streak line to form on Ozalid paper attached to the surface downstream of the pressure tap. The technique is particularly well suited to the rotating frame of reference.

The rotating frame radial-circumferential traverse system has also been described earlier in Refs. 4 and 6 and is shown in some detail in Ref. 3. The device can traverse circumferentially over two blade pitches and radially from hub to tip. In the present programs data was acquired from 5 percent span to 97 percent span. The traverse can be located at various positions ($\Delta X/B_x$) downstream of the rotor (as in Ref. 4). For the present program, however, at midspan the traverse was 30 percent of the rotor axial chord axially downstream of the isolated rotor. For the two stage rotor it was located 25 percent downstream, midway between the rotor trailing edge and the second stator leading edge. These locations were chosen based on mechanical constraints (i.e., the two stage rotor-stator axial gap) and on aerodynamic constraints. Aerodynamically it was desirable to have the traverse close to the trailing edge to show detail in the flow and not so close as to be in any locally stalled region as occurred for the isolated rotor at a traverse location only 10 percent downstream (Ref. 4).

The traverse probe used was a United Sensor five hole probe (USC-F-152) modified to include a cobra probe for traversing very close to the hub. The probe tip was small relative to the flow field (Dia. = 0.093 inches, 2.4 mm). The probe was operated in a computer controlled yaw nulling mode. Data was acquired at approximately 20 radial locations and at typically 50 circumferential locations for 1000 measurement sites per plane. Measurement locations were concentrated in the hub and tip endwall regions and in the airfoil wake.

FLOW VISUALIZATION

The results of the surface flow visualization will be discussed first, before any of the detailed traverse data, in order to provide some physical insight into the nature of the flows in the three rotor tests. Generally speaking there were many very similar features in the three flow visualization results (Figs. 1, 2 and 3). The suction surfaces were very nearly two-dimensional in nature over much of their area. The major departure from two-dimensionality is the corner stall region present in all three tests.

The corner stall region for the two isolated rotor tests (thin and thick inlet boundary layers) are very similar in size and shape. The flow in the stalled region is generally outward (toward the tip) and there is a region of reversed flow out to about 25 percent span. The corner stall region begins slightly downstream of midchord and it displaces the profile boundary layer outward (toward the tip) to about midspan (a distance of about 50% chord from the endwall). The corner stall region on the two stage rotor was slightly

smaller, starting slightly aft of midchord, but it displaced the profile boundary layer outward a distance somewhat larger than half the chord. Note that these comparisons of the nature of the corner stall region are at the nominal design flow coefficients and that their spanwise and chordwise extent will be a strong function of loading (Ref. 4). The spanwise extent of the corner stall region will depend on the relative "health" of the suction surface boundary layer above it. The spanwise extent will increase as boundary layer separation is approached. Low momentum fluid in the hub stall regions tends to be centrifuged toward the tip and can eventually reach the tip (Ref. 4).

The tip region of the suction surface has a weak outflow due to the leakage flow over the tip entraining the suction surface flow. There is, however, no evidence of a strong suction surface corner stall at the tip. This is consistent with the results of Ref. 7 (Plate 5) where it was observed that the tip clearance flow tends to "wash away" the corner stall. It was observed in Ref. 7 that a clearance to chord ratio of 0.04 was optimum in terms of minimizing the extent of the corner stall region. This is very close to the relatively large clearance to chord ratio of the two stage rotor (Table I).

The pressure surfaces of the three rotors were very nearly two dimensional (collateral) over most of the airfoil. The radial component of surface flow was small except in the immediate vicinity of the tip. Here there was a weak radial outflow due to leakage and no indication of a scraping vortex (i.e., flow toward the hub).

On the hub the effects of secondary flow in the endwall boundary layer were minimal. The endwall flows were nearly collateral with a trajectory close to the airfoil mean camber line. The corner stall region had no significant impact on the hub endwall boundary layer.

In conclusion, the flow visualization results indicate that the major departures from what would be otherwise highly two-dimensional boundary layer flow, are due to the corner stall region at the hub and to the leakage flow at the tip.

CONTOURS OF ROTARY TOTAL PRESSURE

Contour plots of rotary total pressure measured in the flow downstream of the three rotors are shown in Figs. 4, 5 and 6. The data for the isolated rotor with the thin inlet boundary layers covers 1.32 pitches. The data for the thick inlet boundary layer and for the two stage rotor covers two pitches. Recall that for the two isolated rotor tests the traverse plane was 30 percent aft of the rotor and that for the two stage test it was 25 percent aft. In all cases the suction surface side of the wake is to the left and the pressure surface side of the wake is to the right.

Rotary total pressure is defined as follows:

$$P_{T,rot} \equiv P + \tfrac{1}{2}\rho(W^2 - U^2) = P_{T,abs} - \rho U C_\theta \qquad (1)$$

where W, U and C_θ are the relative flow speed, the wheel speed and the absolute swirl velocity, respectively. Rotary total pressure was chosen for the present discussions since (unlike relative total pressure) for inviscid flow it is invariant with radius change along a stream line in the rotating frame of reference. It is also desirable to look at rotary total pressure from the point of view of secondary flow. For flow with uniform density, gradients in rotary total pressure are the driving potential for secondary flow in the rotating frame of reference in the same manner as gradients in absolute total pressure are the driving potential for secondary flow in the stationary frame of reference (Ref. 8). The increment between the values of the rotary total pressure on the various contours has been normalized by a dynamic pressure based on wheel speed at midspan.

For the isolated rotor with the thin inlet boundary layer (Fig. 4) there is a large "free stream" region of constant rotary total pressure between the wakes and the endwalls. This is present due to the thinness of the inlet boundary layers (δ = 5 and 10% span) and the constant absolute total pressure in the inlet core flow region. The contours for the isolated rotor with the thick inlet boundary layers (Fig. 5) are quite different. The circumferential contours in the free stream region between the wakes and the endwalls are due to the radial gradients in absolute total pressure in the thick boundary layers (δ = 37% span) in the fluid entering the rotor. For the two stage rotor (Fig. 6) the contours in the free stream region are due to the upstream inlet guide vane, rotor and stator. Comparatively speaking, however, the flow in the free stream region has a relatively uniform rotary total pressure. In general, many of the same features can be seen in varying magnitude in all three rotor exit flow fields.

At the hub, the data for both isolated rotor tests (Figs. 4 and 5) show little evidence of Bernoulli surface rotation due to secondary flow. The streamwise component of vorticity generated by turning the flow is insufficient to overcome the initial inlet streamwise vorticity. The former would move endwall fluid from the pressure to the suction surface side of the channel while the latter (due to inlet skewing) tends to drive the endwall boundary layer fluid toward the pressure surface (Ref. 9). There is some indication of flow toward the hub on the pressure surface side of the passage. Finally, for both isolated rotor cases there is a thickening of the blade wake in the hub region due to the corner stall. The thickening for the thin and thick cases is very similar. This observation is

consistent with those of Ref. 10 where it was demonstrated that the severity of the corner stall was insensitive to the thickness of the inlet boundary layer.

The data for the two stage rotor (Fig. 6) indicated that the flow in the hub region was relatively clean, that is, similar to the isolated rotor with the thin inlet boundary layer in that no strong shear regions were evident. There is some evidence of Bernoulli surface rotation due to secondary flow near the suction surface. The corner stall region is very thin relative to those of the two isolated rotor cases and appears as little more than a thickening of the blade wake. The corner stall begins to deepen and thicken the wake at about midspan.

From the hub region the following conclusions can be drawn. The corner stall is the major source of hub loss and blockage. The corner stall behaves more like a thickened blade wake rather than a thickening of the hub endwall boundary layer. Finally, for the two isolated rotor cases, the effects of secondary flow were minimized due to the skewing and energizing of the hub boundary layer as it comes onto the rotating hub.

When comparing the flows in the tip region recall that the clearance for the two isolated rotor tests was 1.6 percent of chord while for the two stage test it was 3.9 percent of chord. The flow in the tip regions is influenced by tip leakage, wall motion (toward the pressure surface) and the inlet boundary layer. For the two isolated rotor cases (Fig. 4 and 5) the low total pressure region is nearly midway between adjacent airfoil wakes. This is similar to results presented for tip leakage in a stationary cascade without an endwall present and with a clearance to chord ratio of 4 percent (Ref. 7, experiments A and B).

The tip region of the two stage rotor was considerably different in that the low total pressure region was very close to the pressure surface. For this case the center of the low total pressure region was located 30 percent further from the tip endwall, inspite of the shorter chord. These differences must in some measure be due to the much larger tip clearance of the two stage rotor.

ROTOR TOTAL PRESSURE LOSS

One of the more significant pieces of information to be derived from the traverse data presented above is the spanwise distribution of the rotor total pressure loss. In the present discussion the total pressure loss coefficient ($C_{PT,rel}$) is defined as the difference between the mass averaged inlet and exit relative (or rotary) total pressures at a fixed radius, normalized with a dynamic pressure based on the wheel speed at midspan. Strictly speaking the total pressure difference should be taken along a fixed (axisymmetric) stream surface. For all three rotors the maximum radial displacement of a stream surface was about 1 percent span (near midspan). Finally, the mass averaging of the total pressures was based on the measured circumferential distributions of flow speed, yaw and pitch from which the local C_x could be calculated.

The data for the thin and thick inlet boundary layer tests on the isolated rotor are shown in Fig. 7. For the thin case, since the rotary total pressure is constant over the core flow at inlet radial shifting of the stream surfaces is of no consequence in computing the net loss. In fact, for this case the inlet boundary layer only affected the loss at the two or three data points closest to the endwalls. The corner stall region (Fig. 1) and the low rotary total pressure region associated with it (Fig. 4) have caused a loss level which is very high relative to two-dimensional (profile) loss levels and which penetrates out to 40 percent span. The high loss region at the tip is felt from 75 percent span outward. The loss in the midspan region is representative of two-dimensional cascade levels (Ref. 4, Fig. 6).

For the isolated rotor with the thick inlet boundary layers (Fig. 7) there is a region of very low loss out to 10 percent span due to the weak radial redistribution of the inlet rotary total pressure profile. As mentioned above, high total pressure fluid moved toward the hub near the pressure surface side of the wake (Fig. 5) causing an increase in rotary total pressure in the region and hence a local reduction to the mass averaged loss. Similar effects can be seen in the cascade results of Ref. 7 (Fig. 21) and in the rotating rig data of Ref. 11 (Fig. 6) where spanwise redistribution of high and low total pressure fluid caused a negative mass averaged total pressure loss near the endwalls. These observations regarding endwall flow in compressor airfoil passages and the dominant contributions of corner stall relative to endwall secondary flow are consistent with similar observations made in Ref. 10.

The thick inlet boundary layer isolated rotor test indicated no well defined low loss region at midspan as occurred for the thin case. Both the hub and tip high loss regions occupied a larger portion of the span than in the thin case. The reason for this difference is not evident in the flow visualizations (Figs. 1 and 2) but it is somewhat suggested by the rotary total pressure contours (Figs. 4 and 5).

The loss data for the two stage rotor is presented in Fig. 8. The radial distribution of the rotor inlet relative total pressure was computed by mass averaging the circumferential distributions of relative total pressure computed from the absolute frame traverse data taken at the first stator exit. The nature of the loss distribution near the hub is similar to that of the thick inlet boundary layer isolated rotor tests, with a low (negative) loss region close to the endwall. Here, as above, the low and negative loss region

at the hub is due to the high total pressure fluid moving toward the hub near the pressure surface side of the blade wake (Fig. 6).

In the midspan region the loss level is slightly negative (1.3% at midspan). There are a number of possible explanations for this result, any one or all of which may be contributing to the negative loss. (1) It may be a result of experimental error. An error of 0.5 percent in the measured total pressure at the rotor inlet and at the rotor exit could account for the negative loss. (2) The negative loss could actually be present due to a radial redistribution of high and low total pressure fluid such as occurred near the hub. (3) The negative loss is in part due to a radial shift of the axisymmetric stream surfaces between the rotor inlet and exit measurement planes. This is possible due to the relatively large radial gradient in rotary total pressure in the midspan region of the flow. The radial shift of slightly more than 1 percent span between rotor inlet and exit is sufficient to explain half of the negative loss at the 40 percent span location where it is maximum.

FLOW ANGLES

The rotor inlet and exit metal angles (θ^*) and the inlet and exit flow angles (θ) are presented in Figs. 9 and 10. For the two isolated rotor cases the inlet flow angles were calculated from wheel speed and the measured radial variation of C_x. The inlet flow angle for the two stage rotor is based on mass averaged relative flow angles calculated from the stationary frame measurements made at the first stator exit. The rotor exit flow angles were measured in the rotating frame of reference and mass averaged based on the circumferential distributions of flow angle and C_x. Mass averaging reduces the impact of the nearly axial flow in the low velocity region immediately downstream of the corner stall.

Since both isolated rotor tests (thin and thick inlet boundary layers) were run at the same flow coefficient based on area averaged C_x the thin case was running closer to the stall from 20 percent span to 80 percent span. In the endwall regions the thick case was running closer to stall, causing the hub and tip boundary layers at the rotor inlet to be more heavily skewed in the direction opposing secondary flow due to turning. Aside from a shift in level (of approximately 2°) the exit angle profile was relatively insensitive to inlet boundary layer thickness. The 2° drop in deviation for the thick inlet boundary layer case is in part due to its lower inlet angle over the midspan region.

The large under turning in the tip region of both isolated rotor cases is due to at least three mechanisms. (1) Tip leakage contributes to the under turning. This was shown in Ref. 7 for a cascade and in Ref. 11 (Fig. 3) for a large scale multistage rotor. (2) Wall motion also contributes to the under turning. As the wall is approached the flow angle must approach 90°. Finally (3) the inlet boundary is skewed toward the rotor pressure surface due to the rotor motion, leading to under turning.

The flow angle data for the two stage rotor in Fig. 10 are similar in many ways to the isolated rotor data. There is over turning at the hub due to corner stall and under turning at the tip due to leakage and wall motion. The results are also very similar to those of Ref. 11 (Fig. 3).

BLOCKAGE

Through-flow analyses are axisymmetric calculations of the radial distributions of mass averaged quantities. Mass flow (M), however, is related to the area average of ρC_x. The mass averaged quantities are related to this area average in the continuity equation by the blockage factor ($\bar{K}$).

$$M = 2\pi \int_{r_h}^{r_t} \bar{K} \rho \bar{C}_x^{PT} \, r dr \qquad (2)$$

According to this expression $\bar{K}$ is the ratio of the area averaged axial velocity (or $\bar{C}_x^a$) to $\bar{C}_x^{PT}$, the axial velocity based on the mass averaged total and static pressures and the mass averaged yaw (θ) and pitch (ϕ) angles. This relationship may be expressed as follows.

$$\bar{K} \equiv \left(\bar{C}_x^a / \bar{C}_x^{PT} \right) = f(r) \qquad (3)$$

where (for incompressible flow)

$$\bar{C}_x^{PT} \equiv \left(\sqrt{\bar{P}_T^m - \bar{P}_S^m / \tfrac{1}{2}\rho} \right) \cos \bar{\theta}^m \cos \bar{\phi}^m \qquad (4)$$

In this notation (-a) indicates an area average and (-m) indicates a mass average. The description of blockage as a function of radius is consistent with what is referred to as "tangential" blockage in Ref. 2 (p. 329). It reflects all departures from axisymmetry from hub to tip including profile wakes, corner stall, tip leakage and so on. "Endwall" block-

age does not reflect a departure from axisymmetry but rather the inability of a small number of computational stream tubes to accurately account for the endwall boundary layers. Endwall blockage reflects the computational approach of coupling a through-flow calculation to an endwall boundary layer calculation. For example, endwall blockage would not be required in the single pass axisymmetric analysis of Ref. 12 which simultaneously solves both the viscous and inviscid regions of the flow. For this approach endwall blockage is unnecessary and only tangential blockage would be required.

Blockage distributions have been calculated from the measured data according to the above definition. They reflect the departure from axisymmetry from the hub to the tip, i.e., the fullspan distribution of tangential blockage. The major contribution to blockage for these three rotor test cases came from the total pressure. The area and mass averages of the static pressure and the yaw and pitch angles were generally very close to one another.

Recall that the traverse planes for the isolated rotor and for the two stage compressor are 30 percent and 25 percent respectively aft of the rotors. This is significant since blockage will be a strong function of distance downstream due to wake mixing.

The blockage distributions for the two isolated rotor tests are shown in Fig. 11. The spanwise variations are very similar to the spanwise variation of total pressure loss (Fig. 7). The similarity in blockage profiles is particularly interesting in view of the factor of 4 difference in the inlet boundary layer thickness for the two cases. The blockage data also points to the dominant role of corner stall relative to secondary flow and to the insensitivity of corner stall to inlet boundary layer thickness. The blockage profile for the two stage rotor is generally lower in the endwall regions than either of the two isolated rotor cases, even with the much larger relative tip clearance.

In conclusion, the blockage profiles bear a qualitative similarity to the loss profiles with the major contributions being due to hub corner stall and tip endwall and leakage flow. The midspan blockage for all three cases (at their nominal design flow coefficients) is very small.

CONCLUSIONS

This paper has presented a comparison of several types of data acquired on three compressor rotor configurations: an isolated rotor with very thin inlet hub and tip boundary layers, the same rotor with thick inlet boundary layers, and a two stage compressor second stage rotor, each running at its nominal design flow coefficient. The data examined for each configuration consisted of surface flow visualization, a radial-circumferential distribution of rotary total pressure in the flow aft of the rotor, and the spanwise distribution of loss, flow angle and blockage.

There were many strong similarities in the main features of the flow over the three rotors. The most striking was the strong influence of hub corner stall (as opposed to the hub endwall boundary layer) on the loss, deviation and blockage and its insensitivity to inlet boundary layer thickness. The tip boundary layer and leakage flow were also seen to have a strong impact. Although secondary flow was generally seen to be rather weak, as evidenced by the slight rotation of the Bernoulli surfaces and the lack of cross flow in the hub boundary layers, radial redistribution of high and low total pressure fluid through the rotor passage and in the downstream flow was observed to produce spanwise distributions of the total pressure loss which were locally negative. This radial redistribution could have been due to mechanisms other than the weak secondary flow, e.g., it could have been a result of the radial outflow in the corner stall region.

The present two stage compressor program is being continued with particular emphasis in the areas of tip clearance effects, off-design performance and the stator. As a result of these and the earlier experimental studies and companion analytical work it is expected that a more complete and detailed understanding of multi-stage compressor aerodynamics will emerge.

REFERENCES

1. -----, AGARD Conference Proceedings No. 195 on Through-Flow Calculations in Axial Turbomachinery, 47th meeting of AGARD/PEP, AGARD-CP-195, May 20-21, 1976.
2. -----, AGARD Advistory Report No. 175, Propulsion and Energetics Panel Working Group 12 on Through-Flow Calculations in Axial Turbomachines, AGARD-AR-175, October 1981.
3. Dring, R, P., H. D. Joslyn and L. W. Hardin: "Experimental Investigation of Compressor Rotor Wakes," AFAPL-TR-79-2107, Air Force Aero Propulsion Laboratory, Technology Branch, Turbine Engine Division (TBX), Wright-Patterson Air Force Base, OH.
4. Dring, R. P., H. D. Joslyn and L. W. Hardin: "An Investigation of Compressor Rotor Aerodynamics," ASME, Journal of Engineering for Power, January 1982, Vol. 104, p. 84-96.
5. Wagner, J. H., R. P. Dring and H. D. Joslyn: "Axial Compressor Middle Stage Secondary Flow Study," final report submitted to NASA-Lewis Research Center for Contract No. NAS3-23157, December 1982.
6. Dring, R. P. and H. D. Joslyn: "Measurements of Turbine Rotor Blade Flows," ASME Gas Turbine Conference, New Orleans, LA, Measurement Methods in Rotating Components of Turbomachinery, p. 51-58.
7. Lakshminarayana, B. and J. H. Horlock: "Leakage and Secondary Flows in Compressor Cascades," ARC, R&M No. 3483, 1967.
8. Hawthorne, W. R.: "Secondary Vorticity in Stratified Compressible Fluids in Rotating Systems," CUED/A-Turbo/TR 63, University of Cambridge, England, 1974.
9. Moore, R. W. and D. L. Richardson: "Skewed Boundary Layer Flow Near the Endwalls of a Compressor Cascade," Trans. ASME, Vol. 79, November 1957.
10. Horlock, J. H., J. F. Louis, P. M. E. Percival and B. Lakshminarayana: "Wall Stall in Compressor Cascades," Trans. ASME, Journal of Basic Engineering, Vol. 88, September 1966, pp. 637-648.
11. Adkins, G. G. and L. H. Smith: "Spanwise Mixing in Axial-Flow Turbomachines," ASME, Journal of Engineering for Power, January 1982, Vol. 104, p. 97-110.
12. Anderson, O. L.: "Calculation of Internal Viscous Flows in Axisymmetric Ducts of Moderate to High Reynolds Numbers," Computers and Fluids, Vol. 8, p. 391-411, 1980.

ACKNOWLEDGEMENTS

TABLE I - ROTOR GEOMETRY & TEST CONDITIONS

	Isolated Rotor	Two-Stage Rotor
Number of Airfoils	28	44
τ_m/B	1.01	0.97
Span/B	1.00	1.50
Clrnc/B	0.016	0.039
α_s	35.5°	47.1°
Camber	49°	35°
Hub/Tip	0.8	0.8
N (rpm)	510	650
$\bar{C}_x$ (f/s)	102	78
Re (W_1, B)	4.9×10^5	3.0×10^5
ϕ	0.85	0.51
$(\Delta X/B_x)$	0.30	0.25
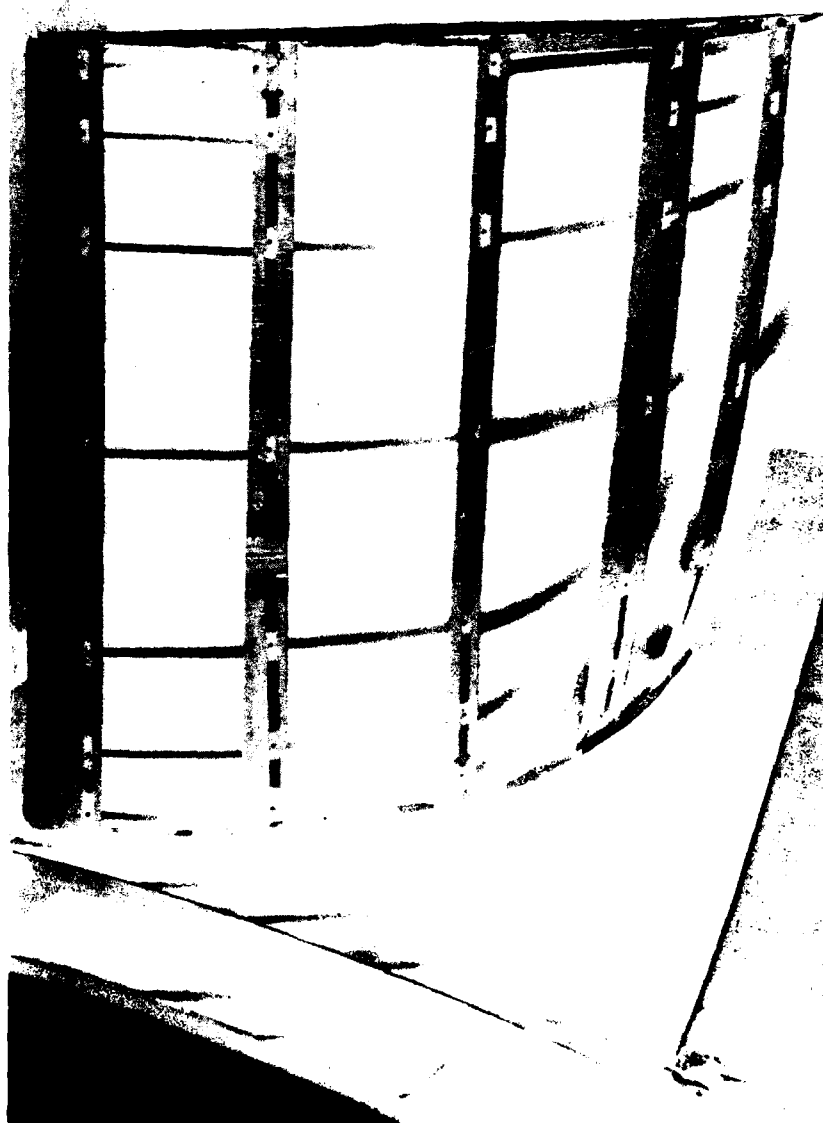
Figure 1   Isolated Rotor, Thin Inlet Boundary Layers, Suction Surface, $\phi = 0.85$
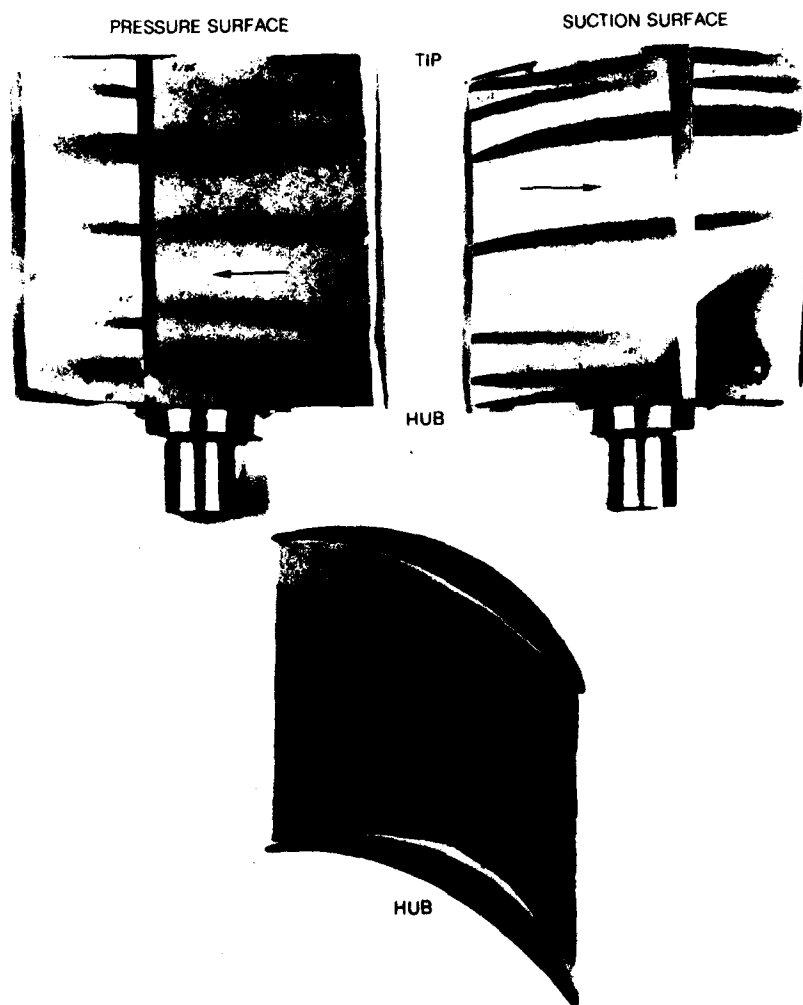
Figure 2   Isolated Rotor, Thick Inlet Boundary Layers, $\phi = 0.85$
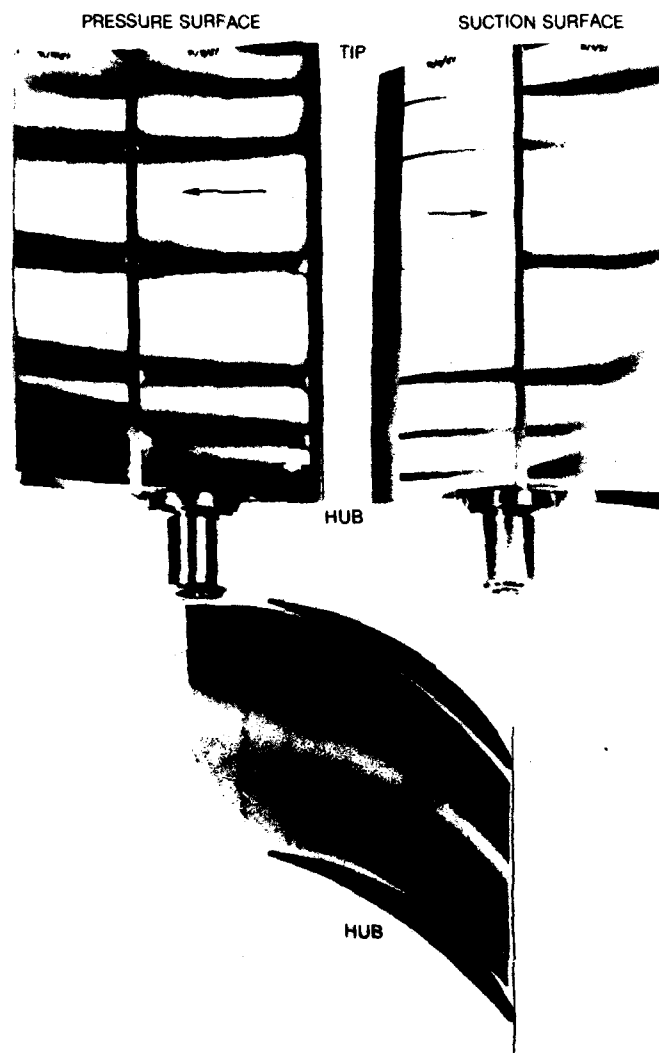
Figure 3   Two Stage Compressor, Second Stage Rotor, ϕ = 0.51
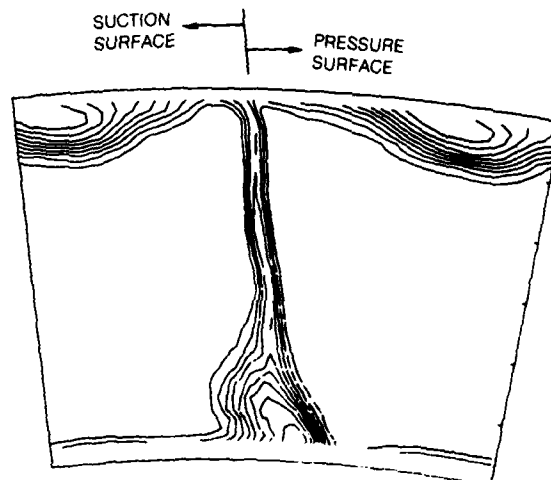
Figure 4 Isolated Rotor, Thin Inlet Boundary Layers,
Rotary Total Pressure, $\phi \approx 0.85$, 30% aft,
1.32 Pitches, $\Delta Cp_T = 0.1$
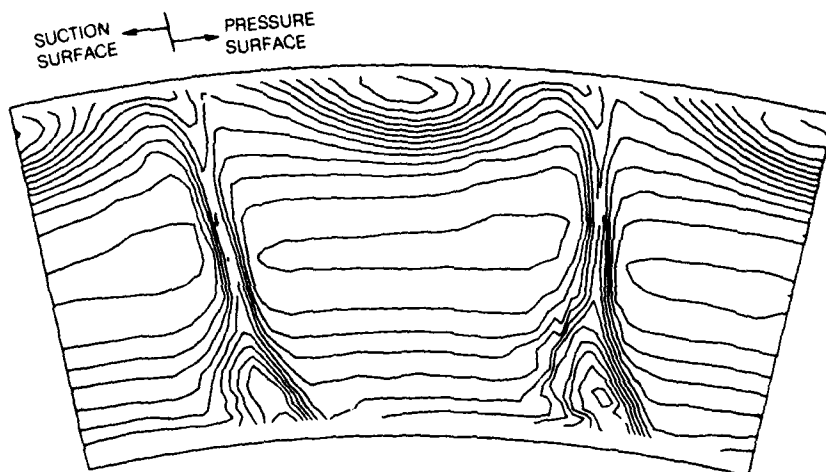
Figure 5 Isolated Rotor, Thick Inlet Boundary Layers,
Rotary Total Pressure, $\phi = 0.85$, 30% aft,
2.0 pitches, $\Delta Cp_T = 0.1$
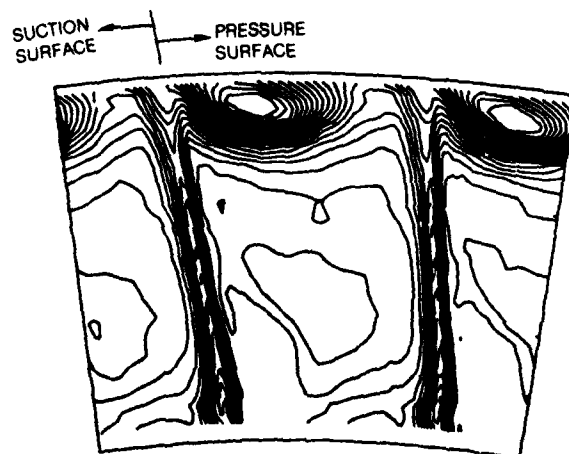
Figure 6 Two Stage Compressor, Second Stage Rotor,
Rotary Total Pressure, $\phi = 0.51$, 25% aft,
2.0 pitches, $\Delta Cp_T = 0.025$
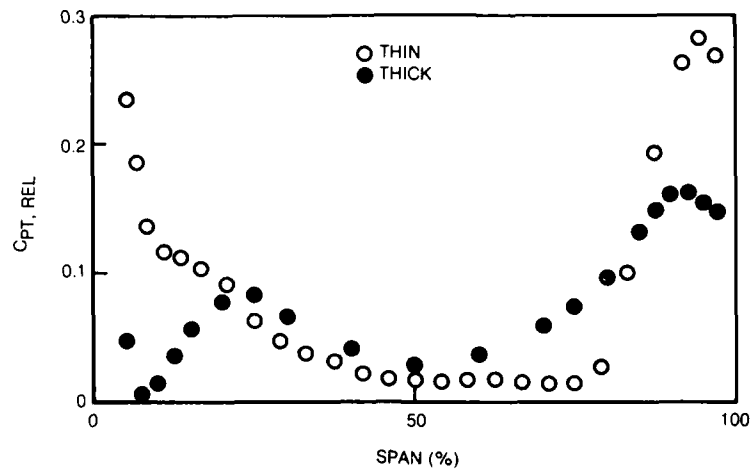
Figure 7   Isolated Rotor, Thin and Thick Inlet
           Boundary Layers, Total Pressure Loss,
           $\phi = 0.85$
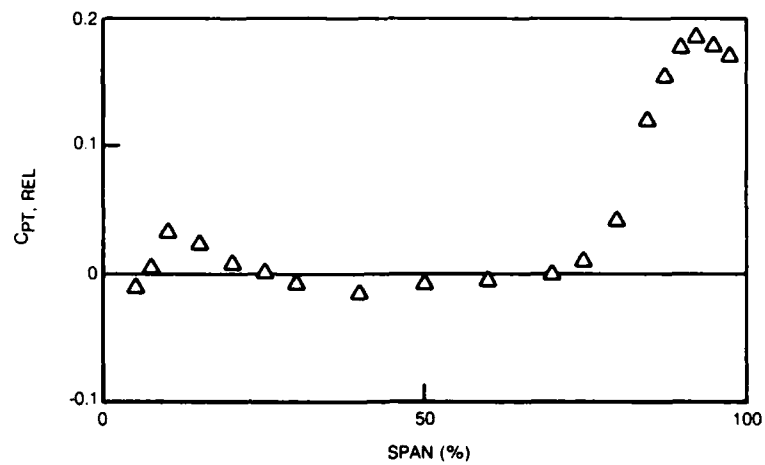
Figure 8   Two Stage Compressor, Second Stage Rotor,
           Total Pressure Loss, $\phi = 0.51$
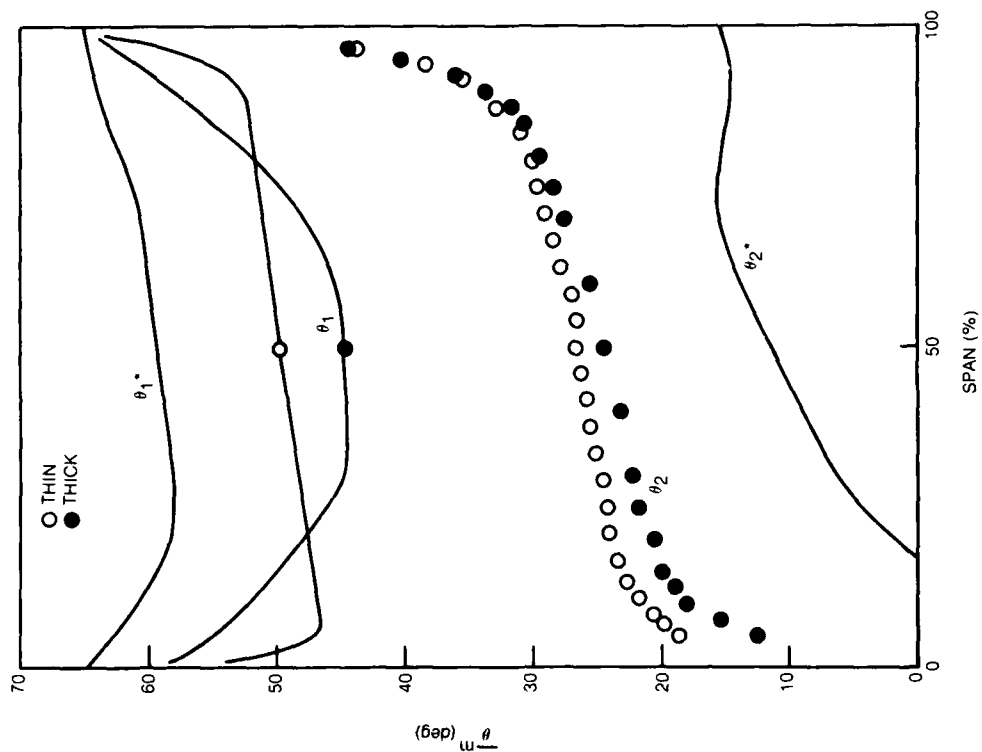
Figure 9 Isolated Rotor, Thin and Thick Inlet Boundary Layers, Relative Flow Angles, $\phi = 0.85$
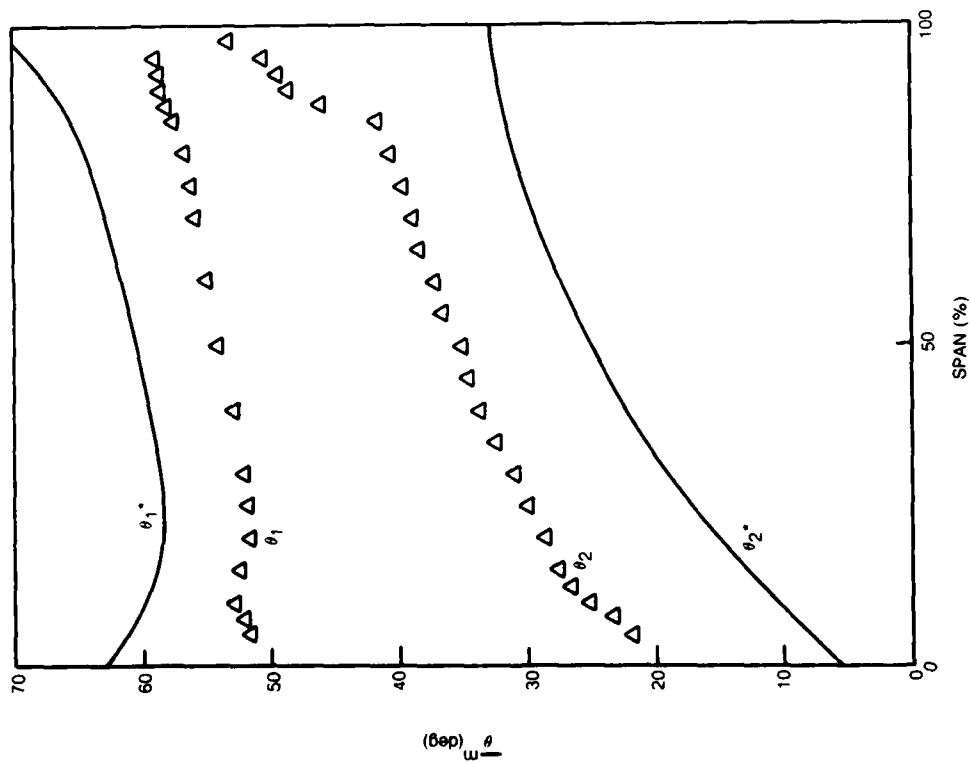
Figure 10 Two Stage Compressor, Second Stage Rotor, Relative Flow Angles, $\phi = 0.51$
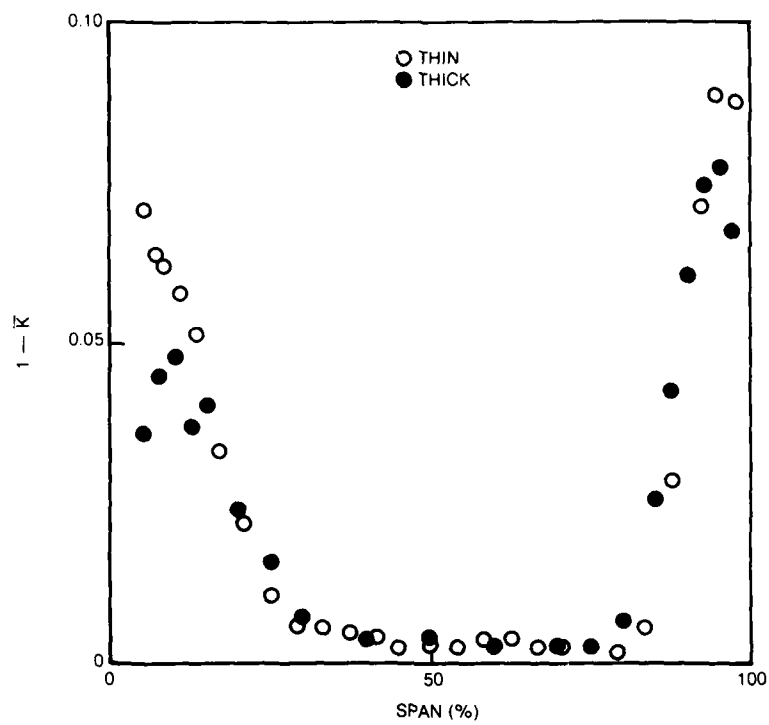
Figure 11   Isolated Rotor, Thin and Thick Inlet
            Boundary Layers, Blockage, $\phi = 0.85$
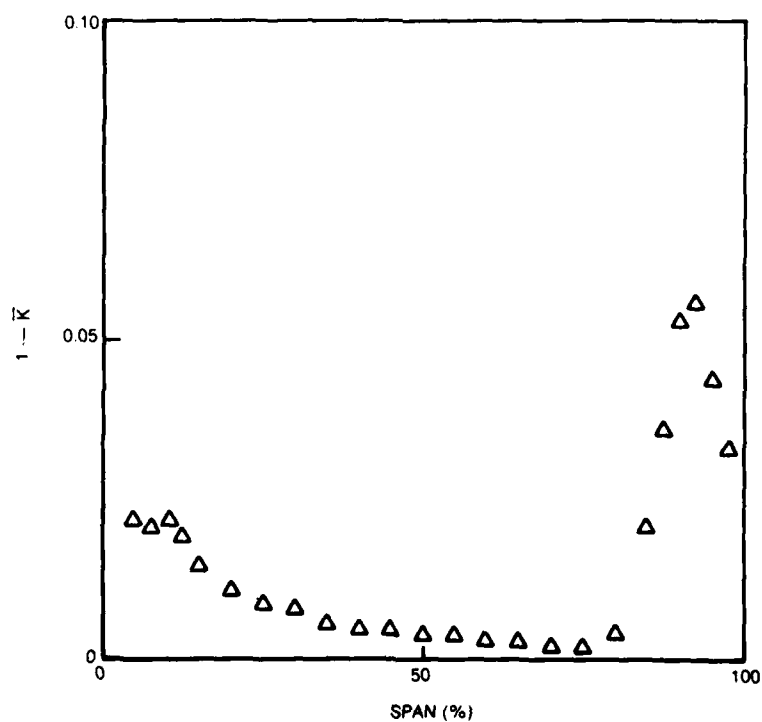
Figure 12   Two Stage Compressor, Second Stage Rotor,
            Blockage, $\phi = 0.51$

DISCUSSION

Ph.Ramette, Fr

In Figure 8, which gives the total pressure losses for the second stage rotor of the two-stage compressor, the total pressure loss is close to zero near the hub, because of the high total pressure fluid moving towards the hub near the pressure surface side of the blade wake, as you said. In the midspan region, the negative loss could be due to the large tip clearance, which is 4%, so that the flow near the tip of the blades is moving toward midspan at the exit of the rotor, redistributing the radial total pressure profile. Could you comment about this?

Author's Reply

As mentioned in the paper, aside from small measurement errors, the two prime candidates for explaining the negative loss at the midspan of the second stage rotor are radial redistribution of high and low total pressure fluid. and radial displacement of the axisymmetric stream surface. Both of these possibilities could be accentuated by the very large tip clearance. This question may become clearer as we examine additional data.

B.Lakshminarayana

(1) I would like to congratulate you on a large amount of fine data.

(2) The thick boundary layer case had very small velocity gradients near the wall and had almost a linear profile from hub to mid-radius. Since the secondary flow is very sensitive to the velocity gradients, rather than the thickness, it is not surprising that the thick boundary layer case did not have severe secondary flow. It would be useful to generate a thick boundary layer with steep velocity gradients near the wall.

Author's Reply

The thin and thick inlet C_x profiles in the isolated rotor tests were very similar in terms of their shape factors (H = 1.3 and 1.5 respectively). Since to a first approximation the secondary flow process varies linearly with the initial streamwise and normal components of vorticity the factor of 4 variation in inlet boundary layer thickness was felt to be a fairly significant variation. Finally, the two-stage test lends strong evidence that secondary flow will in general be relatively weak, particularly in comparison with the effects of corner stall.

C.L.Ball, US

My comment is not made in terms of trying to generalize between your results and that which we noted in the two-stage fan, but it is interesting to note that the circumferential blockage near the walls behind the low speed rotor is higher than in the core flow region, which is further evidence of the highly non-axisymmetric flows in the endwall boundary layer region as compared to free stream, as we observed behind the stators in the two-stage fan.

Author's Reply

I agree. Our data on these and other tests have indicated that the flow in the endwall regions is in general far more non-axisymmetric than the flow in the midspan region.

Ch.Hirsch, Be

I would like, first of all, to congratulate the authors for their continuous effort in the production of such high quality data.

I am very pleased by the importance given to the concept of tangential blockage distinct from the end-wall blockage. We are using this distinction in our through-flow calculation method and connect the blockage K to the local loss coefficient through the momentum thickness of the wake. Therefore it is not surprising that the variation of K is similar to the variation of the total pressure loss. Actually we think that the variation could be deduced from the other. Have you tried to derive the variation of K from the radial variation of wake thickness?

Author's Reply

As we noted in the paper, "the blockage profiles bear a qualitative similarity to the loss profiles". To date, however, we have not attempted to quantify this relationship. This will definitely be something to look into as we evaluate the rest of our data.

J.Moore, US

(1) Is the ammonia neutrally buoyant in these flows?

(2) Is there enough shear work at the shroud, combined with secondary flow from the shroud to cause the local increases in rotary total pressure which you observe?

Author's Reply

Strictly speaking, the ammonia used in the flow visualization is not neutrally buoyant but we believe that it does accurately follow the surface streamlines. This belief is based on numerous previous tests where density ratio and blowing rate effects were demonstrated to have no noticeable impact on the indicated surface streamline direction.

The increase in rotary total pressure was observed primarily on the two-stage compressor second stage rotor in the midspan region and very close to the hub (Fig.8). From Figure 6 it is difficult to see how shear work and secondary flow at the shroud could influence the rotary total pressure of the midspan and hub fluid other than by radial displacement of the axisymmetric stream surfaces due to blockage at the tip. The flow visualization (Fig.3) also suggests that it is unlikely that fluid originating at the rotor shroud could find its way radially into the midspan region.

EXPERIMENTAL VERIFICATION OF AN ENDWALL BOUNDARY LAYER PREDICTION METHOD

Charles W. Elrod
AFWAL/POTX
Wright-Patterson AFB

James L. Bettner
Detroit Diesel Allison Div.
General Motors Corporation

An endwall boundary layer code was verified in a low speed compressor facility and used to compute casing blockage and efficiency penalty in a full-scale engine. Detailed endwall boundary layer measurements and overall compressor performance measurements were obtained for various conditions of surface roughness, porosity and tip clearance in the low speed compressor facility. Stage pressure ratio and stall margin were determined for the single-stage compressor at three corrected speeds. Shroud roughness did not markedly reduce overall compressor performance at design conditions, but did result in some loss of stall margin. Shroud wall porosity, on the other hand, did reduce design point performance, but also substantially increased stall margin. The shroud endwall boundary layer code exhibited overall satisfactory agreement with solid smooth/rough endwall experimental results, but was not as effective for the T56-A-100 experimental results. The code was effective in predicting tip clearance effects.

INTRODUCTION

Losses in the gas turbine engine compressors are receiving increasing attention as efficiency becomes a critical design parameter. Escalating fuel costs have prompted the turbine engine research community to intensify their efforts to understand the loss mechanisms and reduce their overall effect. One of the major loss mechanisms in the gas turbine engine is leakage over the tips of both compressor and turbine rotors. A large portion of the decrement in performance attributed to tip losses is due to clearance increases during the first few hundred on wing hours, after the engine break-in. The increase in clearance results from tip wear when the rotor rubs into the case.

Through the years, attempts have been made to develop an abradable coating for the case to prevent or minimize blade tip wear. The attempts have been marginally success-ful, with wear ratios of 1:1 (blade tip to case coating ratio) being typical. The search for rub tolerant coatings has resulted in a wide variety of material character-istics and configurations. The purpose of these variations has been primarily to pro-vide a rub strip on the compressor case which will tolerate interference from the rotor without wearing the blade tip. The rub strip material must also be configured to resist erosion, oxidation and thermal fatigue.

The payoff for this material development and design effort is enormous. A change in engine performance (specifically fuel consumption) of 1% can result in savings of millions of dollars in fuel costs. This magnitude of fiscal savings is leading engine designers to consider other factors (factors involving aerodynamic considerations rather than mechanical parameters), as well as blade tip wear. Two such factors are rub strip roughness and porosity.

Intuitively, one would suspect that both factors would influence stage and overall engine performance; however, only limited evidence of an empirical basis for this con-clusion was available. A program was, therefore, initiated by the Air Force, through the Detroit Diesel Allison Division of General Motors Corporation, to study the effects of surface roughness and porosity on stage and overall compressor performance in a controlled environment (Reference 1). This paper will summarize the results of the experimental program and, in particular, the porosity effects. The analytical portion of this program will not be described in this report. A detailed summary of the endwall boundary layer code can be found in Reference 1.

FACILITY DESCRIPTION

The experimental program involved the use of two facilities. The first was a low-speed compressor (LSC) rig, and the second was a full-scale engine test (FSET) facility. The LSC rig was used to provide detailed endwall boundary layer measurements for various conditions of endwall roughness, endwall porosity, and tip clearance at several differ-ent operating conditions. The FSET facility was used to correlate and verify the use of the three-dimensional, turbulent, compressible endwall boundary layer flow prediction method for full-scale engine applications (Reference 1).

LOW SPEED COMPRESSOR RIG

The LSC rig layout is shown in Figure 1 and consists of a single-stage, zero inlet swirl, low-speed (184 ft/sec) compressor which was designed to reflect realistic aero-dynamic values of blockage, blade loading and loss levels for typical aft stages of modern compression systems. The compressor design parameters are summarized in Table 1.

The major modification to the rig for this program was the installation of differ-ent shroud endwall geometries. Four different configurations were employed in the test program. Three different size roughness elements and one porous endwall were tested, as shown in Table 2.

The roughness elements were uniform glass spheres whose diameters (K_s) were 0.020, 0.030, 0.080 inch. These spheres produced roughness Reynolds number values of 100 to 400 from

$$K^+ = \frac{U_\tau K_s}{\nu} \tag{1}$$

where U_τ is the friction velocity, K_s is the roughness element height, and ν is the kinematic viscosity. Therefore, roughness experiments were conducted in the fully rough zones. Porosity, on the other hand, was provided by a material configuration which permitted airflow radially into or out of the shroud and circumferentially around the shroud. Figure 2 illustrates the test section, including the shroud insert and reference planes.

INSTRUMENTATION

Multi-element total pressure rakes distributed circumferentially around the annulus at the stage inlet and exit, boundary layer rakes on the hub and tip walls located at the rotor inlet and stator exit, total temperature rakes at the stator exit, and various static pressure taps on the hub and tip walls make up the bulk of the steady state instrumentation. Vane tip static pressure distribution was mapped through the use of 45 static pressure taps on the outer wall of one stator passage.

Hot wire anemometry was employed in the exit planes of the rotor and stator, as well as three axial locations inside the stator passage (Figure 3). DISA constant temperature anemometry equipment was used to obtain the streamwise velocity and air angle.

A Dynamic Data Capacitance gage provided blade tip clearances. Individual variances in tip clearances are measured and used to determine an average running clearance. The output of the probe is nearly linear in the range of interest, namely 0.070 - 0.140 inch. Most blades were found to be within ±0.005 of the nominal clearance of 0.071 inch for Configuration I.

EXPERIMENTAL RESULTS

The effects of tip clearance, shroud roughness, and shroud porosity on stage flow versus pressure ratio can be observed in Figures 4 through 11 at three different corrected speeds. Figure 4 presents the effect of varying clearance for the smooth wall configuration. The design pressure ratio is reduced slightly at the design point, while the stall margin (SM), defined by

$$SM = \left[\frac{\left(\frac{R_c}{W_c} \right)_{sp}}{\left(\frac{R_c}{W_c} \right)_{op}} - 1 \right]_{N_c = C} \tag{2}$$

where R_c = total pressure ratio
W_c = corrected flow rate
N_c = corrected speed

is significantly affected, reduced by over 12%. This overall performance decrement is typical when tip clearances are increased in this magnitude.

The effects of roughness on performance are presented in Figures 5 through 8. Compared to the smooth wall, the stage pressure ratio remains relatively unchanged at the near design point as roughness is increased from a smooth wall to progressively rougher surfaces. (For close clearances, see Figure 5.) The stall margin defined by Eq.(1) decreases by 6-7%, transitioning from smooth to rough wall. At partial speeds, the pressure ratio decreases as surface roughness is increased.

When the clearances were doubled, the pressure ratio decreased slightly at the near design point for rough shrouds versus the smooth configuration (Figure 6). Stall margin, on the other hand, was seen to increase for rough walls, and, in fact, the largest increase occurred with the .030 inch diameter element. The reason for this apparent anomaly is not altogether clear at this time.

The relative effect of clearance when the roughness was held constant is presented in Figures 7 and 8. For the .030 inch elements, the stall margin is relatively unaffected, but the pressure ratio is less as clearance is increased. The .080 inch elements have no apparent effect on pressure ratio at the near design point, while the stall margin is reduced 3% as the clearance is increased.

A more dramatic effect is observed in Figure 9. The use of a porous shroud resulted in both a measurable decrease in pressure ratio and a significant increase in stall margin. This latter effect also holds when the clearance is doubled (Figure 10).

Flow pressure ratio was slightly affected, but not as severely as seen in Figure 9. Even more interesting, however, is the comparison of porous shrouds when the clearance is increased (Figure 11). The stall margin is approximately 26% higher at the clearance/span of 1.56, compared to the clearance/span of 2.92. Although the magnitude of the difference is somewhat unexpected, the trend is not. Examining the pressure ratio, however, the clearance/span effect is quite unexpected. The larger clearance produces measurably higher flow pressure ratio.

Another way to look at these effects is to examine the hub and tip wall static pressure distributions, particularly the static pressure ratio for the hub and tip sections at the design operating point. Figure 12 illustrates the axial hub and tip static pressure distributions for Configuration I. The other configurations produced very similar static pressure distributions and would serve no purpose if presented. The data listed in Table 3, however, does present the effect of porosity. The pressure ratio at the hub was noticeably consistent, while the porous configuration static pressure rise was higher than any of the other configurations. The boundary layer growth on the casing wall at the rotor and through the stator was found to be significantly less for the porous wall than the solid or rough walls. The reduction in boundary layer produces a larger flow area, lower wall velocities and, hence, larger static pressures.

FULL-SCALE TEST

The full-scale test was conducted in a T56 engine, modified to permit testing with different roughness levels in the last four stages of the compressor. The T56 compressor is basically a constant tip, fixed geometry, 14-stage machine with an inlet hub/tip radius of 0.49 (Figure 13).

Fixed, total temperature and pressure rakes in the compressor upstream plenum and in the compressor exit plane were used to measure overall performance. Total temperature and pressure elements were also positioned at several locations around the circumference and on the leading edge of each of the 14 stator rows. Rub pins were included in the last four stages to indicate clearance.

Performance tests were conducted with three different shroud configurations for stages 11 through 14.

1. Configuration I - Wire sprayed aluminum machine surface finished to 70 microinches. This is the as-delivered T56 baseline compressor.

2. Configuration II - The sprayed aluminum coating is grit blasted to a 500 microinch surface condition.

3. Configuration III - The sprayed aluminum coating is further grit blasted to an 800 microinch surface condition.

EXPERIMENTAL RESULTS

The compressor inlet Reynolds number was established to be the same for each of the three shroud roughness configurations, and the test points were presurge operating points. In particular, performance was examined at altitude (100% speed) and sea level takeoff (96.3% speed). The data point serial numbers are shown in Table 4.

The interstage performance maps for Configurations II and III at altitude (100% speed), from open throttle to past design, short of surge, are depicted in Figures 14 through 18. Inlet flow was measured, while pressure ratio and efficiency were calculated from the averaged total temperatures and pressures. Configuration I was not included because performance analysis indicated the results were in error.

Examination of the performance maps for the two shroud roughness levels reveals a performance loss as flow proceeds through the compressor. The effect of roughness on efficiency was negligible, although the rougher shroud did result in a lower overall value. Similar results for pressure ratio are noted.

The sea level (96.3% speed) performance maps are presented in Figures 19 through 23. Efficiency levels were seen to decrease as flow continued through the compressor in a manner similar to the 100% speed results. More significantly, however, is the decrease in performance with shroud roughness levels from 70 microinches to 500 microinches. Further increases in roughness produced only slightly deteriorated performance.

One speculation on the differences between the 100% speed (altitude) and the 96.3% speed (sea level conditions) is due to Reynolds number effects. Some surface finish effects correlation with the work of Shaffler, Reference 3, might suggest that the shroud flow could be superimposed on the efficiency versus Reynolds number plot (Figure 24). The depressed inlet conditions of the altitude test place these test points in the intermediate zone, where Reynolds number has a significant effect, while roughness has little influence. The third region, characterized by a critical Reynolds number above which efficiency is constant for increasing Reynolds numbers, is a hydrodynamically rough region where roughness does reduce efficiency.

COMPARISON OF ANALYTICAL AND EXPERIMENTAL RESULTS

The comparisons of predicted and measured boundary layer growth characteristics are presented in Figures 25 through 30. Examining Figures 25 and 26, one observes a prediction that agrees relatively well with experimental or measured data and indicates the effects of clearance on the smooth wall boundary layer development.

Figures 27 and 28 depict the agreement between predicted and measured data relating axial displacement thickness and axial shape factor with the axial location in the LSC rig for roughened endwalls. The agreement is once again fairly good; however, the prediction capability appears to favor the larger roughness element size. Part of the problem may be due to the type of roughness elements chosen and the buried configuration. This design probably precluded the elements from penetrating the laminar sublayer and producing a realistic aerodynamically rough surface. Furthermore, the LSC rig is a single-stage facility and may be of insufficient length for the flow to react to roughness.

The prediction capability of the endwall code for the porous configuration is seen to be ineffective (Figures 29 and 30). The code assumption for porosity was to presume the flow entered the endwall material and moved axially, resulting in an effective tip clearance larger than the actual mechanical clearance. The effective tip clearance then is the sum of the mechanical clearance and the clearance addition due to porosity. Had the code been modified to account for flows normal to the endwall, the predictions would probably have been more accurate.

Streamwise boundary layer development was also predicted, with results similar to the axial displacement thickness (Figures 31 through 33). Although streamwise displacement thickness was calculated for each configuration, the figures presented are included to illustrate the general code prediction capability.

The T56 smooth and rough wall boundary layer computations are presented in Figure 34. The axial displacement thickness and shape factor are shown throughout the 14 compressor stages and are seen to vary in a saw-tooth fashion. When shroud roughness was varied in the last four stages, no apparent change in displacement thickness was found for stage 11, whereas the 14th stage thickness was seen to increase by approximately .002 inch for 500 microinch roughness and .004 inch for the 800 microinch roughness.

CONCLUSIONS

The program was conducted to quantify the effects of roughness and porosity on compressor performance as the primary goal. In addition, a boundary layer prediction code was to be developed for prediction capability in future engine design tasks. The program, for the most part, was successful. A pitch averaged, three-dimensional, compressible, turbulent, integral boundary code for compressor endwalls was developed and does agree relatively well with experimental results for smooth and solid/rough endwalls. In particular, the effects of clearance on boundary layer development were well demonstrated.

Performance of both the LSC rig compressor and the T56 compressor were found to be affected by clearance and roughness. As clearance increased, efficiency and stall margin were both reduced. Roughness had a minor effect on LSC efficiency, but did measurably reduce stall margin.

Porosity was noted to produce significant effects in stall margin and lesser effects on pressure ratio. Stall margin increased by 25-30%, whereas pressure ratio was reduced slightly. The code was found, however, to be inadequate for the porous shroud configuration. Part of the code's inability could be traced to the assumption that the effect of porosity was merely an increase in clearance and neglected the potential axial recirculation within the wall boundary layer leading to radial inflow and outflow.

For the most part, a code has been developed which models boundary layer development for solid endwalls with variable roughness. Some modifications of the model will be required for porosity effects.

REFERENCES

1. Bettner, J. L. and Elrod, C. W., "The Influence of Tip Clearance, Stage-Loading, and Wall Roughness on Compressor Casing Boundary Layer Development," April 1982, ASME Paper 82-GT-153.

2. Schaffler, A., "Experimental and Analytical Investigation of the Effects of Reynolds Number and Blade Surface Roughness on Multistage Axial Flow Compressor," Arpil 1979, ASME Paper 79-GT-2.

TABLE 1

AIRFOIL CHARACTERISTICS - MEAN SECTION DESIGN VALUES

	Blade	Stator
Type of Airfoil	65 series	65 series
Chord, C-in (m)	4.489	5.089
Solidity, $\sigma = C/S$	1.435	1.516
Camber, $\emptyset$ - deg.	20.42	48.57
Aspect Ratio, AR - L/C	1.046	0.943
Leading Edge Radius/C	0.0044	0.0049
Trailing Edge Radius/C	0.0028	0.0030
Inlet Angle, β_1 - deg.	59.38	37.84
Exit Angle, $\beta_2{}^1$ - deg.	42.41	0.00
Loss Coefficient, $\bar{\omega}$	0.043	0.056
Diffusion Factor, D_f	0.449	0.410

TABLE 2

Test Configuration	Blade Tip Clearance % Span	Type of Shroud Wall Surface	Surface Condition Roughness - Element Size (in.)/Porosity
I	1.48	Solid/Smooth	-
II	1.56	Porous/Smooth	30% Oper
III	1.44	Solid/Rough	0.080
IV	1.30	Solid/Rough	0.030
V	1.13	Solid/Rough	0.020
VI	2.96	Solid/Smooth	-
VII	2.92	Porous/Smooth	30% Open
VIII	2.81	Solid/Rough	0.080
IX	2.77	Solid/Rough	0.030

TABLE 3

ROTOR HUB AND TIP SECTION STATIC PRESSURE RATIO NEAR DESIGN OPERATING POINT

	Configuration								
	I	II	III	IV	V	VI	VII	VIII	IX
Wall Condition	Solid/ Smooth	Porous/ Smooth	Solid/ Rough 1	Solid/ Rough 2	Solid/ Rough 3	Solid/ Smooth	Porous/ Smooth	Solid/ Rough 1	Solid/ Rough 2
Tip Clearance	1.48	1.56	1.44	1.30	1.13	2.96	2.92	2.81	2.77
$R_{c_{s_h}}$	1.00604	1.00598	1.00609	1.00614	1.00599	1.00594	1.00613	1.00602	1.00678
$R_{c_{t_h}}$	1.0089	1.0091	1.0089	1.0089	1.0089	1.0087	1.0095	1.0086	1.0085

TABLE 4

T56-A-100 COMPARATIVE DATA POINTS

T56-A-100 Configuration	Shroud Wall Roughness-- Microinches	Comparative Data Points (S/N) 96.3% N/	Comparative Data Points (S/N) 100% N/
I	70	43	
II	500	199	190
III	800	200	211
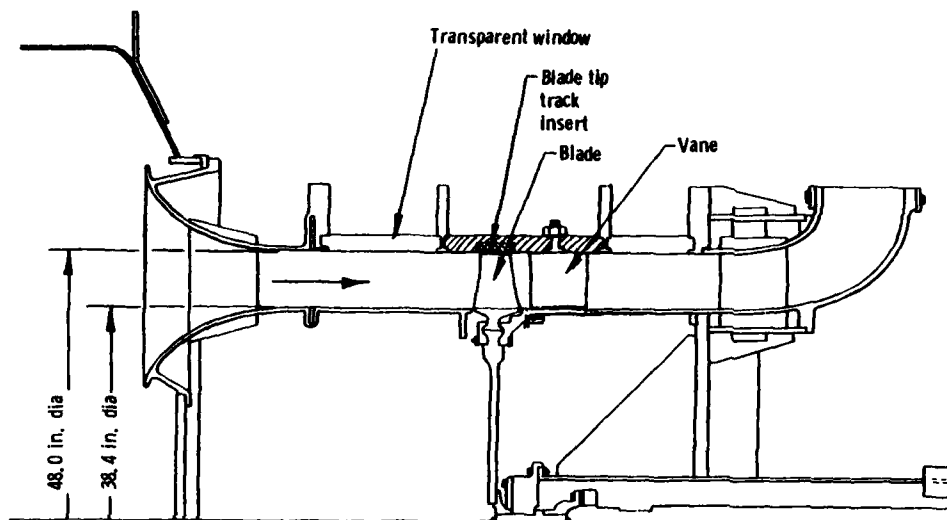
Figure 1. Low Speed Compressor Facility
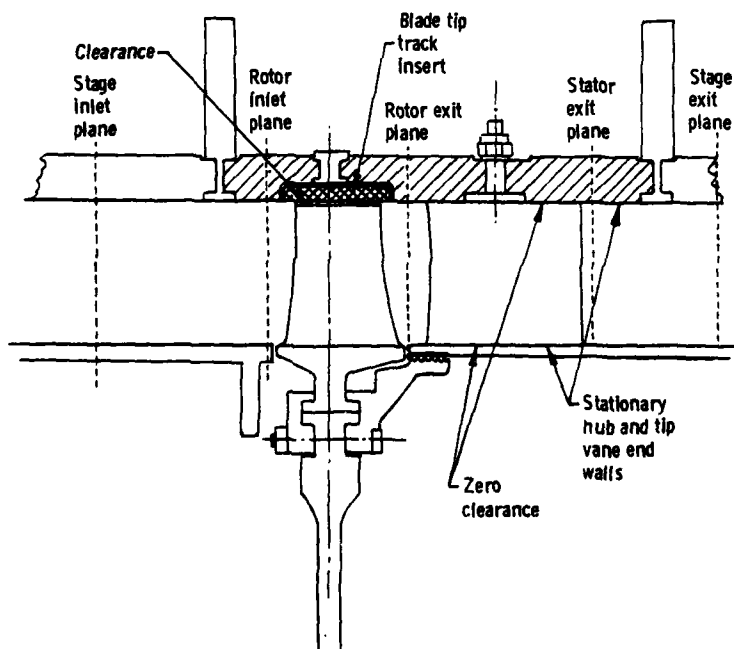
Figure 2. Blade Track Shroud Wall Insert Detail
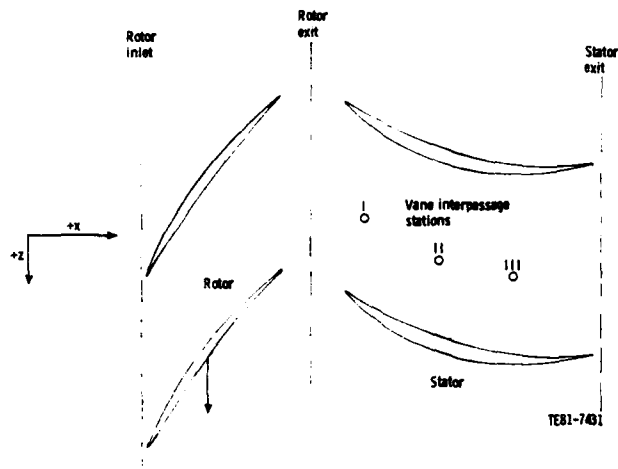
Figure 3. Low Speed Compressor Tip Section
Measurement Stations
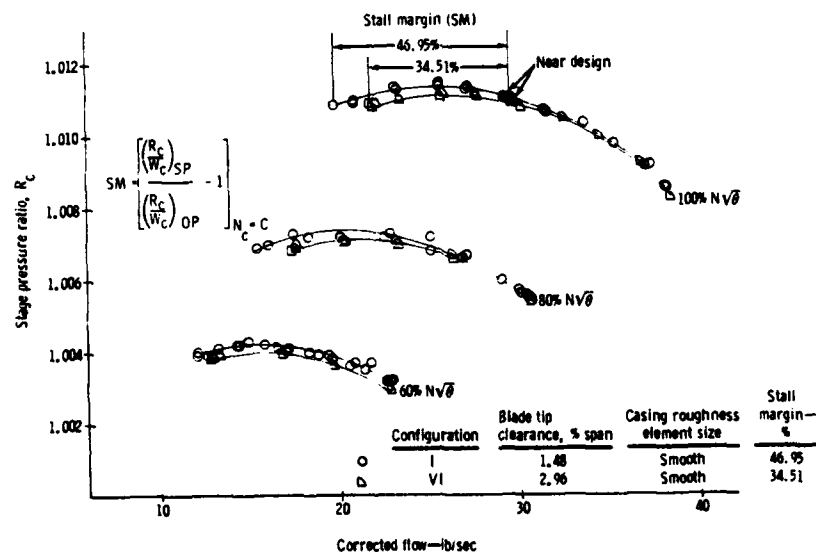
Figure 4. Effect of Tip Clearance on LSC Stage Performance
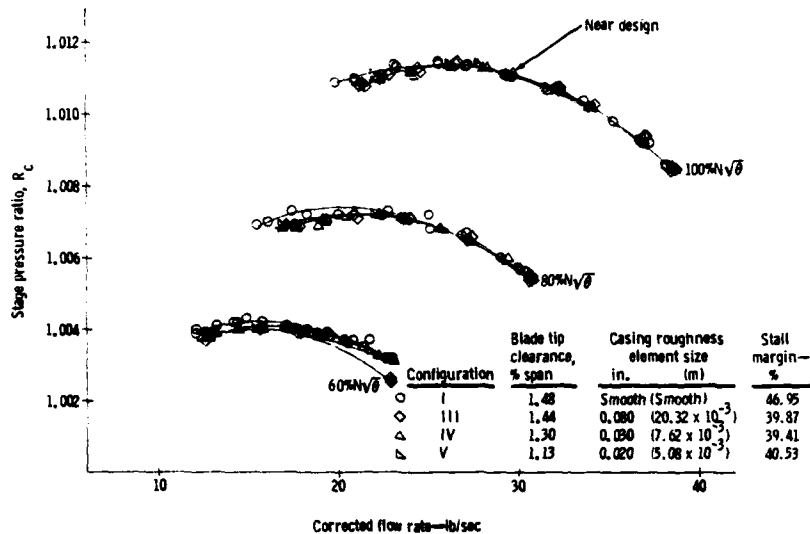
Figure 5. Effect of Shroud Roughness on Small Clearance LSC Stage
Performance
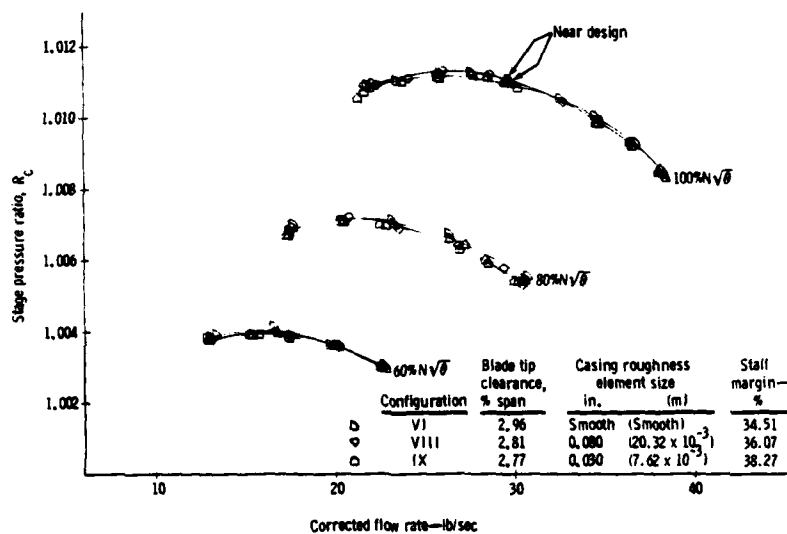
Figure 6. Effect of Shroud Roughness on Large Clearance LSC Stage
Performance
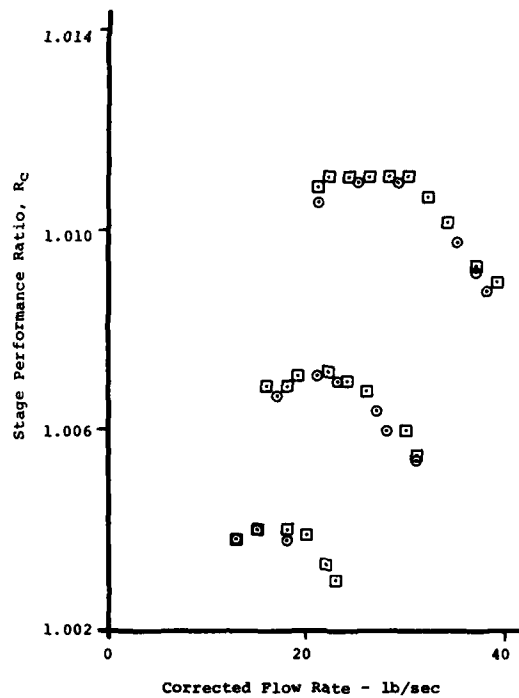
Figure 7. Effect of Tip Clearance on LSC Stage
Performance for .030 inch Element Roughness
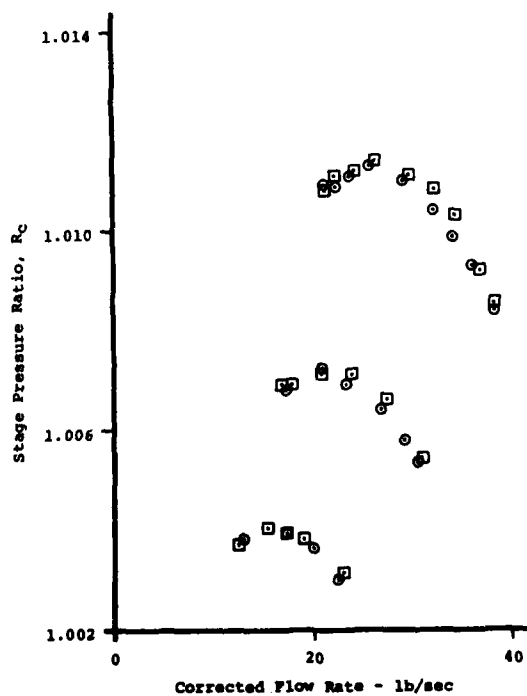
Figure 8. Effect of Tip Clearance on LSC Stage Performance for
the .080 inch Roughness Element
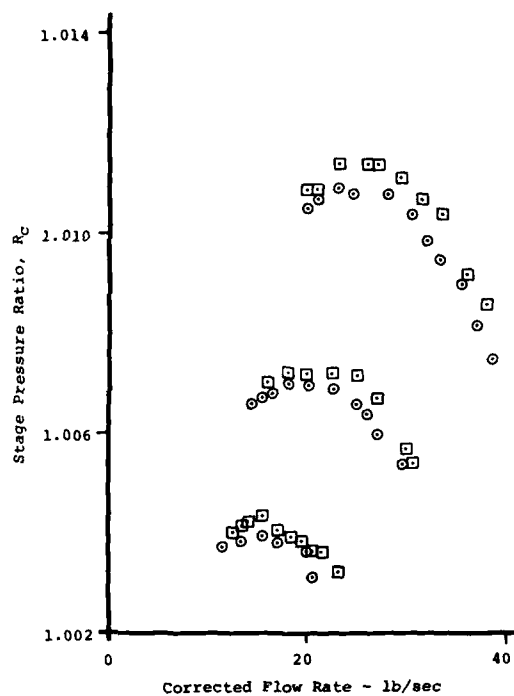
Figure 9. Effect of Porosity on LSC Stage Performance for Small
Clearance
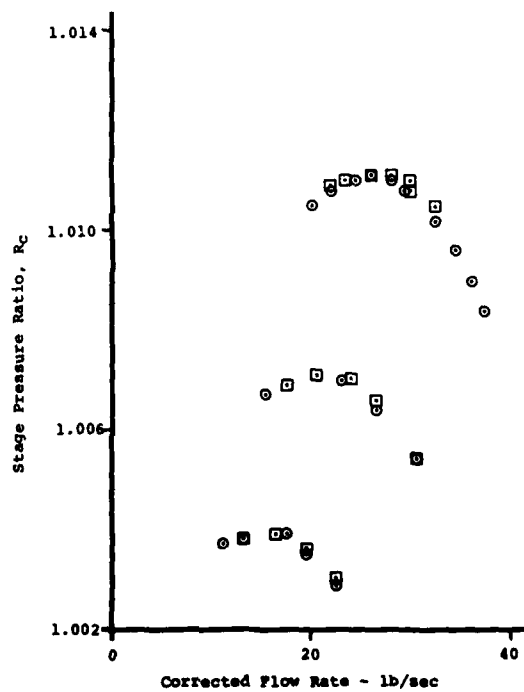
Figure 10. Effect of Porosity on LSC Stage Performance for
Large Clearance
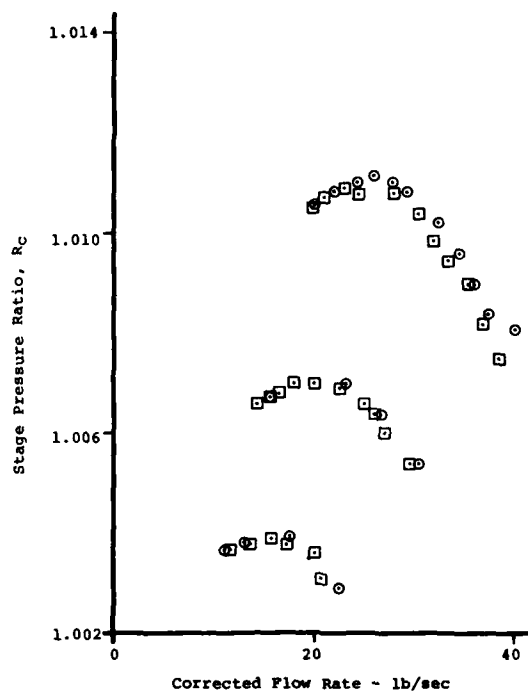
Figure 11. Effect of Clearance on Stage Performance for Porous
            Configuration
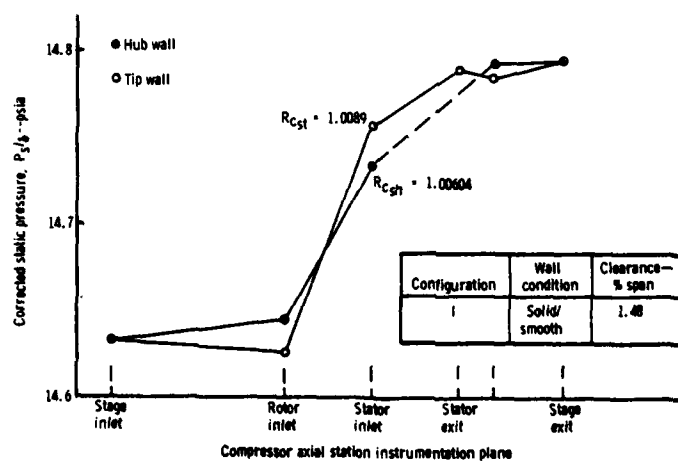
Figure 12. Axial Hub and Tip Wall Static Pressure Distribution
            Through Configuration I at Design Operating Point
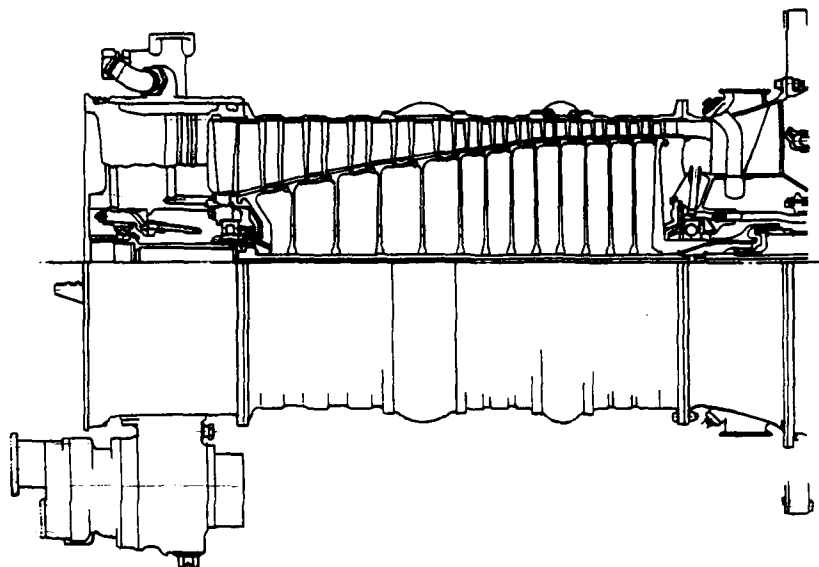
Figure 13.   T56 EMDP Compressor Section
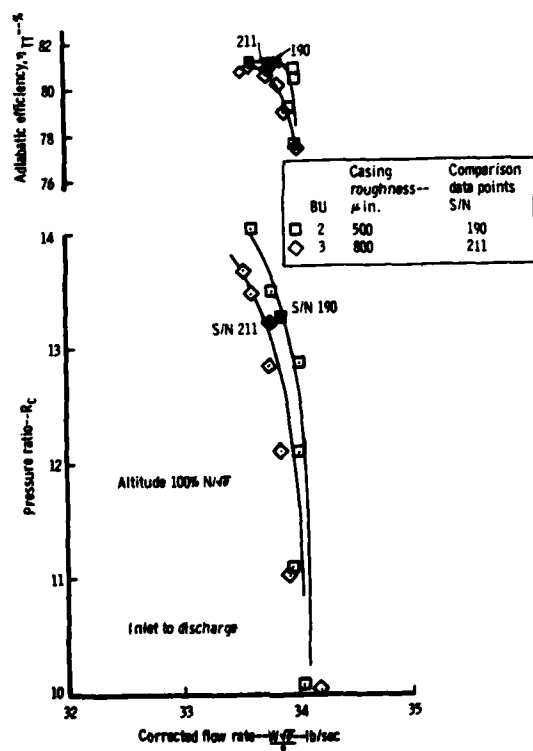
Figure 14. T56-A-100 Compressor Maps from Inlet to Discharge for Two Shroud Roughness Values at 100% Design Speed
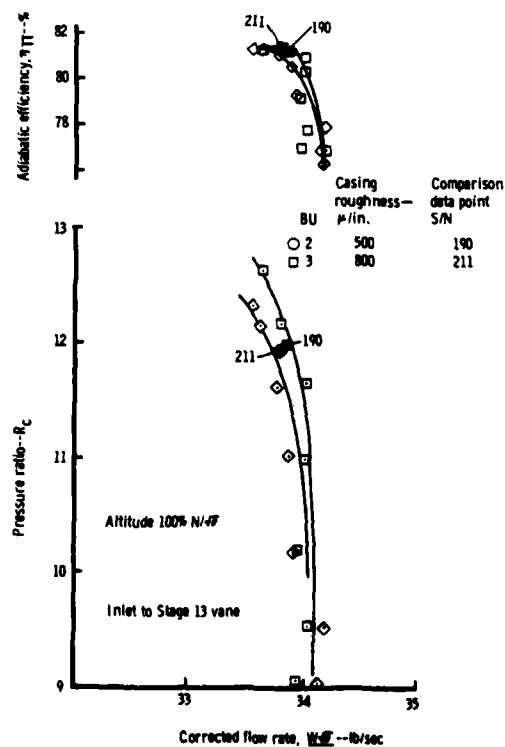
Figure 15. T56-A-100 Compressor Maps from Inlet to 13th-Stage Vane for Two Shroud Roughness Values at 100% Design Speed
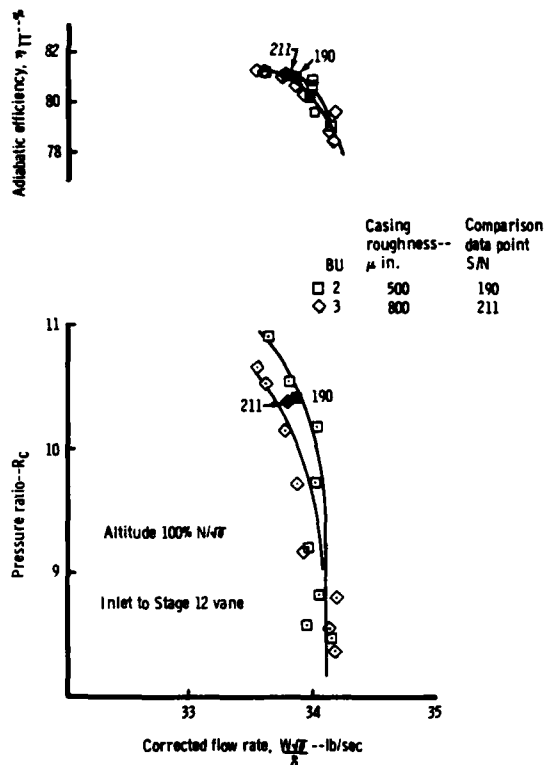
Figure 16. T56-A-100 Compressor Maps from Inlet to 12th-Stage Vane for Two Shroud Roughness Values at 100% Design Speed
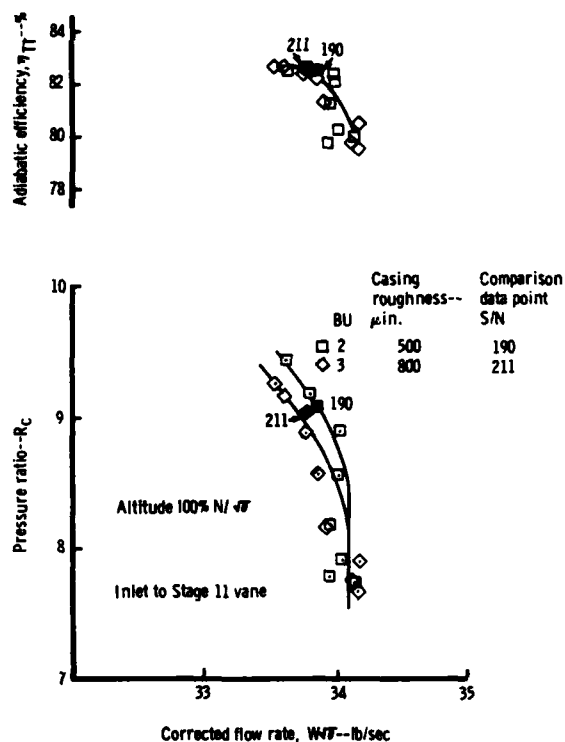
Figure 17. T56-A-100 Compressor Maps from Inlet to 11th-Stage Vane for Two Shroud Roughness Values at 100% Design Speed
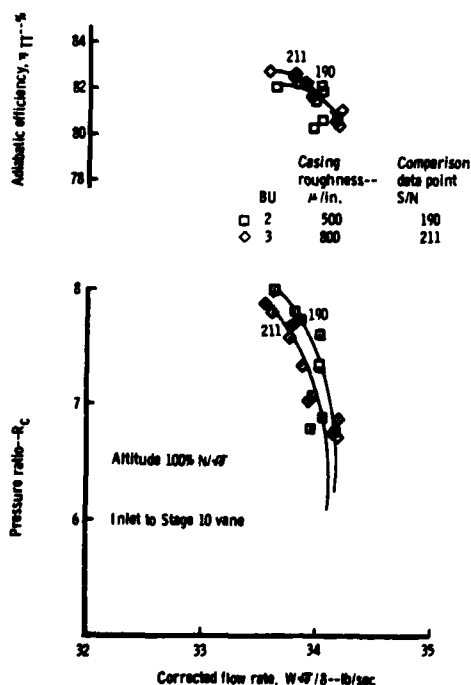
Figure 18. T56-A-100 Compressor Maps from Inlet to 10th-Stage Vane for Two Shroud Roughness Values at 100% Design Speed
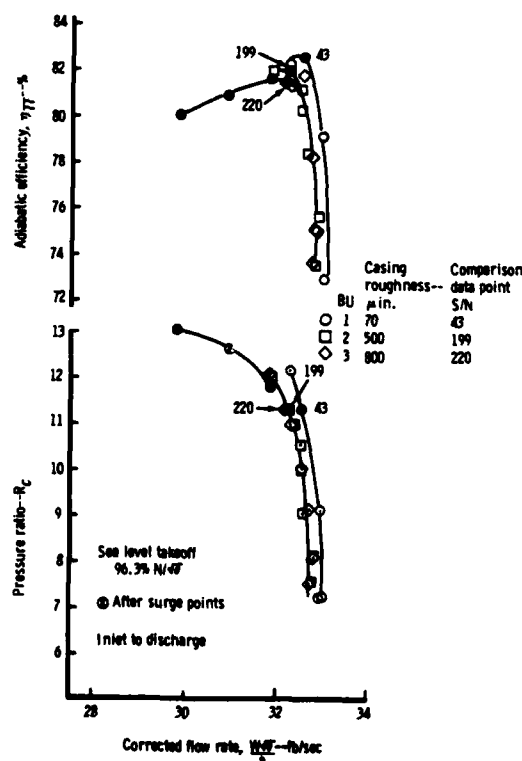
Figure 19. T56-A-100 Compressor Maps from Inlet to Discharge for Three Shroud Roughness Values at 96.3% Design Speed
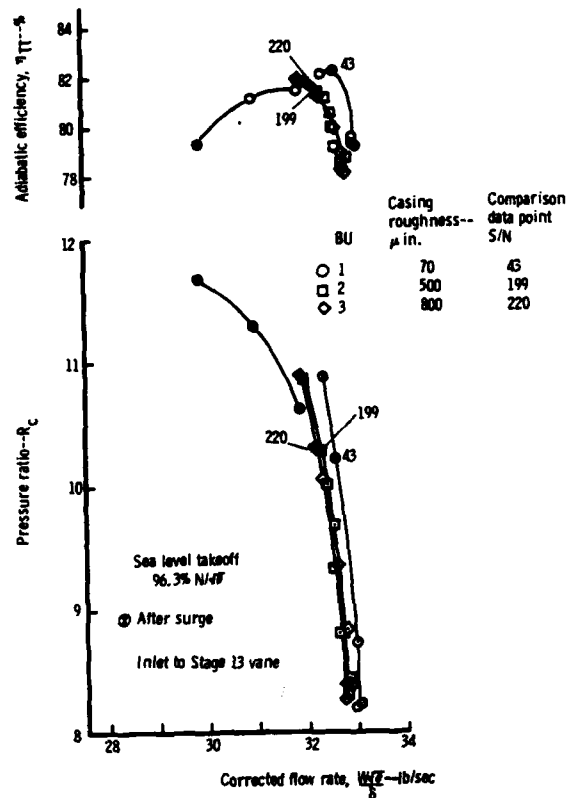
Figure 20. T56-A-100 Compressor Maps from Inlet to 13th-Stage Vane for Three Shroud Roughness Values at 96.3% Design Speed
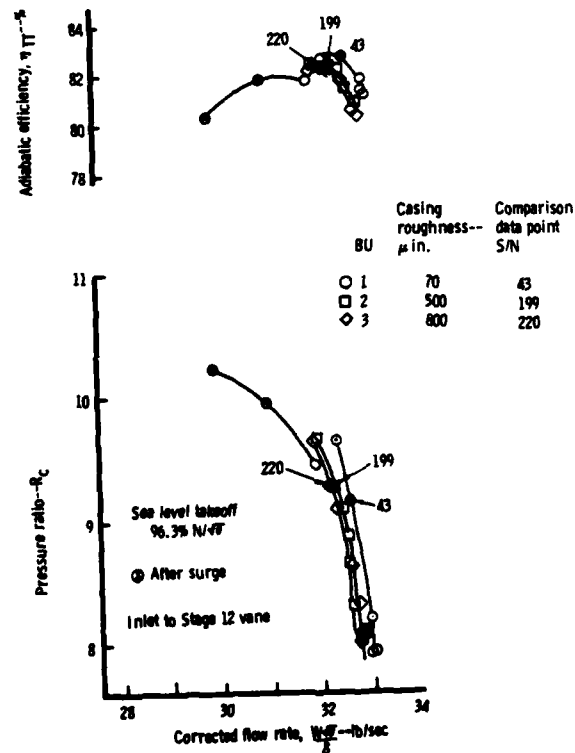
Figure 21. T56-A-100 Compressor Maps from Inlet to 12th-Stage Vane for Three Shroud Roughness Values at 96.3% Design Speed
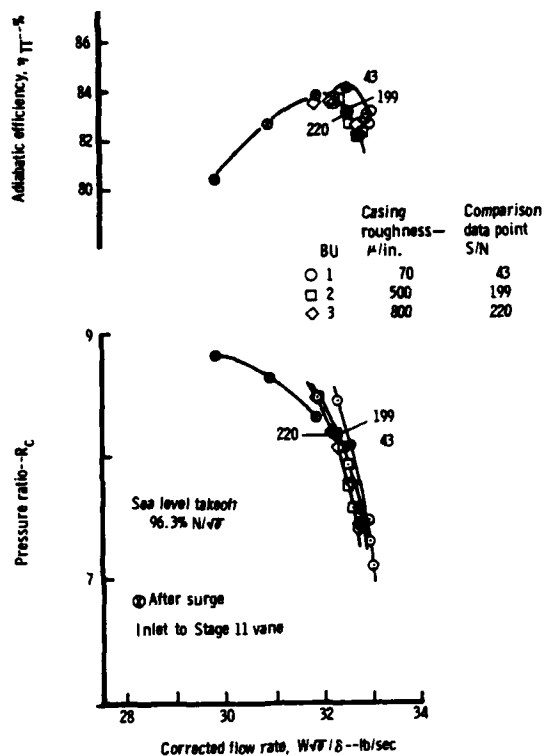
Figure 22.   T56-A-100 Compressor Maps from Inlet to 11th-Stage
Vane for Three Shroud Roughness Values at 96.3%
Design Speed
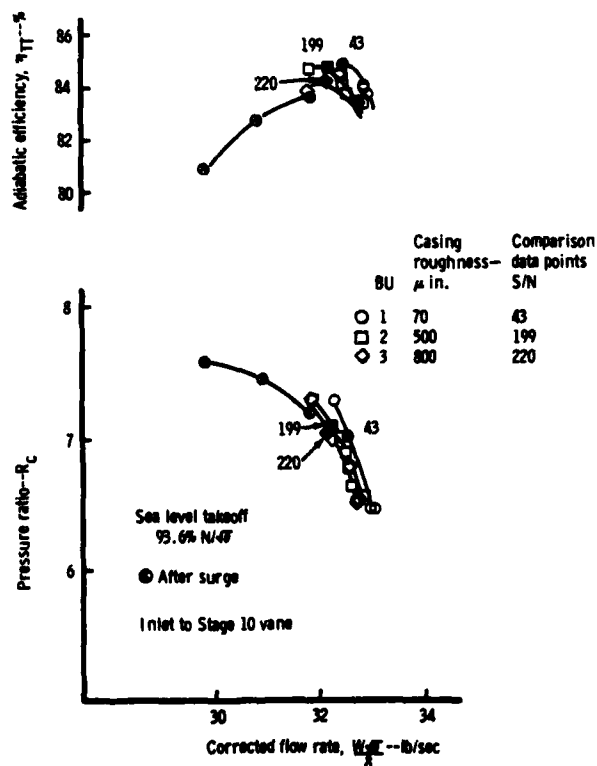
Figure 23.   T56-A-100 Compressor Maps from Inlet to 10th-Stage
Vane for Three Shroud Roughness Values at 96.3%
Design Speed
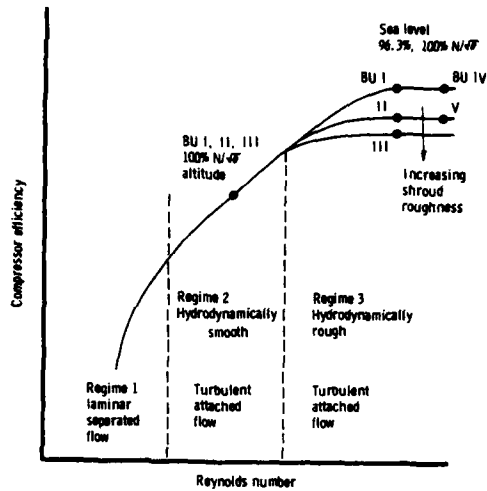
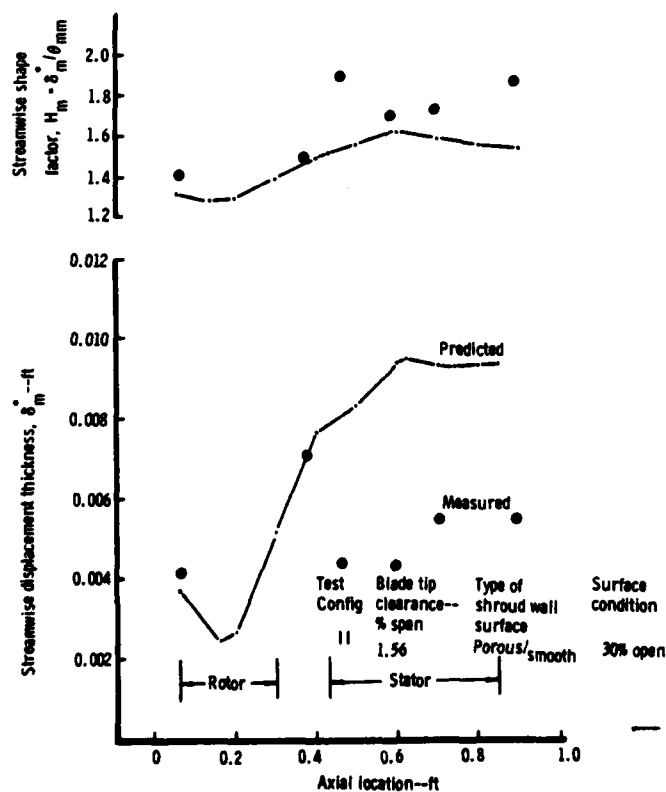Figure 24. Effect of Reynolds Number on Compressor Efficiency
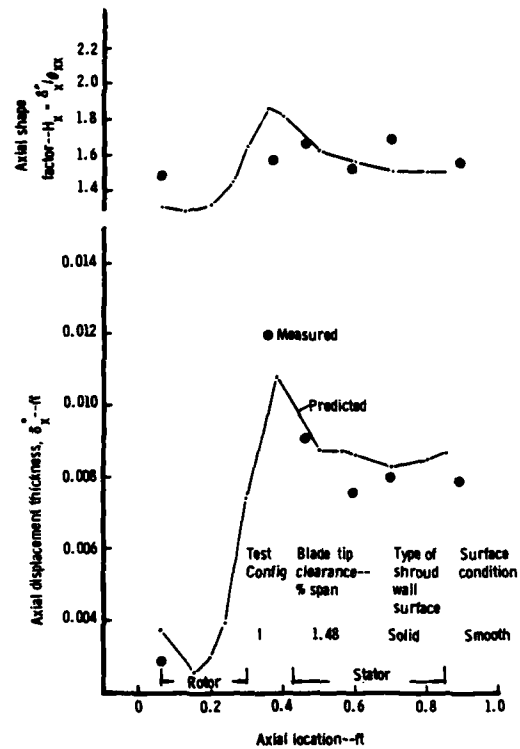
Figure 25. Comparison of Measured and Predicted Axial Displacement Thickness and Shape Factor for LSC Configuration I
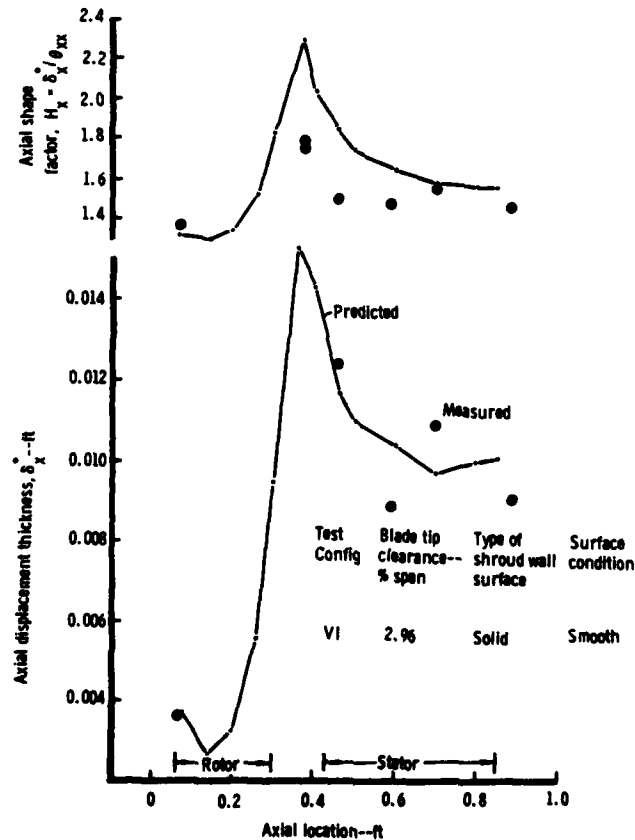
Figure 26. Comparison of Measured and Predicted Axial Displacement Thickness and Shape Factor for LSC Configuration VI
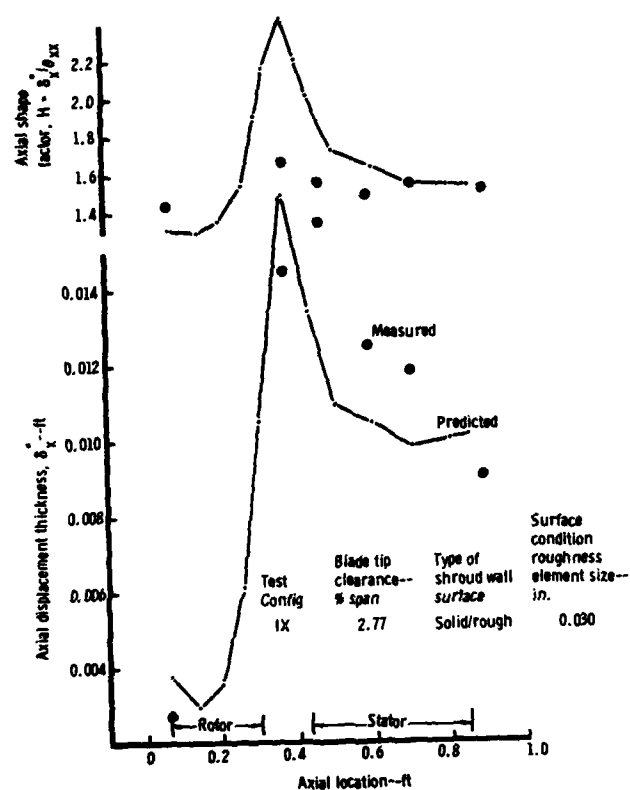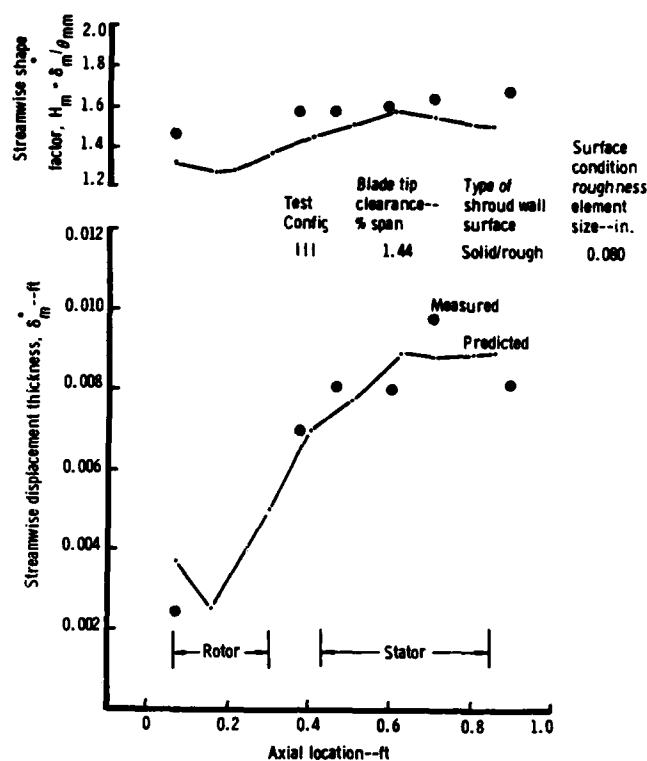
Figure 27. Comparison of Measured and Predicted Axial Displacement Thickness and Shape Factor for LSC Configuration IX
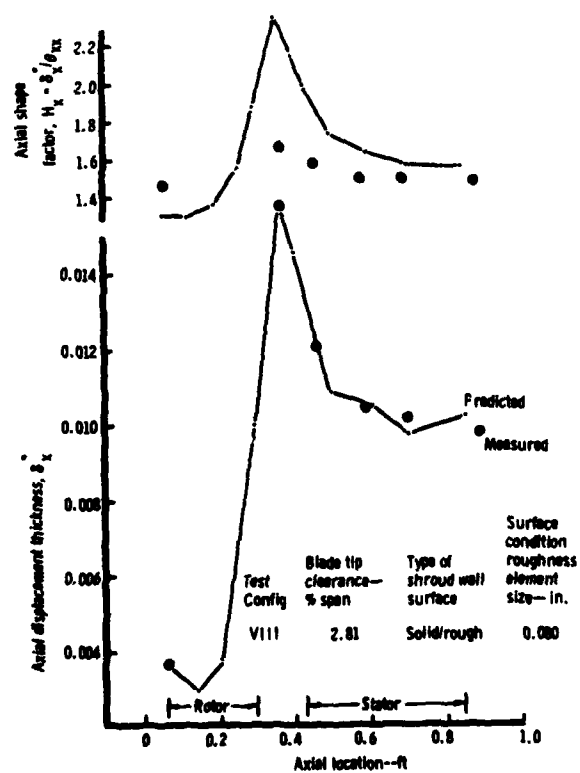
Figure 28. Comparison of Measured and Predicted Axial Displacement Thickness and Shape Factor for LSC Configuration VIII
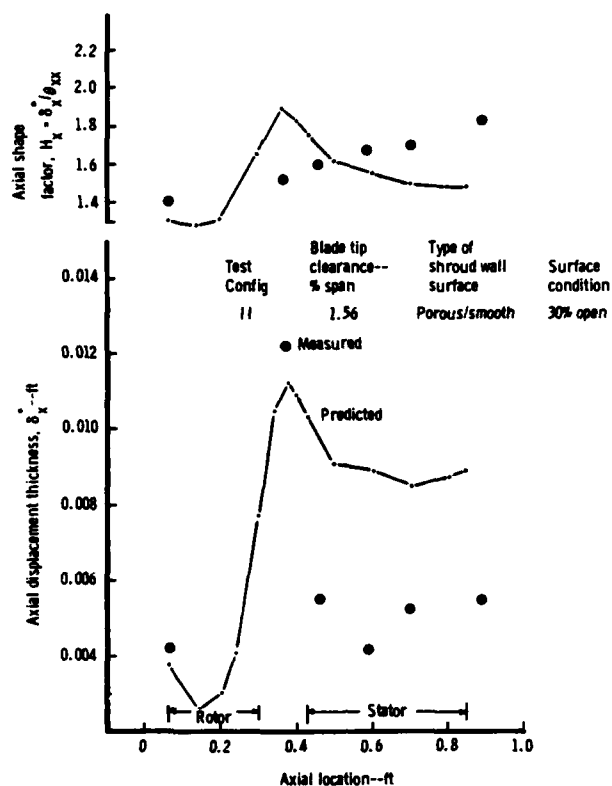
Figure 29. Comparison of Measured and Predicted Axial Displacement
Thickness and Shape Factor for LSC Configuration II
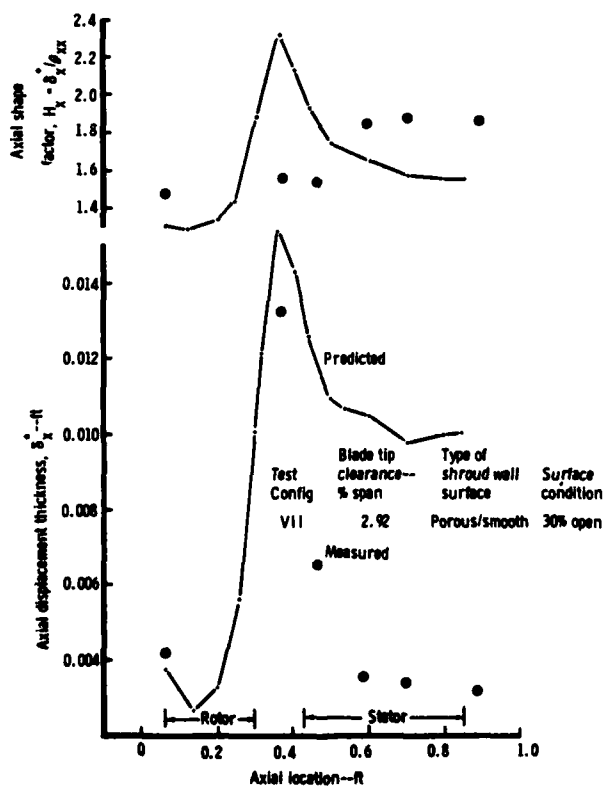
Figure 30. Comparison of Measured and Predicted Axial
Displacement Thickness and Shape Factor for
LSC Configuration VII
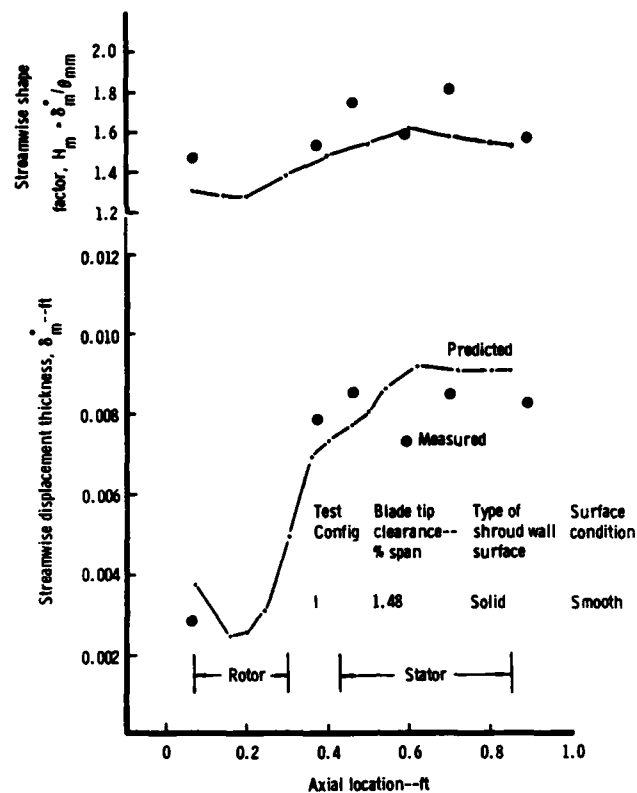
Figure 31. Comparison of Measured and Predicted Streamwise
Displacement Thickness and Shape Factor for LSC
Configuration I

Figure 32. Comparison of Measured and Predicted Streamwise
Displacement Thickness and Shape Factor for LSC
Configuration II

Figure 33. Comparison of Measured and Predicted Streamwise
Displacement Thickness and Shape Factor for
Configuration III
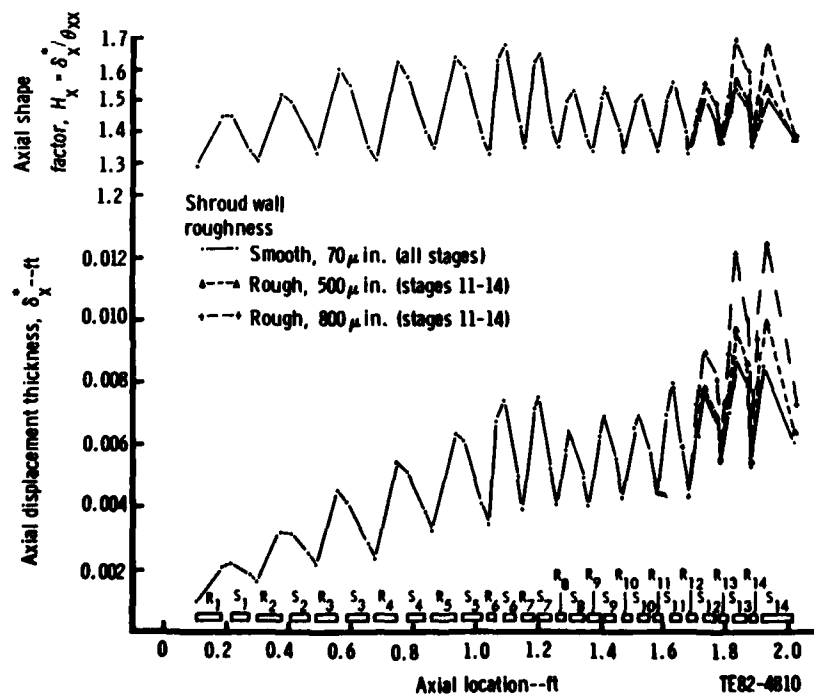
Figure 34. Computed Axial Displacement Thickness (blockage) and Shape Factor for
Smooth and Rough Shroud Wall T56-A-100 Compressors

DISCUSSION

D.K.Hennecke, Ge

You state in your paper that the porous surface was smooth. Could you please tell us what kind of porous material you used, what its surface roughness was, and how thick the layer was.

Author's Reply

The material was alternating layers of metal sheet with multi-holes to provide inflow and axial flow. The surface was smooth and somewhat untypical of compressor shroud porous material.

The thickness was approximately 30 mils and the roughness was unmeasured but probably on the order of about 70 microinch.

Ph.Ramette, Fr

For Figure 29, giving the comparison between experimental results and calculation, you said that the tip clearance was taken as the sum of the mechanical clearance and the clearance addition due to porosity. The code has been modified to account for axial but not normal flow. I think that the difference of velocities has also to be taken into account between the flow in the tip clearance and the flow going through the porous material. Could you comment about this?

Author's Reply

Your observation is correct and that type of correction is under way. The fact of the matter is that both inflow and outflow through the porous media will have their effects on the boundary layer. This is evidenced by the significantly thinner layer seen with the porous media compared to those seen with the rough and smooth walls. The assumption of an additive clearance effect for the porous shroud was an initial assumption for simplification and is obviously erroneous.

REPORT DOCUMENTATION PAGE

1.Recipient's Reference	2.Originator's Reference	3.Further Reference	4.Security Classification of Document
	AGARD-CP-351	ISBN 92-835-0340-6	UNCLASSIFIED

5.Originator	Advisory Group for Aerospace Research and Development North Atlantic Treaty Organization 7 rue Ancelle, 92200 Neuilly sur Seine, France

6.Title	VISCOUS EFFECTS IN TURBOMACHINES

7.Presented at	the Propulsion and Energetics Panel 61st (A) Specialists' Meeting, held in Copenhagen, Denmark, 1–3 June 1983.

8.Author(s)/Editor(s)	9.Date
Various	September 1983

10.Author's/Editor's Address	11.Pages
Various	390

12.Distribution Statement	This document is distributed in accordance with AGARD policies and regulations, which are outlined on the Outside Back Covers of all AGARD publications.

13.Keywords/Descriptors

Viscous flow	Secondary flow
Viscous-Inviscid interaction	Compressor flow
Calculation methods for viscous flow	Turbine flow
Boundary layer	Tip clearance

14.Abstract

The Conference Proceedings contain 23 papers presented at the Propulsion and Energetics Panel 61st A Specialists' Meeting on Viscous Effects in Turbomachines, which was held in Copenhagen, Denmark, on 1–3 June 1983.

The Technical Evaluation Report is included at the beginning of the Proceedings. Questions and answers of the discussions follow each paper. The Specialists' Meeting was arranged in 4 sessions: Viscous-Inviscid Interactions (9); Viscous Flow Computations (4); End-Wall Boundary Layers (6); and Experimental Measurements from Multistage Turbomachines (4).

The purpose of the Specialists' Meeting was to assemble the leading experts and specialists in this field from industry, research institutes and universities in order to establish the latest state-of-the-art.

AGARD Conference Proceedings No.351 Advisory Group for Aerospace Research and Development, NATO VISCOUS EFFECTS IN TURBOMACHINES Published September 1983 390 pages The Conference Proceedings contain 23 papers presented at the Propulsion and Energetics Panel 61st A Specialists' Meeting on Viscous Effects in Turbomachines, which was held in Copenhagen, Denmark, on 1-3 June 1983. The Technical Evaluation Report is included at the beginning of the Proceedings. Questions and answers of the discussions follow each paper. The Specialists' P.T.O	AGARD-CP-351 Viscous flow Viscous-Inviscid interaction Calculation methods for viscous flow Boundary layer Secondary flow Compressor flow Turbine flow Tip clearance
AGARD Conference Proceedings No.351 Advisory Group for Aerospace Research and Development, NATO VISCOUS EFFECTS IN TURBOMACHINES Published September 1983 390 pages The Conference Proceedings contain 23 papers presented at the Propulsion and Energetics Panel 61st A Specialists' Meeting on Viscous Effects in Turbomachines, which was held in Copenhagen, Denmark, on 1-3 June 1983. The Technical Evaluation Report is included at the beginning of the Proceedings. Questions and answers of the discussions follow each paper. The Specialists' P.T.O	AGARD-CP-351 Viscous flow Viscous-Inviscid interaction Calculation methods for viscous flow Boundary layer Secondary flow Compressor flow Turbine flow Tip clearance

AGARD Conference Proceedings No.351 Advisory Group for Aerospace Research and Development, NATO VISCOUS EFFECTS IN TURBOMACHINES Published September 1983 390 pages The Conference Proceedings contain 23 papers presented at the Propulsion and Energetics Panel 61st A Specialists' Meeting on Viscous Effects in Turbomachines, which was held in Copenhagen, Denmark, on 1-3 June 1983. The Technical Evaluation Report is included at the beginning of the Proceedings. Questions and answers of the discussions follow each paper. The Specialists' P.T.O	AGARD-CP-351 Viscous flow Viscous-Inviscid interaction Calculation methods for viscous flow Boundary layer Secondary flow Compressor flow Turbine flow Tip clearance
AGARD Conference Proceedings No.351 Advisory Group for Aerospace Research and Development, NATO VISCOUS EFFECTS IN TURBOMACHINES Published September 1983 390 pages The Conference Proceedings contain 23 papers presented at the Propulsion and Energetics Panel 61st A Specialists' Meeting on Viscous Effects in Turbomachines, which was held in Copenhagen, Denmark, on 1-3 June 1983. The Technical Evaluation Report is included at the beginning of the Proceedings. Questions and answers of the discussions follow each paper. The Specialists' P.T.O	AGARD-CP-351 Viscous flow Viscous-Inviscid itneraction Calculation methods for viscous flow Boundary layer Secondary flow Compressor flow Turbine flow Tip clearance

Meeting was arranged in 4 sessions: Viscous-Inviscid Interactions (9); Viscous Flow Computations (4); End-Wall Boundary Layers (6); and Experimental Measurements from Multistage Turbomachines (4).

The purpose of the Specialists' Meeting was to assemble the leading experts and specialists in this field from industry, research institutes and universities in order to establish the latest state-of-the-art.

DATE
ILMED

8